



University of Tehran

ISSN: 2322-2093

Volume 58, Number 2, December 2025

Civil Engineering Infrastructures Journal

CEIJ

Available online at
www.ceijournal.com

Civil Engineering Infrastructures Journal (CEIJ)

Semiannual Publication

Editor – in - Charge

Ghassemieh, M., Professor
msoltani@ut.ac.ir

Editor – in – Chief

Tabesh, M., Professor
mtabesh@ut.ac.ir

Executive Manager and Contact Person

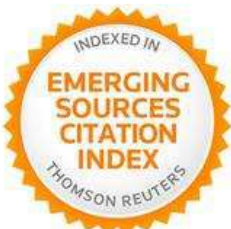
Akhtari, N.
cej@ut.ac.ir

Published by:



University of Tehran
College of Engineering

Indexed by:



Web of Science (ESCI)



Scopus



Civil Engineering Infrastructures
Journal (CEIJ)
College of Engineering
University of Tehran
P.O. Box: 11155-4563
Tehran, Iran.
Tel/ Fax: +98-21-88956097
Email: ceij@ut.ac.ir
Web Site: www.ceij.ir

Editorial Board

Askari, F., Associate Professor, International Institute of Earthquake Engineering and Seismology, Iran.

Aslani, F., Associate Professor, University of Western Australia, Australia.

Babazadeh, A., Associate Professor, University of Tehran, Iran.

Behnamfar, F., Associate Professor, Isfahan University of Technology, Iran.

EskandariGhadi, M., Professor, University of Tehran, Iran.

Fatahi, B., Associate Professor, University of Technology Sydney, Australia.

Gupta, R., Professor, Visvesvaraya National Institute of Technology, India.

Heravi, Gh.R., Professor, University of Tehran, Iran.

Kerachian, R., Professor, University of Tehran, Iran.

Mahmoudzadeh Kani, I., Professor, University of Tehran, Iran.

Mazza, F., Professor, University of Calabria, Italy.

Moghadas Nejad, F., Professor, Amirkabir University of Technology, Iran.

Moridpour, S., Associate Professor, RMIT University, Australia.

Motamed, R., Associate Professor, University of Nevada, USA.

Salehi Neyshabouri, A.A., Professor, Tarbiat Modarres University, Iran.

Nourani, V., Professor, University of Tabriz, Iran.

Ouhadi, V.R., Professor, Bu-Ali Sina University, Iran.

Shafei, B., Associate Professor, Iowa State University, USA.

Naderpajouh, N., Associate Professor, University of Sydney, Australia.

Shekarchizadeh, M., Professor, University of Tehran, Iran.

Shafieezadeh, A., Associate Professor, Ohio State University, USA.

Tanyimboh, T., Associate Professor, University of the Witwatersrand, South Africa.

Touran, A., Professor, Northeastern University, USA.

Towhata, I., Professor, University of Tokyo, Japan.

Zahraei, S.M., Professor, University of Tehran, Iran.

Advisory Board

Ahmadi, M.T., Professor, Tarbiat Modarres University, Iran.

Behnia, K., Associate Professor, University of Tehran, Iran.

Benekohal, R.F., Professor, University of Illinois, USA.

Gatmiri, B., Professor, University of Tehran, Iran.

Mobasher, B., Professor, Arizona State University, USA.

Motavali, M., Professor, Structural Engineering Research Laboratory, EMPA, Switzerland.

Rahimian, M., Professor, University of Tehran, Iran.

Saiedi, M., Professor, University of Nevada, Reno, USA.

Sorooshian, S., Professor, University of California, USA.

CONTENTS

Volume 58, Number 2, December 2025

Review Paper

The Utilization of Plastic Waste for Stabilizing Expansive Soil Subgrade: 203

A Critical Review

Kumar, M., Pratap, B., Azhar, M.D., Mondal, S. and Singh, R.P.

Research Papers

A Comparative Study on the Effect of Fineness of Low-Grade Calcined..... 231

Clays on Engineering Properties of Binary and Ternary Blended Concretes

Moodi, F., Fazelhashemi, A., GivKashi, M.R., Banar, R., Ramezaniapour, A.M. and Ramezaniapour, A.A.

Effects of Macro-Synthetic Fibres Incorporation on the Dimensional..... 253

Change Properties of Bacillus Subtilis Bacterial Concrete

Ghoniem, A.G., Aboul Nour, L. and Hassan, H.

The Free Vibration Characteristics of a Concrete Arch Gravity 265

Dam Using Finite Element Technique

Sougata, M. and Nallasivam, K.

Enhancing Cable-Stayed Bridge Structural Health Assessment 287

Using Phase Space Trajectory and Load Pattern Variability

Mohseni Moghaddam, M., Dehghani, E. and Bitaraf, M.

Impact of High-Strength Reinforcement on Ductility of 309

Normal-Strength Reinforced Concrete Column

Ulfa, A.A. and Piscesa, B.

Date Palm Fibers to Improve Tensile Strength in Self-Compacting 333

Concrete with Silica Fume

Mirzaie Aliabadi, M., Derakhshan Nezhad, A.H., Shahidzadeh, M.S. and Dadpour, A.

Lightweight Fiberglass Concrete Beams of Varying..... 351

Steel Reinforcement and Shear-Span Depth Ratios

Ghoniem, A., Gamal, M. and Aboul Nour, L.

Topology Optimization of Wave Barriers for Mitigating Dynamic..... 369

Compaction-Induced Vibrations Using a Coupled CMA-ES/Finite-Element Method

Abedini, F., Rafiee-Dehkharghani, R. and Laknejadi, K.

Predicting the Efficiency of Using Empty Fruit Bunch of Oil-Palm 391

Fibre in Reinforcing Structural Concrete: A Statistical Analysis

Kilani, A.J., Olubambi, A., Ikotun, B. D., Onjefu, L. and Abdulwahab, R.

Technical Notes

Permeable Triangular Vanes Effect on Turbulent Flow Field..... 419

Ahmadi Adli, S., Abbaspour, A., Hosseinzadeh Dalir, A. and Parsa, J.

Optimizing the Performance of L-Shaped Concrete-Filled Steel 429

Tube Columns Under Eccentric Loading

Labibzadeh, M., Kordi, M., Hosseinlou, F., Rezaeian, A. and Khayat, M.



The Utilization of Plastic Waste for Stabilizing Expansive Soil Subgrade: A Critical Review

Kumar, M.¹, Pratap, B.², Azhar, M.D.¹, Mondal, S.^{3*}, and Singh, R.P.⁴

¹ Ph.D. Candidate, Department of Civil Engineering, National Institute of Technology Jamshedpur, India.

² Assistant Professor, Department of Civil Engineering, Graphic Era (Deemed to be University), Dehradun, India.

³ Assistant Professor, Department of Civil Engineering, National Institute of Technology Jamshedpur, India.

⁴ Associate Professor, Department of Civil Engineering, National Institute of Technology Jamshedpur, India.

© University of Tehran 2024

Received: 9 Dec. 2023;

Revised: 7 Mar. 2024;

Accepted: 7 Apr. 2024

ABSTRACT: In developing countries like India, plastic waste has become a menace to the environment and civilization. Moreover, it challenges the sustainable waste management practice since plastic waste is non-biodegradable. The reuse and recycling of plastic are the best way to handle it and can be used as a good construction material. Researchers have explored potential applications of plastic waste in civil engineering construction. In this context, it is worth mentioning that efforts have been made to utilize plastic waste as reinforcement material in ground improvements. However, the suitability of plastic strips as a reinforcing material for various types of soil remains a concern. Different studies have been conducted to explore the potential of plastic waste as a reinforcing material for ground improvement. This paper presents a review of the scope and applicability of plastic waste for reinforcing expansive soils and its other impacts.

Keywords: Plastic Waste, Soil Reinforcement, Ground Improvement, Expansive Soil.

1. Introduction

From paper clips to space crafts, from cell phones to computers, and various other items in our daily use, plastic products have found their use in a variety of applications.

In the last 60 years after its invention, plastic has taken center stage in our daily life due to its favorable attributes such as low weight, durability, reliability, easy adaptability, highly convenient to use, and easy availability (Fadhil et al., 2021). Due to these qualities of plastic, its demand

increased substantially from 0.5 million tons in 1950 to above 260 million tons by 2008, and similar growth is expected in the future (Fadhil et al., 2021). Plastic is non-biodegradable, and its increased use leads to some adverse effects on the environment by littering roadsides, clogging sewer lines, and filling land. The CPCB India has undertaken a study on plastic trash production in 60 different Indian cities, predicting that it will be 15342.5 tons per day, or about 5.6 million tons per year. In addition, almost 6000 tons of trash remain

* Corresponding author E-mail: smondal.ce@nitjsr.ac.in

uncollected and littered (Peddaiah et al., 2018). During the survey, it was also found that one of the most important reasons for the Mumbai city flood in 2005 was the choking of sewer drains by plastic waste materials thrown indiscriminately by the people (Peddaiah et al., 2018). One of the efficient methods to limit plastic waste is to recycle or reuse it by blending it with various products under high pressure and temperature. During an investigation, it was found that reinforcing the soil with plastic waste strengthens the soil; hence, it can be used as a reinforcing material. Improving the strength of soil by plastic waste reinforcement is a meaningful and efficient way, and is cost-effective.

Some examples of utilizing such materials for civil engineering applications include soil stabilization of the base, sub-base courses of pavements, strengthening of earthen embankments, and reducing soil settlements in foundations. (Peddaiah et al., 2018). The growth of cities and industrial areas implies that the land available for buildings of sufficient capacity and occupancy is exhausted to a certain extent.

Geotechnical engineers have to construct structures like foundations, embankments, and pavements at a given site with given soil conditions available to them. In such situations, different ground improvement techniques are available to be utilized for the improvement of poor soil conditions.

Soil modification through the addition of admixtures and the use of soil reinforcement techniques are popular ground improvement techniques among engineers. Fly ash, pond ash, Rice Husk Ash (RHA), Ground Granulated Blast Furnace Slag (GGBS), stone dust, terrazyme, etc., can be utilized as an admixture to improve the soil properties (Aswar et al., 2023; Gautam et al., 2022; Priyadarshree et al., 2021). Since soils are susceptible to differential settling due to their low shear strength, heavy loads from civil engineering structures on soft or weak soils can lead to failure if not properly

handled (Correia and Rocha, 2021). Certain needs, such as loading capacity, shear strength, and permeability, may be addressed by using ground enhancement techniques such as prefabricated vertical drains or soil stabilization (Abdel-Rahman, 2021). Many studies on soil strengthening have been conducted in recent years utilizing randomly distributed natural and synthetic fiber material (Mirzababaei et al., 2013).

Compaction with randomly distributed fiber-reinforced soil has several advantages. Previous research has shown that the strength properties of randomly distributed fiber-intensified soil are a function of the fiber concentration and fiber-surface interaction (Bahrami and Marandi, 2020).

Random reinforcement of soil with High-Density Polyethylene (HDPE) plastic strips obtained from waste bags or bottles may be a simple and cost-effective method to enhance the engineering properties of existing soil (Vijayan and Parthiban, 2020).

The main emphasis of many researchers is on the usage of plastic strips as fiber materials in the construction of different geotechnical structures. In addition to the recycling of plastic and rubber waste fiber, this will allow fiber to be reused for the stabilization of soils. The large terrain of the world is covered with expansive soil. There is a great change in volume after wetting and drying, which is the main problem associated with expansive soils. Due to its volume change behavior, damages to structures have been observed extensively. Hence, it makes expansive soil problematic. Thus, in the regions with pronounced wet and dry seasons, it poses a great hazard. In a large number of such cases, vertical or horizontal cracks develop, and due to this damage in pavement, buildings, canals, and conduits in basement walls take place. The proper technique to improve the soil condition by reducing estimated structural damage from expanding soil has been the point of focus of many investigations carried out by various researchers. The main purpose of techniques used for soil

improvement is to prevent or limit moisture ingress, change of properties of the soil, and super movement with overburden. Materials used recently for the improvement of soil conditions are geosynthetics, including geotextiles, geogrids, geomembranes, plastic waste bottles, carry bags, and many such objects.

By using geotextiles, plastic waste bottles, and carry bags with lateral resistance, tensile diaphragm, support, and build-up capacity, it may be able to increase the expanding terrestrial subgrade's capacity. It is economical to use plastic waste bottles and carry bags in any type of structure, such as buildings, pavements, canals, and conduits (Kumar et al., 2022; Mahajan et al., 2022). This paper provides a comprehensive overview of the intricate relationship between plastic waste and soil stabilization, with a primary focus on expansive soils. The initial section succinctly outlines the prevalent issue of plastic waste and conducts a literature review on soil stabilization techniques, setting the stage for a more focused discussion on expansive soils. The literature

review critically evaluates existing methods, establishing a foundation for understanding the complexities associated with stabilizing soils. Subsequently, the paper delves into an in-depth analysis of expansive soil behavior, elucidating the challenges posed by its unique characteristics. The state-of-the-art approaches to enhancing the engineering properties of expansive soils are thoroughly examined, offering a comprehensive understanding of current methodologies and their effectiveness. The paper concludes by identifying a research gap in the current body of knowledge, indicating a need for further investigation into specific aspects of improving expansive soil engineering behavior. By synthesizing existing research, critiquing methodologies, and pinpointing gaps in knowledge, the paper contributes to the academic discourse on soil stabilization, particularly in the context of expansive soils. This fosters a deeper understanding of this multifaceted and crucial environmental challenge. The flow chart of this review article is shown in Figure 1.

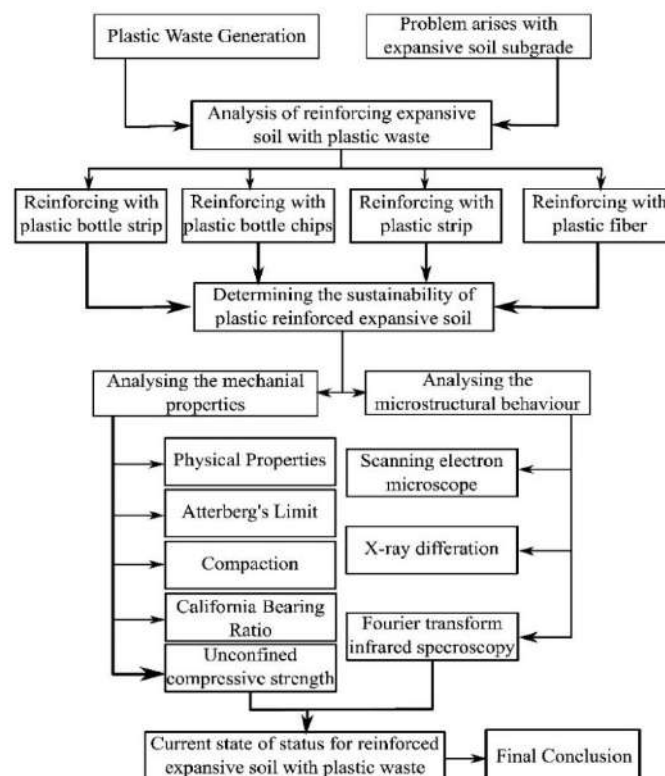


Fig. 1. Overview of stabilization of expansive soil with plastic waste

2. Plastics

Plastics, derived from lighter fractions of natural gas or oil, consist of polymers or resins. The term 'plastics' encompasses a diverse array of resins, each possessing unique capabilities and properties. Also, the properties of every resin can be changed with the addition of substances. Various resin types and added substances permitted a wide scope of item production that meets a variety of specifications. Polymers are large synthetic particles composed of repeating chemical units called monomers which combine to form polymers or long chains. Polymers are pure materials formed through the polymerization procedure; however, they cannot be utilized individually, yet. Additional substances are added for plastic shape. Such added substances comprise of reinforcements, fire retardants, fillers, coupling operators, antistatic specialists, oils, shades, plasticizers, and stabilizers. Unadulterated polymer might incorporate cellulose, cotton, wood, cowhide, elastic, shellac, fleece, bitumen, and silk (Khalid and Alshawmar, 2023).

3. Soil Stabilization with Reinforcing Materials

It is standard practice to use a range of ground improvement additives (for example, calcium, cement, and fly ash) to deal with poor shear strength and soil capabilities when constructing on weak ground. Henry Vidal of France created a new and improved method later to decrease the risk of stability in slopes, enhance the capacity to carry the load, and reduce lateral deformation by reinforcing tensile materials (geo-synthesis, etc.) into deficient soils. direct shear tests were performed on dry sand reinforced with various fiber types. Natural and synthetic fibers, as well as metal wires mixed with soil, were subjected to rigorous testing. A theoretical model, based on a force equilibrium for fiber-reinforced sand, has been developed.

Theoretical predictions of the model for fiber-reinforced sand were compared with the experimental results. It was also obtained that the shear strength of the reinforced soil was improved. An increase in the peak shear strength and a reduction in post-peak strength were found. The important parameters that affect the results were the concentration and orientation of fibers in the sand-fiber mix, irrespective of the density of the sand.

These findings are directly applicable to the protection of slopes of weathered granite rocks and sand dunes formed along coastal beaches. The mechanical properties of kaolinite soil and fiber composite were examined. The results of various laboratory tests such as unconfined compression test, splitting tension, three-point bending, and hydraulic conductivity, indicated appreciable enhancement in the all-round strength of the composite. The additional strength was found to be a function of fiber length, fiber content, and soil-fiber water content. The more the fiber content, the higher is the compressive strength, the tensile strength, and the toughness index.

The influence is more at low water content. It is also noted that the higher fiber length provides less increase in tensile and compressive strength but makes the composite more ductile. Though there is a slight increase in the hydraulic conductivity of the composite, it remains low enough to be used as a liner in landfills. It was mentioned in an experimental study on the evaluation of the strength of reinforced sand with small strips of recycled HDPE. The strength tests used included California Bearing Ratio (CBR), secant modulus, robust modulus, and shear strength. Experiments were carried out to examine the interactions between portage sand and HDPE strips. According to the results, the addition of waste plastic to the soil enhances its strength and stiffness. The effects of characteristics of fiber (e.g., weight, aspect ratio, and surface friction), its density, and confining stress on the shear strength of fiber-reinforced soils are

evaluated. The results of several triaxial compression tests on reinforced soil have been used to develop a mathematical model through regression analysis. This model can find the shear strength of soils reinforced with any other type of fiber for a given confining stress. The model results compare well with the many other experimental studies reported in the literature. This introduces the concept of "critical confining stress", which means that the failure envelope of soil fiber composite is curvilinear with the transition at critical confining stress, and below which the fibers may slip in the soil matrix on loading. It was also reported that the critical confining stress is dependent upon the aspect ratio of the fiber. The shear strength of the soil was found to increase considerably by fiber insertion, and the rise in strength depended on the fiber weight, the aspect ratio, and the size of the grain. Kumar et al. (2022) provided the findings of laboratory experiments on expansive soil reinforced with randomly dispersed polyester fibers.

The addition of fiber to soils improved the maximum compressive strength, CBR value, peak friction angle, and ductility of the specimens, as shown by the test results. The fiber content and pond ash content are found to be optimal at 0.3% to 0.4% of dry weight. It was described the benefits of using randomly distributed polyethylene terephthalate fiber, obtained from the recycled waste plastic bottles (as reinforcement) to uniform fine sand as well as cemented sand. The various tests conducted for the study were unconfined compression tests, splitting tensile tests, and saturated drained triaxial compression tests with local strain measurements. The strength and deformation characteristics of soil, reinforced soil, and reinforced cemented soil were studied separately through regression analysis of experimental data. It is concluded that the peak strength of cemented and non-cemented soil improves with the inclusion of fiber; however, the ultimate strength is a little bit reduced. Further, the inclusion of fiber

makes the cemented soil somewhat ductile, but the initial stiffness remains unaltered. The results of drained triaxial compressive tests on fiber-reinforced sand specimens were provided. After adding a small amount of synthetic fiber, the composite's failure stress has been found to increase. A reduction in early stiffness and an increase in stress, on the other hand, are related to strain at failure. Steel fibers have little effect on the composite's initial stiffness. The failure phases increase up to 70% when the fiber structure is 2% (by volume) and the aspect ratio is 85. Increases in fiber concentration and aspect ratio enhance the reinforcing advantage, but it also depends on relative grain size and fiber length. Fine sand produces more shear strength than coarse sand, and the maximum benefit is attained at low fiber content (0.5%).

However, with a greater fiber concentration, this trend is reversed (1.5%). Under triaxial compression, a model has been developed to predict failure stress. There are two segments in the failure envelope: linear segment with fiber and non-linear segment with respect to fiber material generation. The results indicate that the fiber yield is much higher than the stress range seen in experimental results. To explain the failure criteria of fiber-reinforced sand, the concept of a microscopic internal friction angle was created. This idea is a simple method of integrating fiber reinforcement in the stability analysis of earthen constructions.

Later, after a few years, the mechanical behavior of sand reinforced with strips of waste plastic was reported. Consolidated drained tests were conducted on sand and reinforced sand with strips of waste carry bags and packing materials (HDPE plastic).

The analysis of the experimental results shows improvement in the engineering behavior of reinforced sand. The dilation of reinforced sand is restricted, and the shear strength parameter, i.e., angle of shearing resistance, is increased. It is also established that the improvement is more at low confining pressure as compared to that of

high confining pressure. According to the findings of the study, the behavior of polypropylene reinforced sand under high shear strain has been investigated through a ring shear test. Shear testing was performed on sand with and without reinforcement.

The reinforcement used was randomly dispersed fiber. Under high distortional strains, the influence of the fiber was investigated by looking at the impact of the length of the fiber, the content of the fiber, and the effective normal stress at differing relative densities of the sand. Higher fiber content and denser fiber-reinforced sand components have been studied specifically to demonstrate the effects of longer fibers more clearly. The results showed that this kind of fiber strengthening has a tremendous amount of promise since the enhanced strength does not diminish even when subjected to quite high strain. The fibers were taken out after failure to observe their status. It is concluded that the long fibers are broken after large plastic deformation, and short fibers are created. It is also found that the denser sands acquire more shear strength on reinforcement, and the shear strength enhancement is more with higher fiber content. It was considered that the distribution of fiber strips in the fiber-sand mix creates anisotropy. Keeping this in view, an anisotropic yield condition is developed for fiber-reinforced sand with the ellipsoidal distribution of fibers. The maximum shear stress, in an anisotropic yield condition, is dependent on the direction of principal stress and in-plane mean stress.

The anisotropic shear strength can be found from the plot of the yield condition on the plane of maximum shear stress and the shear stress on the z -plane. This yield condition has been used for limit equilibrium analysis employing a kinematic approach. As the fiber-reinforced sand is anisotropic, the angle of internal friction will vary with the direction of the major principal stress.

However, for boundary value problems, the unique value of the angle of internal

friction can be determined. The proposed approach has been used to evaluate the performance of fiber-reinforced sand with a retaining wall and a strip foundation. It is concluded that the inclusion of fibers in sand reduces the load on the retaining wall and improves the bearing capacity of the strip footing. Dutta et al. (2016) presented a study on stone dust reinforced with waste plastic strips overlying the soft clay. The experimental study is limited to the impact of reinforcement on the CBR value of the stone dust above soft clay (commercial grade of kaolinite). Three lengths of low-density polyethylene waste plastic strips (12 mm, 24 mm, and 36 mm) with strip content (0.1%, 0.2%, 0.4% and 0.8% by weight) were used. The results were interpreted in terms of CBR value and secant modulus. It is concluded that the inclusion of waste plastic in stone dust above soft clay results in little improvement of CBR value and secant modulus, and the improvement is more with plastic strip content and length of the strips. Kumar et al. (2022) developed a novel shape of plastic strips termed disciplined HDPE by reinforcing it with locally available soil to enhance the engineering performance of sub-grade soil. HDPE strips of various concentrations (0.25, 0.5, 0.75, 1, 2, and 4%), as well as lengths and sizes, were put into the sandy soil with random orientation. It was noted that an increase in HDPE strip content and size, improves CBR values and significantly reduces sub-grade thickness. It is assumed that the confining pressure is so high that the fibers get broken before reaching to pull-out condition. The simple force equilibrium model was used to predict the shear behavior of reinforced soil, which depends on factors like fiber content, aspect ratio, specific gravity, elastic modulus of fiber material, skin friction, the orientation of fiber concerning shear plane, confining stress, void ratio, angle of internal resistance, and specific gravity of soil. This introduces the existence of apparent cohesion due to the presence of fibers in the soil that increases the shear strength. The

shear strength improvement is found to be proportional to fiber content and its aspect ratio. However, the validation of the model has not been done with any experimental results. Landfill closure essentially requires a cover barrier for the safety of the surrounding environment. A suitable cover barrier was provided that is somewhat ductile, impermeable, and good for site safety as required. The silty clay cover barriers of landfills are subjected to differential settlement due to the non-uniform settlement of the garbage mass in the landfills. This causes cracks in the cover material, and the purpose of protecting the pollution from the closed landfills is lost.

For this reason, it has been proposed to use polypropylene fiber-reinforced silty clay as a cover material. Authors have reported the results of direct tensile and compression tests of reinforced silty clay and have shown that the composite material is improved in compression as well as in tension. The rigidity and ductility of the proposed composite material become quite good to improve the mechanical performance of the reinforced clay. This leads to a better solution to the problems of covering barriers of landfills. The shear strength of fiber-reinforced soils is evaluated by the test results of triaxial compression on the specimens of the composite soil. For rational designing of a fiber-reinforced soil structure, it is essential to develop the mechanics of reinforcement as well as failure of this composite material.

Li and Zornberg (2013) presented a methodology by which the equivalent shear strength of fiber-reinforced soil can be predicted by knowing the shear strength of the soil matrix and the pull-out tensile capacity of the fiber through the soil. It is proposed to evaluate the shear strength in a discrete framework, which requires experimental assessment of shear strength parameters of soil by triaxial compression test and results of fiber pull-out test through soil, which indicates the tension mobilized at various shear strain levels. The shear strength of reinforced soil is governed by

strain compatibility at peak failure or post-peak residual shear strength of the unreinforced soil. The study concludes that the fiber-induced tension is mobilized at the high strain stage, high fiber content provides shear strength by the use of residual shear strength of the soil, and low fiber content gives shear strength with peak shear strength of the soil. However, the equivalent shear strength of the reinforced soil should be calculated corresponding to the strain level at peak failure and residual shear strength of the soil, and the maximum of the two values may be taken as equivalent shear strength. Bahrami and Marandi (2020) gave the formulation of failure criteria of fiber-reinforced sand considering the isotropic and anisotropic distribution of fiber in the soil matrix. A concept of cross-anisotropy concerning three planes (x , y , and z) has been followed to define the anisotropy due to the distribution of fibers in the soil. This defines an anisotropic variable ' A ' as a joint invariant of the deviator stress tensor and deviator fiber distribution tensor. The value of ' A ' ranges from -1 to 1, and for the isotropic fiber distribution, its value is zero.

The strength of the composite sand is also influenced by the degree of anisotropy of fiber distribution. It is assumed that the host soil alone is isotropic, and anisotropy in the composite is contributed by the reinforcing fibers only. One of the failure criteria developed and presented for the isotropic distribution of fibers considers the major, intermediate, and principal stresses. The criteria can predict the shear strength of the composite at a given confining pressure and can also predict the strength of unreinforced soil. The other expression gives the shear strength of the composite with the anisotropic distribution of fibers.

This criterion may assess the shear strength of the reinforced soil, which is tested under true triaxial compression under the three-dimensional (3D) loading, where the intermediate and minor stresses differ in magnitude. It has been noted that the predictions made by the proposed criteria

match well with the test results. The study is applicable for analyzing the stabilized slopes with reinforcement of soil by synthetic fibers, plant roots, and soil nails, etc. Correia and Rocha (2021) described an experimental study on the effect of plastic fibers on the compressibility behavior of soils. Materials used were waste HDPE plastic bottle fibers and silty sand with clay content. A series of odometer tests were conducted on specimens of compacted composite soil at Optimum Moisture Content (OMC) reinforced with plastic strips of aspect ratios (2, 4, and 8) and varied plastic content (0.0%, 0.25%, 0.5%, and 1% by weight). The test results reveal that the Maximum Dry Density (MDD) reduces with an increase in fiber content, but the OMC remains almost the same. The compression index (C_c) and coefficient of volume change (m_v) decrease up to 0.5% and these are increased thereafter. The coefficient of consolidation (C_v) increases with an increase in aspect ratio of fibers. It is eventually found that 96% consolidation gets completed within 96 seconds with the inclusion of 1% fibers of aspect ratio 8, which shows the potential of plastic fibers in achieving early consolidation settlement of soil. Mirzababaei et al. (2013) reported the rise in the amount of residential, commercial, and industrial carpet waste that may be used to control the swelling characteristics of compacted expansive soils. Two different soil samples with plasticity indices (17.0% and 31.5%) were taken for the study. Two different types of carpet waste fibers were mixed with the soil. The fiber contents in the sample soils were kept at 1%, 3% and 5% by the dry weight of soil. The MOCs and maximum dry unit weights of reinforced and unreinforced samples were determined.

The two types of fibers used were GBF (synthetic carpet shred) and ABF (short fibers from shearing processes). It was ensured that fiber and water distribution remained uniform. Many compaction tests and swelling tests were done. The results show that the maximum dry unit weights

decrease with an increase in the fiber content, and the OMC is increased with the rise in fiber content.

The specimens prepared with fiber content at MDD and OMC have shown a reduction in swelling pressure values. The highest drop in swelling pressure has been found with 1% GBF fiber content. It has also been noted that minimum swelling pressure is attained at 1% ABF fiber content. Vijayan and Parthiban (2020) present the use of plastic waste as a reinforcing material for improving the strength of clayey and sandy soil. It was found that reinforcing the soil with waste plastic pieces strengthens and improves the stability of the soil. The plastic waste pieces are mixed with clayey and sandy soil. The shear strength parameters of reinforced and unreinforced samples were investigated by a direct shear test. A significant improvement is shown in terms of soil strength. The internal friction angle is increased more in sandy soil, but it is improved marginally in the case of clayey soil. The influence of reinforcement on cohesion is negligible. The compaction tests on reinforced and unreinforced clay revealed that the MDD and OMC of reinforced soil are decreased due to the use of those plastic pieces, which obviously have low specific gravity. Fadhil et al. (2021) investigated experimentally the performance of local sand reinforced with HDPE strips. Here, two sandy soils, i.e., Klipheuwel sand and Cape Flats sand, were used, and the tests conducted were direct shear tests and plate load tests. Shredded plastic material strips were mixed at concentrations up to 0.3% by weight. The dimensions of the plastic strips were varied, and the effect of variation in strip sizes was also studied. The strip lengths were between 15 mm and 45 mm, and the width was between 6 mm and 18 mm. To find the extent of soil improvement, soil strength parameters were obtained for the composite specimen. The results obtained from the tests suggest that in the case of sandy soils, the induction of plastic strips is an effective

reinforcement. It was considered that the reactive soils exhibit volume changes due to climatic variations, which cause damage to pavements and foundations of various structures. The specimens were prepared by mixing slag, construction wastes (crushed masonry, tiles, etc.), and commercial bentonite in different proportions and cured for 28 days. The specimens were tested for shear strength by a direct shear test. The test results and microstructural study of specimens showed considerable improvement in the shear strength and stability of the proposed mix. It is also mentioned that the microstructural study supports the test results, as the slag has cementing properties.

Mahajan et al. (2022) reported the research with the objective of exploring the underlying challenges of expanding soils and providing realistic economic solutions for expanded Sudanese soil development. The concern was the field performance of expanding soils with a focus on design requirements and construction safeguards for large-scale buildings. The results indicated that high swelling pressure led to the heaving of soil below the foundations of structures and was the main cause of failure.

Correia et al. (2015) worked on the mechanical impact of the soft soil "Baixo Mondego" on the amount of binder and fiber used in the production of a chemically stabilized concrete mix that is reinforced or not with short polypropylene fibers. One test was for determining compressive strength (unconfined compressive strength test), while the other three were for determining tensile strength. There were four distinct kinds of tests (direct tensile strength test, split tensile strength test, and flexural strength test). Increased binder concentration increased stiffness, compressive strength, and resistance in fiber-reinforced specimens, but had less effect on nanofiber-reinforced specimens, according to the findings. Stiffness, compressive force, and direct tensile force are reduced, strength losses after the peak are minimized, and the soil's behavior

transforms from fragile to ductile by adding a tiny number of fibers to soft soil that has been stabilized. The research also discovered that the effect of fiber addition on strength varied based on the straining mechanism used in each test. Therefore, the impact of the fiber on bending strength testing is considerable, while the presence of fibers in direct strength tests is insignificant. The relationship between compressive strength and tensile strength, as well as the relationship between the tensile strengths, are presented at the end of the trial, as well as the relationship between the tensile strengths, as determined by direct tensile strength testing, split strength testing, and flexural tests. Abdel-Rahman (2021) described the soil at construction sites which is not suitable for bearing heavy loads as needing to be improved to enhance bearing capacity and decreased the effective settlement. An overview and concept of major ground improvement techniques and their practical applications were described.

As a result, the techniques may be used in a variety of soil types, from coarse to fine-grained soils. A large portion of India's red soil is typically covered by water. These soils are found in low-precipitation areas and are not capable of absorbing moisture from the atmosphere. Because of the high concentration of iron in these soils, they are red. Because of the porous structure of the red soil, it has a lower strength than other soils. Soil stabilization is accomplished via the application of certain chemicals to soils to improve their engineering and strength properties.

Peddaiah et al. (2018) globally stated that since the non-biodegradable plastics are being incinerated because the hazardous gases are thrown into the atmosphere, it is causing a major environmental problem. Research on the compliance and usage of waste plastics in soil enhancement is shown here. Experimentally, it was investigated that reinforced plastic soil resulted in effective stabilization to encounter waste disposal problems and to provide economic solutions for soil stabilization. The

compaction test, direct shear test, and CBR test are all used in this study to explore the effect of plastic bottle strips on silty sand. According to the results, the maximum dry weight of the plastic unit, shear strength parameters, and CBR values increased. With each passing day, the usage of plastic items such as plastic bags, bottles, chairs, toys, and many other plastic products is

increasing. Therefore, the environmental problems caused by plastic waste are becoming more severe. Therefore, the use of waste plastics as a soil stabilizer is an effective use of waste, since suitable soil is missing for a variety of technical applications. In Table 1, the summary of different studies is presented.

Table 1. Literature review with critical remarks

Author	Soil location	Country	Type of soil/work	Remarks
Machado et al. (2024)	Salvador	Brazil	<ul style="list-style-type: none"> Sand Reinforced with randomly distributed polypropylene fibers, 0.5% by weight, 12.5-51 mm in length. 	<ul style="list-style-type: none"> Improvement in the isotropic compression test, triaxial test Reinforced with polypropylene fibers under isotropic compression.
Amena and Chakeri (2022)	Jimma town	India	<ul style="list-style-type: none"> Expensive soil Used plastic water bottles that are easily available, economical and a waste substance posing a problem for safe disposal. 	<ul style="list-style-type: none"> 0.75% improvement in the shear strength, cohesion, and loads settlement. 1% improvement in the CBR. Poorly graded sand added with shredded plastic strips.
Kumar et al. (2022)	Sasaram, India	India	<ul style="list-style-type: none"> Black Cotton Soil (BCS) Waste plastic strip Soil was stabilized with waste plastic strips of three different aspect ratios in varying proportions (i.e., 0.4%, 0.7% and 1%) 	<ul style="list-style-type: none"> Find a significant improvement in CBR and shear strength characteristics. Soaked CBR significantly increased by 223%. Slight increase in MDD and significant decrease in OMC.
Abukhetta la and Fall (2021)	Ottawa-Gatineau area in Ontario	Canada	<ul style="list-style-type: none"> BCS reinforced with plastic waste. 	<ul style="list-style-type: none"> Plastic Fiber is used. MDD reduced due to the addition of plastic waste CBR value is improved, and the thickness of pavement is reduced.
Bozyigit et al. (2021)	Kaolin clay, Bornova	Turkey	<ul style="list-style-type: none"> Kaolin clay. Waste plastic fibers used for the improvement of soil for its geotechnical parameters. 	<ul style="list-style-type: none"> 1% improvement in the angle of shear strength and cohesion. Waste plastic fibers are used. Geotechnical parameter improvement of soil in terms of its parameters.
Fadhil et al. (2021)	Mustansiriyah University, Baghdad	Iraq	<ul style="list-style-type: none"> Sand Two selected sandy soils: Utilizing polyethylene shopping bags waste to reinforce soils. 	<ul style="list-style-type: none"> 0.75% improvement in the angle of friction, plate load test. Inclusion of discrete polypropylene fibers in soil as reinforcement material.
Hassan et al. (2021)	Hawshki area, Iraq	Iraq	<ul style="list-style-type: none"> Clayey soil Plastic bottle strip Plastic bag strip Both strips were mixed with soil to improve the mechanical properties of the soil 	<ul style="list-style-type: none"> Modulus resilient of soil was improved with an increase in fiber content. MDD was improved significantly CBR was also increased with an increase in fiber content.

Yang et al. (2021)	Hunana	China	<ul style="list-style-type: none"> • Granular Soil • This scientific paper explains how to use a simple analytical model to estimate the shear strength of granular soils reinforced with fibers. The model is intended to be basic and simple. 	<ul style="list-style-type: none"> • Because of the existence of fibers in the granular soil, cohesion contributes to the soil's increased shear strength, but it contributes very little to the increased shear resistance due to increased stress.
Kassa et al. (2020)	Bole, Ethiopia	Ethiopia	<ul style="list-style-type: none"> • Expansive soil • Rectangular PET bottle strip • Mixing plastic strip in three different aspect ratios in 0.5, 1, and 2 % with expansive soil to improve its strength 	<ul style="list-style-type: none"> • MDD and OMC are reduced. • Swelling is reduced by using a plastic strip. • Huge improvement in Uniaxial Compressive Strength (UCS). • Angle of internal friction and cohesion increases with an increase in reinforcement material.
Peddaiah et al. (2018)	Patna Ganga alluvial soil	India	<ul style="list-style-type: none"> • Silty sand • Use of waste • Plastic soil improvement. • Plastic may be utilised as an efficient waste stabiliser as well as a cost-effective option for stabilising poor soils. 	<ul style="list-style-type: none"> • 0.4% improvement in the CBR value, MDD and shear strength. • Plastic bottle strips are used. • Improvement in the engineering properties of soil for its stabilization.
Naeini and Rahmani (2017)	Silty soil, Qazvin	Iran	<ul style="list-style-type: none"> • Silty soil • Laboratory CU tri-axial tests on randomly plastic waste bottle chips. 	<ul style="list-style-type: none"> • 1.25% improvement in the angle of internal friction, cohesion, pore water pressure, OMC, and MDD. • Silty soils are used. • The influence of different fiber length and different fiber content on the shear strength is detected.
Dutta et al. (2016)	Koradi thermal power plant, Nagpur	India	<ul style="list-style-type: none"> • Fly ash • This article raises concerns about two types of industrial waste: old plastic water bottles and fly ash. • It emphasizes the repurposing of old, discarded plastic water bottles in the field of civil engineering. 	<ul style="list-style-type: none"> • 13% improvement in the tensile strength-strain, deformation. • Waste plastic water bottles and plastic bags are used. • Reinforcement materials in the field of geotechnical engineering.
Dutta et al. (2016)	Badarpur sand	India	<ul style="list-style-type: none"> • Sand • For consolidated three-axial compression testing, a mixture of sand-waste plastic strips was used. 	<ul style="list-style-type: none"> • 0.15% improvement in the stress-strain behavior by the neural network method. • Neural network architectures are used.
Mirzababaei et al. (2013)	Clayey soil, Balton	United kingdom	<ul style="list-style-type: none"> • Clay soil • Utilization of carpet waste fibers. • In order to improve the swelling characteristics of compacted cohesive soils. 	<ul style="list-style-type: none"> • 3% improvement in the swelling condition • Investigated the effect of adding two carpet waste fibers on the swelling characteristics of two clay soils.

4. Behavior of Expansive Soil

4.1. Mechanism of Expansive Clay

Clay particles have superficial negative charges due to isomorphous substitution. This happens due to the chemistry of exchangeable cations, which depends on

the electrostatic forces between the pore fluid medium in the clay and the negatively charged clay surface. To preserve neutrality within the fluid media of the clay pore, normal affinity draws counter ions to the surface of clay particles, distancing them from the clay surface by reducing their

concentration.

The diffuse double layer is produced because of variations in concentration caused by the electrostatic surface characteristics and cation exchange capacity of the clay, i.e., the number of cations needed to permeate the clay surfaces (Aswar et al., 2023; Yadav and Tiwari, 2017). The dual layer employs an inflammatory reaction to separate minerals and expandable minerals such as montmorillonite from particles. Diffuse double layers significantly affect the technical characteristics of clay soils, most notably hydraulic conductivity. Hydraulic conductivity should be decreased because of the diffuse thickness expansion of the dual layer, and vice versa when the dual layer has been reduced. In fact, this forms the basis for the swell-shrinking behavior of varying moisture on expansive soils.

Because of its expandable clay mineral, for example, montmorillonite, the morphology of which is characterized by an expanding clay lattice. Volume variations in expansive soil are inherent because of the behavior of the diffuse dual layer.

Expandable clay minerals have low intermolecular attraction forces among adjacent unit cells; however, major isomorphous substitution shows negative surface charges, significant capability for cation exchange, and large specific surface during clay mineral formation.

4.2. Identification of Clay Minerals

Two methods, mineralogical identification and the inferential testing method, have been introduced for evaluating the presence of expandable clay lattice. The inferential testing procedure consists of the indirect methods used for calibrating index characteristics like liquid limit, limit of shrinkage, and distribution of particle size, and direct methods including odometer testing and free swell testing (free swell ratio, free swell value, and differential free swell) (Aswar et al., 2023). The method of mineralogical identification is comprised of differential thermal analysis, X-ray

diffraction analysis, Scanning Electron Microscopy (SEM), dye adsorption, and chemical analysis. Though mineralogical identification methods are good enough in expansive soils to identify clay minerals, their use to classify swelling behavior is limited due to a few shortcomings. Because of higher-level tools, complexity, as well as expert review of findings, mineralogical detection procedures were not cost-effective as suggested in the literature. Mineralogical detection approaches become unfeasible for an extensive variety of applications. The inferential testing approaches appear useful to identify and classify the swelling behaviors of clay minerals because they depend on index properties, and direct approaches when testing the swell potential, it is neither costly nor advanced. Though, for literature, the free swell ratio technique (the most encouraging method used to identify the dominant clay mineral in expansive soil) was introduced because it tends to be compatible with the methods used recently for the identification of mineralogical soils (Soltani et al., 2018). The ratio of free swell, in combination with the fluid limit test, is used to assess the dominant clay mineral using a cone approach with carbon tetrachloride and water as pore fluids, due to its inherent nature of certain soils, which consist of a combination of montmorillonite and non-expandable kaolinitic clay mineral. This knowledge derives from the non-polarity of carbon tetrachloride, which prevents the development of a diffusing dual-layer and allows flocks to form, resulting in high liquid limits for kaolinite-rich soils. Expansive soils are categorized using the free swell ratio technique, as given in Table 2. Figure 2 shows the plasticity chart classification of Black Cotton Soil (BCS), which is collected from different locations of India (Reddy et al., 2020).

4.3. Identification of Clay Minerals

BCSs are the black clays generated by the breakdown of simple igneous rocks because of very severe seasonal weather

variation. It is called BCS as it is suitable for cotton cultivation. The colors vary from light grey to dark grey and black. BCS are limited to the tropical and temperate climate zones of semi-arid regions and are plentiful in the regions where the yearly evaporation is greater than the precipitation. BCSs have been documented to exist as superficial deposits in continuous stretches and are typical of the low drainage flat terrain. The lack of quartz for clay's mineralogy helps to establish impermeable and waterlogged fine-grained soil material.

4.4. BCS's General Characteristics

During any road construction project, expansive soils generally appear as sub-grade material, and these sub-grades can vary from highly expansive to expansive.

The soil is very clayey and is very hard like the clods, often measuring 70 mm wide and 1.0 m thick, which cannot be quickly pulverized for treatment to use in constructing a road due to the formation of cracks. This raises serious problems with subsequent road performance. Besides, the softened subgrade tends to rise to the top

layers of the pavement, especially when there are many voids in the stone soling of the subsurface. Invariably, the incremental infiltration of wet BCS contributes to road collapse.

Owing to the loss of the subgrade strength through softening during the rainy season, roads laid on BCS bases build undulations on their surfaces. A low concentration of titanium oxide induces the black color of the BCS. There may be a high percentage of clay in the BCS, which is mainly the composition of montmorillonite that is black or blackish grey. The physical characteristics of BCS vary from location to location. As a result, the bearing capacity of BCS is low and it may depict high shrinkage/swelling characteristics. The physical characteristics of BCS vary from position to location. It is estimated that approximately 40-60% of BCS in grain has a size of less than 0.001 mm. In general, these soils have a higher liquid and plasticity limit index and an extremely low CBR value. Swelling pressure as high as 785-981 kN/m².

Table 2. Free swell ratio expansive classification of soils (Asuri and Keshavamurthy, 2016)

Oedometer expansion (%) ^a	Type of clay	Free swell ratio	Shrinkage limit	Soil expansively
< 1	Non-swelling	≤ 1	<5	Negligible
1-5	Mixture of swelling and non-swelling	1-1.5	5-13	Low
5-15	Swelling	1.5-2	8-18	Moderate
15-25	Swelling	2-4	30-60	High
>25	Swelling	>4	>60	Very high

Note: ^awith 7 kPa surcharge from air-dried to saturated.

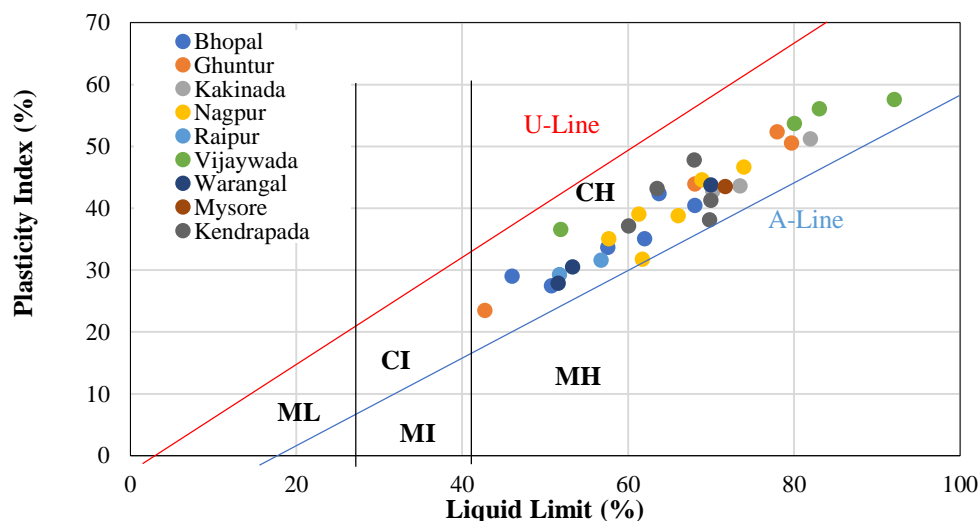


Fig. 2. Plasticity chart classification of BCS (Reddy et al., 2020)

Because of the extremely low CBR values of this soil, pavement construction becomes expensive.

4.5. State of the Art in the Stabilization of Expansive Soil

Over the years, advancements in understanding expansive soil behaviour have yielded numerous outcomes in the realm of soil stabilization. Geotechnical engineers, employing scientific principles, have dedicated substantial efforts to comprehend how expansive soils behave under various loading conditions. The latter half of the 20th century witnessed a plethora of experiments conducted by the geotechnical community, aimed at elucidating and classifying the fundamental behaviour of expansive soils. A method was developed to determine the swelling pressure of the BCS, revealing an increase in swelling pressure despite incomplete relationship maturation. In the pursuit of comprehending the heave phenomenon, odometer tests were conducted to procure data. Subsequent research endeavours sought to determine the swell capacity of expansive clays through predictive, field, and laboratory observations. The concept of soil suction, associated with a negative pore water pressure resulting from the humidity demand of hydro-mechanical clays, was introduced and correlated with swelling in sub-grade clay during moisture occurrence.

Researchers have contributed to the development and application of definitions and methods for quantifying characteristics of expansive soil, including swelling and resilient modulus. Laboratory experiments, such as Atterberg limits, particle size distribution (sieve investigation and hydrometer), dry density, and humidity content, have been instrumental in identifying key properties of expansive clays. In summary, these research endeavours offer valuable insights into expansive soil behaviour and various laboratory identification methods.

4.6. Utilizations of Waste Plastic in the Field of Civil Engineering

Plastics find diverse applications across

various sectors, including development, packaging, automotive, furniture, sports, electrical and electronics, health and safety, consumer goods, and household appliances.

In the field of civil engineering, plastics play a crucial role in the construction of bridges, buildings, water-retaining structures, landfills, terminals, ports, roads, railways, and landscaping, among others (Kumar et al., 2022; Khalid and Alshawmar, 2023). Construction-related plastic components encompass materials for partitions, erosion control, foundation inlays, bike racks, walkways, boardwalks, docks, bulkheads, curbs/wheel stop, pallets, railroad ties, piles, piers, guardrails, and sound walls. For a material to qualify as an effective construction material in structural engineering, it should possess qualities such as durability, strength, flexibility, ease of installation, fire resistance, and cost-effectiveness. However, this research focuses on reinforced soil using PET (Polyethylene Terephthalate) waste plastics, as outlined in Table 2, which compares the characteristics of plastic with other construction materials.

5. Mechanical Technique

Mechanical techniques for soil modification encompass compaction, vibration (utilizing various methods), and blasting. The mechanical enhancement of soil through compaction involves densifying the soil by imparting mechanical energy. This process entails adjusting the water content and the gradient of the soil.

Cohesionless soils are compacted by confining the soil and applying vibration energy. Hand-operated vibratory plates and motor-powered vibratory rollers of various sizes prove highly effective in compacting sand and gravel soils. Dynamic compaction of loose granular fills is achieved using substantial dropping weights. In areas with fine-grained cohesive soils, common compaction devices such as sheep foot rollers, rubber tire rollers, and others are employed. Mechanical compaction is

directed towards enhancing the engineering properties of the soil mass. This includes reducing settlement through decreased void ratios, bolstering soil strength, and minimizing shrinkage (Ikeagwuani and Nwonu, 2019).

5.1. Reinforcement

Utilizing fibrous materials like waste plastic strips and geosynthetics, along with composites such as geotextiles, geocomposites, geocells, geogrids, and geonets, represents a strategy for stabilizing weak soils and enhancing soil strength (de Azevedo et al., 2021). This approach creates a 3D spatial strengthening network that interweaves or interlocks soil grains into a cohesive mass with improved mechanical efficiency. Typically, these materials are introduced into the soil system, either randomly or with specific engineering, before components are integrated. Table 3 illustrates various forms and configurations of natural and synthetic fibers used for reinforcing soil. de Azevedo et al. (2021) extensively analysed the technical effects of randomly dispersed fibers on soil properties, encompassing both natural and synthetic soil reinforcement fibers.

Notably, the analysis did not delve into the stabilization effects of waste rubber fibers or carpet waste fibre (de Azevedo et al., 2021). The influence of waste rubber

fibers on the geotechnical properties of clay was studied by Yadav and Tiwari (2017).

The rubber fibers were added between 0% and 10% content, with a constant increase of 2.5% by weight of the dry soil. Progressive decreases in both MDU: "Maximum Dry Unit weight" and OMC from 16.35 kN/m³ to 14.78 kN/m³ and from 20.1% to 18.25% were due to the result of the humidity density relationship. The Uniaxial Compressive Strength (UCS) in the soil has improved slightly from 60.59 kPa to 62.69 kPa with a rubber fiber content of 2.5%. However, additional rubber fiber decreased the maximum axial stress by a maximum decrease of approximately 21.7% with 10% of the rubber fiber material. The results of the test for split tensile strength of the soil demonstrated a steady rise in split tensile stress with a volumetric strain until a total of 2.5% rubber fiber was reached for all percentages; the peak strength of the tensile has increased by 8.6% but has decreased at high content of rubber fibers with the highest drop of around 7.3% with a maximum level of 10%. The soaked CBR decreased steadily with rubber fiber content, whereas the unsoaked CBR reached around 38.6% with 2.5% rubber fiber addition. The swelling pressure in the soil was steadily decreased by the rise in fiber from 70.12% for natural soil to 39.58% with a 10% content of rubber fiber.

Table 3. Description of the natural/synthetic fibers used in soil reinforcement

Information source	Type of fiber	Dosage/Optimal content (%)	Fiber configuration (length)/Optimal length (mm)
Chompoorat et al. (2023)	Palm fiber	0-1	20-40
Ekinci et al. (2022)	Carbon and polypropylene fiber	0.3	10-30
Kumar et al. (2022)	Waste plastic strip	0-1	10-20
Ma et al. (2022)	Polyethylene fiber	4-5	Pellets
Hassan et al. (2021)	Plastic bottle strip	1-4	10-20
Lv et al. (2021)	Polypropylene fiber	1 ^a	12 ^a
Kassa et al. (2020)	Pet bottle strip	0.5-2	15-20
Wang et al. (2017)	Jute fiber	0.3-0.9	6-18
Yadav and Tiwari (2017)	Waste rubber fiber	0-10	≤ 15
Jayasree et al. (2015)	Natural coir fiber	0.2-1	> 4.5
Jayasree et al. (2015)	Coir pith	0.5-3	< 4.75
Mirzababaei et al. (2013)	Synthetic carpet waste fiber	1-5	2-20

Note: ^aThe optimal values

Mirzababaei et al. (2013) presented the analysis of the impact of the swelling properties of two forms of carpet waste fibers from various sources. Type 1 consisted of short nylon fibers derived from shearing piles of carpets, while Type 2 consisted of a mixture of polyester, polypropylene, and wool derived from trim carpet edges. The addition of the additives into dry soil was at 1%, 3%, and 5% by weight. The results indicate that the swelling pressure for compacted clay, with an activated content of sodium bentonite at MDU and OMC, has reduced to around 20% with 1% of type 1 fiber content, and strengthened by 10% at other fiber content. On the other side, the soil swelling pressure has risen exponentially for type 2 fibers, with a rise of approximately 83% with a fiber content of 3%. The impact of different moisture levels at a fixed dry unit weight and different dry unit weights at constant moisture levels has been studied. The findings demonstrate that the swelling pressure declines with the rise of the moisture level in constant dry unit weight, but the rise of dry unit weight in a fixed moisture content is raised. The same findings for fiber-reinforced soils have also been recorded (Mirzababaei et al., 2013).

5.2. The Relation Between the Microstructural and Engineering Properties

In addition to the volumetric and gravimetric condition variables-void ratio, the content of water, saturation level, and stress (back history) both hydraulic as well as mechanical, various macroscopic soil characteristics can also be seen in terms of microstructural behavior, distribution of pores and connectivity; shape, size, distribution, and arrangement as well as contacts of grain. A typical example is a difference in the permeability of soil at various compaction water content; a compacted soil wet optimal is less than the same compacted soil with an optimal dryness to the same porosity. Initially, it was because of a transition from the

flocculated to a dispersed clay particle structure, but the latest research on the permeability of clay aggregates caused by compaction was explained at distinctive water level contents. The inapplicability of the specific connections between macroscopic parameters and hydraulic compressibility, conductivity, and swelling/shrinkage behavior was also explained using clay microstructure imaging. The significance of the size, shape, as well as aggregations of structure, distribution, and connectivity of pores, is illustrated by these studies, along with the behavior of the soil, and how these aggregations and pores would alter throughout. It has also been studied by several variables, such as the type of clay mineral, the rate of drying or wetting, wetting/drying periods, and separating or combining.

Generally, the shape as well as the amount of clay minerals in soils and the interactions with pore water within the soil were illustrated to have a major impact on their strength, compressibility, as well as permeability over time. In the study, it is identified that there may be a relationship between the fabric of natural clays and their engineering properties. A microscopic review of thin parts, prepared by a special technique, in both the undisturbed and remolded specimens of many types of clays at natural water content, has provided direct information on the fabric. It presents various fabric features such as parallel clay orientation and photomicrographs. In terms of the inter-particle forces and the past of the material subsequent deposition or remolding, the fabrics produced in the undisturbed and remolded clays are clarified. To determine the engineering properties of the soil, experiments on micro-analysis of soil particles with regard to micrographs, chemical analysis using energy-dispersive X-ray spectroscopy, fabric orientation, and pores in compacted clay can be used. The effect of using soil enhancement additives can also be effectively determined using microanalysis.

6. Microanalysis of Soil

It was reported that it has always been important to understand the essence of materials/soil and their structures. In deciding the form of environmental processes and in estimating their resistance, the fine soil microscopic structure can be used as an index. During the evaluation of the soil structure on a small scale, some new nanometer research methods and particulate analysis were proposed. SEM: "Scanning Electron Microscopy"; AFM: "Atomic Force Microscopy"; and TEM: "Transmission Electron Microscopy"; are direct methods of nanoscale particle imaging, providing data such as particle size, shape, and morphology. SEM was invented in 1931, Which offers a wider picture of the electron by using specimens.

In this procedure, an electron beam is vertically centered on the specimen. When the beam interacts with the specimen in the vacuum, X-rays and electrons are emitted from the specimen. X-rays are then obtained by the detectors, converted into signals, and passed onto the screen to prepare for the final picture via the interaction between primary electrons and the sample. The nanostructure of soil particles has been widely used by SEM for research. TEM uses the emission of electrons in the direction of the TEM; however, the electrons emitted pass through the specimen and enter a phosphorous detector to reveal a pattern of sample composition.

This unit was also used for imagery of soil nanostructures. AFM has been used in recent years to assess the topography of surfaces and Surface Forces analysis. The surface of a sample is scanned with a sharp tip connected to a cantilever in AFM. In geotechnics, AFM images are also used to analyze soil nanoparticles' surface morphology, calculate the adhesive force between the soil particles, and measure the friction angle between them.

6.1. Determination of Clay Fabric by SEM

A clay fabric (or microstructure of clay)

describes the orientation or structure, or spatial solid particle distribution and particle-to-particle relations. Clay variations are primarily associated with mineralogy, consolidation, diagenesis, and the size of a grain. The sediments' mechanical and physical properties are extremely influenced and primarily regulated by the microstructure of clay fabric, which includes its consolidation behavior. Due to greater contact surface area and greater bonding ability, clay fabric with a preferred orientation offers superior sediment integrity and greater shear strength than clay sediments with less shear resistance and random microstructure.

Fabric modification, therefore, tends to be a significant variable affecting both the rise in the core sample's shear intensity as well as the speed of the shear wave. In the early stages of consolidation, the microstructure of this portion of the sediment will most likely be of sufficient strength to cope with pressure impressed on it by the reduced overload. The soil's micro pores provide valuable information on shear intensity, compressibility, hydraulic conductivity, and soil-water characteristics.

It is difficult to determine the structure of the soil micro-pores, and they are highly variable for one type of soil. The arrangement of micro pores shifts with the stress conditions, water and air movement, temperature, flocculation, gravimetric behavior, and weathering in the long term.

Several experiments were performed on the composition of soil micro-porosity. The intra, as well as inter-aggregate pores, have been studied in compacted clays. This kind of micro-porosity structure was called a double structure or dual structure by subsequent researchers. The findings have shown that the inter-aggregate pores shift quickly during soil compaction, consolidation, and drying.

6.2. Formation of Image in The SEM

SEM images of 3D objects and electron lenses are interpreted. The purpose of the electron lenses on the specimen was to

create a focused, small electron probe. SEM produces an electron beam on the surface of a specimen with a spot size having a diameter < 10 nm while still having enough current for forming an appropriate image. Furthermore, the electron beam is usually characterized through the diameter of the probe (d) that ranges from 1nm-1 μ m, the current of the probe (I)-nA $^{\circ}$ to μ A $^{\circ}$, as well as the convergence of the probe (α) - 10^{-4} - 10^{-2} radians. The electron beam images are concentrated into a fine probe that is scanned with the aid of scanning coils around the surface of the sample. In the form of electromagnetic radiation, a signal is emitted by every specimen point that has been hit through accelerated electrons.

Also, this radiation's selected portions received by a detector, generally Back Scattered Electrons (BSE) and/or Secondary Electrons (SE), as well as the subsequent signal, are amplified and presented on a computer monitor or TV screen.

6.3. Lenses Within the SEM

The electron lenses aim to achieve the desired crossover diameter of a convergent electron beam. The lenses are cylindrical-hole metal cylinders that work in a vacuum.

The magnetic field is produced within the lenses that vary to concentrate or defocus the electron beam that passes across the lens hole. In the electron gun, the electron-beam crossing diameter is demagnified to a small size by SEM using one to three condenser lenses. The amount of demagnification is regulated by the first and second condenser lenses. There is typically a resolution, condenser, spot size, or single control mark in the microscopes. The beam-limiting aperture, the stigmator, as well as space for the scanning coil are also included in the design of the lenses.

6.4. Formation of Image

The SEM picture in the analog or digital domain is a two-dimensional (2D) intensity map. In each picture, a pixel on the monitor appears for the same point on the sample

that is proportional to the force of the signal collected on each point by the detector. The picture is created and electronically displayed.

Electronic synthesis shapes the images in the SEM; there is no optical transformation, and no virtual optical images are created. The beam is continuously pushed in an analog scanning system; at a predefined number of lines, along the X-axis (line scan), a fast scan is complemented along the Y-axis through a stepwise slow scan. The frame time is given by the time for a single line scanning multiplied by the total frame lines. Only discrete beam positions are permitted in digital scanning systems. The beam is located there for a fixed time in a specific spot, known as dwell time, as well as afterward it is shifted to the next point.

Analog signal strength is determined by the detector while the beam is centered on the specimen. The voltage signals produced through the amplifier from the detector are digitized and stored in the corresponding database registry as a discrete numerical value. By translating the numerical values into an analog signal that is stored in the computer memory for displaying it on a monitor. Thus, the digital image is displayed.

6.5. Focus on Microstructural Interaction

Engineers need to understand the physicochemical changes of the stabilized soil. Therefore, for the physicochemical changes, a convincing explanation is given by the microstructural study. It is possible to present such analysis in the qualitative digital image analysis context, for example, X-Ray Diffraction (XRD), or quantitative charts, SEM.

They help in explaining the influence on the pore structure of stabilization, micro fabric, and soil components. Mirzababaei et al. (2013) studied the microstructural investigation of the polymers' impact on soil micro fabrics. The furan polymer, applied to the soil at 3%, 5% and 10% by

weight, steadily decreased the three expansive soils' free swell percentage compressed at MDD and OMC having approximately 83.5% average maximum drop. Figures 3-5 represent the alterations in the micro fabric of the soil due to the result of the furan addition at 5% as well as 10%.

A natural soil, from various magnification ratios picture (500x and 1000x), when combined with a few silt grains, sparse aggregations, and a few connectors consisting of discrete granular soil. There exist clear inter-assemblage pores among scattered and discrete aggregations.

Although, the soil fabric transitions into denser aggregation with intra-assemblage pore creation resulting from the denser aggregations' formation with inter-assemblage pore being less visible, with the addition of furan at 5% and 10%, suggesting a decrease in the size of the pore. Clothed silt grains in the natural soil are even more noticeable than that. In the soil's swelling properties, the observed reduction is responsible for improvements in the pore structure and soil fabric. The microstructural inquiry performed here, however, is only qualitative.

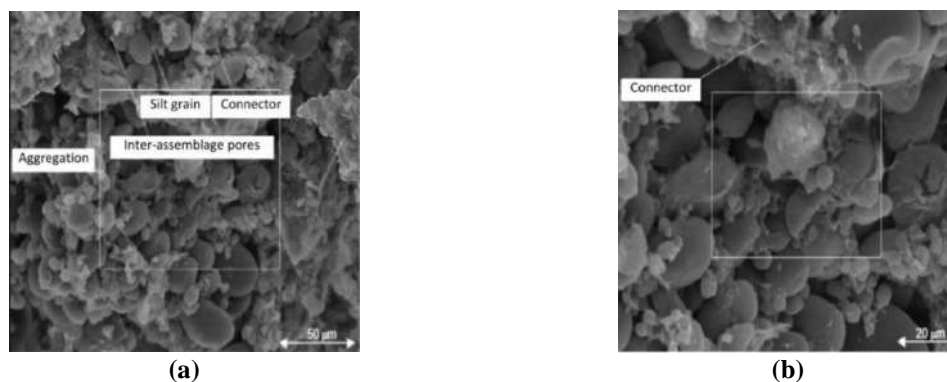


Fig. 3. Micro fabric of natural soil modified from (Mirzababaei et al., 2013): a) 500x magnification; and b) 1000x magnification

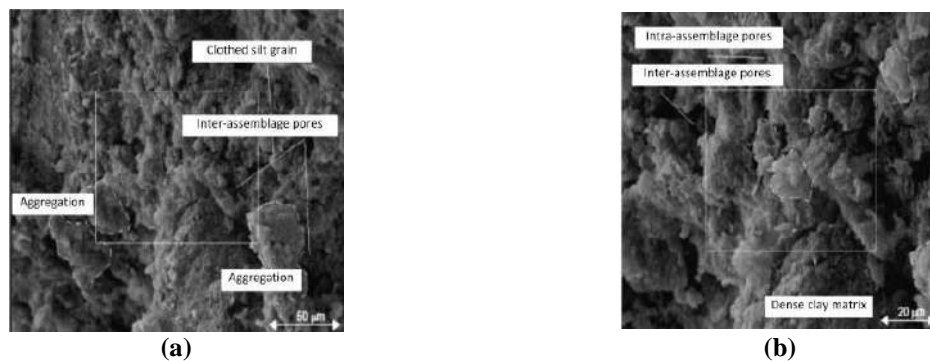


Fig. 4. Micro fabric of Soil with 5% furan modified from (Mirzababaei et al., 2013): a) 500x magnification; and b) 1000x magnification

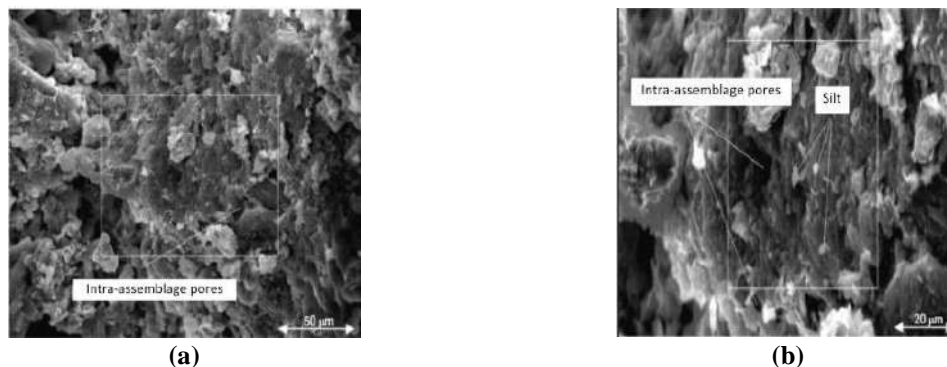


Fig. 5. Micro fabric of clayey soil with 10% furan modified from (Mirzababaei et al., 2013): a) 500x magnification; and b) 1000x magnification

7. Solid Wastes

In municipal areas, the production of solid waste is usually found in large quantities as a common phenomenon. Glass, paper, plastics, wood, rubber scraps, reusable goods, metals, plant debris, and organic materials are the main components of such waste. Depositories and the disposal of waste generated in large amounts involve environmental challenges. However, most of these materials have demonstrated their suitability in recent years for use in soil stabilization. Signes et al. (2016) analyzed the effect of the addition of rubber particle crumbs on the swelling potential for the soil to argillaceous marlstones and observed a decline from 3.71% to 1.37% for the addition of rubber crumb particles at 25%. The impact of cement-modified soft clay on durability has been investigated with solid waste from gypsum wastes (recycled basanite). The soil has lost a slight part of its UCS between cycle 1 and cycle 3, and was almost recovered in cycle 5 with a ratio of basanite-soil of 10% and a cement-to-soil ratio of 5% on the application of 10%, so stabilized soil is confirmed to be sustainable.

7.1. The Transition from State of the Practice to State of the Art

The geotechnical group is carrying out a great deal of work on expansive soil stabilization in the 21st century. However, problems emerging from such practice areas need to be resolved to be more effective and achievable. It's not so very limited, although rather a potential way to maximize the use of available methods for the sustainable and productive implementation of comprehensive soil stabilization. When such problems are solved, expansive soil stabilization becomes a realistic method. The approach will best be implemented in the area without the requirement for strict, time-consuming, and expensive research, which might not be feasible in situ application (Ikeagwuani and Nwonu, 2019).

7.2. Geo Environmental Issue

The soil stabilization technology should be used to avoid adverse environmental effects. Applications involving the use of an additive that contains high-carbon or hydrogen sulfide must be avoided, as emissions of such compounds have proven to be detrimental to the environment. No recommendation is made for products made up of heavy metals that would pollute the groundwater by leaching. The soil value of pH must also be taken into consideration when using any stabilizer. To make the study more sustainable, researchers must conduct geo-environmental assessments, based on the additive used, according to their research (Ikeagwuani and Nwonu, 2019). The use of gypsum waste plasterboard at dosages after evaluation of the soil pH and hydrogen sulfide release after completing the stabilization procedure did not contribute to any adverse effect. Etim et al. (2017) showed the quantity of iron that could be generated from an additive in the groundwater through batch equilibrium analyses and compared it with the prescribed level in drinking water given by the World Health Organization (WHO).

The use of engineered deposits as deposit liners is another approach used to prevent heavy metal dumping into groundwater. This form of liner serves as an obstacle to heavy metals being sorbed and prevents groundwater pollution. A deposit filler was used with a mixture of clay, 17% of RHA, and 2% bentonite. Similarly, the sawdust-resistant clay soil is used to contain cadmium and lead leachate from waste disposal.

7.3. Reuse of Waste

In expansive soil stabilization, waste tire rubber has shown great potential. The Expansive Soil-Rubber (ESR) technique has been used and suggests that it might significantly minimize in situ heaving in soil, particularly where the deposit of sulphate-rich natural soil exists. Also, it can prevent traditional agents of soil use; whereas it has been significantly restricted

by ESR, which is not appropriate where material rigidity is necessary.

7.4. Sustainable Practice

For efficient waste management, waste reuse should be tested in soil stabilization to ensure safe disposal of waste material for a green environment. The stabilization studies, therefore, use materials to determine the possible effect of the additives on the environment to make its use safe. However, few researchers regard this as a crucial parameter for applying these in expansive soil stability (Ikeagwuani and Nwonu, 2019). Recycled gypsum from waste plasterboard to improve the soil used as an embankment material and enhance the properties of the stabilized soil, while making sure that the stabilizer has no wrong environmental impact within its administration dosage. The studies were carried out to calculate the effect of recycled gypsum as regards hydrogen sulfide, pH, as well as toxic substances like boron, chromium, and fluorine. Low-carbon sodium silicate liquid was used to enhance the UCS and expansive clay compressibility features. Due to the low carbon additive used, this can be seen as a sustainable enhancement.

7.5. Focus on the Application of Nanotechnology

Using highly fine particles was the other practice that has been embraced in recent years (within the context of nanoparticles).

It was presented for improving the tensile strength as well as its parameters of lime-treated marine clay with nano-modified coir fiber that preserved durability by increasing the wetting cycles of the stabilized soil matrix. Sharo and Alawneh (2016) described a similar analysis to change the expansive clay soil, for the purpose of using nano-clay materials. A regressive pattern has been shown by increasing clay content, which also demonstrates the soil swelling potential, with a peak decline of approximately 65.5% with 3% nano-clay content, and with 0.6%

nano-clay content, a peak increase of about 42% is achieved for UCS.

Nanomaterial (nano-z) has been used by Ugwu et al. (2013) to improve the subgrade strength of soil in plastic clay. At varying ratios of nano-z/water at 1:150, 1:200, and 1:300 nanomaterial is applied. The increase in the material ratio shows a monotonous decrease with the change in the tested soil characteristics and the ideal ratio found is 1:150. The additive causes a reduction of about 74.5% in the soil Plasticity Index (PI) and an improvement of about 120% in CBR. The nanomaterial stabilization mechanism has been clearly shown. The nano-z material is a non-functional alkyl organic matter, and silanol (Si-OH) is generated in terms of hydrolyzation (reaction with water).

Siloxane can be formed from reactive silanol ($=\text{Si-O-Si}=\text{}$), which attaches to the silanol surface of soil, providing the soil with molecular hydrophobicity and making it water repellent on the treated soil surface.

7.6. Problem Statement

With rapid technological development worldwide, plastic usage, such as waste plastic carry bags, is rising. Every year around the world, about 500 billion bags are used. Used waste plastic carry bags disposal is a major issue, as most plastic waste can no longer be biodegraded and cannot be incinerated, as it emits toxic gases.

The stabilization of soil enhances the mechanical properties of fragile soils, with managed compaction or the use of stabilizers, like asphalt or lime, although these additives in the recent few years have become expensive.

7.7. Solution Statement and Aim

To have a solution for the alternative management of the waste plastic carry bags is their use in soil stabilization, which is cost-effective. The trash is clean; it just needs recycling. Since it is eco-friendly, it will protect the environment and improve soil properties, CBR value, tensile strength, as well as shear resistance by reducing the compressibility of the soil. Advantages of

using waste plastic for soil enhancement:

- Reduces the field permeability of the soil.
- Load-bearing capacity improves.
- Soil shear strength increases.
- Soil cracks and swelling are minimized.
- Durability boosts.
- Soil settlement reduction.
- CBR improves.
- The improvement of soil quality is cost-effective and energy-intensive.
- The problem of waste plastic can be solved.
- Abundantly available.

8. Focus on the Economic Implication

Since soil properties need to be improved to achieve some default values while stabilizing poor soil, the engineer's role is to provide geotechnical soil modification and cost-effectively obtain the desired properties. Besides, researchers have performed comparative research to determine the efficacy and economy of various additives. This is evident from studies in the year 2000, conventional stabilizers are frequently being used for expansive soil stabilization as stand-alone products (Zhao et al., 2015; Dafalla et al., 2015; Soltani et al., 2018). Many problems related to this, however, have provided space for potential alternatives as illustrated by Firoozi et al. (2017). In spite of this, the stabilizing impact of conventional agents appears to exceed other stabilizer effects during comparative studies, unless electrolytic lignin is marginally superior to fly ash, especially as regards soil plasticity.

Even among the conventional agents, although fly ash is a waste product, it appears to beat both lime and cement economically. Some non-traditional agents were also used for comparative research compared to traditional agents. These were commonly used in soil cushions. Soil cushioning strategies are also implemented to avoid moisture content variations in the soil since it is understood that the soil

instability is due to the difference in moisture in water content. To alleviate the swelling behavior of expansive clays, the approach utilizes a coherent non-expansive soil cushion. To stabilize the overlapping soil, cushioned materials are typically spread over extensive soil beds in the sheet of mattress formation and are sand beds, geocells, and others, as described in the research carried out by Dutta et al. (2016). Waste for manufacturing by-products, polymeric waste, and geotextiles are the most important substances for cushioning.

Geocell is a rigid geosynthetic product of complicated blended cells with 3D honeycomb structures requiring limited effects. Dutta et al. (2016) recommended that the shear strength of compact products should be substantially enhanced due to the geocell system boundary impact. They also claimed that by using geocell confinement for distributing base load, settlement reduction is superior to other mesh-shaped 2D composites. Other researchers (Sharma and Nallasivam, 2023) endorsed this claim, which found that the geocell reinforcement system delivered greater output than the material quantity equivalence of the planar reinforcement system. The efficacy of the process is illustrated by laboratory experiments performed using soil cushioning techniques for comparative research purposes. GGBS and fly ash were used as cushions on expansive soil treated with lime. Both GGBS and fly ash increased the CBR and, with increasing the cushion thickness, reduced the expansive soil swell potential.

The same results were obtained using Expanded Geofoam Polystyrene (EPS) and sand as cushions. It was found by using sand as a cushion, the cushioning technique performs in the same way as the additive mixing technique. The EPS geofoam, however, worked better in stabilizing the soil than sand. In a 3D geocell mattress and EPS geofoam embankment, a finite element approach was used to test soil cushion and fill materials. The component materials of geocell and geofoam are modeled using

elastic models or linear-elastic, excluding the concrete and geogrid layers, by applying the Mohr-Coulomb failure criterion. The findings of the study show a decrease in the geocell-stabilized soil's vertical displacement and also a decline in the geocell-stabilized soil's vertical and horizontal displacement. To calibrate these results, however, further laboratory work is required. As several of the researchers demonstrate, comparative analyses of the efficacy of one substance over another can be differentiated easily (Dafalla et al., 2015). However, a minor variation is found in the evaluation of comparative stabilizers' efficiency in other situations. Besides, the need for successful and economically sustainable stabilization has led investigators to try to optimize each of these two steps-based information: first, a potential combination of different materials following a comparative analysis, and Second, data obtained using a single material on the outcomes of numerous independent works. It is typically an optimization technique to make good use of the advantages of diverse materials.

9. Issue of Optimization

During expansive soil stabilization, researchers also strived to achieve both economy and efficiency. To optimize the advantages of each, they used different trial approaches to combine different stabilizers.

These findings are consequent as well from the work of individual and their comprehension of the chemistry behind physical-chemical variations caused by a certain stabilizer to achieve such optimal efficiency. Because of cost consequences and time-consuming nature, the conventional trial approach is not so adequate; however, using a combination of stabilizers, the need arose for better approaches to achieving optimum efficiency (Ikeagwuani and Nwonu, 2019).

10. Research Limitations

This article investigates the usefulness of

waste plastic carry bags in improving the behavior of expansive soil. Some research limitations in the present review article are listed below.

- The investigation has not been done to stabilize the expansive (BCS) soil using waste carry bags.
- The usefulness of HDPE was investigated to improve all the soil parameters.
- Further studies and research are needed to reduce the cost by using waste plastic carry bags as reinforcing materials for improving all soil parameters. The exploration has not handled the hypothetical parts of soil stabilization, reused waste plastic management, immaculateness, and the type of water. Due to a lack of laboratory facilities, accessible distributed index information and mechanical properties of HDPE (carry bags) plastic strips, a portion of the HDPE (carry bags) strip study (e.g., tensile strength at break, tensile modulus, flexural strength, and elongation at break, heat redirection, and melting point) has not been explored. Besides, water was assumed to be usable during the mixing of the soil and the waste soil HDPE (carry bags) plastic composite during the laboratory equipment program; afterward, no testing was carried out. Additionally, field reinforcement of the soil was not taken care of. Besides, the soil type received for this exploration was cohesionless, a portion of the tests couldn't be conducted on soil-HDPE (carry bags) plastic waste, as well as soil examples such as triaxial shear test, and others.

11. Conclusions

This paper discusses recent advances in soil stabilization technology. The paper aims to analyze the stabilization of expansive soil, emphasizing those critical areas like microstructural interaction for deciding the stabilization process, the economic consequences of comparative research, the topic of sustainability and reuse of waste, and the use of nanotechnology. Many test

methods for the analysis of variations in the microstructure of expansive as well as stable soils have been developed in recent years. Changes in soil micro fabrics, pore sizes, and constituents are often concerned with these changes. This is generally achieved by maximizing the use of different additives for achieving economic efficiency. Sustainable practice is also very critical. Efficient methods of waste management and recycling have been provided by soil stabilization technologies, by reusing waste products. Nanotechnology has also shown that it is a viable instrument for expansive soil stabilization. While achieving the stabilization of expansive soil, some insights have been found to resolve some of the issues that impede the applicability of the available soil. Below is the summary of the critical reviews:

- After soil stabilization, geo-environmental problems can occur. To ensure that the stabilization process is sustainable, it is, therefore, important for researchers to conduct the required experiments. Criteria with adverse environmental implications should be checked in accordance with the form and dosage of the additive used. This includes the soil's pH value, the release of hazardous compounds such as carbon, and the leaching of heavy metals into groundwater.

- For the field application of expansive soil stabilization by various additives, the standardization problem has not been resolved. When field experts investigate the potential to establish such a norm based on practice, along with the findings of individual stabilization, and the possible implementation of artificial intelligence techniques, this issue can be resolved.

- When using a mixture of different additives, optimization problems occur in attempting to achieve maximum efficiency.

- The research findings show that the prospect of its usage to improve and stabilize the soil is a good sign.

- The usage of waste plastic carry bags has led to the soil's improvement.

- The use of waste plastic carry bags on

the soil is an economic option.

- In the value, there is a significant increase. It can also be suggested to use it to build roads like temporary roads, village roads, or pathways, because the material is waste and non-biodegradable.

- Using waste plastic carry bags in the clay soil allows the overall weight of the dry device to decrease and the ideal moisture content to increase. The ideal humidity content is decreased by an increase in waste plastic carry bags.

- The effect of waste plastic carry bags on the improvement of soil properties depends primarily on the size of the strip, the quality of the plastic, and the form. The plastic strips may be a successful soil enhancement technique.

12. Availability of Data and Material

Data will be made available on request from the corresponding author.

13. Acknowledgement

We are thankful to the National Institute of Technology Jamshedpur, Jharkhand, India, for providing all the facilities for the research work.

14. Author's Contribution

Mantu Kumar: Investigation, Writing-original draft, Bheem Pratap: Writing-review and editing, Md Azhar: Investigation, Writing-review and editing, Somenath Mondal: Writing-review, editing, and Supervision, Rakesh Pratap Singh: Conceptualization, Methodology, editing, and Supervision.

15. Declarations

- Competing interests: The authors declare that there is no conflict of interest regarding the publication of this paper.

- Ethics approval and consent to participate: The survey research directed has received ethical clearance from the ethics committee

of National Institute of Technology Jamshedpur, Jharkhand, India. All respondents provided consent to participate in the research.

- Consent for publication: not applicable.

16. References

- Abdel-Rahman, M.M. (2021). "Review of soil improvement techniques", In: Shehata, H., Badr, M. (eds), *Advancements in Geotechnical Engineering, Sustainable Civil Infrastructures*, Springer, Cham, https://doi.org/10.1007/978-3-030-62908-3_14.
- Abukhettala, M. and Fall, M. (2021). "Geotechnical characterization of plastic waste materials in pavement subgrade applications", *Transportation Geotechnics*, 27, 100472, <https://doi.org/10.1016/j.trgeo.2020.100472>.
- Amena, S. and Chakeri, D. (2022). "A study on the effects of plastic waste strips and lime on strength characteristics of expansive soil", *Advances in Civil Engineering*, 2022(1), 6952525, <https://doi.org/10.1155/2022/6952525>.
- Asuri, S. and Keshavamurthy, P. (2016). "Expansive soil characterization: an appraisal", *INAE letters*, 1, 29-33, <https://doi.org/10.1007/s41403-016-0001-9>.
- Aswar, D.S., Bajad, M.N. and Ambadkar, S.D. (2023). "Performance evaluation of terrazyme as soil stabilizer", *Civil Engineering Infrastructures Journal*, 56(2), 277-299, <https://doi.org/10.22059/cej.2022.342784.184.1>.
- Bahrami, M. and Marandi, S.M. (2020). "Effect of strain level on strength evaluation of date palm fiber-reinforced sand", *Geomechanics and Engineering*, 21(4), 327-336, <https://doi.org/10.12989/gae.2020.21.4.327>.
- Bozyigit, I., Bulbul, F., Alp, C. and Altun, S. (2021). "Effect of randomly distributed pet bottle strips on mechanical properties of cement stabilized kaolin clay", *Engineering Science and Technology, an International Journal*, 24(5), 1090-1101, <https://doi.org/10.1016/j.jestch.2021.02.012>.
- Chompoorat, T., Likitlersuang, S., Buathong, P., Jongpradist, P. and Jamsawang, P. (2023). "Flexural performance and microstructural characterization of cement-treated sand reinforced with palm fiber", *Journal of Materials Research and Technology*, 25, 1570-1584, <https://doi.org/10.1016/j.jmrt.2023.06.036>.
- Correia, A.A., Oliveira, P.J.V. and Custódio, D.G. (2015). "Effect of polypropylene fibres on the compressive and tensile strength of a soft soil, artificially stabilized with binders", *Geotextiles and Geomembranes*, 43(2), 97-106, <https://doi.org/10.1016/j.geotexmem.2014.11.008>.
- Correia, N.D.S. and Rocha, S.A. (2021). "Reinforcing effect of recycled polypropylene fibers on a clayey lateritic soil in different compaction degrees", *Soils and Rocks*, 44, e2021061520, <https://doi.org/10.28927/SR.2021.061520>.
- Dafalla, M., Mutaz, E. and Al-Shamrani, M. (2015). "Compressive strength variations of lime-treated expansive soils", In *IFCEE 2015*, 1402-1409, <https://doi.org/10.1061/9780784479087.126>.
- de Azevedo, A.R., Cruz, A.S., Marvila, M.T., de Oliveira, L.B., Monteiro, S.N., Vieira, C.M.F. and Daironas, M. (2021). "Natural fibers as an alternative to synthetic fibers in reinforcement of geopolymer matrices: a comparative review", *Polymers*, 13(15), 2493, <https://doi.org/10.3390/polym13152493>.
- Dutta, S., Nadaf, M.A. and Mandal, J.N. (2016). "An overview on the use of waste plastic bottles and fly ash in civil engineering applications", *Procedia Environmental Sciences*, 35, 681-691, <https://doi.org/10.1016/j.proenv.2016.07.067>.
- Ekinci, A., Abki, A. and Mirzababaei, M. (2022). "Parameters controlling strength, stiffness and durability of a fibre-reinforced clay", *International Journal of Geosynthetics and Ground Engineering*, 8(1), 6, <https://doi.org/10.1007/s40891-022-00352-8>.
- Etim, R.K., Eberemu, A.O. and Osinubi, K.J. (2017). "Stabilization of black cotton soil with lime and iron ore tailings admixture", *Transportation Geotechnics*, 10, 85-95, <https://doi.org/10.1016/j.trgeo.2017.01.002>.
- Fadhil, S.H., Al-Soud, M.S. and Kudadad, R.M. (2021). "Enhancing the strength of clay-sand mixture by discrete waste plastic strips", *Journal of Applied Science and Engineering*, 24(3), 381-391, [https://doi.org/10.6180/jase.202106_24\(3\).0013](https://doi.org/10.6180/jase.202106_24(3).0013).
- Firoozi, A.A., Guney Olgun, C., Firoozi, A.A. and Baghini, M.S. (2017). "Fundamentals of soil stabilization", *International Journal of Geo-Engineering*, 8, 1-16, <https://doi.org/10.1186/s40703-017-0064-9>.
- Gautam, D.N., Azhar, M. and Sinha, A.K. (2022). "Experimental study on black cotton soil stabilization using GGBS", In: *Advances in Geo-Science and Geo-Structures: Select Proceedings of GSGS 2020*, 261-268, Springer Singapore, <https://doi.org/10.1007/978-981-16-1993-928>.
- Hassan, H.J.A., Rasul, J. and Samin, M. (2021). "Effects of plastic waste materials on geotechnical properties of clayey soil", *Transportation Infrastructure Geotechnology*,

- 8(3), 390-413, <https://doi.org/10.1007/s40515-020-00145-4>.
- Ikeagwuani, C.C. and Nwonu, D.C. (2019). "Emerging trends in expansive soil stabilization: A review", *Journal of Rock Mechanics and Geotechnical Engineering*, 11(2), 423-440, <https://doi.org/10.1016/j.jrmge.2018.08.013>.
- Jayasree, P.K., Balan, K., Peter, L. and Nisha, K.K. (2015). "Volume change behavior of expansive soil stabilized with coir waste", *Journal of Materials in Civil Engineering*, 27(6), 04014195, [https://doi.org/10.1061/\(ASCE\)MT.1943-5533.0001153](https://doi.org/10.1061/(ASCE)MT.1943-5533.0001153).
- Kassa, R.B., Workie, T., Abdela, A., Fekade, M., Saleh, M. and Dejene, Y. (2020). "Soil stabilization using waste plastic materials", *Open Journal of Civil Engineering*, 10(1), 55-68, <https://doi.org/10.4236/ojce.2020.101006>.
- Khalid, B. and Alshawmar, F. (2023). "Exploring the feasibility of using recycled pet strips with palm leaf ash for sustainable soil stabilization", *Sustainability*, 15(18), 13542, <https://doi.org/10.3390/su151813542>.
- Kumar, M., Azhar, M., Mondal, S. and Singh, R.P. (2022). "Stabilization of expansive soil subgrade by waste plastic", *Arabian Journal of Geosciences*, 15(10), 936, <https://doi.org/10.1007/s12517-022-10112-7>.
- Li, C. and Zornberg, J.G. (2013). "Mobilization of reinforcement forces in fiber-reinforced soil", *Journal of geotechnical and geoenvironmental engineering*, 139(1), 107-115, [https://doi.org/10.1061/\(ASCE\)GT.1943-5606.0000745](https://doi.org/10.1061/(ASCE)GT.1943-5606.0000745).
- Lv, C., Zhu, C., Tang, C.S., Cheng, Q., Yin, L.Y. and Shi, B. (2021). "Effect of fiber reinforcement on the mechanical behavior of bio-cemented sand", *Geosynthetics International*, 28(2), 195-205, <https://doi.org/10.1680/jgein.20.00037>.
- Ma, J., Nawarathna, H.M. and Hesp, S.A. (2022). "On the sustainable use of recycled plastics in flexible asphalt pavements", *Journal of Cleaner Production*, 359, 132081, <https://doi.org/10.1016/j.jclepro.2022.132081>.
- Machado, S.L., Vilar, O.M., Carvalho, M.F., Karimpour-Fard, M., Pinto, C.M. and Conceição, M.P. (2024). "Modeling the mechanical behaviour of fibre reinforced sands", *Geomechanics and Geoengineering*, 19(5), 800-822, <https://doi.org/10.1080/17486025.2024.2319619>.
- Mahajan, G.R., Radhika, B. and Biligiri, K.P. (2022). "A critical review of vehicle-pavement interaction mechanism in evaluating flexible pavement performance characteristics", *Road Materials and Pavement Design*, 23(4), 735-769, <https://doi.org/10.1080/14680629.2020.1860806>.
- Mirzababaei, M., Mirafteb, M., Mohamed, M. and McMahon, P. (2013). "Impact of carpet waste fibre addition on swelling properties of compacted clays", *Geotechnical and Geological Engineering*, 31, 173-182, <https://doi.org/10.1007/s10706-012-9578-2>.
- Naeini, S.A. and Rahmani, H. (2017). "Effect of waste bottle chips on strength parameters of silty soil", *International Journal of Civil and Environmental Engineering*, 11(1), 6-10, <https://doi.org/10.5281/zenodo.1128141>.
- Peddaiah, S., Burman, A. and Sreedeeep, S. (2018). "Experimental study on effect of waste plastic bottle strips in soil improvement", *Geotechnical and Geological Engineering*, 36, 2907-2920, <https://doi.org/10.1007/s10706-018-0512-0>.
- Priyadarshree, A., Chandra, S. and Kumar, V. (2021). "Performance of grass ash with mix of black cotton soil and lime", *Innovative Infrastructure Solutions*, 6(3), 150, <https://doi.org/10.1007/s41062-021-00518-9>.
- Reddy, P.S., Mohanty, B. and Rao, B.H. (2020). "Influence of clay content and montmorillonite content on swelling behavior of expansive soils", *International Journal of Geosynthetics and Ground Engineering*, 6, 1-12, <https://doi.org/10.1007/s40891-020-0186-6>.
- Sharma, A. and Nallasivam, K. (2023). "Comparison of bearing capacity behavior of strip footing resting on sand-admixed pond ash reinforced with natural fiber and geogrid", *Indian Geotechnical Journal*, 53(6), 1262-1279, <https://doi.org/10.1007/s40098-023-00745-0>.
- Sharo, A.A. and Alawneh, A.S. (2016). "Enhancement of the strength and swelling characteristics of expansive clayey soil using nano-clay material", *In Geo-chicago 2016*, 451-457, <https://doi.org/10.1061/9780784480120.046>.
- Signes, C.H., Garzón-Roca, J., Fernández, P.M., de la Torre, M.E.G. and Franco, R.I. (2016). "Swelling potential reduction of spanish argillaceous marlstone facies tap soil through the addition of crumb rubber particles from scrap tyres", *Applied Clay Science*, 132, 768-773, <https://doi.org/10.1016/j.clay.2016.07.027>.
- Soltani, A., Deng, A., Taheri, A. and Mirzababaei, M. (2018). "Rubber powder-polymer combined stabilization of South Australian expansive soils", *Geosynthetics International*, 25(3), 304-321, <https://doi.org/10.1680/jgein.18.00009>.
- Ugwu, O.O., Arop, J.B., Nwoji, C.U. and Osadebe, N.N. (2013). "Nanotechnology as a preventive engineering solution to highway infrastructure failures", *Journal of Construction Engineering and Management*, 139(8), 987-993, [https://doi.org/10.1061/\(ASCE\)CO.1943-7862.0000670](https://doi.org/10.1061/(ASCE)CO.1943-7862.0000670).

- Vijayan, D.S. and Parthiban, D. (2020). "Effect of solid waste based stabilizing material for strengthening of expansive soil, A review", *Environmental Technology and Innovation*, 20, 101108, <https://doi.org/10.1016/j.eti.2020.101108>.
- Wang, Y.X., Guo, P.P., Ren, W.X., Yuan, B.X., Yuan, H.P., Zhao, Y.L. and Cao, P. (2017). "Laboratory investigation on strength characteristics of expansive soil treated with jute fiber reinforcement", *International Journal of Geomechanics*, 17(11), 04017101, [https://doi.org/10.1061/\(ASCE\)GM.1943-5622.0000998](https://doi.org/10.1061/(ASCE)GM.1943-5622.0000998).
- Yadav, J.S. and Tiwari, S.K. (2017). "Effect of waste rubber fibres on the geotechnical properties of clay stabilized with cement", *Applied Clay Science*, 149, 97-110, <https://doi.org/10.1016/j.clay.2017.07.037>.
- Yang, N., Chen, X., Li, R., Zhang, J., Hu, H. and Zhang, J. (2021). "Mesoscale numerical investigation of the effects of fiber stiffness on the shear behavior of fiber-reinforced granular soil", *Computers and Geotechnics*, 137, 104259, <https://doi.org/10.1016/j.compgeo.2021.104259>.
- Zhao, H., Liu, J., Guo, J., Zhao, C. and Gong, B.W. (2015). "Reexamination of lime stabilization mechanisms of expansive clay", *Journal of Materials in Civil Engineering*, 27(1), 04014108, [https://doi.org/10.1061/\(ASCE\)MT.1943-5533.0001040](https://doi.org/10.1061/(ASCE)MT.1943-5533.0001040).



This article is an open-access article distributed under the terms and conditions of the Creative Commons Attribution (CC-BY) license.



A Comparative Study on the Effect of Fineness of Low-Grade Calcined Clays on Engineering Properties of Binary and Ternary Blended Concretes

Moodi, F.^{1*}, Fazelhashemi, A.², GivKashi, M.R.², Banar, R.³, Ramezaniapour, A.M.⁴ and Ramezaniapour, A.A.⁵

¹ Assistant Professor, Department of Civil and Environmental Engineering, Amirkabir University of Technology, Tehran, Iran.

² M.Sc. Student, Department of Civil and Environmental Engineering, Amirkabir University of Technology, Tehran, Iran.

³ Ph.D. Candidate, Department of Civil and Environmental Engineering, Amirkabir University of Technology, Tehran, Iran.

⁴ Associate Professor, School of Civil Engineering, College of Engineering, University of Tehran, Tehran, Iran.

⁵ Professor, Department of Civil and Environmental Engineering, Amirkabir University of Technology, Tehran, Iran.

© University of Tehran 2024

Received: 4 Mar. 2023;

Revised: 17 Apr. 2024;

Accepted: 24 Apr. 2024

ABSTRACT: The fineness of low-grade Calcined Clay (CC) particles in limestone calcined clay cement (LC3) and calcined clay cement (C3) plays an important role in terms of grinding time and energy consumption. In this regard, two low-grade kaolinitic clays (kaolinite content of less than 40%) from domestic sources were firstly calcined and then ground using a laboratory ball mill to achieve three fineness values of $\sim 8 \pm 2$, 20 ± 2 , and 32 ± 2 wt% retaining on a 45 μm sieve. According to experimental results, the substitution of finer low-grade CCs in binary C3 and ternary LC3 concretes had a marginal improvement in the compressive strength, bulk water absorption, and electrical resistivity by 4.7, 5.2, and 14.5%, respectively, compared to their counterpart coarser low-grade CCs mixtures. However, the chloride ions migration coefficients of mixtures containing low-grade CCs with the lowest fineness were 81-107% and 100-134% of their counterpart mixtures with the highest fineness of CC particles at 28 and 91 days, respectively. Overall, the low-grade CCs with a fineness of $\sim 32 \pm 2$ wt% retaining on a 45 μm sieve using less grinding time and energy consumption delivered a satisfactory mechanical and durability performance against chloride attack.

Keywords: Limestone Calcined Clay Cement (LC3), Fineness, Low-Grade Calcined Clay, Kaolinite Content, Chloride Ions Attack.

1. Introduction

The production and availability constraints of common Supplementary Cementitious Materials (SCMs), such as fly ash, silica

fume, blast furnace slag, and natural pozzolans, prevent them from satisfying the increasing demands of the construction industry (Scrivener et al., 2018a; Riahi Dehkordi and GivKashi, 2024). On the

* Corresponding author E-mail: fmoodi@aut.ac.ir

other hand, kaolinitic clays and calcium carbonate minerals like aragonite and calcite are plentiful resources that have the potential to broaden the utilization of SCMs in blended cements (Scrivener et al., 2018a; Zolfagharnasab et al., 2021; Du and Dai Pang, 2020; Díaz et al., 2017). In fact, calcined clays (CCs) are clays that have been thermally activated through dihydroxylation in the temperature range of 650-850 °C (Richardson, 2002). By comparing different types of clay, kaolinite-based CCs have the highest pozzolanic reactivity and have the potential to improve the mixture's properties (Fernandez et al., 2011). A novel approach has been introduced, combining kaolinitic CCs with Limestone Powder (LP) as SCMs. This method has resulted in the development of ternary blends known as limestone calcined clay cement (LC3) (Scrivener et al., 2018a).

Additionally, this new ternary blend also has the potential for use in advanced mixes like self-compacting concrete or self-compacting lightweight concrete (Mazloom et al., 2020; Mazloom and Salehi, 2018; Afzali-Naniz et al., 2021). Although other SCMs, such as slag and fly ash, are generally regarded as having no additional emissions and energy consumption, CC, due to the need for calcination, does have an impact. However, the calcination process for clay involves significantly lower temperatures compared to the clinker production, and there is no CO₂ emitted during the decomposition of clay (Sharma et al., 2021). Studies have indicated that the energy needed for the clays calcination is approximately 60% of that needed for clinker production, and the CO₂ emissions are around 30% of those generated by clinker production (Gettu et al., 2019). In terms of environmental impact, a study by Pillai et al. (2019) found that LC3 concretes, which exhibit comparable compressive strengths to Portland cement concretes, could potentially have a CO₂ footprint that is 16% to 30% lower. Due to the use of Metakaolin (MK) by other industries (mainly painting, paper, and

ceramic industries), pure kaolinite clay has become more expensive (Barata and Angélica, 2011). Therefore, using CCs with low purity is proposed as an alternative option. Studies on LC3 production show that clay with at least 40% kaolinite can be used as a 50% substitution of Portland cement. So, the utilization of low-grade clays with reduced kaolinite content could potentially address these constraints and also facilitate the utilization of waste materials in cement manufacturing.

Initiatives have been undertaken in this direction, such as incorporating 30% rejected clay brick (FRCB) in the formulation of LC3-50 (with a 50% clinker ratio) (Krishnan et al., 2020). Du and Dai Pang (2020) investigated the concrete durability with various replacement levels of cement by CC and LP. Permeability, electrical conductivity, RCMT, and water sorptivity of LC3 concretes were decreased compared to the control mixture. Maraghechi et al. (2018) concluded that the purity of CC has a remarkable effect on the concrete durability against chloride ion transport. Investigating the influence of fineness of particles and kaolinite content of low-grade CCs on the technical properties of binary and ternary blends containing CC, respectively named calcined clay cement (C3) and limestone calcined clay cement (LC3), is one of the necessary studies in this field. For instance, Bishnoi et al. (2018) produced LC3 blends by mixing 50% clinker, 31% CC, 15% LP, and 4% gypsum on a laboratory scale. The test results showed that while Blaine's fineness test could be a useful initial indicator for controlling the grinding process, laser diffractometry can offer a more comprehensive evaluation of the grinding of all cementing constituents. Krishnan et al. (2018) discussed that the industrial production of LC3 concretes comprises 50% clinker, 30% CC, 15% LP, and 5% gypsum. The findings indicated that grinding-based improvement in fine particles of MK did not always lead to enhanced early-stage hydration of C₃S. In a

research by Lapeyre et al. (2019), the role of the Particle Size Distribution (PSD) of MK in the hydration kinetics of tricalcium silicate paste (C_3S-T1) was investigated.

Also, Dumani and Mapiravana (2020) investigated the influence of different fineness of MK on the compressive strength of cementing pastes containing MK. The findings showed that the compressive strengths of the cementing pastes containing MK were not remarkably affected by the MK fineness, within the particle size range of 45 to 75 μm . This means that even the coarser MK can be used as a substitute for OPC, thus helping to decrease the expenses associated with grinding. Malacarne et al. (2021) investigated the influence of utilizing low-grade clay as a clinker substitute on the fresh properties of ternary cements. Their results demonstrated that the influence of the fineness of calcined limestone and clay on the thixotropic and water demand of pastes is more considerable relative to their mineralogical compositions. Ayati et al. (2022) used eight types of low-grade CC as a replacement for cement. The index of pozzolanic activity and the strength activity index of clays were determined. They also showed that mortars containing CC have higher compressive strengths than mortars containing pulverized fuel ash. Li et al. (2022) studied the influence of calcined MK content on water demand, pozzolanic activity, and mixture efficiency. The results showed higher pozzolanic reactivity and improved compressive strength with increasing MK content. In addition, higher MK content and fineness increased the water demand significantly. Kluge and Assmann (2018) investigated the effect of different mills of CCs on the short-term strength (7 days) of mixtures. The variables used in this study were cement fineness, CC fineness, and the amount of CC by considering three variables for each factor.

The results indicated that the effect of CC fineness was less significant compared to that of cement and the amount of cement. Also, with increasing fineness, the strength

increased, but with increasing the amount of CC, the strength decreased. Andrés et al. (2015) studied the impact of fineness of clinker, LP, and CC on compressive strength and mercury penetration porosity.

They showed that CC fineness is almost as important as clinker fineness, but LP's fineness has a significant effect only at early ages. Ferreiro et al. (2019) studied the influence of fineness and calcination temperature of raw clays on the LC3 binders' performance. They showed that the 2-day strength of blended cement was affected by clinker substitution. In contrast, the long-term efficiency and strength were influenced by LP content, fineness, raw clay composition, and temperature. Pérez and Martirena-Hernandez (2020) studied the concurrent grinding of LC3 binders and assessed how grinding duration affects the PSD of CC, LP, and clinker in the performance of these blends. The findings suggested that as grinding time increased, fineness improved, leading to enhanced compressive strength, albeit with an increase in water demand. CC fineness is the main influencing factor on rheology and water demand, while compressive strength is controlled by clinker fineness. Zunino and Scrivener (2020) compared two fragmentation methods to increase kaolinite content in low-grade CC. The findings indicated that kaolinite tends to be concentrated in finer particles after the grinding process, and the separation of particles can elevate the kaolinite content of CCs and enhance their pozzolanic reaction.

Zolfagharnasab et al. (2021) investigated the durability of LC3 binders containing low-grade CCs against chloride attack. They showed that these mixtures could be recognized as a promising option with sufficient durability. Yadak Yaraghi et al. (2022) investigated the suitability of conventional tests for assessment of the durability and permeability of low-grade CC mixtures. Based on the findings, it was determined that the water absorption test based on BS 1881-122 (2020), could not effectively determine the penetration

characteristics of binary and ternary binders containing CC. Siline and Mehsas (2022) researched to explore the impact of enhancing the MK fineness on its chemical reactivity. Their findings indicated that increasing the MK fineness does not appear to enhance its chemical reactivity. This conclusion was drawn based on the observation that the strength activity index remained unchanged. Luzu et al. (2022) investigated the optimal ratio of LC3 binders to obtain the highest possible packing density. The results showed that grain size distribution is not a critical parameter, especially in mortars, and adding LP fillers improves packing density.

Also, Ferreiro et al. (2017) studied the impact of fineness and type of raw clay on the efficiency and strength of binders. The early strength of blended cements appears to be mainly independent of particle fineness. On the other hand, the long-term performance can be remarkably enhanced by increasing the fineness of CC. Although research has been conducted in this area, studies are still limited, and there are discrepancies between opinions among researchers. Most existing studies have only investigated these concrete's pozzolanic reactivity, hydration kinetics, and efficiency. Among the hardened properties, compressive strength has often been the only investigated parameter. Nevertheless, more research is still needed to attain a better understanding of the effect of CC's fineness and kaolinite content on the mechanical, permeability, and chloride-induced durability of ternary LC3 and

binary C3 concretes. This study aimed to fill the gap in existing studies regarding the effect of the fineness of low-grade CC on the technical properties of C3 and LC3 and compare the results with Portland Cement (PC) concrete. In this regard, two types of low-grade CCs with kaolinite content of 19.4% and 28.7% from local resources were used. Low-grade CCs were ground by a laboratory ball mill to achieve three fineness values of $\sim 8 \pm 2$, 20 ± 2 , and 32 ± 2 wt% retaining on a 45 μm sieve. The results of ternary blends (containing 20% CC and 10% LP) were compared with corresponding binary blends (containing 30% CC). In other words, the potential of using lower fineness of low-grade CCs to produce LC3 concretes while maintaining desirable engineering properties has been studied. Also, a Distance-Based Approach (DBA) has been performed to compare the performance of different mix designs.

2. Experimental Program

2.1. Material

In this research, a Type II Portland Cement (PC) was used. The C_2S , C_3S , C_3A and C_4AF phases contents of PC were 17.75%, 58.64%, 5.10% and 11.81%, respectively. It should be noted that the used PC meets the requirements of ASTM C150 (2020). In addition, two types of low-grade CCs with different kaolinite contents were gathered from local resources located in the north-western parts of Iran. The preparation of powdered samples of these raw clays for calcination is shown in Figure 1.



Fig. 1. Samples of raw clays before the calcination process (Bahman-Zadeh et al., 2022): a) Clay Sample 1 (kaolinite content: 19.4%); and b) Clay Sample 2 (kaolinite content: 28.7%)

Both raw clays were calcined in a fixed-bed electrical furnace at 800 °C for 1 hr. The calcination process of CCs is shown in Figure 2. The kaolinite content of the CCs was measured by determining the weight loss between approximately 400-600 degrees Celsius using Thermogravimetric Analysis (TGA) with the tangential method (Scrivener et al., 2018b). TGA was performed using the STA 504 instrument in an atmosphere of AR gas, with a heating

rate of 10 °C per minute. The IR spectrum of raw clay samples and TGA results are presented in Figure 3 and Table 1, respectively. Binders including ASTM C150 (2020) Type II PC, two various CCs from different domestic deposits, and LP. The chemical composition as achieved by X-Ray Fluorescence (XRF) and the physical properties of PC, CCs, and LP are given in Table 2.

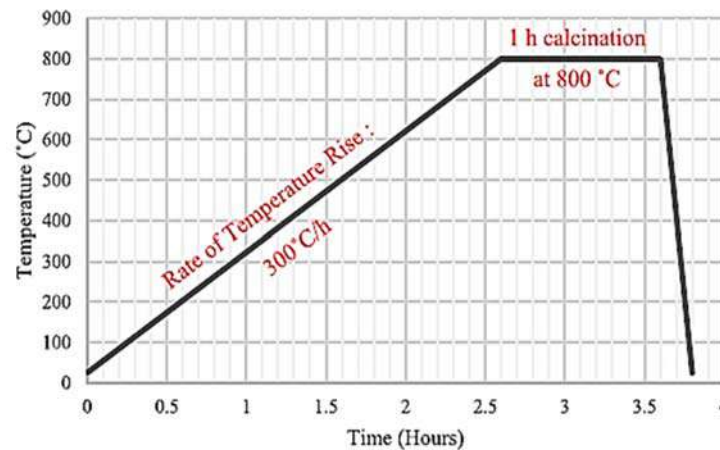


Fig. 2. The process of calcination of CCs (Yadak Yaraghi et al., 2022)

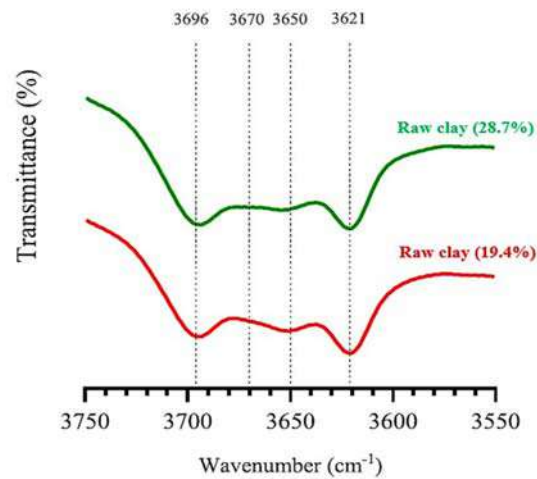


Fig. 3. IR test spectrums of the studied raw clays

Table 1. TGA test results for CCs

Material	Approximate temperature range for dihydroxylation (°C)	Mass loss (%)	Amount of kaolinite from TGA test (%)
CC (19.4%)	540-640	2.71	19.4
CC (28.7%)	420-600	4.00	28.7

Table 2. Chemical characteristics of cementitious materials by XRF analysis

Chemical compounds	SiO ₂	Al ₂ O ₃	Fe ₂ O ₃	CaO	Na ₂ O	K ₂ O	MgO	SO ₃	L.O.I.	Density (gr/cm ³)
PC	21.62	4.29	3.88	64.89	0.41	0.78	2.29	2.41	1.52	3.10
CC (19.4%)	78.71	19.4	0.23	0.04	0.04	0.74	-	0.06	0.60	2.58
CC (28.7%)	71.30	22.6	0.09	2.70	0.05	0.33	0.09	0.01	2.57	2.55
LP	1.78	0.47	0.26	49.9	-	0.32	2.26	0.97	43.83	2.62

The composition of aggregates consisted of 55% sand, 20% fine gravel, and 25% coarse gravel, to be within the range recommended by the National Concrete Regulations. Table 3 shows the maximum size, density, and moisture percentage of aggregate components. Figure 4 shows the aggregate grading curve. Considering that CCs and LP absorb water and reduce the workability of the mixture, and due to the need to keep the ratio of water to binder constant for making samples, using Super Plasticizer (SP) as a chemical admixture was inevitable in this research. The SP admixture used in this research was based on polycarboxylate ether according to the specification of G class of ASTM C494 standard (2020).

2.2. The Process of Preparing Blended Cements

In this research, in addition to ternary blends (including PC, CC, and LP), binary blends (including PC and CC) and a plain mixture containing PC have also been used to compare the results. In total, 13 types of binders were prepared in this research, and 13 mix designs were obtained by keeping

other variables constant. Using low-grade CC with two different purity percentages and three different fineness values has been investigated. The clays were calcined in a furnace at 800 °C, and then the CCs were ground using a laboratory ball mill to make their particle diameter smaller than 4 mm. Low-grade CCs with 19.4% and 28.7% purity were used. CCs were crushed into three levels of fineness using a ball mill. All the CCs were passed through a 100-grade sieve during grinding. The percentage of retaining on the 45-micron sieve was used to measure fineness. The highest fineness, close to the fineness of PC, i.e., the remaining percentage of 8 ± 2 on the 45-micron sieve, was selected. The lowest fineness, the lowest allowed limit according to ASTM regulations, i.e., 32 ± 2 percentage of residue on a 45-micron sieve, and average fineness, $20 \pm 2\%$ residue on a 45-micron sieve, were selected. According to the ASTM standard, the maximum percentage of residue on the 45-micron sieve can be 34%. LP was also ground using a ball mill close to the fineness of PC, i.e., the remaining percentage was 8 ± 2 on a 45-micron sieve.

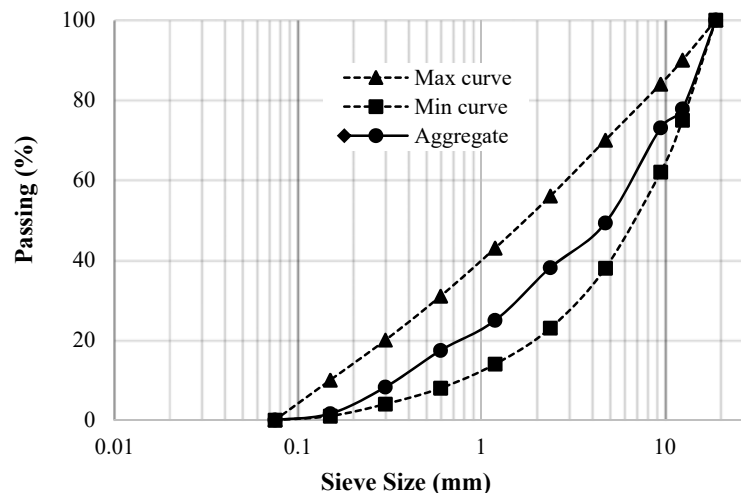
**Fig. 4.** Aggregate grading curve with a maximum size of 19 mm

Table 3. Specifications of aggregates used include, density, water absorption, and moisture content

Aggregate	Maximum size (mm)	Density (gr/cm ³)	SSD (%)	Moisture available (%)
Coarse gravel	19	2.57	1.97	0.27
Fine gravel	12.5	2.55	2	0.5
Sand	9.5	2.54	2.2	0.65

Figure 5 shows the process of calcining, crushing, and grinding of CCs. micron sieve was considered to be

almost similar in the two types of CC, the CC (28.7%) particles were softer than the CC (19.4%) particles.

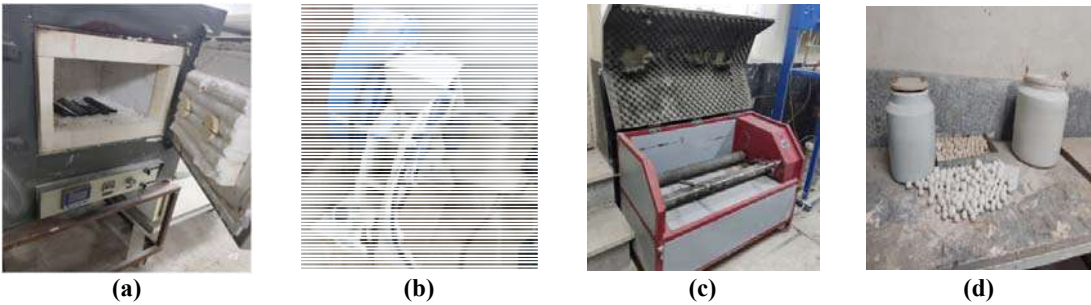


Fig. 5. Preparation of blended cements: a) Calcination of clay in the furnace; b) Crushing machine; c) Grinding machine; and d) Ball mill grinding

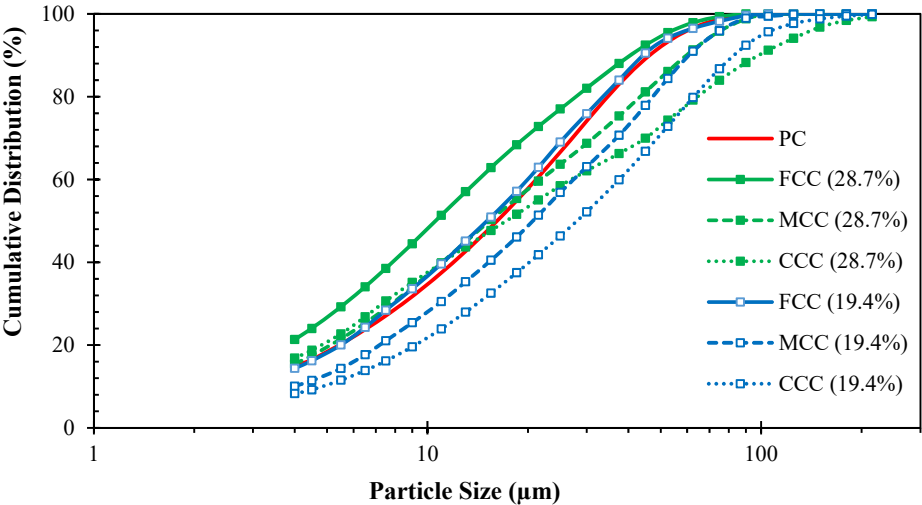


Fig. 6. Comparison of cumulative particle size distribution

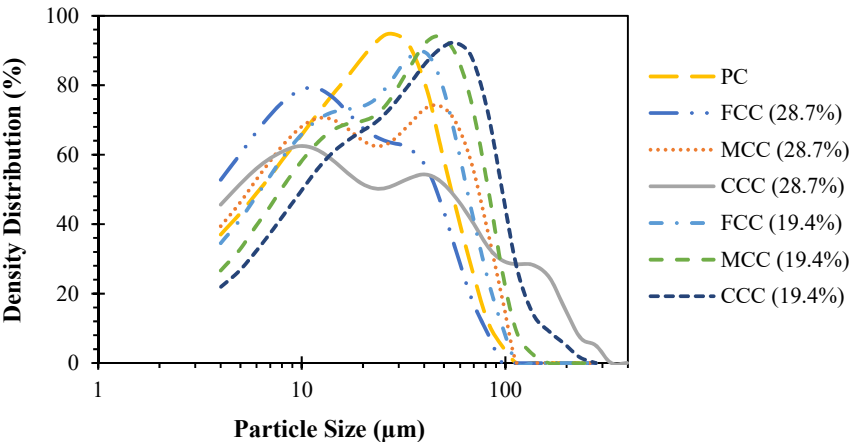


Fig. 7. Comparison of particle size density distribution

2.3. Mixing Procedure

Table 4 shows the design of the mixtures used in this study according to the components. In this study, thirteen concrete mixtures with total binder contents of 400 kg/m³ and a constant water to binder ratio of 0.4 were considered. In binary blends, the amount of PC replaced by CCs was 30%. In ternary blends, the substitution levels of PC were 20% for CCs and 10% for LP. The slumps of all mixtures were adjusted between 30 and 60 mm (S1-S2) using SP.

The dosages of SP have been expressed as weight percentages of binders. The concrete mixing process was done using a 60-liter pan mixer. The following steps outline the sequence for mixing materials and preparing concrete samples:

- Mixing gravel and sand with 1/3 of water for 1 min;
- Adding dry SCMs to the mix and mixing for 0.5 min;
- Adding PC, the remaining water, and mixing for 1.5 min;

- Modifying the slump by incorporating SP and thoroughly mixing for 1.5 min;

- Molding concrete samples and 24 hour-curing under a plastic sheet at room temperature (~25 °C);

- Demolding samples and curing until testing days in a saturated limewater (RH~100%, ~21 °C).

2.4. Test Methods

As previously stated, this research aimed to assess the durability of concretes with varying levels of fineness of low-grade CCs. Therefore, the conducted experiments were divided into three main categories: mechanical properties, permeability, and durability (Figure 8).

2.4.1. Compressive Strength

The compressive strength test (Figure 8c) was performed at 3, 7, 28, 90, and 180 days of curing according to the ASTM C39 standard (2021).

Table 4. Specifications of concrete mix designs (Kg/m³)

Mix. ID	Binders			Gravel	Sand	Water	SP (gr)
	PC	CC	LP				
OPC	400	797.3	-	797.3	967.0	160	60
FC3 (19.4%)	280	787.7	-	787.7	955.3	160	74
MC3 (19.4%)	280	787.7	-	787.7	955.3	160	67
CC3 (19.4%)	280	787.7	-	787.7	955.3	160	67
FC3 (28.7%)	280	788.2	-	788.2	955.9	160	63.9
MC3 (28.7%)	280	788.2	-	788.2	955.9	160	58.1
CC3 (28.7%)	280	788.2	-	788.2	955.9	160	54.2
FLC3 (19.4%)	280	788.2	40	788.2	955.9	160	59.7
MLC3 (19.4%)	280	788.2	40	788.2	955.9	160	55.1
CLC3 (19.4%)	280	788.2	40	788.2	955.9	160	55.4
FLC3 (28.7%)	280	788.6	40	788.6	956.3	160	57.2
MLC3 (28.7%)	280	788.6	40	788.6	956.3	160	54.1
CLC3 (28.7%)	280	788.6	40	788.6	956.3	160	51.3

Note: (F: Fine, M: Medium, C: Coarse), (C3: Calcined Clay Cement), (LC3: Limestone Calcined Clay Cement), (CC: Calcined Clay), (LP: Limestone Powder), (SP: Superplasticizer)

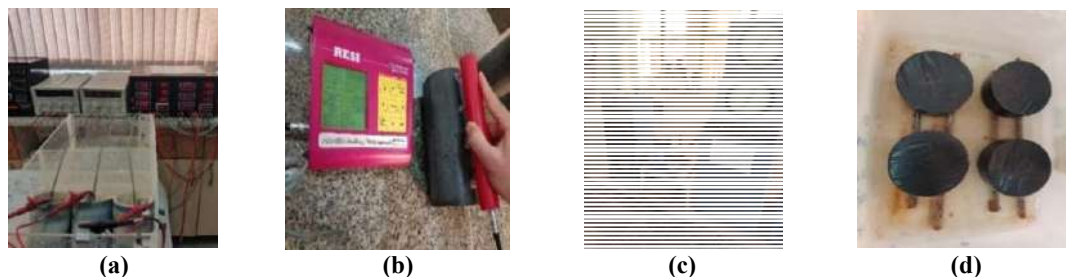


Fig. 8. Pictures of different experiments: a) Chloride ion migration; b) Surface electrical resistance; c) Compressive strength test; and d) Capillary water absorption

Cubic samples with dimensions of 10 cm were stored to test the compressive strength until the test age in saturated lime water. For each test age, the average results of three samples were reported.

2.4.2. Bulk Water Absorption

Bulk water absorption of the samples was conducted based on the BS 1881-122 standard (2020). As mentioned in previous studies (Yadak Yaraghi et al., 2022; Antoni et al., 2012), ettringite exhibits strong stability in LC3 blends attributed to the incorporation of LP and the creation of CO3-AFm compounds, with the presence of this phase noted in matured samples. However, ettringite becomes unstable at temperatures exceeding 50 °C; thus, preparation techniques involving high temperatures are not advised (Scrivener et al., 2018b).

Therefore, following the sample preparation procedure outlined in BS 1881-122 (2020) for water absorption measurement (drying concrete samples for 72 hours at 105 °C) could lead to notable modifications in the microstructure of LC3 binders and affect the mixtures. Consequently, utilizing BS 1881-122 (2020) for evaluating the permeability of LC3 concrete presents significant limitations, and adjustments to the sample preparation method are necessary for this type of mixture.

Alternative techniques, such as extended drying at 50 °C and vacuum drying of specimens, could be considered for the modified water absorption test preparation (Yadak Yaraghi et al., 2022). For this reason, all studied samples were kept at 50 °C for 14 days and then placed in a sealed room for 24 hours to overcome this drawback.

2.4.3. Water Sorptivity

To measure the amount of water sorptivity, disk-shaped samples with a diameter of 10 and a height of 5 cm, which were obtained by cutting cylindrical samples of 20 × 10 cm, were used, and the

test was performed according to the ASTM C1585 standard (2020). First, the samples were kept in an oven at a temperature of 50 °C for 14 days. Then, after weighing, the samples were placed in a container of water, so that the water level was 2 ± 1 mm above the bottom of the samples, while the water with the bottom of the sample should be in complete contact (Figure 8d). It should be noted that after removal from the oven, the samples were completely covered with insulating tape to prevent the absorption of moisture from the environment. For each sample, three specimens were prepared at the ages of 28 and 90 days.

2.4.4. Electrical Resistivity

For this test, cylindrical concrete samples with dimensions of 10 × 20 cm were made and stored in saturated lime solution until the test age. For each mixture design, three samples were tested, and the average results were reported. The electrical resistance results were read in all four directions in each sample. The test was performed according to ASTM C1760 (2021) at 7, 28, 90, and 180 days. Figure 8b shows a picture of this experiment.

2.4.5. Rapid Chloride Migration Test (RCMT)

This test was performed according to NT BUILD 492 (1999) at the ages of 28 and 90 days. One sample was tested for each age. Samples with a diameter of 10 cm and a height of 5 cm obtained by cutting cylindrical samples were tested. Figure 8a shows a view of the RCMT test.

2.4.6. Mercury Intrusion Porosimetry (MIP)

Mercury Intrusion Porosimetry (MIP) was performed on paste samples that had been cured in limewater for 28 days. To stop the hydration process, the samples with dimensions of around 10 × 10 × 3 mm, underwent treatment using the solvent exchange technique outlined in Snellings et al. (2018). Thermo Finnigan Pascal 440 and 140 porosimeters, featuring a maximum

mercury injection pressure of 182 MPa, were employed in this investigation. The contact angle between the solid and mercury was adjusted to 140°, and the surface tension of mercury was determined as 0.480 N/m. These parameters were used to compute the pore radius.

3. Results and Discussion

3.1. Compressive Strength

Figure 9 indicates the compressive strength development of C3 and LC3 concretes between 3 and 91 days. At all ages, the compressive strengths of all concretes containing CCs were lower than OPC concrete. It can be due to the dilution effect of using 30% SCMs (20% CC + 10% LP) instead of clinker (Yadak Yaraghi et al., 2022).

As it is illustrated, C3 mixtures containing CC (28.7%) showed higher compressive strength in comparison with CC (19.4%) binary mixtures. Elevating the kaolinite content in CCs typically leads to enhanced compressive strengths of C3 concretes. This improvement can be primarily attributed to the increased reactivity of CCs, particularly when they possess higher purity levels of MK (Zolfagharnasab et al., 2021). However, in LC3 concretes, there was no remarkable difference between compressive strength results of CC (19.4%) and CC (28.7%) ternary mixtures. Comparing the results of

binary and ternary samples containing CCs, ternary LC3 (19.4%) concretes had a compressive strength comparable to that of binary C3 (19.4%) concretes. In comparison, the compressive strength of LC3 (28.7%) concretes was lower than corresponding C3 concretes. The comparable compressive strength of C3 and LC3 concretes containing low-grade CC (19.4%) attributed to the filling effect of LP and the reactions of alumina-containing phases in CCs with CaCO_3 from LP (synergic reactions) leads to the formation of additional $\text{CO}_3\text{-AFm}$ phases. Therefore, it appears that in LC3 (19.4%) mixtures, the filler effect of LP and synergistic reactions may compensate for the lower pozzolanic reactivity of CC at 19.4%. However, when CC content is increased to 28.7%, the impact of the pozzolanic reaction on compressive strength may outweigh the positive effects of using LP and CC together. Specifically, replacing 20% of OPC with CC in LC3 (28.7%) mixtures could result in the formation of fewer pozzolanic hydrates compared to binary mixtures containing 30% CC (Bahman-Zadeh et al., 2023). In order to understand the effect of the fineness of CC particles on C3 and LC3 concretes, the relative compressive strength of each mixture compared to their corresponding mixtures with the highest fineness of CCs (i.e., FC3 or FLC3 mixtures) is demonstrated in Figure 10.

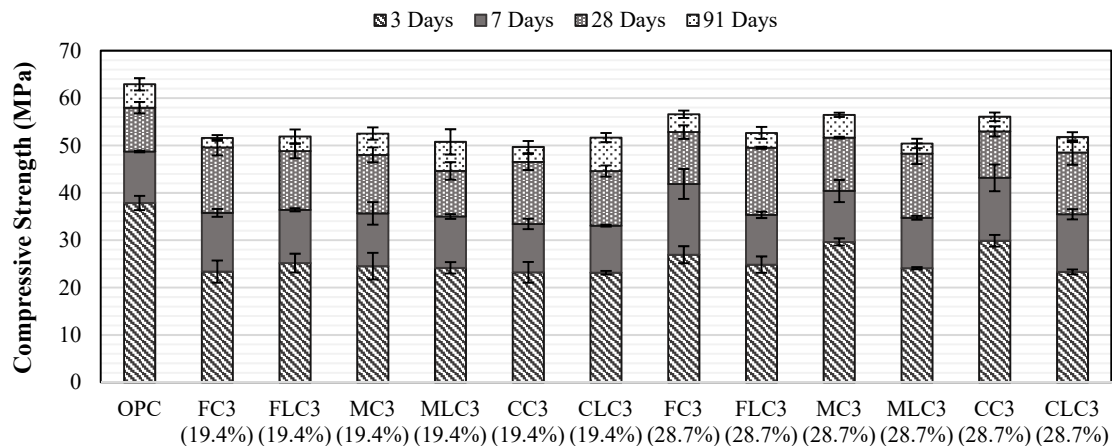


Fig. 9. Compressive strength of studied mixtures

Generally, the coarser CCs containing mixtures showed less compressive strength than finer CCs mixtures. The fineness of CCs had more influence at early ages, so the difference between the minimum and maximum relative compressive strengths of mixtures varied from 19% to 6% at 3 and 91 days, respectively. The better early age-compressive strength of finer CC mixtures can be attributed to the smaller PSD of CC, which can lead to improved particle packing, and fills the gaps between clinker grains (Poon et al., 2001). Additionally, the finer CC particles can act as nucleation sites, promoting nucleation effects and potentially enhancing the overall performance of the cementitious system (Andrés et al., 2015). However, the results confirmed that the coarser CCs obtained by

less grinding time and energy consumption had great potential of being used in C3 and LC3 concretes in terms of compressive strength.

3.2. Bulk Water Absorption

The results of the water absorption test are shown in Figure 11. According to the results, incorporating CCs (either in binary or ternary binders) led to increased permeability by up to 34% compared to the OPC mixture. These findings are in contradiction with the results of Zolfagharnasab et al. (2021), and Yadak Yaraghi et al. (2022), which reported lower water absorption for CCs mixtures. These contradictory results can be attributed to differences in test methods.

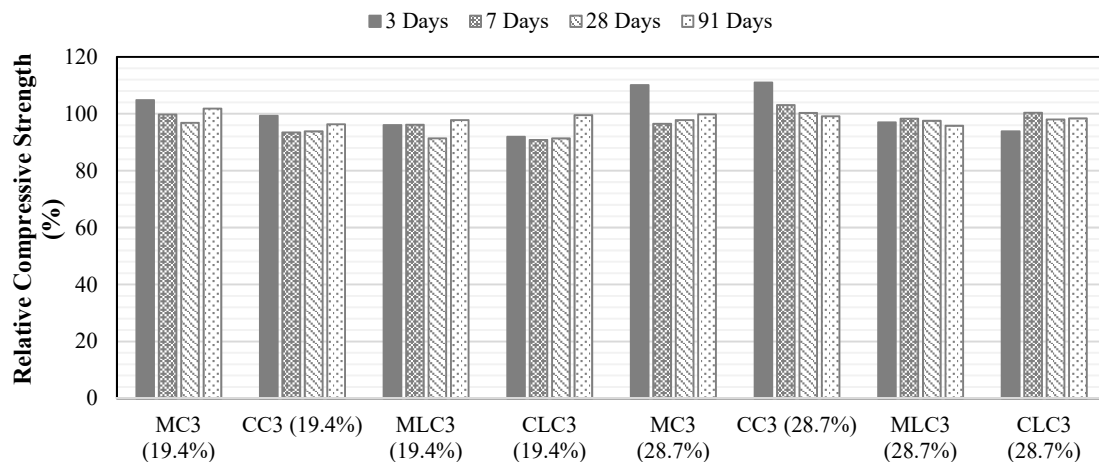


Fig. 10. Relative compressive strength of mixtures compared to the corresponding mixture with the finest CCs

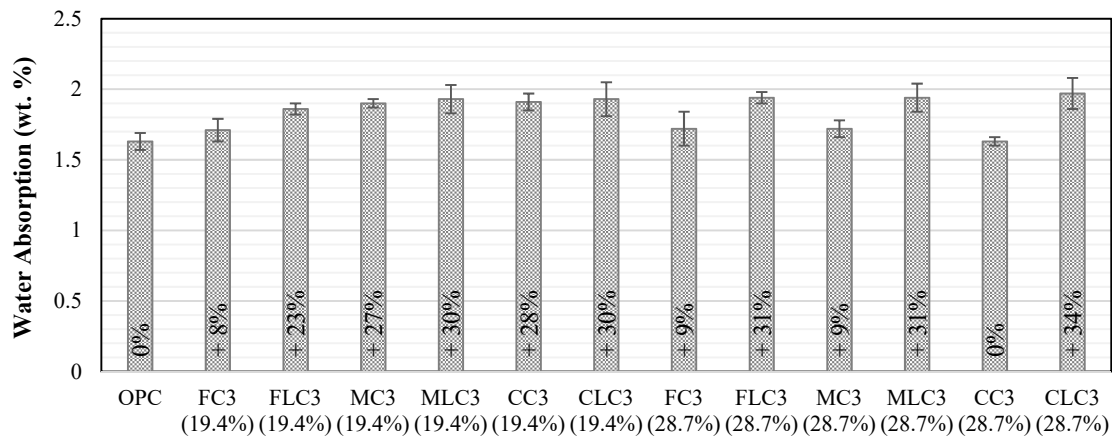


Fig. 11. 28-day water absorption values and difference with OPC mixture

Both of them (Zolfagharnasab et al., 2021; Yadak Yaraghi et al., 2022) have determined that using the BS 1881-122 (2020) method may change the hydrated cement system and result in inaccuracies when assessing permeability. The lower water absorption of binary blends containing CCs compared to their counterpart ternary mixtures is primarily due to the higher amounts of CCs in C3 concretes and the greater formation of pozzolanic products. This enhancement is more noticeable in the CC (28.7%) mixtures, which was up to 34% difference between CC3 (28.7%) and CLC3 (28.7%).

Moreover, because of the higher pozzolanic reactivity of CC (28.7%) compared to CC (19.4%), the water absorption rates of CC (28.7%) mixtures were slightly lower than those of CC (19.4%) blends. It can be concluded that the blends made with the finer CCs exhibited a little less and almost identical water absorption values compared to the coarser CCs. The water absorption of mixtures with the highest fineness of CC, including FC3 (19.4%), FLC3 (19.4%), and FLC3 (28.7%) was 20%, 7%, and 3% lower than CC3 (19.4%) and CLC3 (19.4%), respectively.

However, in FC3 (28.7%), the water absorption was 9% higher than in CC3 (28.7%). This exception can be due to the agglomeration of finer platy particles of CC around the clinker grains which resulted in higher permeability (Andrés et al., 2015).

3.3. Water Sorptivity

Table 5 illustrates the initial and secondary rates of water absorption after 28 and 91 days of curing. According to the findings, the water sorptivity of the mixtures is reduced as the curing time advances, as a result of the completion of hydration reactions of cementitious materials that alter the micro-pore structure and diminish the water transport rate of capillary suction. From 28 to 91 days of curing, the initial rate of water absorption for OPC, C3 binary, and LC3 ternary concretes has been reduced by up to 33%, 53%, and 45%, and the secondary rate of water absorption reduced by up to 36%, 72%, and 54%, respectively. As a general deduction, all C3 binary mixtures except MC3 (19.4%) and CC3 (19.4%) showed lower initial and secondary rates of water absorption after 91 days. Nevertheless, until 28 days, only binary mixtures including FC3 (19.4%), FC3 (28.7%), and CC3 (28.7%) had similar or lower initial and secondary rates of water absorption. These can be due to the filling effect of the finer particles in the cementitious matrix of binary mixtures containing the finest CCs in FC3 (19.4%) and FC3 (28.7%), and the highest content of MK in CC3 (28.7%) and FC3 (28.7%) mixtures. Generally, LC3 ternary mixtures had more S_i and S_s relative to their corresponding C3 binary mixtures, which can be attributed to the lower content of CCs in LC3 mixtures.

Table 5. Initial and secondary rates of water absorption

Mixture ID	28 Days		91 Days	
	$S_i \times 10^{-4}$ (mm/ \sqrt{s})	$S_s \times 10^{-4}$ (mm/ \sqrt{s})	$S_i \times 10^{-4}$ (mm/ \sqrt{s})	$S_s \times 10^{-4}$ (mm/ \sqrt{s})
OPC	128.7	33.9	85.7	21.9
FC3 (19.4%)	134.0	21.4	63.1	11.7
FLC3 (19.4%)	166.7	37.7	101.6	21.8
MC3 (19.4%)	142.9	41.2	96.6	11.4
MLC3 (19.4%)	157.6	34.7	99.6	24.9
CC3 (19.4%)	136.6	36.1	100.7	15.2
CLC3 (19.4%)	159.0	34.4	98.3	25.8
FC3 (28.7%)	133.3	17.9	78.6	10.6
FLC3 (28.7%)	137.1	34.1	84.7	29.9
MC3 (28.7%)	140.3	36.4	84.4	12.9
MLC3 (28.7%)	175.2	22.8	96.6	27.4
CC3 (28.7%)	112.8	36.3	76.9	10.5
CLC3 (28.7%)	150.4	33.1	136.5	15.2

Note: S_i : Initial rates of water absorption, S_s : Secondary rates of water absorption

In binary blends containing CC (19.4%) and ternary blends containing CC (28.7%), the initial rate of water absorption decreased with increasing the fineness of CCs; however, in other cases, it remained almost constant.

3.4. Electrical Resistivity

Figure 12 shows the surface electrical resistivity of concretes. The electrical resistivity of concrete is directly influenced by the permeability, the ionic composition of the pore solution, and the connectivity of pores in the concrete microstructure (Ramezani-pour et al., 2011). At 7 days, the electrical resistivity of C3 binary blends incorporating CC (19.4%) was up to 10.3% lower than that of the OPC mixture. It can be due to the dilution effect, pozzolanic reactivity, and lower kaolinite content of CC (19.4%) at early ages. Besides, C3 binary concretes containing CC (28.7%) showed higher electrical resistivity compared to binary CC (19.4%) mixtures by about 1.5 times after 91 days. After 28 and 91 days of curing, all CC containing concretes displayed higher electrical resistivity. This enhancement is primarily associated with the refinement of the concrete's pore structure, as well as the

increased tortuosity of the paths for ion transport within the concrete pore solution (Du and Dai Pang, 2020). All ternary LC3 concretes demonstrated lower electrical resistivity in comparison with their corresponding binary mixtures. This difference was more remarkable between binary and ternary concretes containing CC (28.7%). It seems that the replacement of LP in LC3 concretes resulted in lower electrical resistivity due to the lower kaolinite content of ternary binders as opposed to binary mixtures, as also reported by Yadak Yaraghi et al. (2022). In comparison with three different fineness of CCs, Figure 13 showed that the binary and ternary binders demonstrated slightly better electrical resistance relative to coarser CC particles mixtures. In other words, at 91 days, the electrical resistivity of FC3 (19.4%), FLC3 (19.4%), FC3 (28.7%), and FLC3 (28.7%) was 6%, 7%, 1%, and 4% than those of CC3 (19.4%), CLC3 (19.4%), CC3 (28.7%), and CLC3 (28.7%), respectively. Thus, the mixtures with lower fineness (coarser particles) of CCs had comparable electrical resistivity while using less energy consumption and grinding time compared to higher fineness (finer particles) mixtures containing CCs.

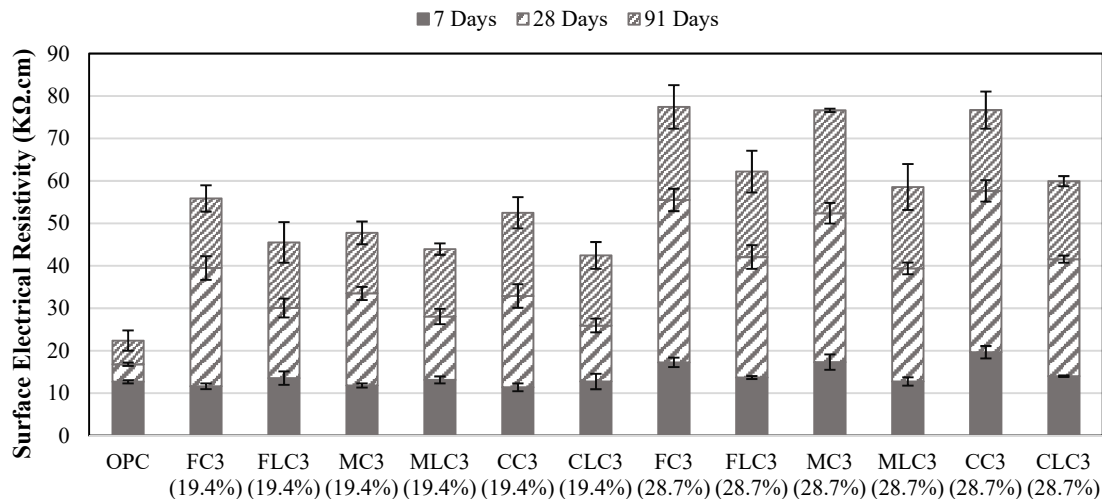


Fig. 12. Surface electrical resistivity of concrete mixtures

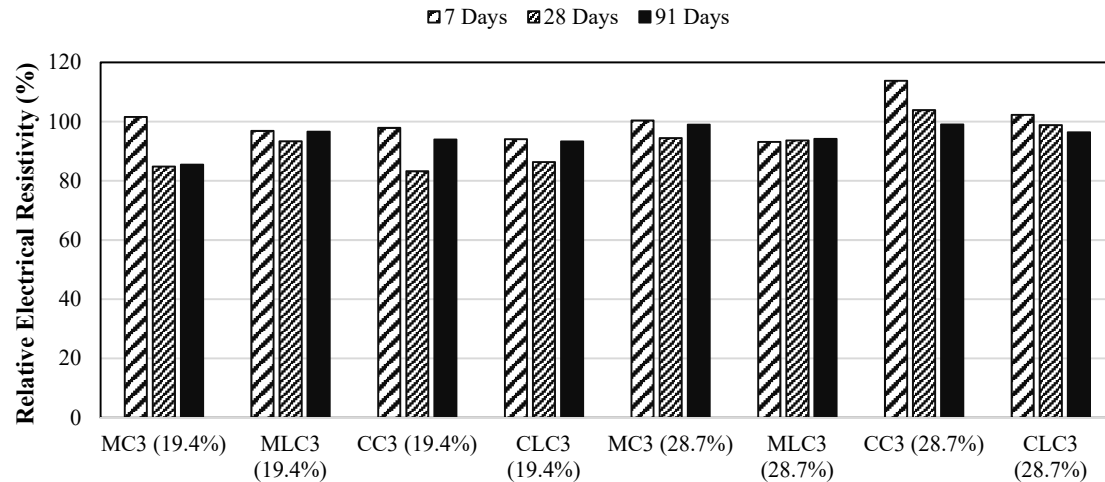


Fig. 13. Relative electrical resistivity of mixtures compared to the corresponding mixture with the finest CCs

3.5. Rapid Chloride Migration Test (RCMT)

The RCMT results for concrete specimens after 28 and 91 days of curing are demonstrated in Figure 14. The results show that a 30% replacement of PC drastically reduced the D_{nssm} values for concretes incorporating SCMs, especially at 90 days. The C3 binary mixtures containing CC (19.4%) outperformed the counterpart ternary LC3 mixtures at 28 and 91 days. In binary and ternary blends containing CC (28.7%), LC3 mixtures had comparable D_{nssm} values at 28 days, but after 91 days of curing, C3 mixtures showed lower D_{nssm} relative to LC3 concretes. This could

suggest that the creation of carboaluminate compounds was not sufficient to offset the impact of using reduced amounts of low-grade CC in LC3 mixtures (Yadak Yaraghi et al., 2022). As expected, the C3 and LC3 concretes containing the higher kaolinite content of CC (28.7%) had remarkably reduced the chloride coefficient compared to CC (19.4%) containing mixtures. As for the various fineness of CCs mixtures, the results in Figure 15 revealed that the chloride ions migration coefficient of mixtures with the coarser particles were from 81-107% and 100-134% of their counterpart mixtures with the finest CC particles at 28 and 91 days, respectively.

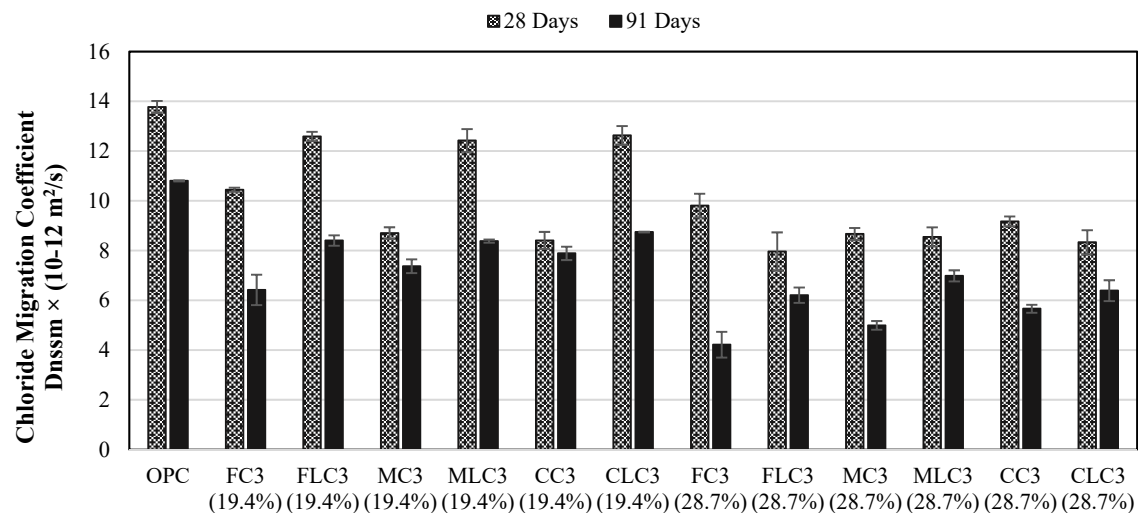


Fig. 14. Results of the rapid chloride migration test

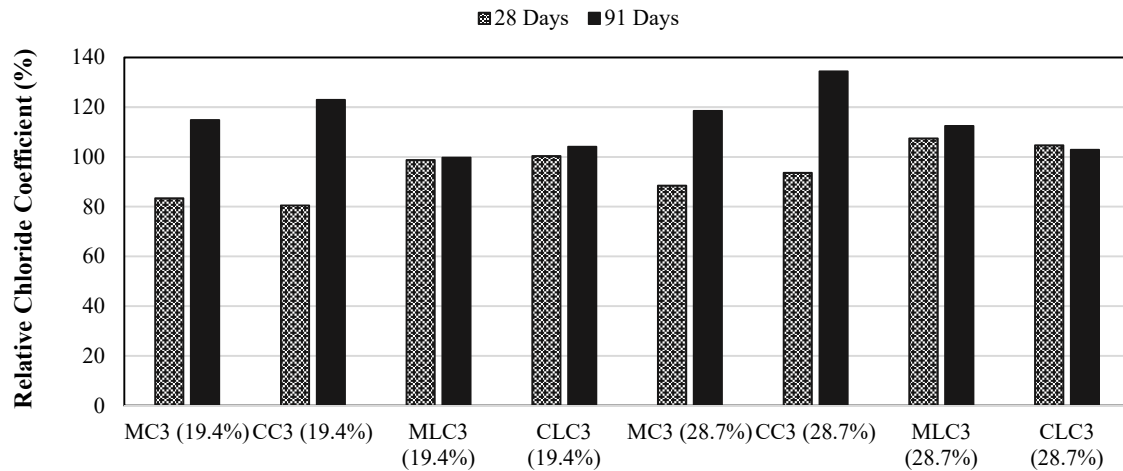


Fig. 15. Relative chloride ions migration coefficient of mixtures compared to the corresponding mixture with the finest CCs

Therefore, by the progress of cementitious materials' hydration and pozzolanic reaction at later ages, the durability of mixtures containing the lower fineness of CC against chlorides was enhanced significantly compared to their corresponding mixtures with higher fineness. In C3 and LC3 concretes, the

fineness of low-grade CCs was more effective in the reduction of D_{nssm} values at early ages until 28 days.

3.6. Mercury Intrusion Porosimetry (MIP)

The cumulative intrusion of mercury in cementitious pastes is shown in Figure 16.

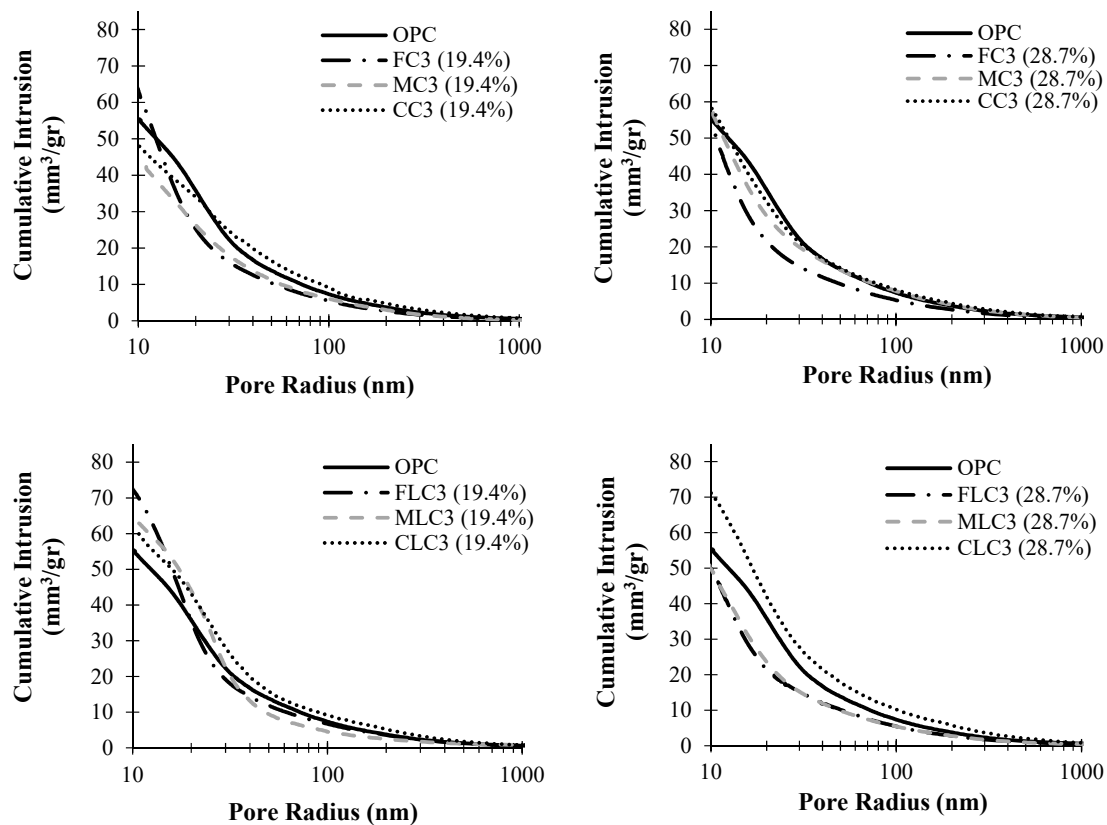


Fig. 16. MIP results of CC pastes in comparison with PC paste

Generally, the C3 binary pastes exhibited a more refined pore structure and finer pore connectivity compared to the OPC paste. In addition, in LC3 ternary pastes (except for CLC3 (19.4%) and CLC3 (28.7%) due to the coarser particles of CC), the impermeability of pastes was enhanced in comparison with the control paste. According to the results, the blends made with finer CCs (i.e., FC3 and FLC3) demonstrated a lower total porosity and significantly greater pore refinement compared to the blend containing coarser CCs. This pore refinement may be attributed to the combined effect of enhanced particle packing resulting from a much smaller PSD, which could fill the gaps between cement grains (Poon et al., 2001) and the higher pozzolanic reaction of the CCs, as similarly stated by other researchers (Andrés et al., 2015; Bahman-Zadeh et al., 2022). The pozzolanic hydrates formation in the pastes containing CC may contribute to the densification of the microstructure and pore refinement (Bahman-Zadeh et al., 2022). In addition, the threshold pore diameter (as defined in Scrivener et al. (2018b) and average pore diameter of pastes are given in Table 6. It can be seen that by increasing the fineness of CCs in binary and ternary blends, the average diameter of pores had changed towards smaller values, and a reduced threshold pore diameter was achieved. In addition, the C3 binary pastes had smaller average pore diameters than their corresponding LC3 ternary blends.

A similar trend for threshold pore diameter has been observed for binary and ternary binders containing CCs except for MC3 (19.4%) and CC3 (19.4%) relative to their corresponding LC3 pastes. Also, the average pore diameter of all CC containing pastes was smaller than OPC paste (19.4 nm) except for MLC3 (19.4%) and CLC3 (19.4%), which were 25.2 and 26.1 nm, respectively. In addition, based on the results in Table 6, the threshold and average pore diameters of mixtures containing CC (28.7%) were smaller than CC (19.4%) mixtures. This further refinement of the porosity in higher kaolinite content CC pastes was observed in previous studies (Avet and Scrivener, 2018; Bahman-Zadeh et al., 2022).

3.7. Discussion

In this study, a Distance-Based Approach (DBA) (Kashi et al., 2017) is utilized for comparing different mix designs and achieving an optimal design. In this technique, the first step is to determine the decision criteria. Two criteria of strength and durability have been selected as decision criteria. The durability criterion includes various experimental results such as bulk water absorption, water sorptivity, electrical resistivity, RCMT, and MIP.

Table 7 illustrates the normalized values of decision criteria. After determining the decision criteria, they need to be standardized for calculating the distance index.

Table 6. Threshold and average pore diameters of the studied mixtures

Mixture ID	Threshold pore diameter (nm)	Average pore diameter (nm)
OPC	50.6	19.4
FC3 (19.4%)	26.6	11.6
MC3 (19.4%)	54.7	11.5
CC3 (19.4%)	110.2	10.0
FLC3 (19.4%)	32.9	17.0
MLC3 (19.4%)	43.3	25.2
CLC3 (19.4%)	69.1	26.1
FC3 (28.7%)	27.1	11.3
MC3 (28.7%)	37.0	10.5
CC3 (28.7%)	42.5	12.6
FLC3 (28.7%)	26.7	11.7
MLC3 (28.7%)	39.5	10.2
CLC3 (28.7%)	59.2	16.4

Table 7. Normalized values of different decision parameters

Criterion	Strength		Durability			
	Mix. ID	Compressive strength	Bulk water absorption	Water sorptivity	Electrical resistivity	RCMT MIP
	OPC	2.70	1.63	0.50	-1.95	-2.18 -0.84
	FC3 (19.4%)	-0.43	0.98	1.66	-0.02	0.11 0.61
	FLC3(19.4%)	-0.29	-0.25	-1.17	-0.65	-1.12 0.63
	MC3 (19.4%)	-0.40	-0.57	-0.13	-0.51	0.34 0.91
	MLC3(19.4%)	-0.81	-0.82	-0.85	-0.79	-1.06 -0.39
	CC3 (19.4%)	-0.92	-0.65	-0.03	-0.38	0.28 -1.92
	CLC3 (19.4%)	-0.95	-0.82	-0.87	-0.93	-1.23 -2.09
	FC3 (28.7%)	0.76	0.90	1.37	1.49	0.95 0.67
	FLC3 (28.7%)	-0.29	-0.90	0.05	0.36	0.91 0.82
	MC3 (28.7%)	0.75	0.90	0.39	1.35	1.06 0.43
	MLC3(28.7%)	-0.61	-0.90	-1.00	0.11	0.50 0.59
	CC3 (28.7%)	1.01	1.63	1.48	1.62	0.71 0.87
	CLC3 (28.7%)	-0.51	-1.14	-1.38	0.28	0.74 -0.28

Ultimately, the distance between each alternative for the optimal state is derived from Eq. (1).

$$D_k = \left\{ \sum_j [W_j * (z_{kj} - z_{*j})]^2 \right\}^{0.5} \quad (1)$$

where k: is the number of alternatives; D_k : is distance index for the k^{th} alternative; j : is the number of criteria; z_{kj} : is the standardized value of the k^{th} alternative with respect to criterion j ; z_{*j} : is the benchmark value of criterion j and W_j : is the weight of criterion j .

Another point regarding calculating the distance index is that different criteria need to be weighted to determine their importance. Various weighting scenarios are considered. Equal importance between two criteria and considering only one criterion are among the investigated scenarios. Furthermore, Figure 17 depicts the changes in the distance index for different mix designs based on different weights. According to the DBA concept, the optimal alternative has the lowest distance index. According to the results in Table 8, the mixture of OPC will be the best design when the importance of both decision criteria is equal. Among clay-containing specimens, the binary combination CC3 (28.7%) shows the best

performance considering both strength and durability criteria. Considering only the strength criterion, the OPC sample outperforms the binary and ternary mixtures containing CC considerably. This is due to the decrease in strength caused by using CCs. Also, as indicated by the durability criterion, FC3 (19.4%), CC3 (28.7%), and FC3 (28.7%) will be the best mixtures. The finer particle size and higher grade of CC-containing mixtures have improved the performance. However, among ternary mixtures containing CC and LP, FLC3 (28.7%) will be the best mixture.

In general, according to the results in Table 8 and Figure 17, increasing the fineness and grade of CCs in mixtures reduces their distance index, and they exhibit better performance in various tests.

Only in the CC3 (28.7%) sample, the effect of increasing particle size was not observed in the results. Additionally, the distance index for all ternary mixtures increased compared to their corresponding binary mixtures, indicating decreased strength and durability. According to the results in Figure 17a, with an increase in the importance of strength, FC3 (19.4%) preferred relative to the OPC mixture. When the weight of the strength criterion is less (more important to the durability criterion), binary mixtures containing CC with a grade of 28.7% will be preferable.

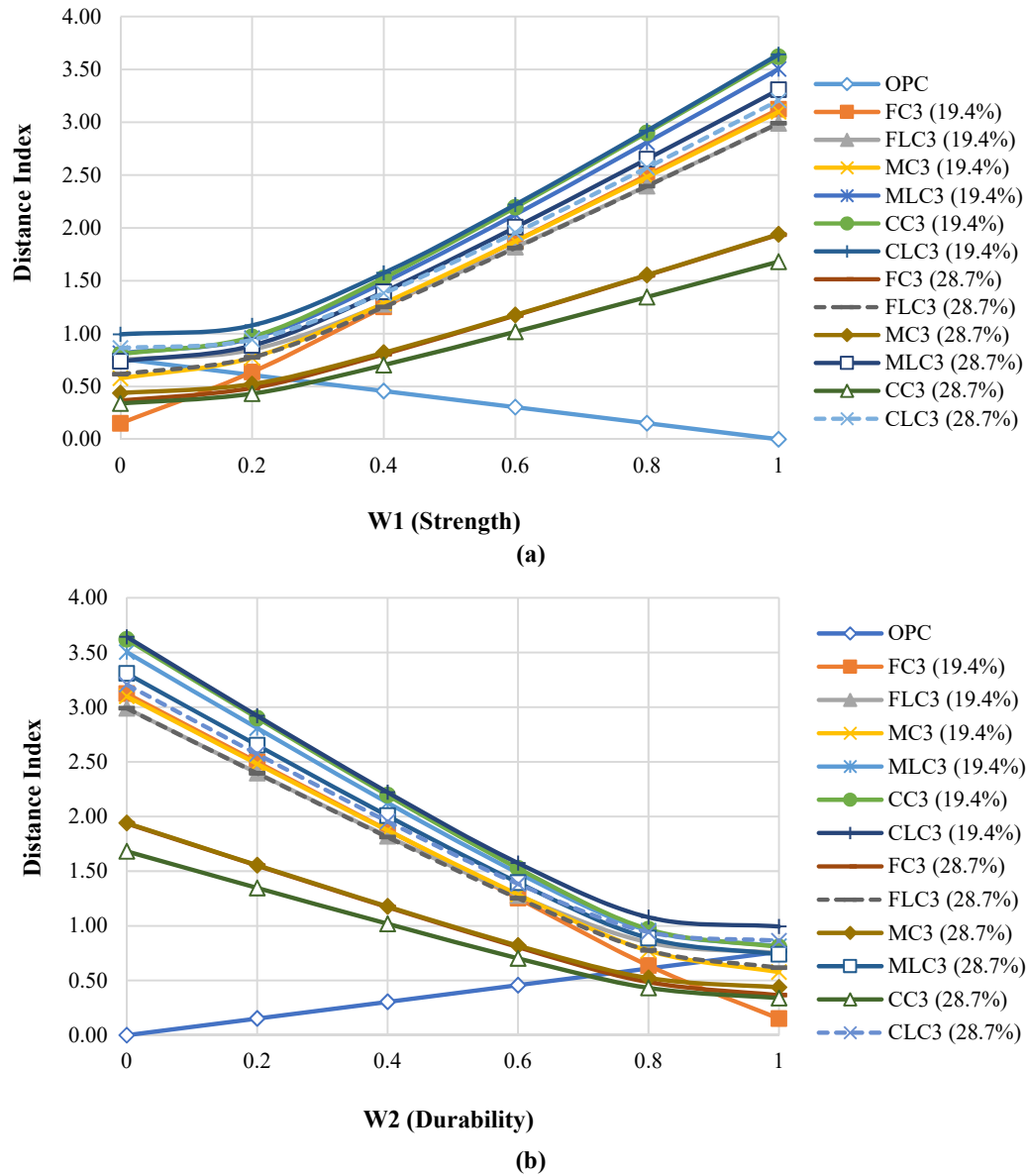


Fig. 17. Distance index values according to different weighting: a) Strength criterion; and b) Durability criterion

Table 8. Distance index for different W_j

Mix. ID / W_j	$W_1 = W_2 = 0.5$	$W_1 = 1$	$W_2 = 1$
OPC	0.38	0.00	0.76
FC3 (19.4%)	1.56	3.12	0.15
FLC3 (19.4%)	1.54	2.99	0.75
MC3 (19.4%)	1.58	3.10	0.58
MLC3 (19.4%)	1.80	3.50	0.81
CC3 (19.4%)	1.85	3.62	0.81
CLC3 (19.4%)	1.89	3.64	0.99
FC3 (28.7%)	0.99	1.94	0.37
FLC3 (28.7%)	1.53	2.99	0.62
MC3 (28.7%)	0.99	1.94	0.44
MLC3 (28.7%)	1.69	3.31	0.74
CC3 (28.7%)	0.86	1.68	0.34
CLC3 (28.7%)	1.66	3.21	0.86

FC3 (19.4%) will have the lowest distance index when the weight is less than 0.1. In the distance of 0.1-0.3 (weight of strength), CC3 with a 28.7% grade will be better. According to the results, a significant difference in the distance index between binary and ternary mixtures is observed. This is due to the effect of adding LP in ternary blends of LC3 concrete. Due to considering two decision criteria, the interpretation of the results in Figure 17b is very similar to Figure 17a. Only when the importance of the durability criterion exceeds 0.7, the results obtained for samples containing CC with the lower grade will be the preferred option.

However, it is necessary to mention that the environmental impact of using CC compared to Portland cement is considerable, and further studies need to consider other criteria such as environmental and economic assessments, including carbon footprint, energy consumption, and cost.

4. Conclusions

This study mainly focused on the effect of the fineness of low-grade calcined clays (CCs) on their reactivity in binary and ternary concretes. For this purpose, two kaolinitic low-grade CCs were ground by a laboratory ball mill to achieve three fineness values of $\sim 8 \pm 2$, 20 ± 2 , and 32 ± 2 wt% retaining on a 45 μ m sieve, named fine, moderate, and coarse CCs, respectively.

Experimental investigations of binders with the 30% substitution of the PC by CCs (C3 binary blends) or combined 20% CCs and 10% LP (in LC3 ternary blends) were compared with the control mixture without CCs and LS. It is worth noting that the experiments were conducted in a controlled laboratory environment, so the results may not completely represent how the C3 and LC3 concretes would perform in actual construction situations. The following conclusions can be drawn:

- Utilizing low-grade CCs (kaolinite

contents < 30wt%) in C3 and LC3 concretes resulted in lower compressive strength, higher water absorption, higher electrical resistivity, and lower chloride ions migration coefficient than PC concrete.

- Binary blends incorporating higher kaolinite content CC (28.7%) showed superior performance in comparison with corresponding LC3 concretes in terms of compressive strength, bulk water absorption, and electrical resistivity.

However, in binary and ternary blends containing CC (19.4%), the difference between these results was insignificant.

- Regarding RCMT results, the C3 binary mixtures containing CC (19.4%) outperformed the counterpart ternary LC3 mixtures at 28 and 91 days. In binary and ternary blends containing CC (28.7%), LC3 mixtures had comparable D_{nssm} values at 28 days, but after 91 days of curing, C3 mixtures showed lower D_{nssm} relative to LC3 concretes.

- Regarding the chloride ions migration coefficient of mixtures with various fineness of CCs, results revealed that the chloride ions migration coefficient of mixtures with the coarser particles were 81-107% and 100-134% of their counterpart mixtures with the finest CC particles at 28 and 91 days, respectively.

- Based on MIP results, the blends made with the highest fineness of CCs demonstrated a lower total porosity and a considerably greater pore refinement compared to the blend made with the coarser CCs. This can be attributed to the filling effect and higher pozzolanic reaction of the highest fineness-containing mixtures.

- Substitution of finer low-grade CCs in C3 and LC3 mixtures had a marginal improvement in the compressive strength, bulk water absorption, and electrical resistivity by up to 4.7, 5.2, and 14.5% relative to coarser low-grade CCs mixtures, respectively. In other words, the mixtures with the CCs' fineness of $\sim 32 \pm 2$ wt% retaining on 45 μ m sieve performed a comparable compressive strength, bulk water absorption, and electrical resistivity

with the counterpart mixtures containing CCs with higher fineness of $8 \pm 2\text{wt}\%$ retaining on 45 μm sieve.

- Overall, C3 and LC3 concretes containing low-grade CCs with the fineness of $\sim 32 \pm 2\text{wt}\%$ retaining on 45 μm sieve obtained using less grinding time and energy consumption delivered a satisfactory mechanical and durability performance compared to their corresponding CC mixtures with the fineness of $\sim 8 \pm 2\text{wt}\%$ retaining on 45 μm sieve.

- According to the results of the distance index, mixtures containing low-grade CCs will be the more suitable option compared to the control mixture, when the importance of durability exceeds approximately 70%. This percentage will change with changes in decision criteria and alterations in the grade of CCs.

5. References

- Afzali-Naniz, O., Mazloom, M. and Karamloo, M. (2021). "Effect of nano and micro SiO₂ on brittleness and fracture parameters of self-compacting lightweight concrete", *Construction and Building Materials*, 299(13), 124354, <https://doi.org/10.1016/j.conbuildmat.2021.124354>.
- Andrés, L.M., Antoni, M.G., Alujas Diaz, A., Martirena Hernandez, J.F. and Scrivener, K.L. (2015). "Effect of fineness in clinker-calcined clays-limestone cements", *Advances in Cement Research*, 27(9), 546-556, <https://doi.org/10.1680/jadcr.14.00095>.
- Antoni et al. (2012). "Cement substitution by a combination of metakaolin and limestone", *Cement and Concrete Research*, 42(12), 1579-1589, <https://doi.org/10.1016/j.cemconres.2012.09.006>.
- ASTM C150/C150M-20. (2020). "Standard Specification for portland cement", *ASTM International*, West Conshohocken, PA, https://www.astm.org/c0150_c0150m-20.html.
- ASTM C1585-20. (2020). "Standard test method for measurement of rate of absorption of water by hydraulic-cement concretes", *ASTM International*, West Conshohocken, PA, <https://www.astm.org/c1585-20.html>.
- ASTM C1760-12. (2021). "Standard test method for bulk electrical conductivity of hardened concrete", *ASTM International*, West Conshohocken, PA, <https://www.astm.org/c1760-12.html>.
- ASTM C39/C39M-21. (2021). "Standard test method for compressive strength of cylindrical concrete specimens", *ASTM International*, West Conshohocken, PA, https://www.astm.org/c0039_c0039m-20.html.
- ASTM C494/C494M-17. (2020). "Standard specification for chemical admixtures for concrete", *ASTM International*, West Conshohocken, PA, <https://www.astm.org/c0494c0494m-17.html>.
- Avet, F. and Scrivener, K. (2018). "Investigation of the calcined kaolinite content on the hydration of limestone calcined clay cement (lc3)", *Cement and Concrete Research*, 107, 124-135, <https://doi.org/10.1016/j.cemconres.2018.02.016>.
- Ayati, B., Newport, D., Wong, H. and Cheeseman, C. (2022). "Low-carbon cements: potential for low-grade calcined clays to form supplementary cementitious materials", *Cleaner Materials*, 5, 100099, <https://doi.org/10.1016/j.clema.2022.100099>.
- Bahman-Zadeh, F., Ramezaniapour, A.A. and Zolfagharnasab, A. (2022). "Effect of carbonation on chloride binding capacity of limestone calcined clay cement (lc3) and binary pastes", *Journal of Building Engineering*, 52, 104447, <https://doi.org/10.1016/j.jobbe.2022.104447>.
- Bahman-Zadeh, F., Zolfagharnasab, A., Pourebrahimi, M., Mirabrishami, M. and Ramezaniapour, A.A. (2023). "Thermodynamic and experimental study on chloride binding of limestone containing concrete in sulfate-chloride solution", *Journal of Building Engineering*, 66, 105940, <https://doi.org/10.1016/j.jobbe.2023.105940>.
- Barata, M.S. and Angélica, R.S. (2011). "Pozzolanic activity of kaolin wastes from kaolin mining industry from the amazon region", *Matéria (Rio de Janeiro)*, 16, 797-810, <https://doi.org/10.1590/S1517-70762011000300007>.
- Bishnoi, S., Maity, S., Kumar, M., Saxena, S.K. and Wali, S.K. (2018). "Pilot scale production of limestone calcined clay cement", *Calcined Clays for Sustainable Concrete: Proceedings of the 2nd International Conference on Calcined Clays for Sustainable Concrete*, 69-74, https://doi.org/10.1007/978-94-024-1207-9_12.
- BS 1881-122. (2020). "Testing concrete method for determination of water absorption", <https://standardsdevelopment.bsigroup.com/projects/2020-01169>.
- Díaz, Y.C., Berriel, S.S., Heierli, U., Favier, A.R., Machado, I.R.S., Scrivener, K.L., Hernández, J.F.M. and Habert, G. (2017). "Limestone calcined clay cement as a low-carbon solution to

- meet expanding cement demand in emerging economies”, *Development Engineering*, 2, 82-91, <https://doi.org/10.1016/j.deveng.2017.06.001>.
- Du, H. and Dai Pang, S. (2020). “High-performance concrete incorporating calcined kaolin clay and limestone as cement substitute”, *Construction and Building Materials*, 264, 120152, <https://doi.org/10.1016/j.conbuildmat.2020.120152>.
- Dumani, N. and Mapiravana, J. (2020). “Evaluation of age strengths of metakaolin blend pastes with varying fineness of grind”, *Calcined Clays for Sustainable Concrete: Proceedings of the 3rd International Conference on Calcined Clays for Sustainable Concrete*, 339-348, <https://doi.org/10.1007/978-981-15-2806-440>.
- Fernandez, R., Martirena, F. and Scrivener, K.L. (2011). “The origin of the pozzolanic activity of calcined clay minerals: a comparison between kaolinite, illite and montmorillonite”, *Cement and Concrete Research*, 41(1), 113-122, <https://doi.org/10.1016/j.cemconres.2010.09.013>.
- Ferreiro, S., Canut, M.M.C., Lund, J. and Herfort, D. (2019). “Influence of fineness of raw clay and calcination temperature on the performance of calcined clay-limestone blended cements”, *Applied Clay Science*, 169, 81-90, <https://doi.org/10.1016/j.clay.2018.12.021>.
- Ferreiro, S., Herfort, D. and Damtoft, J.S. (2017). “Effect of raw clay type, fineness, water-to-cement ratio and fly ash addition on workability and strength performance of calcined clay - Limestone Portland cements”, *Cement and Concrete Research*, 101, 1-12, <https://doi.org/10.1016/j.cemconres.2017.08.003>.
- Gettu, R., Patel, A., Rathi, V., Prakasan, S., Basavaraj, A.S., Palaniappan, S. and Maity, S. (2019). “Influence of supplementary cementitious materials on the sustainability parameters of cements and concretes in the Indian context”, *Materials and Structures*, 52, 1-11, <https://doi.org/10.1617/s11527-019-1321-5>.
- Kashi, A., Ramezani pour, A.A. and Moodi, F. (2017). “Durability evaluation of retrofitted corroded reinforced concrete columns with FRP sheets in marine environmental conditions”, *Construction and Building Materials*, 151, 520-533, <https://doi.org/10.1016/j.conbuildmat.2017.06.137>.
- Kluge, W. and Assmann, B.O. (2018). “Grinding of calcined clays and its effects on cement properties”, *Calcined Clays for Sustainable Concrete: Proceedings of the 2nd International Conference on Calcined Clays for Sustainable Concrete*, 244-248, <https://doi.org/10.1007/978-94-024-1207-939>.
- Krishnan, S., Emmanuel, A.C., Shah, V., Parashar, A., Mishra, G., Maity, S. and Bishnoi, S. (2018). “Industrial production of limestone calcined clay cement: experience and insights”, *Green Materials*, 7(1), 15-27, <https://doi.org/10.1680/jgrma.18.00003>.
- Krishnan, S., Gopala Rao, D. and Bishnoi, S. (2020). “Why low-grade calcined clays are the ideal for the production of limestone calcined clay cement (lc3)”, *Calcined Clays for Sustainable Concrete: Proceedings of the 3rd International Conference on Calcined Clays for Sustainable Concrete*, 125-130, <https://doi.org/10.1007/978-981-15-2806-414>.
- Lapeyre, J., Ma, H. and Kumar, A. (2019). “Effect of particle size distribution of metakaolin on hydration kinetics of tricalcium silicate”, *Journal of the American Ceramic Society*, 102(10), 5976-5988, <https://doi.org/10.1111/jace.16467>.
- Li, R., Lei, L. and Plank, J. (2022). “Impact of metakaolin content and fineness on the behavior of calcined clay blended cements admixed with hpeg pce superplasticizer”, *Cement and Concrete Composites*, 133, 104654, <https://doi.org/10.1016/j.cemconcomp.2022.104654>.
- Luzu, B., Trauchessec, R. and Lecomte, A. (2022). “Packing density of limestone calcined clay binder”, *Powder Technology*, 408, 117702, <https://doi.org/10.1016/j.powtec.2022.117702>.
- Malacarne, C.S., Longhi, M.A., Silva, M.R.C., Gonçalves, J.P., Rodríguez, E.D. and Kirchheim, A.P. (2021). “Influence of low-grade materials as clinker substitute on the rheological behavior, hydration and mechanical performance of ternary cements”, *Case Studies in Construction Materials*, 15, e00776, <https://doi.org/10.1016/j.cscm.2021.e00776>.
- Maraghechi, H., Avet, F., Wong, H., Kamyab, H. and Scrivener, K. (2018). “Performance of limestone calcined clay cement (lc 3) with various kaolinite contents with respect to chloride transport”, *Materials and Structures*, 51, 1-17, <https://doi.org/10.1617/s11527-018-1255-3>.
- Mazloom, M., Karimpanah, H. and Karamloo, M. (2020). “Fracture behavior of monotype and hybrid fiber reinforced self-compacting concrete at different temperatures”, *Advances in Concrete Construction*, 9(4), 375-386, <https://doi.org/10.12989/acc.2020.9.4.375>.
- Mazloom, M. and Salehi, H. (2018). “The relationship between fracture toughness and compressive strength of self-compacting lightweight concrete”, *IOP Conference Series: Materials Science and Engineering*, 431(6), 62007, <https://doi.org/10.1088/1757-899X/431/6/062007>.

- NT Build 492. (1999). "Nord test method: chloride migration coefficients from non-steady-state", <https://www.nordtest.info/wp/1999/11/21/nt-build-492>.
- Pérez, A. and Martirena-Hernandez, J.F. (2020). "Influence of limestone content and psd of components on properties of clinker-calcined clay-limestone cements produced by intergrading", *Proceedings of the International Conference of Sustainable Production and Use of Cement and Concrete: ICSPCC 2019*, 31-37, <https://doi.org/10.1007/978-3-030-22034-14>.
- Pillai, R.G., Gettu, R., Santhanam, M., Rengaraju, S., Dhandapani, Y., Rathnarajan, S. and Basavaraj, A.S. (2019). "Service life and life cycle assessment of reinforced concrete systems with limestone calcined clay cement (lc3)", *Cement and Concrete Research*, 118, 111-119, <https://doi.org/10.1016/j.cemconres.2018.11.019>.
- Poon, C.S., Lam, L., Kou, S.C., Wong, Y.L. and Wong, R. (2001). "Rate of pozzolanic reaction of metakaolin in high-performance cement pastes", *Cement and Concrete Research*, 31(9), 1301-1306, [https://doi.org/10.1016/S0008-8846\(01\)00581-6](https://doi.org/10.1016/S0008-8846(01)00581-6).
- Snellings, R., Chwast, J., Cizer, "O., De Belie, N., Dhandapani, Y., Durdzinski, P., Elsen, J. Haufe, J., Hooton, D., Patapy, C. and Santhanam, M. (2018). "Rilem tc-238 scm recommendation on hydration stoppage by solvent exchange for the study of hydrate assemblages", *Materials and Structures*, 51(6), 1-4, <https://doi.org/10.1617/s11527-018-1298-5>.
- Ramezani pour, A.A., Pilvar, A., Mahdikhani, M. and Moodi, F. (2011). "Practical evaluation of relationship between concrete resistivity, water penetration, rapid chloride penetration and compressive strength", *Construction and Building Materials*, 25(5), 2472-2479, <https://doi.org/10.1016/j.conbuildmat.2010.11.069>.
- Riahi Dehkordi, E. and GivKashi, M.R. (2024). "Considerations for the construction, implementation and economic evaluation of geopolymer permanent formworks (gpfs): a new approach to protect concrete structures against aggressive environmental factors", *Arabian Journal for Science and Engineering*, 49(4), 4861-4875, <https://doi.org/10.1007/s13369-023-08081-4>.
- Richardson, M.G. (2002). "Fundamentals of durable reinforced concrete", <http://doi.org/10.1201/9781003261414>.
- Scrivener, K., Martirena, F., Bishnoi, S. and Maity, S. (2018a). "Calcined clay limestone cements (lc3)", *Cement and Concrete Research*, 114, 49-56, <https://doi.org/10.1016/j.cemconres.2017.08.017>.
- Scrivener, K., Snellings, R. and Lothenbach, B. (2018b). "A practical guide to microstructural analysis of cementitious materials", Crc Press, <https://api.taylorfrancis.com>.
- Sharma, M., Bishnoi, S., Martirena, F. and Scrivener, K. (2021). "Limestone calcined clay cement and concrete: A state-of-the-art review", *Cement and Concrete Research*, 149, 106564, <https://doi.org/10.1016/j.cemconres.2021.106564>.
- Siline, M. and Mehsas, B. (2022). "Effect of increasing the Blaine fineness of metakaolin on its chemical reactivity", *Journal of Building Engineering*, 56, 104778, <https://doi.org/10.1016/j.jobbe.2022.104778>.
- Yadak Yaraghi, A.H.Y., Ramezani pour, A.M., Ramezani pour, A.A., Bahman-Zadeh, F. and Zolfagharnasab, A. (2022). "Evaluation of test procedures for durability and permeability assessment of concretes containing calcined clay", *Journal of Building Engineering*, 58, 105016, <https://doi.org/10.1016/j.jobbe.2022.105016>.
- Zolfagharnasab, A., Ramezani pour, A.A. and Bahman-Zadeh, F. (2021). "Investigating the potential of low-grade calcined clays to produce durable lc3 binders against chloride ions attack", *Construction and Building Materials*, 303, 124541, <https://doi.org/10.1016/j.conbuildmat.2021.124541>.
- Zunino, F. and Scrivener, K. (2020). "Increasing the kaolinite content of raw clays using particle classification techniques for use as supplementary cementitious materials", *Construction and Building Materials*, 244, 118335, <https://doi.org/10.1016/j.conbuildmat.2020.118335>.



This article is an open-access article distributed under the terms and conditions of the Creative Commons Attribution (CC-BY) license.



Effects of Macro-Synthetic Fibres Incorporation on the Dimensional Change Properties of Bacillus Subtilis Bacterial Concrete

Ghoniem, A.G.^{1*}, Aboul Nour, L.² and Hassan, H.²

¹ Ph.D., Instructor, Structural Engineering Department, Faculty of Engineering, Zagazig University, Egypt.

² Professor, Structural Engineering Department, Faculty of Engineering, Zagazig University, Egypt.

© University of Tehran 2024

Received: 21 Dec. 2023;

Revised: 14 Mar. 2024;

Accepted: 29 May 2024

ABSTRACT: Immediate dimensional changes during loading are critical characteristics that must be thoroughly understood to ensure the long-term durability and performance of concrete. In the current study, the effects of fixed bacterial content and different macro-synthetic fibre mechanical properties and fibre percentages on concrete dimensional changes were evaluated using 34 mixed designs. The influence of low- and high-strength macro-synthetic fibre with nine contents ranging from 0% to 4% on M40 concrete was investigated with and without calcium carbonate precipitation of *Bacillus subtilis* activity at a cell concentration of 105 cells/ml. The ANSYS package was used to compute the homogenized properties of the composite materials, such as the elastic modulus, shear modulus, and Poisson's ratio. For validation, the numerical results showed good agreement with the analytical results of the dilute distribution model and the Mori-Tanaka model. Compared to the reference conventional concrete, the results showed that adding bacteria and 2% high-strength macro-synthetic fibre simultaneously improved elasticity, shear moduli, and Poisson's ratio by 17.89%, 15.16%, and 3.30%; however, low-strength macro-synthetic fibres caused 3.54%, 1.32%, and 2.98% reduction, respectively. Overall, high-strength macro-synthetic fibre improves the properties of bacterial concrete composite for a variety of structural applications when compared to other traditional concrete.

Keywords: Composite Materials, Elasticity and Shear Moduli, Numerical Homogenized Simulation, Poisson's Ratio, Polyethylene Fibre.

1. Introduction

Conventional Concrete (CC) cracks can lead to steel reinforcement corrosion; however, Bacterial Concrete (BC), also known as self-healing concrete, offers a solution by using bacteria to repair cracks and enhance the properties of fibre concrete (Chithambar Ganesh et al., 2019). The sustainable immediate self-repair of the

formed micro- and macro-cracks can prevent crack growth by limiting the paths for liquids and gases that may contain harmful chemical substances (Hameed et al., 2023). Biogenic origins, such as ureolytic bacteria, can induce CaCO_3 precipitation, leading to the self-healing of cracks in concrete when exposed to different environmental conditions or

* Corresponding author E-mail: agghoneim@zu.edu.eg

mechanical loads (Rameshkumar et al., 2020). *Bacillus subtilis* embedded in BC can repair cracks and restore the original mechanical properties of concrete for up to 200 years (Jena et al., 2020). *Subtilis* can repair a cement mortar crack width of 0.3 mm within 1-5 days in the laboratory (Vijay et al., 2017) and may take several weeks for the total rehabilitation of the macro-cracks up to 0.46 mm (Wiktor and Jonkers, 2011) or 0.5 mm (Wang et al., 2014). This self-healing increased the compressive strength f_c' by an average value of 23% at 28 d, and the split tensile strength f_t improved in the range of 13.7 - 25.3% (Ghoneim et al., 2020). Moreover, self-healing can reduce porosity, increase durability, guarantee a reduction in degradation rates, lower repair frequency, minimize the costs of strength monitoring/damage detection, and extend the ultimate service life of concrete structures (Alshalif et al., 2020; Bhaskar, 2021). Incorporating fibres in concrete, which serve as reinforcement, improves the self-healing performance by bridging cracks and reducing the amount of healing product required (Zhang et al., 2020).

Calcite sediment remediation techniques can fill inaccessible concrete pores caused by the use of fibres in concrete. Polypropylene fibres can prevent cracking, thereby affecting the dimensional changes and quality of the material (Tiwari and Singh, 2024). The dimensional stability of concrete depends on the environmental conditions and applied loads; however, it is also related to the concrete mix components. This study demonstrates the effectiveness of a dual-component composite material consisting of randomly distributed fibres and bacteria in immediate elastic dimensional changes related to the applied loading of concrete. Because of their ease of application, low density, and non-breakability, synthetic fibres have been commonly considered for use in concrete.

Macro fibres are defined as fibres with a diameter greater than 0.3 mm and a specific surface area of approximately 10 cm²/g (Jawhar et al., 2024). Increasing the

fibre content in Fibre-Reinforced Concrete (FRC) to 4% strikes a balance between achieving maximum strength and maintaining workability (Hasan et al., 2019), while also improving ductility and toughness (Yoo and Moon, 2018). In addition, Fibre-Reinforced Bacterial Concrete (FRBC) is a composite material with greater stability over shelf-life and multiple significant environmental footprints. In the last 10 years, the major advantages of FRBC have been investigated by many researchers, as follows: i) Crack bridging recovery, as provided by ESEM/XEDS microscopic images (Feng et al., 2019); ii) Improving healing participation to fill the crack-controlled width pattern (Qian et al., 2009); iii) Enhancing the ultimate load capacity and ductility (Hao et al., 2018; Ghoniem et al., 2021); iv) Enhancing fibrous concrete porosity and extending the service life of the structure (Kua et al., 2019; Karimi and Mostofinejad, 2020); (v) Recycling nonbiodegradable thermoplastic materials in fibrous concrete is an environmentally safe procedure (Merli et al., 2019).

Understanding the concept of dimensional change in synthetic fibrous bacterial concrete requires an exploration of how fibres contribute significantly to the overall properties of the material, including reducing shrinkage and enhancing toughness, crack resistance, and flexural strength (Amjad et al., 2023; Damodaran and Thangasamy, 2023). Hence, the elastic dimensional change of synthetic fibrous bacterial concrete is a multifaceted topic that requires a thorough understanding of the composition of the material, the effects of synthetic fibres on bacterial activity, and influencing factors. The dimensional change properties have scarcely been investigated from a numerical analysis point of view to avoid time-consuming laboratory experiments. The main issue of numerical simulation is that the synthetic fibre diameter is a few micrometers, while the structural dimension is in meters.

Therefore, the mechanical properties of

such composites are a multiscale modelling problem (Geers et al., 2010; Montero-Chacón et al., 2019). There are two approaches to the numerical simulation of composite structures. 1) The hierarchical approach is called the FE2 approach because there is a separate microscopic finite element simulation for every integration point of the macroscopic Finite Element (FE) simulation. The stress and strain are computed in the smaller length scale, and the averaged values are sent back to the larger length scale (Raju et al., 2021).

2) The homogenization approach is called the unit cell approach, as it is the most popular approach to eliminate the scale problem in FE2 analysis. The homogenization/unit cell approach for composite structure simulation has been described in the literature, in which the composite properties were averaged based on microstructure analysis rather than simulating the entire complex microstructure. Full-field approaches, based on periodic homogenization theory, estimate the overall behavior of an equivalent homogeneous material by defining a Repeated/representative Volume Element (RVE) (Naili et al., 2020). An equivalent inclusion Dilute Distribution (DD) model can predict the effective bulk modulus K_{eff} and shear modulus G_{eff} of a composite in which a single inclusion/fibre is in an infinite elastic host material matrix (Eshelby, 1957). The DD model is more suitable for small volume fractions of inclusions, where interactions between inclusions are negligible as they are far apart. Another widely used model is the Mori-Tanaka (MT) model, which is very close to the experimental results for the prediction of the effective bulk modulus and shear modulus. The MT model, based

on the average matrix stress assumption, imposes an additional condition on the DD model to consider the effect of multiple inclusions by combining the DD theory with the effective field concept (Benveniste, 1987). The current study numerically investigated the composite properties by considering the unit cell approach of the composite structure simulated by ANSYS material designer as an integrated component system in the ANSYS software package. The elastic modulus, shear modulus, and Poisson's ratio were estimated to explore the synergistic effects of bacteria and fibres.

The effects of high- and low-strength macro-synthetic fibres introduced by different volumes on the properties of concrete incorporating *Bacillus subtilis* bacteria at a concentration of 105 cells/ml in mixing water were evaluated. Finally, the gradual changes in the material properties obtained from the numerical results are compared with the analytical results of the dilute distribution model and the MT model.

2. Materials and Methods

Simulations were performed based on the known properties of their component base materials. The study material properties were chosen based on previous technical investigations and experiments to provide reliable inputs for the numerical models as follows: i) *Bacillus subtilis* JC3 was identified as a spore-forming aerobic alkaliphilic bacterium. Peptone, NaCl, and yeast extract were used as growth media.

The matrix characteristics for the control and bacterial concrete BC were developed at the age of 28 days, as shown in Table 1, with an optimum *B. Subtilis* cell.

Table 1. Plain and bacterial concrete characteristics

Matrix type	Control concrete CC	Bacterial concrete BC
Density (g/cm ³)	2300	2300
Elastic modulus E (MPa)	32200	36700
Poisson's ratio ν	0.18	0.18
Tensile strength f_t (MPa)	4.51	5.13
Compressive strength f_c (MPa)	52.01	61.06

Subtilis cell concentration equal to 105 cells/ml of mixing water (Rao et al., 2017).

ii) The macro-synthetic polyethylene fibres have a unit diameter d_f , aspect ratio $AR_f = l_f / d_f$, density, elastic modulus E , Poisson's ratio ν , and ultimate tensile strength as shown in Table 2. High-strength fibre/type 1 (Monishaa and Namitha, 2017) and low-strength fibre/type 2 (Bentur and Mindess, 2006) were provided. To investigate the target homogenized characteristics, the synthetic fibre matrix included different volume contents ($v_f = 0.3, 0.5, 0.75, 1, 1.5, 2, 3$, and 4%) for both the M40 control and bacterial concrete. The scheme of the specimen sets used to generate the RVE models is shown in

Figure 1. The generated 34 models were modelled to explore the synergistic effects of bacteria and fibres. For macroscopic simulation and computing the homogenized properties of chopped fibre composites, the study presents numerical RVE modelling of fibrous composite concrete modelled using ANSYS material designer integrated in the ANSYS software package, as shown in Figure 2. The Material designer modelling procedure of a chopped fibre composite is summarized using different parameters until the geometric meshing of the internal shape, as follows: 1) The seed number against which the random fibre directions are calculated.

Table 2. Macro-synthetic fibre characteristics

Fibre type	Type 1	Type 2
Fibre strength type	High	Low
Diameter d_f (μm)	433	625
Aspect ratio AR_f	90	48
Density (g/cm^3)	0.97	0.94
Elastic modulus E_f (MPa)	73000	5000
Poisson's Ratio ν_f	0.422	0.418
Ultimate tensile strength f_{tf} (MPa)	2580	600

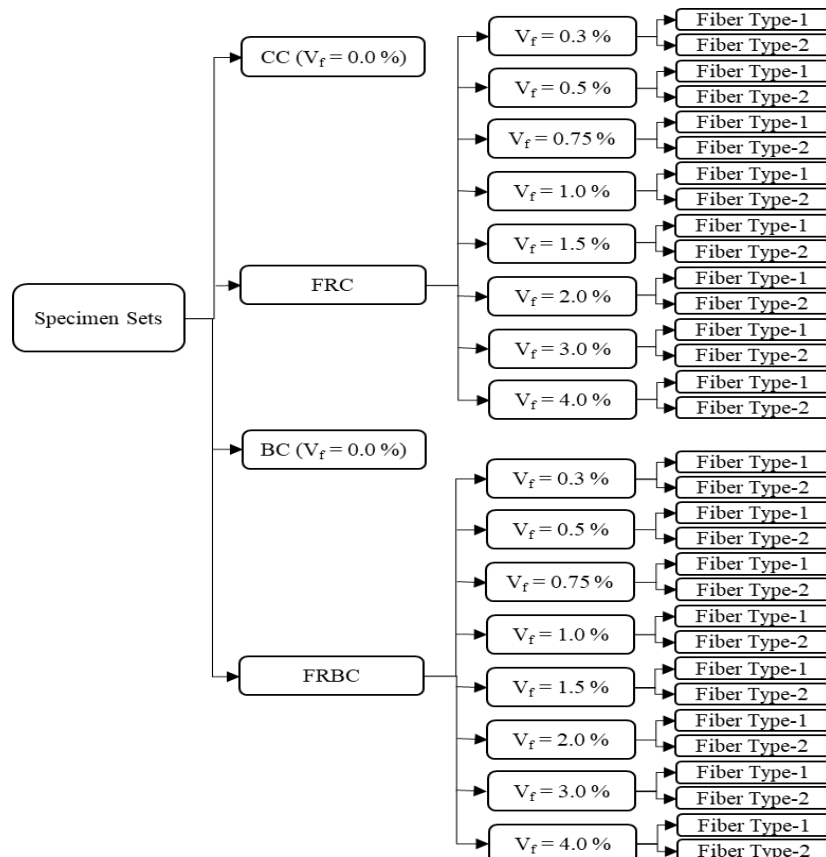


Fig. 1. Scheme of the study specimen sets

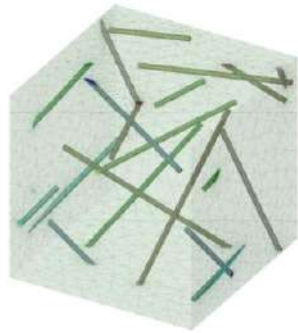


Fig. 2. Meshed chopped fibre composites of ANSYS material designer typical RVE

2) The repeat count specifies whether a given volume is sufficiently large to

represent the number of fibres in the RVE. If the RVE size is insufficient, the software may fail to generate an RVE geometry with self-intersecting fibres that are longer than the RVE size. Consequently, increasing the variable size of the RVE is essential. Table 3 shows the actual numerically corrected size effects for various RVE models.

3) Tensor of symmetric fibre orientation. The initial fibre orientations were specified as uniform in all directions with diagonal values of 0.33, 0.33, 0.33, and zero values for the off-diagonal entries.

Table 3. Actual numerical entries and orientation tensor entries of the RVE geometry

The actual numerical entries for various RVE models						The actual orientation tensor entries of the RVE geometry	
Fibre type	Volume fraction V_f %	Actual V_f %	Seed	Repeat count	No. of fibres /RVE	Diagonal values (a_{11} , a_{22} , a_{33})	Off-diagonal values (a_{12} , a_{13} , a_{23}) and (a_{21} , a_{31} , a_{32})
Type 1	0.0	-	-	-	-	-	-
	0.3	0.3131	1	4	12	0.2632, 0.2502, 0.4866	-0.03205, 0.01635, -0.09209
	0.5	0.5044	1	4	9	0.3616, 0.2778, 0.3606	-0.07518, -0.01506, -0.1615
	0.75	0.8246	1	4	8	0.3191, 0.2141, 0.4668	0.01058, -0.05301, -0.1623
	1	1.11	1	4	7	0.1123, 0.2199, 0.6677	0.039, -0.07615, -0.1813
	1.5	1.641	1	5	11	0.2887, 0.2881, 0.4232	0.083, -0.06024, -0.2119
	2	2.066	1	5	9	0.1458, 0.2446, 0.6096	0.06223, -0.1672, -0.1258
	3	3.17	8	6	13	0.3567, 0.2763, 0.367	0.06598, 0.02428, -0.05158
	4	4.131	10	6	11	0.2648, 0.4444, 0.2908	-0.05631, 0.01301, -0.2039
Type 2	0.0	-	-	-	-	-	-
	0.3	0.3296	1	3	10	0.3147, 0.3333, 0.352	-0.04782, -0.02756, -0.05366
	0.5	0.5673	1	3	8	0.3417, 0.3304, 0.3278	-0.03748, -0.1053, -0.0703
	0.75	0.7694	1	4	14	0.2839, 0.2198, 0.4963	-0.01388, -0.07003, -0.04152
	1	1.015	1	4	12	0.2819, 0.2261, 0.492	0.02245, -0.03927, -0.08307
	1.5	1.511	8	5	19	0.3634, 0.3177, 0.3189	0.04143, -0.04234, 0.03576
	2	2.082	8	5	17	0.4302, 0.2271, 0.3427	0.0165, -0.0994, 0.03733
	3	3.15	8	5	14	0.3587, 0.3012, 0.3401	0.008798, -0.205, 0.03489
	4	4.156	8	5	12	0.2957, 0.402, 0.3024	0.09896, -0.02228, 0.1095

Table 3 shows the actual values of the orientation tensor entries determined after generating the actual RVE geometry size and fibre fractions.

3. Results and Discussion

The dimensional change in fibrous bacterial concrete affects the performance and service life of structures. Excessive loading can lead to cracking, reduced serviceability, and compromised durability, while unexpected cracks can result in structural damage and loss of functionality. A numerical RVE model was used to study the improvement of certain properties, such as the elasticity modulus E_y , shear modulus G_{yz} , Poisson's ratio ν_{xz} , and density ρ . The

mean and Standard Deviation (SD) of results are displayed in Figure 3 with SD below 2.14%. The target samples were mentioned as “matrix type - fibre type”.

With respect to plain concrete, high-strength fibre reinforced concrete FRC-1, bacterial concrete BC, high-strength fibre reinforced bacterial concrete FRBC-1, and low-strength fibre reinforced bacterial concrete FRBC-2, the mean values of elasticity modulus E_{eff} and shear modulus G_{eff} increased by 1.52% and 1.11%, 13.98% and 13.98%, 15.46% and 14.97%, and 11.09% and 10.60%, respectively. The mean values decreased by 2.39% and 2.85% for the low-strength fibre reinforced concrete FRC-2.

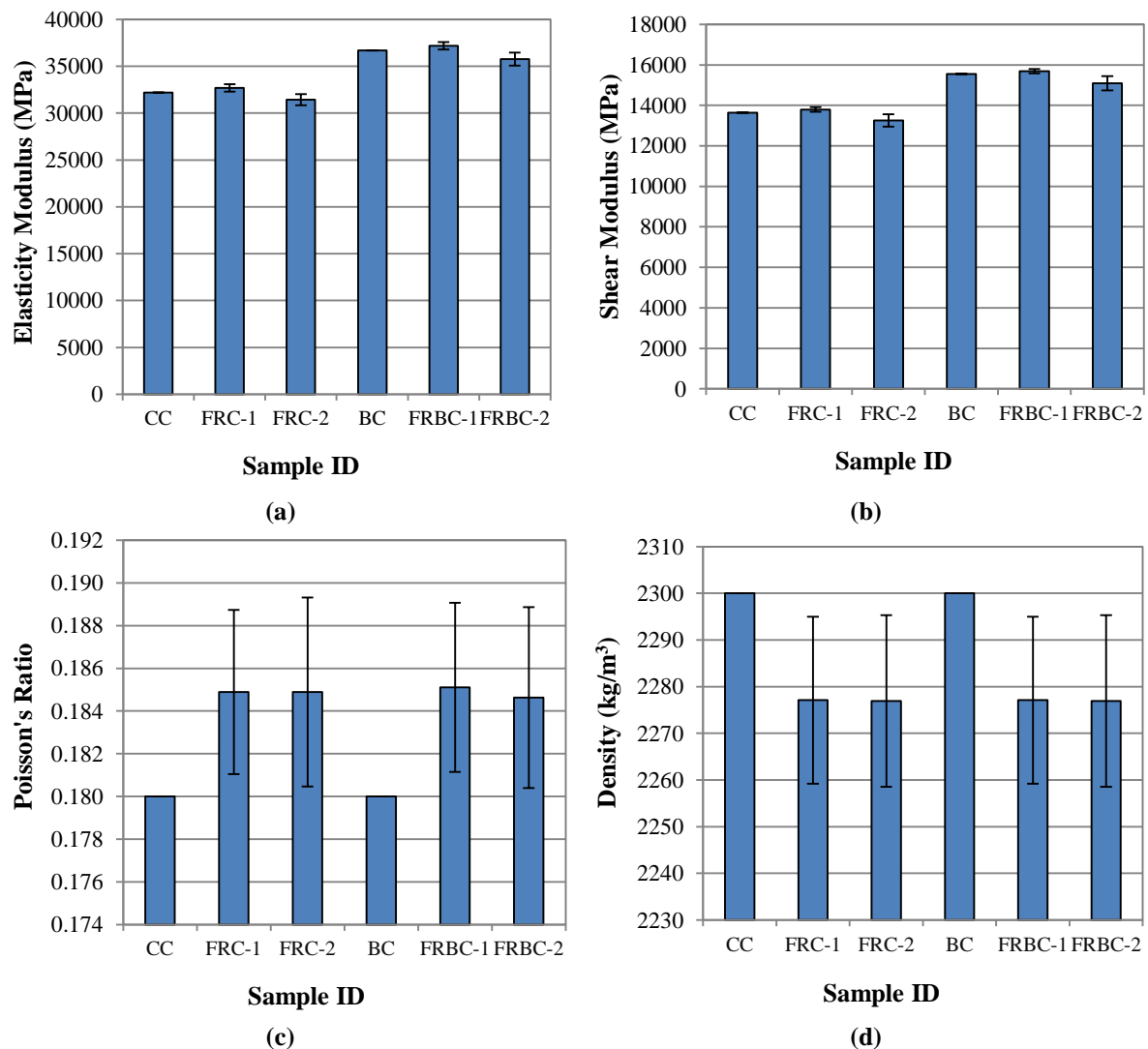


Fig. 3. Concrete properties of the study samples: a) Elasticity modulus; b) Shear modulus; c) Poisson's ratio; and d) Density

Detailed improvements in elasticity and shear moduli for both the FRC and FRBC relative to the M40 conventional concrete are illustrated in Figure 4. The target samples are mentioned as “matrix type - fibre type - homogenized moduli”. The elastic and shear moduli for both the FRC and FRBC increased with the high-strength fibre content, whereas the enhancement in the homogenized moduli decreased with the low-strength fibre content. This innovative result supports the fact that high-strength fibres improve ductility because fibre pull-out is the desired failure mode for dissipating energy in the matrix (Richardson, 2005; Khan and Ayub, 2016).

Polyethylene macro-synthetic fibres can enhance the pre-peak elastic modulus of an element, causing an increase in flexural strength and shear capacity (Pantazopoulou and Zanganeh, 2001; Majdzadeh et al., 2006). Bhosale et al. (2019) concluded that

increasing the energy-absorbing capability during fracture improved post-peak ductility (Bhosale et al., 2019).

Polyethylene macro-synthetic fibres provide post-cracking tensile resistance across cracks (Yıldırım et al., 2015). With respect to plain or bacterial concrete, both high- and low-strength fibre-reinforced concrete and fibre-reinforced bacterial concrete mean values of density decreased by 1%. While high-strength fibre reinforced concrete FRC-1, low-strength fibre reinforced concrete FRC-2, high-strength fibre reinforced bacterial concrete FRBC-1, and low-strength fibre reinforced bacterial concrete FRBC-2, mean values of Poisson's ratio v_{eff} increased by 2.72%, 2.71%, 2.84%, and 2.57%, respectively. The detailed enhancements in Poisson's ratio for FRC and FRBC compared to conventional concrete are illustrated in Figure 5.

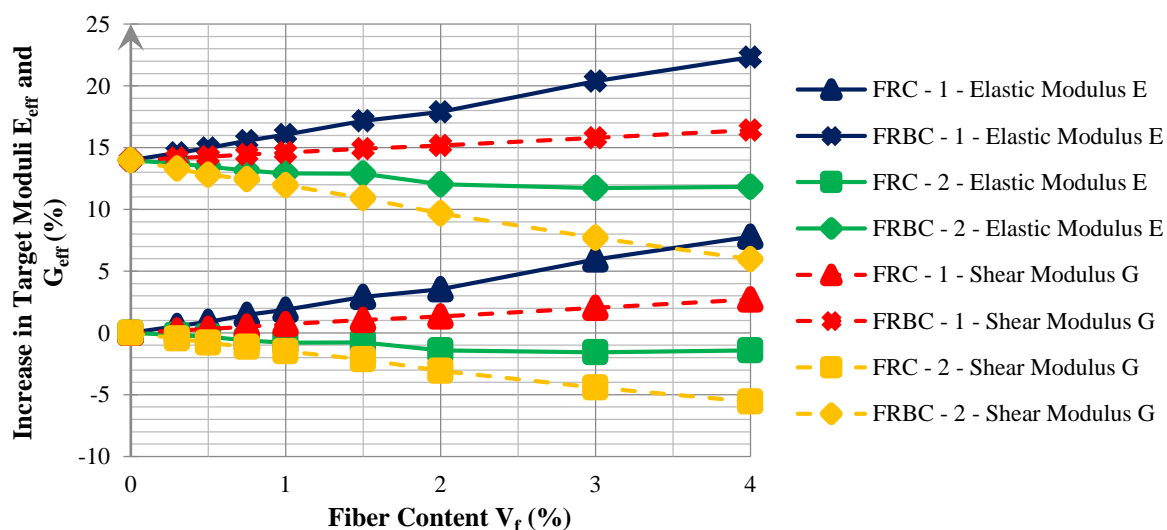


Fig. 4. Enhancement in the target numerical elastic and shear moduli

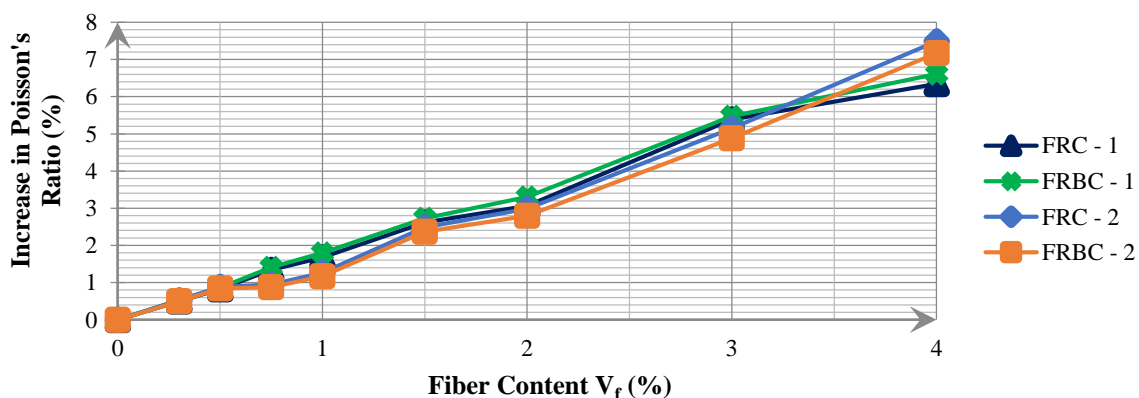


Fig. 5. The enhancement in the target numerical Poisson's ratio, v_{eff}

The Poisson's ratio enhancement increased with the content of high-strength or low-strength fibres in both fibrous concrete and fibrous bacterial concrete, indicating improved crack formation arrest and post-peak strength (Tiberti et al., 2014).

Related to the reference conventional concrete, the results indicated that the inclusion of high-strength fibre from 0% to 2% and constant content of *Bacillus subtilis* bacteria increased the elastic modulus, shear modulus, and Poisson's ratio in the range of 13.98-17.89%, 13.98-15.16%, and 0-3.30%, respectively. However, the inclusion of only high-strength fibre from 0% to 2% without *Bacillus subtilis* bacteria increased the elastic modulus, shear

modulus, and Poisson's ratio in the range of 0-3.54%, 0-1.32%, and 0-2.98%, respectively. Hence, the contribution of *Bacillus subtilis* bacteria distinguished in concrete mixtures with different fibre percentages from 0% to 2% was in the ranges of 13.98-14.35%, 13.98-13.84%, and 0-0.32% for the elastic modulus, shear modulus, and Poisson's ratio, respectively.

One of the current research objectives is to verify the numerical bulk modulus and shear modulus results using the analytical DD and MT models. As depicted in Figures 6 and 7, the homogenized numerical results are in good agreement with the analytical results for the bulk and shear moduli.

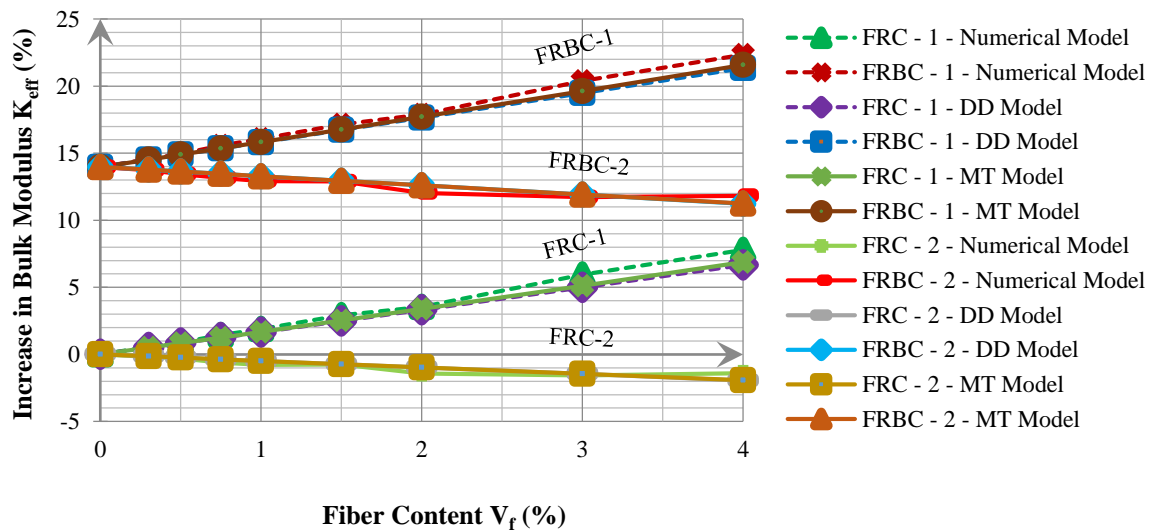


Fig. 6. Validation of target bulk modulus, K_{eff}

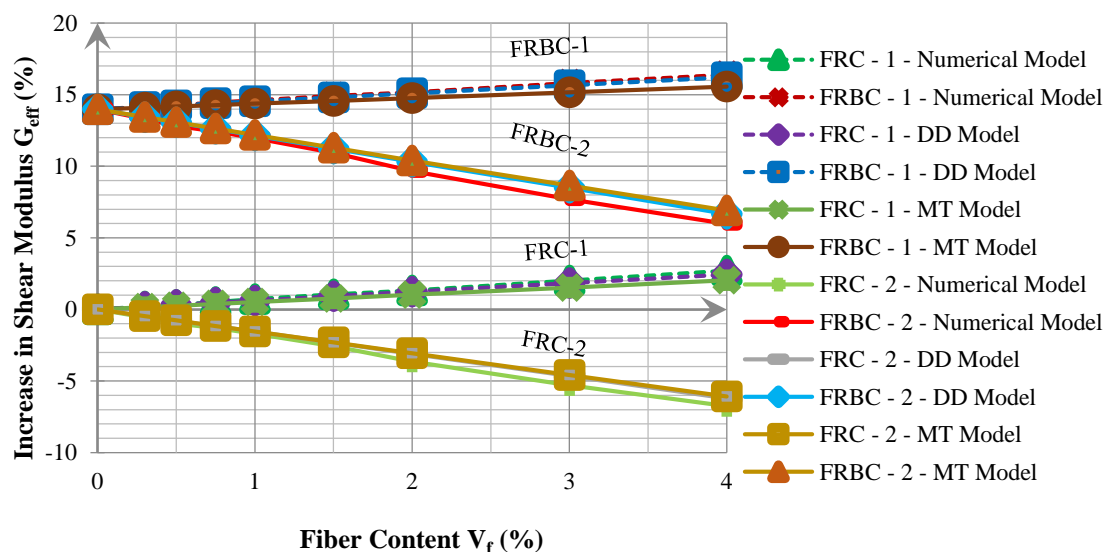


Fig. 7. Validation of target shear modulus, G_{eff}

The target samples are mentioned as “matrix type - fibre type - modelling method”. In addition, the statistical hypothesis factorial ANOVA test in SPSS V25 software was used to compare the effect of analysis methods on composite moduli, finding no significant differences between the numerical and analytical results and no significant differences between FRBC and FRC in terms of poisson’s ratio, but significant differences among different matrix types in elastic and shear moduli. Figure 8 shows target composite properties E_{eff} , G_{eff} , and ν_{eff} that are equal to -0.5%, -1%, and 2.75% for FRC, 13.98%, 13.98%, 0% for BC, and 13.25%, 12.75%, 2.75% for FRBC, respectively, with a 99% confidence level. The mean values show that fibrous FRBC and non-fibrous BC had better elasticity and shear moduli than traditional concrete. The biological self-repairing concept of traditional concrete has more effective advantages, and the addition of high-strength fibres only slightly enhances these properties. This result is broadly consistent with the major trends of other studies, in which the initial tangent modulus E_{it} changed slightly with the addition of fibres (Ezeldin and Balaguru, 1992; Algihtwel, 2018). Fibrous bacterial concrete mitigates dimensional changes through the network incorporation of high-strength fibres, which reduces strain and restrains the concrete

matrix. The bacterial components in synthetic fibrous bacterial concrete, such as calcium carbonate-producing bacteria, play a vital role in mitigating dimensional change cracks by producing calcite crystals as fillers in the microstructure. The controlled crack pattern in synthetic fibrous bacterial concrete improves the bond strength between the fibres and the low-porosity matrix, resulting in enhanced flexural strength and shear capacity. As a result, the biological self-repairing concept of traditional and fibrous concrete achieved more effective advantages for the elastic and shear moduli. These findings are consistent with those of previous studies (Qian et al., 2009; Hao et al., 2018; Feng et al., 2019; Kua et al., 2019; Karimi and Mostofinejad, 2020). Despite its inherent benefits, fibrous bacterial concrete can undergo long-term dimensional changes owing to environmental conditions, chemical reactions, and material properties.

Factors such as high temperature, humidity, and exposure to aggressive chemicals can accelerate the growth of bacteria, leading to an increase in the production of calcite crystals, resulting in dimensional changes. Therefore, laboratory testing techniques, including strain gauges and expansion tests, can help researchers understand the behavior of the material and develop predictive models.

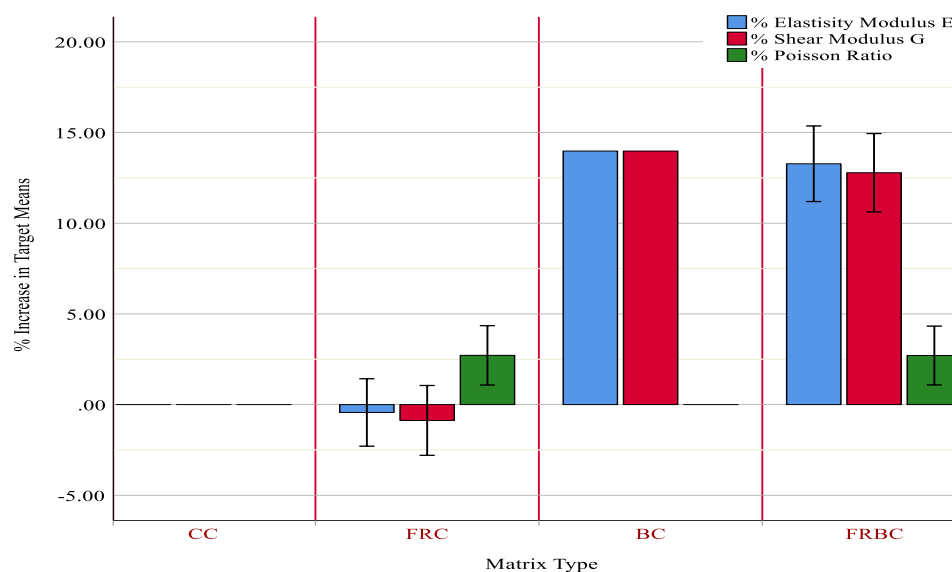


Fig. 8. Enhancement of the properties of different matrix types

Furthermore, as the scope of the investigation expands beyond the prediction of linear elastic properties of composites, the limitations of numerical models become more apparent in modelling post-failure behavior and predicting damage and cracking patterns. Future studies will focus on other dimensional changes of concrete related to the applied loadings as creep deformation, or related to environmental aspects, such as early thermal expansion/contraction and swelling/shrinkage, which account for the majority of cracking in concrete structures.

The fibre parameters, matrix grades, and self-repair techniques require further investigation. In addition, the macroscopic stress, strain distributions, and failure responses require intensive surveys. More data are required to facilitate the design and production of FRBC.

4. Conclusions

The current study investigated the dimensional change properties of concrete that included macro-synthetic fibres and *Bacillus subtilis* bacteria, such as Poisson's ratio, elasticity, and shear moduli. Proper incorporation of fibres and bacteria, coupled with careful mixture design and construction practices, can effectively manage immediate dimensional changes, mitigate long-term dimensional changes, and ensure the optimal performance and longevity of structures constructed using this innovative material. The main findings are as follows: 1) Using high-strength macro-synthetic fibres instead of low-strength synthetic fibres improves the concrete target properties; 2) It is essential to acknowledge that the process of Bacterial-Induced Calcite Precipitation (BICP) involves the conversion of the calcium lactate or urea present in the concrete mixture into calcite, effectively counteracting dimensional changes. The bacterial strain treatment combined with macro-synthetic fibre inclusion increased the conventional concrete homogenized

elastic modulus, shear modulus, and Poisson's ratio properties by 13.25%, 12.75% and 2.75%, respectively, according to the statistical analysis, regardless of the content and mechanical properties of the fibre. Ongoing research has direct positive effects on the design of practical structural elements by developing stronger synthetic fibres and optimizing bacterial activity to further enhance the performance of fibrous bacterial concrete with respect to dimensional changes.

5. References

- Algihwel, M. (2018). "A review on effect of different fiber types on fiber reinforced concrete behavior", *Sustainable Structures and Materials, An International Journal*, 1(2), 36-43, <https://doi.org/10.26392/SSM.2018.01.02.036>.
- Alshalif, A.F., Irwan, J.M., Othman, N., Al-Gheethi, A.A. and Shamsudin, S. (2020). "A systematic review on bio-sequestration of carbon dioxide in bio-concrete systems: a future direction", *European Journal of Environmental and Civil Engineering*, 26(3), 1209-1228, <https://doi.org/10.1080/19648189.2020.1713899>.
- Amjad, H., Arsalan Khushnood, R. and Ali Memon, S. (2023). "Biomimetic robust self-healing of *Bacillus subtilis* immobilized through sisal fiber for next-generation concrete infrastructure", *Construction and Building Materials*, 368(3), 130299, <https://doi.org/10.1016/j.conbuildmat.2023.130299>.
- Bentur, A. and Mindess, S. (2006). *Fibre reinforced cementitious composites*, CRC Press.
- Benveniste, Y. (1987). "A new approach to the application of Mori-Tanaka's theory in composite materials", *Mechanics of Materials*, 6(2), 147-157, [https://doi.org/10.1016/0167-6636\(87\)90005-6](https://doi.org/10.1016/0167-6636(87)90005-6).
- Bhaskar, S. (2021). "Self-healing bacterial cementitious concrete composites: development and performance evaluation", Ph.D. Thesis, Toronto Metropolitan University, <https://doi.org/10.32920/ryerson.14656461.v1>.
- Bhosale, A., Rasheed, M.A., Prakash, S.S. and Raju, G. (2019). "A study on the efficiency of steel vs. synthetic vs. hybrid fibers on fracture behavior of concrete in flexure using acoustic emission", *Construction and Building Materials*, 199, 256-268, <https://doi.org/10.1016/J.CONBUILDMAT.2018.12.011>.
- Chithambar Ganesh, A., Muthukannan, M.,

- Malathy, R. and Ramesh Babu, C. (2019). "An experimental study on effects of bacterial strain combination in fibre concrete and self-healing efficiency", *KSCE Journal of Civil Engineering*, 23(10), 4368-4377, <https://doi.org/10.1007/s12205-019-1661-2>.
- Damodaran, P. and Thangasamy, L. (2023). "Experimental investigation on mechanical properties and characterization of steel fibre concrete with *Bacillus subtilis*", *E3S Web of Conferences*, EDP Sciences, 03002, <https://doi.org/10.1051/e3sconf/2F202338703002>.
- Eshelby, J.D. (1957). "The determination of the elastic field of an ellipsoidal inclusion and related problems", *Proceedings of the Royal Society of London, Series A, Mathematical and Physical Sciences*, 241(1226), 376-396, <https://doi.org/10.1098/rspa.1957.0133>.
- Ezeldin, A.S. and Balaguru, P.N. (1992). "Normal and high-strength fiber-reinforced concrete under compression", *Journal of Materials in Civil Engineering*, 4(4), 415-429, <https://doi.org/10.1061/%28ASCE%290899-1561%281992%294%3A4%28415%29>.
- Feng, J., Su, Y. and Qian, C. (2019). "Coupled effect of pp fiber, pva fiber and bacteria on self-healing efficiency of early-age cracks in concrete", *Construction and Building Materials*, 228, 116810, <https://doi.org/10.1016/j.conbuildmat.2019.116810>.
- Geers, M.G., Kouznetsova, V.G. and Brekelmans, W. (2010). "Multi-scale computational homogenization: trends and challenges", *Journal of computational and applied mathematics*, 234(7), 2175-2182, <https://doi.org/10.1016/j.cam.2009.08.077>.
- Ghoneim, A., Hassan, H. and Aboul-Nour, L. (2020). "Self-repairing polyethylene fiber-reinforced-concrete with *bacillus subtilis* bacteria a review", *International Journal of Engineering and Technology*, 9(2), 437-447, <http://doi.org/10.14419/ijet.v9i2.30172>.
- Ghoniem, A., Hassan, H. and Aboul-Nour, L. (2021). "Behavior of macro-synthetic fiber-reinforced high-strength concrete beams incorporating *bacillus subtilis* bacteria", *Latin American Journal of Solids and Structures*, 18, 1-14, <https://doi.org/10.1590/1679-78256378>.
- Hameed, N.A., Othman, F.M. and Abdul-Hameed, A.A. (2023). "Integration of fdm and self-healing technology: evaluation of crack sealing by durability and mechanical strength", *Materials Research Express*, 10(12), 125701, <https://doi.org/10.1088/2053-1591/2Fad0c7d>.
- Hao, Y., Cheng, L., Hao, H. and Shahin, M.A. (2018). "Enhancing fiber/matrix bonding in polypropylene fiber reinforced cementitious composites by microbially induced calcite precipitation pre-treatment", *Cement and Concrete Composites*, 88, 1-7, <https://doi.org/10.1016/j.cemconcomp.2018.01.001>.
- Hasan, A., Maroof, N. and Ibrahim, Y. (2019). "Effects of polypropylene fiber content on strength and workability properties of concrete", *Polytechnic Journal*, 9(1), 7-12, <https://doi.org/10.25156/PTJ.V9N1Y2019.PP7-12>.
- Jawhar, A.A., Al-Hadithi, A.I. and Mansoor, Y.A. (2024). "An experimental investigation of mechanical properties of wet-mixed shotcrete reinforced with different types of plastic fiber", *AIP Conference Proceedings*, AIP Publishing, <https://doi.org/10.1063/5.0190540>.
- Jena, S., Basa, B. and Panda, K. (2020). "Bacterial concrete for the development of sustainable construction-a review", *Recent Trends in Civil Engineering: Select Proceedings of ICRITICE 2019*, 587-600, <https://doi.org/10.1007/978-981-15-5195-646>.
- Karimi, N. and Mostofinejad, D. (2020). "*Bacillus subtilis* bacteria used in fiber reinforced concrete and their effects on concrete penetrability", *Construction and Building Materials*, 230, 117051, <https://doi.org/10.1016/j.conbuildmat.2019.117051>.
- Khan, S.U. and Ayub, T. (2016). "Modelling of the pre and post-cracking response of the pva fibre reinforced concrete subjected to direct tension", *Construction and Building Materials*, 120, 540-557, <https://doi.org/10.1016/j.conbuildmat.2016.05.130>.
- Kua, H.W., Gupta, S., Aday, A.N. and Srubar, W.V. (2019). "Biochar-immobilized bacteria and superabsorbent polymers enable self-healing of fiber-reinforced concrete after multiple damage cycles", *Cement and Concrete Composites*, 100, 35-52, <https://doi.org/10.1016/j.cemconcomp.2019.03.017>.
- Monishaa, M. and Namitha, S.T. (2017). "Experimental study on strength of self-healing concrete", *SSRG International Journal of Civil Engineering- (ICRTCEM-2017)* (Special Issue), 476-484, <https://www.internationaljournalssrg.org/uploads/specialissuepdf/ICRTCEM/2017/CE/IJCE-ICRTCEM-P189.pdf>.
- Majdzadeh, F., Soleimani, S.M. and Banthia, N. (2006). "Shear strength of reinforced concrete beams with a fiber concrete matrix", *Canadian Journal of Civil Engineering*, 33(6), 726-734, <https://doi.org/10.1139/L05-118>.
- Merli, R., Preziosi, M., Acampora, A., Lucchetti, M.C. and Petrucci, E. (2019). "Recycled fibers in reinforced concrete: A systematic literature

- review", *Journal of Cleaner Production*, 248, 119207, <https://doi.org/10.1016/j.jclepro.2019.119207>.
- Montero-Chacón, F., Sanz-Herrera, J.A. and Doblaré, M. (2019). "Computational multiscale solvers for continuum approaches", *Materials*, 12(5), 691, <https://doi.org/10.3390/ma12050691>.
- Naili, C., Doghri, I., Kanit, T., Sukiman, M.S., Aissa-Berraies, A. and Imad, A. (2020). "Short fiber reinforced composites: Unbiased full-field evaluation of various homogenization methods in elasticity", *Composites Science and Technology*, 187, 107942, <https://doi.org/10.1016/j.compscitech.2019.107942>.
- Pantazopoulou, S.J. and Zanganeh, M. (2001). "Triaxial tests of fiber-reinforced concrete", *Journal of Materials in Civil Engineering*, 13(5), 340-348, <https://doi.org/10.1061/%28ASCE%290899-1561%282001%2913%3A5%28340%29>.
- Qian, S., Zhou, J., De Rooij, M., Schlangen, E., Ye, G. and Van Breugel, K. (2009). "Self-healing behavior of strain hardening cementitious composites incorporating local waste materials", *Cement and Concrete Composites*, 31(9), 613-621, <https://doi.org/10.1016/j.cemconcomp.2009.03.003>.
- Raju, K., Tay, T.E. and Tan, V.B.C. (2021). "A review of the fe2 method for composites", *Multiscale and Multidisciplinary Modeling, Experiments and Design*, 4, 1-24, <https://doi.org/10.1007/s41939-020-00087-x>.
- Rameshkumar, V., Prabhath Ranjan Kumar, S., Poornima, V., Venkatasubramani, R. and Sreevidya, V. (2020). "Improvements in mechanical and durability parameters of bio-engineered concrete with metakaolin as a partial substitute for cement", *European Journal of Environmental and Civil Engineering*, 1-14, <https://doi.org/10.1080/19648189.2020.1767696>.
- Rao, M.V.S., Reddy, V.S. and Sasikala, C. (2017). "Performance of microbial concrete developed using bacillus subtilis JC3", *Journal of The Institution of Engineers (India): Series A*, 98(4), 501-510, <https://doi.org/10.1007/s40030-017-0227-x>.
- Richardson, A. (2005). "Bond characteristics of structural polypropylene fibres in concrete with regard to post-crack strength and durable design", *Structural Survey*, 23(3), 210-230, <https://doi.org/10.1108/02630800510610143>.
- Tiberti, G., Minelli, F., Plizzari, G.A. and Vecchio, F.J. (2014). "Influence of concrete strength on crack development in SFRC members", *Cement and Concrete Composites*, 45, 176-185, <https://doi.org/10.1016/j.cemconcomp.2013.10.004>.
- Tiwari, P.K. and Singh, V.K. (2024). "Assessment of polypropylene fiber for effect on fresh and physical performance with durability of self-compacted recycled aggregate concrete", *Civil Engineering Infrastructures Journal*, 58(1), 15-34, <https://doi.org/10.22059/cej.2024.362561.1943>.
- Vijay, K., Murmu, M. and Deo, S.V. (2017). "Bacteria based self-healing concrete - a review", *Construction and Building Materials*, 152(Supplement C), 1008-1014, <https://doi.org/10.1016/j.conbuildmat.2017.07.040>.
- Wang, J., Dewanckele, J., Cnudde, V., Van Vlierberghe, S., Verstraete, W. and De Belie, N. (2014). "X-ray computed tomography proof of bacterial-based self-healing in concrete", *Cement and Concrete Composites*, 53, 289-304, <https://doi.org/10.1016/j.cemconcomp.2014.07.014>.
- Wiktor, V. and Jonkers, H.M. (2011). "Quantification of crack-healing in novel bacteria-based self-healing concrete", *Cement and Concrete Composites*, 33(7), 763-770, <https://doi.org/10.1016/j.cemconcomp.2011.03.012>.
- Yıldırım, G., Keskin, Ö.K., Keskin, S.B., Şahmaran, M. and Lachemi, M. (2015). "A review of intrinsic self-healing capability of engineered cementitious composites: recovery of transport and mechanical properties", *Construction and Building Materials*, 101, 10-21, <https://doi.org/10.1016/j.conbuildmat.2015.10.018>.
- Yoo, D.Y. and Moon, D.Y. (2018). "Effect of steel fibers on the flexural behavior of rc beams with very low reinforcement ratios", *Construction and Building Materials*, 188, 237-254, <https://doi.org/10.1016/j.conbuildmat.2018.08.099>.
- Zhang, W., Zheng, Q., Ashour, A. and Han, B. (2020). "Self-healing cement concrete composites for resilient infrastructures: A review", *Composites Part B: Engineering*, 189, 107892, <https://doi.org/10.1016/j.compositesb.2020.107892>.



This article is an open-access article distributed under the terms and conditions of the Creative Commons Attribution (CC-BY) license.



The Free Vibration Characteristics of a Concrete Arch Gravity Dam Using Finite Element Technique

Sougata, M.¹ and Nallasivam, K.^{2*}

¹ P.G. Student of Structural Engineering, Department of Civil Engineering, National Institute of Technology (NIT) Hamirpur, Himachal Pradesh, India.

² Assistant Professor, Department of Civil Engineering, National Institute of Technology (NIT) Hamirpur, Himachal Pradesh, India.

© University of Tehran 2024

Received: 4 Dec. 2023;

Revised: 21 Mar. 2024;

Accepted: 29 May 2024

ABSTRACT: The objective of this study is to ascertain the free vibration analysis of an arch dam, which needs to be identified prior to doing a dynamic analysis of the dam in response to hydrodynamic and seismic loads. This work focuses on analyzing the free vibration analysis of an arch dam under several conditions: dam-soil contact, dam without soil interaction, and dam in a soil-reservoir system. The analysis is conducted using the finite element software ANSYS. This study's findings include an estimation of the natural frequency and mode shape of various dam systems by free vibration analysis. When foundation interaction is taken into account, the dam's natural frequency is found to be lower than that of a dam with fixed support, which is related to a reduction in stiffness and an increase in the vibrating system's mass. This paper focuses exclusively on analyzing the natural vibration of a concrete arch-gravity dam structure. Dam engineers can conduct additional evaluation of this research to enhance the structural effectiveness and functionality of the dam. Additionally, this research can serve as a basis for analyzing the concrete arch-gravity dam's response to different dynamic loads.

Keywords: Concrete Arch Dam, Free Vibration, Eigen Value Problem, Modal Analysis, Finite Element Method, FEM ANSYS Model.

1. Introduction

The concrete arch-gravity dams are visually appealing due to their arch action formed between two hills. This unique design presents new challenges in its application for irrigation, cultivation, flood safety, and the generation of renewable energy. These dams can be utilized to promote the growth and sustainability of a nation. The arch dam's design serves a structural purpose by facilitating the redistribution of hydrostatic pressure across the dam. These structural systems are characterized by their geometric complexity, which includes

combinations of different external and interior radius or arc angles. Additionally, they include variable and irregular centers for both exterior and interior arches. The vibrational characteristics of these dams can have an impact on their longevity, safety, and livability, as well as resulting in societal, economical, and ecological damages. Therefore, the objective of this work is to determine the natural oscillation behavior of an arch dam, which is crucial to understand prior to doing a dynamic analysis of the dam in response to hydrodynamic and seismic stresses. Yaghin and Hesari (2008) employed the ABAQUS

* Corresponding author E-mail: nallasivam@nith.ac.in

finite element technique software to assess the dynamic properties of arch concrete dams that do not have supports and dams that do not have bedrock support systems.

The temporal evolution of the primary stress, secondary stress, deformation of the dam crest, and river bed level has been computed using the collected data. The maximum values of these parameters during the seismic event have been thoroughly analyzed. Berrabah et al. (2012) conducted a comprehensive modal analysis of the Brezina Arch dam using the Finite Element Method (FEM) and ANSYS software. Three-dimensional (3D) models were created to analyze the impact of the foundation on the arch dam. The models included dams without a soil foundation, dams with soil but no mass, and dams with a soil foundation. Additionally, a study on the phenomenon of damped vibration was conducted. It was determined that the basic frequency of undamped and damped vibrations obtained from a dam with a soil foundation model was much lower than that of a dam without a soil foundation model, and also considerably lower than those obtained from a dam without a soil mass model. The results indicated that any damped vibration ratio was deemed to be lower in value compared to the dam without soil mass and the dam with soil foundation. Furthermore, it was significantly lower than the dam without a soil foundation model. The fundamental frequency of each undamped and damped mode was significantly lower than that of the dam without soil material.

Zhuan-Yun (2014) conducted a study to examine the specific load-bearing properties and seismic behavior of the largest elevated arch dam in a hydroelectric network. They developed a 3D finite element numerical model using ANSYS to analyze the interaction between the arch dam and its foundation. The study focused on static analysis under basic combined effects and dynamic behavior under key factors that contribute to the behavior of the elevated arch dam. The initial order had a

frequency of 3.34 Hz, and its vibrating mode was determined by the orientation along the river, as revealed by the examination of the vibrating characteristics of the elevated arch dam using the Lanczos method. The dam's planned system was deemed appropriate and reliable as the largest dynamic deformation and earthquake stress remain below the required limitations.

Patil and Awari (2015) investigated the impact of soil interaction on gravity dams by employing the finite element analysis program ANSYS. The analysis revealed that when taking into account soil stiffness and mass, the displacement of a dam with a soil foundation contact is greater than that of a dam without such an interface. Khosravi and Heydari (2015) utilized the finite element program ANSYS to ascertain the most advantageous configuration of concrete gravity dams, while also considering the interaction between the dam, water, and foundation rock. A two-dimensional (2D) finite element model comprising the dam, reservoir, and base was available. The dam was considered in four different modeling scenarios: a) Dam with a fixed foundation and an empty reservoir; b) Dam with a flexible foundation and an empty reservoir; c) Dam with a fully functional reservoir and a stable foundation; and d) A reservoir dam with a pliable foundation is required. A study was conducted on the modal characteristics and mode shapes of the Pine Flat, Koyna, and modelled triangular dams. The results were then compared to existing reference data in order to assess the accuracy and reliability of this modeling approach. The numerical findings confirmed the effectiveness of the suggested method for simulating the geometry of gravity dams. It was acknowledged that the inclusion of the dam-water-foundation-rock interaction is crucial in order to build a secure gravity dam.

Varughese and Nikithan (2016) utilized the finite element software ANSYS to assess the static, modal, and transient

analyses of the dam reservoir-foundation system. The reservoir was simulated using the FLUID 29 fluid acoustic element, while the dam and foundation were simulated using the PLANE 42 2D planar strain element. This combination accurately captured the fluid-structure interaction. A formulation for the fundamental period of concrete dams was established using modal analysis.

Pandey et al. (2016) conducted a comparative analysis between 3D and 2D models of a monolith gravity dam using ANSYS software. The researchers determined that a modal analysis can accurately determine the attendance for out-of-plane frequency by studying 3D models, which 2D models may not accurately depict. Consequently, the 3D models exhibited higher levels of stress in comparison to the 2D models when analyzing loads. The 3D model experienced higher tensile strains at the heel of the shorter cross-section due to hydrostatic loads.

Altunişik et al. (2016) investigated the impact of reservoir water on the vibration properties of a model arch dam, both before and after reinforcement. A model of an arch dam-reservoir-foundation was created for the purpose of this experiment. Experiments were conducted on arch dam models, both demolished and strengthened, to study the impact of water on the dynamic characteristics. These experiments involved analyzing ambient vibrations in both unoccupied and filled reservoir conditions. The dynamic properties were acquired by an improved frequency domain decomposition method. Afterwards, the dynamic characteristics obtained from the damaged and reinforced dam models were compared. The study also examined the natural frequencies of both damaged and strengthened models to determine if the impact of strengthening on the frequencies is detectable.

Esmailzadeh et al. (2019) conducted research to detect and determine the extent, location, and elevation of any structural

harm to the dam. Three finite element models of the Pine Flat, Bluestone, and Folsom dams were selected as case studies to achieve these objectives. The dams were modeled using SAP2000 software to analyze their geometric, physical, and mechanical characteristics in both undamaged and damaged conditions. Multiple modal inquiries determined the frequencies and configurations of the structural movements.

Messaad et al. (2021) conducted a modeling study to analyze the occurrence of dam reservoir-foundation coupling, taking into account the presence of both the reservoir and the foundation. This approach allowed for a more accurate assessment of the overall performance of the system. The study utilized the ANSYS FEM to examine the dynamic properties of a dam-reservoir foundation system when subjected to seismic forces.

Verma and Nallasivam (2020, 2021a,b) conducted a study on the static and free vibration analysis of box-girder bridges. Hariri-Ardebili et al. (2021) performed a sensitivity study on dams using a hybrid surrogate model that combines Random Field (RF) and Polynomial Chaos Expansion (PCE). The results illustrated the dam's free vibration characteristics using natural frequencies and mode shapes.

Hariri-Ardebili et al. (2016) conducted a parametric research on a concrete gravity dam using finite element analysis. The researchers determined that the primary causes of failure for these dams were cracking, overturning, and sliding. Additionally, they found that the vibration characteristics of the dams were primarily influenced by the first six modes.

Amini et al. (2021) conducted a sensitivity study on aging concrete gravity dams using Kriging and PCK meta-models. It was discovered that these models were efficient in conducting reliability analysis while reducing computing time.

Abdollahi et al. (2022) highlighted the increasing requirement for a comprehensive dam form design framework that considers

uncertainties and can handle many hazards. This framework should also incorporate time-dependent demand and capacity models. The technique was employed to optimize the configuration of gravity dams by utilizing a collection of time-varying and time-invariant performance indicators at both the local and global scales. Ultimately, the framework was expanded to encompass a versatile dam class that incorporates different heights, strengths of concrete, and flexibility from the base to the concrete structure.

Li et al. (2022) conducted a study on the interaction of dams, water, and foundation rocks in a complicated layered half-space. A novel Scaled Boundary Finite Element Method (SBFEM) was devised for the purpose of examining the interaction between a 3D dam and its foundation. The foundation rock was represented by three unique models: A homogeneous half-space, a horizontal layered half-space, and an inclined half-space.

Rasa et al. (2024a) proposed a computational model that efficiently examined the seismic behavior of concrete gravity dams using the Laplace domain-FEM methodology. The study findings suggested that longer periods of large earthquakes were linked to greater deformations, stress fluctuations, and an increased probability of damage to the dam structure.

Rasa et al. (2024b) examined the dynamic reactions of a concrete machine foundation when subjected to impact loads. The study also considered the deterioration of concrete due to chemical and mechanical processes over time. The deterioration of concrete over time significantly affected the dynamic reactions of machine foundations. There was a direct relationship between the severity of high stress responses at the foundation and the rate at which concrete deteriorates. Machine foundations built on medium soil types exhibited a reduction of 32.6% in stress responses between the ages of 0 and 50 years.

Sharma and Nallasivam (2023) utilized

the ANSYS program, a commercial finite element software, to compute the static response of a 2D model of the Bhakra concrete dam. Several 2D models were created to represent different types of dams, including those with a solid basis, as well as those with a foundation that had mass and those with a foundation that was weightless.

Rasa et al. (2024c) examined the dynamic behavior of the interaction problem between aging concrete gravity dams and reservoirs. Due to concrete deterioration, the dam undergoes elongation in its lifespan, resulting in dynamic responses such as horizontal and vertical displacements, as well as changes in its basic periods. This elongation ultimately resulted in a reduction in the seismic stability of the dam.

Rasa et al. (2024d) presented a dam-reservoir interaction model that integrates many parameters like water compressibility, surface water sloshing, and radiation damping at the far-end reservoir. The purpose of this model was to analyze the influence of concrete degradation on the seismic response and effectiveness of gravity dams. The deterioration of concrete was assumed to take place due to both mechanical and chemical processes over the whole lifespan of the dam.

Hashempour et al. (2023) proposed a simplified nonlinear model to analyze earthquake effects on concrete arch dams. It captured concrete's behaviour under load changes better than complex models. The model accurately predicted crack patterns and final strength. The analysis of the Morrow Point dam considered dam-water interaction and used two damping algorithms. The research suggested that this efficient model can replace complex ones while highlighting the importance of choosing appropriate damping for accurate results.

Heshmati et al. (2013) compared stress and strain methods for evaluating arch dam seismic response. A detailed dam model considered interaction with the reservoir and foundation. While both stress and strain

(cumulative inelastic strain) were analyzed and showed some correlation, the paper argued that the strain-based method provided a more refined picture of dam damage. This potentially leads to different conclusions about dam safety compared to relying solely on stress analysis. In essence, the paper suggested strain-based methods offer a more nuanced approach to dam safety assessments.

Rezaiee-Pajand et al. (2023) proposed a novel method for analyzing vibrations in concrete dams. The traditional approach was computationally expensive due to a complex problem type. They introduced a new strategy that avoids this issue. They formulated two new, easier-to-solve eigenvalue problems and claimed their method was more accurate than existing techniques. The paper validated this with tests on benchmark dams. While the details of the method and the extent of accuracy improvement were not provided here, this new approach had the potential to improve efficiency and accuracy in dam vibration analysis significantly.

Tavakoli et al. (2023) addressed a vulnerability in Roller-Compacted Concrete (RCD) dams: thermal cracks stemming from cement variations. These cracks can worsen during earthquakes. The study examined this phenomenon by utilizing a 3D FEM constructed in the ABAQUS program. The model considered both translational and rotational earthquake motions to analyze crack propagation. Results showed that existing cracks significantly propagated during earthquakes, with rotational motion playing a crucial role. It could increase crack propagation energy by up to 50% for some earthquakes. This highlighted the importance of considering both crack presence and rotational motion for improved earthquake safety assessments of RCD dams.

According to the literature reviews, most researchers have performed both closed-form solution and non-closed-form-

based free vibration analysis of the concrete gravity dam system. In addition, a small number of researchers have performed parametric studies on the free vibration characteristics of several types of concrete gravity dam systems. The objective of this work is to develop a 3D FEM using ANSYS software to examine the free vibration properties of the concrete gravity dam system, with a focus on natural frequencies and mode shapes. The model's reliability is validated using mesh convergence analysis and comparison with findings from prior researchers' investigations. Several parametric experiments are conducted to examine the free vibration properties of concrete gravity dams. The study's findings are crucial for dam engineers as they provide significant insights to enhance their comprehension of the modal features of a concrete gravity dam. Engineers will benefit from this knowledge as it will assist them in studying the dynamic behavior of concrete gravity dams caused by hydrodynamic and earthquake loads.

2. Materials and Methods

2.1. Finite Element Modelling of Concrete Arch Gravity Dam System

Figure 1 depicts the sequential steps for assessing a FEM model of a concrete arch gravity dam system.

2.2. Modelling of a Concrete Arch-Gravity Dam

2.2.1. Dimensional Configurations of The Dam

Table 1 presents the configuration variables of the dam, whereas Figure 2 illustrates the cross-section of the dam using these geometry variables.

This study examines the proposed construction of a concrete arch-gravity dam proposal at Jankar Jangal, located near Chamba, Himachal Pradesh, India, in the Ravi riverbed basin.

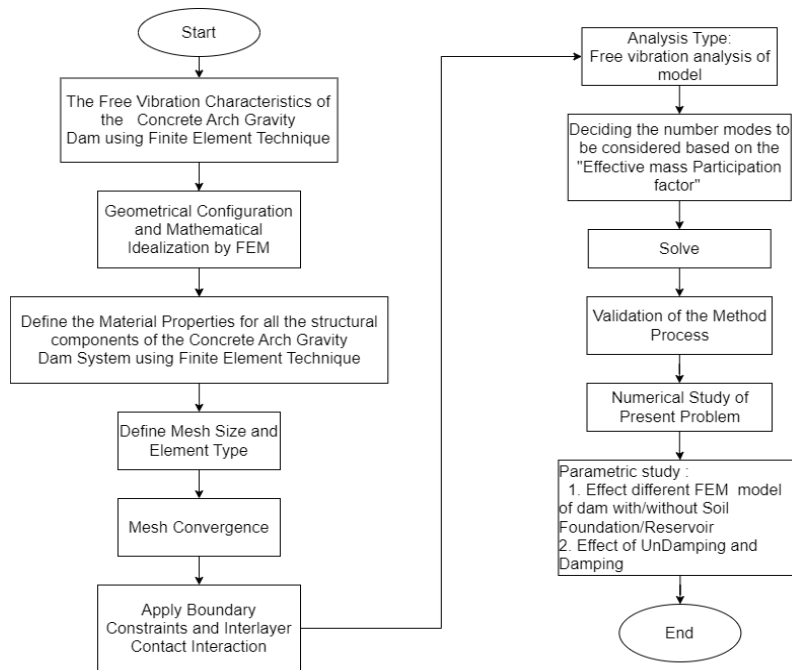


Fig. 1. The schematic sequence used to calibrate the FEM model

Table 1. The parameters of the geometry of the dam

	Model category	Concrete arch-gravity dam (m)
Concrete dam	Width(at Crest Level)	4
	Width(at foundation level)	36.3
	Height	25.94
	Curve span	20.05
	Max water depth	25.44
Foundation	Model category	Soil layer in m
	x	27
	y	48.3
	z	95

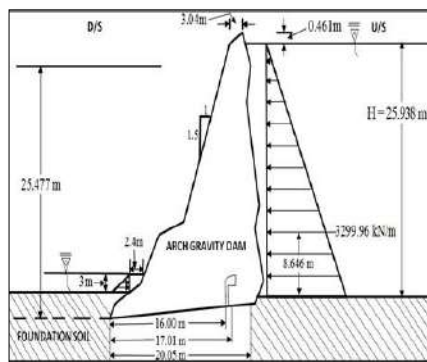


Fig. 2. Geometry configuration of the dam

2.2.2. Concrete Arch-Gravity Dam Mathematical Idealization Using Finite Element Modelling

The FEM has become an indispensable tool for computationally addressing a diverse range of technical problems. The finite element-based software (Zhang et al., 2013; ANSYS Manual, 2019; Tickoo,

2021) was utilized to model the concrete arch-gravity dam in this study. Figures 3-5 display the three distinct methods of discretizing the dam model. In order to examine the modal behavior of the dam, three distinct model situations are selected as follows: Model 1 refers to a dam that has a fixed support and does not have a soil base. The reservoir associated with this dam is called "fixed-empty" and is seen in Figure 3. Model 2 refers to a dam that has a dirt base and an empty reservoir. This particular model is called "mass-empty" and may be seen in Figure 4. Model 3 refers to a dam that has a soil foundation and a reservoir that is completely filled with water. This particular dam is known as the "mass-fluid" dam, as seen in Figure 5. For Model 1, the dam is considered as a fixed boundary constraint at the base.

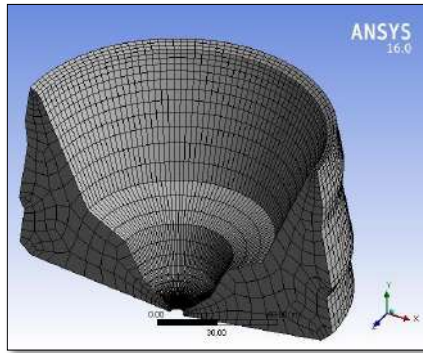


Fig. 3. Dam with a fixed support and does not have a soil base

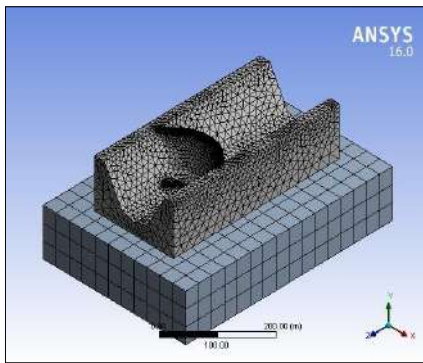


Fig. 4. Dam with a dirt base and an empty reservoir

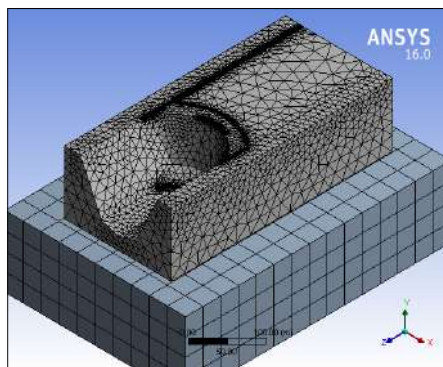


Fig. 5. Dam with a soil foundation and a reservoir that is completely filled with water

In Models 2 and 3, the dam is fixed at the base of the foundation. The length of the reservoir is determined by multiplying the

depth by a factor of 1.5. The dam has undergone a comprehensive 3D analysis. The implementation of ANSYS was utilized for the purpose of modeling and analysis. The dam, soil base, and reservoir have all been created with 3D solid components. Each node of an element possesses six degrees of freedom, encompassing translations and rotations along the x, y, and z axes.

2.3. Material Properties

Table 2 provides the characteristics of the material for the base soil of a concrete arch dam and the water in the reservoir. Multiple organizations provide specific guidelines for ensuring safe construction.

The concrete mass is regarded as homogeneous, isotropic, and elastic. An ideal foundation soil is a uniform, equally responsive, and flexible medium. Herein, the Viscous damping of the structure is assumed to be Rayleigh damping form (Chopra, 2007). In this parametric investigation, the classical viscous damping ratio will be varied at 2%, 5%, and 10%.

2.4. Element Type and Meshing

Figure 6 illustrates the SOLID186 elements, which are 3D solid elements with 20 nodes and exhibit quadratic displacement behavior. Meshing is a crucial component in a finite element model. Using finer meshes in the FEM model can yield more accurate outcomes, but it also results in a larger number of elements and nodes, which in turn leads to higher computational costs. Choosing the optimal element size is critical since it directly affects the trade-off between computational expense and solution precision.

Table 2. Material properties of the concrete dam, reservoir water, and foundation soil

Concrete dam	The mass density of concrete ρ (kg/m ³)	2500
	Modulus of elasticity of concrete E (MPa)	28500
	Poisson's ratio (μ)	0.2
Reservoir water	Density of water (kg/m ³)	1000
	Bulk modulus of elasticity of water K (MPa)	2020
	Sonic velocity or Speed of pressure wave (m/s)	14500
	Wave reflection coefficient	0.25
Foundation soil	The mass density of foundation Soil ρ (kg/m ³)	2100
	Modulus of elasticity of foundation soil E (MPa)	14500
	Poisson's ratio μ	0.25

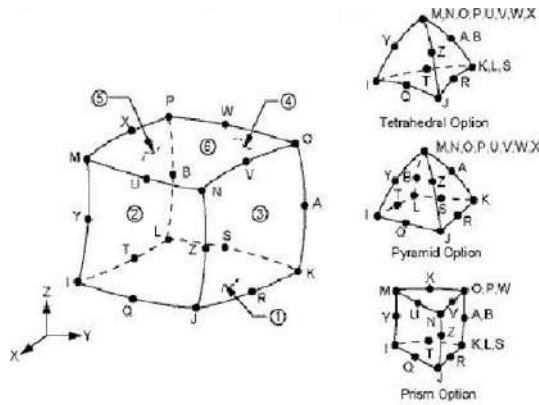


Fig. 6. Multiple sorts of elements utilized to model different components of a concrete arch-gravity dam

The ANSYS Manual (2019) is a robust FEM tool that offers users the ability to define and adjust element sizes according to the specific characteristics of the investigated model or system. The choice of element size and suitable meshing procedures is a critical determinant in ensuring the accuracy and efficiency of simulations conducted using software like ANSYS in the domain of FEM. The characteristics of the element type and meshing size employed for different components of the current model are described in Table 3.

Table 3. Types of elements and meshing size (ANSYS manual, 2019)

Components	Mesh size (mm)	Element type
Concrete dam	250	3D Solid 186
Soil foundation	300	3D Solid 186
Reservoir water	300	3D Solid 186

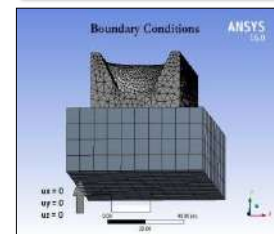
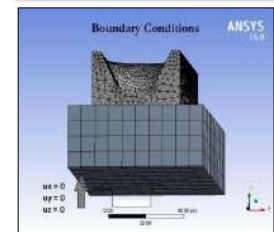
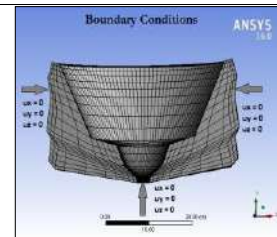
A denser mesh with a greater number of smaller pieces typically produces more precise outcomes, particularly in regions with intricate geometry, as depicted in Figures 3-5.

2.5. Boundary Conditions

When creating a finite element model, the selection of boundary conditions is crucial. It is vital to choose appropriate boundary conditions in order to accurately produce meaningful results. The boundary condition for the structure, as indicated in Table 4, may be categorized into two primary parts: internal boundary conditions, which involve the interaction between each component, and outer boundary conditions, which involve the interaction with the external environment.

Table 4. Boundary conditions (Berrabah et al., 2012)

Components	Boundary condition
Model-1	Fixed boundary constraints at the base of the dam and the side of the dam
Model-2	Fixed boundary constraint at the base of the foundation and side of the dam, and bonded boundary constraint between the interface of the dam and foundation
Model-3	Fixed boundary constraint at the base of the foundation and side of the dam, and bonded boundary constraint between the interface of the dam and foundation



Regarding the outer boundary condition, it is important to note that the bottom and four sides of the foundation were simulated with fixed conditions, meaning that all degrees of freedom were restrained. The internal boundary condition was established by implementing a bonded interaction requirement between the interface of the dam and foundation.

2.6. Modal Analysis of Concrete Gravity Dam System

A frequently utilized technique in the field of structural dynamics is the mode superposition approach. This approach enables the analysis of various dynamic loads acting on structures, including both transient and steady-state responses. Modal frequencies and modal vectors of a structure are usually calculated in the absence of dampening. The hypothesis put forth by Borino and Muscolin (1986) posits that the precise frequencies of structures, commonly referred to as damped frequencies, demonstrate a negligible departure from their un-damped counterparts. The elucidation of the topic is efficiently achieved by employing illustrative situations (Rasa and Budak, 2021).

2.6.1. Un-Damped Modal Analysis

Before doing dynamic analysis, it is essential to carry out free vibration analysis to ascertain the inherent dynamic characteristics of the model structure. Free vibration refers to the phenomenon of vibrations occurring at the inherent frequency of a system without any external influence or interference. The utilization of mode analysis allows for a thorough depiction of the dynamic properties of a vibrating system, encompassing its mode shapes and inherent frequency. The equation of motion for an undamped free vibration system is dictated by the overall structural system, which includes the cross-section, materials utilized, and other important aspects. These parameters collectively govern the fundamental

frequencies and mode shapes of the vibration equation.

$$[M][\ddot{\delta}] + [K][\delta] = 0 \quad (1)$$

where $[M]$: is global mass matrix, $[\ddot{\delta}]$: is global acceleration matrix, $[K]$: is global stiffness matrix, and $[\delta]$: is global displacement matrix. When analyzing the un-damped free vibration, it can be assumed that the motion follows a harmonic pattern in its natural mode. Therefore, the reaction is depicted as follows:

$$[\delta] = [X]\sin(\omega t + \phi) \quad (2)$$

where $\{X\}$: is nodal amplitude of vibration, ω : is angular natural frequency (rad/sec), and ϕ : is phase angle. From Eqs. (1) and (2), a generalized eigenvalue problem can be obtained (Eq. (3)).

$$[[K] - \omega^2[M]][X] = 0 \quad (3)$$

When solving Eq. (3), a standard Eigen solver is utilized to ascertain the inherent frequency and mode shapes of the structures. To get the dam's dynamic characteristics, the equation (Clough and Penzien, 1995) is solved using an ordinary eigen solver. The theoretical natural frequency, as mentioned in Clough and Penzien (1995), can be written as Eq. (4).

$$f_n = n^2 \pi^2 \sqrt{\frac{EI}{mL^4}} n \quad (4)$$

$$= 1.2.3. \dots$$

where f_n : is the frequency of each order, EI : is the flexural stiffness of the cross-section, m : is mass per unit length, and L : is the length of the beam. The corresponding mode shape, ϕ_n , can be written as Eq. (5).

$$\phi_n(x) = C_1 \sin \frac{n\pi x}{L} \quad (5)$$

2.6.2. Damped Modal Analysis (Yaghin and Hesari, 2008; Berrabah et al., 2012)

Damping is a phenomenon that affects

every dynamic process in nature. The existence of an utterly undamped vibration is not observed in actuality. ANSYS offers multiple options for simulating the impact of structural damping. In the context of modal analysis, it is possible to employ both Rayleigh damping and material-dependent damping techniques. In addition, distinct dampening components can be utilized. The two eigen solvers that can be utilized for this objective are the Damped Method and the QR-Damped method. Recall that the equations of free-damped vibration are as Eq. (6).

$$[M][\ddot{x}] + [C][\dot{x}] + [K][x] = 0 \quad (6)$$

where $[M]$, $[C]$ and $[K]$ are the global mass, damping and stiffness matrix, $[\ddot{x}]$, $[\dot{x}]$ and $[x]$ are the global acceleration, velocity and displacement matrix.

In this case, it is assumed that the dam's viscous damping follows the Rayleigh damping form, as described by Chopra (2007). The damping matrix in this scenario is regarded as being proportional to either the mass or the stiffness matrix, or a combination of both. This is because the undamped mode forms are orthogonal for each of these factors, as indicated by the following equations.

$$[c] = \alpha[m] + \beta[k] \quad (7)$$

It is also known as Rayleigh damping. Rayleigh damping determines the relationship between the damping ratio and frequency.

$$\xi_n = \frac{\alpha}{2\omega_n} + \frac{\beta\omega_n}{2} \quad (8)$$

The proportionality constants α and β have units of seconds to the power of negative one and seconds, respectively. The terms "mass proportional damping constant" and "stiffness proportional damping constant" are used to refer to these concepts. If the damping ratio ξ_m, ξ_n

associated with two frequencies in the m^{th} and n^{th} modes is known, the two damping factors can be determined by solving a pair of simultaneous equations. By substituting Eq. (8) into the equations for each of these two examples and representing the resulting equations in matrix form, Eq. (9) is obtained.

$$\begin{Bmatrix} \xi_m \\ \xi_n \end{Bmatrix} = \frac{1}{2} \begin{bmatrix} 1/\omega_m & \omega_m \\ 1/\omega_n & \omega_n \end{bmatrix} \begin{Bmatrix} \alpha \\ \beta \end{Bmatrix} \quad (9)$$

If the damping coefficients of the two modes are equal, the ($\xi = \xi_m = \xi_n$) solution of the simultaneous equations leads to Eq. (10).

$$\begin{Bmatrix} \alpha \\ \beta \end{Bmatrix} = \frac{2\xi}{\omega_m + \omega_n} \begin{bmatrix} \omega_m\omega_n \\ 1 \end{bmatrix} \quad (10)$$

According to ANSYS (2019), alpha damping, also known as mass damping, may be disregarded in numerous practical structural issues when the value of ($\alpha = 0$) is equal to zero. This disregard is typically observed in bodies that exhibit resistance to wind or in undersea applications. In such instances, one of the proportionality constants value (β) can be assessed based on the known value of damping and frequency, ξ_i and ω_i , as follows.

$$\xi_i \text{ and } \omega_i, \text{ as: } \beta = \frac{2\xi_i}{\omega_i} \quad (11)$$

In Eq. (11), the damping ratio (ξ) is assumed to be 2%, 5%, and 10%.

3. Results and Discussion

3.1. Free Vibration Characteristics of a Concrete Arch-Gravity Dam

The response time of a structure is affected by the ratio of force-frequency (ϖ) resulting from outside loads such as live loads and seismic forces, to the inherent frequency (ω) of the structure in relation to its weight. The natural frequencies align with the force frequency, which may result

in resonance and cause structural harm.

3.1.1. Validation of the Method

The modal analysis results for the first five modes of the current work's concrete arch-gravity dam have been confirmed by the study conducted by Berrabah et al. (2012). The validity of this analysis regarding the dam problem, considering both the presence and absence of soil-structure interaction, is confirmed by comparing it with ANSYS results obtained from simplified analyses of the fundamental mode response. The solid 186 elements were employed to replicate the behavior of the concrete arch-gravity dam. The concrete arch-gravity dam was meshed with a mesh size of 200 mm. The numerical problem at hand involves a concrete arch-gravity dam with specific geometric dimensions. The problem focuses on the material properties, element types, and boundary conditions of different components of the dam, as outlined in Tables 1-4.

By utilizing ANSYS software, the outcomes of prior research publications are juxtaposed with the findings of the present study, as depicted in Figure 7. Given the strong concurrence between the current findings and the established results in existing literature, the methodology employed in this study is deemed suitable

for addressing the dam-soil interaction phenomenon and accurately determining the fundamental natural frequency.

3.1.2. Present Problem

Several modal analyses were performed to determine the fundamental natural frequency range of the concrete arch-gravity dam, as depicted in Figures 3-5. The solid 186 elements were employed to replicate the behavior of the concrete arch-gravity dam. The concrete arch-gravity dam was meshed with a mesh size of 400 mm.

The numerical problem at hand concerns a concrete arch-gravity dam with specific geometric dimensions. It involves analyzing the material properties, element types, and boundary conditions of different components of the dam, as outlined in Tables 1-4. An arch dam was subjected to modal analysis in order to ascertain the primary frequencies and mode configurations of the dam construction. The modal frequencies and dynamic responsiveness of gravity dams during earthquakes are influenced by the foundation and water reservoir. An eigenvalue analysis is conducted on the three models mentioned above, and a comparative examination of the modal frequencies is presented in Figures 8-10.

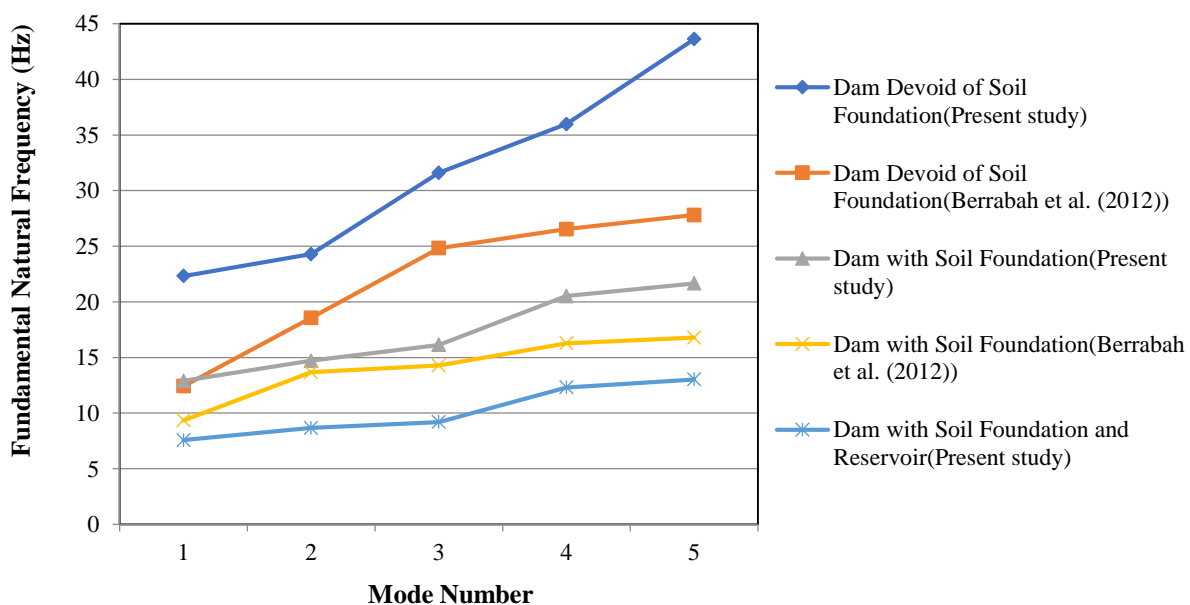
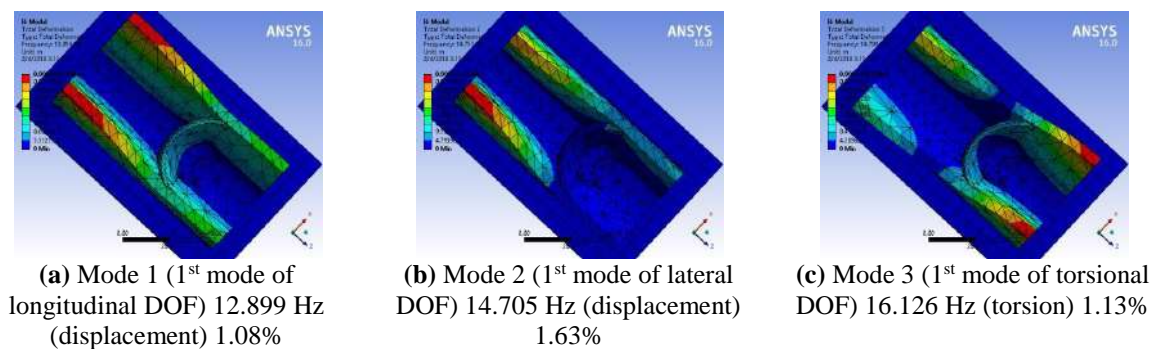
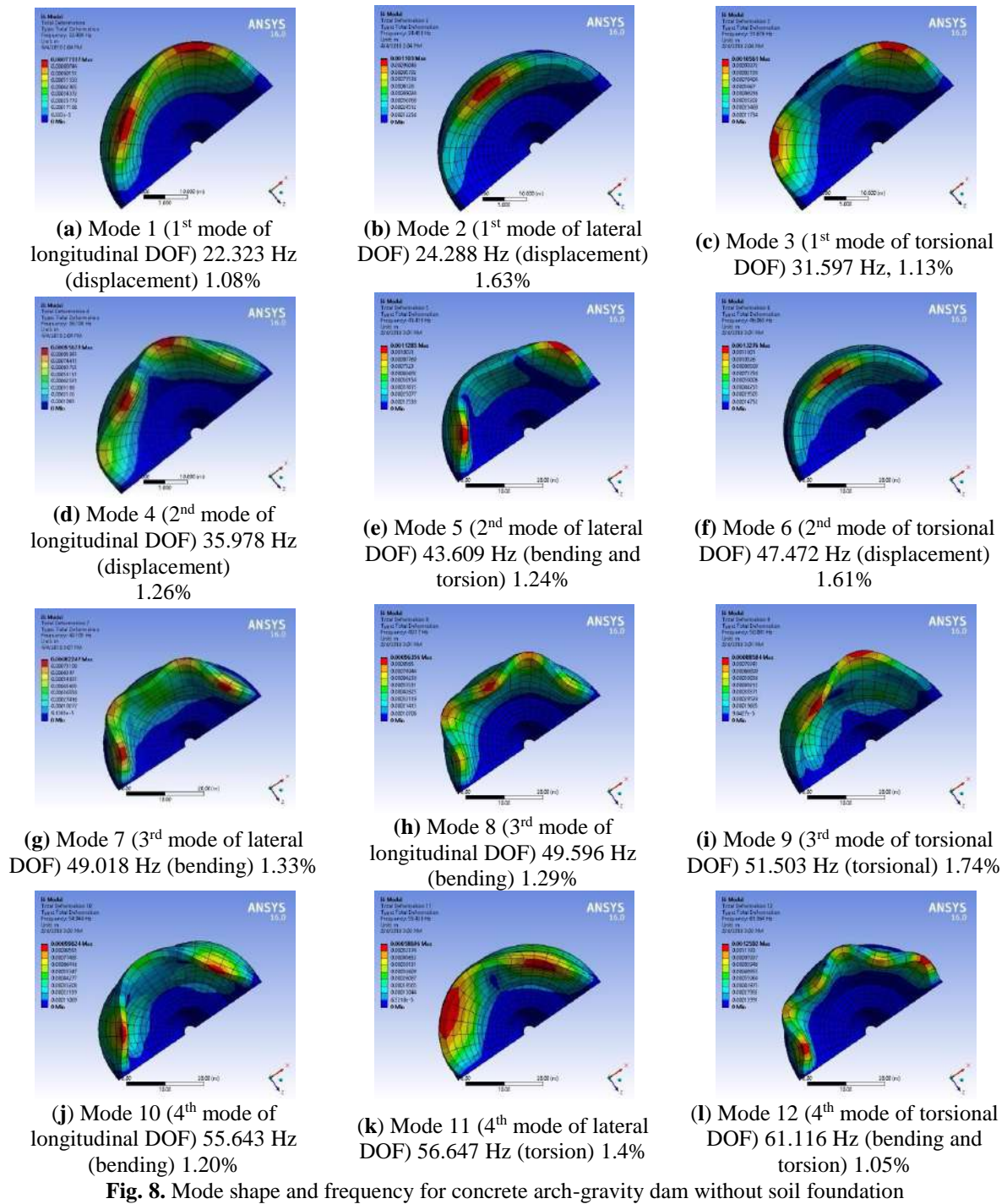
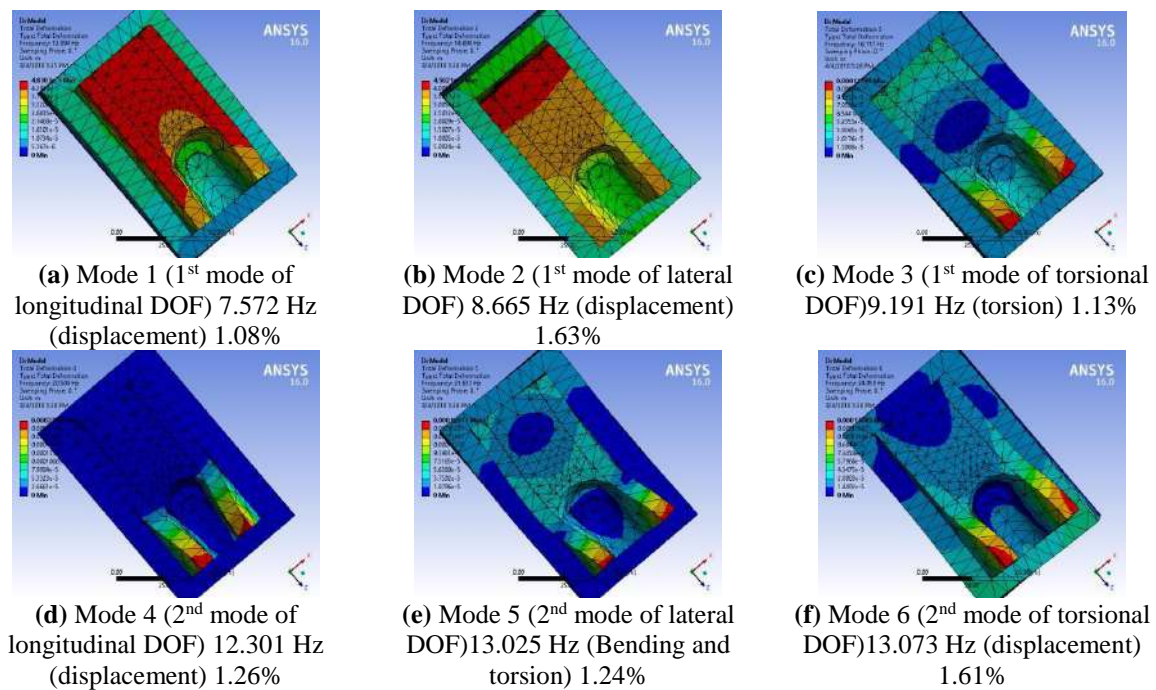
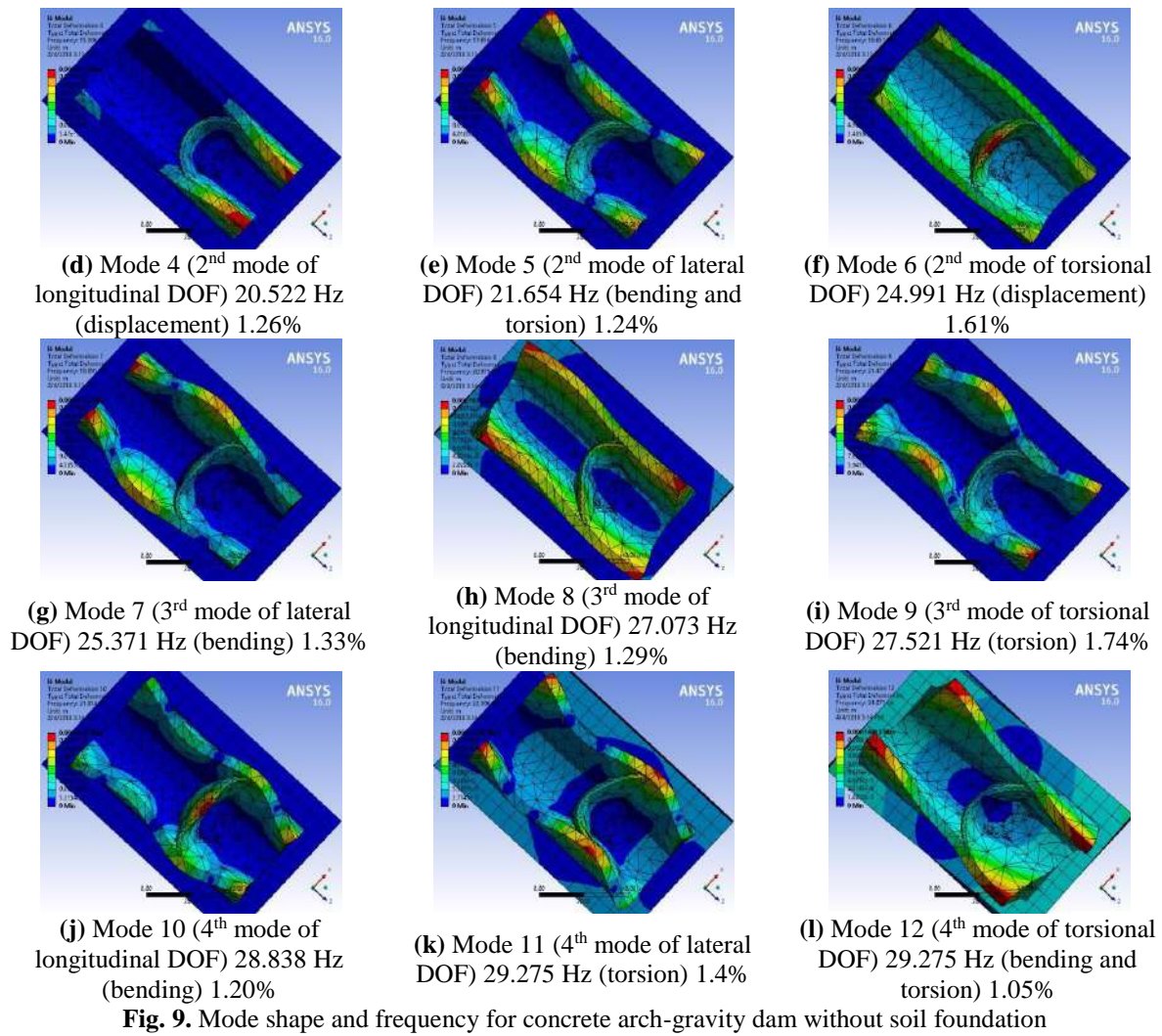


Fig. 7. Frequency of first five modes for undamped free vibration compared with Berrabah et al. (2012) results





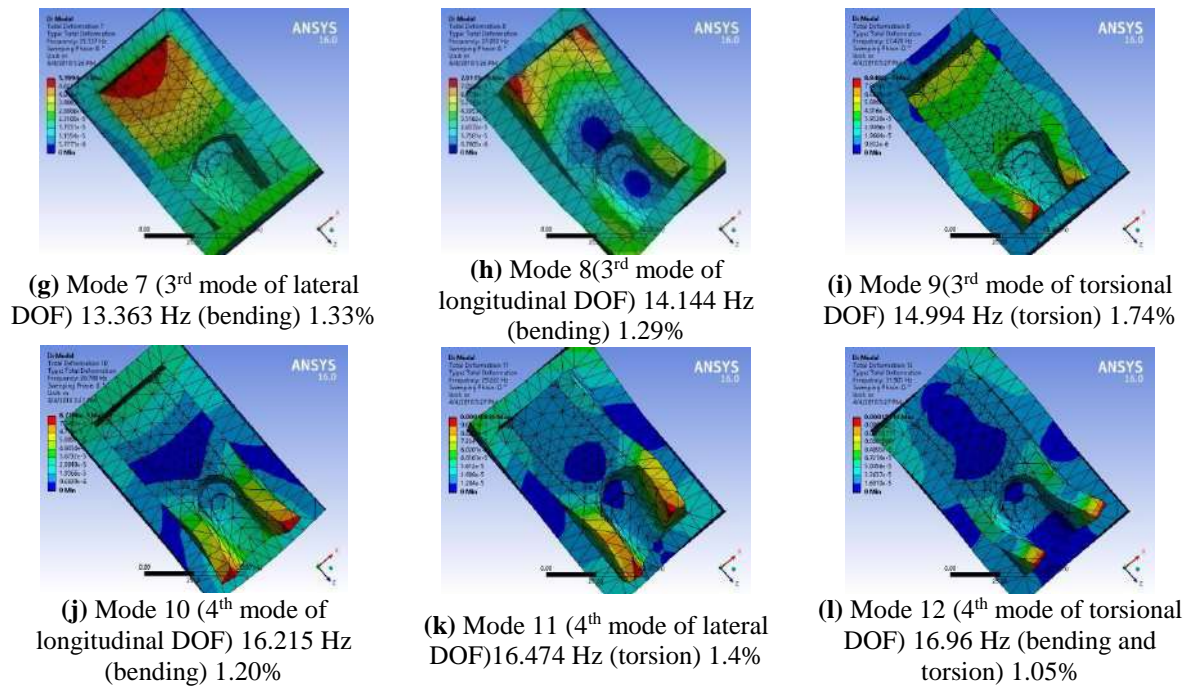


Fig. 10. Mode shape and frequency for concrete arch-gravity dam with soil foundation and reservoir

3.1.2.1. Mesh Convergence Study for Validation Model

The mesh size is a critical factor in the finite element analysis of any structure. For optimal outcomes, it is imperative to select an appropriate mesh size for each component. Mesh convergence is utilized in research to obtain more accurate and detailed information about the free vibration responses of buildings. The study was conducted to analyze fluctuations in the quantity of elements. The model was resolved by decreasing the mesh size and analyzing the results to observe the variations in accordance with the mesh size.

The process of meshing in ANSYS (2019) involves finding a balance between accuracy and computational cost when applying it to any structural model. A crucial aspect of creating an accurate simulation is the development of a top-notch mesh. In this section of the research, mesh convergence is performed to accurately determine the natural frequency of several types of concrete arch-gravity dams. Figure 11 displays the free vibration response for various mesh sizes. The simulation for the structure model in this work is performed using a mesh size of 200 mm, as determined by mesh convergence.

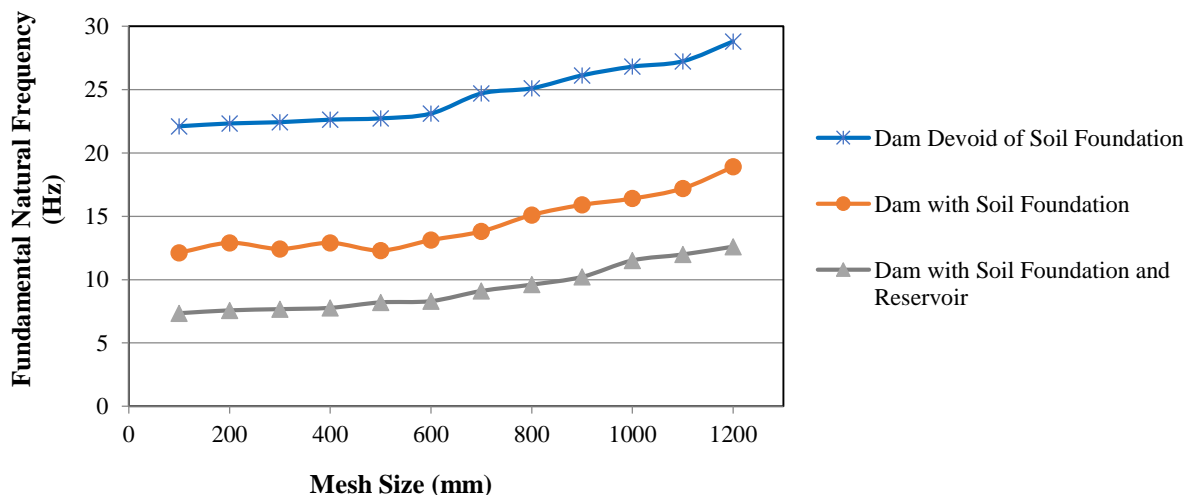


Fig. 11. Mesh convergence study

3.1.3. Parametric Study on Concrete Arch-Gravity Dam System

An analysis is conducted on the FEM model of a concrete arch-gravity dam to identify the several parameters that affect its modal properties. The current study has analyzed multiple parameters and provides a comprehensive explanation of the influence of each parameter.

- Influence of mass participation factor: The number of simulated modes is contingent upon the vibration of various frequencies. According to the Indian standard code "IS 1893 (Part I)", the analysis should evaluate a number of modes that will result in about 90 percent of the modal mass being aroused. Therefore, based on the aforementioned statement, a total of 12 modes are derived from the arch dam, each having distinct configurations. Figure 12 displays the mode forms and associated free vibration frequencies for 30 modes of the dam under three different conditions: without a soil foundation, with a soil foundation, and with a soil foundation and reservoir. The primary mode exhibits a significant mass attendance in the x direction (76%), whereas its effective mass participation is in the y direction (35%). The top five modes constitute 86% of the overall

mass participation, so establishing them as the most significant modes. The relationship between effective mass and total mass is almost similar in the x direction and is greater than that in the y and z directions, as seen in the Appendix (Tables A1-A2).

- Influence of Model Case:

Figure 12 displays the mode forms and associated free vibration frequencies for 30 modes of the dam in three different scenarios: without a soil basis, with a soil foundation, and with both soil and a reservoir.

The modal analysis results indicate that the dam's natural frequency is most prominent in Model 1, which represents a fixed-empty condition of the reservoir and soil foundation. Moreover, when dam-reservoir-soil foundation interaction is recognized (mass-fluid model), the most negligible value for the fundamental frequency is obtained, i.e., there is a 21% decrease in modal frequency for the first fundamental mode as well as more than 30-50% reduction in modal frequencies of all other higher modes if dam structure without soil foundation and dam structure with foundation is considered.

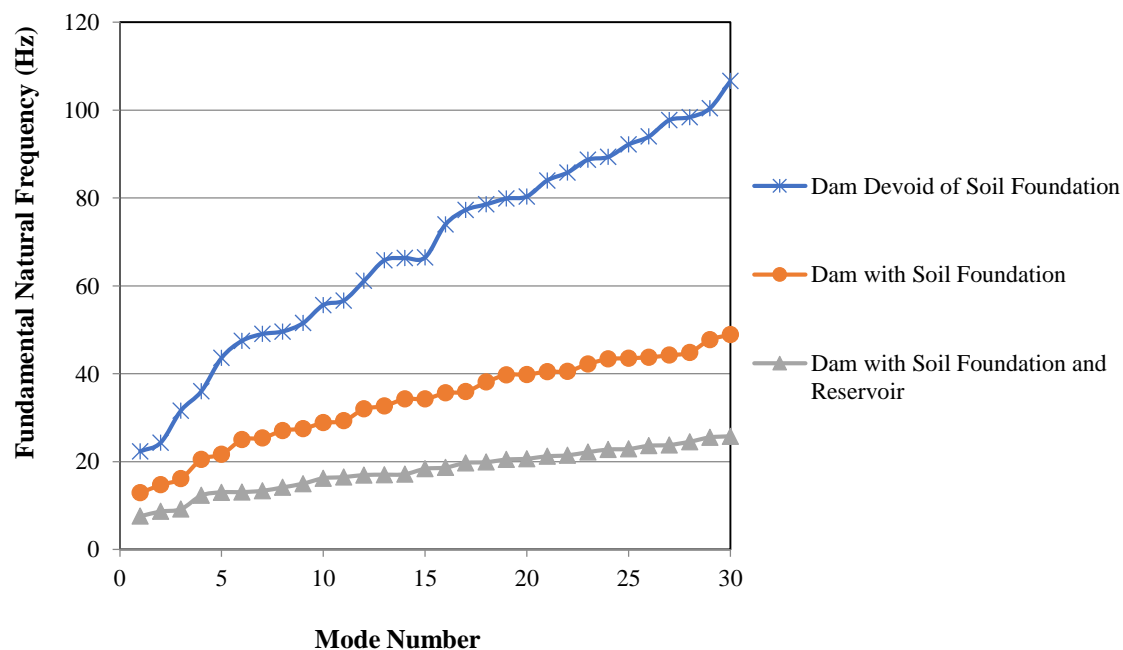


Fig. 12. Frequency of different modes for undamped free vibration

If dam structures with soil foundations and dam structures with soil foundation reservoirs are examined, the modal frequency of the first mode will be reduced by 12%, and the modal frequencies of the subsequent higher modes will be reduced by more than 15%.

When the structure foundation and structure reservoir are taken into account, the modal frequency of the first mode reduces by 22%, while the modal frequencies of other higher modes reduce by more than 51%. This is because when reservoir interaction is taken into account, the water surrounding the structure induces an increase in the inertial force operating on the structure. The hydrodynamic pressure acts on the structure as even the reservoir moves along with the displaced structure. Consequently, the presence of water in the

reservoir affects the dynamic characteristics of the system by altering the patterns of motion and decreasing the frequency of vibrations.

Considering the influence of foundation interaction, the natural frequency of the dam is determined to be lower compared to a dam with fixed support. This is attributed to a reduction in stiffness and an increase in the mass of the vibrating system.

- Influence of Damping Ratio:

Furthermore, a computational analysis was conducted to examine the effects of viscous damping using the Rayleigh form. Figures 12-15 illustrate the mode forms and corresponding free vibration frequencies for 30 modes of undamped and damped systems with different damping ratios ($\xi = 0, 2\%, 5\%, 10\%$).

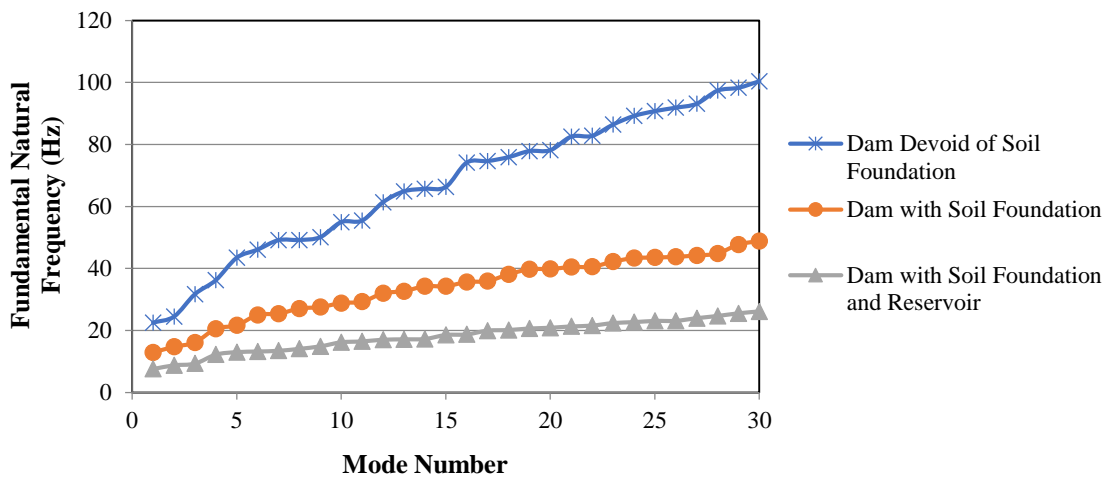


Fig. 13. Frequency of different modes for damped vibration ($\xi = 2\%$)

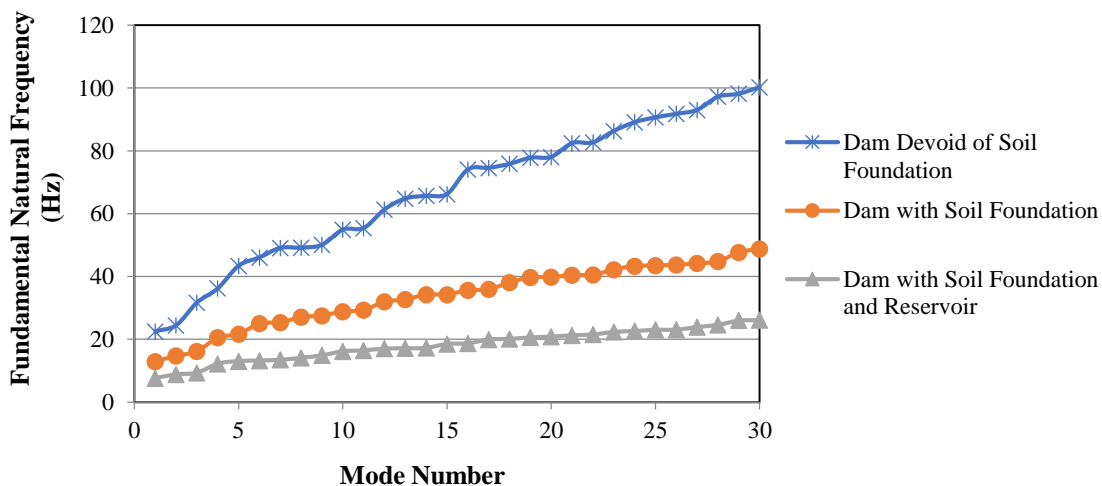


Fig. 14. Frequency of different modes for damped vibration ($\xi = 5\%$)

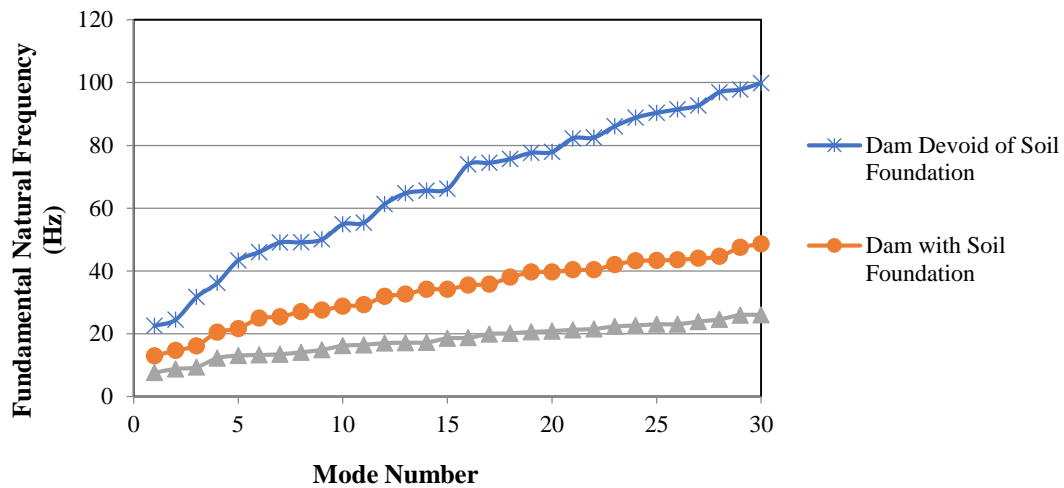


Fig. 15. Frequency of different modes for damped vibration ($\xi=10\%$)

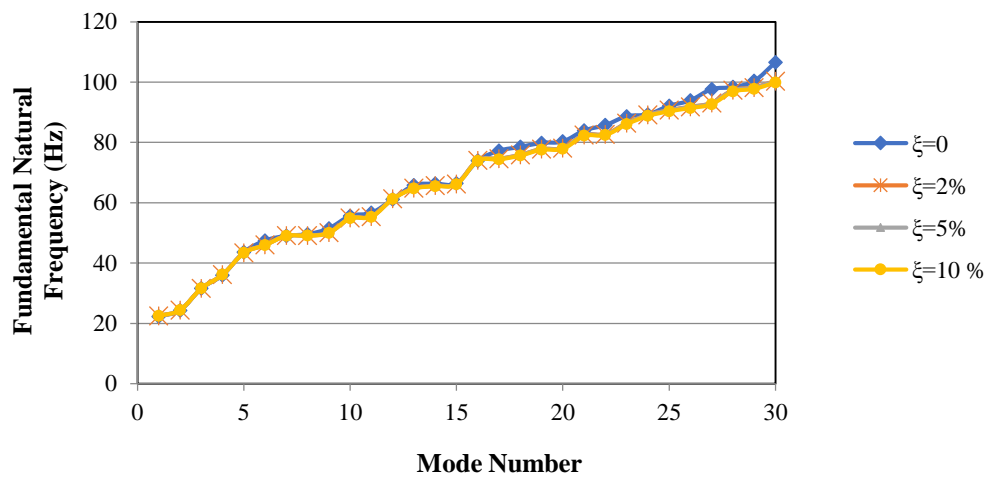


Fig. 16. Dam without a soil foundation

The systems include dams without a soil basis, dams with a soil foundation, and dams with a soil foundation plus a reservoir. Figures 17-18 demonstrate that the

frequency (in Hertz) of undamped free vibration is almost indistinguishable from that of damped (0%, 2%, 5%, and 10%) vibration for all arch dam models.

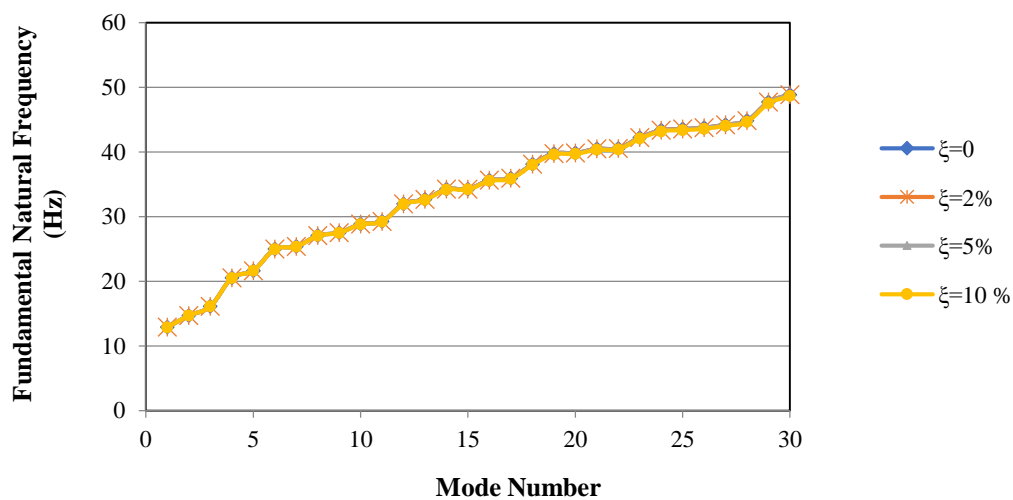


Fig. 17. Dam with soil foundation

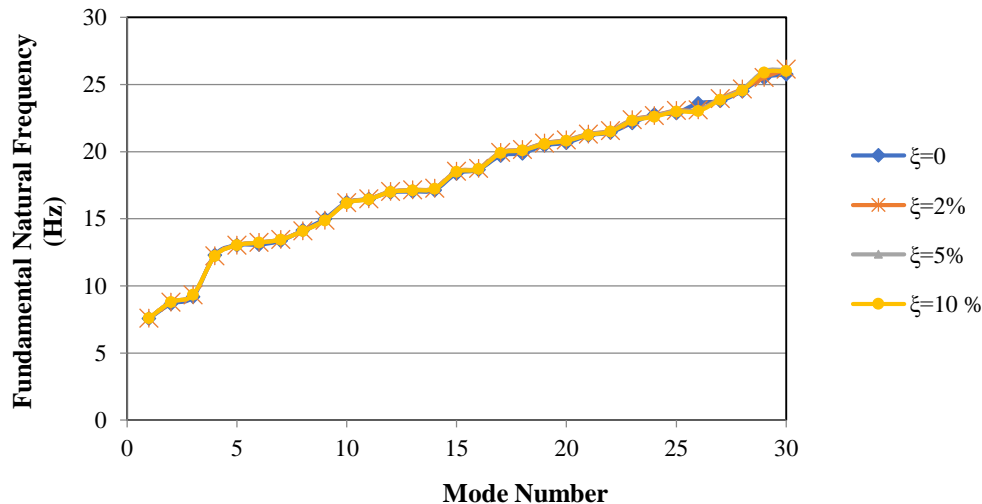


Fig. 18. Dam with soil foundation and reservoir

4. Conclusions

The current work has demonstrated the free vibration behavior of many dam models, including a dam without a soil basis, a dam with a soil foundation, a dam with soil, and a reservoir, using the 3D finite element program ANSYS. The discovered results will facilitate the more accurate design of dams, hence providing substantial advantages to society. The conclusion derived from the comprehensive analyses is succinctly summarized as follows:

The research concludes that the frequency of dams without soil contact is greater than that of dams with soil interaction and dams with both soil and reservoir. It can be described as a dam without a soil basis, a dam with a soil foundation, and a dam with both soil and a reservoir that have the same total mass. However, a dam that includes soil and a reservoir has a lower water stiffness.

Additionally, a dam with a soil foundation is somewhat less rigid due to the fact that the Young's modulus of soil is approximately half the value of a dam without a soil foundation. Consequently, this model is used to replicate lower frequencies. An exploration of the damping has also been conducted using parametric methods. The natural frequencies of both undamped and damped modes obtained from all arch dam models exhibit a high

degree of similarity, with variations of only 2%, 5%, or 10%.

5. References

- Abdollahi, A., Amini, A. and Hariri-Ardebili, M.A. (2022). "An uncertainty-aware dynamic shape optimization framework: Gravity dam design", *Reliability Engineering and System Safety*, 222, 108402, <https://doi.org/10.1016/j.res.2022.108402>.
- Altunışık, A.C., Günaydin, M., Sevim, B., Bayraktar, A. and Adanur, S. (2016). "Dynamic characteristics of an arch dam model before and after strengthening with consideration of reservoir water", *Journal of Performance of Constructed Facilities*, 30(6), 06016001, [https://doi.org/10.1061/\(ASCE\)CF.1943-5509.0000890](https://doi.org/10.1061/(ASCE)CF.1943-5509.0000890).
- Amini, A., Abdollahi, A., Hariri-Ardebili, M.A. and Lall, U. (2021). "Copula-based reliability and sensitivity analysis of ageing dams: Adaptive kriging and polynomial chaos kriging methods", *Applied Soft Computing*, 109, 107524, <https://doi.org/10.1016/j.asoc.2021.107524>.
- ANSYS (2019). *Ansys user's manual*, SAS IP Inc., Southpointe.
- Berrabah, A.T., Belharizi, M., Laulusa, A. and Bekkouche, A. (2012). "Three-dimensional modal analysis of brezina concrete arch dam", *Algeria Earth Science Research*, 1(2), 55-70, <https://doi.org/10.5539/esr.v1n2p55>.
- Borino, G. and Muscolino, G. (1986). "Mode-superposition methods in dynamic analysis of classically and non-classically damped linear systems", *Earthquake engineering and structural dynamics*, 14(5), 705-717, <https://doi.org/10.1016/j.engstruct.2014.11.011>.
- Chopra, A.K. (2007). *Dynamics of structures*,

- Pearson Education India.
- Clough, R.W. and Penzien, J. (1995). *Dynamics of structures*, Computers and Structures, New York.
- Esmailzadeh, S., Ahmadi, H. and Hosseini, S.A. (2019). "A survey of matlab efficiency in damage detection of concrete gravity in concrete gravity dams", *IIUM Engineering Journal*, 20(1), 29-48, <https://doi.org/10.31436/iiumej.v20i1.970>.
- Hashempour, S. A., Akbari, R. and Lotfi, V. (2023). "A simplified continuum damage model for nonlinear seismic analysis of concrete arch dams using different damping algorithms", *Civil Engineering Infrastructures Journal*, 56(2), 235-255, <https://doi.org/10.22059/CEIJ.2023.342419.1837>.
- Heshmati, M., Hariri, A.M., Seyed, K.S. and Mirzabozorg, H. (2013). "Are there any differences in seismic performance evaluation criteria for concrete arch dams?", *Civil Engineering Infrastructures Journal*, 46(2), 233-240, <https://doi.org/10.7508/cej.2013.02.010>.
- Hariri-Ardebili, M.A., Seyed-Kolbadi, S.M. and Kianoush, M.R. (2016). "FEM-based parametric analysis of a typical gravity dam considering input excitation mechanism", *Soil Dynamics and Earthquake Engineering*, 84, 22-43, <https://doi.org/10.1016/j.soildyn.2016.01.013>.
- Hariri-Ardebili, M.A., Mahdavi, G., Abdollahi, A. and Amini, A. (2021). "An rf-pce hybrid surrogate model for sensitivity analysis of dams", *Water*, 13(3), 302, <https://doi.org/10.3390/w13030302>.
- Khosravi, S. and Heydari, M.M. (2015). "Design and modal analysis of gravity dams by ansys parametric design language", *Walailak Journal of Science and Technology (WJST)*, 12(2), 167-180, <http://doi.org/10.2004/wjst.v11i12.866>.
- Li, Z.Y., Hu, Z.Q., Lin, G. and Li, J.B. (2022). "A scaled boundary finite element method procedure for arch dam-water-foundation rock interaction in complex layered half-space", *Computers and Geotechnics*, 141, 104524, <https://doi.org/10.1016/j.compgeo.2021.104524>.
- Messaad, M., Bourezane, M., Latrache, M., Berrabah, A.T. and Ouzendja, D. (2021). "Three-dimensional seismic analysis of concrete gravity dams considering foundation flexibility", *Mechanics and Mechanical Engineering*, 25(1), 88-98, <http://doi.org/10.2478/mme-2021-0012>.
- Pandey, A.D., Das, R., Mahesh, M.J., Anvesh, S. and Saini, P. (2016). "Structural analysis of a historical dam", *Procedia Engineering*, 144, 140-147, <https://doi.org/10.1016/j.proeng.2016.05.017>.
- Patil, S.V. and Awari, U.R. (2015). "Effect of soil structure interaction on gravity dam", *International Journal of Modern Trends in Engineering and Research*, 2(7), 2349-9745.
- Rasa, A.Y. and Budak, A. (2021). "Static and dynamic investigation of structure-foundation-reservoir problem utilizing finite element method", In: *Transactions of International Congress on the Phenomenological Aspects of Civil Engineering* (PACE-2021), 1-6.
- Rasa, A.Y., Budak, A. and Düzgün, O.A. (2024a). "Seismic performance evaluation of concrete gravity dams using an efficient finite element model", *Journal of Vibration Engineering and Technologies*, 12(2), 2595-2614, <https://doi.org/10.21203/rs.3.rs-2361487/v1>.
- Rasa, A.Y., Budak, A. and Düzgün, O.A. (2024b). "Concrete ageing effect on the dynamic response of machine foundations considering-Structure Interaction", *Journal of Vibration Engineering and Technologies*, 12(3), 3417-3429, <https://doi.org/10.1007/s42417-023-01055-8>.
- Rasa, A.Y., Budak, A. and Düzgün, O.A. (2024c). "Concrete deterioration effects on the dynamic behavior of gravity dam-reservoir interaction problems", *Journal of Vibration Engineering and Technologies*, 12(1), 259-278, <https://doi.org/10.1007/s42417-022-00842-z>.
- Rasa, A.Y., Budak, A. and Düzgün, O.A. (2024d). "The influence of concrete degradation on seismic performance of gravity dams", *Earthquakes and Structures*, 26(1), 59, <https://doi.org/10.12989/eas.2024.26.1.059>.
- Rezaiee-Pajand, M., Sadegh Kazemiyani, M. and Mirjalili, Z. (2023). "A novel method for modal analysis of dam-reservoir systems", *Civil Engineering Infrastructures Journal*, 57(1), 33-59, <https://doi.org/10.22059/CEIJ.2023.349505.1873>.
- Sharma, A. and Nallasivam, K. (2023). "Static analysis of a concrete gravity dam using the finite element technique", *Asian Journal of Civil Engineering*, 24(8), 2939-2957, <https://doi.org/10.1007/s42107-023-00686-2>.
- Standard, IS. (1893). *Criteria for earthquake resistant design of structures*, Bureau of Indian Standards, Part 1.
- Tickoo, S. (2021). *ANSYS workbench 2021 R1: A tutorial approach*, Purdue University and CAD/CIM Technologies.
- Tavakoli, H., Mofid, T. and Dehestani, M. (2023). "Dynamic analysis of thermal crack propagation in roller-compacted Concrete dams considering rotational component of ground motion", *Civil Engineering Infrastructures Journal*, 57(2), 287-302, <https://doi.org/10.22059/CEIJ.2023.361667.19>.

- 35.
- Varughese, J.A. and Nikithan, S. (2016). "Seismic behaviour of concrete gravity dams", *Advances in Computational Design*, 1(2), 195-206, <https://doi.org/10.12989/acd.2016.1.2.195>.
- Verma, V. and Nallasivam, K. (2020). "One-dimensional finite element analysis of thin-walled box-girder bridge", *Innovative Infrastructure Solutions*, 5, 1-24, <https://doi.org/10.1007/s41062-020-00287-x>.
- Verma, V. and Nallasivam, K. (2021a). "Free vibration behaviour of thin-walled concrete box-girder bridge using Perspex sheet experimental model", *Journal of Achievements in Materials and Manufacturing Engineering*, 106(2), 56-76, <https://doi.org/10.5604/01.3001.0015.2418>.
- Verma, V. and Nallasivam, K. (2021b). "Static response of curved steel thin-walled box-girder bridge subjected to Indian railway loading", *Journal of Achievements in Materials and Manufacturing Engineering*, 108(2), 63-74, <https://doi.org/10.5604/01.3001.0015.2418>.
- Yaghin, M.A. and Hesari, M.A. (2008). "Dynamic analysis of the arch concrete dam under earthquake force with ABAQUS", *Journal of Applied Sciences*, 8(15), 2648-2658, <https://doi.org/10.3923/jas.2008.2648.2658>.
- Zhang, X.Z., Sun, X.N. and Tang, K.D. (2013). "Static and dynamic analysis of concrete gravity dam by ANSYS", *Applied Mechanics and Materials*, 438, 1334-1337, <https://www.scientific.net/AMM.438-439.1334>.
- Zhuan-Yun, Y. (2014). "Static and dynamic analysis of high arch dam by three-dimensional finite

element method", *Electronic Journal of Geotechnical Engineering*, 19, 2537-2551.

6. Abbreviations

2D: Two Dimensional,
 3D: Three Dimensional,
 ABAQUS: Finite Element Method software,
 ANSYS: Analysis System,
 DOEA: Disregard of Off-diagonal Elements in the non-classical damping matrix,
 DOF: Degree of Freedom,
 DR: Damping Ratio,
 DRFI: Dam-Reservoir-Foundation Interaction,
 DRI: Dam-Reservoir Interaction,
 DFI: Dam-Foundation Interaction,
 FEM: Finite Element Method,
 FORTRAN 90: Programming Language,
 IS: Indian Standard,
 MATLAB: Matrix Laboratory,
 PCE: Polynomial Chaos Expansion surrogate model,
 RF: Random Field,
 SAP 2000: Structural Analysis and Design,
 SBFEM: Scaled Boundary Finite Element Method,
 UQ: Uncertainty Quantification.

7. Appendix

Tables A1-A2 show the participation factor calculation in the dam's x , y , and z directions without and with soil interaction.

Table A1. Participation factor (without soil interaction)

Mode	Frequency in Hz	Time period in sec	Partic. factor	Ratio	Effective mass	Cumulative mass fraction	The ratio of eff. mass to the total mass
x - x direction							
1	22.323	0.4e-01	-0.4e-03	0.000	0.20e-06	0.122e-13	0.765e-14
5	43.609	0.2e-01	-0.1e-02	0.001	0.22e-05	0.765e-01	0.860e-13
15	66.458	0.1e-01	1093.0	0.491	0.12e+07	0.944	0.452e-01
25	92.152	0.1e-01	-761.23	0.342	579465	0.989	0.219e-01
30	106.568	0.9e-01	-318.85	0.143	101668	1.000	0.384e-02
y - y direction							
1	22.323	0.4e-01	0.3e-02	0.001	0.93e-05	0.5085e-12	0.352e-12
5	43.609	0.2e-01	-0.1e-02	0.000	0.12e-05	0.383	0.468e-13
15	66.458	0.1e-01	919.76	0.401	845966	0.835	0.320e-01
25	92.152	0.1e-01	-321.53	0.140	103382	0.982	0.391e-02
30	106.568	0.9e-01	-298.90	0.130	89339.9	1.000	0.338e-02
z - z the direction							
1	22.323	0.4e-01	0.3e-02	0.001	0.93e-05	0.5085e-12	0.352e-12
5	43.609	0.2e-01	-0.1e-02	0.000	0.12e-05	0.383	0.468e-13
15	66.458	0.1e-01	919.76	0.401	845966	0.835	0.320e-01
25	92.152	0.1e-01	-321.53	0.140	103382	0.982	0.391e-02
30	106.568	0.9e-01	-298.90	0.130	89339.9	1.000	0.338e-02

Table A2. Participation factor calculation in y- y direction (with soil interaction)

Mode	Frequency in Hz	Time period in sec	Partic. factor	Ratio	Effective mass	Cumulative mass fraction	The ratio of eff. mass to the total mass
<i>x- x direction</i>							
1	7.572	0.13206	20490	1.000	0.42e+09	0.737	0.589
5	13.025	0.7e-01	5118.3	0.249	0.26e+08	0.7843	0.368e-01
15	18.366	0.5e-01	-332.26	0.016	110400	0.997	0.155e-03
25	22.879	0.4e-01	622.41	0.030	387393	0.999	0.544e-03
30	25.768	0.3e-01	-204.53	0.009	41333.2	1.000	0.597e-04
<i>y-y direction x- x direction</i>							
1	7.57	0.13206	53.096	0.002	2819.15	0.568e-05	0.396e-05
5	13.025	0.7e-01	832.88	0.042	693684	0.224e-01	0.974e-03
15	18.366	0.5e-01	13.328	0.001	177.625	0.885	0.249e-06
25	22.879	0.4e-01	-137.68	0.006	18956.0	0.989	0.266e-04
30	25.768	0.3e-01	-908.44	0.045	825264	1.000	0.115e-02
<i>z-z the direction</i>							
1	7.572	0.13206	-1.1196	0.001	1.25354	0.211e-08	0.176e-08
5	13.025	0.7e-01	429.20	0.019	184215	0.843	0.258e-03
15	18.366	0.5e-01	215.87	0.009	46600.4	0.944	0.654e-04
25	22.879	0.4e-01	13.964	0.001	195.00	0.999	0.273e-06
30	25.768	0.3e-01	-500.25	0.022	250248	1.0000	0.351e-03



This article is an open-access article distributed under the terms and conditions of the Creative Commons Attribution (CC-BY) license.



Enhancing Cable-Stayed Bridge Structural Health Assessment Using Phase Space Trajectory and Load Pattern Variability

Mohseni Moghaddam, M.¹, Dehghani, E.² and Bitaraf, M.^{3*}

¹ Ph.D. Candidate, Department of Civil Engineering, Faculty of Engineering, University of Qom, Qom, Iran.

² Associate Professor, Department of Civil Engineering, Faculty of Engineering, University of Qom, Qom, Iran.

³ Associate Professor, School of Civil Engineering, College of Engineering, University of Tehran, Tehran, Iran.

© University of Tehran 2024

Received: 7 Feb. 2024;

Revised: 06 May 2024;

Accepted: 12 Jun. 2024

ABSTRACT: A novel approach for assessing the structural health of cables in cable-stayed bridges, under varying load patterns, was presented. The method aimed to evaluate cable conditions by utilizing phase space analysis while minimizing traffic disruptions and reducing the necessity for extensive sensor deployment. Through comprehensive numerical investigations on the Manavgat cable-stayed bridge, the efficacy of the proposed method was demonstrated. For this purpose, the time-domain responses of the deck were utilized. The combination of Change in Phase Space Topology (CPST) and Mahalanobis Distance (MD) indices was applied to detect cable damage by discerning nuanced deviations in phase space trajectories. The results revealed that both the MD and CPST indices exhibited impressive accuracy in identifying damage severity and location. To emphasize the robustness of the phase space-based damage detection method, a comparative analysis between the CPST and modal parameters was conducted. At the 10% damage level, the accuracy of CPST increased by 84.5% compared to the first mode frequency of the structure in load state 1. It highlighted the high sensitivity of CPST in cable damage detection.

Keywords: Cable-Stayed Bridge, Structural Health Monitoring, Phase Space Method, Damage Detection, Time Domain Responses.

1. Introduction

A cable-stayed bridge is a type of bridge where the deck is supported by a system of cables connected to one or more towers. These cables extend directly from the tower to the deck, forming a pattern that resembles a fan or a series of parallel lines. Cable-stayed bridges are widely used for medium to long spans, ranging from 200 m to well over 1,000 m. Cable-stayed bridges, noted

for their distinctive appearance, structural efficacy, and ability to span significant distances without intermediate piers, are often located in regions where conventional suspension bridge construction is impractical due to geological or environmental constraints.

Stay cables, as the main load-bearing components of a bridge, typically account for approximately 25-30% of the total construction cost. Moreover, the cost of

* Corresponding author E-mail: maryam.bitaraf@ut.ac.ir

replacing cables can be nearly 3-4 times higher than that of new construction (He et al., 2022). As such, ensuring the health of cables throughout the lifespan of the structure and assessing their operational efficiency are paramount concerns, especially for both existing and newly constructed cable-stayed bridges. The practice of Structural Health Monitoring (SHM) for bridges involves continuously collecting and analyzing data about the bridge's condition throughout its operational lifespan. The goal of SHM is to detect and quantify any potential deterioration that may occur during service, while also providing relevant recommendations for maintenance and oversight of the structure. SHM systems typically utilize various sensors, such as accelerometers, strain gauges, and displacement transducers, to capture the structural responses of the bridge to external forces, including traffic, wind, and seismic activity. After data collection, advanced algorithms are employed to analyze the data and identify changes in the structural dynamics of the bridge, including variations in natural frequencies, mode shapes, and damping ratios. This strategic approach enables the early detection of structural impairments, facilitating prompt rectification and maintenance. This technique reduces the risk of catastrophic failures and extends the operational lifespan of the bridge. Furthermore, structural health monitoring helps optimize maintenance schedules and reduce maintenance costs by providing accurate insights into the condition of the bridge (Saidin et al., 2023).

In essence, the core of SHM lies in identifying, locating, and quantifying damage through dynamic responses. This comprehensive methodology involves assessing and predicting damage at both local and global levels (Pamwani and Shelke, 2018). In the field of monitoring performance and ensuring the longevity of engineering structures, the implementation of SHM has provided invaluable insights over extended periods. Over time,

numerous numerical and experimental studies have explored the field of cable-stayed bridge health monitoring. The assessment of bridge health and dynamic characteristics in most studies has typically been examined under various environmental conditions, moving loads, artificial vibrations, or stimuli such as earthquakes. Bakhshizadeh et al. (2023) investigated the impact of Multiple Support Excitations (MSE) on the dynamic response of large-span cable-stayed bridges to seismic hazards. Various system identification methods, including mode shape curvature and modal strain energy techniques, were utilized for health monitoring to assess structural performance and identify potential damages (Bakhshizadeh and Sadeghi, 2023). Numerous researchers have directed their investigations toward ambient vibration (Beton et al., 2016; Hong et al., 2012).

Prawin et al. (2020) introduced a diagnostic scheme for bridges with minimal measurements, considering environmental and operational variations alongside measurement noise. Null subspace analysis was employed in the first stage to confirm the presence of damage using ambient vibration data through online monitoring. It was concluded from the investigations that the proposed approach was capable of detecting and localizing multiple, as well as subtle, damages under varying environmental conditions with very limited noise-contaminated measurements.

Vibration-based methods have played a central role in the field of structural health assessment. A prominent approach is the modal-based damage detection algorithm, which requires the automated identification and continuous tracking of modal parameters for real-time analysis (Li et al., 2014). These methodologies have been validated through comprehensive computational modeling and empirical investigations. A notable study was the work by Saidin et al. (2023), which focused on structural health monitoring using a vibration-based approach for an Ultra-

High-Performance Concrete (UHPC) bridge. In this study, researchers extracted mode shapes, natural frequencies, and damping ratios to understand the modal characteristics of the bridge. These parameters were then used to assess the bridge's performance and monitor its health over time. The main objective of this study was to highlight the effectiveness of SHM in detecting structural impairments and predicting the behavior of engineering structures. Also, Vibration-based methodologies are extensively utilized for estimating cable tension and evaluating the comprehensive health of cable structures.

Fatigue and corrosion have presented recurring challenges that can affect cables, leading to decreased stiffness and compromised force transmission.

Therefore, monitoring tension, as the primary indicator of cable health, is of paramount importance. This consideration arises from the relationship between cable tension, its strength, and stiffness. Cable tension can be determined using various methodologies, including direct force sensor measurements, non-contact measurements, or assessments of parameters like stress, strain, or natural frequency (Cheng et al., 2024; Fathali et al., 2020; Rinaldi et al., 2023; Yu, 2020). An illustrative example is the study conducted by Zarbaf et al. (2018), who utilized this technique to evaluate the cables of the Ironton-Russell Bridge. Their findings were subsequently compared with those obtained from lift-off tests. These approaches have utilized the natural frequencies, mechanical properties, and geometric features of cables to estimate tension. Jana et al. (2022) introduced a framework that utilized video-based measurements as multiple sensors to minimize estimation errors in real-time cable tension determination. Non-contact video-based sensing offered superior spatial resolution and lower costs compared to conventional sensors. The algorithm was implemented on the Fred-Hartman cable-stayed bridge in Texas, demonstrating accurate tension estimation from video-

based measurements. This showcased the significant potential of the framework in structural health monitoring. Damage detection methods under moving load can be categorized into two methods: the frequency domain method and the time domain method (He et al., 2017; Wu et al., 2017, 2019).

While frequency measurement provides high precision, it tends to offer a global perspective. It has posed challenges for local damage detection. Conversely, mode shape and its derivatives, such as modal curvature and modal flexibility, have theoretically shown sensitivity to damage.

However, they are often affected by measurement noise, compromising their reliability in practical civil structural health monitoring scenarios when using displacement or acceleration data (Hong et al., 2012; Wu et al., 2017). In some investigations, Time Domain Responses (TDR) have proven to be effective tools for identifying localized damage. TDR-based methods directly identify damage from the output, bypassing the need for conversion into structural modal information. Zhang et al. (2020) introduced a rapid output-only technique for detecting damage in highway bridges under moving vehicles, relying on the fractal dimension of long-gauge FBG strain responses. The feasibility of both single and multiple damage scenarios was demonstrated through numerical simulations and an indoor bridge-vehicle model experiment. Additionally, the method's resistance to noise was assessed by adding a Signal-Noise Ratio (SNR) of 30 dB in the numerical simulation, and the impact of varying sensor quantities was investigated. In another study, Kordi and Mahmoudi (2022) presented a new method for detecting damage in truss bridges under moving loads. Damage was identified by comparing the displacement response curve shapes of the intact and damaged models with the axial force influence line curve shape. The results showed that the proposed method can accurately identify the damaged members. Cable-stayed bridges are

renowned for their flexibility. In this structural configuration, the girder operates like a beam resting on a flexible foundation, while the cables provide flexible support from their anchoring points. The primary load paths across the bridge deck provide valuable insights into the condition of secondary structural elements, such as the stay cables. Nazarian et al. (2016) introduced a straightforward approach to recognizing damage in the cables of cable-stayed bridges. This method involved monitoring variations in support reactions by analyzing shear forces acting upon deck components near the support locations. The researchers also proposed a technique to identify cables that have experienced partial or complete loss of tensile force, achieved by measuring strains along the bridge deck.

It is important to acknowledge that this technique may face challenges in accurately modeling geometric constraints and boundary conditions, potentially resulting in inaccuracies. Displacements of the main beam and towers are key indicators of bridge performance, commonly tracked using Global Positioning System (GPS) sensors. For example, in long-span cable-stayed bridges, these displacements are often measured statically during load testing before the bridge is opened to traffic. Although acceleration measurements can also provide displacement data, their precision is lower (Zhang et al., 2023).

Additionally, various factors such as temperature fluctuations, wind forces, and vehicular traffic impact the displacement of long-span bridges. Lei et al. (2023) proposed an approach involving the use of a one-dimensional residual convolutional autoencoder model to estimate displacement responses of a cable-stayed bridge under various loading conditions. To implement this approach, the researchers collected monitoring data from a cable-stayed bridge, including comprehensive measurements of varied loads and corresponding displacement responses.

Subsequently, temperature, wind, and vehicle load characteristics were used as

input variables, while the displacement responses at the mid-span of the main girder and the tops of the two pylons were used as output variables. The model underwent training and validation procedures using the collected monitoring data. It achieved an accuracy exceeding 95% in predicting a range of displacement responses associated with multiple critical loads, all used simultaneously as inputs. Within the field of civil engineering, phase space analysis has emerged as a valuable tool for damage detection. This methodology initially relies on strain history data, transforming time series data into a spatial domain, where even slight changes in parameters can propagate throughout the entire system. The Change in Phase Space Topology (CPST) index has been introduced as an immensely effective method, capable of increasing in value proportionally to the severity of damage, regardless of its location (Nie et al., 2012, 2013). Zhang et al. (2017) introduced a model-free method for detecting damage in bridge structures under moving loads, relying on changes in phase trajectory across multiple vibration measurements. The sensitivity and reliability of this approach were examined through numerical analysis of a simply supported beam structure. Experimental validation revealed that shear connection failures in a composite bridge structure model subjected to moving loads were effectively identified by the method. In multidimensional statistical analysis, the MD is another index that refers to a measure of distance on the scale of standard deviation between an observation and a reference sample. Like CPST, it has been introduced as a damage index in studies related to health monitoring (De Maesschalck et al., 2000; Pamwani and Shelke, 2018). The significant sensitivity of phase space analysis to damage has made it widely used in various studies on structural damage detection (Li et al., 2021; Paul et al., 2017; Peng et al., 2022; Tuttipongsawat et al., 2019). According to the studies, modal parameters such as natural frequency

have shown limited sensitivity to local damages in bridges. Additionally, vibration-based methods for detecting damage have often disrupted traffic flow or required complete bridge closures if necessary. In examining the structure's behavior in the frequency domain, time is also dedicated to converting responses from the time domain to the frequency domain, resulting in a large volume of data. In the literature review on moving loads, the assessment of structural health has typically been conducted using a single type of load pattern. In this article, a novel approach was introduced for tracking cable health in cable-stayed bridges subjected to various load patterns. The approach included a comprehensive examination of phase space reconstruction and damage-sensitive indexes. This method observed how the structure behaves over time with minimal traffic disruptions or bridge closures, achieved by applying a specific load. The need for multiple and costly sensors was removed throughout the bridge deck using displacement sensors or non-contact methods. In this study, a rapid method was provided for early damage detection in cable-stayed bridges by using only one type of response. The research conducted in the realm of damage detection using phase portraits has often focused on structures such as frames, buildings, and highway bridges. In this research, the efficacy of phase space analysis was assessed on a cable-stayed bridge using both the change in phase space topology and the Mahalanobis distance indexes. A cable-stayed bridge located in Turkey, featuring a steel pylon, a composite deck, and 28 steel cables, was investigated. Numerous damage scenarios, encompassing distinct load patterns and speeds, were evaluated.

The proposed method involved reconstructing the deck's displacement at the cable connection points in the phase space and subsequently examining the resulting damage indexes.

2. Methods

2.1. Phase Space Reconstruction

Phase space analysis is a novel method for structural damage detection. The method demonstrates exceptional sensitivity to damage because it magnifies changes in time-domain responses by converting them into a spatial domain. In phase space, each variable represents a distinct dimension in a multi-dimensional space, indicating that any change in one parameter will propagate throughout the entire system. Dynamic systems can be defined by their measured time-series responses in phase space. The phase space can be reconstructed using multiple variables or the time series of a single measured variable, incorporating parameters such as time lag (T) and embedding dimension (d) (Takens, 1981).

Given a time series measurement denoted as $x(i)$ with N data points (where $i = 1, \dots, N$), the reconstruction of the phase space can be formulated as follows (Tuttiyongsawat et al., 2019):

$$X(n) = [x(n).x(n + T). \dots x(n + (d - 1)T)] \quad (1)$$

Each dimension can be expressed as:

$$\begin{aligned} x(n) &= [x(1).x(2). \dots x(N - (d - 1)T)] \\ x(n + T) &= [x(1 + T).x(2 + T). \dots x(N - (d - 2)T)] \\ &\dots \\ x(n + (d - 1)T) &= [x(1 + (d - 1)T).x(2 + (d - 1)T). \dots x(N)] \end{aligned} \quad (2)$$

The set of all dimensions plotted is called the phase space topology. The geometry of the phase trajectory is closely related to the behavior of the structure. Any damage to the structure leads to changes in responses, which are accurately depicted in the topology of the phase space. By assessing the dissimilarity of the topology when damage occurs, it is possible to detect the presence of damage. Selecting an appropriate time lag is crucial during the reconstruction process.

The time lag can be determined using methods such as the Autocorrelation Function and the Average Mutual Information Function (AMIF). Typically, the lag for reconstruction is chosen as the time corresponding to the first zero crossing of the Autocorrelation Function or the first minimum of the AMIF (Abarbanel, 2012; Jiang et al., 2010). Similarly, the optimal choice of the embedding dimension (d) is essential in the reconstruction process.

Prominent techniques used to determine the appropriate embedding dimension include Singular System Analysis (SSA) and False Nearest Neighbor (FNN) methods (Broomhead and King, 1986; Nichols, 2003; Rhodes and Morari, 1997). In this study, the Average Mutual Information Function and False Nearest Neighbor methods were employed to determine the time lag and embedding dimension, respectively.

2.2. Damage Sensitive Feature

In this study, the relationship between the geometry of the phase space trajectory and the dynamic response of the structure was discussed. As damage gradually occurs, discernible changes are triggered within the dynamic response, which are distinctly reflected in the topology of the phase space. Two damage indices were used for damage detection in cable-stayed bridges: The CPST and the MD between phase space trajectories. These indices have been proposed as valuable tools for evaluating the health of the structure using phase space analysis (Nichols, 2003).

2.2.1. Change in Phase Space Topology (CPST)

The CPST index concept aims to measure the difference between the predicted damage case and the actual damage case. Assume $X(n)$ and $Y(n)$ are phase space reconstructions of a healthy case and a damaged case, respectively. The calculation concept is illustrated in Figure 1 (Tuttipongsawat et al., 2019). To begin, a fiducial point $Y(r)$ at time index r from the damage case is selected, and mapped on the healthy case. By minimizing the Euclidean norm, the nearest p neighbors of this fiducial point are chosen in the healthy case (Nie et al., 2013; Pamwani and Shelke, 2018; Tuttipongsawat et al., 2019):

$$NN(n_j): \min \|X(n_j) - Y(r)\|. \quad j = 1, \dots, p \quad (3)$$

where P : denotes the total number of neighborhood points, and the operator $\|\cdot\|$: calculates the Euclidean norm. The set of nearest neighbor points to the fiducial point $Y(r)$: is denoted as NN . These selected neighborhood points are used to quantify the dissimilarity between the healthy and damaged cases. The predicted damage case at the 's' time step can be computed using Eq. (4) (Nie et al., 2013; Pamwani and Shelke, 2018; Tuttipongsawat et al., 2019).

$$\hat{Y}(r+s) = \frac{1}{p} \sum_{j=1}^p X(n_j + s). \quad j = 1, \dots, p \quad (4)$$

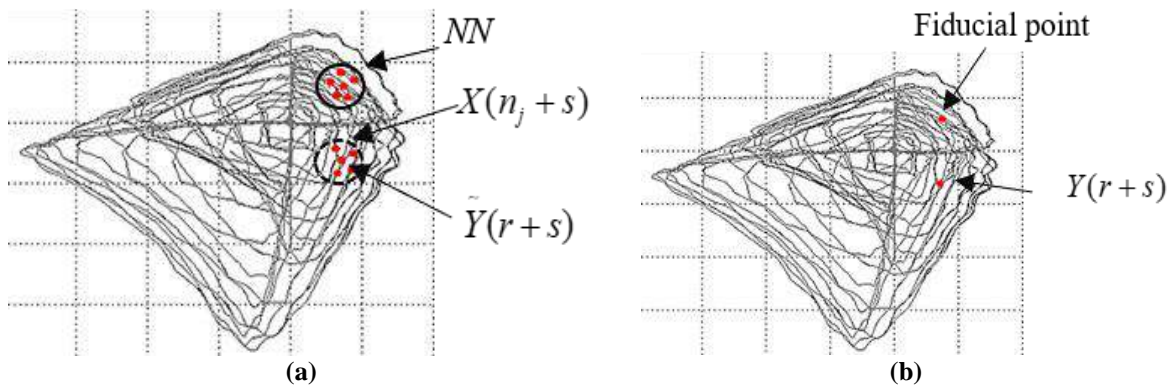


Fig. 1. Diagram of CPST calculation process: a) Healthy phase space topology; and b) Damaged phase space topology

Hence, the difference between the damage case Y and the predicted damage case \tilde{Y} of the fiducial point at time index r is determined as shown in Eq. (5) (Nie et al., 2013; Pamwani and Shelke, 2018; Tuttipongsawat et al., 2019).

$$CPST(i) = \frac{1}{P} \|\tilde{Y}(r+s) - Y(r+s)\|, \quad i = 1, \dots, nt \quad (5)$$

The calculation process will be repeated to obtain an average value of the $CPST$ difference. The number of repetitions or fiducial points is denoted as nt . It is recommended to choose at least 5% of the total number of points in the reconstructed trajectory as the number of fiducial points to achieve a reasonable estimate of $CPST$ (Nichols, 2003). In some references, the number of fiducial points is calculated using Eq. (6) (Nie et al., 2013).

$$nt = N - (d - 1)T \quad (6)$$

where N , d , and T : represent the total number of data points, embedding dimension, and time lag of reconstruction, respectively.

2.2.2. Mahalanobis Distance (MD)

The Mahalanobis Distance (MD) is commonly utilized to measure the distance of an individual point from a cluster of points and evaluate its deviation from the overall population. The observations of the coordinate vectors for each point from the healthy and damaged cases are represented in matrix form as $[X]$ and $[Y]$, respectively.

The matrices are of dimensions $(m \times d)$, where ' m ' is the number of points sampled on the embedded phase portrait, equal to the number of rows. The number of columns ' d ' represents the number of embedding dimensions. The healthy and damaged phase portraits are represented by two random vectors, $\{X\}$ and $\{Y\}$, respectively.

The centroid of these portraits is obtained by calculating the mean of these random vectors, denoted as $\{\mu\}_X$ and $\{\mu\}_Y$, respectively. Their covariance matrices can

also be estimated as $[C_{XX}]$ and C_{YY} , respectively. To compute the MD , a single weighted covariance matrix is derived by assigning relative weights to each of these covariance matrices. This is expressed as (George et al., 2018):

$$[C_{WW}] = W_1[C_{XX}] + W_2[C_{YY}] \quad (7)$$

The weight factors are determined based on the ratio of the number of points sampled in each phase portrait to the total number of points sampled in both. In this paper, equal weights were assigned to each covariance matrix, $W_1 = W_2 = 0.5$. The MD between the phase portraits is calculated using the following formula (George et al., 2018):

$$MD = \sqrt{(\{\mu\}_X - \{\mu\}_Y)^T [C_{WW}] (\{\mu\}_X - \{\mu\}_Y)} \quad (8)$$

This modified version of the MD was used as a damage index in this study. More detailed information on MD calculation can be found in the reference (George et al., 2018).

3. Case Study

The Manavgat cable-stayed bridge, shown in Figure 2, was selected for numerical analysis. This bridge is Turkey's first cable-stayed bridge, designed to accommodate two lanes of road traffic. The bridge is 202 meters long, with each span measuring 101 meters. It features a 13.7-m-wide deck connected to a steel tower by 28 cables. The tower stands approximately 42 m high and has a hollow hexagonal cross-section, mounted on a concrete foundation. The deck is constructed with a composite cross-section, comprising 25 cm of concrete, 10 cm of asphalt, and two continuous steel girders that are laterally restrained. I-shaped steel profiles are embedded continuously along the length of the deck. The deck is supported by 28 steel cables, which are interconnected with the tower. The nearest cable to the pylon is 19.6 m away, with a distance of 12 m between each subsequent cable. The last cables are situated 9.4 m

from the supports. The arrangement of the cables, as well as the cross sections of the deck and the pylon, are shown in Figure 3 (Pan et al., 2018).

3.1. Finite Element Modeling

For the assessment of the structural behavior of the Manavgat cable-stayed bridge, a three-dimensional finite element model was created utilizing SAP2000 software. The deck and pylon were modeled using frame elements, and the pylon was fixed to the foundation. Truss elements were used for the cables. The details of the stay cables, labeled A1-A7 and including

14, 16, 19, 19, 22, 19, and 24 strands, respectively, are provided in Table 1 (Pan et al., 2018).



Fig. 2. Manavgat cable-stayed bridge (Elkady et al., 2023)

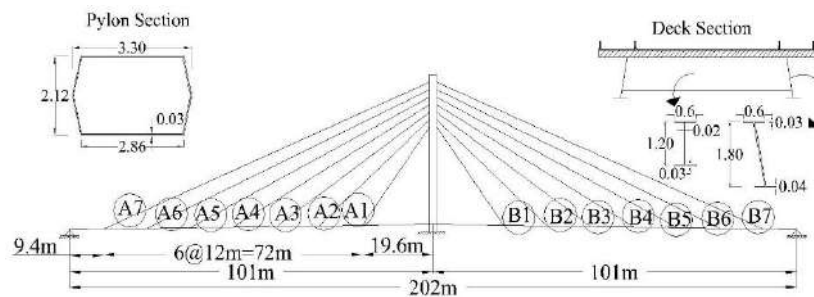


Fig. 3. Manavgat cable-stayed bridge arrangement and the cross-section of the bridge members

Table 1. Numbering and details of stay cables

Cable number	Cable name	Number of strands	Total area of cable (mm ²)
1	A7	24	4355
2	A6	19	3448
3	A5	22	3992
4	A4	19	3448
5	A3	19	3448
6	A2	16	2903
7	A1	15	2722
8	B1	15	2722
9	B2	16	2903
10	B3	19	3448
11	B4	19	3448
12	B5	22	3992
13	B6	19	3448
14	B7	24	4355
15	A7	24	4355
16	A6	19	3448
17	A5	22	3992
18	A4	19	3448
19	A3	19	3448
20	A2	16	2903
21	A1	15	2722
22	B1	15	2722
23	B2	16	2903
24	B3	19	3448
25	B4	19	3448
26	B5	22	3992
27	B6	19	3448
28	B7	24	4355

Each strand has an elastic modulus of 197 GPa, a cross-sectional area of 150 mm^2 , and an ultimate strength of 1,860 MPa.

Moreover, the elastic moduli for the concrete and steel materials were specified as 34 GPa and 200 GPa, respectively. To simulate the interaction between the bridge and vehicle, examples of a five-axle and a two-axle truck, similar to the AASHTO standard load, were employed in the finite element bridge model, as illustrated in Figure 4 (Aashto, 2008). This five-axle

truck is also specified in the Australian Bridge Design Code as T44 (Australasian Railway Association, 1992). The analysis of the bridge under moving load was conducted using simulated time history analysis in the SAP2000 software. The moving load was applied to the deck through the distribution of multiple point loads at uniform intervals. Breaking down the moving load into multiple point loads and their corresponding time history function is illustrated in Figure 5.

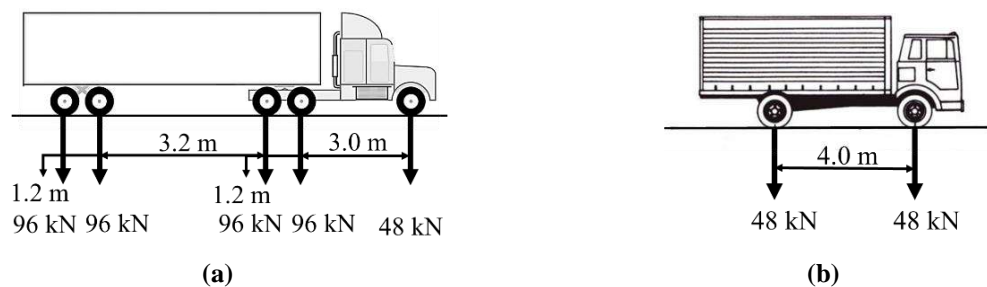


Fig. 4. Truck loadings for 3D model analysis: a) 5-axle truck (T5A); and b) 2-axle truck (T2A)

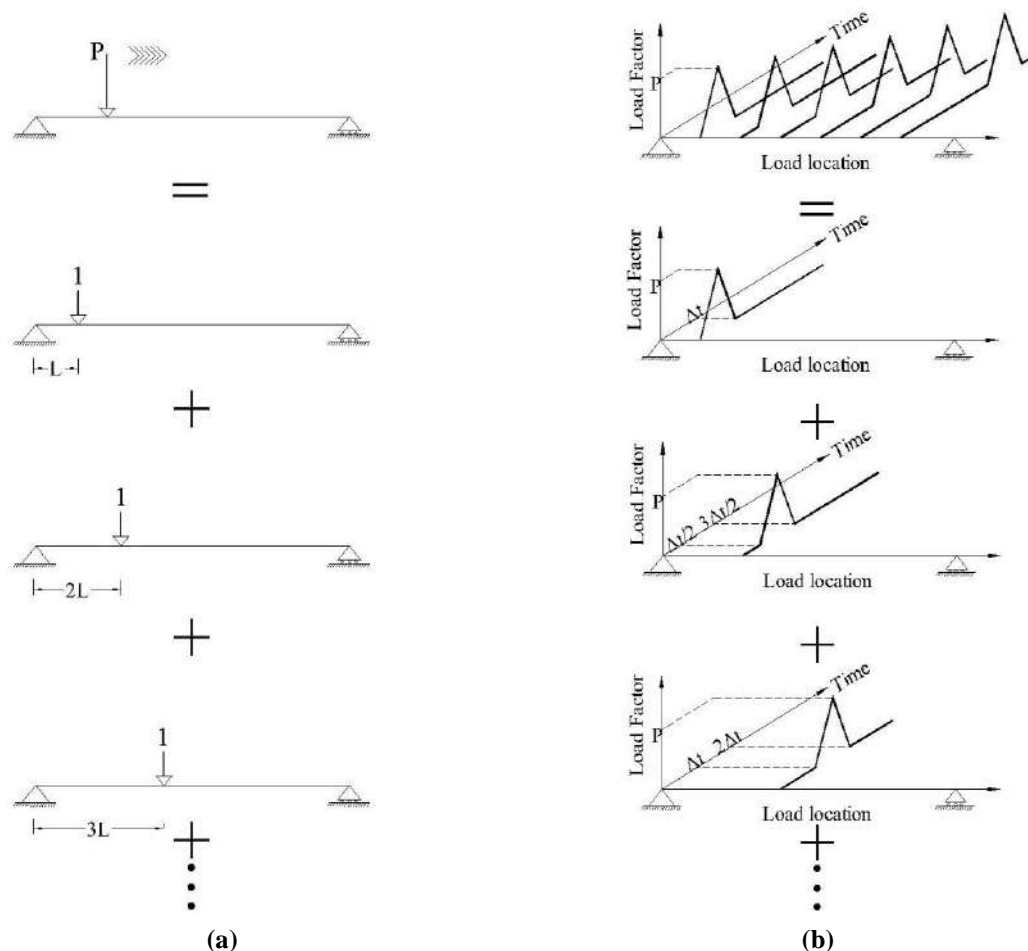


Fig. 5. Breaking down: a) The moving load into point loads at uniform intervals; and b) The time history functions

Point loads, following the load pattern depicted in Figure 5, were applied and removed from the deck. Loads were successively passed over the bridge, with Δt determined by the formula below:

$$\Delta t = \frac{L}{V} \quad (9)$$

where L : denotes the distance between point loads, while V : indicates the speed of the moving load.

4. Results and Discussion

As mentioned, the deck girder in cable-stayed bridges functions like a beam supported by elastic foundations, owing to the presence of cables. The changes in the deck's response provide crucial insights into the condition of the stay cables. In this paper, a time history analysis was performed, involving a round-trip truck at an average speed of 10-15 km/h. Dynamic effects were ignored in the analysis. The evaluation of the vertical displacement of the deck at the points of cable attachment was conducted to assess the health of the

cable-stayed bridge. The displacement of each point was reconstructed using parameters of time lag and embedding dimension, extracted from the displacement vector in the phase space. To identify damaged cables through disparities in phase space trajectories between healthy and damaged cases, two distinct damage indexes were utilized: the CPST and the MD. This paper aimed to detect damage within the cables of cable-stayed bridges using two distinct loading types. A comprehensive overview of the methodology is outlined in the workflow depicted in Figure 6. The process of damage detection typically involves the comparison of two cases: one healthy and the other damaged. In this study, the first investigation of cable damage detection was focused on five distinct cable damage scenarios under ideal conditions. The term 'ideal conditions' indicates that the passing load was consistent in both the healthy and damaged cases. The speed of the passing load was variable in the three damage scenarios. The extent of damage varied from a reduction of 10% to 45% in the cross-sectional area of the cables.

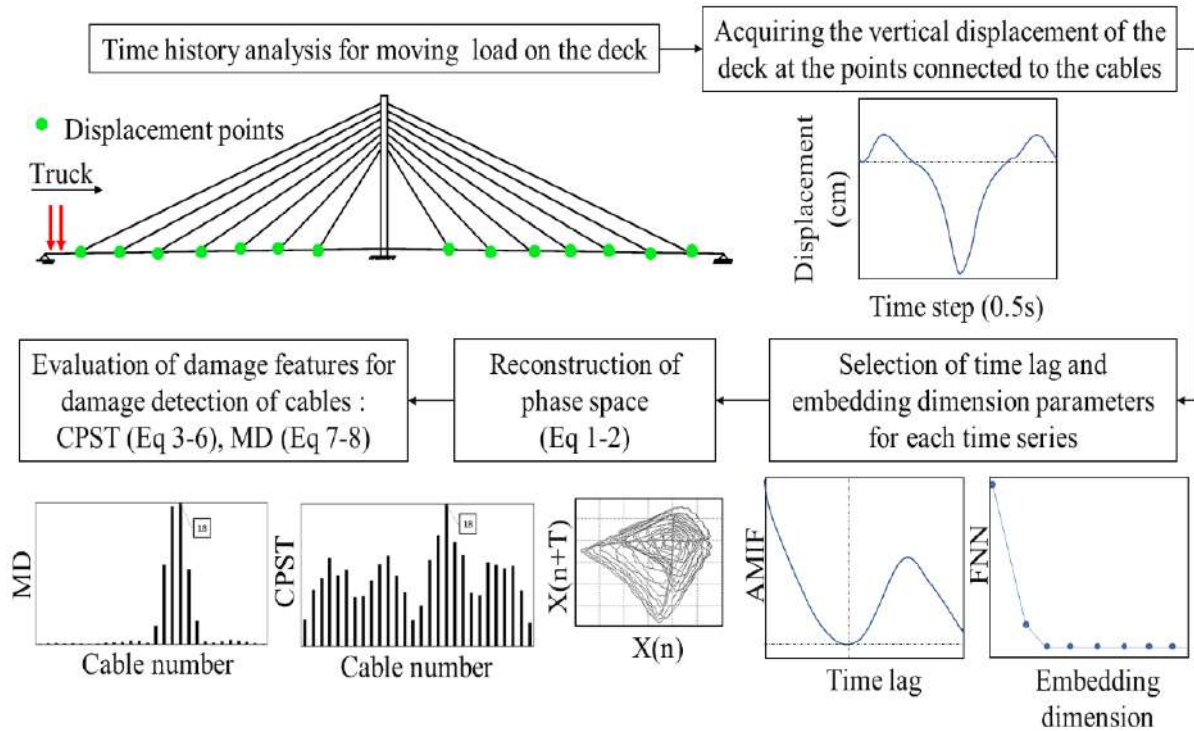


Fig. 6. Workflow of the proposed damage detection method

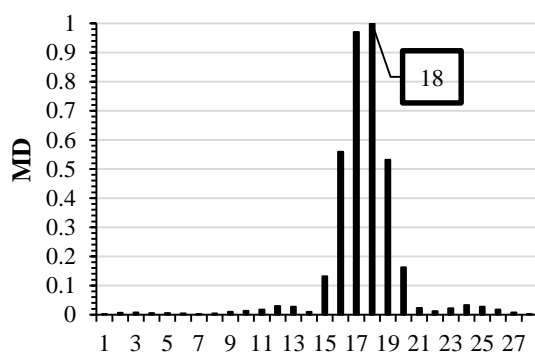
After reconstructing the phase space of deck displacements at the cable connection points, the two damage indices, MD and CPST, were computed and presented in Table 2. The discussion of these indices can be found in the ‘damage sensitive feature’ section. Except Cable 1, both MD and CPST indices (or at least one of them) accurately identified the damaged cables, namely Cables 6, 11, 18, and 25. Cable 1, which acted as a backstay cable supporting all the bridge cables, remained undetected even with a significant damage intensity of 45%.

Damage to this cable has affected all other cables. It is important to note that the index values are normalized to the highest value for ease of evaluation. Cables 1, 2, 13, 14, 15, 16, 27, and 28 were categorized as backstay cables. The damage detection

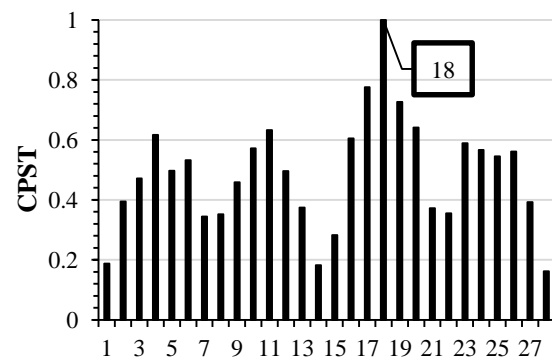
index curve for Cable 18 is illustrated in Figure 7. In this particular scenario, the speed of the passing load in the healthy case was 10 km/h, while in the damaged case, it was 15 km/h. The results were examined under a 5-axle truck (T5A). The second part of the considered damage scenarios involved the passage of trucks with varying load patterns and speeds in both healthy and damaged cases. The severity of damage in these scenarios varied from 20% to 40% of the cable cross-sectional area. These scenarios were analyzed across five distinct states, as shown in Table 3. In the first state, the passing load in the healthy case was the 2-axle truck (T2A), while in the damaged case, the displacements were acquired from the passage of the 5-axle truck (T5A). The passing speed for both trucks in this state remained consistent at 10 km/h.

Table 2. Damage scenarios under ideal conditions

Cable number	Passing load (intact/damaged)	Passing speed (intact/damaged) km/h	Damage percentage (%)	Mahalanobis distance (MD)	Change in phase space topology (CPST)
1	T5A/T5A	10/10	45	26	26
6	T5A/T5A	10/10	40	5	6
11	T2A/T2A	15/15	10	11	11
18	T5A/T5A	10/15	30	18	18
25	T2A/T2A	15/10	30	25	17



(a)



(b)

Fig. 7. Damage detection curves for Cable 18: a) MD; and b) CPST

Table 3. Five states of load passing scenarios

	Intact Passing load	Passing speed km/h	Damaged Passing load	Passing speed km/h
State 1	T2A	10	T5A	10
State 2	T5A	15	T2A	10
State 3	T2A	15	T5A	10
State 4	T5A	10	T2A	15
State 5	T2A	10	T5A	15

In the second state, data were examined for the passage of the T5A truck at 15 km/h in the healthy case and the passage of the T2A truck at 10 km/h in the damaged case.

The third state was the opposite of the second one, where the trucks passing in the healthy and damaged cases changed places, but the passing speeds remained the same as

in the second state. In the fourth state, the T5A truck was used at 10 km/h in the healthy case, whereas the T2A truck was utilized at 15 km/h in the damaged case. In the fifth state, the trucks were opposite to those in the fourth state, but the passing speeds remained the same as in the fourth state.

Table 4. Results of damage detection for the damage level of 20%, excluding backstay cables

Cable number	State 1		State 2		State 3		State 4		State 5	
	MD	CPST	MD	CPST	MD	CPST	MD	CPST	MD	CPST
3	3	3	3	25	17	16	3	12	3	17
4	3	4	4	26	17	17	3	12	4	17
5	4	18	5	25	17	18	12	12	4	5
6	5	6	26	12	17	12	12	12	5	5
7	12	3	26	11	26	17	12	12	12	3
8	25	3	3	11	12	12	17	17	9	3
9	25	24	3	3	12	12	17	12	25	26
10	25	11	10	3	12	12	17	12	11	11
11	26	26	11	3	12	12	26	12	26	26
12	26	25	12	26	12	12	26	17	12	12
17	3	16	17	26	17	16	3	17	17	17
18	3	18	18	25	17	16	3	12	3	17
19	3	18	19	25	17	18	12	12	18	4
20	4	4	26	12	17	17	12	12	5	5
21	12	26	26	12	26	16	12	12	12	26
22	25	22	3	25	12	12	17	12	24	26
23	25	24	3	3	12	17	17	13	24	24
24	25	24	24	3	12	17	17	12	25	25
25	26	26	25	3	12	13	26	13	25	11
26	26	26	26	17	12	12	26	11	26	12

Table 5. Results of damage detection for the damage level of 30%, excluding backstay cables

Cable number	State 1		State 2		State 3		State 4		State 5	
	MD	CPST	MD	CPST	MD	CPST	MD	CPST	MD	CPST
3	3	2	3	3	3	4	13	13	3	4
4	4	4	4	4	17	12	4	12	4	18
5	4	4	5	26	17	17	4	12	4	4
6	5	6	26	25	17	18	12	12	5	5
7	12	26	26	3	26	17	12	17	26	3
8	9	8	3	25	3	12	17	12	9	8
9	24	24	10	3	12	17	17	12	10	10
10	25	10	10	10	12	11	25	12	11	10
11	26	10	11	18	12	17	26	12	11	12
12	26	26	12	12	12	12	26	12	12	12
17	3	3	17	17	17	16	3	12	17	17
18	18	18	18	19	17	18	18	19	18	18
19	4	18	18	18	17	13	4	12	18	19
20	5	20	26	26	17	17	12	13	19	20
21	12	12	26	26	26	12	12	12	12	17
22	23	23	3	12	12	17	17	12	23	22
23	24	24	3	3	12	12	17	12	24	24
24	25	24	24	3	12	12	25	12	25	24
25	25	26	25	25	12	13	25	17	25	26
26	26	26	26	26	12	17	26	12	26	26

All cables, except for the backstay cables (totaling 20 cables), were analyzed and examined under these five states, each with three different levels of damage intensity: 20%, 30%, and 40%. The aim of examining the cables in these scenarios was to assess how well the damage detection method performs when exposed to various load patterns. The results of the damage detection indexes for cable cross-section damage levels of 20%, 30%, and 40% under the five different states are presented in Tables 4, 5, and 6, respectively. As depicted in Figure 8, to maintain uniformity in the number of data points for phase space analysis resulting from the passage of different trucks at various speeds, the arrival and departure times of the resultant load were considered.

Additionally, since the load values of

the axles in the trucks were different, all initial data were normalized to the maximum displacement at the middle point of the bridge span. The damage indices, especially MD, accurately detected damaged cables at different levels of damage in specific cases, such as Cables 3, 12, 17, and 26. Furthermore, in several cases involving Cables 5, 10, 18, 19, 23, and 24, the MD index frequently indicated the damaged cable with a difference of one cable before or after it. However, in many cases involving cables near the pylon (Cables 7, 8, 21, and 22), the indices failed to detect the damage using this method, resulting in inconclusive outcomes. Notably, more favorable results were obtained for damage levels of 30% and higher.

Table 6. Results of damage detection for the damage level of 40%, excluding backstay cables

Cable number	State 1		State 2		State 3		State 4		State 5	
	MD	CPST	MD	CPST	MD	CPST	MD	CPST	MD	CPST
3	3	3	3	3	17	16	3	18	3	2
4	4	3	4	4	17	16	4	12	4	4
5	4	4	4	5	4	5	4	5	4	5
6	5	6	26	12	17	12	12	12	5	6
7	12	3	26	26	26	17	12	17	26	26
8	10	10	10	15	10	18	17	12	10	9
9	24	9	10	3	12	12	17	12	10	24
10	25	10	10	10	12	11	25	12	11	10
11	11	25	11	11	12	12	25	17	11	12
12	12	12	12	12	12	12	26	17	12	26
17	17	2	17	17	17	17	3	12	17	17
18	18	17	18	18	17	12	3	18	18	17
19	4	19	19	19	17	17	4	12	18	19
20	19	20	26	25	17	18	12	16	19	20
21	12	26	26	25	26	18	12	12	26	3
22	23	22	3	27	3	12	17	17	23	22
23	24	24	23	18	12	17	17	13	24	23
24	25	24	24	10	12	11	25	12	25	25
25	25	26	25	25	12	12	25	12	25	26
26	26	26	26	26	12	13	26	13	26	13

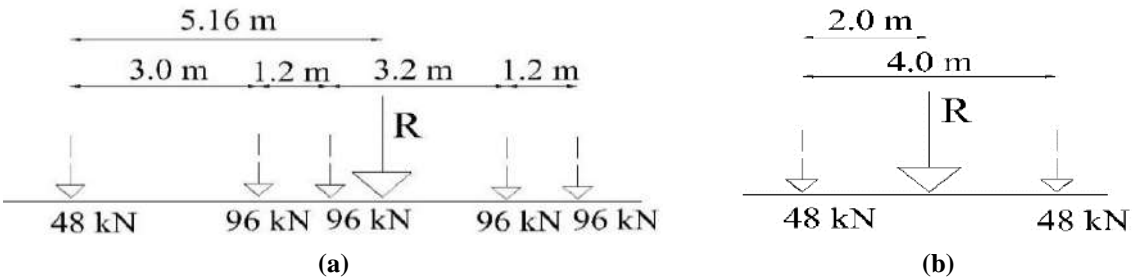


Fig. 8. Resultant load for: a) T5A truck; and b) T2A truck

The MD and CPST curves for the 40% damage level of Cables 5 and 21 are presented in Figures 9-12. The choice of Cable 5 was an example of cables for which the indexes often detected a cable before or after the damaged cable in most states.

Cable 21 was selected as one of the four

nearest cables to the pylon that could not be identified through this method. Although in cases like Cables 8 and 22 in the fifth state at damage levels of 30% and 40%, CPST correctly detected the damaged cables, it's worth noting that the accuracy of this method was limited.

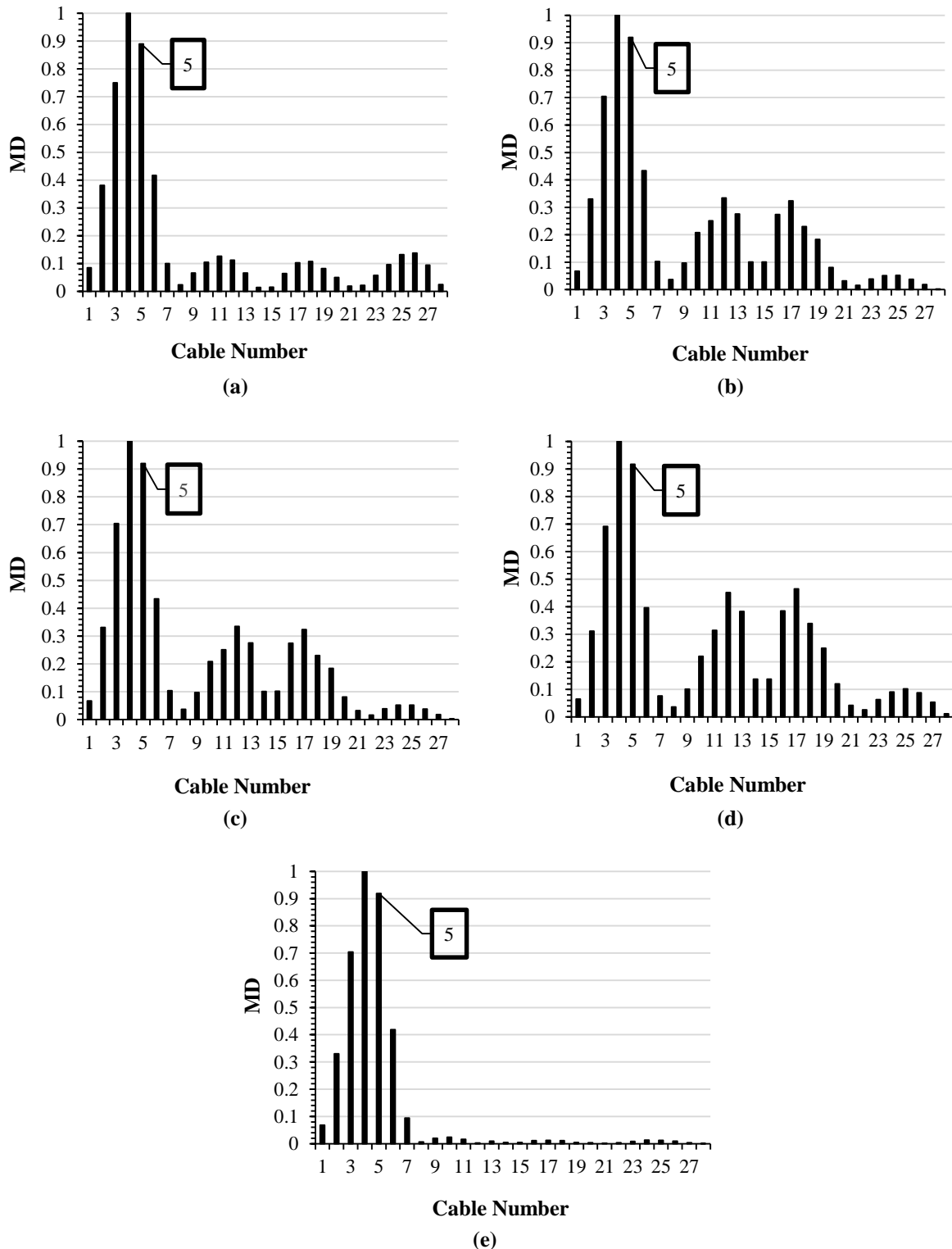


Fig. 9. MD curves of cable 5 for five states: a) State 1; b) State 2; c) State 3; d) State 4; and e) State 5

In addition, the values of the indexes in states two and five for all scenarios showed that the changes in other cables, except the damaged cable, were relatively less

compared to the other states. In essence, when the T5A truck passed at a higher speed than the T2A, the changes observed in the other cables were less pronounced.

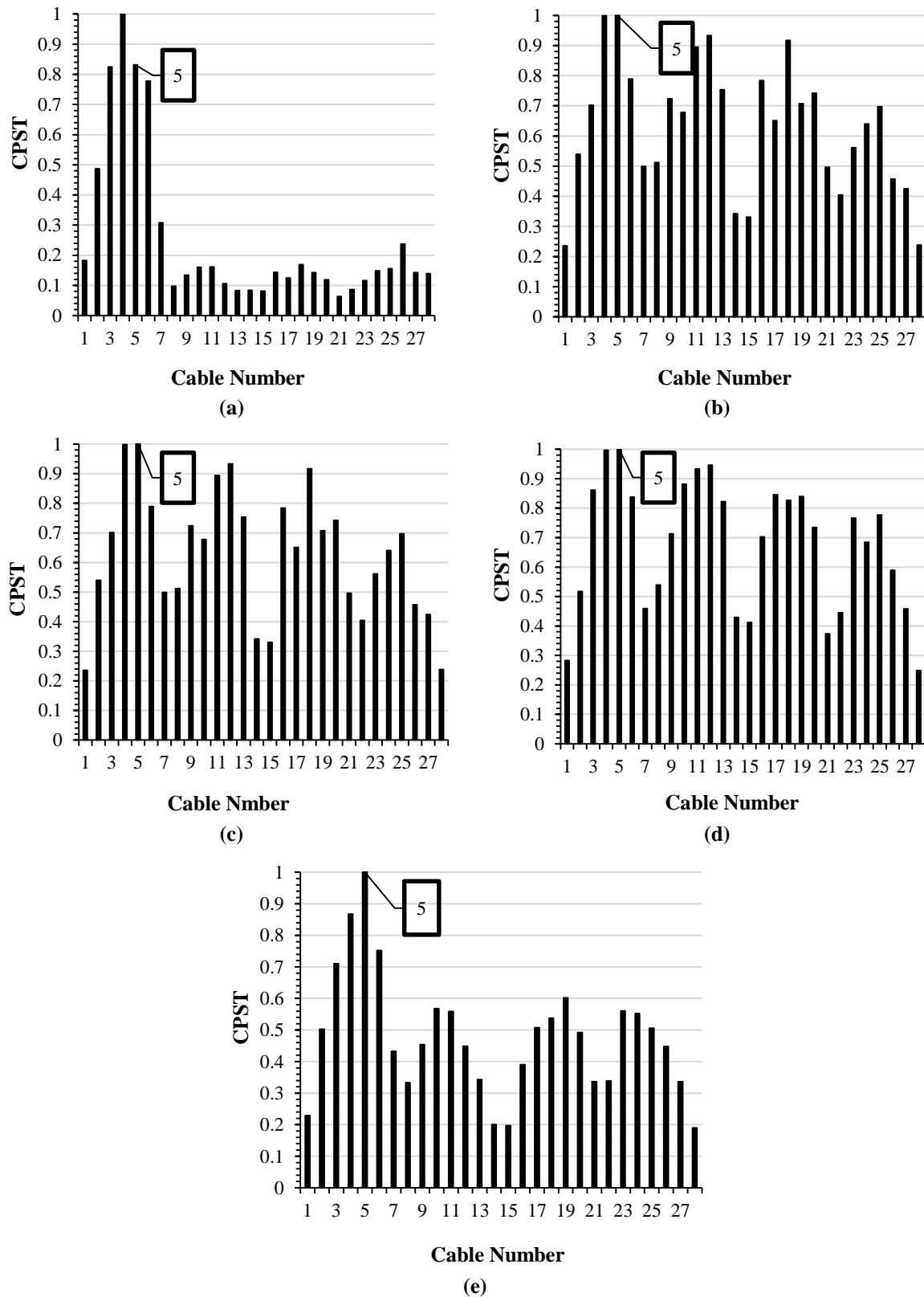


Fig. 10. CPST curves of cable 5 for five states: a) State 1; b) State 2; c) State 3; d) State 4; and e) State 5

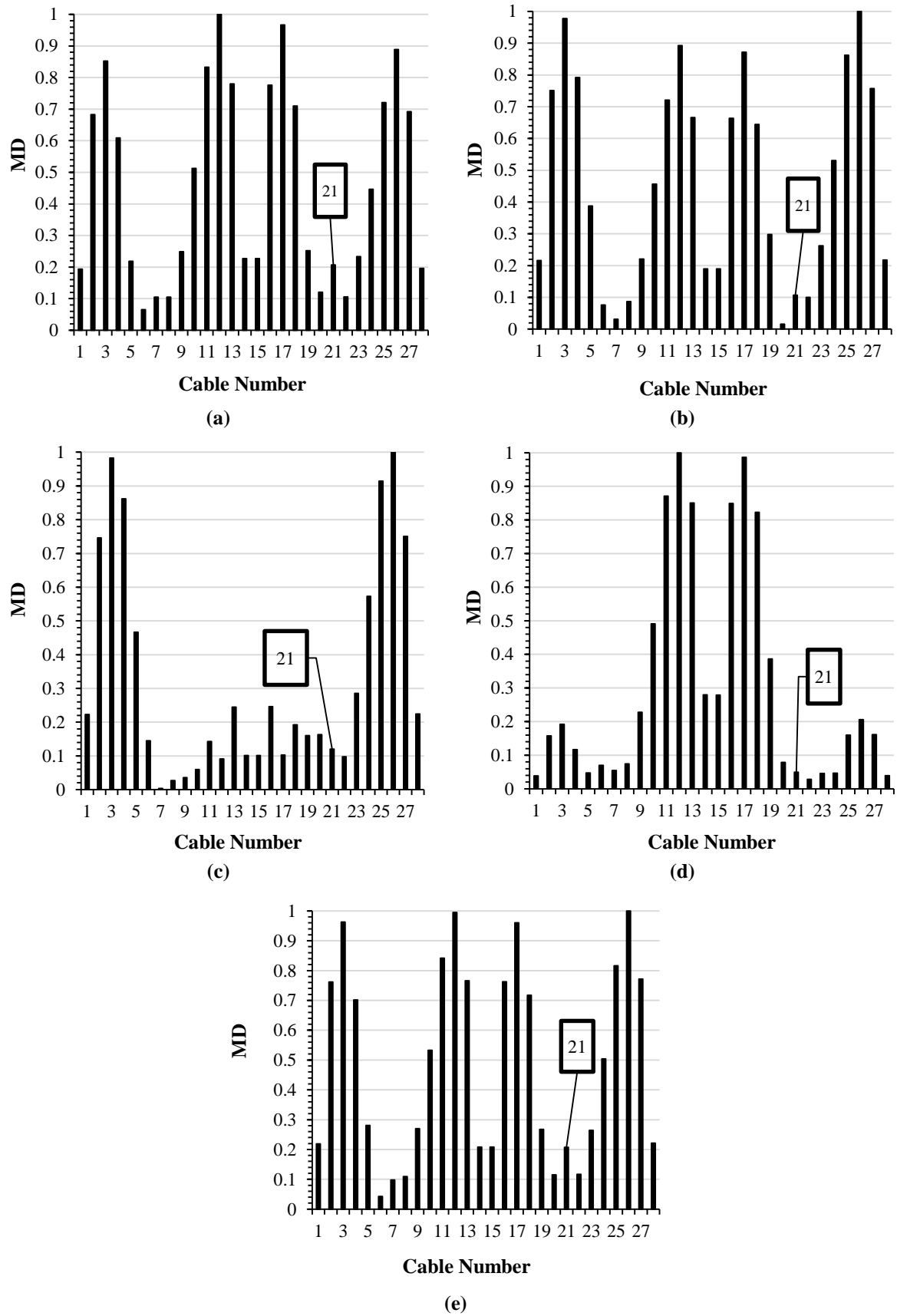


Fig. 11. MD curves of cable 21 for five states: a) State 1; b) State 2; c) State 3; d) State 4; and e) State 5

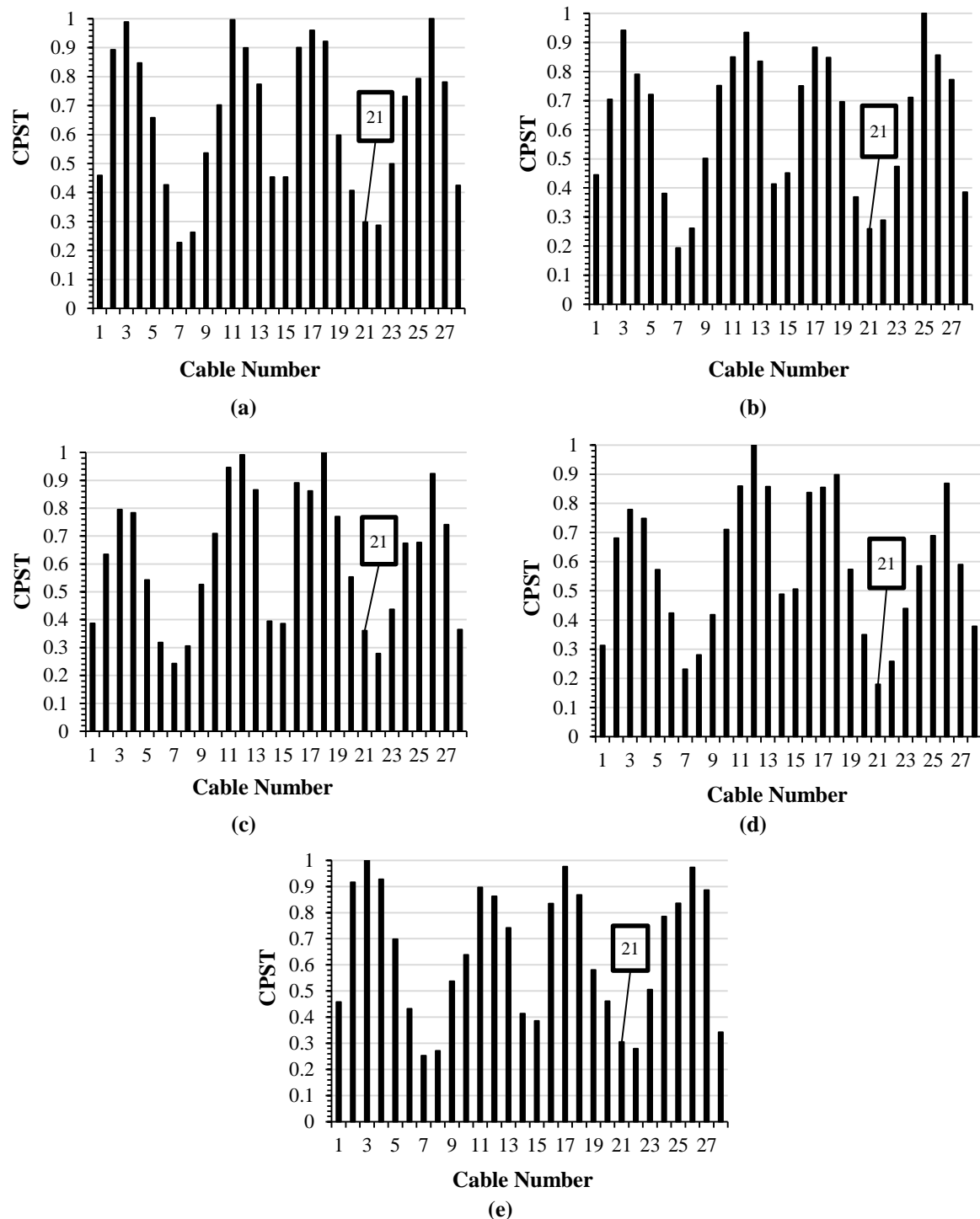


Fig. 12. CPST curves of cable 21 for five states: a) State 1; b) State 2; c) State 3; d) State 4; and e) State 5

The summary of results evaluation for MD and CPST damage indexes is presented in Table 7. Out of 100 analyses conducted, MD correctly identified 24% of scenarios when the cable damage level was 20%, while CPST correctly identified 12% of scenarios. For a damage level of 30%, these values increased to 31% for MD and 28% for CPST. When the damage level was

40%, MD and CPST indexes demonstrated the ability to detect 34% and 35% of the damaged cables across various states, respectively. Moreover, a significant percentage of the diagnoses were near the damaged cable. The MD index showed an accuracy of approximately 56%, considering both accurately and nearly detected cases for the 40% damage level.

Table 7. Results of damage detection for the damage level of 40%, excluding backstay cables

Damage percentage	20%		30%		40%	
Damage index	MD	CPST	MD	CPST	MD	CPST
Total number of analyses	100	100	100	100	100	100
Exactly detected	24	12	31	28	34	35
Nearly detected	15	14	19	20	22	12
Accuracy	39%	26%	50%	48%	56%	47%

4.1. Comparison with Modal-Based Methods

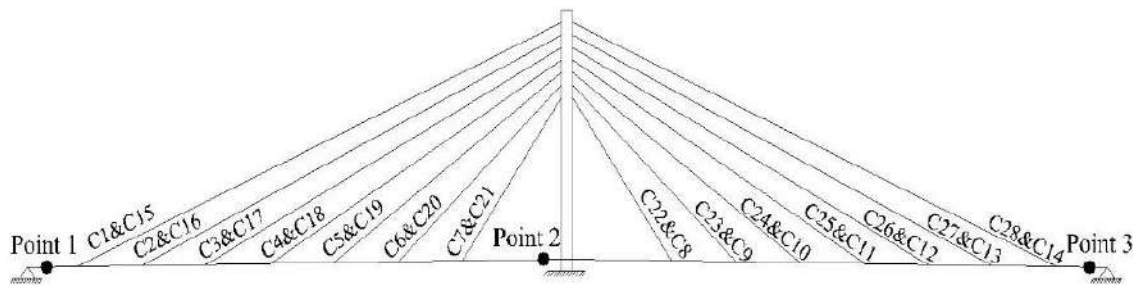
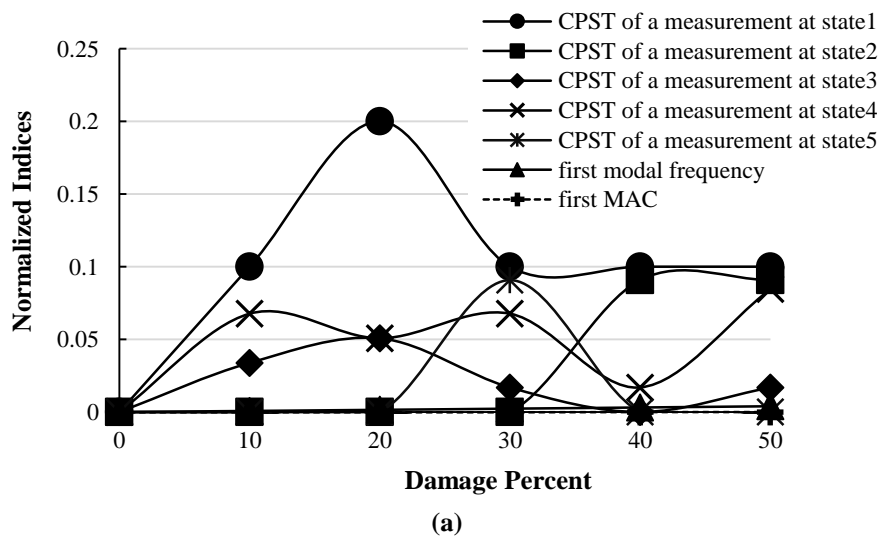
To highlight the robustness of the phase space-based damage detection method, a comparative analysis between CPST and modal parameters was conducted. CPST was derived from the displacement measurements at three distinct points on the deck, as shown in Figure 13: near the support in the first span (Point 1), adjacent to the pylon (Point 2), and in proximity to the support in the second span (Point 3). It was meticulously examined across damage levels of 10% to 50% for cable number 25 under all five aforementioned states. Modal

parameters such as the frequency of the bridge's first mode and the Modal Assurance Criterion (MAC) were analyzed. All indexes were normalized as follows (Nie et al., 2013):

$$CPST_{norm} = \frac{|CPST^d - CPST^u|}{CPST^u} \quad (10-1)$$

$$\omega_{norm} = \frac{|\omega^d - \omega^u|}{\omega^u} \quad (10-2)$$

$$MAC_{norm} = \frac{|MAC^d - MAC^u|}{MAC^u} \cdot MAC = \frac{\{(\varphi^u)^T \varphi^d\}^2}{\{(\varphi^u)^T \varphi^u\} \{(\varphi^d)^T \varphi^d\}} \quad (10-3)$$

**Fig. 13.** Location of measurement points

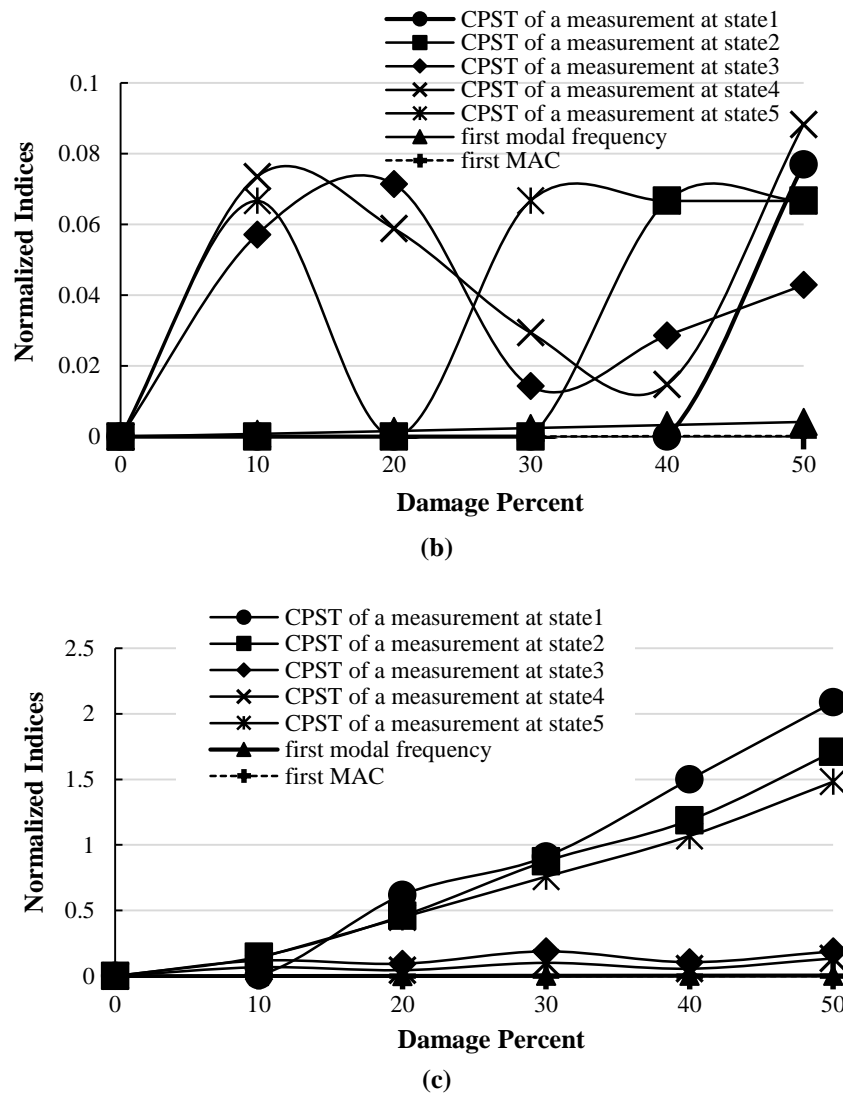


Fig. 14. A comparison of the normalized CPST and modal parameters: a) Measurement point 1; b) Measurement point 2; and c) Measurement point 3

The subscripts ‘u’ and ‘d’ denote the healthy and damaged cases, respectively. φ refers to the mode shape. Figures 14a and 14b illustrate the CPST index values and the modal parameters at Point 1 in the first span and Point 2 adjacent to the pylon. CPST exhibited heightened sensitivity to damage compared to frequency analysis. While CPST may not consistently specify the exact location of damaged cables under different load patterns and speeds, its changes were much more noticeable than those of the first mode frequency and MAC coefficient. Although they have served as significant indicators of structural damage. Figure 14c depicts the results from Point 3, which is situated near the damaged cable. Based on the previous analysis, a noticeable

correlation was observed between the CPST values and increasing damage levels across load-passing States 1, 2, and 5. For instance, at the 10% damage level, the accuracy of CPST increased by 84.5% compared to the first mode frequency of the structure across load State 1. CPST emerged as a powerful index for identifying damage in cable-stayed bridges, showcasing its robustness regardless of the location of the damage.

5. Conclusion and Future Work

A method for assessing cable health in cable-stayed bridges using phase space analysis was introduced. The proposed approach was validated through comprehensive numerical investigations

conducted on the Manavgat cable-stayed bridge. The evaluation encompassed a range of scenarios, which included various loading patterns and speeds. The combination of two indices, namely the CPST and MD, was used for damage detection by identifying subtle deviations in phase space trajectories. Some important conclusions are summarized as follows:

- The damage indices accurately identified the most damaged cables in scenarios where the passing load was the same in both healthy and damaged cases. However, cables near the pylon and backstay cables presented challenges due to their interconnected role.

- The MD index displayed accuracy ranging from 39% to 56% for damage levels of 20% to 40% under various loading patterns and speeds, while the CPST index achieved accuracy between 26% and 47%. In many cases, these indexes detected cables adjacent to the damaged cable, effectively identifying the location of the damage. In states where the T5A truck passed at higher speeds, the indices demonstrated superior effectiveness.

- Some scenarios involving cables near the pylon challenged the MD and CPST in detecting damage, resulting in inconclusive responses. For damage levels of 30% and above, improved results were noted, indicating the method's heightened sensitivity to higher levels of damage.

- The comparison with modal parameters highlighted the enhanced sensitivity of CPST, derived from the phase-space response method, in detecting damage within the time domain. CPST was presented as a valuable tool for monitoring the health of cable-stayed bridges, even when the measurement point is distant from the damaged location. This paper presented an initial approach for a practical solution aimed at ensuring the health of cable-stayed bridges and exploring real-world implementations. Suggestions for enhancing this method in the future include incorporating dynamic effects from high-speed loading, refining parameters with

increased precision and sensitivity (especially concerning backstay cables and those near the pylon), and considering different load placement locations within the passing lanes.

6. Declaration of Competing Interest

The authors declare that they have no known competing financial interests or personal relationships that could have appeared to influence the work reported in this paper.

7. References

- AASHTO. (2008). *LRFD bridge design specifications*, American Association of State Highway and Transportation Officials, Washington, DC.
- Abarbanel, H. (2012). *Analysis of observed chaotic data*, Springer Science and Business Media.
- Australasian Railway Association. (1992). *Bridge design code*, Austroads, Sydney, Australia.
- Bakhshizadeh, A. and Sadeghi, K. (2023). "Health-monitoring methods for long-span cable-stayed bridges", *Infrastructure Asset Management*, 11(1), 41-54, <https://doi.org/10.1680/jinam.23.00030>.
- Bakhshizadeh, A., Sadeghi, K., Ahmadi, S. and Royaei, J. (2023). "Damage identification in long-span cable-stayed bridges under multiple support excitations", *International Journal of Civil Engineering*, 21, 1275-1290, <https://doi.org/10.1007/s40999-023-00823-7>.
- Bedon, C., Dilella, M. and Morassi, A. (2016). "Ambient vibration testing and structural identification of a cable-stayed bridge", *Meccanica*, 51(11), 2777-2796, <https://doi.org/10.1007/s11012-016-0430-2>.
- Broomhead, D.S. and King, G.P. (1986). "Extracting qualitative dynamics from experimental data", *Physica D: Nonlinear Phenomena*, 20(2-3), 217-236, [https://doi.org/10.1016/0167-2789\(86\)90031-X](https://doi.org/10.1016/0167-2789(86)90031-X).
- Cheng, Y., Su, Z. and Zhang, J. (2024). "Mode shape-aided cable force estimation of a double-hanger system using a vision-based monitoring method", *Measurement*, 227, 114214, <https://doi.org/10.1016/j.measurement.2024.114214>.
- De Maesschalck, R., Jouan-Rimbaud, D. and Massart, D.L. (2000). "The mahalanobis distance", *Chemometrics and Intelligent Laboratory Systems*, 50(1), 1-18, [https://doi.org/10.1016/S0169-7439\(99\)00047-7](https://doi.org/10.1016/S0169-7439(99)00047-7).

- Elkady, A.Z., Youssef, A.F., Abuelnadr, I., DePeder, D. and Seleemah, A.A. (2023). "Optimum location of seismic isolation for manavgat cable-stayed bridge", *International Journal of Advanced Engineering, Management and Science*, 9(11), 39-58, <https://doi.org/10.22161/ijaems.911.3>.
- Fathali, M.A., Dehghani, E. and Hoseini Vaez, S.R. (2020). "An approach for adjusting the tensile force coefficient in equivalent static cable-loss analysis of the cable-stayed bridges", *Structures*, 25, 720-729, <https://doi.org/10.1016/j.istruc.2020.03.054>.
- George, R.C., Mishra, S.K. and Dwivedi, M. (2018). "Mahalanobis distance among the phase portraits as damage feature", *Structural Health Monitoring*, 17(4), 869-887, <https://doi.org/10.1177/1475921717722743>.
- He, W.Y., Ren, W.X. and Zhu, S. (2017). "Baseline-free damage localization method for statically determinate beam structures using dual-type response induced by quasi-static moving load", *Journal of Sound and Vibration*, 400, 58-70, <https://doi.org/10.1016/j.jsv.2017.03.049>.
- He, Z., Li, W., Salehi, H., Zhang, H., Zhou, H. and Jiao, P. (2022). "Integrated structural health monitoring in bridge engineering", *Automation in Construction*, 136, 104168, <https://doi.org/10.1016/j.autcon.2022.104168>.
- Hong, W., Wu, Z., Yang, C., Wan, C. and Wu, G. (2012). "Investigation on the damage identification of bridges using distributed long-gauge dynamic macrostrain response under ambient excitation", *Journal of Intelligent Material Systems and Structures*, 23(1), 85-103, <https://doi.org/10.1177/1045389X11430743>.
- Jana, D., Nagarajaiah, S. and Yang, Y. (2022). "Computer vision-based real-time cable tension estimation algorithm using complexity pursuit from video and its application in fred-hartman cable-stayed bridge", *Structural Control and Health Monitoring*, 29(9), e2985, <https://doi.org/10.1002/stc.2985>.
- Jiang, A.H., Huang, X.C., Zhang, Z.H., Li, J., Zhang, Z.Y. and Hua, H.X. (2010). "Mutual information algorithms", *Mechanical Systems and Signal Processing*, 24(8), 2947-2960, <https://doi.org/10.1016/j.ymssp.2010.05.015>.
- Kordi, A. and Mahmoudi, M. (2022). "Damage detection in truss bridges under moving load using time history response and members influence line curves", *Civil Engineering Infrastructures Journal*, 55(1), 183-194, <https://doi.org/10.22059/cej.2021.314109.1723>.
- Lei, X., Siringoringo, D.M., Sun, Z. and Fujino, Y. (2023). "Displacement response estimation of a cable-stayed bridge subjected to various loading conditions with one-dimensional residual convolutional autoencoder method", *Structural Health Monitoring*, 22(3), 1790-1806, <https://doi.org/10.1177/14759217221116637>.
- Li, D., Cao, M., Manoach, E., Jia, H., Ragulskis, M., Shen, L. and Sha, G. (2021). "A multiscale reconstructed attractors-based method for identification of structural damage under impact excitations", *Journal of Sound and Vibration*, 495, 115925, <https://doi.org/10.1016/j.jsv.2020.115925>.
- Li, S., Li, H., Liu, Y., Lan, C., Zhou, W. and Ou, J. (2014). "SMC structural health monitoring benchmark problem using monitored data from an actual cable-stayed bridge", *Structural Control and Health Monitoring*, 21(2), 156-172, <https://doi.org/10.1002/stc.1559>.
- Nazarian, E., Ansari, F. and Azari, H. (2016). "Recursive optimization method for monitoring of tension loss in cables of cable-stayed bridges", *Journal of Intelligent Material Systems and Structures*, 27(15), 2091-2101, <https://doi.org/10.1177/1045389X15620043>.
- Nichols, J.M. (2003). "Structural health monitoring of offshore structures using ambient excitation", *Applied Ocean Research*, 25(3), 101-114, <https://doi.org/10.1016/j.apor.2003.08.003>.
- Nie, Z., Hao, H. and Ma, H. (2012). "Using vibration phase space topology changes for structural damage detection", *Structural Health Monitoring*, 11(5), 538-557, <https://doi.org/10.1177/1475921712447590>.
- Nie, Z., Hao, H. and Ma, H. (2013). "Structural damage detection based on the reconstructed phase space for reinforced concrete slab: Experimental study", *Journal of Sound and Vibration*, 332(4), 1061-1078, <https://doi.org/10.1016/j.jsv.2012.08.024>.
- Pamwani, L. and Shelke, A. (2018). "Damage detection using dissimilarity in phase space topology of dynamic response of structure subjected to shock wave loading", *Journal of Nondestructive Evaluation, Diagnostics and Prognostics of Engineering Systems*, 1(4), 1-13, <https://doi.org/10.1115/1.4040472>.
- Pan, H., Azimi, M., Yan, F. and Lin, Z. (2018). "Time-frequency-based data-driven structural diagnosis and damage detection for cable-stayed bridges", *Journal of Bridge Engineering*, 23(6), [https://doi.org/10.1061/\(ASCE\)BE.1943-5592.0001199](https://doi.org/10.1061/(ASCE)BE.1943-5592.0001199).
- Paul, B., George, R.C. and Mishra, S.K. (2017). "Phase space interrogation of the empirical response modes for seismically excited structures", *Mechanical Systems and Signal Processing*, 91, 250-265, <https://doi.org/10.1016/j.ymssp.2016.12.008>.
- Peng, Z., Li, J. and Hao, H. (2022). "Data driven structural damage assessment using phase space embedding and koopman operator under stochastic excitations", *Engineering Structures*,

- 255, 113906, <https://doi.org/10.1016/j.engstruct.2022.113906>.
- Prawin, J., Lakshmi, K. and Rao, A.R.M. (2020). "Structural damage diagnosis under varying environmental conditions with very limited measurements", *Journal of Intelligent Material Systems and Structures*, 31(5), 665-686, <https://doi.org/10.1177/1045389X19898268>.
- Rhodes, C. and Morari, M. (1997). "The false nearest neighbors algorithm: An overview", *Computers & Chemical Engineering*, 21, S1149-S1154, [https://doi.org/10.1016/S0098-1354\(97\)87657-0](https://doi.org/10.1016/S0098-1354(97)87657-0).
- Rinaldi, C., Lepidi, M., Potenza, F. and Gattulli, V. (2023). "Identification of cable tension through physical models and non-contact measurements", *Mechanical Systems and Signal Processing*, 205, 110867, <https://doi.org/10.1016/j.ymssp.2023.110867>.
- Saidin, S.S., Kudus, S.A., Jamadin, A., Anuar, M.A., Amin, N.M., Ya, A.B.Z. and Sugiura, K. (2023). "Vibration-based approach for structural health monitoring of ultra-high-performance concrete bridge", *Case Studies in Construction Materials*, 18, e01752, <https://doi.org/10.1016/j.cscm.2022.e01752>.
- Takens, F. (1981). "Detecting strange attractors in turbulence", *Dynamical Systems and Turbulence*, Warwick, Berlin, Heidelberg, <https://doi.org/10.1007/BFb0091924>.
- Tuttipongswat, P., Sasaki, E., Suzuki, K., Fukuda, M., Kawada, N. and Hamaoka, K. (2019). "PC tendon damage detection based on phase space topology changes in different frequency ranges", *Journal of Advanced Concrete Technology*, 17(8), 474-488, <https://doi.org/10.3151/jact.17.474>.
- Wu, B., Wu, G., Lu, H. and Feng, D. (2017). "Stiffness monitoring and damage assessment of bridges under moving vehicular loads using spatially-distributed optical fiber sensors", *Smart Materials and Structures*, 26(3), 35058, <https://doi.org/10.1088/1361-665X/aa5c6f>.
- Wu, B., Wu, G. and Yang, C. (2019). "Parametric study of a rapid bridge assessment method using distributed macro-strain influence envelope line", *Mechanical Systems and Signal Processing*, 120, 642-663, <https://doi.org/10.1016/j.ymssp.2018.10.039>.
- Yu, C.P. (2020). "Tension prediction for straight cables based on effective vibration length with a two-frequency approach", *Engineering Structures*, 222, 111121, <https://doi.org/10.1016/j.engstruct.2020.111121>.
- Zarbafe, S.E.H.A.M., Norouzi, M., Allemang, R.J., Hunt, V.J., Helmicki, A. and Venkatesh, C. (2018). "Ironton-russell bridge: application of vibration-based cable tension estimation", *Journal of Structural Engineering*, 144(6), 04018066, [https://doi.org/10.1061/\(asce\)st.1943-541x.0002054](https://doi.org/10.1061/(asce)st.1943-541x.0002054).
- Zhang, W., Li, J., Hao, H. and Ma, H. (2017). "Damage detection in bridge structures under moving loads with phase trajectory change of multi-type vibration measurements", *Mechanical Systems and Signal Processing*, 87(A), 410-425, <https://doi.org/10.1016/j.ymssp.2016.10.035>.
- Zhang, H., Mao, J., Wang, H., Zhu, X., Zhang, Y., Gao, H. and Ni, Y. and Hai, Z. (2023). "A novel acceleration-based approach for monitoring the long-term displacement of bridge cables", *International Journal of Structural Stability and Dynamics*, 23(05), 2350053, <https://doi.org/10.1142/S0219455423500530>.
- Zhang, L., Wu, G. and Cheng, X. (2020). "A rapid output-only damage detection method for highway bridges under a moving vehicle using long-gauge strain sensing and the fractal dimension", *Measurement: Journal of the International Measurement Confederation*, 158, 107711, <https://doi.org/10.1016/j.measurement.2020.107711>.



This article is an open-access article distributed under the terms and conditions of the Creative Commons Attribution (CC-BY) license.



Impact of High-Strength Reinforcement on Ductility of Normal-Strength Reinforced Concrete Column

Ulfa, A.A.^{1*}  and Piscesa, B.² 

¹ M.D., Instructor, Civil Engineering Department, Politeknik Negeri Balikpapan, Balikpapan, Indonesia.

² Ph.D., Instructor, Civil Engineering Department, Institut Teknologi Sepuluh Nopember, Indonesia.

© University of Tehran 2024

Received: 22 Sep. 2023;

Revised: 2 May 2024;

Accepted: 29 May 2024

ABSTRACT: The ductility of reinforced concrete columns can be significantly influenced by the configurations and material properties of the confining bars. Extensive research is required to comprehend the limitations on yield strength imposed by certain building codes, particularly concerning high-strength reinforcement. AS 3600:2017 and ACI 318-19 codes restrict the yield strength of confinement reinforcement to 800 MPa and 700 MPa, respectively. This study investigates the ductility of reinforced concrete columns using five different confining bar configurations, two concrete compressive strengths (30 MPa and 50 MPa), two longitudinal reinforcement yield strengths (420 MPa and 500 MPa), and four transverse reinforcement yield strengths (420 MPa, 500 MPa, 700 MPa, and 1000 MPa). The diameter of the confining bars is adjusted to meet the required area estimates from ACI 318-19 and AS 3600:2017 codes. Additionally, finite element analysis is conducted using the 3D-NLFEA package. The results demonstrate the safety and adequate ductility provided by high-strength steel in reinforced concrete columns. Furthermore, a simple formulation for column ductility, which integrates the confining bar configurations, is proposed based on the numerical study.

Keywords: Confinement, Configuration, Ductility Index, 3D-NLFEA, Finite Element Method.

1. Introduction

Silpa and Sreevalli (2021) have emphasized the need to understand the behavior of reinforced concrete structures under various conditions to ensure safety. For example, the review highlights the importance of analyzing and simulating structural elements to comprehend failure mechanisms and improve design practices (Silpa and Sreevalli, 2021). Column failure is a critical issue that occurs when a column cannot resist shear forces and exhibits low

ductility, typically due to insufficient confinement requirements. To mitigate the risk of column collapse, it is essential to adopt effective solutions that can delay the failure process in a ductile manner. One such solution is to use lateral reinforcement as concrete column confinement. This technique has been widely recognized as an effective measure to enhance the ductility of concrete columns, delay the onset of failure, and improve the overall structural performance.

The collapse of concrete is typically

* Corresponding author E-mail: anis.aulia@poltekba.ac.id

caused by continuous axial loading, leading to uncontrolled volume expansion.

However, the expected collapse can be significantly slowed down and controlled by using sufficient confinement to the concrete core. Thus, it is possible to delay the onset of failure and improve the overall structural behavior of the column. Previous research has delved into the augmentation of stress-strain characteristics in concrete through the use of transverse reinforcement, such as hoops or ties. The findings from Ding et al. (2017) suggested that the restraining impact of stirrups boosts the peak stress, leading to an improvement in the load-bearing capacity of the specimen.

Moreover, the seismic performance of a short column can be elevated by increasing the volume-stirrup ratio and shear span ratio (Ding et al., 2017). These investigations underscore the potential of transverse reinforcement in augmenting axial stress capacity and deformability in Reinforced Concrete (RC) columns. The overarching aim is to elevate ductility by intensifying stress and strain within the column, consequently delaying the risk of column collapse. Kim et al. (2021) showcased a more pronounced ductile response post-flexural yielding with increased yield strength of transverse reinforcement, indicating heightened lateral confinement (Kim et al., 2021). Furthermore, the utilization of high-strength reinforcing bars offers cost-saving benefits while maintaining column strength and ductility (Alavi-Dehkordi and Mostofinejad, 2018).

Enhancing the strength of the stirrups has minimal impact on the reduction in stiffness (Wang et al., 2020). High-strength reinforcement enables larger pitch spacing of transverse reinforcement, enhancing the workability of concrete during casting. It is imperative to recognize the limitations imposed by building codes. AS 3600:2017 restricts the yield stress of transverse reinforcement to 800 MPa, while ACI 318-19 imposes a limit of 700 MPa, ACI 318-19 mandates a minimum level of confinement reinforcement to ensure ductility, whereas

AS 3600:2017 allows for various design approaches, specifying a minimum effective confining pressure of 0.01 times the concrete strength. The configuration of transverse reinforcement, including the detailing of hooks, significantly contributes to enhancing concrete core confinement.

This aspect plays a crucial role in preventing longitudinal bar buckling. It is essential to explore different transverse reinforcement configurations to understand their impact on confining pressure and, consequently, on both column strain ductility and ductility index. This study explores the ductility of RC columns crafted from normal-strength concrete and high-strength reinforcement. Beyond this primary objective, the research scrutinizes the influence of various reinforcement configurations and confinement parameters on the ductility of reinforced concrete columns. Moreover, it aims to provide valuable insights into the structural behavior guided by diverse design standards.

2. Materials and Methods

This study is the extended research carried out by Ulfa et al. (2020), by incorporating various confinement configurations. Analysis of the model will be implemented using the finite element method with an in-house 3D-NLFEA package developed by Piscesa et al. (2018). The 3D-NLFEA utilizes the plasticity-fracture model for concrete, which is restraint sensitive and incorporates premature cover spalling due to restrained shrinkage (Piscesa et al., 2019). The RC columns designed with high-strength rebar based on ACI 318-19 and AS 3600:2017 will be evaluated for their ductility and axial load-carrying capacity.

The analysis result of these columns will enable the determination of the peak load and provide insights into the impact of confinement parameters and reinforcement configurations on the ductility index (I_{10}).

High-strength reinforcing bars serve as

earthquake-resistant alternatives, offering comparable normalized energy dissipation to standard-strength bars (Kamaruddin et al., 2018). However, incorporating high-strength reinforcement reduces the member's stiffness, resulting in increased elastic deformation prior to yielding. On the other hand, Prasetya's test results (Ou and Kurniawan, 2015) indicate that transverse reinforcement yielded after the column reached its peak strength. For shear reinforcement, Ou and Kurniawan (2015) recommended a limit of 600 MPa. The AS 3600:2017 regulation restricts stirrup reinforcement yield stress to 800 MPa, while ACI 318-19 limits it to 700 MPa. This study aims to ensure an equal confinement pressure across various reinforcement configurations. Each increase in reinforcement strength corresponds to a distinct confinement pressure, with higher strength leading to greater restraint stress.

To maintain uniform confinement pressure, the diameter of the confinement rebar reinforcement is adjusted. The variation in diameter is determined based on the minimum required stirrup reinforcement specified in AS 3600:2017 and ACI 318-19 regulations. By adhering to these guidelines, the study ensures compliance with design standards while enabling a comprehensive analysis of the impact of confinement pressure on reinforced elements' behavior. The longitudinal reinforcement area of columns, as per ACI 318-19, is determined by $A_{st} \geq 0.01 A_g$, where A_g : is the column cross-sectional area and A_{st} : is the required area of longitudinal reinforcement:

$$\begin{aligned} A_g &= 600 \text{ mm} \times 600 \text{ mm} = 360000 \text{ mm}^2 \\ A_{st} &\geq 0.01 \times 360000 \text{ mm}^2 \\ &\geq 3600 \text{ mm}^2 \end{aligned}$$

Based on different types of confinement reinforcement configurations, the number of longitudinal bars in Type I and II columns differs from the number in Type III, IV, and V columns. For Type I and II columns with the number of longitudinal bars, $n_b = 8$ and $d_b = 25$ mm, with $\frac{A_{st}}{A_g} = 0.011$. While for Types III, IV, and V

columns with the number of longitudinal bars, $n_b = 12$ and $d_b = 20$ mm, with $\frac{A_{st}}{A_g} = 0.0105$. As per the guidelines specified in ACI 318-19 Clause 18.7.5.4, for normal strength concrete with a compressive strength $f'_c \leq 10000$ psi (i.e., 68.94757 MPa) the requirement for transverse reinforcement dictates that $A_{sh}/(b \cdot s)$ should meet or exceed the criteria outlined in Eqs. (1) and (2) as follows:

$$\frac{A_{sh}}{b_c s} = 0.3 \left(\frac{A_g}{A_{ch}} - 1 \right) \frac{f'_c}{f_{yt}} \quad (1)$$

$$\frac{A_{sh}}{b_c s} = 0.09 \frac{f'_c}{f_{yt}} \quad (2)$$

$$A_{sh} = n_s \frac{1}{4} \pi d^2 \quad (3)$$

where A_g : is the gross area of the column cross-section, A_{ch} : is the centre-to-centre bounded core area of the longitudinal reinforcement, b : is the overall width of the column, and s : is the distance between the confining bars along the column.

According to AS 3600:2017, the triaxial stress across all sections and the effectiveness of confining bars are used to obtain the confining pressure in the core (Samani et al., 2015). Clause 10.7.3.3, the effective stress confinement ($f_{r,eff}$) is:

$$f_{r,eff} = k_e \cdot f_r \geq 0.01 f'_c \quad (4)$$

$$k_e = \left(1 - \frac{n \cdot w^2}{6 \cdot A_c} \right) \left(1 - \frac{s}{2 \cdot b_c} \right) \left(1 - \frac{s}{2 \cdot d_c} \right) \quad (5)$$

where k_e : is the effectiveness factor of the reinforcement confinement and f_r : is the confinement stress that can be calculated using the following equations:

$$f_r = \frac{\sum_{i=1}^m A_{bf, it} \cdot f_{syf} \sin \theta}{d_s \cdot s} \quad (6)$$

$$\sum_{i=1}^m A_{bf, it} \cdot \sin \theta = \frac{f_r \cdot d_s \cdot s}{f_{syf}} \quad (7)$$

where n : is the number of longitudinal reinforcements, w : is the average net distance among adjacent longitudinal

reinforcements, b_c and d_c : are the centre-to-centre measurements of outermost reinforcement, and A_c : is the core area bounded by the centre-to-centre of the outermost confinement. A_{bf} : is the cross-sectional area of one bar, f_{syf} : is the yield stress of the lateral reinforcement, m : is the number of legs intersecting the confinement section, θ : is the angle between the reinforcing tie to the plane, and d_s : is the

dimension measured from the centre-to-centre of the outer confinement reinforcement.

Square column confinement is more effective than that of rectangular columns. Hence, this study examines the ductility of square-reinforced concrete columns through analysis of five different configurations. Figure 1 illustrates these configurations.

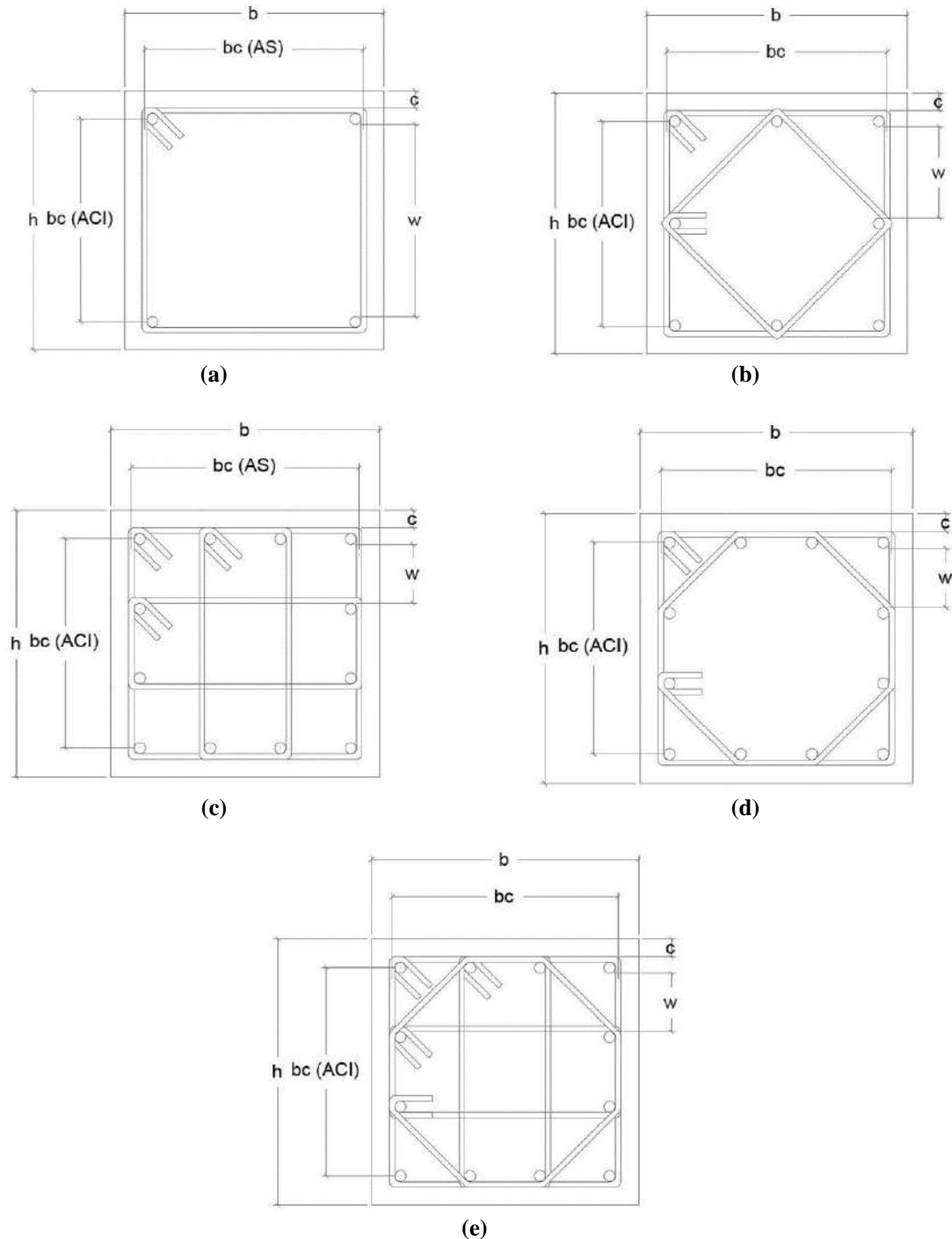


Fig. 1. Confinement configuration of the test specimen: a) Type 1; b) Type 2; c) Type 3; d) Type 4; and e) Type 5

A total of 120 square reinforced concrete columns were used in the study, each measuring $600 \times 600 \times 1800$ mm. The columns feature a concrete cap that is 40 mm thick and have a pitch spacing of 100 mm. The test specimens based on the material's strength are labelled as shown in Tables 1 and 2. The label can be interpreted as follows: Specimen I3.L4.T4. The Roman numeral I represents the specimen configuration type, number 3 indicates the compressive strength of concrete (Type 3

for 30 MPa and Type 5 for 50 MPa), L4 signifies the strength of longitudinal reinforcement at 420 MPa, and T4 denotes the type of transverse reinforcement at 420 MPa. Concrete under effective confinement exhibits full arching action, primarily expressed within the core area of the concrete. Additionally, each confinement configuration generates a distinct confinement pressure, influenced by the quantity and arrangement of the confining bars.

Table 1. Labelling of column specimens ($f_c = 30$ MPa)

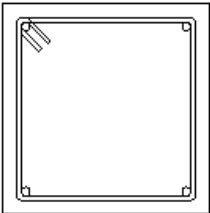
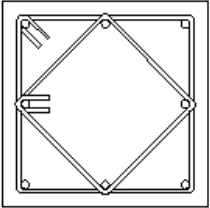
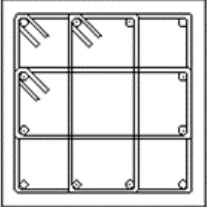
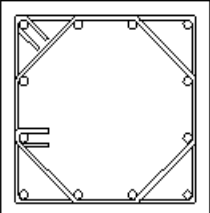
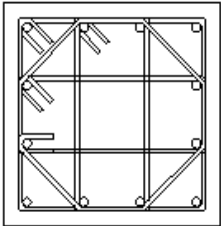
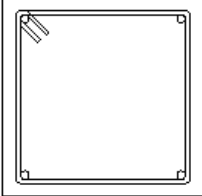
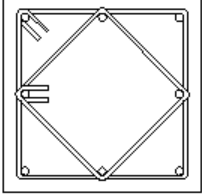
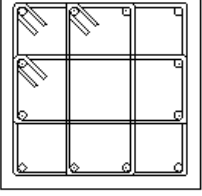
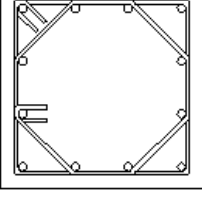
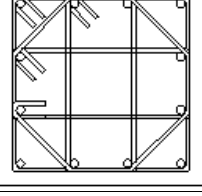
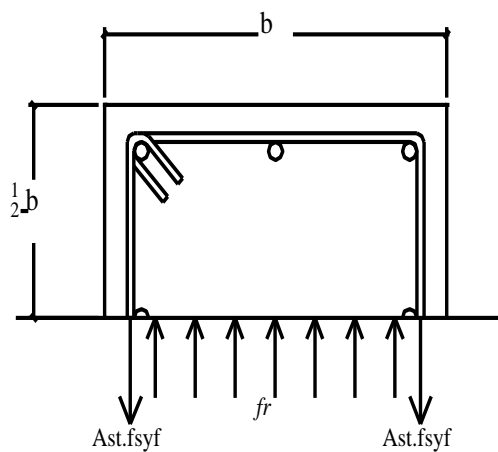
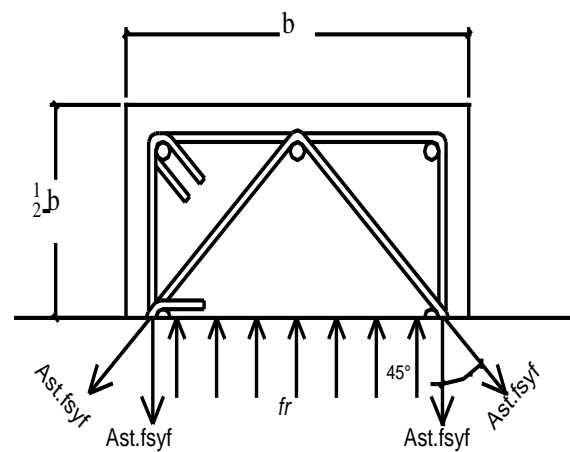
Compressive strength of concrete (f_c)		30 MPa					
Longitudinal rebar yield strength (f_y)		420 MPa			500 MPa		
Transversal rebar yield strength (f_{yt})		420 MPa	700 MPa	1000 MPa	500 MPa	700 MPa	1000 MPa
		I3.L4.T4	I3.L4.T7	I3.L4.T10	I3.L5.T5	I3.L5.T7	I3.L5.T10
		II3.L4.T4	II3.L4.T7	II3.L4.T10	II3.L5.T5	II3.L5.T7	II3.L5.T10
		III3.L4.T4	III3.L4.T7	III3.L4.T10	III3.L5.T5	III3.L5.T7	III3.L5.T10
		IV3.L4.T4	IV3.L4.T7	IV3.L4.T10	IV3.L5.T5	IV3.L5.T7	IV3.L5.T10
		V3.L4.T4	V3.L4.T7	V3.L4.T10	V3.L5.T5	V3.L5.T7	V3.L5.T10

Table 2. Labelling of column specimens ($f'_c = 50$ MPa)

Compressive strength of concrete (f'_c)	50 MPa					
Longitudinal rebar yield strength (f_y)	420 MPa			500 MPa		
Transversal rebar yield strength (f_{yt})	420 MPa	700 MPa	1000 MPa	500 MPa	700 MPa	1000 MPa
	I5.L4.T4	I5.L4.T7	I5.L4.T10	I5.L5.T5	I5.L5.T7	I5.L5.T10
	II5.L4.T4	II5.L4.T7	II5.L4.T10	II5.L5.T5	II5.L5.T7	II5.L5.T10
	III5.L4.T4	III5.L4.T7	III5.L4.T10	III5.L5.T5	III5.L5.T7	III5.L5.T10
	IV5.L4.T4	IV5.L4.T7	IV5.L4.T10	IV5.L5.T5	IV5.L5.T7	IV5.L5.T10
	V5.L4.T4	V5.L4.T7	V5.L4.T10	V5.L5.T5	V5.L5.T7	V5.L5.T10



(a)



(b)

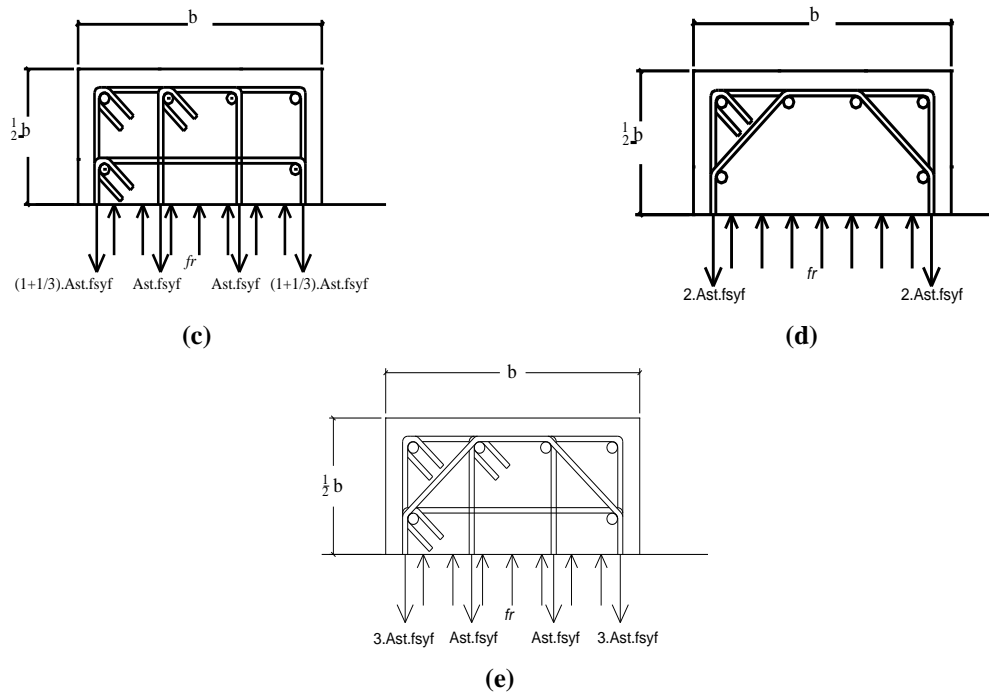


Fig. 2. The effect of confinement configuration on the concrete confinement pressure in the test specimens: a) Type 1; b) Type 2; c) Type 3; d) Type 4; and e) Type 5

The calculation of confinement pressure involves analyzing the cross section's free body, enabling the determination of f_r and $A_{b,fit}$ based on the equilibrium stress illustrated in Figure 2. Table 3 presents the influence of the confining bar on the concrete confinement pressure and the number of tie legs in each confinement configuration, as depicted in Figure 2. The specimens consist of normal-strength concrete with compressive strengths of 30 MPa and 50 MPa, along with high-strength steel confining bars. These specimens are varied based on the strengths of longitudinal and transverse reinforcements.

The variations are as follows: a) Longitudinal reinforcement yield strength (f_y) of 420 MPa, with confinement yield strengths (f_{yt}) of 420 MPa, 700 MPa, and 1000 MPa. b) Longitudinal reinforcement yield strength (f_y) of 500 MPa, with confinement yield strengths (f_{yt}) of 500 MPa, 700 MPa, and 1000 MPa. The stress-strain behavior of the longitudinal reinforcement is assumed to be perfectly

elastic-plastic. For the lateral reinforcement, stress-strain models from various researches are employed: 1) Seliem (Seliem et al., 2009) is referenced for confining steel rebar with a yield strength $f_{yt} = 420$ MPa; 2) Nehrp (Moehle et al., 2010) provides the stress-strain model for confining steel rebar with a yield strength $f_{yt} = 500$ MPa; 3) Hung (Hung and Chueh, 2016) is consulted for the stress-strain model of confining steel rebar with a yield strength $f_{yt} = 700$ MPa, and 4) Cai (Cai et al., 2018) is utilized for the stress-strain model of confining steel rebar with a yield strength $f_{yt} = 1000$ MPa. Figure 3 depicts the stress-strain diagram of the confining steel rebar. To comply with the requirements of ACI 318-19 Clause 18.7.4.1, which mandates $A_{st} \geq 0.01 A_g$ for the longitudinal reinforcement area, the following design decisions were made:

- Types I and II columns have a reinforcement diameter of 25 mm, equivalent to 1.09% of the gross cross-sectional area.

Table 3. The number of tie legs in each configuration

Column type	I	II	III	IV	V
Tie legs	2	3.414	4.667	3.61	6.28

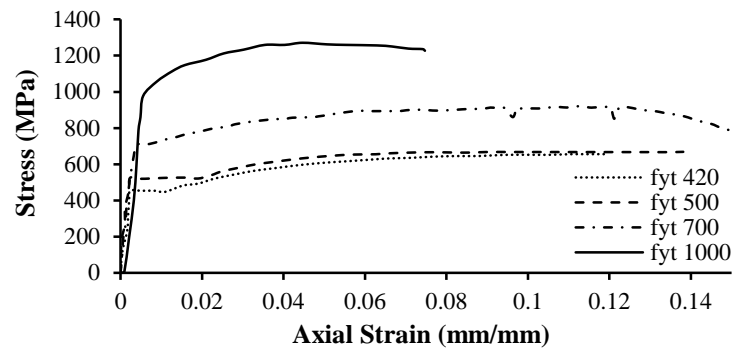


Fig. 3. Stress-strain diagram of lateral reinforcement

- Types III, IV, and V columns feature a 20 mm longitudinal reinforcement diameter, representing 1.05% of the gross cross-sectional area. These design choices ensure adherence to the specified longitudinal reinforcement area requirements. Each specimen will be analyzed by systematically adjusting the diameter of the confining rebar, taking into account the minimum diameter criteria specified in AS 3600:2017 and ACI 318-19. The material properties of the columns include a presumed density of 2200 kg/cm³ and a Young's modulus of 200,000 MPa for the reinforcement.

- Furthermore, by using Eq. (3), the diameter of the transverse reinforcement is analytically determined to meet the required area specifications stated in Eqs. (1) and (2).

The values of k_e and f_r vary based on the number of longitudinal reinforcements and their corresponding A_s values, leading to specific calculations. For column samples designed according to AS 3600 standards (with a minimum $f_{r,eff} = 0.01 f'_c$), the values of k_e and f_r can be computed using Eqs. (4) and (5), respectively, and the results are summarized in Table 4. ACI 318-19 provides guidelines for the area of confinement reinforcement based on Eq. (4), while AS 3600:2017 enables the calculation of the required diameter of the confinement rebar using Eq. (7) to satisfy the minimum $f_{r,eff}$ requirements. Table 5 presents the obtained reinforcement diameters for each specimen based on the requirements specified in AS 3600:2017 and ACI 318-19.

Table 4. k_e and f_r correspond to the number of longitudinal bar

	Column type	
	I and II	III, IV, and V
k_e	0.62214	0.68935
f_r (30 MPa)	0.48221	0.43519
f_r (50 MPa)	0.80368	0.72532

Table 5. Minimum confinement rebar diameter (mm) of specimen X, indicating the specific configuration type according to the corresponding column type outlined in Tables 1 and 2

Column type	AS 3600:2017					ACI 318-19				
	I	II	III	IV	V	I	II	III	IV	V
X3.L4.T4	6.13	4.69	3.81	4.33	3.29	14.59	11.17	9.60	10.92	8.28
X3.L4.T7	4.75	3.63	2.95	3.36	2.55	11.30	8.651	7.44	8.46	6.41
X3.L4.T10	3.97	3.04	2.47	2.81	2.13	9.46	7.238	6.22	7.08	5.37
X3.L5.T5	5.62	4.3	3.49	3.97	3.01	13.37	10.24	8.80	10.01	7.59
X3.L5.T7	4.75	3.63	2.95	3.36	2.55	11.30	8.651	7.44	8.46	6.41
X3.L5.T10	3.97	3.04	2.47	2.81	2.13	9.46	7.238	6.22	7.08	5.37
X5.L4.T4	7.91	6.06	4.92	5.6	4.24	18.84	14.42	12.4	14.1	10.7
X5.L4.T7	6.13	4.69	3.81	4.33	3.29	14.59	11.17	9.60	10.92	8.28
X5.L4.T10	5.13	3.92	3.19	3.63	2.75	12.21	9.344	8.03	9.14	6.93
X5.L5.T5	7.25	5.55	4.51	5.13	3.89	17.26	13.21	11.36	12.92	9.8
X5.L5.T7	6.13	4.69	3.81	4.33	3.29	14.59	11.17	9.603	10.92	8.28
X5.L5.T10	5.13	3.92	3.19	3.63	2.75	12.21	9.344	8.034	9.14	6.93

It is important to note that the structural frame design in AS 3600:2017 is specifically intended for ordinary to Intermediate Resisting Moment Frames (OMRF to IMRF), while the ACI 318-19 confinement equation is intended for Special Resisting Moment Frames (SRMF).

Figure 4 displays a 3D mesh model of column specimens, which comprises solid elements representing concrete, along with five different reinforcement configurations.

The mesh model was created using SALOME 9.2.0 software. The column core and cover regions are clearly differentiated, as illustrated in Figure 4a. In the analysis,

the load is applied to the top surface of the column, while the bottom surface is fixed as a restraint.

3. Results and Discussion

The 3D-NLFEA simulation provides data on load and deformation. These values are then used to calculate the axial stress by dividing the load by the cross-sectional area of the column. Similarly, the axial strain is determined by dividing the deformation by the original length of the column. The resulting stress-strain diagram of the column is depicted in Figures 5-14.

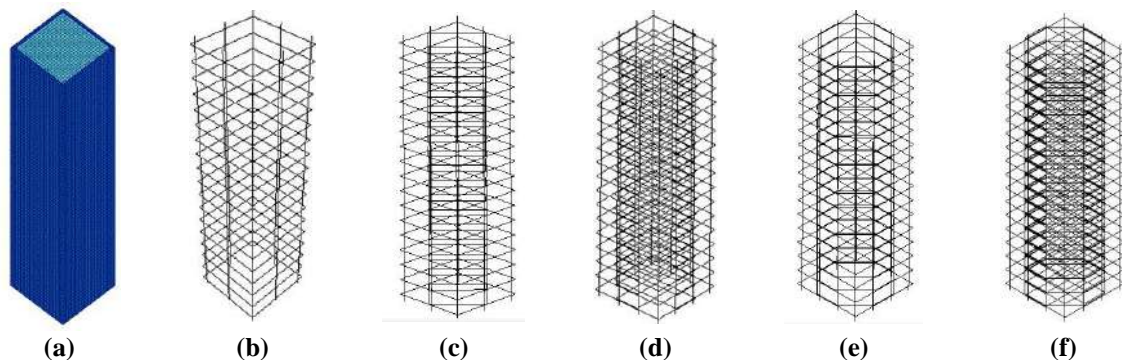


Fig. 4. Modeling of specimens: a) Concrete; b) Type I; c) Type II; d) Type III; e) Type IV; and f) Type V

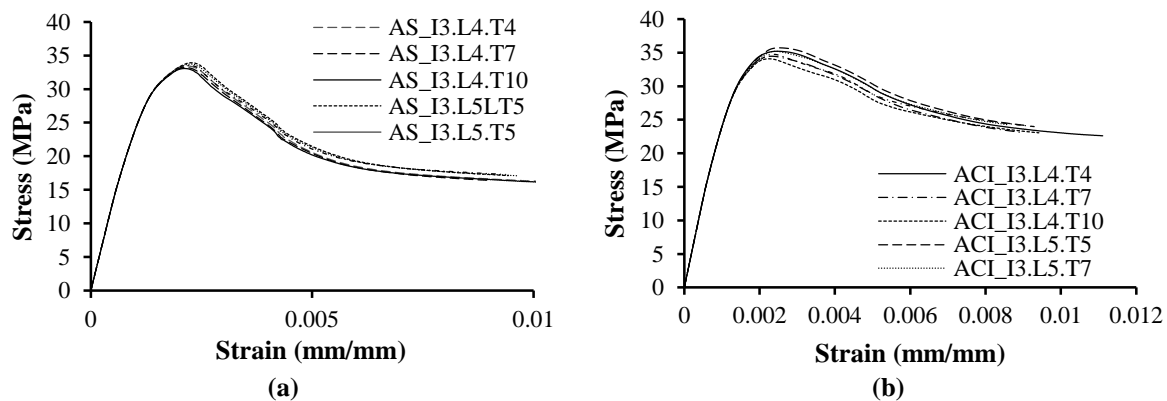


Fig. 5. Specimen stress-strain diagram Type I f'_c 30 MPa: a) AS 3600:2017; and b) ACI 318-19

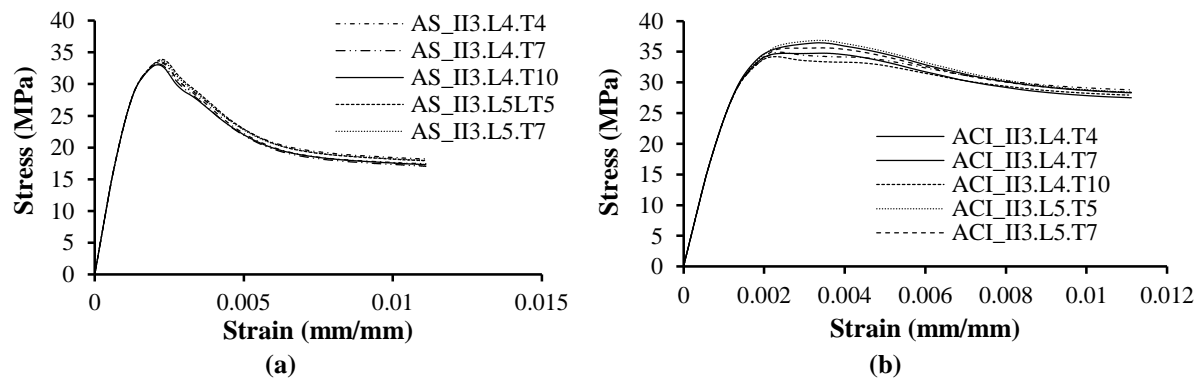


Fig. 6. Specimen stress-strain diagram Type II f'_c 30 MPa: a) AS 3600:2017; b) ACI 318-19

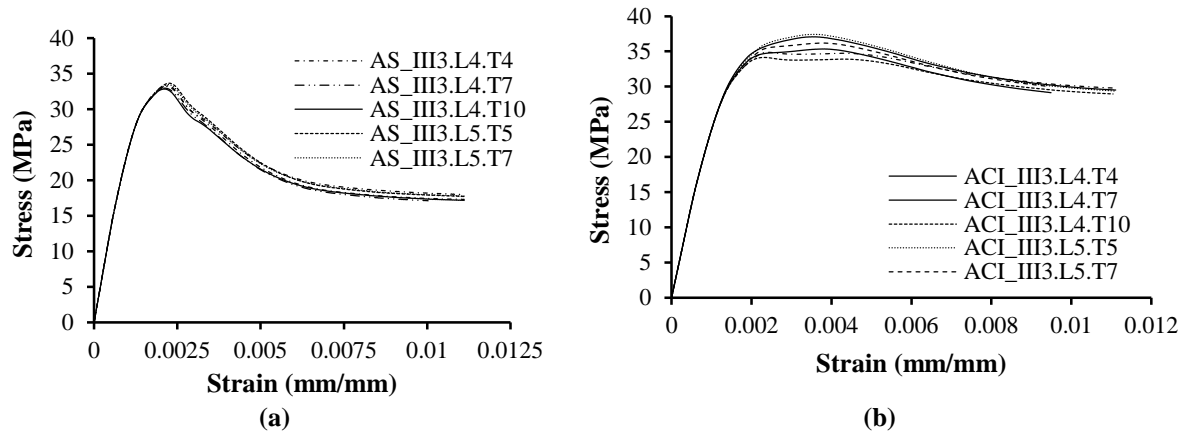


Fig. 7. Specimen stress-strain diagram Type III f'_c 30 MPa: a) AS 3600:2017; b) ACI 318-19

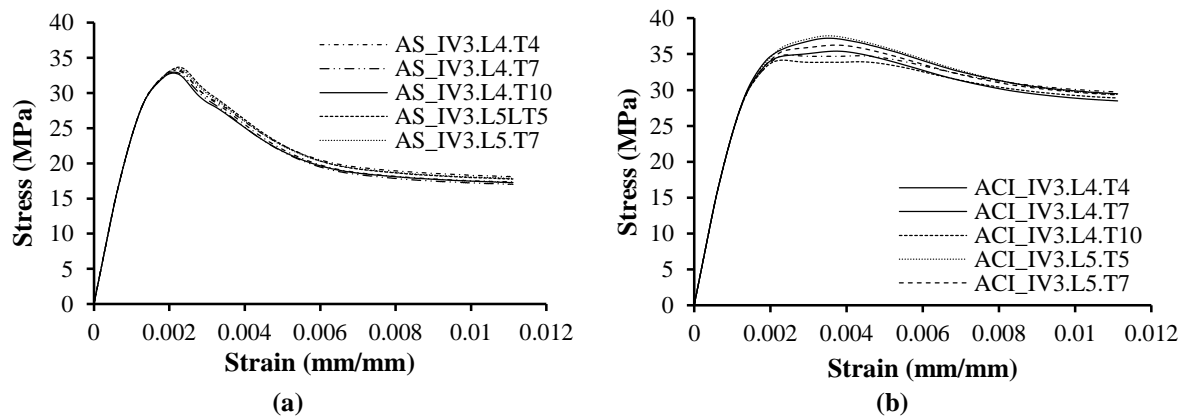


Fig. 8. Specimen stress-strain diagram Type IV f'_c 30 MPa: a) AS 3600:2017; b) ACI 318-19

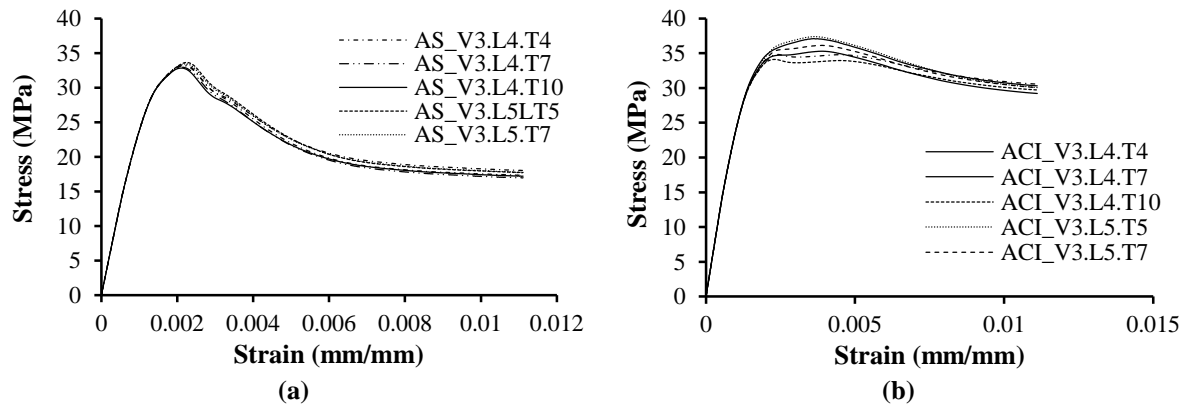


Fig. 9. Specimen stress-strain diagram Type V f'_c 30 MPa: a) AS 3600:2017; b) ACI 318-19

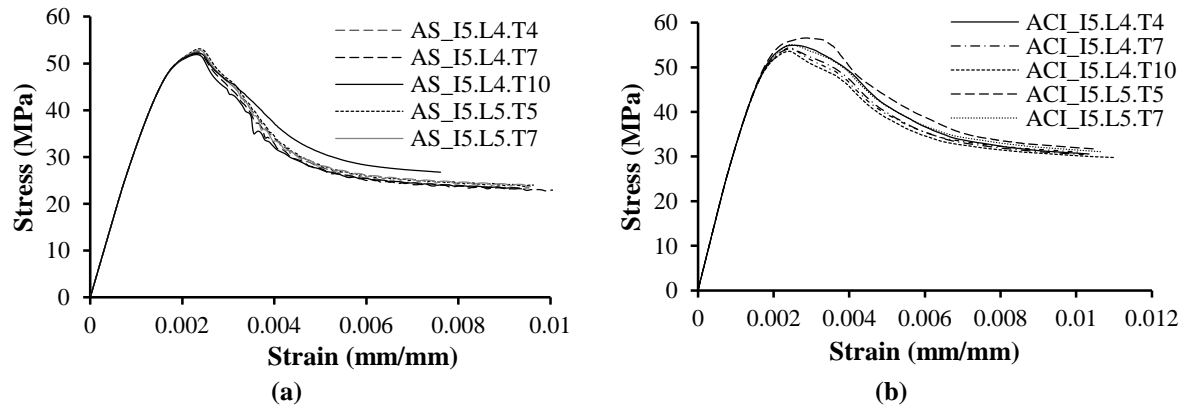


Fig. 10. Specimen stress-strain diagram Type I f'_c 50 MPa: a) AS 3600:2017; b) ACI 318-19

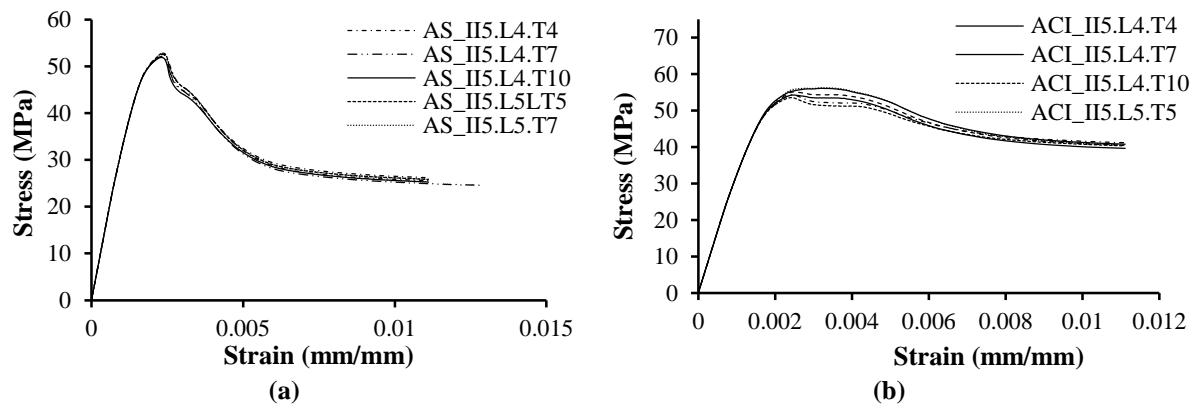


Fig. 11. Specimen stress-strain diagram Type II f_c 50 MPa: a) AS 3600:2017; b) ACI 318-19

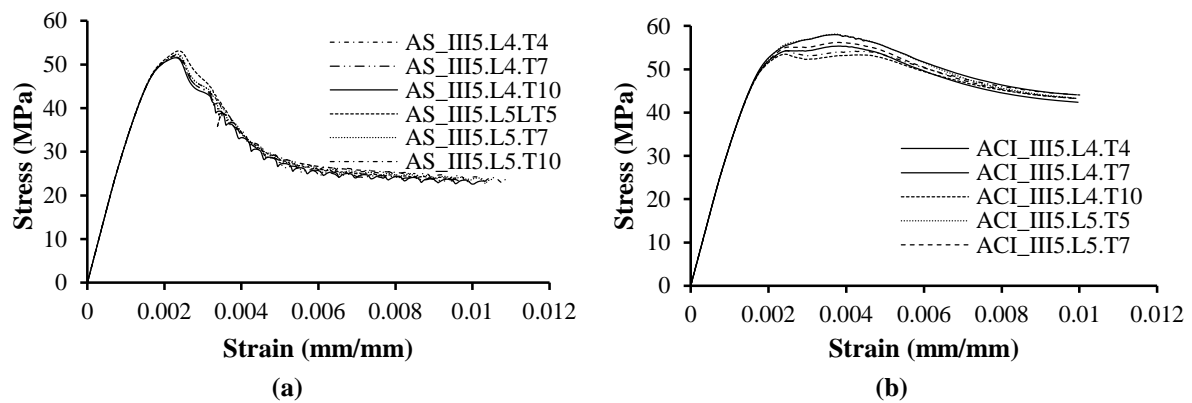


Fig. 12. Specimen stress-strain diagram Type III f_c 50 MPa: a) AS 3600:2017; b) ACI 318-19

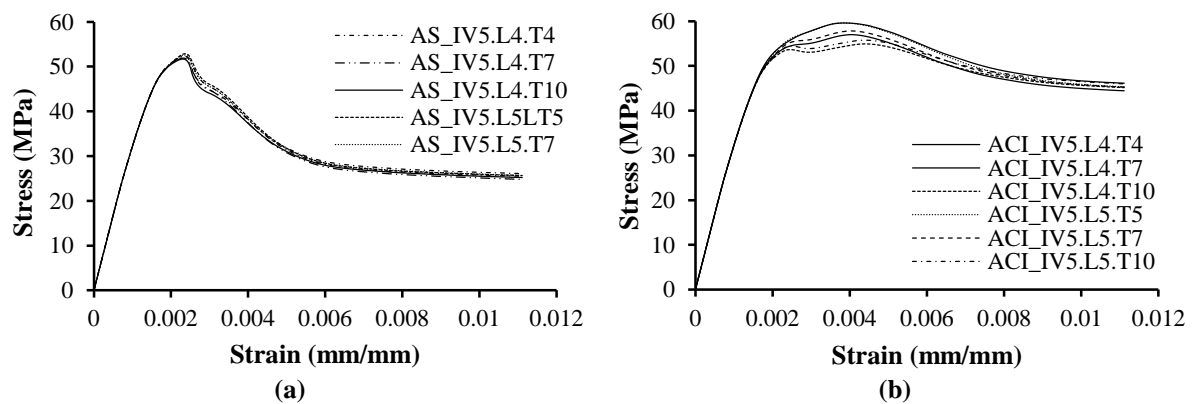


Fig. 13. Specimen stress-strain diagram Type IV f_c 50 MPa: a) AS 3600:2017; b) ACI 318-19

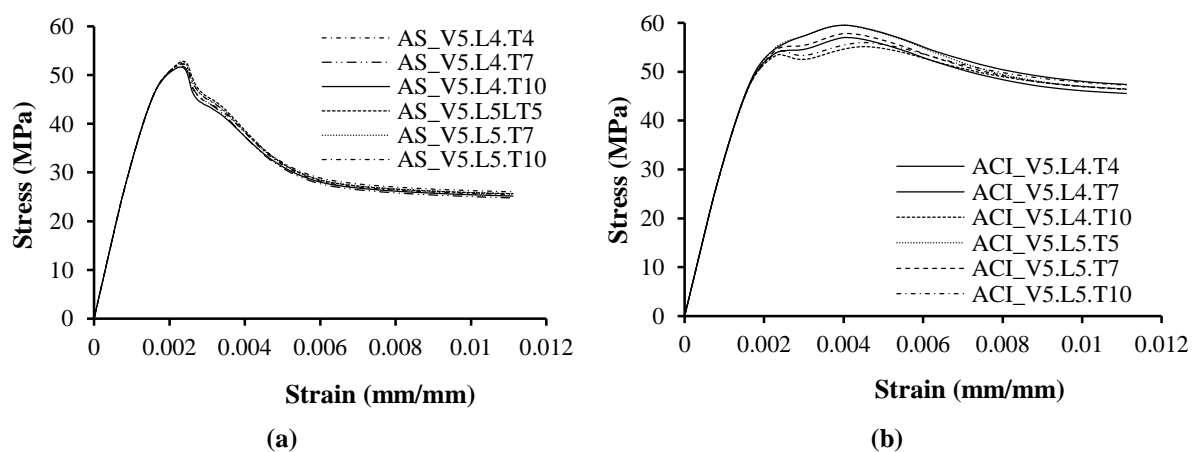


Fig. 14. Specimen stress-strain diagram Type V f_c 50 MPa: a) AS 3600:2017; and b) ACI 318-19

Figures 5 to 14 demonstrate that columns with the minimum reinforcement exhibit a similar strain-stress relationship within the same configuration type. The peak stress values for the test specimens are presented in Tables 6 and 7. Figure 15 demonstrates the influence of varying the yield stress of longitudinal reinforcement (f_y) and confinement reinforcement (f_{yt}) on the peak stress of column Type 1. Figure 15 illustrates that a column featuring 500 MPa longitudinal reinforcement exhibits a higher

peak stress compared to a column with 420 MPa longitudinal reinforcement. This distinction arises from the initial planning phase, where the diameter of the longitudinal reinforcement is kept constant within each configuration type. However, columns that employ longitudinal reinforcement with higher yield stresses will exhibit greater strength due to the amplified restraint effects resulting from varying yield stresses of the transverse reinforcement.

Table 6. Peak stress of RC column with constant A_{sh}/b_s ratio (ACI 318-19)

Column type	I	II	III	IV	V
X3.L4.T4	35.22	36.46	37.08	37.21	37.10
X3.L4.T7	34.47	34.77	35.35	35.41	35.29
X3.L4.T10	34.09	34.20	34.14	34.16	34.11
X3.L5.T5	35.73	36.87	37.43	37.55	37.39
X3.L5.T7	34.47	35.64	36.19	36.25	36.13
X3.L5.T10	34.77	34.92	34.87	34.89	34.83
X5.L4.T4	54.93	56.12	58.00	59.59	59.52
X5.L4.T7	54.10	54.28	55.35	56.99	57.01
X5.L4.T10	53.58	53.56	53.47	54.92	55.13
X5.L5.T5	56.57	56.25	58.12	59.63	59.53
X5.L5.T7	55.06	55.12	56.20	57.82	57.83
X5.L5.T10	54.38	54.39	54.27	55.75	55.96

Table 7. Peak stress of RC column with constant confining pressure (AS 3600:2017)

Column type	I	II	III	IV	V
X3.L4.T4	33.46	33.45	33.23	33.24	33.21
X3.L4.T7	33.20	33.18	32.97	32.98	32.96
X3.L4.T10	33.06	33.04	32.84	32.84	32.83
X3.L5.T5	33.91	33.88	33.67	33.68	33.65
X3.L5.T7	33.72	33.67	33.48	33.48	33.46
X3.L5.T10	33.53	33.51	33.31	33.32	33.31
X5.L4.T4	52.53	52.53	52.02	52.32	52.27
X5.L4.T7	52.11	52.10	51.69	51.89	51.86
X5.L4.T10	52.27	51.89	51.55	51.68	51.65
X5.L5.T5	53.12	53.11	53.12	52.88	52.83
X5.L5.T7	52.84	52.81	52.37	52.59	52.55
X5.L5.T10	51.89	52.57	52.21	52.36	52.32

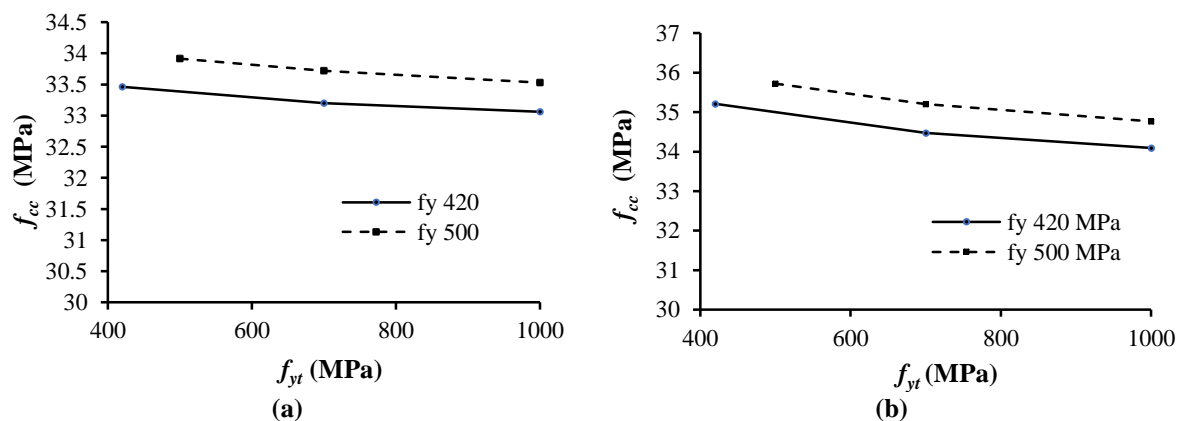


Fig. 15. Peak stress of column Type I with f_y and f_{yt} variation; a) AS 3600:2017; and b) ACI 318-19

The column's peak stress variation is influenced by the lateral stiffness, which depends on the stirrup reinforcement diameter. Stirrups with lower yield stresses have larger bar diameters, resulting in increased lateral stiffness. Eqs. (8) and (9) can be utilized for calculating the lateral stiffness of a restraint:

$$L_{atstiff} = \frac{E_s \cdot A_{b,fit}}{L_{tieleg}} \quad (8)$$

$$L_{tieleg} = n_{tieleg} \cdot \frac{1}{2} b_c \quad (9)$$

The lateral stiffness of the column can be observed in Table 8. The disparity in confinement pressure between columns designed according to AS 3600:2017 and

ACI 318-19 has a notable impact on the lateral stiffness. Columns designed under ACI 318-19 exhibit a lateral stiffness approximately six times greater than those designed under AS 3600:2017.

Consequently, columns designed per AS 3600:2017 experience a more rapid decline in stress after reaching the peak compared to columns designed according to ACI 318-19 standards. Following the previous explanation, Figure 16 illustrates the comparison of peak stress among columns with a compressive strength of 30 MPa (f'_c), longitudinal reinforcement yield stress (f_y) of 420 MPa, and the confinement yield stress (f_{yt}) of 420 MPa for each configuration.

Table 8. Lateral stiffness of specimen Type I, f'_c 30 MPa

	Lateral stiffness	
	AS	ACI
I3.L4.T4	11481,095	71005,917
I3.L4.T7	6888,657	42603,550
I3.L4.T10	4822,060	29822,485
I3.L5.T5	9644,119	59644,970
I3.L5.T7	6888,657	42603,550
I3.L5.T10	4822,060	29822,485

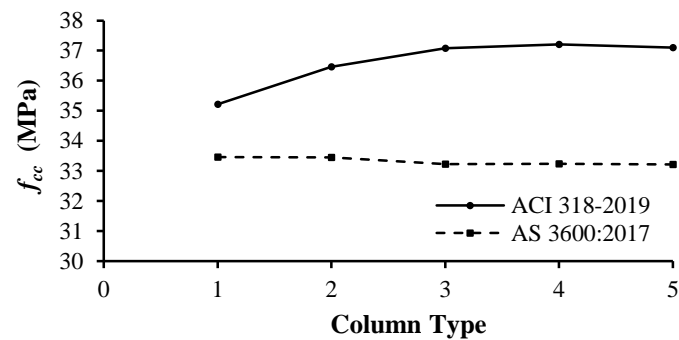


Fig. 16. Comparison of f_{cc} column with f'_c 30 MPa, f_y 420 MPa, and f_{yt} 420 MPa each configuration

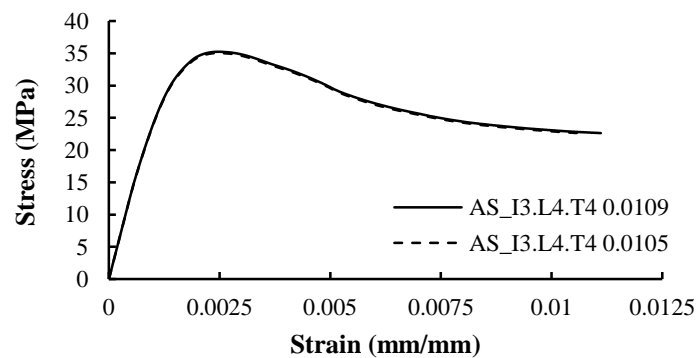


Fig. 17. AS_I3.L4.T4 column stress-strain comparison between 0.0109 and 0.0105 longitudinal reinforcement ratio

In Figure 16, columns Types I and II designed according to AS 3600:2017, show similar peak stresses due to their comparable reinforcement ratios. Similarly, columns III, IV, and V exhibit nearly identical peak stresses. Figure 17 illustrates the stress-strain relationship of the AS_I3.L4.T4 column, with a longitudinal reinforcement ratio of 0.0105, obtained from additional simulations for comparison.

Figure 17 compares the stress-strain relationship between two columns: AS_I3.L4.T4 with a longitudinal reinforcement ratio of 0.0109 and AS_I3.L4.T4 with a longitudinal reinforcement ratio of 0.0105. The results show that the ductility and ductility index are not significantly different. However, columns Types I and II can achieve peak stresses similar to columns Types III, IV, and V by adjusting the longitudinal reinforcement ratio. Table 10 displays the peak stresses of columns with f'_c 30 MPa, f_y 420 MPa, and f_{yt} 420 MPa for each configuration.

Additionally, Figure 18 compares the maximum f'_c 30 MPa of each configuration with a longitudinal reinforcement ratio of 0.0105. Columns designed according to ACI 318-19 exhibit distinct peak stress compared to those designed according to AS 3600:2017. This disparity can be attributed to the differences in the formulations used by AS 3600:2017 and ACI 318-19 to determine the requirements

for confinement reinforcement. The columns designed according to AS 3600:2017 comply $A_{b,fit}$ in Eq. (10) with the specified confinement requirements, where f_{reff} equal to $0.01 f'_c$ as indicated in Eqs. (4) to (7).

$$A_{b,fit} = \frac{0.01 f'_c d_s \cdot s}{k_e f_{sf}} \quad (10)$$

Meanwhile, columns designed according to ACI 318-19 adhere $A_{b,fit}$ in Eqs. (11) and (12) to the confinement reinforcement requirements specified in Eqs. (1) to (3) as below:

$$A_{b,fit} = \rho \cdot b \cdot s \quad (11)$$

$$A_{b,fit} = \rho \cdot b \cdot s = 0.3 \left(\frac{A_g}{A_{ch}} - 1 \right) \frac{f'_c}{f_{sf}} b \cdot s \quad (12)$$

The above equations demonstrate the contrasting approaches of the two codes. AS 3600:2017 incorporates the effective arrangement of longitudinal and transverse reinforcement, considering triaxle confinement. On the other hand, ACI 318-19 takes into account the ratio between the gross cross-sectional area and the core column's cross-sectional area when determining the need for confinement reinforcement. As a result, columns designed according to the transverse reinforcement requirements of AS 3600:2017 exhibit similar peak stresses.

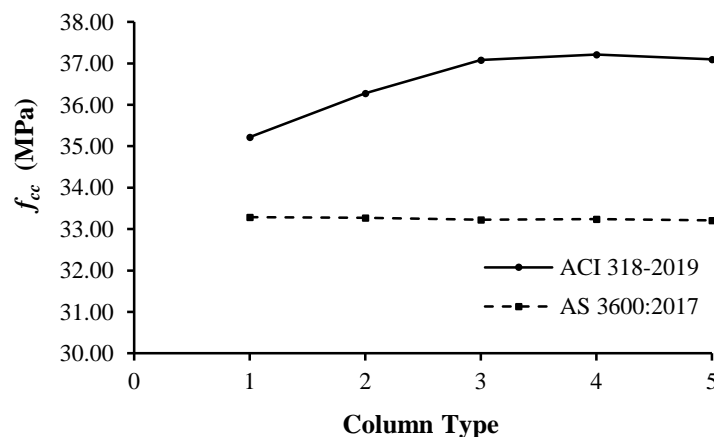


Fig. 18. Comparison of f_{ce} column with f'_c 30 MPa, f_y 420 MPa, and f_{yt} 420 MPa each configuration with longitudinal reinforcement 0.0105

In contrast, columns designed following the standards of ACI 318-19 show negligible variations in peak stress, which

are influenced by the core effective volume and configuration type, as depicted in Figure 19.

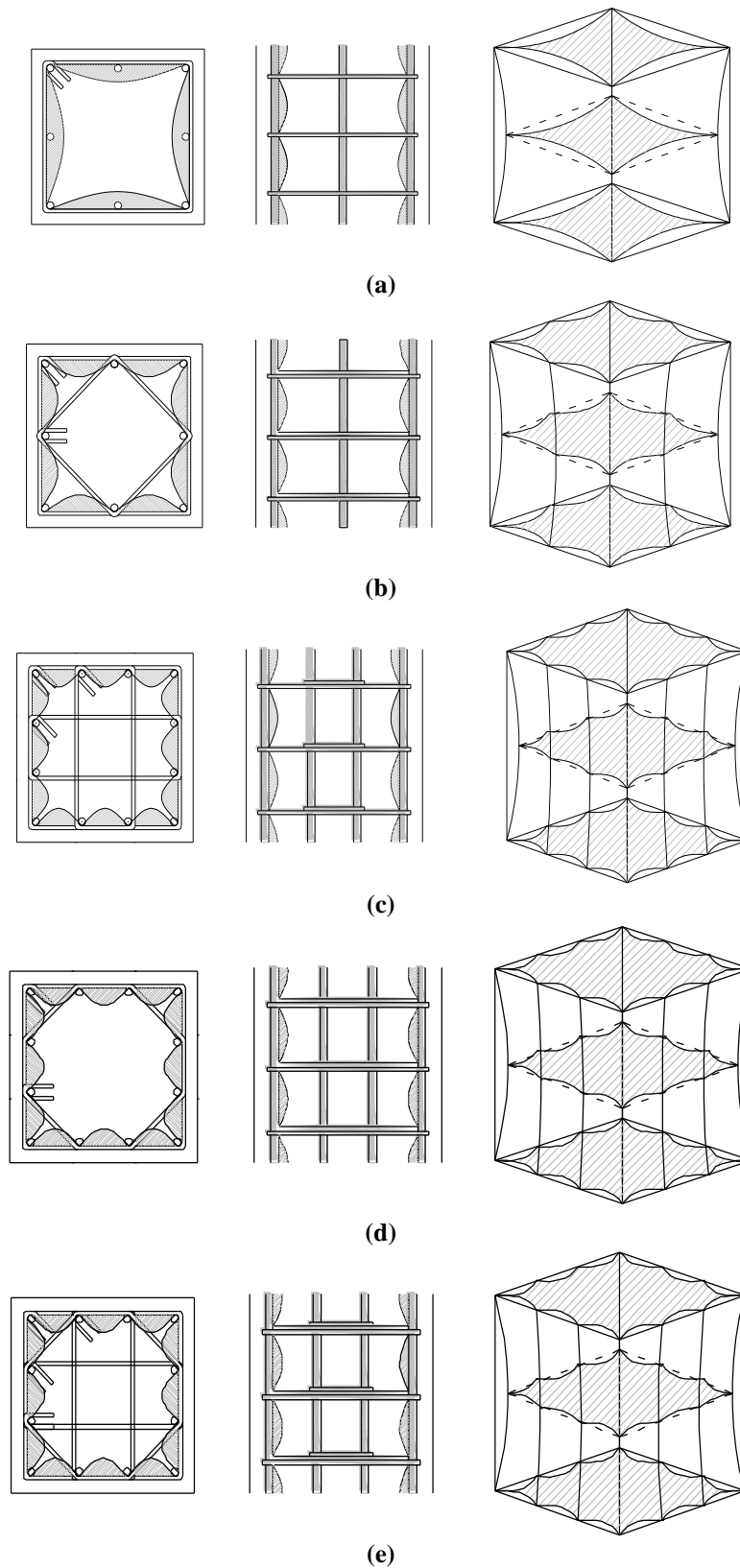


Fig. 19. Effect of stirrup configuration on the concrete confinement area: a) Type 1; b) Type 2; c) Type 3; d) Type 4; and e) Type 5

Figure 20 illustrates a comparison of the peak stress attainment for columns designed to comply with the minimum diameter specifications of ACI 318-19 and AS 3600:2017. Figure 20 reveals insights into the performance of reinforced concrete columns under varying design parameters.

Notably, columns featuring 500 MPa longitudinal reinforcement exhibit higher peak stresses compared to their 420 MPa counterparts, emphasizing the substantial influence of longitudinal reinforcement yield strength on overall column strength.

The lateral stiffness, determined by stirrup reinforcement diameter, proves to be a critical factor, with lower-yield-stress stirrups exhibiting larger bar diameters and increased lateral stiffness. Moreover, the observed disparities in confinement pressure between AS 3600:2017 and ACI

318-19-designed columns significantly impact lateral stiffness, leading to distinct stress distribution patterns. The nuanced variations in peak stress, particularly in columns designed per ACI 318-19, underscore the importance of understanding and optimizing column behavior based on specific code requirements and design objectives. Ductility is associated with the configuration of a structural system or member and its section behavior. The ductility of the test specimen column I3. L4. T4, designed according to the reinforcing requirements specified in the AS 3600:2017 standard, can be assessed using the graphical approach depicted in Figure 20. In Figure 21, the yield strain of the column is determined by drawing tangents from coordinates 0.0 and 0.75 to the peak stress value.

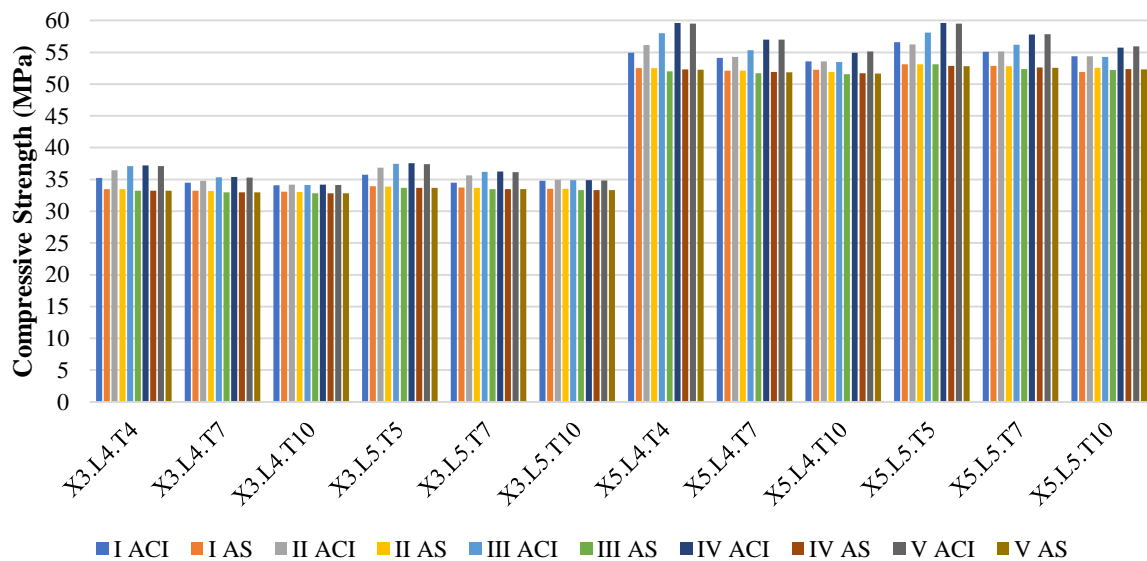


Fig. 20. Comparison of the peak stress attainment for columns designed to ACI 318-19 and AS 3600:2017

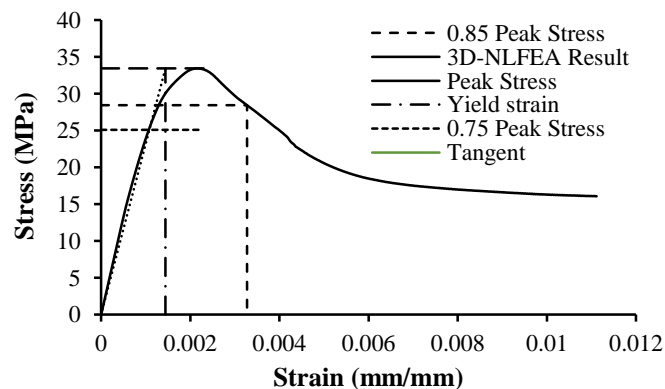


Fig. 21. Ductility calculation of column type I3.L4.T4 designed according to ACI 318-19

For column I3.L4.T4, the yield strain is obtained at the intersection of the tangent with the peak stress. Additionally, the concrete reaches its ultimate strain when the stress is reduced to 15% of the peak stress.

Therefore, the ductility can be calculated using Eq. (13) as follows.

$$\mu = \frac{\varepsilon_u}{\varepsilon_y} \quad (13)$$

By employing the same methods, Table 9 presents the ductility values of reinforced concrete columns (test specimens)

constructed with confinement reinforcement according to the provisions of AS 3600:2017. Table 9 demonstrates that columns meeting the minimum diameter requirements of AS 3600:2017 exhibit comparable ductility. This suggests that by adhering to the standard confining pressure specified in AS 3600:2017, the desired level of ductility can be achieved, even if the yield stress of the stirrup reinforcement exceeds the specified value. Table 10 presents the ductility of reinforced concrete columns designed according to ACI 318-19.

Table 9. Strain ductility of RC column with constant confining pressure (AS 3600:2017)

Column type	I	II	III	IV	V
X3.L4.T4	2.263	2.344	2.292	2.345	2.324
X3.L4.T7	2.291	2.356	2.327	2.340	2.306
X3.L4.T10	2.300	2.343	2.321	2.321	2.307
X3.L5.T5	2.288	2.341	2.329	2.329	2.321
X3.L5.T7	2.303	2.392	2.326	2.337	2.627
X3.L5.T10	2.324	2.378	2.357	2.394	2.648
X5.L4.T4	1.864	1.908	1.858	1.917	1.869
X5.L4.T7	1.856	1.863	1.838	1.875	1.815
X5.L4.T10	1.911	1.802	1.850	1.796	1.777
X5.L5.T5	1.837	1.846	1.840	1.875	1.842
X5.L5.T7	1.835	1.849	1.852	1.865	1.835
X5.L5.T10	1.820	1.794	1.831	1.789	1.789

Table 10. Strain ductility of RC column with constant A_{sh}/b_s (ACI 318-19)

Column type	I	II	III	IV	V
X3.L4.T4	3.257	4.500	4.727	4.639	5.181
X3.L4.T7	3.238	5.000	5.325	5.095	5.905
X3.L4.T10	3.264	5.695	7.095	7.071	10.000
X3.L5.T5	3.186	4.390	4.491	4.478	6.588
X3.L5.T7	3.222	4.936	5.156	5.156	6.463
X3.L5.T10	3.200	5.724	7.616	7.584	11.242
X5.L4.T4	2.388	3.279	3.497	3.564	3.861
X5.L4.T7	2.392	3.389	3.806	3.774	4.158
X5.L4.T10	2.312	3.457	4.466	4.788	5.698
X5.L5.T5	2.270	3.235	3.420	3.431	3.688
X5.L5.T7	2.363	3.306	3.739	3.782	4.145
X5.L5.T10	2.303	3.427	4.489	4.768	5.722

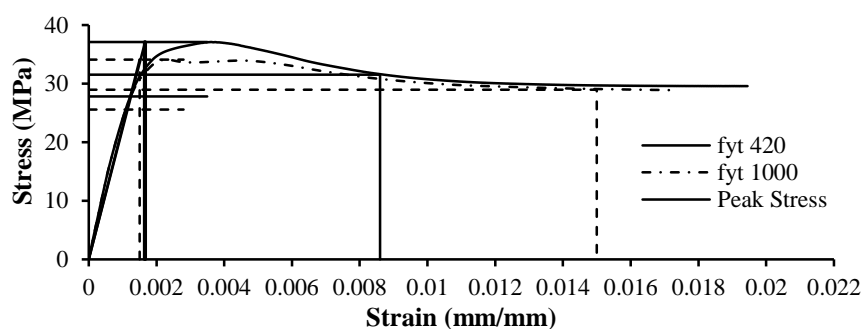


Fig. 22. Column ductility comparison (ACI 318-19) between f_{yt} 420 MPa and f_{yt} 1000 MPa column type V f_c 30 MPa

It reveals a range of strain ductility among columns constructed per the ACI 318-19 standards. This variation in ductility is further depicted in Figure 22. ACI 318-19 focuses only on the ratio between the column's gross cross-sectional area and its core area for confinement reinforcement. This results in minimal variations in peak stresses among columns designed according to this standard, primarily influenced by lateral stiffness.

The choice of confinement strength (f_{yt}) significantly impacts the ductility of column strain. Higher f_{yt} values, such as 1000 MPa, allow for greater strain of 0.85 f'_c compared to lower f_{yt} values like 420 MPa. Consequently, higher f_{yt} values lead to larger strain ductility, as the column can deform more before reaching its ultimate limit.

ε_y column with f_{yt} 420 MPa $>$ ε_y column with f_{yt} 1000 MPa

$\varepsilon_{0.85}$ columns with f_{yt} 420 MPa $<$ $\varepsilon_{0.85}$ columns with f_{yt} 1000 MPa

$\frac{\varepsilon_{0.85}}{\varepsilon_y}$ column with f_{yt} 1000 MPa

$>$ $\frac{\varepsilon_{0.85}}{\varepsilon_y}$ column with f_{yt} 420 MPa

μ column with f_{yt} 1000 MPa $>$ μ column with f_{yt} 420 MPa.

Based on this explanation, it can be concluded that columns designed according to ACI 318-19 standards, with minimum stirrup variations, exhibit varying levels of strain ductility, despite meeting the same reinforcement requirements. Figure 23 depicts a contrast in the achievement of strain ductility for columns designed in accordance with the minimum diameter requirements of ACI 318-19 and AS 3600:2017. The examination of Figure 23 provides crucial insights into the structural performance of reinforced concrete columns across diverse design standards.

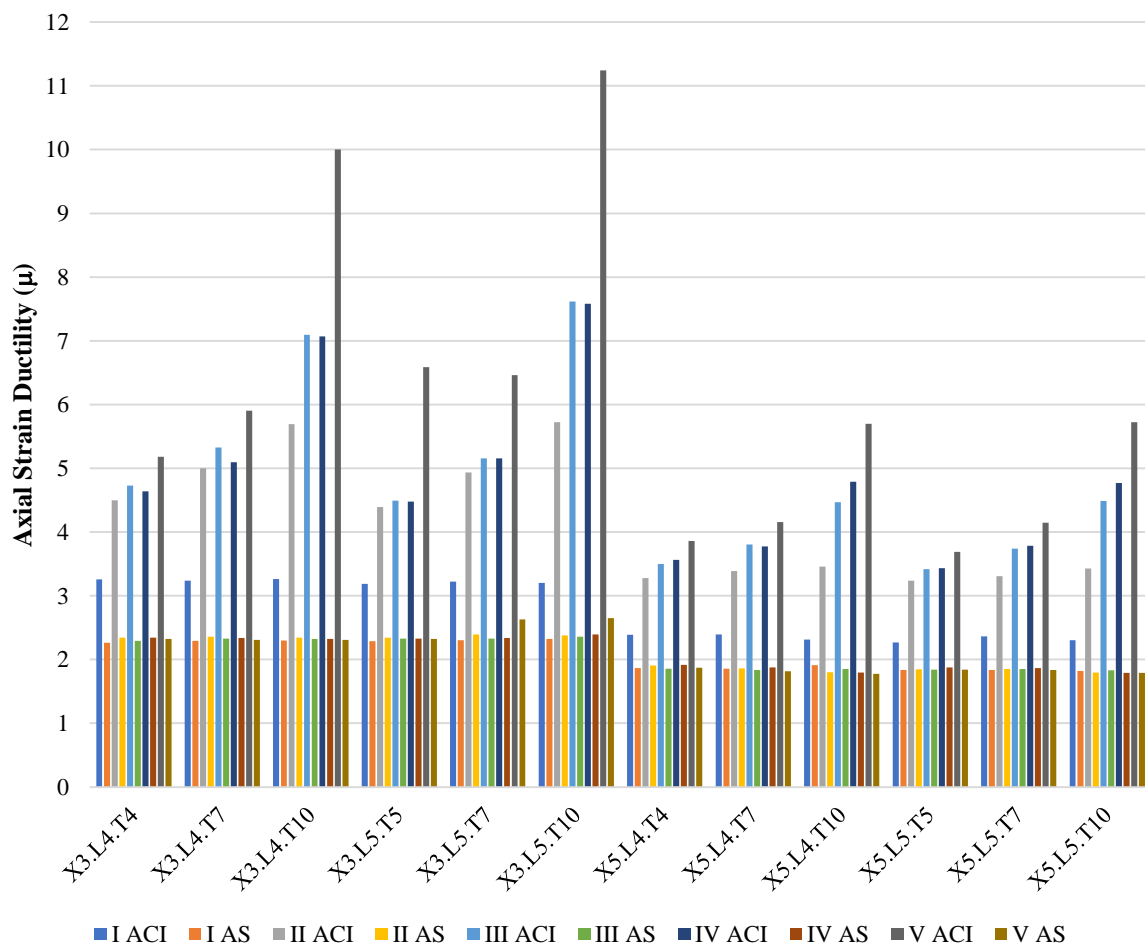


Fig. 23. Strain ductility for columns designed in ACI 318-19, and AS 3600:2017

Firstly, columns complying with AS 3600:2017's minimum diameter requirements exhibit consistent ductility, showcasing the reliability of the prescribed confining pressure. Secondly, ACI 318-19's emphasis on the gross-to-core area ratio influences peak stress uniformity, primarily dictated by lateral stiffness.

Additionally, the substantial impact of confinement strength (f_{yt}) on strain ductility is evident, highlighting the role of f_{yt} in enhancing deformation capacity. Lastly, variations in strain ductility among columns designed per ACI 318-19, despite minimal stirrup differences, suggest nuanced factors at play beyond mere reinforcement quantity. The ductility of a column in the potential plastic hinge region is typically characterized by an idealized trilinear force-deformation diagram, which comprises three regions: ascending, plateau, and softening. Ductility is commonly evaluated when the peak load decreases to 85% of its capacity. The ductility index (I_{10}) is derived from the energy area beneath the load-strain curve of the column. The ductility of the RC column is quantified using the I_{10} ductility index, which assesses the energy ratio. This energy is determined by calculating the area

under the curve of the axial load (P) versus nominal strain (ϵ). In the case of concentrically loaded RC columns, the nominal strain is equivalent to the axial strain. It is worth noting that the I_{10} ductility index has been employed by Samani et al. (2015) for evaluating the ductility of RC columns. The I_{10} considers the yield strain (ϵ_y) and 5.5 times the nominal yield strain ($5.5 \epsilon_y$) for calculation. It measures the ratio of the area under the curve from $5.5 \epsilon_y$ to ϵ_y . An I_{10} index of one represents an elastic-perfectly brittle material, while an I_{10} index of ten corresponds to an elastic-perfectly plastic model. Figure 24 provides a detailed explanation of the I_{10} measurement. The ductility index of specimen Column I3.L4.T4, designed according to the reinforcement requirements of AS 3600:2017, can be determined using the graphical method depicted in Figure 25.

The ductility index can then be calculated by evaluating the area under the curve, as expressed in Eq. (14).

$$I_{10} = \frac{\text{Area under curve to } 5.5\epsilon_y}{\text{Area under curve to } \epsilon_y} \quad (14)$$

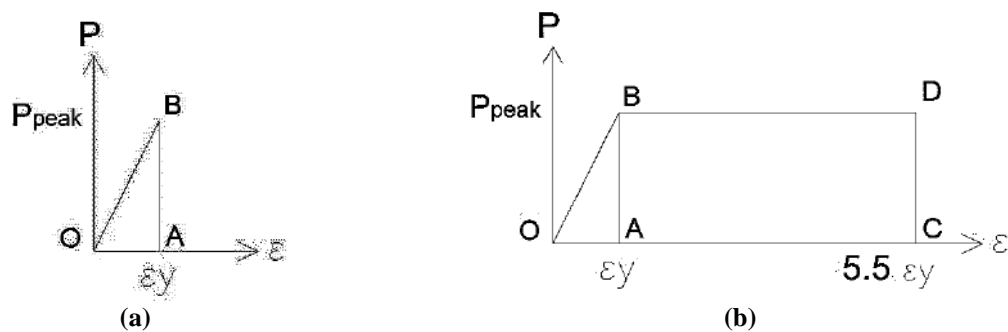


Fig. 24. I_{10} ductility index for: a) Elastic-perfectly brittle material; and b) Elastic-perfectly plastic material

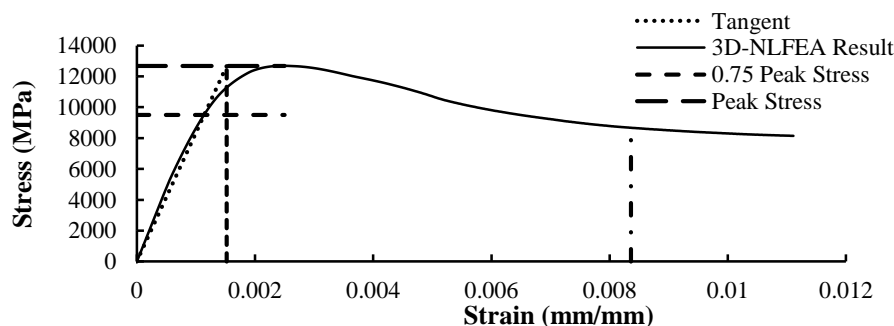


Fig. 25. Ductility index calculation of column type I3.L4.T4 designed according to AS 3600:2017

Table 11 presents the ductility index of reinforced concrete columns designed in accordance with AS 3600:2017 standards. It demonstrates that columns (test specimens) designed according to AS 3600:2017 confinement requirements, considering variations in configuration, longitudinal reinforcement yield strength, and transverse reinforcement yield strength, exhibit a consistent ductility index (I_{10}). This implies that by adjusting the confinement pressure requirements in accordance with AS 3600:2017 standards, the desired level of ductility can be achieved, even when the confinement yield strength exceeds the code-specified value of 1000 MPa.

Additionally, Table 12 presents the ductility index (I_{10}) of reinforced concrete columns designed according to ACI 318-19 using the same approach. Table 12 demonstrates a consistent ductility index for columns designed per ACI 318-19, regardless of variations in configuration and

yield strength of reinforcement. This suggests that achieving the desired ductility index in high-strength columns can be accomplished by maintaining uniform confinement strength across different yield stresses. Figure 26 illustrates a comparison of the ductility index achievement for columns designed to adhere to the minimum diameter specifications of ACI 318-19 and AS 3600:2017. The bar graph in Figure 26 provides compelling insights into the comparative performance of columns designed under AS 3600:2017 and ACI 318-19 standards. Columns conforming to AS 3600:2017 exhibit consistent ductility index across varied configurations and reinforcement yield strengths, emphasizing the reliability of achieving desired ductility through adjusted confinement pressure. Meanwhile, ACI 318-19-designed columns consistently maintain a uniform ductility index, underscoring the importance of a consistent confinement strength for desired performance in high-strength columns.

Table 11. I_{10} ductility index of RC column with constant confining pressure (AS 3600:2017)

Column type	I	II	III	IV	V
X3.L4.T4	7.1166529	7.4691619	7.3768913	7.47007	7.460995
X3.L4.T7	7.265861	7.4837516	7.456004	7.45562	7.651411
X3.L4.T10	7.2931671	7.5457574	7.4869508	7.511647	7.506907
X3.L5.T5	7.2415735	7.4414874	7.4056108	7.431082	7.344545
X3.L5.T7	7.3034621	7.5651303	7.4445493	7.433756	7.543412
X3.L5.T10	7.3762808	7.5687152	7.5060432	7.589289	7.545897
X5.L4.T4	6.389787	6.811318	6.492846	6.794314	6.747175
X5.L4.T7	6.324716	6.7644	6.461826	6.719558	6.712184
X5.L4.T10	6.761192	6.828948	6.947423	6.787364	6.787051
X5.L5.T5	6.354541	6.68235	6.361365	6.728676	6.607029
X5.L5.T7	6.355158	6.738293	6.437094	6.793737	6.787393
X5.L5.T10	6.360145	6.853521	6.551679	7.018206	6.929423

Table 12. I_{10} ductility index of RC column with constant A_{sh}/bs (ACI 318-19)

Column type	I	II	III	IV	V
X3.L4.T4	8.439448	9.050173	9.0815934	9.0401	8.699055963
X3.L4.T7	8.415725	9.129695	9.2423233	9.059597	9.1530027
X3.L4.T10	8.587081	9.22032	9.3908361	9.363342	9.396854283
X3.L5.T5	8.412246	8.928137	9.0272252	9.013962	8.006013257
X3.L5.T7	8.415967	9.103203	9.1636645	9.195624	9.818547776
X3.L5.T10	8.523426	9.217122	9.4667608	9.580538	9.422981565
X5.L4.T4	7.520316	8.659733	8.689585	8.70404	8.81442026
X5.L4.T7	7.611878	8.778546	8.940826	8.86798	8.637399957
X5.L4.T10	7.507538	8.713933	9.081247	9.201794	9.323091093
X5.L5.T5	7.534136	8.583219	8.670677	8.655809	8.763608863
X5.L5.T7	7.551625	8.698117	8.891821	8.859737	8.966636908
X5.L5.T10	7.591402	8.689093	9.280597	9.151548	9.127884141

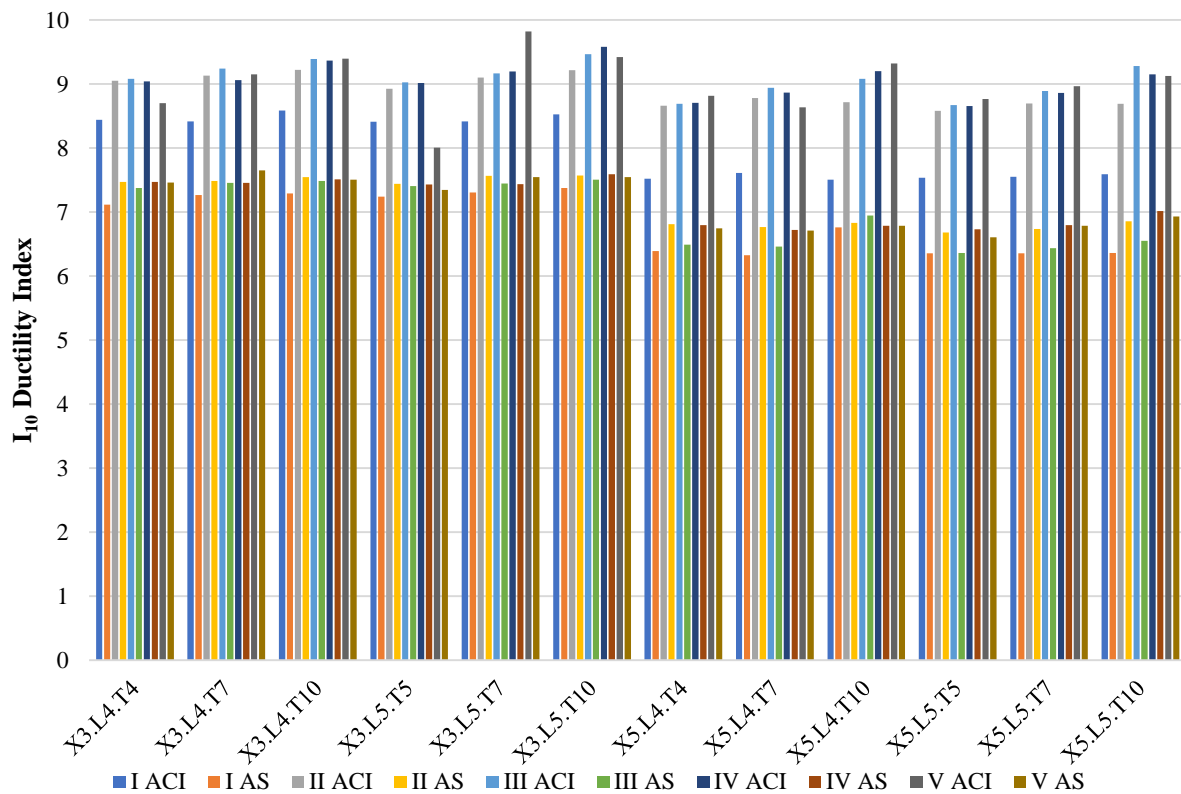


Fig. 26. Ductility index calculation of column type X3.L4.T4 designed according to AS 3600:2017

Multiple studies (such as Foster and Attard, 1997, 2001) have proposed a relationship between column ductility and the confinement parameter $k_e \rho_s f_{yt} / f'_c$ %. Foster and Attard (1997) established a regression Eq. (15) to predict the ductility index based on this parameter:

$$I_{10} = 1.9 \ln (1000 k_e \rho_s f_{yt} / f'_c) \quad (15)$$

Figure 27a shows the correlation between confinement parameters and I_{10} values of examined columns, while Figure 27b displays the percentage of errors in the attard and stunge model.

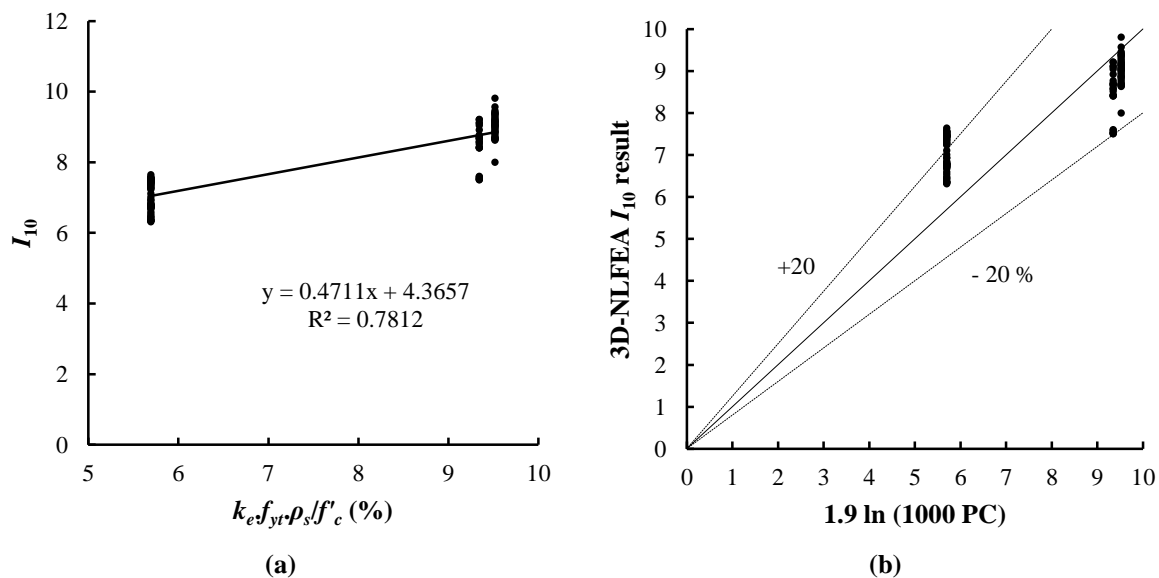


Fig. 27. a) Correlation between confinement parameters and I_{10} values from 3D-NLFEA; and b) Comparison of I_{10} results: 3D-NLFEA vs. constitutive model

In this test, the specimens are subjected to the same confinement pressure, resulting in similar confinement parameters for specimens with the same value. However, the test results reveal a range of ductility indices due to the influence of longitudinal and confinement reinforcement yield stresses. To approach the ductility index results of the column specimens, new confinement parameters have been proposed. These parameters are represented by Eq. (16).

$$\text{Proposed Confinement Parameter (PC)} = k_e \rho_s \frac{f_y f_{yt}}{(f_c)^2} \quad (16)$$

Figure 28 illustrates the relationship between the proposed confinement parameter and the achieved ductility index of the test specimens. Eq. (17) presents the proposed confinement parameters for predicting the I_{10} .

$$\text{Proposed } I_{10} = 0.9 \ln \left(k_e \rho_s \frac{f_y f_{yt}}{(f_c)^2} \right) + 4.17 \quad (17)$$

4. Conclusions

This study extensively investigated axially loaded square-reinforced concrete columns comprising normal-strength concrete and

high-strength confinement rebar's with diverse configurations. The study findings are summarized as follows:

- Columns designed according to AS 3600:2017 standards consistently demonstrated a mean strain ductility range of 1.78 to 1.92, indicating relatively minor variation under identical minimum confining pressure.
- In contrast, columns designed per ACI 318-19 standards exhibited a wider range of strain ductility, ranging from 2.27 to 11.24, despite comparable Ash values.
- This finding indicates that the utilization of high-strength steel confining rebar's (exceeding 800 MPa) in columns adhering to minimum confinement requirements resulted in a mean ductility index of 7.93, ensuring the columns' safe and reliable performance.
- Additionally, the proposed predictive model for the column's ductility index demonstrated an average deviation of 3.53%, underscoring its accuracy and reliability in ductility estimation. These quantified results offer insights into the variations in strain ductility, shedding light on the nuanced impacts of different design standards and reinforcement configurations on the ductility and performance of reinforced concrete columns.

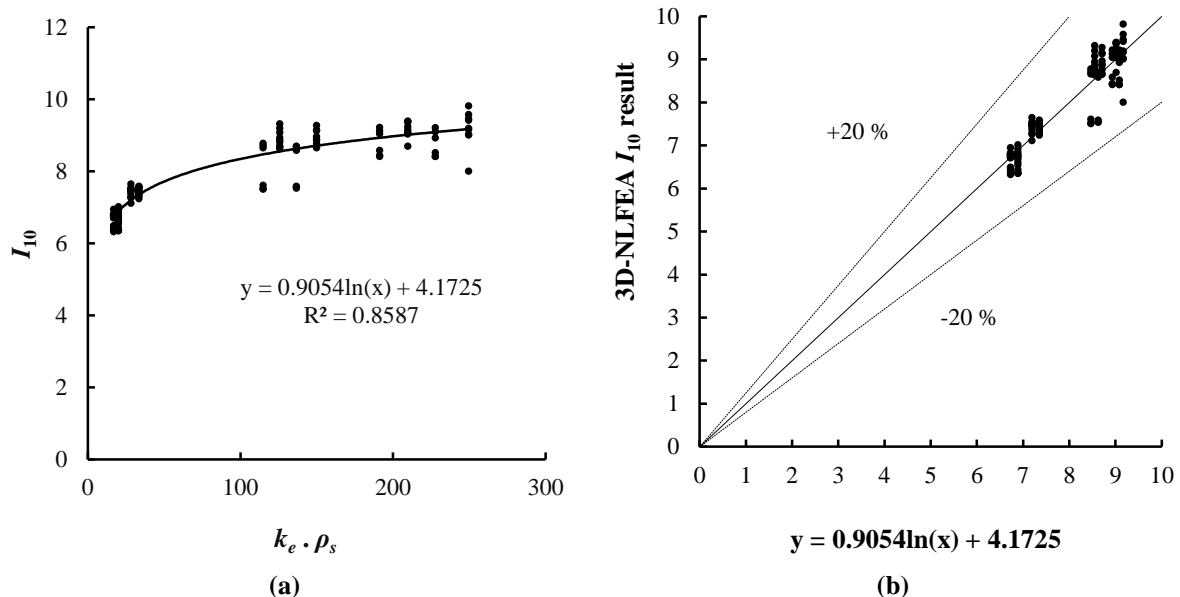


Fig. 28. a) Relationship between confinement parameters with 3D-NLFEA I_{10} result; and b) Comparison of test specimen ductility index with proposed confinement parameters

However, several key considerations emerged during the study, which must be addressed:

- An increase in the yield stress of steel bars may lead to a reduction in ductility, which warrants attention in future research and design considerations. Additionally, the primary purpose of using transverse bars in RC columns is to enhance ductility rather than strength, aligning with the fundamental objectives of reinforced concrete design.
- While the study provides valuable insights, it's important to exercise caution in asserting that its results can directly influence or alter existing building code regulations. Emphasis is placed on the research aiming to inform rather than dictate regulatory changes. The practical implications of utilizing high-strength steel bars, including potential increases in construction costs and implications for the strong column-weak beam condition, suggest the need for further research and careful evaluation in real-world applications.
- Finally, the basic assumption underlying valid building codes regarding plastic hinge formation in moment frames during strong earthquakes highlights the importance of considering seismic design principles in structural engineering practice.

If in moment frames, the ductility demand of the column exceeds that of the beam, the formation of the plastic moment is prioritized in columns. This can lead to the unwanted phenomenon of a weak column-strong beam during earthquakes.

- Additionally, the use of high-strength rebar's has two major drawbacks: an increase in construction costs and potential shortages when supplying the construction materials. These issues can result in difficulties in executing the project. Despite the valuable insights provided by this research, it's important to recognize that its results alone cannot alter established regulations of accredited building codes.

This paper serves as a technical note rather than a means to change regulations.

In conclusion, this research enriches understanding regarding the impact of high-strength reinforcement on the ductility of normal-strength reinforced concrete columns, providing valuable insights that can guide future research efforts and inform engineering decision-making processes.

5. Acknowledgments

My gratitude to Mr. Saifuddin and Mrs. Heni for providing the funds to complete this research.

6. References

- ACI 318. (2019). Building code requirements for structural concrete (ACI 318-19) commentary on building code requirements for structural concrete (ACI 318R-19) *Reported by ACI Committee* 318. https://www.concrete.org/Portals/0/Files/PDF/Previews/318-19_preview.pdf.
- Alavi-Dehkordi, S.M. and Mostofinejad, D. (2018). "Behavior of concrete columns reinforced with high-strength steel rebar's under eccentric loading", *Materials and Structures*, 51(6), 145, <https://doi.org/10.1617/s11527-018-1271-3>.
- AS:3600. (2017). "Concrete structures (draft for public comment Australian standard)", Standards Australia Ltd., <https://www.mbawa.com/wp-content/uploads/2017/07/DR-AS-3700-2017-Masonry-structures.pdf>.
- Cai, Z.K., Wang, Z. and Yang, T.Y. (2018). "Experimental testing and modeling of precast segmental bridge columns with hybrid normal- and high-strength steel rebar's", *Construction and Building Materials*, 166, 945-955, <https://doi.org/10.1016/j.conbuildmat.2018.01.159>.
- Ding, H., Liu, Y., Han, C. and Guo, Y. (2017). "Seismic performance of high-strength short concrete column with high-strength stirrups constraints", *Transactions of Tianjin University*, 23, 360-69, <https://doi.org/10.1007/s12209-017-0059-9>.
- Foster, S.J. and Attard, M.M. (1997). "Experimental test on eccentrically load high strength concrete columns", *Structural Journal*, 94(3), 295-303,
- Foster, S.J. and Attard, M.M. (2001). "Strength and ductility of fiber-reinforced high-strength concrete columns", *Journal of Structural Engineering*, 127(1January), 28-34, [http://doi.org/10.1061/\(ASCE\)0733-9445\(2001\)127:1\(28\)](http://doi.org/10.1061/(ASCE)0733-9445(2001)127:1(28)).
- Hung, C.C. and Chueh, C.Y. (2016). "Cyclic

- behavior of uhpfrc flexural members reinforced with high-strength steel rebar”, *Engineering Structures*, 122, 108-120, <http://doi.org/10.1016/j.engstruct.2016.05.008>.
- Kamaruddin, K.S., Imran, I., Derry Imansyah, M., Riyansyah, M. and Ariyanto, A. (2018). “Application of high strength reinforcing bars in earthquake-resistant structure elements”, *The 4th International Conference on Rehabilitation and Maintenance in Civil Engineering*, 02015, 1-10, <https://doi.org/10.1051/mateconf/201819502015>.
- Kim, M.J., Lee, B.S., Kim, D.H., Han, S.P. and Kim, K.H. (2021). “Effect of configuration and yield strength of transverse reinforcement on lateral confinement of RC columns”, *Applied Sciences*, 11(15), 6696, <https://doi.org/10.3390/app11156696>.
- Moehle, J.P., Hooper, J.D., Kelly, D.J. and Meyer, T.R. (2010). *NEHRP seismic design technical brief seismic design of cast-in-place concrete diaphragms, chords and collectors: A guide for practicing engineers*, (NIST GCR 10-917-4), National Institute of Standards and Technology, US Department of Commerce, <https://www.nehrp.gov/pdf/nistgcr10-917-4.pdf>.
- Ou, Y.C. and Kurniawan D.P. (2015). “Shear behavior of reinforced concrete columns with high-strength steel and concrete”, *ACI Structural Journal*, 112(1), 35-46, https://www.academia.edu/101663107/shear_behavior_of_reinforced_concrete_columns_with_high_strengthsteelandconcrete.
- Piscesa, B., Attard, M.M., Prasetya, D. and Samani, A.K. (2019). “Modeling cover spalling behavior in high strength reinforced concrete columns using a plasticity-fracture model”, *Engineering Structures*, 196, 109336, <https://doi.org/10.1016/j.engstruct.2019.109336>.
- Piscesa, B., Attard, M.M. and Samani, A.K. (2018). “3D finite element modeling of circular reinforced concrete columns confined with frp using a plasticity based formulation”, *Composite Structures*, 194, 478-493, <https://doi.org/10.1016/j.compstruct.2018.04.039>.
- Samani, A.K., Attard, M.M. and Foster, S.J. (2015). “Ductility in concentrically loaded reinforced concrete columns”, *Australian Journal of Structural Engineering*, 16(3), 237-250, <https://doi.org/10.1080/13287982.2015.1092688>.
- Seliem, H.M., Hosny, A., Rizkalla, S., Zia, P., Briggs, M., Miller, S., Darwin, D., Browning, J., Glass, G.M., Hoyt, K. and Donnelly, K. (2009). “Bond characteristics of ASTM A1035 steel reinforcing bars”, *ACI Structural Journal*, 106(4), 530-539.
- Silpa, G. and Sreevalli, I.Y. (2021). “A review on progressive collapse of reinforced concrete flat slab structures”, *Civil Engineering Infrastructures Journal*, 54(1), 181-194, <https://doi.org/10.22059/cej.2020.291570.1624>.
- Ulfa, A.A., Piscesa, B., Attard, M.M., Faimun, F. and Aji, P. (2020). “Parametric studies on the ductility of axial loaded square reinforced concrete column made of normal-strength concrete and high-strength steel confining rebar with various ties configuration”, *E3S Web of Conferences*, 156, 03002, EDP Sciences, 2020, <https://doi.org/10.1051/e3sconf/202015603002>.
- Wang, P., Shi, Q., Wang, F. and Wang, Q. (2020). “Seismic behaviour of concrete columns with high-strength stirrups”, *Earthquake and Structures*, 18(1), 15-25, <https://doi.org/10.12989/eas.2020.18.1.015>.



This article is an open-access article distributed under the terms and conditions of the Creative Commons Attribution (CC-BY) license.



Date Palm Fibers to Improve Tensile Strength in Self-Compacting Concrete with Silica Fume

Mirzaie Aliabadi, M.^{1*} , Derakhshan Nezhad, A.H.² , Shahidzadeh, M.S.¹ and Dadpour, A.³

¹ Assistant Professor, Department of Civil Engineering, Faculty of Engineering, Behbahan Khatam Alanbia University of Technology, Behbahan, Iran.

² M.Sc. Student, Department of Civil Engineering, Faculty of Engineering, Behbahan Khatam Alanbia University of Technology, Behbahan, Iran.

³ M.Sc., Laboratory Expert, Department of Civil Engineering, Faculty of Engineering, Behbahan Khatam Alanbia University of Technology, Behbahan, Iran.

© University of Tehran 2024

Received: 3 Dec. 2023;

Revised: 26 May 2024;

Accepted: 23 Jun. 2024

ABSTRACT: Today, the use of new additives in self-compacting concrete leads to the improvement of its mechanical properties. Palm groves are one of the vegetation covers of Behbahan city in Iran, which cover a large area of land in this region. In this research, due to the abundance of palm groves in the south of Iran, the idea of using date palm fibers in the self-compacting concrete mixing plan has been proposed. The fibers were cut into 3 cm lengths and used in self-compacting concrete as a natural, cheap, and readily available admixture. In this research, palm fibers were used to make self-compacting concrete to improve the mechanical properties of this concrete with percentages of 0%, 0.5%, 1%, 1.5%, and 2% weight of cement. The results of the tests showed that the tensile strength of self-compacting concrete with and without date palm fibers with percentages of 0.5%, 1%, 1.5%, and 2% by weight of cement in 7 and 28 days of processing were 16.37%, 34.27%, 56.39%, 82.24% and 13.56%, 27.61%, 46.96%, and 67.6% tensile strength increased compared to the self-compacting concrete sample without date fibers. The compressive strength of self-compacting concrete with and without date palm fibers with 0.5%, 1%, 1.5%, and 2% by weight of cement in 7 and 28 days of processing are 5.19%, 10.87%, 17.81%, 22.60%, and 4.11%, 9.51%, 15.48%, 22.47% respectively of the compressive strength decreased compared to the self-compacting concrete sample without date fibers.

Keywords: Self-Compacting Concrete, Date Palm Fibers, Compressive Strength, Tensile Strength.

1. Introduction

Self-compacting concrete is an important material in the construction industry (Abani et al., 2018), which consists of fine and coarse aggregates (Alatshan et al., 2017), cement, additives, and water (Al-Hadithi et

al., 2023). Self-compacting concrete is widely used in the construction industry due to its advantages, such as the availability of materials, smoothness, and efficiency (Askar et al., 2023; Ahmad et al., 2021a). The importance of self-compacting concrete is due to its high durability (Ayub

* Corresponding author E-mail: mirzaie@bkatu.ac.ir

et al., 2021), low cost in implementation compared to ordinary concrete (Asmaa and Khashaa, 2022), its efficiency and resistance (Abdullah and Sivakumar, 2023). One of the important characteristics of self-compacting concrete is its viscosity and stability compared to other types of concrete (Bozorgmehr Nia and Adlparvar, 2022).

This concrete is widely recommended in the construction of safe and durable structures that can withstand various loads (Bhat et al., 2023; Ahmad et al., 2021b). In addition, self-compacting concrete can be considered a cost-effective material to reduce costs in implementation, such as time and vibration due to compaction under its own weight (Dounia et al., 2023). This type of concrete flows easily in the mold, easily passes through the rebars (Djoudi et al., 2012), and under natural conditions (Ramli and Dawood, 2010), it condenses under the effect of its own weight. This concrete has a very high efficiency (Akhmetov et al., 2022). The use of fibers in concrete started four decades ago (Eskandari et al., 2021), and has continued to expand in order to improve the properties and mechanical behavior of concrete (Falahtabar Shiade and Tavakoli, 2018).

Fibers in concrete reduce the brittleness of concrete and ensure its plasticity (Fokam et al., 2020). Fibers may be vegetable (Ghobadi et al., 2019), synthetic, or metallic (IRIB News Agency, 2020). It improves the mechanical properties of concrete under compressive, tensile, bending, and shear loads (Jawad et al., 2021a), as well as resistance to erosion, creep, shrinkage, freezing, wear, and erosion, and creates a unified material (Ahmad et al., 2021). Using waste in concrete mix is one of the effective ways to reduce waste materials (Wang et al., 2022). In addition, the use of waste materials as a substitute for part of cement in concrete mix design is an effective solution to solve environmental problems (Modarres and Ghalehnovi, 2023). One of the natural fibers used in concrete is palm fiber (Mirabi Moghadam

2021). Considering that there are more than 45 thousand hectares of palm groves in Khuzestan province. Of this amount, there are more than 2 thousand hectares of palm groves in Behbahan city (Sor et al., 2022). So easy and cheap access to date palm fibers is possible in this region (Ramhormozy et al., 2023; Tawfeeq and Ganesh, 2022).

Various studies have been conducted in relation to the use of palm fibers to improve the properties of concrete, some of which have been reviewed below: Falahtabar Shiade and Tavakoli (2018) investigated the estimation of mechanical properties and durability of self-compacting concrete with fibers using ultrasonic pulse speed.

Boutarfa et al. (2018) studied cement mortar reinforced with plant fibers alpha, date, and dis on the mechanical properties of concrete in the field of construction. Abani et al. (2018) evaluated the flexural properties and tensile strength of concrete reinforced with palm fibers in the desert climate. Fokam et al. (2020) investigated cement mortar reinforced with natural fibers and palm kernel in a study of mechanical properties. Mirabi Moghadam (2021) evaluated the effect of the shape and amount of date palm sis fibers on the compressive and tensile strength of concrete. Modarres and Ghalehnovi (2023) investigated the effect of recycled steel fibers from waste tires on concrete properties.

One of the most important elements in the production of science is to consider the approach of sustainable development. Sustainable development with the concept of using existing potential and facilities and taking into account the needs of future generation, in line with the optimal use of available natural resources, is important (Alatshan et al., 2017; Abani et al., 2018). Many studies have been done on the possibility of using plant waste in concrete to strengthen tensile and compressive strength. Natural fibers are one of the existing solutions that can be used as a substitute for common fibers in cement and concrete mortar (Hosseini Bar et al., 2017;

Ghobadi et al., 2019).

The innovative aspect of this project is the optimal use of waste resources and the minimization of waste and environmental pollution. Cement has tensile properties, but its tensile strength is very low compared to fibers. In order to reduce the amount of cement consumption in concrete and increase the tensile strength of concrete in the mixing design, palm fibers were used according to the weight of cement and silica fume, and Viscosity Modifying Admixtures (VMA) to increase the strength and strengthen the transfer zone of concrete in this mixing design. The difference between this research and other studies is the use of micro silica gel and VMA, which is an innovative aspect of this project. In this article, the mechanical behavior and compressive and tensile strength of self-compacting concrete with palm fibers in the Behbahan region are investigated considering the weather conditions.

2. Laboratory Program

2.1. Materials

2.1.1. Cement

In all 5 mixed designs, Portland cement Type 5 of Behbahan cement factory was used based on ASTM C150 (2012). The specifications are shown in Tables 1 and 2.

2.1.2. Date Palm Fibers

Date palm fibers are obtained by separating the two parts. First, the palm fiber should be separated from the main trunk of the palm (Figure 1). Then the fiber should be cut, and the broken fibers should be created with a suitable length of 3 cm as a natural, cheap, and accessible additive. It can be used in different weights in self-compacting concrete (Figure 2). According to Table 3, the specifications of date fibers have been determined for the mixed design (Figure 3). The values mentioned in Table 3 may be different depending on the type of palm fibers of each region and the test conditions used.

Table 1. Type 5 Portland cement specifications

Symbol	IR	SiO ₂	Al ₂ O ₃	Fe ₂ O ₃	CaO	MgO	SO ₃
(%)	0.18	21.38	4.40	5.40	64.64	2.28	0.50
Symbol	O ₂ Na	K ₂ O	LOI	C ₃ S	C ₂ S	C ₃ A	C ₄ AF
(%)	0.26	0.77	0.19	61.12	15.23	2.52	16.42

Table 2. Mechanical characteristics of Type 5 Portland cement

Standard levels	Blaine's elegance (cm ² /g) BF	Initial setup time (minutes) IST	Final setup time (minutes) FST
Standard	3350	155	260
Standard levels	3-day compressive strength (kg/cm ²)	7-day compressive strength (kg/cm ²)	28-day compressive strength (kg/cm ²)
Standard	224	288	422



Fig. 1. Behbahan date palm

However, in general, palm fibers have good thermal insulation properties, and due to their low thermal conductivity, they can have different applications for temperature regulation and prevention of heat loss in concrete. The elemental composition of date palm fibers was investigated by Scanning Electron Microscope (SEM) analysis, which indicates the presence of

silicon dioxide in their composition.

This element is effective in the mechanical properties of self-compacting concrete (Figure 4). According to the tensile test results of date palm fibers, male palm fibers have the highest tensile strength compared to female date palm fibers, and male date palm fibers were used for this project.

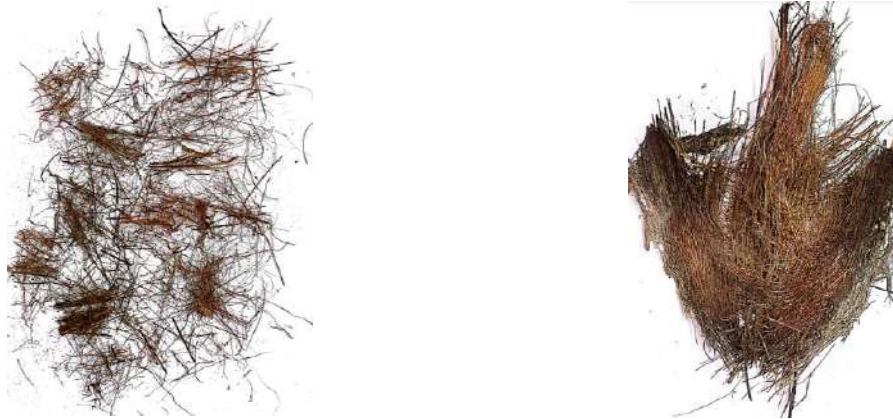


Fig. 2. Palm fiber components

Table 3. Characteristics of date palm fibers (Falahtabar Shiade and Tavakoli, 2018; Mirabi Moghadam, 2021; ASTM C496, 2002)

Characteristics	Fiber diameter (mm)	Maximum tensile strength (MPa)	Modulus of elasticity (MPa)	Special Weight (gr/cm ³)	Extension (24 hours)	Cross-section increase (24 hours)
Amount of	0.50	70.59	780.60	0.80	10.19%	1.94%
Characteristics	Water absorption (24 hr)	Thermal conductivity coefficient (W/m.K)	Thermal conductivity (W/m.K)	Specific heat capacity (Kj/k)	Thermal emission rate (mm ² /s)	Natural humidity percentage
Amount of	162%	0.045%	0.060	1.26	0.83	1.96



Fig. 3. Tensile test of date fibers with Bongshin device to determine tensile strength

2.1.3. Aggregates

In this mixed design, coarse aggregate with a maximum size of 19 mm and sand with a maximum size of 4.75 mm were used. The sand used in this design was mixed from Ramhormoz, Khuzestan. Gravel (peas, almonds) and sand were granulated using a suitable sieve. For pea sand passed through a 8/3 sieve, almond sand passed through a 1/2 sieve, and sand passed through a 8 sieve were used, which conforms to ASTM C33 (2003) (Table 4 and Figure 5).

2.1.4. Superplasticizer and Silica Fume

In order to achieve the mechanical properties of self-compacting concrete,

super plast PC 5000, which is made based on polycarboxylate, was used as a type of water-reducing and reinforcing concrete. Also, to achieve rheological properties in the pasty state and to improve the quality of self-compacting concrete, silica fume was used, which is based on silica fume and is a strong reducer of concrete water. The use of silica fume increases the compressive strength, reduces the permeability of concrete, and eases concreting by increasing concrete slump and high efficiency. Also, silica fume can strengthen the transition zone and affect the final strength of concrete. It is in accordance with ASTM C494 (2002) (Table 5).

Element	Weight%	Atomic%
C K	49.81	57.67
O K	47.48	41.27
Si K	0.76	0.38
Ca K	1.95	0.68
Totals	100.00	

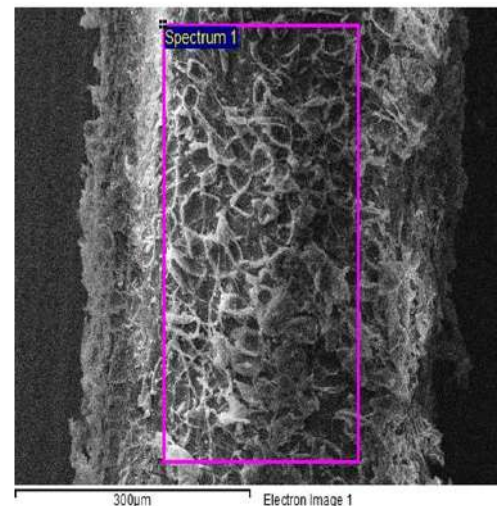


Fig. 4. Scanning Electron Microscope (SEM) analysis of date palm fibers

Table 4. Characteristics of aggregates

Characteristics	Sand water absorption percentage	Water absorption percentage of pea sand	Water absorption percentage of almond sand
(%)	2.2	0.80	0.90



Fig. 5. Washed sand and graded gravel (pea- and almond-sized aggregates)

2.1.5. Water

The water used in the self-compacting concrete mix design was potable. It was used to produce and process the samples, which conforms to the requirements of ASTM C94 (2009) (Table 6).

2.1.6. Limestone Powder

One of the necessary materials to ensure proper viscosity in self-compacting concrete is stone powder. Due to the presence of very fine particles, fillers such as stone powder fill the voids and voids between the cement and aggregate particles and therefore reduce the porosity and increase the bulkiness of concrete. This category of filler elements, due to having a very high specific surface area, increases the friction between grains and increases the viscosity of concrete. Therefore, the use of super-lubricants in order to increase the fluidity of concrete in the construction of such concrete is inevitable. The results of chemical analysis and physical characteristics of cement and limestone powder are shown in Table 7. In this design,

Qom limestone powder was used.

2.1.7. VMA (Solidifier and Controller of Concrete Rheology)

VMA powder additive is developed to produce self-compacting concrete with increased viscosity and controlled rheological properties. VMA plays a significant role in controlling excess water in concrete. In this research, the master matrix VMA 358 additive was used based on heavy polymer molecular strands with extraordinary stability. The amount of this material in the concrete mix plan is calculated in relation to the percentage of cement. When all the ingredients were mixed in the mixer. At the last moment, when the concrete is formed, the mixer is turned off for a few seconds, and the concrete is allowed to rest. A certain amount of VMA is spread on the concrete so that the excess water in the concrete is controlled through VMA, and the concrete becomes fluid and more efficient, which is in accordance with the ASTM C494/C494 M (2002) (Figure 6).

Table 5. Technical specifications of superplasticizer and silica fume

Characteristics	Physical condition	Specific gravity (kg/liter)	PH	Color	Special weight (kg/m ³)
Super plast PC5000 superplasticizer					
General	Liquid	1.1	6.2	Yellow	1.008
Silica fume					
General	Thick liquid	1.35	9	Gray	320

Table 6. Characteristics of drinking water

Characteristics	Temperature (°C)	PH	Chloride ion concentration
amount of	20	6	50

Table 7. Qom limestone powder

Characteristics	SiO ₂	Al ₂ O ₃	Fe ₂ O ₃	MgO	CaO	SO ₃	LOI
(%)	2.8	0.35	0.50	1.8	51.22	1.24	43.2



Fig. 6. VMA (solidifier and controller of concrete rheology)

2.2. Mixed Design

5 mixing plans of self-compacting concrete with date palm fibers were investigated in this research. The percentage of date palm fibers is in different ratios (0%, 0.5%, 1%, 1.5%, 2% weight of cement). In all 5 mixed designs, the amount of materials is constant, and the percentage of date palm fibers is variable (Table 8).

2.3. Doing Experiment

To achieve the right mixing plan, first, different combinations of benefits such as; cement, sand, gravel (peas, almonds), water, superplasticizer, micro silica, rock powder, date palm fibers and VMA were mixed in a mixer in suitable and uniform environmental conditions, and as a result, self-compacting concrete with and without date palm fibers was produced. For the benefits mixture, the mixer was used for 8 min to prepare self-compacting concrete with and without fibers. The order of pouring benefits in the mixer is as follows: First, gravel (peas and almonds) and sand ASTM C33 (2003) were added in the mixer for 1 min, then stone powder and date palm fibers were added to the mixture for 3 min and mixed in the mixer. In the next step cement ASTM C150 (2012), water ASTM C94 (2009), superplasticizer, micro silica ASTM C494 (2002) and VMA ASTM C494/C494M (2002) were added in the mixer and were mixed for 4 min to produce a self-compacting concrete. After mixing the mentioned materials in the mixer, the slump flow test (ASTM C1611, 2009), v-

funnel test (INSO 3203-9, 2013), l-box test (INSO 3203-10, 2013), and j-ring test (INSO 11271, 2014) are necessary for the properties of fresh-self-compacting concrete with and without palm fibers.

2.3.1. Slump Flow Test

The slump flow test is very common to determine the efficiency of self-compacting concrete due to its simplicity. The slump flow test was based on the ASTM C1611 (2009).

2.3.2. V-Funnel Test

The v-funnel test was performed to measure the ability of self-compacting concrete to change the flow direction and pass through the reinforced and bound sections, without separating the grains and blocking the flow. V-funnel tests were in accordance with the INSO 3203-9 (2013).

2.3.3. L-Box Test

The purpose of the L-Box test is to check the fluidity, the strength of the concrete passing between the rebar, the stability against the separation of the grains, and the filling ability. The L-Box test was in accordance with the INSO 3203-10 (2013).

2.3.4. J-Ring Test

The J-Ring test actually simulates the passage of concrete through rebar and is used to check the ability to pass. The J-Ring test was in accordance with the INSO 11271 (2014).

Table 8. Mixing design of self-compacting concrete with and without date palm fibers (Kg/m³)

Superplasticizer	Palm fibers	Self-compacting concrete without date palm fibers (0%)							Cement
		VMA	Stone powder	Silica fume	Water	Sand	Almond sand	Pea sand	
10	-	0.160	160	5	135	1240	150	300	400
			Self-compacting concrete with palm fibers (0.5%)						
10	2	0.160	160	5	135	1240	150	300	400
			Self-compacting concrete with palm fibers (1%)						
10	4	0.160	160	5	135	1240	150	300	400
			Self-compacting concrete with palm fibers (1.5%)						
10	6	0.160	160	5	135	1240	150	300	400
			Self-compacting concrete with palm fibers (2%)						
10	8	0.160	160	5	135	1240	150	300	400

2.4. Molding of Concrete Samples

Fresh self-compacting concrete was poured into cubic molds with dimensions of $150 \times 150 \times 150$ mm and cylindrical molds with dimensions of 150×300 mm and molded. They were kept at a temperature of 25°C for 24 hr to harden, and after 24 hr, the samples were taken out of the molds and kept in a water tank for curing for 7 and 28 days. A total of 300 self-compacting concrete samples were made with and without date palm fibers. Of these, 150 specimens were made in a cube mold, and 150 specimens were made in a cylindrical mold. After the 5 mix designs reached the ages of 7 and 28 days, the compressive strength test of cubic specimens was performed according to the ISIRI 3206 (2003), and the tensile strength test of cylindrical specimens was performed according to the ASTM C496 (2002). A concrete breaker jack was used to break the concrete samples. Finally, after the failure test of the concrete samples, the results of the samples were compared and analyzed with self-compacting concrete without fibers.

3. Testing the Compressive Strength of Cubic Specimens

The results of compressive strength tests of

concretes based on the ages of 7 and 28 days, with cubic dimensions of $150 \times 150 \times 150$ mm on cubic test pieces according to the ISIRI 3206 (2003) showed that by adding date palm fibers to self-compacting concrete, the compressive strength decreases (Figure 7).

4. Testing the Tensile Strength of Cylindrical Samples

The tensile strength of concretes based on the ages of 7 and 28 days, with cylindrical dimensions of 150×300 mm was investigated. The results of tests on cylindrical specimens based on the ASTM C496 (2002) showed that the tensile strength increases with the addition of date palm fibers to self-compacting concrete (Figure 8).

5. Results and Interpretation

5.1. Slump Flow Test

The results of the slump flow test showed that with the increase in the percentage of date palm fibers in the self-compacting concrete, the slump diameter decreased, and the time also increased, which indicates a decrease in concrete flow. This issue was in accordance with the ASTM C1611 (2009).



Fig. 7. The failure of the cube specimen with the compressive strength device, and the specimen broken with palm fibers

5.2. V-Funnel Test

The results of the V-Funnel test showed that with the increase in the percentage of date palm fibers, the test time increased, which indicates that the concrete becomes harder and its flow decreases with the increase in the percentage of date palm fibers, which is in accordance with the INSO 3203-9 (2013).

5.3. L-Box Test

The results of the L-Box test showed that with the increase in the percentage of date palm fibers, the test time increased and

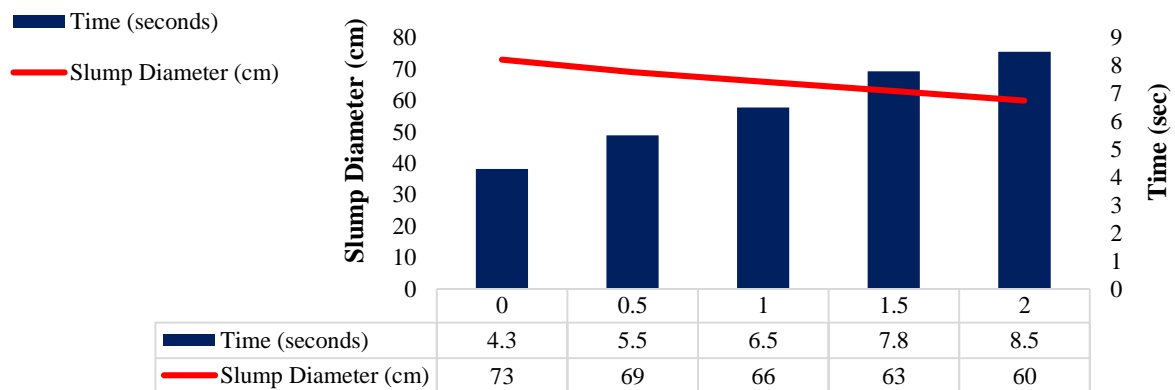
the height of the edge of the box to the vertical surface and the height of the edge of the box to the horizontal surface decreased, which is in accordance with the INSO 3203-10 (2013).

5.4. J-Ring Test

The results of the J-Ring test showed that with the increase in the percentage of date palm fibers, the test time increased and the diameter of the slump decreased, which is in accordance with the INSO 11271 (2014).

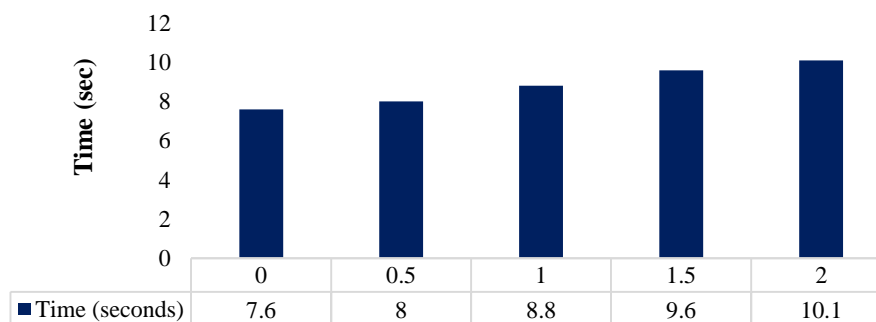


Fig. 8. Failure of the cylindrical test piece with the Brazilian device and the test piece broken with palm fibers



Self-Compacting Concrete with and without Palm Fibers

Fig. 9. Slump flow test results



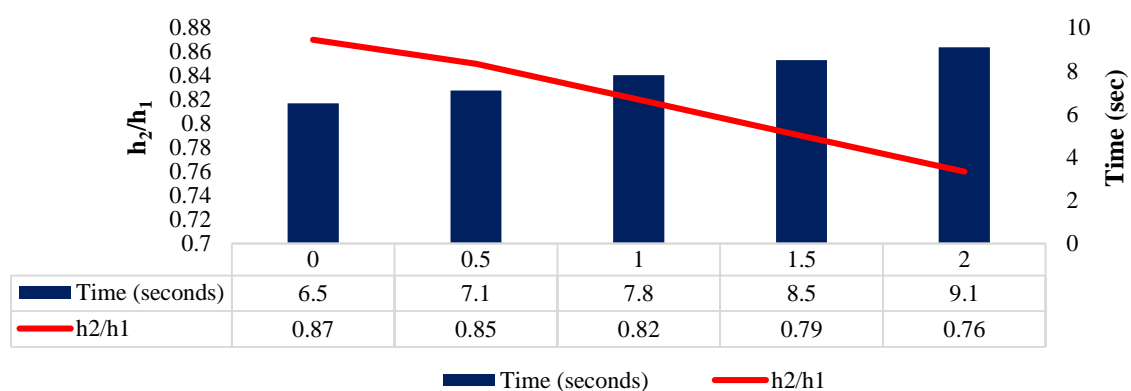
Self-Compacting Concrete with and without Palm Fibers

Fig. 10. V-funnel test results



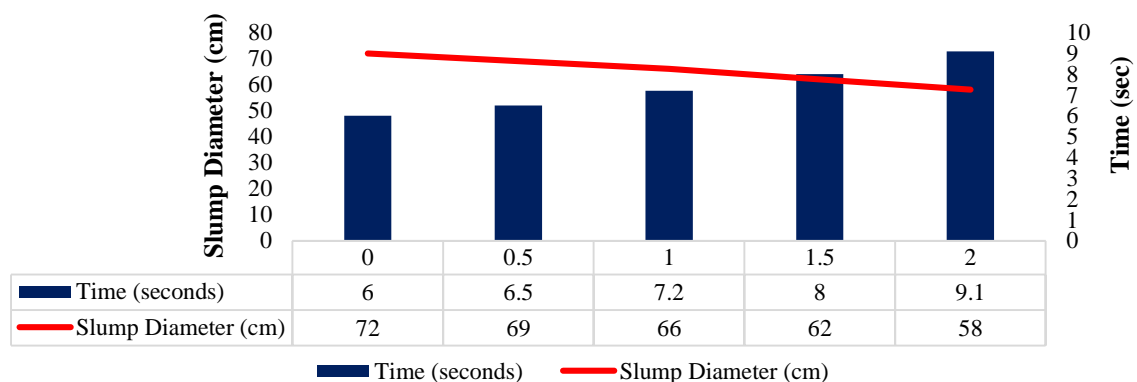
Self-Compacting Concrete with and without Palm Fibers

Fig. 11. Results of the 5-min v-funnel test



Self-Compacting Concrete with and without Palm Fibers

Fig. 12. L-Box test results



Self-Compacting Concrete with and without Palm Fibers

Fig. 13. J-Ring test results

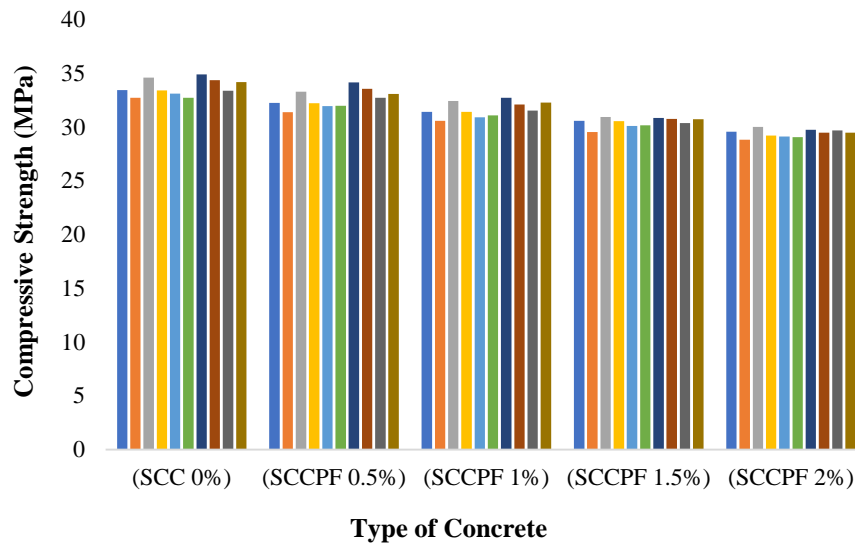
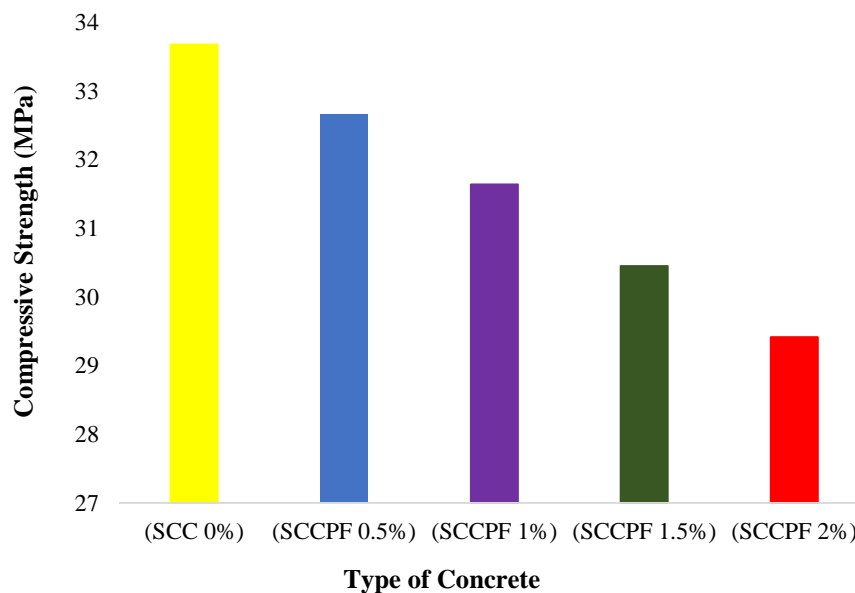
5.5. Testing the Compressive Strength of Cubic Specimens

The reason for the decrease in compressive strength in self-compacting concrete for cubic samples is due to the negative effect of the empty space created in self-compacting concrete due to the amount, shape, and dispersion of fibers in

concrete. Also, increasing the percentage of date palm fibers causes a decrease in porosity due to the addition of fibers and as a result, it causes a decrease in adhesion between cement and aggregates, a decrease in adhesion in the concrete transition area, and a lack of cohesion for sufficient concrete durability.

Table 9. Recorded results of compressive strength test data for cubic samples (MPa)

No	1	2	3	4	5
Type of concrete	(SCC 0%)	(SCCPF 0.5%)	(SCCPF 1%)	(SCCPF 1.5%)	(SCCPF 2%)
Compressive strength test results in 7-day curing for cubic samples (MPa)					
Data range	32.71 - 34.8	31.37 - 34.15	30.57 - 32.72	29.52 - 30.10	28.82 - 30
Average	33.67	32.65	31.63	30.44	29.41
Variance	0.5432	0.6590	0.4490	0.1647	0.1160
Standard deviation	0.737	0.8118	0.6701	0.458	0.3406
Coefficient of variation	0.0218	0.0248	0.0211	0.015	0.0115
Compressive strength test results in 28-day curing for cubic samples (MPa)					
Data range	40.04 - 41.58	38.28 - 39.81	37.37 - 38.80	35.87 - 37.31	34.72 - 35.98
Average	40.75	39.12	38.19	36.76	35.49
Variance	0.3034	0.2671	0.1929	0.2278	0.1852
Standard deviation	0.5522	0.5168	0.4392	0.4773	0.4303
Coefficient of variation	0.0135	0.0132	0.0114	0.0129	0.0121

**Fig. 14.** 7-day compressive strength results of cubic samples**Fig. 15.** Results of the 7-day average compressive strength of cubic samples

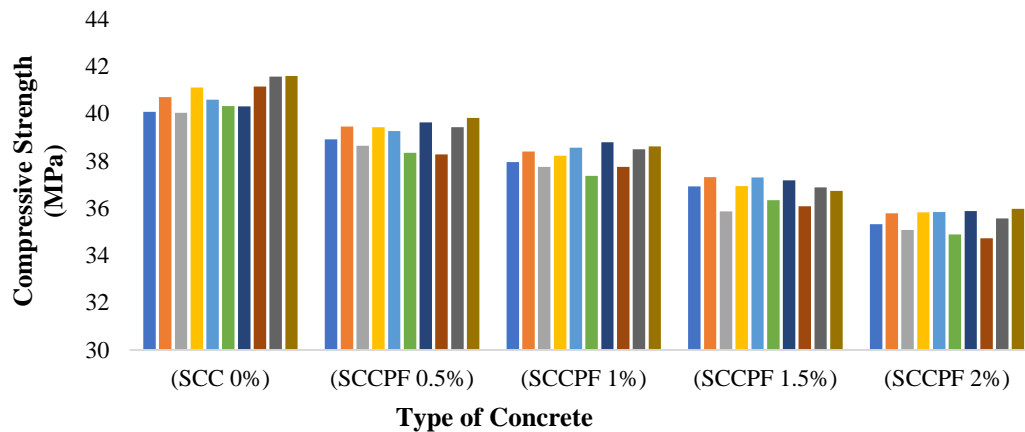


Fig. 16. 28-day compressive strength results of cubic samples

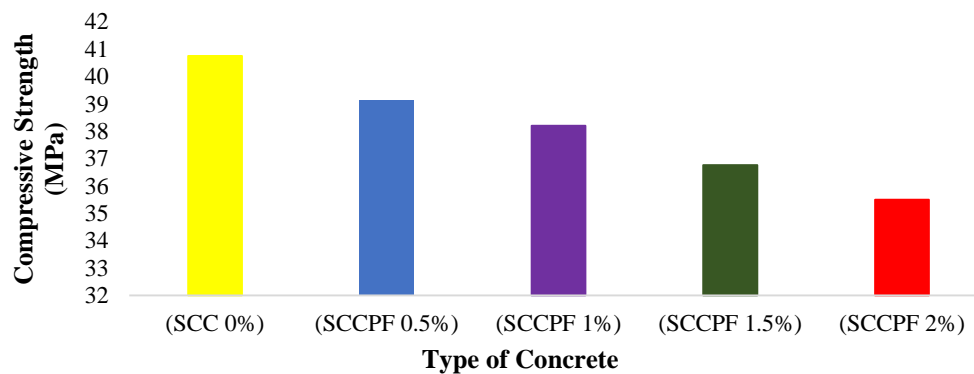


Fig. 17. Results of the 28-day average compressive strength of cubic samples

5.6. Testing the Tensile Strength of Cylindrical Samples

The reason for the increase in the tensile strength test of self-compacting concrete for cylindrical specimens is due to the positive effect of the unique characteristic of fibers with regard to the tensile strength and modulus of elasticity of date palm fibers in self-compacting concrete due to the quantity and size. According to the background of the research in Mirabi Moghadam (2021), with an increase of 2% of date palm fibers in concrete, the tensile

strength increased. According to the results of this research, with an increase of 2% of date palm fibers in self-compacting concrete, the tensile strength increased. In the research of Falahtabar Shiade and Tavakoli (2018), the compressive strength decreased with an increase of 2% of date palm fibers in concrete. According to the results of this research, the compressive strength decreased with an increase of 2% of date palm fibers in self-compacting concrete.

Table 10. Recorded results of tensile strength test data for cylindrical samples (MPa)

No	1	2	3	4	5
Type of concrete	(SCC 0%)	(SCCPF 0.5%)	(SCCPF 1%)	(SCCPF 1.5%)	(SCCPF 2%)
Tensile strength test results in 7-day curing for cylindrical samples (MPa)					
Data range	12.10 – 12.9	14.30 -14.96	16.20 – 17.05	19.30 - 19.80	22.50 – 23.10
Average	12.525	14.61	16.748	19.6	22.831
Variance	0.0494	0.04194	0.05203	0.02346	0.02470
standard deviation	0.222	0.204	0.2281	0.1531	0.1571
Coefficient of variation	0.017	0.0140	0.0136	0.0078	0.0068
Tensile strength test results in 28-day curing for cylindrical samples (MPa)					
Data range	14.2 – 15.1	16.23 – 17.2	18.5 – 19.2	21.3 – 22.63	24.1 – 24.96
Average	14.671	16.587	18.769	21.677	24.731
Variance	0.0875	0.0650	0.0466	0.1232	0.0578
standard deviation	0.2958	0.255	0.216	0.3511	0.2404
Coefficient of variation	0.0201	0.0153	0.0115	0.0161	0.0097

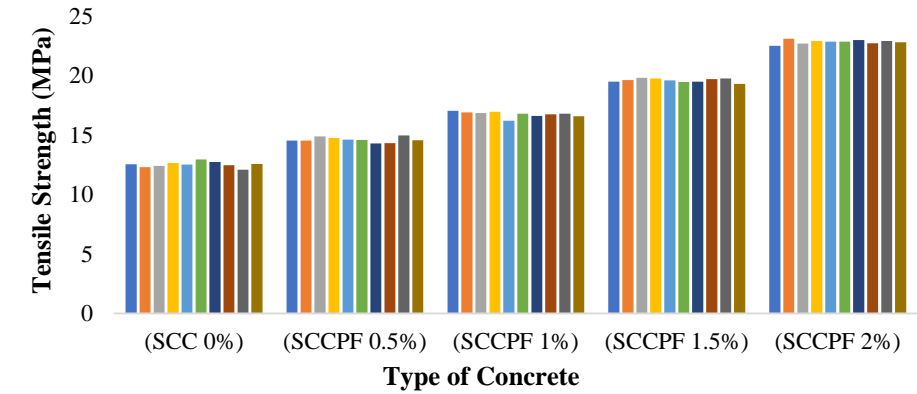


Fig. 18. 7-day splitting tensile strength of cylindrical specimens

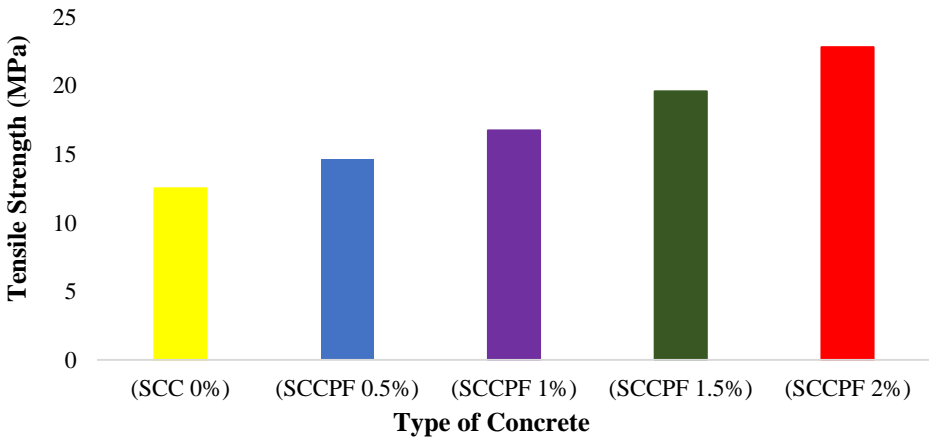


Fig. 19. Results of the 7-day splitting tensile strength of cylindrical specimens

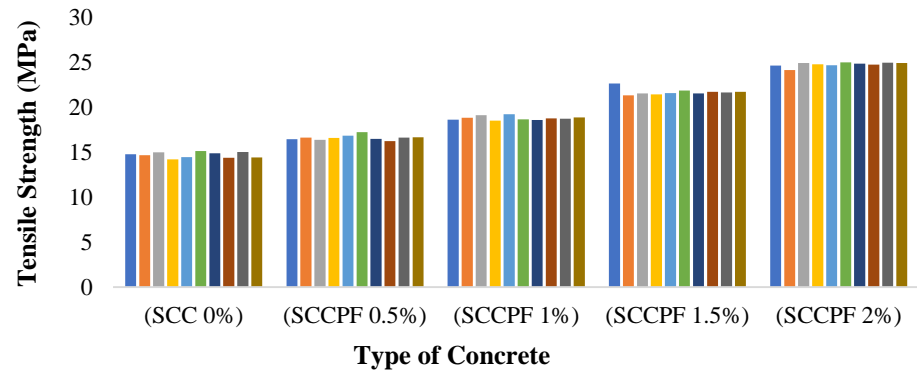


Fig. 20. 28-day splitting tensile strength of cylindrical specimens

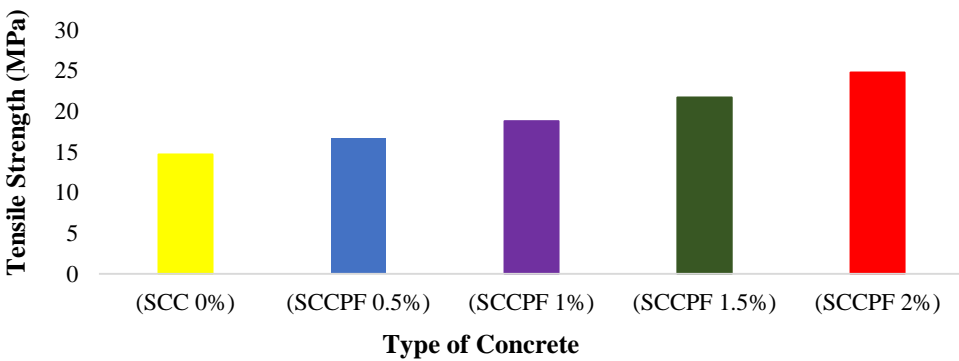


Fig. 21. Results of the 28-day splitting tensile strength of cylindrical specimens

By increasing the bearing capacity of concrete, palm fiber significantly improves tensile strength. This improvement is mainly due to the uniform distribution of stress in the concrete by the fibers. These fibers create bridges within the concrete that prevent the growth and expansion of cracks under loading. Date palm fibers in self-compacting concrete reduce fractures caused by tensile stresses. These fibers can absorb and distribute tensile stresses, which increases the resistance of concrete against bending and tensile loads.

Due to their natural structure and flexibility, date palm fibers help to improve the rheological properties of self-compacting concrete. Date palm fibers can play an important role in improving the resistance of concrete against thawing and thawing cycles. By reducing the permeability of concrete, these fibers prevent the entry of water and the formation of cracks caused by freezing and melting.

Palm fibers can increase the resistance of concrete against chemical attacks and corrosion. Due to its natural properties and special chemical composition, these fibers prevent the penetration of corrosive substances into the concrete. Date palm fibers in self-compacting concrete can significantly improve mechanical, rheological, and durability properties. By increasing tensile strength, improving rheological properties, reducing cracking, increasing resistance to environmental conditions, and having positive effects on microscopic and macroscopic levels, these fibers make self-compacting concrete an ideal option for complex and sensitive construction projects.

6. Conclusions

Self-compacting concrete is one of the most widely used building materials in the world, which is used in construction, but one of the problems of concrete should be kept in mind, its fragility and brittleness, which is considered as one of the mechanical behaviors of concrete. Measures have been

taken to solve it. For this purpose, steel rebars are used to reinforce concrete to limit tension and brittleness. In fact, natural fibers are used to increase the mechanical strength and improve the stability of concrete. In this way, the capacity of palm fibers can be used to limit and control cracks, improve bending and tensile strength, and also improve resistance to stresses.

Due to the presence of many palm trees in the Behbahan region, easy and cheap access to these fibers, in this research, the effect of these fibers on the hardened properties of self-compacting concrete was investigated in a laboratory manner. The main purpose of this research is to investigate the effect of adding palm tree fibers on the tensile strength of self-compacting concrete. The results of the tests are as follows:

- The compressive strength of self-compacting concrete cube specimens with palm fibers with different percentages (0.5%, 1%, 1.5%, and 2% compared to the weight of cement) during 7-day processing, respectively, 5.19%, 10.87%, 17.81%, and 22.60% decreased compared to the sample without date fiber.
- The compressive strength of self-compacting concrete cube specimens with date fibers with different percentages (0.5%, 1%, 1.5%, and 2% compared to the weight of cement) during 28 days curing, respectively, 4.11%, 9.51%, 15.48%, and 22.47% decreased compared to the sample without date fiber.
- Tensile strength of cylindrical specimens of self-compacting concrete with palm fibers with different percentages (0.5%, 1%, 1.5%, and 2% compared to the weight of cement) during 7 days of curing, respectively, 16.37%, 34.27%, 56.39%, and 82.24% increase compared to the sample without date fiber.
- Tensile strength of cylindrical specimens of self-compacting concrete with date fibers with different percentages (0.5%, 1%, 1.5%, and 2% compared to the weight of cement) during 28 days curing,

respectively, 13.56%, 27.61%, 46.96%, and 67.62% increase compared to the sample without date fibers.

Date palm fibers are not useful at the moment, and when they are piled up, they cause environmental pollution, and due to their inflammability, they increase the possibility of fire in palm groves. The use of natural fibers from the point of view of using waste, reducing environmental pollution, reducing economic costs, their abundance and availability, as well as the ease of using this type of concrete due to the flexibility of the fibers, is significant in curved and resistant structures. It is a study and it is compatible with the environment and reduces the harmful effects on the environment.

7. References

- Abani, S., Kriker, A. and Khenfer, M. (2018). "Flexural properties of reinforced date palm fibres concrete in sahara climate", *Technologies and Materials for Renewable Energy*, AIP conference proceedings, 1968, <https://doi.org/10.1063/1.5039267>.
- Abdullah, A. and Sivakumar, K. (2023). "Effect of fibre diameter and tensile strength on the mechanical, fracture, and fibre distribution properties of eco-friendly high-strength self-compacting concrete", *Construction and Building Materials*, 403, 133161, <https://doi.org/10.1016/j.conbuildmat.2023.133161>.
- Ahmad, J., Aslam, F., Zaid, O., Alyousef, R., Alabduljabbar, H. and Manan, A. (2021a). "Self-fibers compacting concrete properties reinforced with propylene fibers", *Science and Engineering of Composite Materials*, 28(1), 64-72, <https://doi.org/64.72.10.1515/secm-2021-0006>.
- Ahmad, J., Zaid, O., Aslam, F., Martinez-Garcia, R., Alharthi, Y.M., El Ouni, M.H., Tufail, R.F. and Sharaky, I.A. (2021b). "Mechanical properties and durability assessment of nylon fiber reinforced self-compacting concrete", *Journal of Engineered Fibers and Fabrics*, 16, 15589250211062833, <https://doi.org/10.1177/15589250211062833>.
- Akhmetov, D., Akhazhanov, S., Jetpisbayeva, A., Pukhareno, Y., Root, Y., Utepov, Y. Akhmetov, A. (2022). "Effect of low-modulus polypropylene fiber on physical and mechanical properties of self-compacting concrete", *Case Studies in Construction Materials*, 16, <https://doi.org/10.1016/j.cscm.2021.e00814>.
- Alatshan, F., Altomate, M., Mashiri, F. and Alamin, W. (2017). "Effect of date palm fibers on the mechanical properties of concrete", *International Journal of Sustainable Building Technology and Urban Development*, 8(2), 68-80, <https://doi.org/10.12972/susb.20170007>.
- Al-Hadithi, A.I., Majid, A. and Midher, A.H. (2023). "Structural behavior of reinforced lightweight self-compacting concrete beams using expanded polystyrene as coarse aggregate and containing polyethylene terephthalate fibers", *Structural Concrete Journal Citation Reports*, 24(5), 5808-5826, <https://doi.org/10.1002/suco.202200381>.
- Askar, M.K., Al-Kamaki, Y.S.S. and Hassan, A. (2023). "Utilizing polyethylene terephthalate pet in concrete", *Journals Polymers*, 15(15), 3320, <https://doi.org/10.3390/polym15153320>.
- Asmaa, H.S. and Khashaa, M. (2022). "Optimum characteristics of plastic fibres for sustainable self-compacting concrete SCC", *European Journal of Environmental and Civil Engineering*, 27(9), 2967-2984, <https://doi.org/10.1080/19648189.2022.2119605>.
- ASTM C150/C150M. (2012). *Standard specification for Portland cement*, American Society of Testing and Materials Standards, West Conshohocken, PA.
- ASTM C33. (2003). *Standard specification for concrete aggregates*, American Society of Testing and Materials Standards, West Conshohocken, PA.
- ASTM C494. (2002). *Standard specification for chemical admixtures for concrete*, Annual Book of ASTM Standards, ASTM International, (Vol. 04.02), West Conshohocken, PA.
- ASTM C494/C494M. (2002). *Standard specification for chemical admixtures for concrete*, Annual Book of ASTM Standards, ASTM International, (Vol. 04.02), West Conshohocken, PA.
- ASTM C94. (2009). *Standard specification for ready-mixed concrete*, American Society of Testing and Materials Standards, ASTM International, West Conshohocken, PA.
- ASTM C94/C94M – 09. (2009). *Standard specification for ready-mixed concrete*, Annual Book of ASTM Standards (Vol. 04.02), ASTM International, West Conshohocken, PA.
- ASTM C1611. (2009). *Standard test method for slump flow of self-consolidating concrete*, ASTM International, West Conshohocken, PA.
- ASTM C1611/C1611M – 09. (2009). *Standard test method for slump flow of self-consolidating concrete*, Annual Book of ASTM Standards (Vol. 04.02), ASTM International, West Conshohocken, PA.
- ASTM C496. (2002). *Ttensile concrete test*

- equipment, ASTM International, West Conshohocken, PA.
- ASTM C496/C496M – 02. (2002). *Standard test method for splitting tensile strength of cylindrical concrete specimens*, Annual Book of ASTM Standards, (Vol. 04.02), ASTM International, West Conshohocken, PA.
- Ayub, T., Khan, S. and Mahmood, W. (2021). "Mechanical properties of self-compacting rubberized concrete containing polyethylene terephthalate fibres", *Iranian Journal of Science and Technology, Transactions of Civil Engineering*, 46, 1073-1085, <https://doi.org/10.1007/s40996-020-00568-6>.
- Bhat, A.H., Naqash, J.A., Habib, T. and Islam, S.U. (2023). "Compressive strength and microstructural properties of sustainable concrete containing nanosilica, alccofine and metakaolin", *Civil Engineering Infrastructures Journal*, 57(1), 1-15, <https://doi.org/10.22059/cej.2023.348240.1866>.
- Boutarfa, M., Belouettar, R. and Makradi, A. (2018). "Comparative study of cement mortar reinforced with vegetable fibers (alfa, date palm and diss): Mechanical properties and shrinkage", *Journal of Materials and Environmental Sciences*, 9(8), 2304-2314. https://www.jmaterenvironsci.com/Document/vol9/vol9_N8/253-JMES-4073-Boutarfa.pdf. [jmaterenvironsci.com](https://www.jmaterenvironsci.com)
- Bozorgmehr Nia, S. and Adlparvar, M.A. (2022). "The effects of waste polyethylene terephthalate particles on the properties of fresh and hardened self-consolidating concrete", *International Journal of Civil Engineering and Construction*, 1(1), 6-12, <https://doi.org/10.22271/27078329.2022.v1.i1a3>.
- Djoudi, A., Khenfer, M.M., Bali, A., Kadri, E.H. and Debicki, G. (2012). "Performance of date palm fibres reinforced plaster concrete", *International Journal of Physical Sciences*, 7, 2845-2853, <https://doi.org/10.5897/IJPS11.1553>.
- Dounia, D., Mourad, B. and Mohammed, B. (2023). "Effect of date palm and polypropylene fibers on the characteristics of self-compacting concrete", *Structural Integrity and Durability of Structures*, 17(64), 31-50, <https://doi.org/10.3221/IGF-ESIS.64.03>.
- Eskandari, A., Omidinasab, F., Sahraei, A.M. and Dalvand, A. (2021). "Investigating the effect of different types of fibers in improving the flexural performance of recycled concrete beams in the elastic and plastic zones", *Journal of Structural and Construction Engineering*, 8(12), 344-362, <https://doi.org/10.22065/JSCE.2021.280477.2411>.
- Falahtabar Shiade, M. and Tavakoli, H.R. (2018). "Estimation of mechanical and durability properties of self-compacting concrete with fibers using ultrasonic pulse velocity", *Journal of Rehabilitation in Civil Engineering*, 6(2), 43-53, <https://doi.org/10.22075/JRCE.2018.798.1099>.
- Fokam, C.B., Kenmeugne, E., Meva'a, L. and Mansouri, K. (2020). "Cement mortar reinforced with palm nuts natural fibers: Study of the mechanical properties", *Revue des Composites et des Matériaux Avancés-Journal of Composite and Advanced Materials*, 30(1), 9-13, <https://doi.org/10.18280/rcma.300102>.
- Ghobadi, M., motaghd, S., Mirzaei Aliabadi, M. and Gharaibi, Y. (2019). "Investigating the fresh and hardened properties of fiber self-compacting concrete", *Scientific Research Journal of Structural and Construction Engineering*, 6(4), 43-61, <https://doi.org/10.22065/JSCE.2018.102143.1366>.
- Hossein Bar, A., Mirabi Moghadam, M.H. and Shahryari, A. (2015). "Investigation of the effect of date palm sisal fibers on the tensile strength of concrete", *Proceedings of the National Conference on Civil and Architectural Engineering and Physical Development*, Saravan, Iran.
- INSO 3203-9. (2013). *Testing fresh concrete - part 9: self-compacting concrete V-funnel test*, Iranian National Standardization Organization, Karaj, Iran, (in Persian).
- INSO 3203-10. (2013). *Testing fresh concrete - part 9: self-compacting concrete -L box test*, Iranian National Standardization Organization, Karaj, Iran, (in Persian).
- INSO 11271. (2014). *Concrete - measurement of passing ability of self-consolidating concrete by J-ring- test method*, Iranian National Standardization Organization, Karaj, Iran, (in Persian).
- IRIB News Agency. (2020). "More than 9 thousand tons of dates were harvested from Behbahan groves", News code: 2851756, <https://www.iribnews.ir/>, (in Persian).
- ISIRI 3206. (2003). *Standard test determining the compressive strength of concrete samples*, Institute of Standards and Industrial Research of Iran, Tehran, Iran, (in Persian).
- Mirabi Moghadam, M.H. (2021). "Investigation of Cis Palamfiber on the mechanical properties of concrete", *Structural and Construction Engineering Scientific-Research Journal*, 8(3), 169-176, <https://doi.org/10.22065/jsce.2019.168289.1766>.
- Modarres, Y., Ghalehnovi, M. (2023). "The effect of recycled steel fibers from waste tires on concrete properties", *Civil Engineering Infrastructures Journal*, 56(1), 1-18,

<https://doi.org/10.22059/CEIJ.2022.339592.1820>.

- Ramhormozy, A., Kazeminezhad, E. and Safakhah, S. (2023). "Effect of polyethylene terephthalate and polypropylene fibers on the shear behavior of rc deep beams", *Revista de la Construcción*, 22(1), 223-241, <https://doi.org/10.7764/RDLC.22.1.223>.
- Ramli, M. and Dawood, E.T. (2010). "Effects of palm fiber on the mechanical properties of lightweight concrete crushed brick", *American Journal of Engineering and Applied Sciences*, 3(2), 489-493, <https://doi.org/10.3844/ajeassp.2010.489.493>.
- Sor, N.H., Ali, T.K.M., Vali, K.S., Ahmed, H.U., Faraj, R.H., Bheel, N. and Mosavi, A. (2022). "The behavior of sustainable self-compacting concrete reinforced with low-density waste Polyethylene fiber", *Materials Research Express*, 9(3), 035501, <https://doi.org/10.1088/2053-1591/ac58e8>.
- Tawfeeq, A.W. and Ganesh, S. (2022). "Study on fresh properties, mechanical properties and microstructure behavior of fiber reinforced self-compacting concrete", *Materials Today: Proceedings*, 62(12), 6663-6670, <https://doi.org/10.1016/j.matpr.2022.04.666>.
- Wang, J., Dai, Q. and Si, R. (2022). "Experimental and numerical investigation of fracture behaviors of steel fiber-reinforced rubber self-compacting concrete", *Journal of Materials in Civil Engineering*, 34(1), 04021379, [https://doi.org/10.1061/\(ASCE\)MT.1943-5533.0004010](https://doi.org/10.1061/(ASCE)MT.1943-5533.0004010).



This article is an open-access article distributed under the terms and conditions of the Creative Commons Attribution (CC-BY) license.



Lightweight Fiberglass Concrete Beams of Varying Steel Reinforcement and Shear-Span Depth Ratios

Ghoniem, A.^{1*} , Gamal, M.²  and Aboul Nour, L.³ 

¹ Assistant Professor, Structural Engineering Department, Faculty of Engineering, Zagazig University, Egypt.

² Instructor, Structural Engineering Department, Faculty of Engineering, Zagazig University, Egypt.

³ Professor, Structural Engineering Department, Faculty of Engineering, Zagazig University, Egypt.

© University of Tehran 2024

Received: 6 Feb. 2024;

Revised: 24 Jun. 2024;

Accepted: 8 Jul. 2024

ABSTRACT: Fiberglass Lightweight Concrete (FLC) combines the advantages of fiber usage in a lightweight concrete matrix. In the present study, 8% of the cement weight was replaced by silica fume. Six specimens containing 2% glass fiber and 75% coarse aggregate replaced with lightweight expanded clay were subjected to a 4-point bending test. The study examined how four shear-span depth ratios (1.5, 3.0, 3.57, and 4.5) and three reinforcement ratios (low, medium, and high) affected collapse performance. Among all low-reinforced samples, the 1.5 shear-span depth exhibited the greatest improvements in resistance, mid-span deflection, stiffness, energy absorption, fracture energy, and toughness, showcasing flexural compression collapse. In contrast, the 3.57 shear-span depth low-reinforced specimen achieved the highest ductility ratio. Compared with all other 3.57 ratio samples, the low-reinforcement sample exhibited mixed flexural-shear crack patterns and the highest ductility ratio, fracture energy, and capacity of energy absorption. However, the highly reinforced sample displayed an oblique shear collapse mode and the highest stiffness enhancement. Finally, the proposed model predicting the shear strength was conducted. So, engineers can adapt the structural role of the fiberglass lightweight concrete beams to meet specific project requirements.

Keywords: Ductility, Fiberglass, LECA, Reinforced Beams Behavior, Stiffness.

1. Introduction

Fiberglass Lightweight Concrete (FLC) has attracted significant attention in the construction industry over the past decade because of its low density, long durability, and excellent thermal and acoustic insulation properties. Owing to its low weight, recent studies have shown that lightweight concrete is one of the best alternatives to traditional concrete in high-

rise buildings and long-span construction.

Lightweight concrete reduces member size, dead loads on construction, and total cost (Deifalla et al., 2020). Lightweight concrete is made by replacing or mixing normal aggregate with a lighter one derived from two main sources: i) natural, such as scoria and pumice. ii) artificial, such as Lightweight Expanded Clay Aggregate (LECA) and expanded shales (Kumar and Srivastava, 2023). To highlight its

* Corresponding author E-mail: agghoneim@zu.edu.eg

suitability as a sustainable structural alternative to conventional concrete for construction practices, lightweight concrete must achieve safety and serviceability by providing sufficient strength and controlling deformation under different loads. Reinforcing elements with longitudinal bars and fibers manages crack characteristics, ensuring the necessary ductility (Vakili et al., 2019). Glass fibers provide exceptional stiffness, strength, and chemical resistance (Sathishkumar et al., 2014) and are also effective in controlling shrinkage cracking (Mirza and Soroushian, 2002). Fiberglass lightweight concrete offers numerous benefits in terms of sustainability and environmental impacts.

The use of glass fibers in composites contributes to the reduction of waste generated by the glass industry (Karuppannan Gopalraj and Kärki, 2020). In addition, the inclusion of LECA lowers the consumption of natural resources, such as sand and gravel (Bozorgmehr Nia and Nemati Chari, 2023).

Aboul-Nour et al. (2023) investigated how different LECA ratios and glass fiber contents affect the density, workability, compression, and split tensile strengths of lightweight concrete. They found that a mix of 2% glass fiber and 75% replaced LECA exhibited the highest compression strength, while a mix of 1% glass fiber showed the greatest tensile strength (Aboul-Nour et al., 2023). Prestressed glass fiber lightweight concrete girders demonstrated a 20% weight reduction and effectively prevented bond-slip damage due to a ridged interface (Li et al., 2024).

Several studies have examined the capacity of steel fiber lightweight concrete girders (Li et al., 2019, 2021). Increasing the content of steel fibers shifts collapse modes from shear collapse to ductile flexural shear collapse, while shear resistance decreases as the shear-span depth ratio increases (Jiao et al., 2017). However, there is a gap in the experimental studies on the performance of longitudinally reinforced fiberglass lightweight concrete

specimens.

This study enhances the understanding of designing and optimizing FLC beams. For structural engineers, a comprehensive grasp of shear-span and reinforcement ratios is essential for accurate analysis and design. In the current study, the results of testing six large-scale reinforced concrete specimens with constant fiber volume fraction and LECA content are presented to explore the significance and implications of the shear-span and reinforcement ratios.

The specimens undergo 4-point loading tests controlled by displacement. The cracking patterns and performance parameters, including the stiffness, ductility, capacity of energy absorption, toughness, and fracture energy of the FLC beam, are discussed. To ensure a reliable design, the results are compared with those obtained from the mathematical model. The finest model for predicting FLC beam shear strength is identified from the proposed model, six code-of-practice provisions, and seven equations from the literature.

2. Materials and Methods

2.1. Test Program

Concrete mixes included cement, sand as a fine aggregate, coarse normal and lightweight aggregates, tap water, Silica Fume (SF), superplasticizer, and glass fiber. The quantities used in the mixes are summarized in Table 1.

Table 1. Concrete mixtures for the research samples (kg/m³)

Materials	Quantity
Cement	500
Water	195
Sand	574.4
Dolomite	248.9
LECA	484.5
Silica fume	40
High-range water reducer	11
Glass fiber (% of volume)	2%

The natural siliceous sand of a 1738 kg/m³ bulk density used in our experiments had a fineness modulus of 2.72. The crushed dolomite aggregate had a 14 mm

maximum size, 1570 kg/m³ bulk density, 2.62 specific gravity, and a 2.35% water absorption ratio. Alex Hydroponics Company locally produces LECA brown pellets, which is a coarse lightweight aggregate fired in a rotary kiln at temperatures ranging from 950 to 1100 °C.

The maximum nominal size of the LECA was 20 mm, its specific gravity was 1.6, its bulk density was 1000 kg/m³, and its water absorption ratio was 16.69. The chemical components of LECA were SiO₂ (61.12%), Al₂O₃ (18.77%), Fe₂O₃ (14.21%), CaO (1.78%), MgO (2.37%), and Loss (0.4%). Table 2 presents a sieve analysis of the aggregates used in our study.

Table 2. Sieve analysis of study aggregate types

Particle size (mm)	% Passing		LECA
	Fine aggregate	coarse aggregate	
20	-	-	95.9
14	-	99.2	19.7
10	-	77.6	-
5	99.4	12.5	-
2.36	95	-	-
1.18	87.4	-	-
0.6	44.4	-	-
0.3	8.6	-	-
0.15	2	-	-

In the current study, the ratio of water to cementitious materials (w/b) is set at 0.36. The study used Type I Portland cement (CEMI 42.5N) to comply with ES 4756-2 (2020) and ASTM C150/C150M-22 (2022). Cementitious materials and water-reduction admixtures were used to enhance the concrete's fresh and hardened characteristics. The study employed sika fume of a 0.65 ± 0.1 kg/L density at 8% of the cement weight manufactured by Sika Egypt and master rheobuild1100 super-

plasticizer at a rate of 2.2 lit/100 kg of cement. At 25 °C, the dark brown liquid master rheobuild1100 had a specific gravity from 1.19 to 1.26 and a pH from 6 to 11.

The research used Type E glass fiber, 12 mm long, 13 µm wide, and tensile strength from 500 to 600 N/mm² from the Egyptian European Steel Fiber Company. The LECA was immersed for 24 hours in water to ensure saturation of the internal voids. The LECA was then removed from the water an hour before its use. All dry components, including sand, dolomite, LECA, cement, and SF, were distributed uniformly in the mixer for two minutes. Half of the mixing water was added to the water reducer, and the other half was added directly to the mix. After two minutes of mixing all these components, the mix was sprinkled with fibers. Finally, hand mixing is performed to ensure the homogeneity of concrete.

Experimental surveys assessed the LECA's effectiveness as a partial replacement for coarse aggregate in concrete. The influence of LECA on the fresh and hardened properties of samples containing 2% glass fiber was also examined. The samples' density, workability, compression, and split tensile strengths were measured according to ASTM C143/C143M-20 (2020), ASTM C642-21 (2021), BS EN 12390-3 (2019), and ASTM C496/C496M-17 (2017), respectively. The changes in physical and mechanical properties compared with a control mix without LECA (Table 3). Using LECA to replace 75% of the coarse aggregate resulted in the smallest weight reduction of 16.14% compared with normal concrete.

Table 3. Physical and mechanical properties of concrete mixes

LECA content	Density			Slump		Compression strength				Split tensile strength			
	Mean (kg/m ³)	SD	Change (%)	(mm)	Change (%)	Mean (kg/m ³)	SD	Change (%)	Strength/weight ratio (MPa/kg)	Mean (kg/m ³)	SD	Change (%)	
0%	2419	17	-	60	-	48.41	1.26	-	5.05	3.40	0.28	-	
75%	2028	28	-16	80	+33	31.13	0.31	-35	3.46	1.58	0.18	-53	
85%	1986	130	-17	93	+55	28.21	1.67	-41	2.85	1.82	0.15	-46	
95%	1930	81	-20	105	+75	25.68	3.43	-46	2.71	2.03	0.08	-40	

However, higher LECA content diminished compression strength. The 75% LECA mix, identified as optimal, achieved the highest strength-to-weight ratio of 3.46 MPa/kg, with a density of 2028 kg/m³, categorizing it as lightweight according to ACI definitions, which classify normal-weight concrete as having a density of 2240 to 2420 kg/m³. Additionally, the compression strength of the LECA concrete met the required standards, as structural lightweight concrete should exceed 15 MPa at 28-days per ASTM C330-23 (2023) and ACI 213R (1987) guidelines. The 75% LECA concrete revealed an experimental split tensile strength of 1.6 MPa. Wang and Wang (2013), Sajedi and Shafigh (2012), and ACI 318 (2019) take into account the influence of glass fiber on strength as ($f_{st} = 3.898 + 2.08 V_f$), ($f_{st} = 0.5245 + 0.0761 f_{cu}$), and ($f_{st} = 0.23 f_c^{0.7}$) that equals 3.9 MPa, 3.35 MPa, and 2.5 MPa for the current study mix, respectively. The experimental split

tensile strengths were approximately 59%, 52%, and 36% lower than the theoretical values for normal aggregate concrete calculated by Wang and Wang (2013), Sajedi and Shafigh (2012), and ACI 318 (2019), respectively.

2.2. Test Specimens

The experimental study examined the structural attitude of LECA concrete specimens by testing girders at various shear-span depth ratios (a/d). The program involved the fabrication and testing of six reinforced concrete specimens, detailed in Table 4, with rectangular cross-sections having 10 cm width, 15 cm depth, 160 cm total length, and 150 cm supported length.

Each specimen comprised 75% LECA as a replacement for normal-weight coarse aggregates and 2% glass fiber. Specimens were labeled "L" followed by numbers indicating the shear-span depth ratio and the reinforcement bar diameter.

Table 4. Details of test beam samples

Beam determination	Shear-span depth ratio, a/d	Beam size $b \times d$ (mm)	Tension reinforcement		
			Number and size	A_s (mm ²)	$\rho = A_s / bd$ (%)
L3.57-R10 (control)	3.57	100×150	2Φ10	157	1.04
L1.5-R10	1.5				
L3-R10	3				
L4.5-R10	4.5		2Φ12	204	1.36
L3.57-R12	3.57				
L3.57-R16	3.57		2Φ16	226	1.5

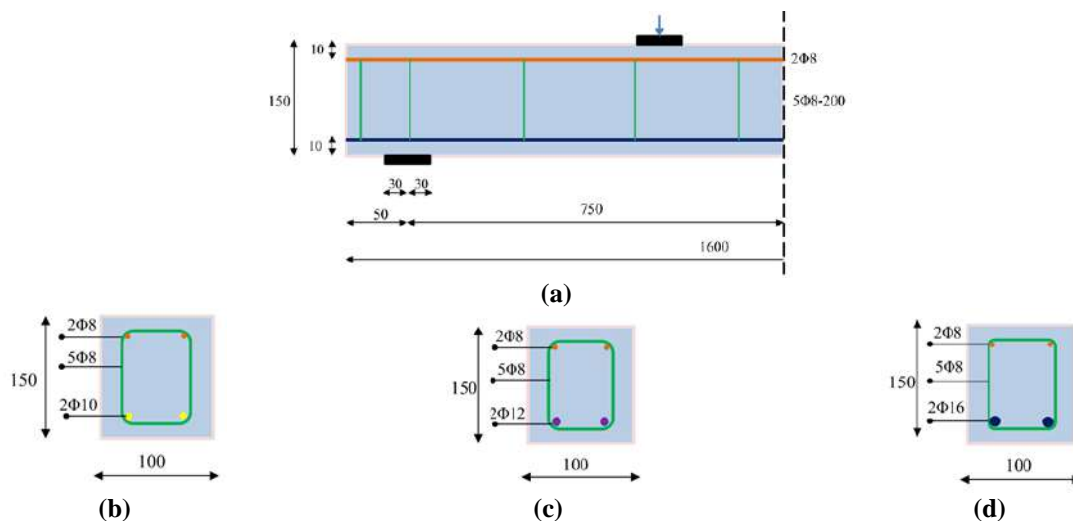


Fig. 1. Dimensions and reinforcement information of FLC beams (units: mm): a) Half elevation of the test beam; b) Cross-section of low-reinforcement-ratio beams; c) Cross-section of medium-reinforcement-ratio beams; and d) Cross-section of high reinforcement ratio beams

Four specimens featured 10 mm bottom tensile reinforcement bars (low reinforcement ratio), including one control specimen with a shear-span depth ratio of 3.57, and three others at ratios of 1.5, 3.0, and 4.5. The remaining two specimens, under a ratio of 3.57, had 12 mm and 16 mm bottom tensile bars, representing medium and high reinforcement ratios. Figure 1 illustrates the reinforcement specifics. A Linear Variable Displacement Transformer (LVDT) and a load cell measured the mid-span displacement and total applied load, respectively. The tensile longitudinal reinforcements (10 mm, 12 mm, and 16 mm) had a f_y / f_{ult} ratio of 40/60. Upper longitudinal reinforcement and stirrups were made of ordinary mild steel with an 8 mm diameter and a strength of $f_y / f_{ult} = 24 / 35$.

3. Results and Discussion

3.1. Load-Deflection Relationship

Figure 2a depicts the relationship between applied load and deflection for various samples with differing shear-span depth ratios. Generally, loading increased until collapse, exhibiting a linear nature before cracking. The curve's slope changed after cracking, indicating decreased stiffness until the tensile steel yielded. Specimens with shear-span depth ratios of 4.5, 3.57, and 3.0 displayed similar load-deformation responses before and after cracking, differing only in the initial curve segment. Sample L3.57-R10 reached the curve's inflection point earlier than the others, followed by the sample with a 4.5

ratio, then the sample with a 3.0 ratio.

Consequently, L3.57-R10 had the lowest stiffness compared with L4.5-R10 and L3-R10. After recording the ultimate load, sample L1.5-R10 showed several changes in inclination as strength increased and then declined, retaining the highest stiffness among all samples. The findings indicate that reducing the shear-span depth ratio significantly enhanced the flexural stiffness of FLC beams. Figure 2b illustrates load vs. mid-span deflection for specimens with varying reinforcement ratios. Loading increased for all girders, resulting in a linear pre-cracking curve. The slope decreased after cracking, indicating reduced stiffness until the tensile steel failed. The low-reinforcement ratio sample, L3.57-R10, reached the curve's inflection point before the other samples. It exhibited a minor strength increase after yielding, followed by a nearly flat plateau and a slight strength decrease. The load-deflection curve for the medium reinforcement ratio sample, L3.57-R12, consisted of two segments connected at the maximum load point, showing a sharp drop in slope post-inflection, and indicating stiffness reduction. The high-reinforcement ratio sample (L3.57-R16) also experienced a sudden strength drop after reaching maximum load. These findings suggest that rising the steel reinforcement ratio improved the total stiffness of the specimens, aligning with previous research on LECA concrete containing varying amounts of steel and polypropylene fibers (Al-Khafaji and Harba, 2023).

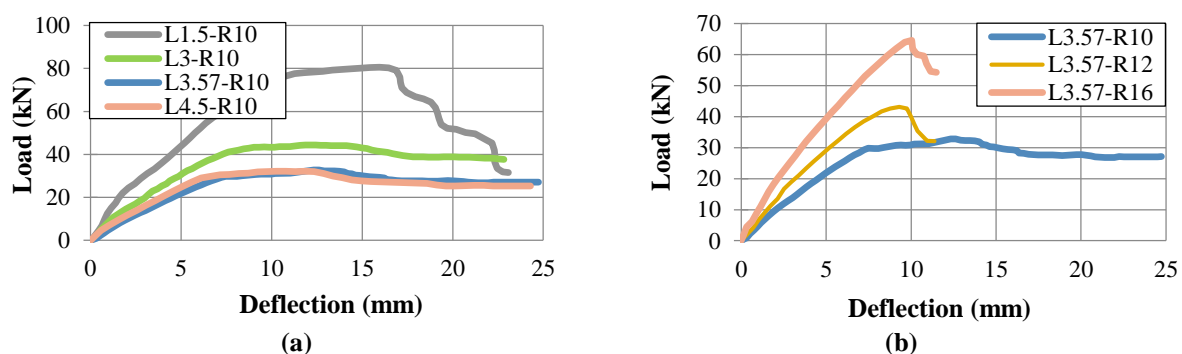


Fig. 2. Load-displacement curves for: a) Same reinforcement and various shear-span depth ratio samples; and b) Same shear-span depth ratio and different bottom tensile reinforcement samples

3.2. Crack Pattern and Collapse Mode

1) Influence of the shear-span depth ratio: Figure 3 shows the specimens' crack patterns and collapse modes with varying shear-span depth ratios: L1.5-R10, L3-R10, L3.57-R10, and L4.5-R10. In the control sample L3.57-R10, an initial flexural crack arose on the tension side in the mid-span zone. As loading enlarged, an extra flexural crack developed between the initial crack and extended vertically, while an additional crack formed in the outer shear-span on the tension side, eventually reaching the load points. This sample exhibited a flexural-compression collapse mode, culminating in concrete crushing at the top compression side between the 2-points of the applied load. During the initial loading level, the specimen with the lowest shear-span depth ratio, L1.5-R10, showed a mid-zone mild flexural crack. A diagonal crack emerged at a load of 59 kN, with more oblique and flexural crack appearing as the load enlarged. At 76 kN, a shear crack formed in the support region, leading to collapse through a diagonal shear crack at approximately 45° from the support.

Previous studies on lightweight

concrete girders with steel fibers support that shear-compression collapse occurs in specimens with shear-span depth ratios of 1.5 to 2.5, involving concrete crushing in the shear compression region and a subsequent larger shear crack in the tension region (Li et al., 2019). Sample L3-R10 exhibited a crack pattern and collapse mode similar to L3.57-R10, although L3.57-R10 developed more extensive flexural and oblique crack.

Sample L4.5-R10 failed likewise, showing only a flexural crack in the mid-span zone, resulting in an exclusively flexural collapse followed by concrete crushing between the two loading points.

While specimens with shear-span depth ratios of 3.0, 3.57, and 4.5 demonstrated similar flexural-compression collapse modes, those with ratios of 3.0 and 3.57 were in a transitional phase from shear collapse to pure flexural collapse, leading to a gradual disappearance of shear crack in favor of additional flexural crack. As the shear-span depth ratio increased, the main crack shifted from the outer shear spans to the middle flexural bending region.

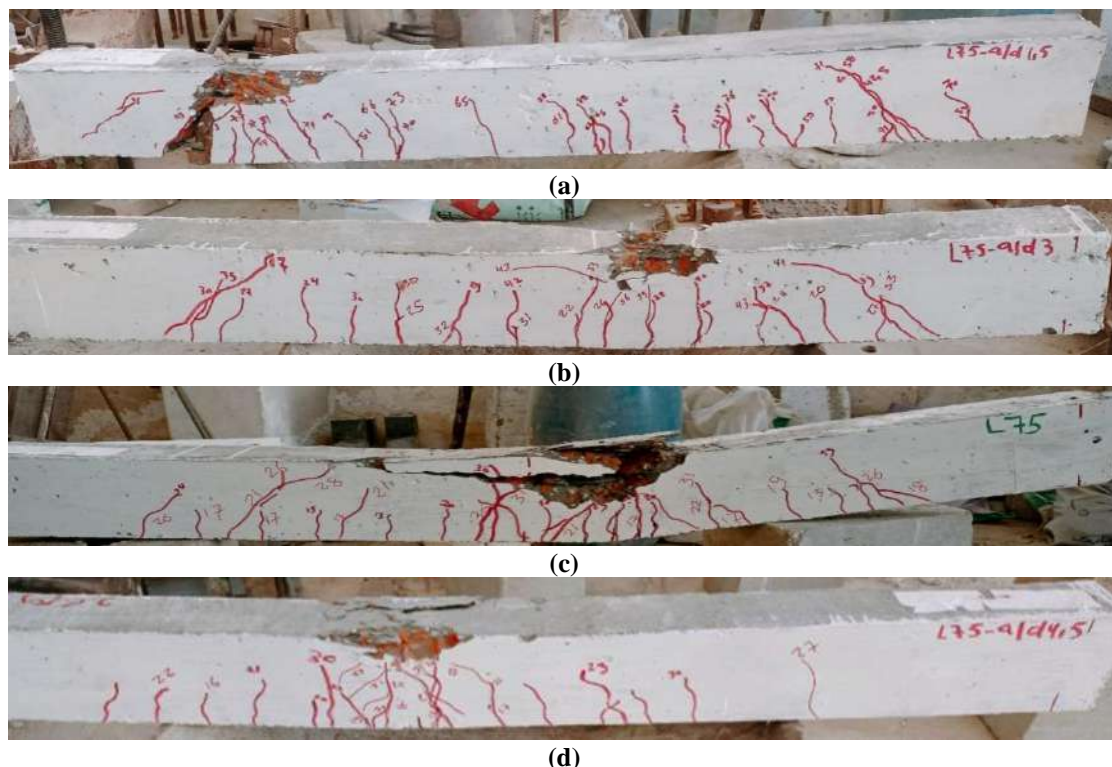


Fig. 3. Crack patterns for beams with various shear-span to depth ratios: a) L1.5-R10; b) L3-R10; c) L3.57-R10; and d) L4.5-R10

Table 5 quantitatively compares the cracking and peak loads, as well as moment resistance, for specimens with different shear-span depth ratios. The control sample (of shear-span depth ratio 3.75, L3.57-R10) exhibited its first crack at 13 kN. In contrast,

the specimen with the smallest shear-span depth ratio (1.5) demonstrated superior crack resistance. At loads of 32 kN and 20 kN, L1.5-R10 and L3-R10 showed approximately 146% and 54% more resistance to the initial crack, respectively.

Table 5. Load, moment resistance capacity, displacement, and collapse modes of samples with different shear-span depth ratios and reinforcement ratios at the cracking and peak stages

Sample ID	Cracking stage			Peak stage			Collapse mode
	Cracking load (kN)	Cracking moment resistance (kN.m)	Displacement at cracking load, Δ_{cr} (mm)	Maximum load (kN)	Maximum moment resistance (kN.m)	Displacement at maximum load, Δ_{max} (mm)	
L3.57-R10	13.00	3.25	2.818	33.35	8.34	10.34	Flexural-compression
L1.5-R10	32.00	8.00	3.272	80.59	20.15	16.11	Shear-compression
L3-R10	20.05	5.02	2.953	44.51	11.13	12.28	Flexural-compression
L4.5-R10	16.20	4.05	3.028	32.36	8.09	10.76	Flexural-compression
L3.57-R16	30.10	7.53	3.552	65.27	16.31	10.02	Shear-compression
L3.57-R12	21.30	5.33	3.390	43.56	10.89	9.65	Shear-compression

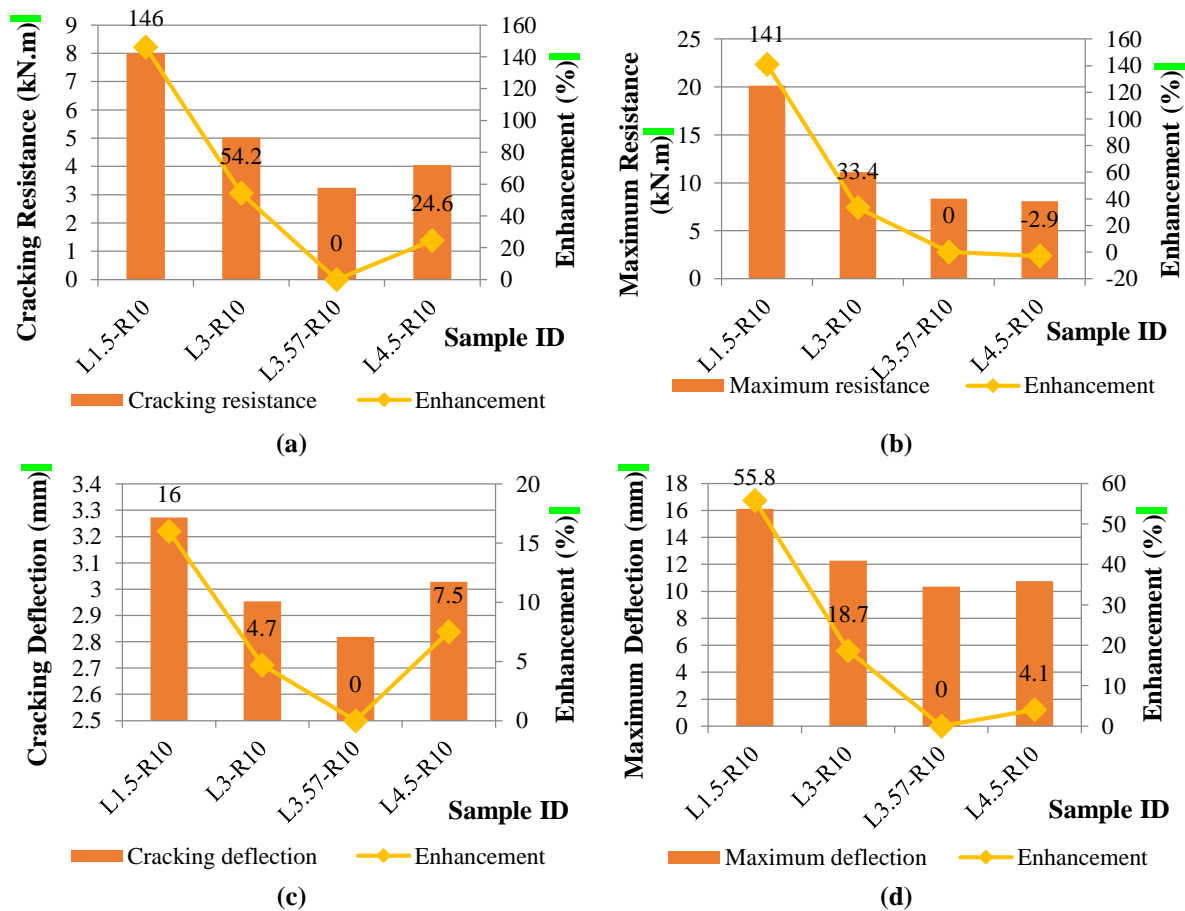


Fig. 4. Enhancement percentage of various shear-span depth ratio samples in: a) Cracking resistance; b) Maximum resistance; c) Cracking deflection; and d) Maximum deflection

At peak load, the control sample reached an ultimate load and resistance of 33.35 kN and 8.33 kN·m, respectively. Specimens with shear-span depth ratios of 1.5 and 3.0 (L1.5-R10 and L3-R10) surpassed the control sample's ultimate load and resistance by approximately 141% and 33.4%, peaking at 80.5 kN, 20.14 kN·m, and 44.51 kN, 11.12 kN·m. Additionally, the sample with a lower shear-span depth ratio (1.5) exhibited the greatest deflection at 16.11 mm, while deflection decreased to 12.28 mm and 10.34 mm for specimens with ratios of 3.0 and 3.57, respectively.

The deflection of the 4.5 shear-span depth ratio specimen slightly increased to 10.76 mm. Consequently, specimens with lower shear-span depth ratios displayed superior anti-cracking performance, indicated by increased cracking deflection and load, as shown in Figures 4a and 4c. Hence, reducing the shear-span depth ratio enhanced ultimate resistance and deflection (Figures 4b and 4d). This finding aligns with Sathiyamoorthy's assertion that lightweight girder shear resistance increases as the shear-span depth ratio decreases (Sathiyamoorthy, 2021). As this ratio reduces, compression struts can effectively transfer internal forces directly to supports through arch action. The specimen with the highest shear-span depth ratio (L4.5-R10) experienced a delay of approximately 24.5% in its first cracking load compared with the control sample.

Despite a higher shear-span depth ratio, L4.5-R10 had a lower ultimate load and resistance of about 2.9%. Yin and Hu (2021) noted that the increase in cracking load is attributed to the load transfer mechanism.

2) Influence of the tensile steel: Figure 5 illustrates crack patterns and collapse modes of established specimens with a constant shear-span depth ratio and varying reinforcement ratios L3.57-R10, L3.57-R12, and L3.57-R16. For L3.57-R12, a minor flexural crack arose at a 26 kN loading. At 29 kN, an oblique crack formed near the 2-points of loading, leading to diagonal shear-compression collapse characterized by a substantial crack under the loading point and compression concrete crushing. Specimen L3.57-R16 exhibited similar diagonal shear-compression collapse but with more cracks before the collapse, particularly in the mid-span zone.

As the load increased, an oblique crack propagated on the tensile side, with a minor shear crack appearing near the supports at 53 kN. Both L3.57-R12 and L3.57-R16 experienced local failures due to stress concentrations at the supports. This crack pattern was linked to the formation of fractures and the nonlinear nature of concrete materials. The tensile reinforcement diameters for 12 mm and 16 mm exceeded the maximum tensile reinforcement ratio (ρ_{max}), while the 10 mm diameter was below it.

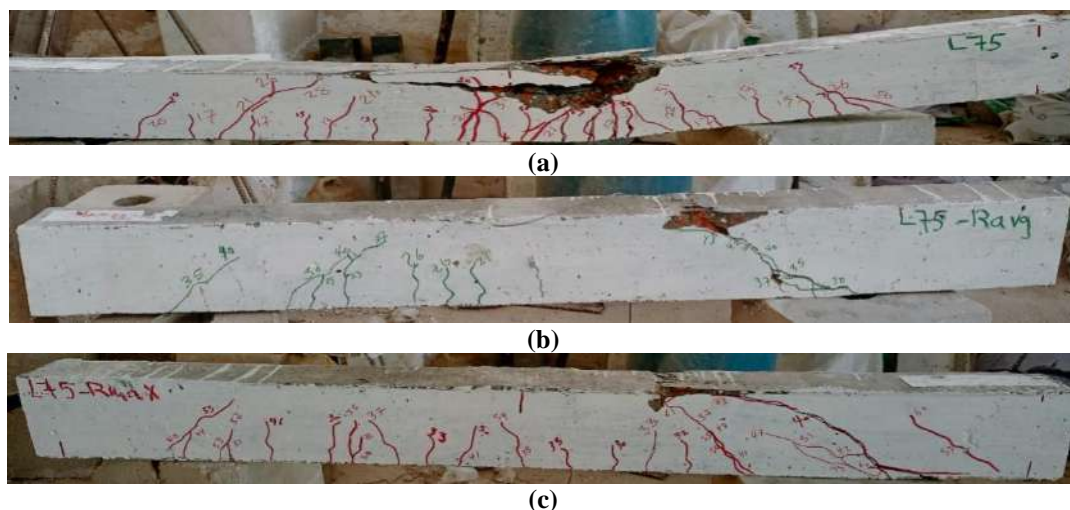


Fig. 5. Crack pattern of beams: a) L3.57-R10; b) L3.57-R12; and c) L3.57-R16

According to ACI 318 (2019), reinforcement ratios were as follows: minimum (ρ_{min}) 0.3, maximum (ρ_{max}) 1.33, and balanced (ρ_b) 1.77, indicating that to ensure ductile collapse, specimens should be under-reinforced ($\rho_b < \rho < \rho_{min}$) (ACI 318, 2019).

Enlarging the steel reinforcement ratio beyond ρ_{max} shifted the collapse mode to undesirable shear-compression collapse, consistent with findings by Alhassan et al. (2017). Specimens with medium and high reinforcement ratios showed deflections of 6.6% and 3% less at maximum load than those with low steel reinforcement ratios, aligning with Shafigh et al. (2011), which highlighted that lighter concrete girders with lower reinforcement deflected more. Thus, higher reinforcement ratios enhance cracking resistance and deflection, delaying crack appearance (Figures 6a and 6b). Figures 6c and 6d demonstrate that a higher reinforcement ratio increases ultimate moment capacity without affecting maximum deflection, supporting similar results from Zhu et al. (2018) and Wang et

al. (2022). The high tensile reinforcement ratio specimen L3.57-R16 exhibited a 131% increase in cracking load (30.1 kN) and moment (7.52 kN.m) compared with the low reinforcement control sample. The medium reinforcement ratio L3.57-R12 showed a 63.8% increase in cracking load (21.3 kN) and moment (5.3 kN.m). The peak load and resistance also increased similarly for both medium and high reinforcement ratios, with L3.57-R12 (43.5 kN, 10.89 kN.m) and L3.57-R16 (65.2 kN, 16.3 kN.m) showing increases of 30.6% and 95.7% compared with the control sample. These trends resonate with findings by Al-Khafaji and Harba (2023), who noted the flexural capacity decrease of lightweight concrete girders as tension reinforcement diminished.

3.3. Performance Parameters

The lightweight nature of FLC makes it particularly suitable for buildings in earthquake-prone areas, reducing seismic strain while maintaining strength.

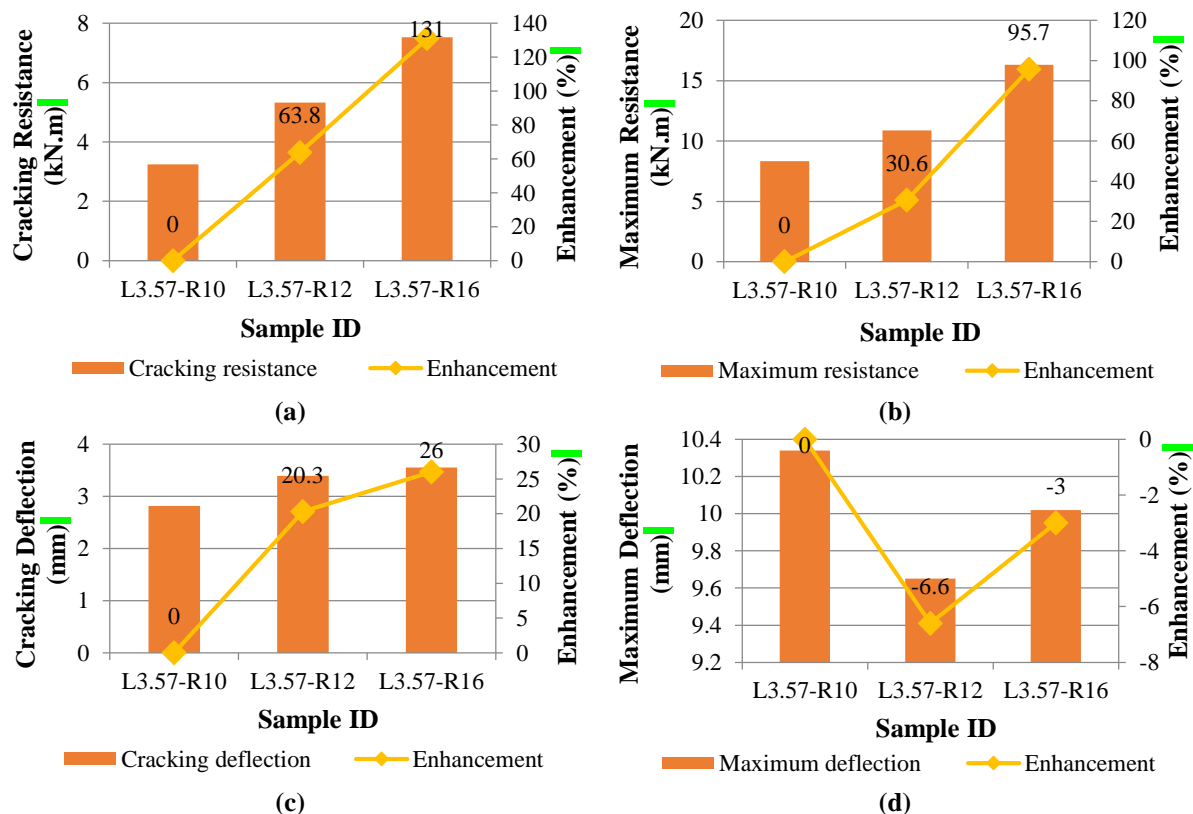


Fig. 6. Enhancement percentage of various bottom tensile reinforcement ratio samples in: a) Cracking resistance; b) Maximum resistance; c) Cracking deflection; and d) Maximum deflection

Therefore, it is essential to calculate the stiffness, ductility, energy absorption capacity, toughness, and fracture energy of FLC beams. According to ACI 318 (2019), the secant method is used to determine stiffness. As shown in Figure 7a, a lower shear-span depth ratio significantly reduces stiffness; it decreased by about 77.9% as the ratio increased from 1.5 to 4.5. Conversely, rising the diameter of the reinforcement steel from 10 to 12 and 16 mm improved stiffness by approximately 34.7% and 80.8%, respectively (Figure 7b).

Ductility and energy absorption reflect

the conversion of mechanical applied energy into internal potential energy within reinforced concrete elements, serving as structural safety indices (Hanoon et al., 2017). Accurate prediction of ductility is crucial for assessing a structure's ability to withstand inelastic deformations without losing its load-carrying capacity. The displacement ductility ratio, μ , was calculated using ASTM E2126-11 (2011) equation. Among various shear-span depth ratios, the shear-collapse mode negatively affected the ductility ratio of the L1.5-R10 sample (Figure 7c).

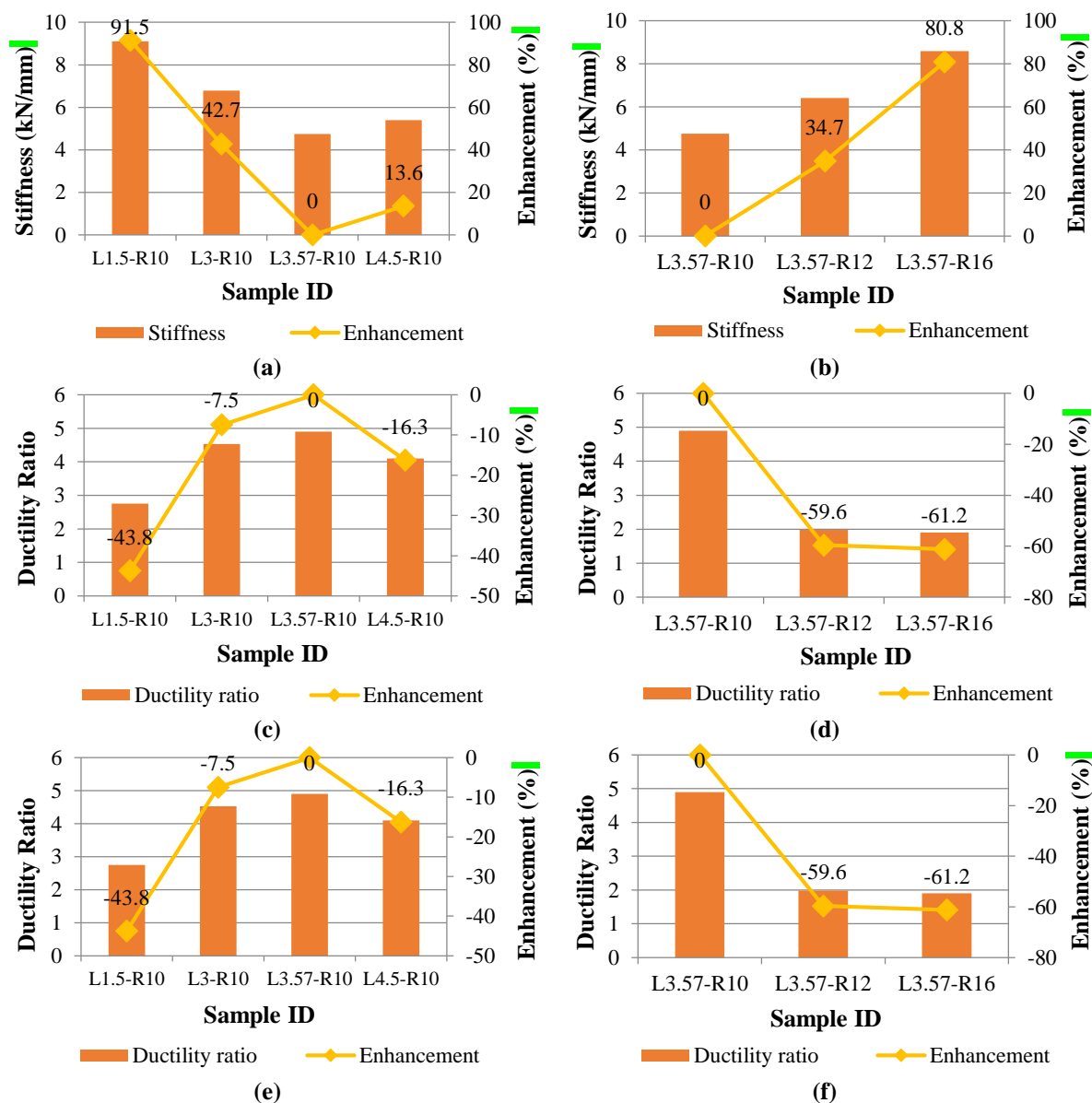


Fig. 7. Enhancement percentage: a) Stiffness of various shear-span depth ratio samples; b) Stiffness of the samples with various reinforcement ratios; c) Ductility of samples with various shear-span depth ratios; d) Ductility of various reinforcement ratio samples; e) Capacity of energy absorption for samples with various shear-span depth ratios; and f) Energy absorption capacities of the samples with various reinforcement ratios

Comparatively, samples L3.57-R16 and L3.57-R12 exhibited lower ductility ratios due to shear collapses versus the flexural collapse mode of sample L3.57-R10, with reductions of 61.2% and 59.6%, respectively (Figure 7d).

Energy absorption, determined as the area below the load-deflection trajectory, remains vital for maintaining structural integrity under unusual loads. Results indicated an inverse relationship between shear-span depth ratio and capacity of energy absorption, which decreased by approximately 108.9% when increasing the ratio (1.5 to 4.5) (Figure 7e). Conversely, changing the reinforcement steel diameter from 12 mm to 16 mm resulted in

reductions of 52.9% and 27% in energy capacity, respectively. Additionally, increasing the bottom tensile reinforcement diminished energy absorption capacity (Figure 7f). Fracture energy is crucial for understanding concrete behavior in large structures and shear tests. Using the equation outlined by Gyawali (2023), the fracture energies were assessed for comparison. Sample L1.5-R10 recorded the highest fracture energy, while sample L3-R10 was 78.2% lower. Figure 8a demonstrates that increasing the shear-span depth ratio to 3.57 and 4.5 reduced fracture energy by 105.6% and 108%, respectively, indicating its direct impact on energy absorption during fracture.

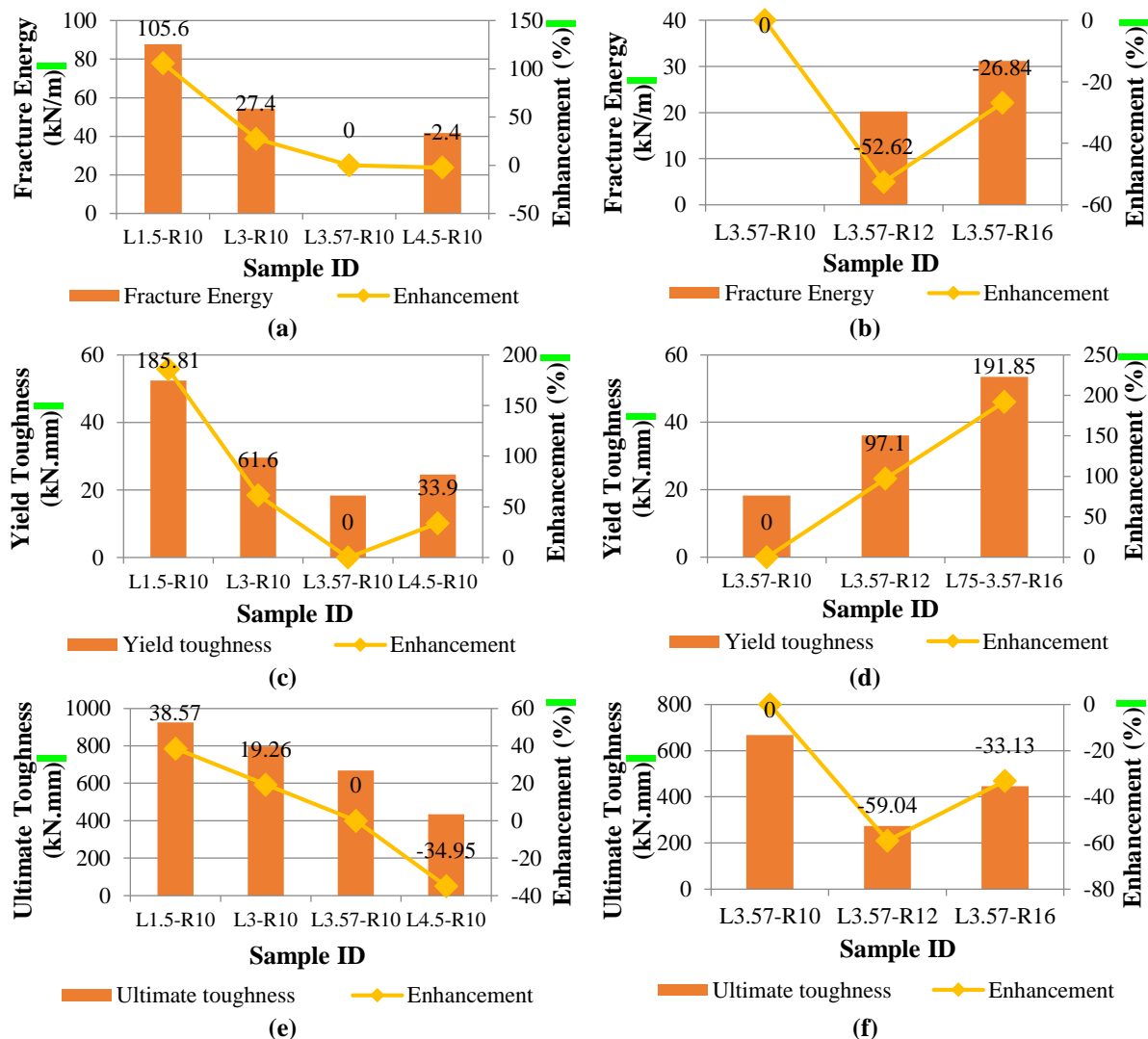


Fig. 8. Enhancement percentage of: a) Fracture energy at various shear-span depth ratios; b) Fracture energies at various reinforcement ratios; c) Yield toughness at various shear-span depth ratios; d) Yield toughness at various reinforcement ratios; e) Ultimate toughness at various shear-span depth ratios; and f) Ultimate toughness at various reinforcement ratios

Although no clear relationship exists between reinforcement ratio and fracture energy, samples with lower ratios showed a more significant effect on fracture energy. For samples L3.57-R16 and L3.57-R12, increasing the reinforcement ratio led to reductions in energy of approximately 26.84% and 52.62%, respectively (Figure 8b). Yield and ultimate toughness values were derived from ASTM C1018-97 (1997) equation. Figures 8c and 8e illustrate that these values decreased by 151.91% and 3.62%, respectively, as the shear-span depth ratio increased from 1.5 to 4.5. A lower shear-span depth ratio positively influences yield and ultimate toughness, with higher yield toughness generally associated with increased initial crack loads (Safiuddin et al., 2022). The high ultimate toughness values suggest that the LECA aggregate and glass fiber mixture enhances the FLC girders' resistance to tensile stresses. A high reinforcement ratio significantly affects yield toughness positively but detracts from ultimate toughness, as shown in Figures 8d and 8f.

Utilizing 75% expanded clay particles reduces concrete density to 2028.6 kg/m³, thereby decreasing the dead load on structures. Furthermore, the 75% LECA concrete demonstrated acceptable compression strength (31 MPa) and split tensile strength (1.6 MPa). These combined properties make FLC ideal for applications where strength and weight are critical, such as in high-rise construction. Despite a low reinforcement ratio, incorporating glass

fibers into the concrete matrix enhanced tension capacity and improved resistance to cracking and shrinkage.

3.4. Experimental Result vs. Theoretical Estimation

The assumptions of the proposed doubly reinforced prediction model for the fibrous concrete beams shear strength include contributions from the nominal shear strength of concrete, longitudinal reinforcement, stirrups, and fibers, as defined in Eq. (1).

$$v_{fc;u} = v_{fc;sf} + v_{fc;st} \quad (1)$$

$$v_{fc;sf} = \left[\frac{\sigma_t (h-e)}{ad} \left(\frac{h}{2} + \frac{e}{2} - \frac{x}{2} \right) \right] + \frac{f_y A_{sc}}{abd} \left(\frac{x}{2} - d' \right) \quad (2)$$

$$\sigma_t = 0.00772 \frac{V_f l_f}{d_f} F_{be} \quad (3)$$

$$e = h - \frac{0.85 f'_c x}{\sigma_t} + \frac{f_y}{\sigma_t b} (A_s - A_{sc}) \quad (4)$$

$$c = \frac{\varepsilon_c d}{\varepsilon_c + \frac{f_y}{E_s}} \quad (5)$$

where, $v_{fc;u}$: represents the longitudinally steel reinforced fibrous girders ultimate shear strength, $v_{fc;st}$: indicates the stirrups shear strength, and $v_{fc;sf}$: accounts for the shear strength from the fibrous matrix, compression steel, and longitudinal bottom steel (ACI 544.4R, 1988).

Figure 9 illustrates the nominal moment calculated using the proposed model, based on the stress and strain distributions in the fibrous concrete sample.

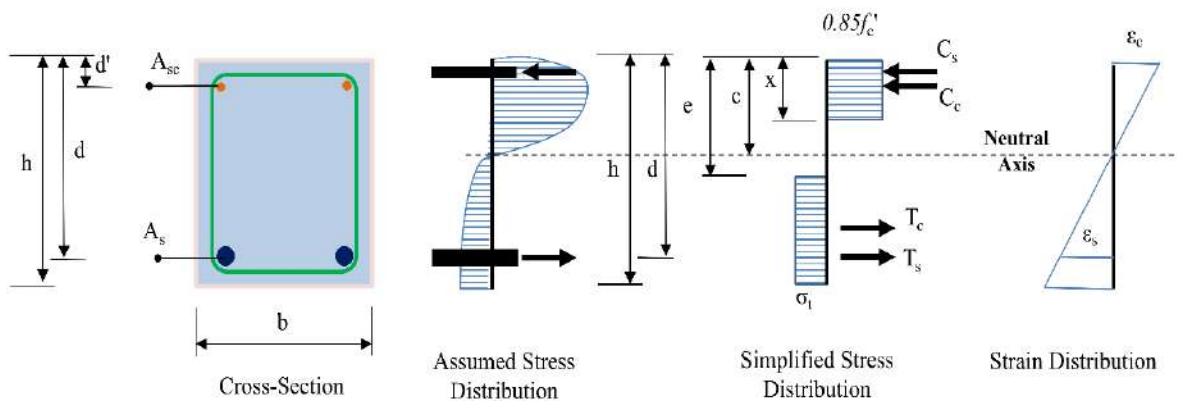


Fig. 9. Design assumptions for reinforced fibrous concrete beams

The shear strength contribution of fibers and reinforcement steel for a doubly reinforced fibrous concrete sample, $v_{fc;sf}$, is determined as shown in Eq. (2). In the equations, σ_t denotes the tension stress in fibrous concrete (Eq. (3)), V_f is the fiber content, and l_f / d_f represents the fiber aspect ratio. F_{be} , the fiber bond effectiveness, varies from 1.0 to 1.2 based on the fiber features (set to 1.0 in this study). Parameters such as the girder total depth (h), shear span (a), girder width (b), distance from the supreme compression fiber to the center of the tension steel bars (d), depth of the rectangular stress block (x), and internal tension and compression forces (e) are distinguished in Eqs. (4) and (5). The yielding strength of the bars (f_y), the area of tension steel (A_s), the compression steel area (A_{sc}), the distance from the supreme compression fiber to the center of compression steel (d'), and the compression strength of plain concrete (f_c') are also specified. The supreme compression fiber to the neutral axis distance (c) is based on the strain distribution and the concrete compression strain (ϵ_c), which is 0.0035 for 1.0% fiber content and 0.004 for 1-3% fiber content, with the steel elasticity modulus (E_s) equal to 200 GPa. Theoretical models are usually considered for integration into design codes due to their simplicity and satisfactory test results for fibrous specimens.

Figure 10 compares the test shear strength values of fibrous concrete girders with those predicted by the proposed model and thirteen existing models. The models AS 3600 (2018), ACI 544.4R (2018), Ashour et al. (1992), ACI 318 (2019), Eurocode 2 (2004), CECS 38 (2004), Kwak et al. (2002), Narayanan and Darwish (1987), Shin et al. (1994), Imam et al. (1995), Li et al. (2019), JGJ12 (2006), Yi et al. (2017), and the current proposed model exhibited similar trends across samples and reasonably predicted experimental shear strength values, except for the 1.5 shear-span depth ratio sample evaluated by Eurocode 2 (2004). The theoretical shear strength of each FLC girder that failed in shear was compared with the actual measured strengths.

Table 6 presents the mean of the $v_{fc;THEO} / v_{fc;EXP}$ ratios for each model. The proposed model, AS 3600 (2018), Ashour et al. (1992), ACI 318 (2019), ACI 544.4R (2018), JGJ12 (2006), and Yi et al. (2017) exhibited mean values close to 1.0 with a total standard deviation of less than 0.5. They demonstrated conservative estimation, with deviations of 7.19%, 7.89%, 23.44%, -35.96%, 45.60%, 52.37%, and 58.41% from experimental results. The previous seven models overestimated shear strength capacity, except ACI 544.4R (2018), which underestimated it.

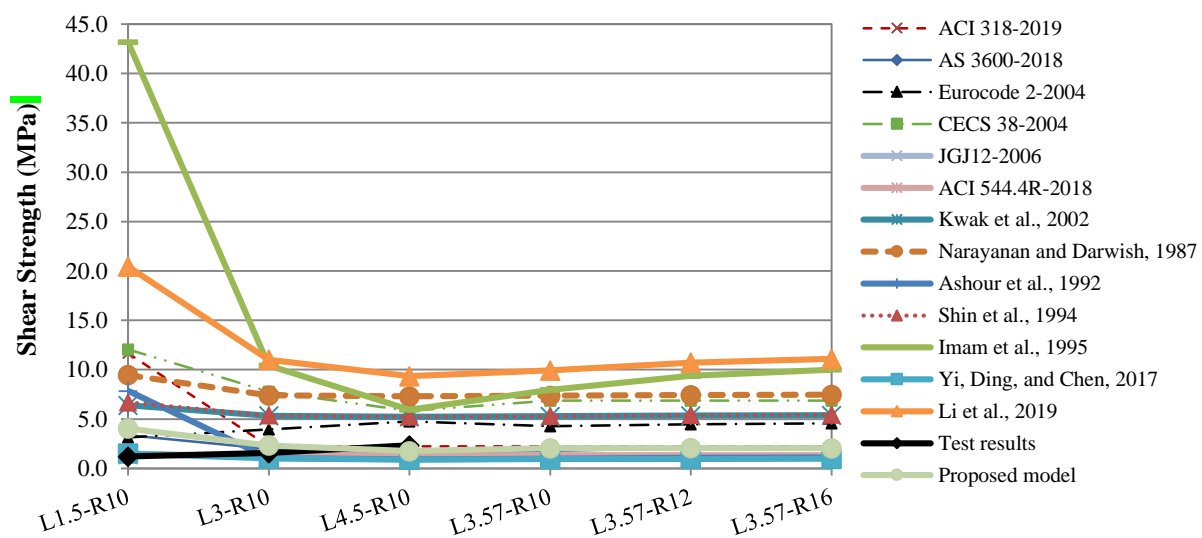


Fig. 10. Shear strength results and values predicted using theoretical and experimental models

The equations of the AS 3600 (2018) and Ashour et al. (2009) models are fundamentally similar, utilizing parameters such as f'_c , A_s , f_y , b , and shear-span depth ratio, with the main distinction being Ashour et al. (2009) including fiber pullout resistance v_b as a shear strength contribution, while ACI 544.4R (2018) does not consider longitudinal reinforcements.

According to Lim et al. (2006), the American code effectively forecasts the ultimate strength of lightweight concrete girders. The remaining seven models, including Euro code 2 (2004), Kwak et al. (2002), Shin et al. (1994), CECS 38 (2004), Narayanan and Darwish (1987), Li et al. (2019), and Imam et al. (1995), consistently underestimated shear strength, with average $v_{fc, THEO} / v_{fc, EXP}$ values below 5.55 and standard deviations under 2, showing deviations exceeding 60% from experimental results.

4. Conclusions

This research investigates the impact of the steel reinforcement ratio and shear-span depth ratio on the FLC beams' behavior. The experimental program provides valuable insights into load capacity, deflection behavior, and fracture propagation. The important conclusions are as follows:

1) The shear-span significantly affects the shear and load capacities of FLC girders. Increasing the shear-span depth ratio from 1.5 to 4.5 reduced shear fracture propagation while increasing flexural crack propagation until a pure flexural crack developed in a low-reinforced sample at a 4.5 shear-span depth ratio. The R10 bars beam with the smallest shear-span depth ratio of 1.5 showed enhanced cracking resistance, cracking deflection, peak resistance, peak deflection, stiffness, ductility ratio, capacity of energy absorption, fracture energy, yield, and ultimate toughness by 146%, 16%, 141%, 55.8%, 91.5%, -43.8%, 106%, 105.6%, 185.81%, and 38.57%, respectively, compared to the R10 bars beam with a 3.57 shear-span depth ratio. Lowering the shear-span depth ratio positively impacted all performance measures except for the ductility ratio. A greater shear span can lead to excessive deflections and increased ductility, with the main crack shifting from the exterior shear spans to the interior flexural bending region, where the girder becomes more flexible.

2) The reinforcement ratio is vital for the load capacity and crack resistance of FLC girders. High-reinforced and medium-reinforced specimens exhibited shear-compression collapse, while the low-reinforced sample showed flexural-compression collapse.

Table 6. Mean, standard deviation, and coefficient of variation of the ratios of the theoretical values of shear strength of FLC beams calculated by each model $v_{fc, THEO}$ to their experimental values $v_{fc, EXP}$

Model	Mean value of $v_{fc, THEO}/v_{fc, EXP}$	Standard deviation SD of $v_{fc, THEO}/v_{fc, EXP}$	Coefficient of Variation CV (%)
Proposed model	0.93	0.37	39.64
ACI 318 (2019)	1.36	0.38	27.94
AS 3600 (2018)	0.92	0.42	45.57
Eurocode 2 (2004)	1.76	1.22	69.21
CECS 38 (2004)	3.04	1.33	43.74
JGJ12 (2006)	0.48	0.25	53.03
ACI 544.4R (2018)	0.54	0.33	60.46
Kwak et al. (2002)	2.23	1.25	56.38
Narayanan and Darwish (1987)	3.12	1.70	54.47
Ashour et al. (1992)	0.77	0.34	44.98
Shin et al. (1994)	2.26	1.25	55.23
Imam et al. (1995)	5.54	1.09	19.66
Yi et al. (2017)	0.42	0.20	47.35
Li et al. (2019)	4.87	1.95	40.06

The R16 bars high-reinforced specimen at a 3.57 shear-span depth ratio demonstrated the greatest improvements in cracking resistance, cracking deflection, peak resistance, stiffness, and yield toughness by 131%, 26%, 95.7%, 80.8%, and 191.85%, respectively, compared with the low-reinforced R10 bars specimen. However, peak deflection, ductility ratio, capacity of energy absorption, fracture energy, and ultimate toughness decreased by -3%, -61.2%, -27%, -26.84%, and -33.13%, respectively. Higher reinforcement ratios enhance tensile strength and crack resistance, but excessive reinforcement can negatively affect the collapse mode, shifting from diagonal tension to shear-compression collapse. High reinforcement ratios may lead to insufficient crack warnings, raising significant safety concerns.

3) Designing FLC beams with varying shear spans and reinforcement ratios necessitates careful attention to relevant design codes and standards. The results of the theoretical to experimental shear strength ratio validate the effectiveness of the current study's model and the AS 3600 (2018) model in accurately predicting the shear strength of fiberglass lightweight concrete girders.

5. References

- Aboul-Nour, L., Gamal, M. and Ghoniem, A. (2023). "Glass fiber for improved behavior of light expanded clay aggregate concrete beams: an experimental study", *Frattura ed Integrità Strutturale (Fracture and Structural Integrity)*, 17(65), 1-16, <https://doi.org/10.3221/IGF-ESIS.65.01>.
- ACI 213R-87. (1987). *Guide for structural lightweight-aggregate concrete*, American Concrete Institute ACI, Farmington Hills, Michigan, USA, <https://www.concrete.org/publications/internationalconcreteabstractsportal.aspx?m=details&id=5099>.
- ACI 318-19. (2019). *Building code requirements for structural concrete (ACI 318-19) commentary on building code requirements for structural concrete (ACI 318R-19)*, American Concrete Institute ACI, Farmington Hills, USA, <https://standards.globalspec.com/std/14349342/aci-318m>.
- ACI 544.4R-88. (1988). "Design considerations for steel fiber reinforced concrete", *American Concrete Institute*, Farmington Hills, Michigan, USA, <https://standards.globalspec.com/std/1210947/aci-544-4r>.
- ACI 544.4R. (2018). "Guide to design with fiber-reinforced concrete", *American Concrete Institute*, Farmington Hills, Michigan, USA, <https://standards.globalspec.com/std/13051488/aci-544-4r>.
- Al-Khafaji, N.H.A. and Harba, I.S.I. (2023). "Shear and flexural behavior of lightweight concrete beams containing hybrid fibers", *Civil and Environmental Engineering*, 19, 206-217, <https://doi.org/10.2478/cee-2023-0018>.
- Alhassan, M., Al-Rousan, R. and Ababneh, A. (2017). "Flexural behavior of lightweight concrete beams encompassing various dosages of macro synthetic fibers and steel ratios", *Case Studies in Construction Materials*, 7, 280-293, <https://doi.org/10.1016/j.cscm.2017.09.004>.
- AS 3600. (2018). *Concrete structures*, Standards Australia Limited, Sydney, <https://store.standards.org.au/product/as-3600-2018>.
- Ashour, S.A., Hasanain, G.S. and Wafa, F.F. (1992). "Shear behavior of high-strength fiber reinforced concrete beams", *American Concrete Institute Structural Journal*, 89(2), 176-184, <https://doi.org/10.14359/2946>.
- ASTM C143/C143M-20. (2020). *Standard test method for slump of hydraulic cement concrete*, American Society of Testing and Materials, ASTM International, West Conshohocken, Philadelphia, USA, <https://standards.globalspec.com/std/14302069/astm-c143-c143m-20>.
- ASTM C150/C150M-22. (2022). *Standard specification for Portland cement*, American Society of Testing and Materials, ASTM International, West Conshohocken, Philadelphia, USA, https://store.astm.org/c0150_c0150m-22.html.
- ASTM C330-23. (2023). *Standard specification for lightweight aggregates for structural concrete*, American Society of Testing and Materials, ASTM International, West Conshohocken, Philadelphia, USA, https://store.astm.org/c0330_c0330m-23.html.
- ASTM C496/C496M-17. (2017). *Standard test method for splitting tensile strength of cylindrical concrete specimens*, American Society of Testing and Materials, ASTM International, West Conshohocken, Philadelphia, USA, <https://standards.globalspec.com/std/4055208/astm-c496-c496m-17>.
- ASTM C642-21. (2021). *Standard test method for*

- density, absorption, and voids in hardened concrete, American Society of Testing and Materials, ASTM International, West Conshohocken, Philadelphia, USA, <https://standards.globalspec.com/std/14510464/astm-c642-21>.
- ASTM C1018-97. (1997). *Standard test method for flexural toughness and first-crack strength of fiber-reinforced concrete (using beam with third-point loading)*, ASTM International, USA, <https://standards.globalspec.com/std/3811416/astm-c1018-97>.
- ASTM E2126-11. (2011). *Standard test methods for cyclic (reversed) load test for shear resistance of vertical elements of the lateral force resisting systems for buildings*, ASTM International, West Conshohocken, PA, USA, <https://doi.org/10.1520/E2126-11>.
- Bozorgmehr Nia, S. and Nemati Chari, M. (2023). "Applied development of sustainable-durable high-performance lightweight concrete: Toward low carbon footprint, durability, and energy saving", *Results in Materials*, 20, 100482, <https://doi.org/10.1016/j.rinma.2023.100482>.
- BS EN 12390-3. (2019). *Testing hardened concrete - Compressive strength of test specimens*, British Standard Institution, London, UK, <https://standards.globalspec.com/std/13376131/bs-en-12390-3>.
- CECS 38. (2004). *Technical specification for fibre reinforced concrete structure*, China Association for Engineering Construction Standardization, <https://www.chinesestandard.net/PDF/English.aspx/CECS38-2004>.
- Deifalla, A., Awad, A., Seleem, H. and Abdelrahman, A. (2020). "Investigating the behavior of lightweight foamed concrete T-beams under torsion, shear, and flexure", *Engineering Structures*, 219, 110741, <https://doi.org/10.1016/j.engstruct.2020.110741>.
- ES 4756-2/2020. (2020). *Cement- Part 2: Assessment and verification of constancy of performance*, Egyptian Organization for Standards and Quality, Egypt, <https://www.eos.org.eg/en/standard/3081>.
- Eurocode 2 (2004). *Design of concrete structures - Part 1-1: General rules and rules for buildings*, European Committee for Standardization (CEN), <https://standards.globalspec.com/std/10010073/aenor-une-en-1992-1-1-eng>.
- Gyawali, T.R. (2023). "Effect of sand types and mixing procedures on the flexural behaviour of the high ductile mortar in monotonic and cyclic loadings", *Heliyon*, 9(3), e14452, <https://doi.org/10.1016/j.heliyon.2023.e14452>.
- Hanoon, A.N., Jaafar, M.S., Hejazi, F. and Abdul Aziz, F.N.A. (2017). "Energy absorption evaluation of reinforced concrete beams under various loading rates based on particle swarm optimization technique", *Engineering Optimization*, 49(9), 1483-1501, <https://doi.org/10.1080/0305215X.2016.1256729>.
- Imam, M.A., Vandewalle, L. and Mortelmans, F. (1995). "Shear - moment analysis of reinforced high strength concrete beams containing steel fibres", *Canadian Journal of Civil Engineering*, 22, 462-470, <https://doi.org/10.1139/L95-054>.
- JGJ12 (2006). *Technical specification for lightweight aggregate concrete structures*, Ministry of Housing and Urban-Rural Construction of the People's Republic of China, China Building Industry Press, Beijing, China, <https://www.chinesestandard.net/PDF/English.aspx/JGJ12-2006>.
- Jiao, C., Xu, B., Gao, J. and Wang, L. (2017). "Experiments on shear resistance of steel fiber reinforced lightweight aggregate concrete beams", *Journal of Civil Engineering and Management*, 34, 9-13, <http://dx.doi.org/10.13579/j.cnki.2095-0985.2017.02.003>.
- Karuppannan Gopalraj, S. and Kärki, T. (2020). "A review on the recycling of waste carbon fibre/glass fibre-reinforced composites: fibre recovery, properties and life-cycle analysis", *SN Applied Sciences*, 2(3), 433, <https://doi.org/10.1007/s42452-020-2195-4>.
- Kumar, R. and Srivastava, A. (2023). "Influence of lightweight aggregates and supplementary cementitious materials on the properties of lightweight aggregate concretes", *Iranian Journal of Science and Technology, Transactions of Civil Engineering*, 47(2), 663-689, <https://doi.org/10.1007/s40996-022-00935-5>.
- Kwak, Y.K., Eberhard, M.O., Kim, W.S. and Kim, J. (2002). "Shear strength of steel fiber-reinforced concrete beams without stirrups", *American Concrete Institute Structural Journal*, 99(4), 530-538, <https://doi.org/10.14359/12122>.
- Li, S., Chen, W., Hu, J., Zhang, D. and Chen, L. (2024). "Flexural behavior of unbounded prestressed concrete composite beams manufactured with glass-fiber-reinforced lightweight aggregate concrete and conventional concrete", *Iranian Journal of Science and Technology, Transactions of Civil Engineering*, 48(4), 2031-2047, <https://doi.org/10.1007/s40996-023-01297-2>.
- Li, X., Li, C., Zhao, M., Yang, H. and Zhou, S. (2019). "Testing and prediction of shear performance for steel fiber reinforced expanded-shale lightweight concrete beams without web reinforcements", *Materials*, 12(10), 1594,

- <https://doi.org/10.3390/ma12101594>.
- Li, C., Zhao, M., Geng, H., Fu, H., Zhang, X. and Li, X. (2021). "Shear testing of steel fiber reinforced expanded-shale lightweight concrete beams with varying of shear-span to depth ratio and stirrups", *Case Studies in Construction Materials*, 14, e00550, <https://doi.org/10.1016/j.cscm.2021.e00550>.
- Lim, H., Wee, T., Mansur, M. and Kong, K. (2006). "Flexural behavior of reinforced lightweight aggregate concrete beams", *Proceedings of the 6th Asia-Pacific Structural Engineering and Construction Conference (APSEC 2006)*, 5-6, https://www.researchgate.net/publication/325146207_flexural_behavior_of_reinforced_light_weight_aggregate_concrete_beams.
- Mirza, F.A. and Soroushian, P. (2002). "Effects of alkali-resistant glass fiber reinforcement on crack and temperature resistance of lightweight concrete", *Cement and Concrete Composites*, 24(2), 223-227, [https://doi.org/10.1016/S0958-9465\(01\)00038-5](https://doi.org/10.1016/S0958-9465(01)00038-5).
- Narayanan, R. and Darwish, I.Y.S. (1987). "Use of steel fibers as shear reinforcement", *American Concrete Institute Structural Journal*, 84(3), 216-227, <https://doi.org/10.14359/2654>.
- Safiuddin, M., Abdel-Sayed, G. and Hearn, N. (2022). "Flexural and impact behaviors of mortar composite including carbon fibers", *Materials*, 15(5), 1657, <https://doi.org/10.3390/ma15051657>.
- Sajedi, F. and Shafigh, P. (2012). "High-strength lightweight concrete using leca, silica fume, and limestone", *Arabian Journal for Science and Engineering*, 37(7), 1885-1893, <https://doi.org/10.1007/S13369-012-0285-3>.
- Sathishkumar, T., Satheeshkumar, S. and Naveen, J. (2014). "Glass fiber-reinforced polymer composites, A review", *Journal of Reinforced Plastics and Composites*, 33, 1258-1275, <https://doi.org/10.1177/0731684414530790>.
- Sathiyamoorthy, K. (2021). "Shear and flexural behaviour of lightweight self-consolidating concrete beams", PhD Thesis, Ryerson University, <https://doi.org/10.32920/ryerson.14662374.v1>.
- Shafigh, P., Hassanpour, M., Razavi, S. and Kobraei, M. (2011). "An investigation of the flexural behaviour of reinforced lightweight concrete beams", *International Journal of Physical Sciences*, 6(10), 2414-2421, <https://doi.org/10.5897/IJPS10.550>.
- Shin, S.W., Oh, J.G. and Ghosh, S.K. (1994). "Shear behavior of laboratory-sized high-strength concrete beams reinforced with bars and steel fibers", *Special Publication*, 142, 181-200, <https://doi.org/10.14359/3917>.
- Vakili, S.E., Homami, P. and Esfahani, M.R. (2019). "Flexural behavior of lightweight concrete beams reinforced with GFRP bars and effects of the added micro and macro fiber", *Civil Engineering Infrastructures Journal*, 52(2), 349-363, <https://doi.org/10.22059/cej.2019.277143.1557>.
- Wang, H.T. and Wang, L.C. (2013). "Experimental study on static and dynamic mechanical properties of steel fiber reinforced lightweight aggregate concrete", *Construction and Building Materials*, 38, 1146-1151, <https://doi.org/10.1016/j.conbuildmat.2012.09.016>.
- Wang, Z., Xie, J., Li, J., Liu, P., Shi, C. and Lu, Z. (2022). "Flexural behaviour of seawater-sea sand concrete beams reinforced with GFRP bars: Effects of the reinforcement ratio, stirrup ratio, shear span ratio and prestress level", *Journal of Building Engineering*, 54, 104566, <https://doi.org/10.1016/j.jobe.2022.104566>.
- Yi, W., Ding, Y. and Chen, H. (2017). "Experimental study on shear behavior of lightweight aggregate concrete beams without stirrups", *Journal of Building Structures*, 6, 123-132, <http://dx.doi.org/10.14006/j.jzjgxb.2017.06.014>.
- Yin, Y. and Hu, S. (2021). "Effects of span-depth ratios on the energy release rate for three-point bending beams", *Engineering Fracture Mechanics*, 244, 107567, <https://doi.org/10.1016/j.engfracmech.2021.107567>.
- Zhu, H., Cheng, S., Gao, D., Neaz, S.M. and Li, C. (2018). "Flexural behavior of partially fiber-reinforced high-strength concrete beams reinforced with FRP bars", *Construction and Building Materials*, 161, 587-597, <https://doi.org/10.1016/j.conbuildmat.2017.12.003>.



This article is an open-access article distributed under the terms and conditions of the Creative Commons Attribution (CC-BY) license.



Topology Optimization of Wave Barriers for Mitigating Dynamic Compaction-Induced Vibrations Using a Coupled CMA-ES/Finite-Element Method

Abedini, F.¹, Rafiee-Dehkharghani, R.^{2*} and Laknejadi, K.³

¹ Ph.D. Candidate, School of Civil Engineering, College of Engineering, University of Tehran, Tehran, Iran.

² Assistant Professor, School of Civil Engineering, College of Engineering, University of Tehran, Tehran, Iran.

³ Assistant Professor, Islamic Azad University, Science and Research Branch, Tehran, Iran.

© University of Tehran 2024

Received: 16 Dec. 2023;

Revised: 26 May 2024;

Accepted: 10 Jun. 2024

ABSTRACT: This paper aims to find optimal wave barriers for mitigating the ground-borne vibrations induced during Dynamic Compaction (DC). Within this context, two types of barriers are considered. The first type of barrier has a classic rectangular shape, and they are arranged in single, double, and quadruple configurations. The second type involves a distributed grout barrier located within a designated area, characterized by varying grout densities. In this research, the Finite Element (FE) method is used to simulate the dynamic compaction problem, and soil nonlinearity is considered due to the development of large deformations around the tamping point in dynamic compaction. Covariance Matrix Adaptation Evolution Strategy (CMA-ES) serves as a robust optimization tool and is coupled to FE simulations using comprehensive Python scripts to find the optimal barrier configuration. The findings from the study reveal that the number of rectangular barriers does not necessarily increase mitigation capacity. Furthermore, the barriers' Mitigation Capacity (MC) depends on their filling material and filled percentage. Moreover, the investigation of distributed grout barriers reveals an interesting observation that the optimal configuration for the grout distribution tends to form an approximate W-shaped pattern.

Keywords: Dynamic Compaction, Ground-Borne Vibration, Optimization, Wave Barrier, CAM-ES, Finite Element.

1. Introduction

Vibration mitigation is a holistic concept, involving a wide array of methods aimed at effectively reducing vibrations. In some cases, base isolation can be implemented; but it is limited to active seismic zones, considering the relatively high costs associated with implementation.

Additionally, cost-effective yet efficient mitigation methods, such as wave barriers and ground improvement techniques, can be used (Jayawardana et al., 2019a). Open and in-filled trenches, piles, sheet piles, heavy mass technology, scrap tire isolation walls, and soil grouting can also be used for mitigating vibrations induced by heavy machinery and trains (Mahdavisefat et al.,

* Corresponding author E-mail: rezarafiee@ut.ac.ir

2017; Saikia and Das, 2014). In general, wave barriers can be classified into two categories: stiff barriers and soft barriers, distinguished by their impedance mismatch with the soil. For instance, concrete-filled trenches are stiff barriers, while bentonite-filled trenches or gas cushions are soft barriers. Svinkin (2004) categorized vibration consequences into three groups: structure vibrations, resonant structure response, and dynamic settlements. In the literature, the parameters of trench width, depth, and location are primarily studied. However, other factors, such as trench shape (Esmaeili et al., 2014; Yarmohammadi et al., 2018; Zakeri et al., 2014), buried depth (Feng et al., 2019; Moussa and El Naggar, 2020), and trench inclination angle (Cho, 2021; Herbut, 2020), are also investigated in the literature.

The conversion of Rayleigh waves to other types of waves, such as primary or secondary waves (p and s waves), is called mode conversion. The barrier functionality is evaluated based on the percentage of the waves spreading, reflecting, or refracting from the barrier. In open trenches, reflection plays the governing role; however, in the filled trenches, mode conversion is also of great importance. Installing trenches in the wave path causes discontinuity and lengthens the path. Thus, it may lead to a considerable decrease in wave energy.

Moreover, the Rayleigh wave amplitude diminishes with depth. It is observed that vibrations decrease by 90% at a depth of $1.5 \lambda_R$ (Rayleigh wavelength). Barriers can be open or filled with different materials, such as water, concrete, and bentonite. Open trenches are the most effective ones since they can block wave transmission. However, researchers have always looked for new materials to fill the trenches. For instance, some studies are performed to evaluate the efficiency of water, geofoam, concrete, bentonite, Tire-Derived Aggregates (TDA), and tire chips (Alzawi, 2011; Ekanayake et al., 2014; Fathi Afshar et al., 2024; Moussa and El Naggar, 2020; Tandon et al., 2023). In case of instability,

geofoam-filled trenches can be used instead of open trenches (Mahdavisefat et al., 2017). One of the novel methods of blocking vibrations is using metamaterials that control wave energy. Gao and Shi (2019) used barriers made of layered metamaterials, and frequency and time-domain analyses proved their satisfactory functionality.

These barriers are called wave-guided barriers. Majumder and Venkatraman (2023) conducted a state-of-the-art review on vibration screening techniques using open and in-filled trenches. Persson (2013) mentioned that when Rayleigh waves impinge on a filled barrier, five different scenarios happen for the incident wave: 1) Rayleigh wave that reflects from the trench; 2) Rayleigh wave that passes through the trench; 3) body wave that disseminates backward and deep in the soil; 4) body-wave that spreads in the domain; and 5) body-wave that travels beneath the trench.

Vibrations occurring in the locations after the trench are mainly due to Types 2, 4, and 5. Optimization has been used in geotechnical engineering for different usages, such as wave barriers (Jayawardana et al., 2019b; Sigmund et al., 2016), dynamic compaction (Bayat et al., 2023), and foundation design (Jelušić and Žlender, 2018; Juang and Wang, 2013; Sadeghi et al., 2021). Specifically, Yarmohammadi and Rafiee-Dehkharghani (2020), Rezaie et al. (2018), and Dolatshahi et al. (2020) applied topology optimization in studying wave barriers. Analytical, numerical, or experimental methods can be utilized to study trenches' functionality. Numerical approaches, such as the Boundary Element Method (BEM), Finite Element Method (FEM), and Finite Difference Method (FDM), are used since closed-form solutions are not always easy to achieve.

Moreover, analytical methods are limited to simple boundary conditions and specific geometries. Additionally, experimental methods are often complex and expensive to implement. The promising results of previous numerical research

validate the fidelity of numerical methods (Ahmad and Al-Hosseini, 1991; Bian et al., 2016; Mahdavisefat et al., 2017). Either two-dimensional (2-D) or three-dimensional (3-D) models can be utilized in the analysis. Saikia and Das (2014) compared 2-D and 3-D models and concluded that 2-D models yield approximately 11-12% error. Moreover, research has demonstrated that 2-D simulations cannot fully capture geometric damping. It is beyond doubt that 3-D models are more accurate; however, their computational cost is significant (Norén-Cosgriff et al., 2019). Therefore, there is still a strong trend toward using 2-D simulations, particularly in optimization problems, where numerous numerical iterations are required. This paper studies different governing parameters that affect the performance of wave barriers, considering DC-induced vibrations. The affecting parameters are the trench's width and depth, the trench's location, and the filled percentage of the trench. Finding the most effective wave barrier is complex since all the previously mentioned affecting parameters are interdependent. Hence, the Covariance Matrix Adaptation Evolution Strategy (CMA-ES) is implemented to find the optimum topology of the wave barriers.

The optimization algorithm is coupled with Finite Element (FE) simulations for finding the fitness function. Moreover, parametric studies and verifications ascertain the reliability of the results. Some researchers have studied the effectiveness of coupling optimization algorithms with FE simulation in complex optimal design problems (Rafiee-Dehkharghani et al., 2018). The studied barriers have two types: 1) rectangular barriers that are open, filled, or partially filled; 2) distributed grout with different densities that are scattered within a discretized domain using the topology optimization concept. The term "rectangular" refers to the barrier cross-section in the FE simulations. The rectangular barriers can be arranged in single, double, and quadrupole

configurations. The studied problem and two proposed vibration mitigation approaches are detailed in the following sections. Further, modelling specifics, optimization methods, and results are presented in subsequent sections.

2. Problem Definition

DC tamping generates surface vibrations due to the generation of Rayleigh waves. Two approaches are chosen to control the vibrations with wave barriers: 1) designing rectangular trenches; and 2) distributing grout in the domain to find the optimal topology of the barrier. In the first approach, one, two, or four (the determination of the maximum number of trenches is based on the limitations imposed by the width and distance within the domain) trenches can be installed in the disturbed zone. The efficiency of the trenches depends on various parameters, such as geometry, location, filling material properties of the barriers, and the filled percentage. The primary objective is to trap these waves by installing wave barriers between the loading and receiving/observation points. It is not feasible to install the barriers in the close vicinity of the excitation and receiving points; thereby, a clear distance of L_R and L_T is considered as shown in Figure 1. The domain that remains in between is called the optimization/disturbed zone. Moreover, a minimum distance of 0.5 m is maintained between trenches in case of multiple trenches to consider practical limitations.

The general schematic of the DC problem studied in this paper is shown in Figure 1, where w_b , d_b , and L stand for the trench's width, depth, and distance from the tamping point, respectively. In the second approach, the grout is distributed in the design domain to find the best topology for the ideal wave barrier. Thereby, the domain is discretized into smaller cells (1×1 m), with grout distributed within these cells. Due to the large solution domain and the interdependence of these parameters,

conducting separate parametric studies to assess their influences is not feasible. As a result, it is required to use optimization algorithms such as CMA-ES to find the optimal configuration. The objective function of the optimization is to minimize the Peak Particle Velocity (PPV) at the receiving point. The 2-D axisymmetric model and Mohr-Coulomb constitutive law are used in FE simulations of the problem.

A similar constitutive law is used by Pan and Selby (2002), and it is observed that the Mohr-Coulomb model can successfully simulate the DC phenomenon. The Mohr-Coulomb model is a suitable option since it is not always easy to find the values of the necessary parameters of other constitutive models (Mehdipour and Hamidi, 2017). In this vein, more complex constitutive models do not always outperform simpler ones, as they often present challenges in parameter calibration. The Mohr-Coulomb model is utilized in this research, considering that the focus is on the optimization process. The schematic of the axisymmetric problem for approaches 1 and 2 is depicted in Figure 1.

3. Numerical Modelling and DC Loading

FE numerical simulations are used for

modelling the DC problem in this paper. To do so, ABAQUS commercial software is used to capture the transient dynamic loading nature of the tamping phenomenon.

Soil is assumed to have a homogeneous, isotropic, and elastoplastic medium. Material nonlinearity is considered as the DC-induced strains are large. The axisymmetric model is used in this study due to the symmetry of the problem, and reducing the computational cost. The FE domain is selected to be large enough to prevent wave reflections from the boundaries (Figure 2). The model dimension is tailored based on the total loading duration to ensure that the waves reach the observation point, but do not reflect and affect the results. The observation point is located 17 m from the tamping point. The location of the observation point is chosen based on practical matters.

3.1. Loading

The impact load induces surface displacements. Regarding propagation, Rayleigh waves are considered to be surface waves, meaning they travel on the top layers of the soil.

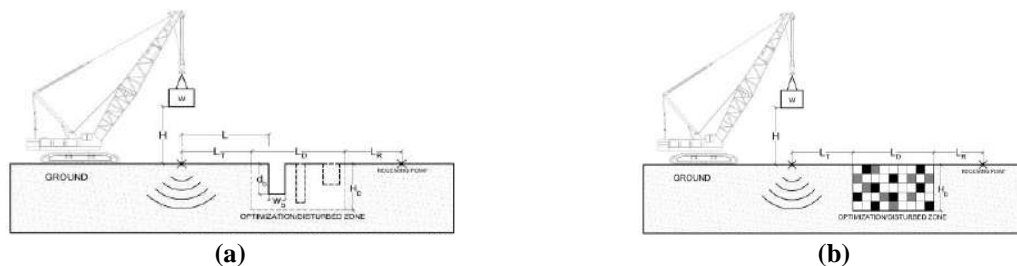


Fig. 1. Schematic of the problem and two approaches for vibration mitigation: a) Approach 1: single or multiple barriers; and b) Approach 2: material distribution or topology optimization

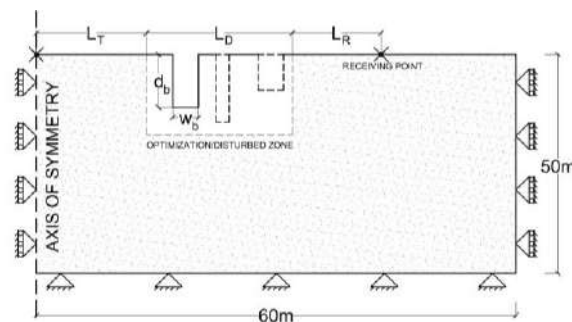


Fig. 2. Axisymmetric FE model

They propagate outward from the source of the excitation, affecting a wide area of the surface. Modelling DC in detail is complex, involving numerous parameters that describe the interaction between the tamper and soil upon impact. Due to DC's cost-effectiveness as a ground improvement technique, these parameters are often not readily accessible. Moreover, incorporating all these intricacies into the model increases computational costs without necessarily improving accuracy. Therefore, it is required to use simplified methods for modelling DC loading. Within this context, Pan and Selby (2002) studied DC using ABAQUS models under two loading cases: 1. applying an approximate half-sine force-time profile on the ground; and 2. detailed tamper impact modelling. It was demonstrated that a half-sine loading graph simulates the tamping scenario well (Mayne and Jones Jr, 1983; Scott and Pearce, 1975).

Figure 3 shows the soil stress induced by a 10-ton rigid mass dropping from a height of 11.5 m (Abedini et al., 2022). To model the impact scenario, the velocity of the $\sqrt{2gh}$ (where g is the gravity acceleration and h is the dropping height) is

applied to the tamper's reference point, and the force history profile is extracted at the tamping interface as shown in Figure 3, considering the rigid contact between the soil and tamper. Furthermore, the *PPV* of the soil nodes at different locations from the tamping points is extracted for two types of loadings (half-sine load estimation and rigid impact modelling) and compared in Figure 4. The results in this figure show that the *PPVs* obtained using the simplified half-sine loading closely align with those from more detailed impact modelling; therefore, the DC loading is simulated by a half-sine profile. This is computationally very efficient as this paper focuses on optimizing the barriers.

3.2. FE Mesh Size and Time Step

Spatial and time discretization are very critical factors for accurate FE modelling. Using small elements increases the accuracy and the computational cost; hence, it is required to find an optimal mesh size using convergence analysis. Since the model is axisymmetric, CAX4R elements (4-node axisymmetric elements in the ABAQUS library) are used to mesh the model domain.

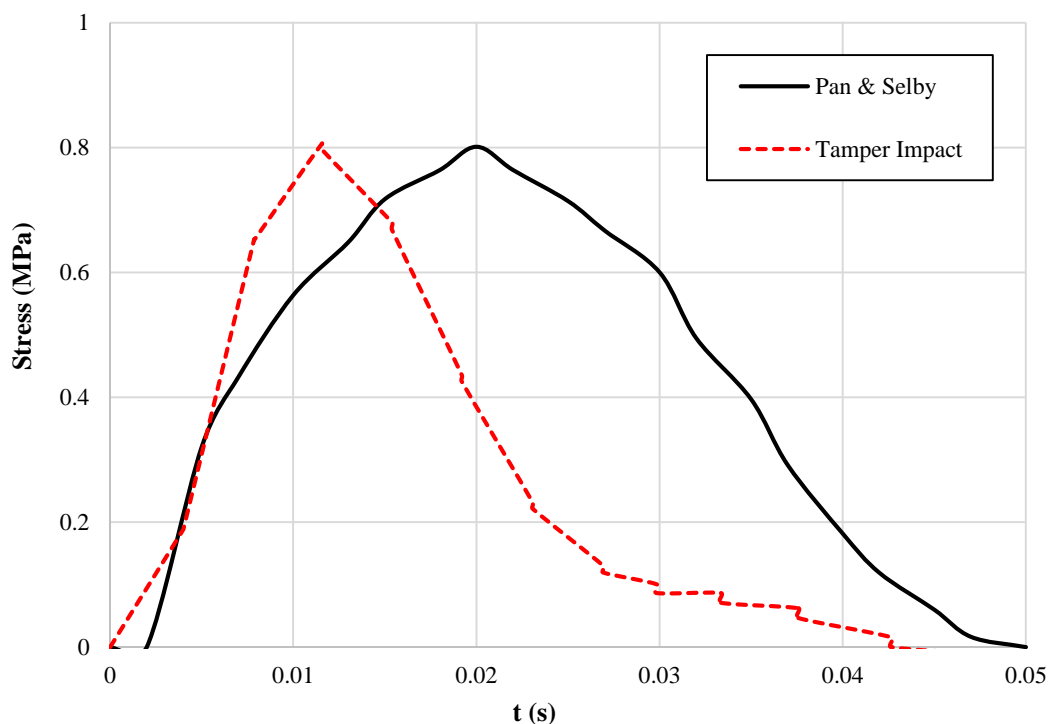


Fig. 3. Half-sine tamping loadings

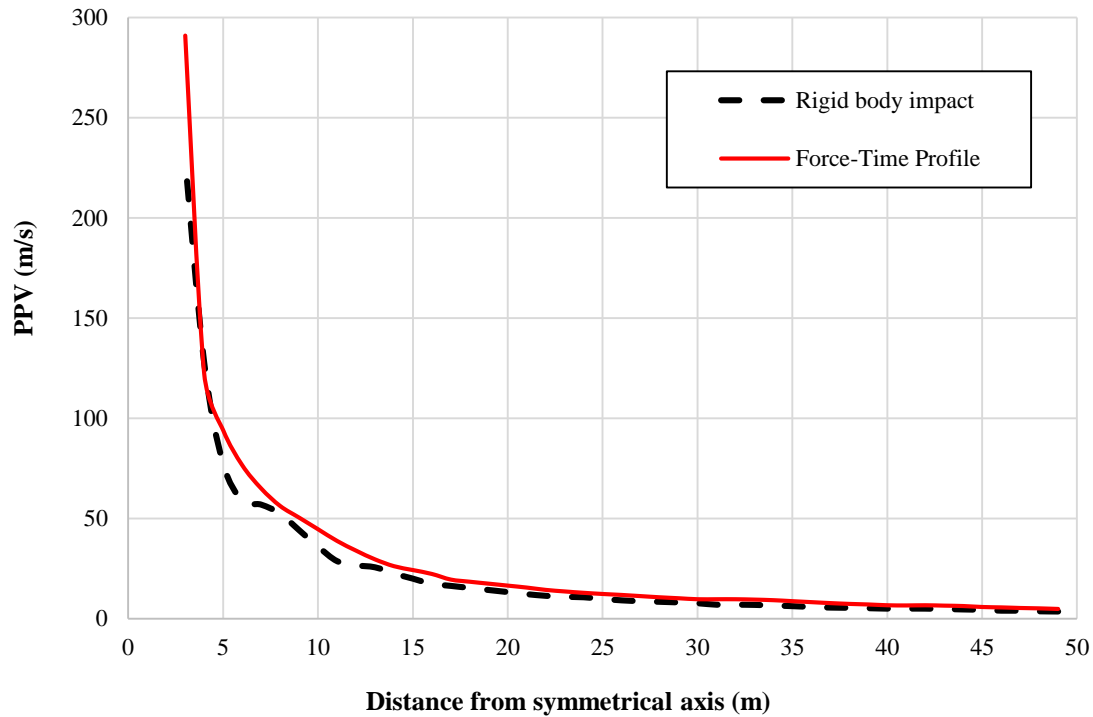


Fig. 4. Soil nodes PPVs at different distances

Having approximately ten nodes per wavelength is recommended, as this directly affects both time and computational costs (Norén-Cosgriff et al., 2019). In this study, the Rayleigh wave velocity of the soil and the loading frequency are 30 m/s and 10 Hz, respectively. Therefore, the maximum mesh size is $0.2 \times 30 / 10 = 0.6$ m.

Additionally, convergence analyses are conducted to ensure accuracy, with the final maximum size selected as 0.5 m. The dynamic analyses are performed using ABAQUS/Explicit Solver. The time increments (Δt) are selected based on the maximum element size and wave speed in the soil. This is automatically selected in the explicit solver. For more detailed information on this topic, it is recommended to refer to the ABAQUS manual (Abaqus, 2014), which provides comprehensive guidance and instructions.

4. FE Model Verification

One of the main challenges in verifying numerical models is the limited availability of comprehensive data. Many field studies, especially older ones, do not provide sufficient data for building and calibrating

numerical models. To verify the results, a model is constructed using sandy soil characterized by the properties listed in Table 1. Two different tampers with masses of 10 and 25 tons are dropped separately from a height of 10 m and 20 m, respectively. Figure 5 exhibits a perfect match between the results obtained from the FE models and the field measurements conducted by Lukas (1986). This correspondence validates the accuracy and reliability of the FE models in capturing the real-world behavior of the DC. In Figure 5, m and H denote the tamper mass and drop height, respectively.

5. Material Properties of the Ground and Barriers

The soil properties are elaborated in Table 2, where V_s and V_R represent the shear wave velocity ($V_s = \sqrt{\frac{E}{2\rho(1+\nu)}}$) and Rayleigh wave velocity ($V_R = V_s \times \frac{(0.862+1.14\nu)}{(1+\nu)}$), respectively. Damping is a critical issue in dynamic analysis. Rayleigh damping is applied in the model with the coefficients of $\eta_1 = 0$ and $\eta_2 = 0.01$, where η_1 and η_2 are the mass and stiffness damping coefficients, respectively.

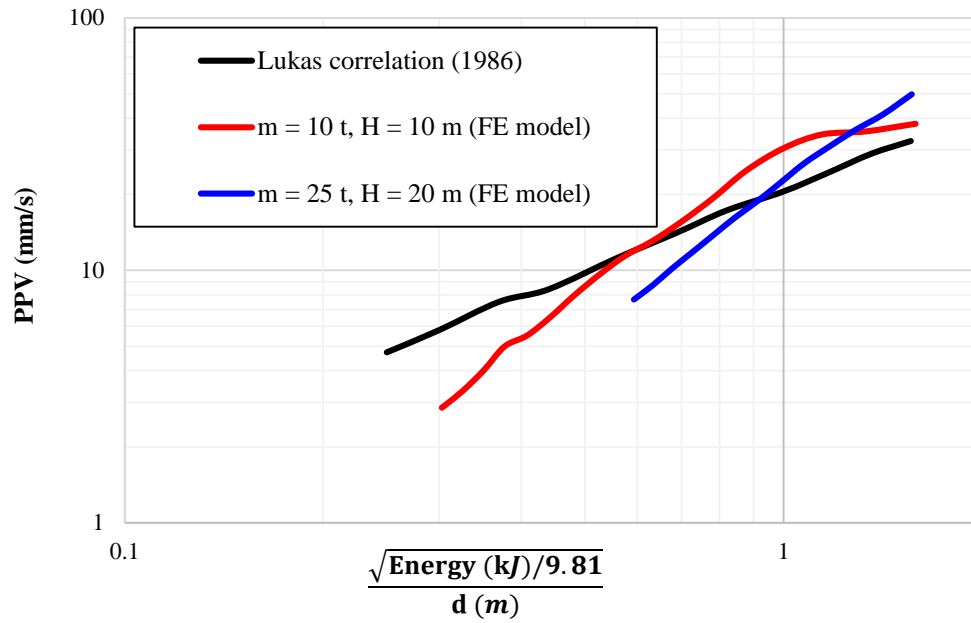


Fig. 5. FE model verification

Table 1. Sandy soil properties for verification

ρ	ν	ϕ	E
1600 kg/m ³	0.25	30 degrees	25 Mpa

Table 2. Ground properties

Elastic modulus (E)	Friction angle (ϕ)	Cohesion (C)	Poisson's ratio (ν)	Density (ρ)	V_s	V_R
5 Mpa	25 degrees	5 KPa	0.35	1800 kg/m ³	32 m/s	30 m/s

Eq. (1) shows the Rayleigh damping formula where ω is the circular frequency, and α and β are Rayleigh damping coefficients (Chopra, 2007).

$$\xi = \frac{1}{2\omega} \alpha + \frac{\omega}{2} \beta \quad (1)$$

Filling material is one of the governing factors in trenches. In other words, the impedance mismatch ratio (IR) between the soil and the filling material of the trench affects waves' transmission. Impedance mismatch between the soil and the filling material significantly affects the efficiency of the wave barriers. A high IR shows a significant difference in impedance between the materials, which leads to reflections of waves at the interface. These reflections can result in wave energy being directed back into the soil or spread through the barrier. IR is defined in Eq. (2) and is zero for the open trench. The mechanical

properties of the filling materials (concrete and Soil-Bentonite Mixture (SBM)) used in this paper are detailed in Table 3.

$$IR = \frac{\rho \times V_{s \text{ filling material}}}{\rho \times V_{s \text{ soil}}} \quad (2)$$

6. Optimization Method

Topology optimization is one of the important methods of optimization. By employing topology optimization techniques, the barriers are engineered to disrupt and attenuate the transmission of waves induced by dynamic compaction.

Rayleigh waves have the highest energy and are the most destructive ones; thereby, the main attention and discussions are on Rayleigh waves. Different objective functions, such as displacement, velocity, and compliance, can be defined based on the problem's purpose. Minimizing the

vertical *PPV* at the receiving point is the objective function of the optimization in the current study. *PPV* is measured by obtaining the velocity record from ABAQUS and finding the maximum of the absolute values. In this paper, topology optimization of barriers is studied using CMA-ES. Meta-heuristic algorithms, such as CMA-ES, treat the problem as a black box, providing a specific response for any given inputs; hence, they can solve a wide range of optimization problems. This strategy is based on the normal distribution and uses the covariance matrix (C), population size (λ), mean (m), and step size (σ).

Covariance shows the variables' dependency and controls the shape of the distribution ellipsoid. The mean vector represents the favourite solution, and the step size controls the step length. These parameters are continually updated in each iteration based on the outcomes of previous steps. Many references on CMA-ES optimization are available in the literature, among which the interested readers are referred to Hansen (2019) and Hansen and Auger (2014). CMA-ES is a robust adaptive meta-heuristic strategy for optimizing continuous variables. Its speed and computational cost are satisfactory.

Therefore, it is a suitable optimization method for the current problem. For instance, CMA-ES has outranked 31 other optimization methods in one research of Black-Box optimizations (Hansen et al., 2010). At each population or optimization step, the geometry of the ABAQUS FE model changes and needs to be updated. Applying these changes in each population using the graphical user interface of ABAQUS is a time-consuming and fairly impossible process.

Therefore, the connection between the optimization algorithm and FE models should be automated; in other words, they need to be coupled. Comprehensive Python codes are developed to couple the optimization algorithm with FE models.

These codes create new FE models

based on different parameters defined within the optimization process. The following steps are performed in the Python scripts created for the coupled CMA-ES/FE procedure: 1) Creating different parts of the FE model, allocating different material properties and sections based on the optimization variables developed in the optimization process; 2) applying loads and boundary conditions to the model; 3) meshing the model with appropriate mesh size; 4) simulating the FE model using dynamic explicit analysis; 5) Exporting the FE model outputs to a file to be used in the updating process of the objective function. This process continues until the termination criterion is satisfied (here set to 10^{-2} , setting 10^{-2} as the termination criterion means optimization stops when the range between the best objective function values of recent and past generations is less than 10^{-2} . The selection of the termination limit depends on the problem.). Multiprocessing is utilized in certain cases due to the high computational cost (multiprocessing with five cores in single trenches, and two cores in dual and quadruple trenches).

6.1. Optimization of the Rectangular Trenches

Optimization variables are width (w_b), depth (d_b) and trench's distance from the tamping point for the open, filled, and partially filled rectangular trenches (L). In addition to the stated variables, a Filled Percentage (FP) is considered as the fourth variable in the partially-filled trenches.

Width varies between 1 and 2 m, depth ranges between 1 and 7 m, location can have values between 2 and 12 m, and filled percentage ranges between 0 and 100 percent. The optimization constraint is applied to the total excavation volume and is set to be $10 \text{ m}^3/\text{m}$. This constraint ensures that the excavation volume remains within the specified limit. It is assumed that an excavation volume of more than $10 \text{ m}^3/\text{m}$ is not economically and operationally suitable.

Table 3. Filling material properties

Filling material	ρ (kg/m ³)	E (MPa)	ν	V_s (m/s)	IR
Concrete	2400	20000	0.15	1903	79
SBM	1200	3.13	0.45	30	0.63

6.2. Material Distribution in the Domain

Topology optimization searches for novel designs within a specified domain, adhering to the specific constraint of an excavation volume of 10 m³/m in this study. In this case, the optimization zone is discretized into 1×1 m cells (77 grids) within a 7 ×11 m domain, as illustrated in Figure 1b. The selection of cell size should achieve a balance between accuracy and computational efficiency, ensuring robust results for the problem. Optimization variables are densities assigned to each cell within the optimization zone. The optimization algorithm generates 77 different densities (optimization variables), each ranging from 0 to 1. A density of 0 indicates the cell is not grouted (pure soil), while 1 signifies a fully grouted cell. While intermediate values between 0 and 1 are generated during the optimization process, the optimal design ideally consists only of 0 and 1. A penalization factor (P) is defined based on Eq. (3), where k : stands for the iteration step to decrease intermediate values. P increases according to generation increase, reaching a value of 5 at maximum (Groenwold and Etman, 2010; Seitz and Grabe, 2016). Soil properties in each cell are calculated by interpolating between the soil and grout properties based on Eq. (4) showing interpolation of elastic modulus for each grid (E_{grid}) using density (ρ) and penalization factor (P).

$$P = \begin{cases} 1 & , k < 10 \\ \min(5, 1.021^{k-10}) & , k \geq 10 \end{cases} \quad (3)$$

$$E_{grid} = E_{soil} + \rho^P \times (E_{grout} - E_{soil}) \quad (4)$$

This interpolation can also be used for other material properties (Seitz and Grabe, 2016). Grout properties are indicated in Table 4. Grout properties are calculated based on the case studies reported in Toraldo et al. (2018). The grout density is chosen to be the same as that of the soil, as

recommended by Croce et al. (2014).

Young's elasticity modulus is calculated based on Eq. (5), where C : stands for cohesion and β : is a dimensionless coefficient, which depends on soil type. Based on case studies reported in Toraldo et al. (2018), β ranges between 330 and 830 for silty sand. For this study, a value of 400 has been selected, and α is subsequently calculated using Eq. (6). Cohesion and friction angle values are chosen based on the study by Toraldo et al. (2018).

$$E = \frac{C}{\alpha} \times \beta \quad (5)$$

$$\alpha = \frac{1}{2 \tan(\frac{\pi}{4} + \frac{\phi}{2})} \quad (6)$$

7. Results and Discussion

This section discusses optimization results. Each optimization process is repeated at least twice to verify its accuracy and avoid local optima. The primary focus of using wave barriers is to attenuate vertical vibrations, particularly in cases where the ground loading is vertical, such as with DC loads in this paper. Attenuation is achieved through spreading, reflecting, or refracting waves from the barrier. Therefore, all simulations, results, and suggestions provided in this section are related to the vertical direction. These results cannot be extrapolated to the horizontal vibrations as their mitigation pattern is entirely different from the vertical vibrations. Results of two different approaches are presented separately in the following subsections.

PPV is 21 mm/s at the receiving point without any trenches or grouting (i.e., pure soil). Mitigation Capacity (MC) is defined by Eq. (7) to quantify the functionality of trenches, where design stands for the disturbed soil, and pure soil indicates the soil without any trench or grouting. The higher the MC, the more the trench

functionality. MC is used to compare the trenches functionality in the subsequent sections.

7.1. Rectangular Trenches

Rectangular trenches have been examined in three distinct scenarios: single, dual, and quadruple trenches. The outcomes of each case are detailed in the following sections.

7.1.1. Single Trench System

Optimization results are reported in Tables 5 and 6, in which L represents the distance between the loading and the trench, w_b and d_b stand for the trench width and depth, respectively.

Table 4. Grout properties

Elastic modulus (E)	Friction angle (ϕ)	Cohesion (C)	Density (ρ)
4 GPa	26 degrees	3.2 MPa	1800 kg/m ³

$$MC = \frac{\text{Objective function}_{\text{design}} - \text{Objective fur}}{\text{Objective function}_{\text{pure soil}}} \times 100 \quad (7)$$

Installing trenches in the wave path causes discontinuity and lengthens the path. As results reveal (Tables 5 and 6), open trenches are more effective compared to in-filled trenches due to the absence of energy transfer through them. Figure 6a to 6c illustrates various trench configurations. Partially filled trenches with concrete have shown effectiveness. Partially concrete-

filled trenches with a 10% filled percentage (FP) have been found to offer the highest MC, which is 48.5% (Figure 6c and Table 6).

However, SBM-filled trenches are not suitable and yield results similar to open trenches (Tables 5 and 6). These tables show that deep active trenches are the most effective open trenches. The optimized depth reaches the maximum allowable value in the optimization procedure, implying the close relationship between the trench depth and vibration mitigation. Table 5 indicates that open trenches can mitigate the vibrations by up to 46%. The field results reported by Fathi Afshar et al. (2024) showed that the open trenches can have an effectiveness of 50%.

7.1.2. Dual System Trench

The performance of open trenches surpasses that of other single trench systems. As a result, the current section focuses only on the study of open dual trenches. In this section, a similar constraint is defined over the volume of excavation (10 m³/m) to make the results comparable with those for the single trenches. Table 7 elaborates on the dual trenches system optimization results. Open dual trenches have similar constraints in width, depth, and distance as single trenches. In addition to the previously mentioned constraints, it is advisable to keep a minimum distance of 0.5 m between each trench to address practical concerns.

Table 5. Optimized variables of open and filled trenches

Material	Impedance ratio	Optimized variables				
		w_b (m)	d_b (m)	L (m)	PPV (mm/s)	MC (%)
Open	0	1.2	7.0	2.0	11.4	46.0
SBM	0.63	2.0	2.8	7.0	18.8	10.3
Concrete	79.0	1.4	7.0	8.7	20.0	4.9

Table 6. Optimized variables of partially-filled trenches

Material	Impedance ratio	Optimized variables					
		w_b (m)	d_b (m)	L (m)	FP (%)	PPV (mm/s)	MC (%)
SBM	0.63	1.2	7	2.1	0	0	45.2
Concrete	79.0	1.3	7	6.3	10	10	48.5

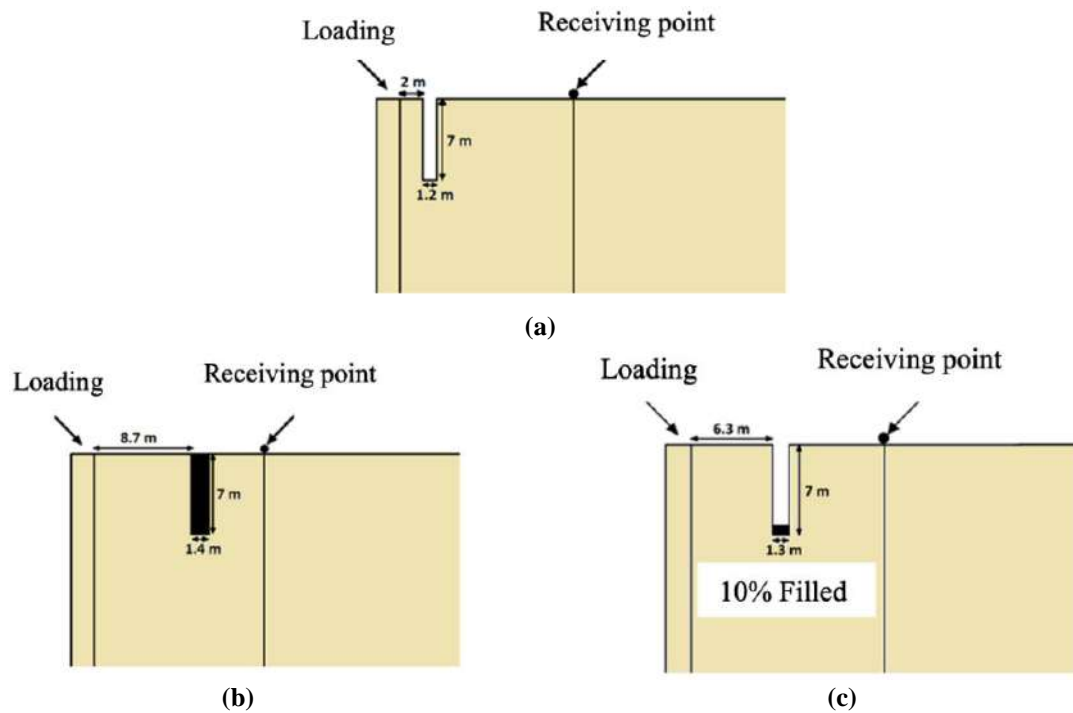


Fig. 6. Optimized configurations of single trench systems: a) Open; b) Concrete-filled; and c) Partially concrete-filled

Table 7. Optimized variables in the dual trenches system

Trench number	Optimized variables				
	w_b (m)	d_b (m)	L (m)	PPV (mm/s)	MC (%)
1	1	7	2	10.7	49
2	1	2.9	10.2		

The optimized layout of open dual trenches decreases the PPV value to 10.7 mm/s. Its performance is improved by 0.5% and 3% compared to the partially concrete-filled and open single trenches, respectively, discussed in the previous section. As observed in Figure 7, these trenches are relatively far from each other. The spatial separation suggests that trenches do not work together or have a significant influence on each other. It can be concluded that doubling the number of trenches does not significantly affect the MC value.

7.1.3. Quadruple Trenches System

In this section, four trenches are installed in the disturbed zone while keeping the total volume of excavation equal to the constraint in previous sections (i.e., $10 \text{ m}^3/\text{m}$). Table 8 shows the optimized variables of the quadruple trenches system. The minimum depth of the trenches is

assumed to be 0.1 m to study whether the increasing number of trenches is effective. In the optimization process, if trenches with very small depths are generated, it can be concluded that those trenches are not functional or effective, and it is better to remove them. As shown in Figure 8, the two middle trenches have the smallest possible depth of 0.1 m. This indicates that increasing the number of trenches does not necessarily increase MC value. By comparing the results in Figure 7 with those in Figure 8, it can be observed that the optimal quadruple trenches are very similar to the optimized dual trenches. This observation verifies the fidelity of the optimization procedure and underscores that increasing the number of trenches might not necessarily be effective. It suggests that blindly adding more trenches does not guarantee improved results and that careful consideration should be given to the design and placement of trenches.

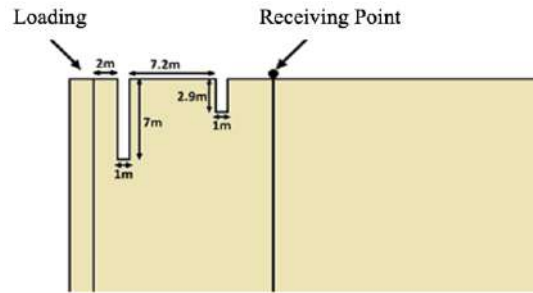


Fig. 7. Optimized variables of dual trenches

Table 8. Optimized variables in the quadruple-trenches system

Trench number	Optimized variables				
	w_b (m)	d_b (m)	L (m)	PPV (mm/s)	MC (%)
1	1	7	2.3	10.77	49
2	1	0.1	4.9		
3	1	0.1	7		
4	1	2.8	10.3		

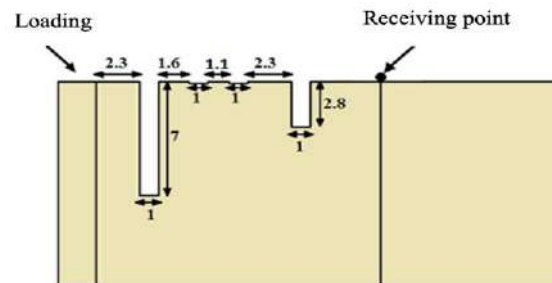


Fig. 8. Optimized variables of the quadruple-trenches system (values are in meters. this is not indicated in the figure due to space constraints)

7.1.4. Changing the Objective Function

In this study, the objective function aims to minimize the vertical PPV at the receiving point. Vertical PPV has been used as the major parameter for measuring vibration in previous research; however, in some papers, acceleration or displacement are considered alternative parameters for measuring vibrations. The choice of the vibration measuring parameter depends on the specific objectives of the study and the available data. To investigate the impact of the objective function definition, two additional optimizations are performed, assessing the objective function using acceleration and displacement values.

These simulations are performed for single open trenches, and the results are presented in Table 9. It is observed that changing the objective function from velocity to acceleration does not make a significant difference in the optimized variables; however, the related MC

increases considerably from 46% to 75% (Table 9). On the other hand, the objective function defined based on the displacement results in a different optimized location for the trench. However, it still emphasizes the necessity of using a deep active trench.

Based on observations, it has been noticed that the variation range of acceleration is more pronounced compared to displacement. Acceleration tends to exhibit more tangible variations in response to changes in each studied variable. On the other hand, displacement shows minimal variation and is not significantly sensitive to variations in optimization variables.

7.2. Material Distribution in the Domain

In this section, a more complex optimization problem is solved using the CMA-ES/FE approach to optimally distribute the grout within the design domain. As previously mentioned, the optimization procedure inevitably generates

intermediate densities (between 0 and 1); however, the penalization factor is applied to the density values to avoid intermediate densities as much as possible. Different densities are allocated to each cell to use these values in practice. Assigning different properties in practice can be achieved by modifying the ratio of materials in the mixture or changing the jet grouting process intensity. Figure 9 illustrates the designed wave barrier with grout distribution, and the presented distribution results in 35% mitigation capacity and a *PPV* of 13.6 mm/s. As illustrated in Figure 9, the grout is mostly concentrated in the lower parts of the disturbed zone due to the low-frequency range of the DC loading. Since the frequency range is low, the Rayleigh wave's penetration depth is deeper, resulting in a denser distribution at the bottom of the zone.

Moreover, grout is mostly located near the excitation source and the receiving point. Density values are larger near the tamping point and create a deep and active pattern similar to the results observed with rectangular trenches. The total material distribution creates an approximate W-shaped design. The W-shaped design traps the wave within the domain and makes waves' transmission to the receiving point harder. As a result, the waves that reach the

receiving point are mitigated in intensity.

The interpretation of W-shaped grout is that the concentration of grout near the excitation source minimizes the initial influence on the surrounding structures, and putting the grout in the proximity of the receiving point ensures blocking the propagated waves before they reach the critical point.

8. Verification of Optimization Results

A comprehensive parametric study is conducted in this section to examine the accuracy of the optimization results. Approximately 3500 models are built to analyze the single trench case, and nearly 6200 models are built to investigate the behavior of the dual trench system. The studied parameters include the width, depth, distance from the tamping point, and filled percentage. The width ranges between 1 and 2 m, depth varies between 1 and 7 m, distance from the tamping point varies between 2 and 12 m, and the filled percentage has values ranging between 0 and 100 percent. For brevity, this section includes only a selected number of graphs (Figures 10 to 13) for reference. Figure 13a illustrates the parametric study results in an open trench.

Table 9. Optimization results for different objective functions

Objective function	Optimized variables			
	w_b (m)	d_b (m)	L (m)	MC (%)
Peak particle velocity	1.2	7	2	46
Peak particle acceleration	1.2	7	2.1	75
Peak particle displacement	1.4	7	5.7	26

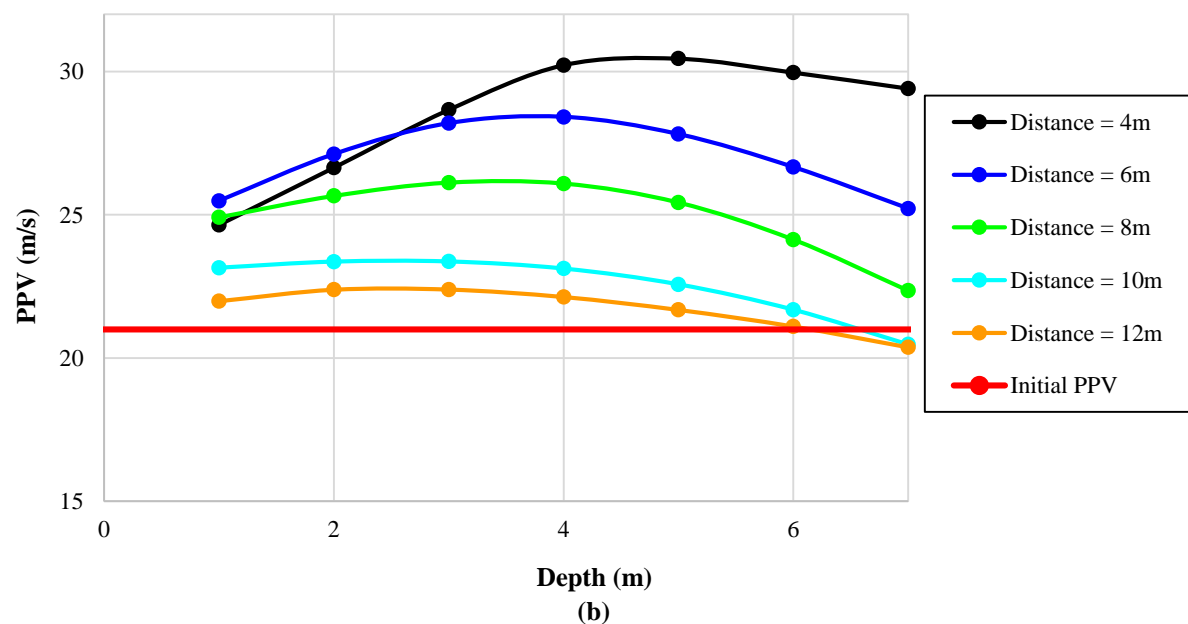
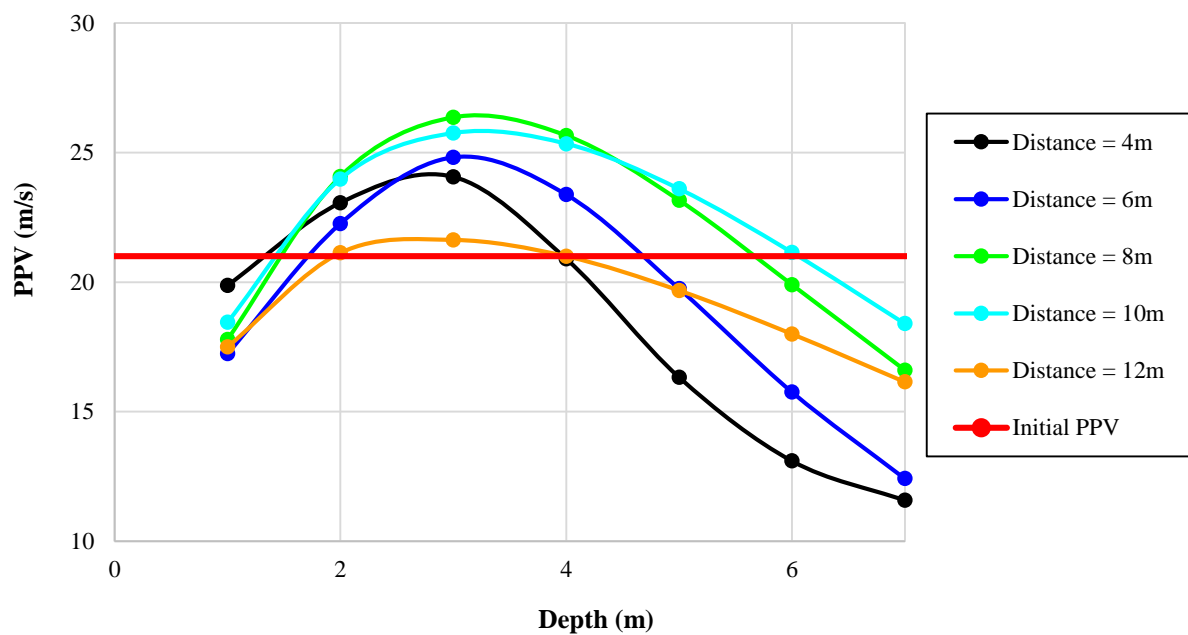
0.21	0	0	0	0	0.29	0.14	0	0.04	0.37	0.15
0	0.25	0.53	0	0	0	0	0	0	0	0.14
0.12	0.01	0.03	0	0.02	0.00	0.31	0	0	0	0.01
0.01	0.95	0.04	0	0.19	0.13	0	0.01	0	0	0.47
0	0.86	0.08	0	0	0	0.24	0	0	0.21	0
0	0.16	0.66	0	0	0.95	0	0.05	0.33	0.24	0.01
0.47	0	0	0	0.15	0.07	0	0.44	0.35	0.08	0.03

Fig. 9. Each cell's density in the disturbed zone grid

A 1 m wide and 7 m deep trench located at 4 m from the centerline of the model has the minimum *PPV*, and it fully aligns with the optimization results presented in Table 5 (the distance values in Table 5 need to be adjusted by 2 m to have the distance from the centerline). Figure 10b depicts the results of the parametric study in the concrete-filled trench. The minimum *PPV* occurs when a 1 m wide and 7 m deep trench is located at 10 m or 12 m from the centerline, to which the optimization suggests a very close result (Table 5).

Figure 10c indicates the parametric studies in an SBM-filled trench. A 1 m wide and 2 m deep trench located 4 m from the centerline generates the minimum *PPV*.

The optimization result (Table 5) leads to a 2.8 m deep trench located at 9 m from the centerline. The optimization result differs from the parametric study, but it can be seen that the variation range is not wide, and the *PPV* of trenches located at 6, 8, 10, and 12 m from the centerline are marginally higher for a 2 m deep trench.



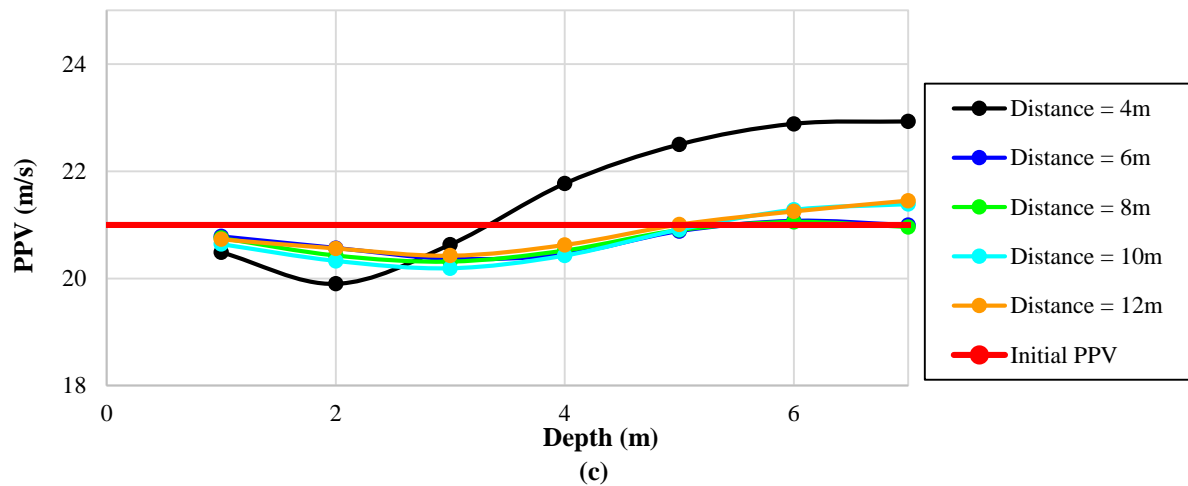
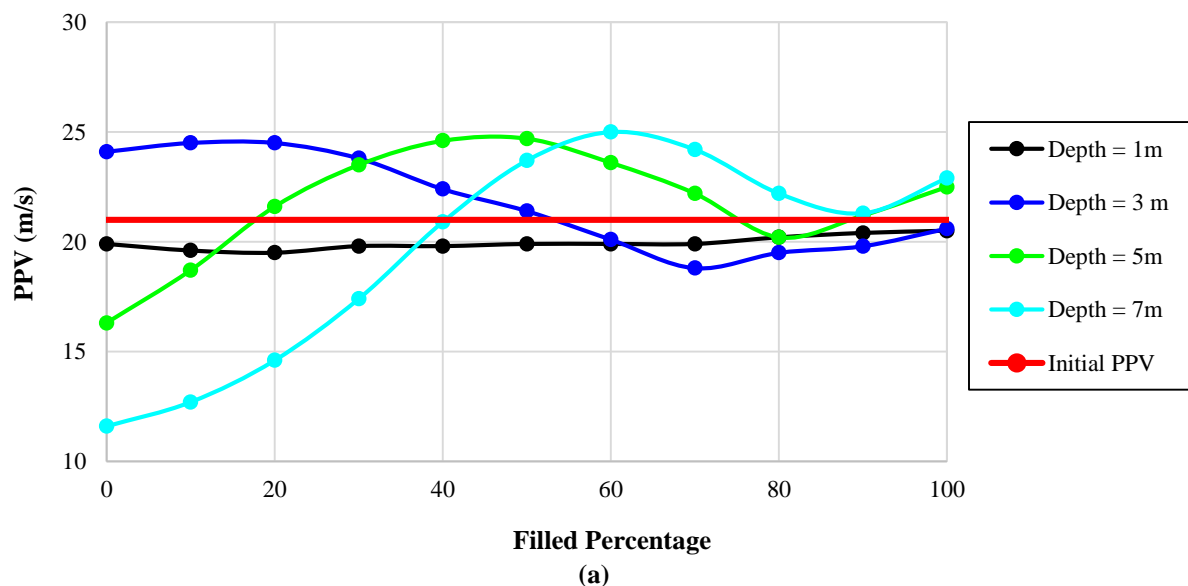


Fig. 10. Parametric study for single trench: a) Open trench; b) Concrete-filled trench; and c) SBM-filled trench

Also, the second minimum happens when a 3 m deep trench is located 10 m from the centerline. As depicted in Figure 10, no specific trend is gleaned in the graphs, emphasizing the need to optimize problems as indefinite and unpredictable as the current study. Figure 10 presents the amplifications observed in the study. It is noteworthy that the amplification phenomenon in impact loadings has been documented in only a limited number of studies. Amplification in vibrations induced by a forge hammer noted by Svinkin (2004) and the occurrence of amplification in open trenches in a pile-driving study reported by Jayawardana et al. (2018), further support the observation of amplification in specific scenarios.

A study by Kermani et al. (2024) also found that increasing the trench depth does not follow a consistent trend, suggesting the presence of an optimal depth range for these barriers. Indeed, the observed trend of amplification in impact loadings can be attributed to the presence of geometrical irregularities introduced during the installation of trenches. These geometrical irregularities can cause wave reflections, diffractions, and scattering. As a result, certain frequencies or points may experience amplification of vibrations. Moreover, Figure 11 shows that partially SBM-filled trenches perform the best when empty (air-filled), especially with a depth of 7 m located at 4 m from the centerline.



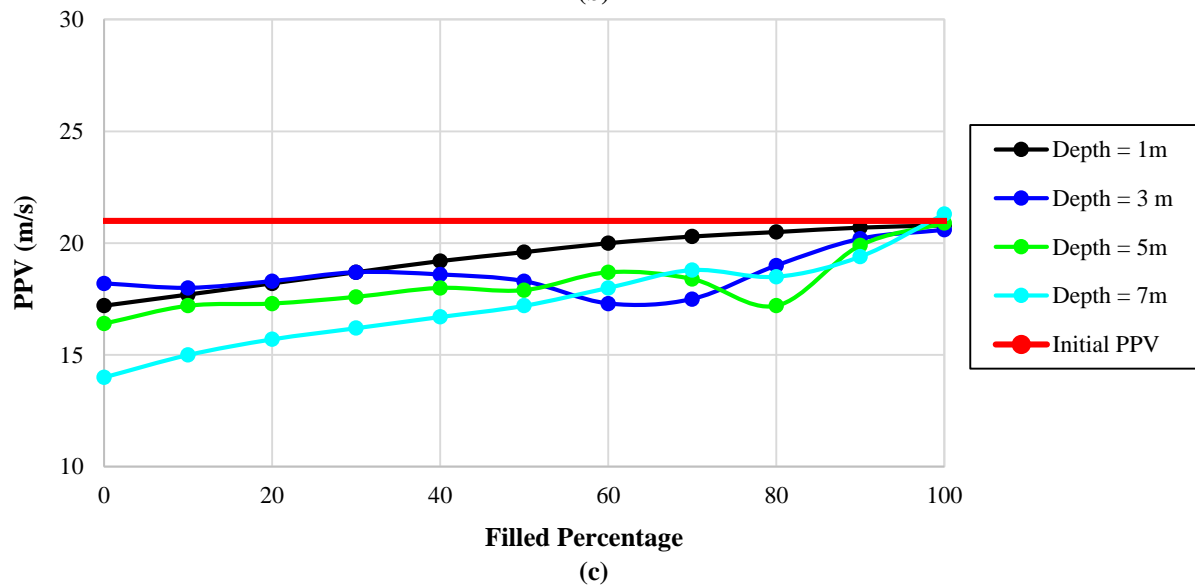
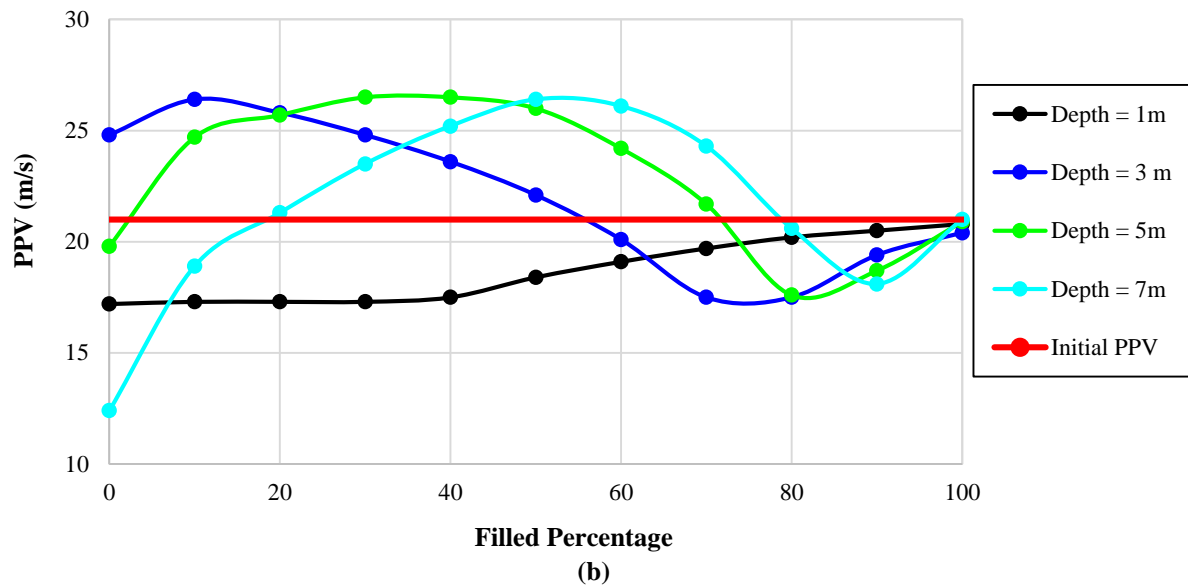
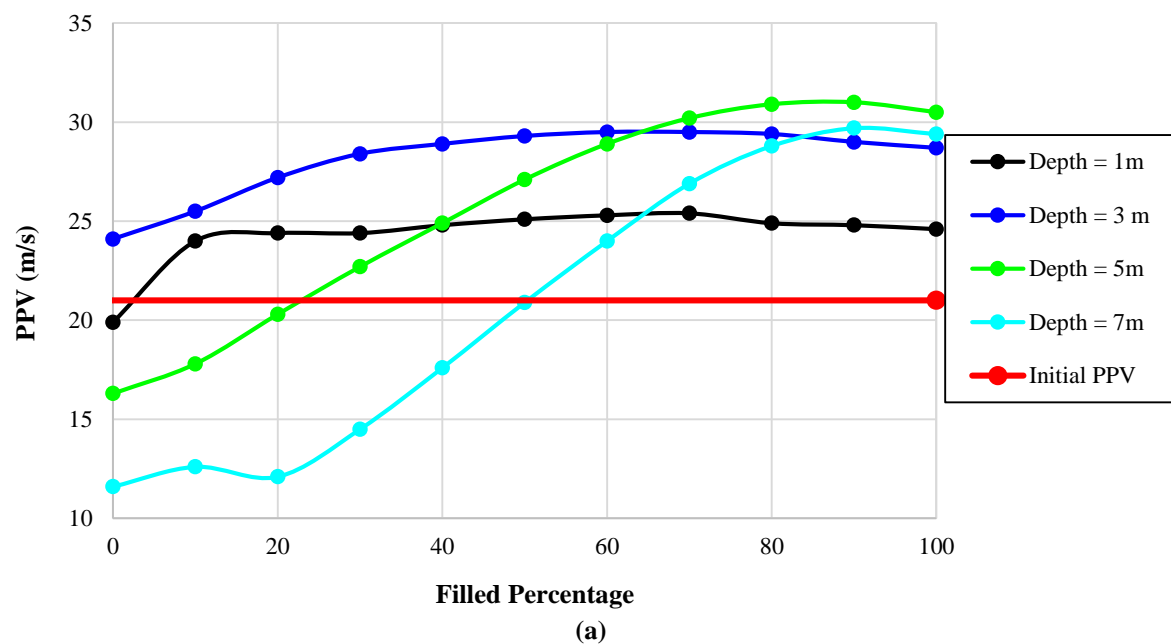


Fig. 11. Parametric study for partially SBM-filled single trenches located at: a) 4 m; b) 8 m; and c) 13 m



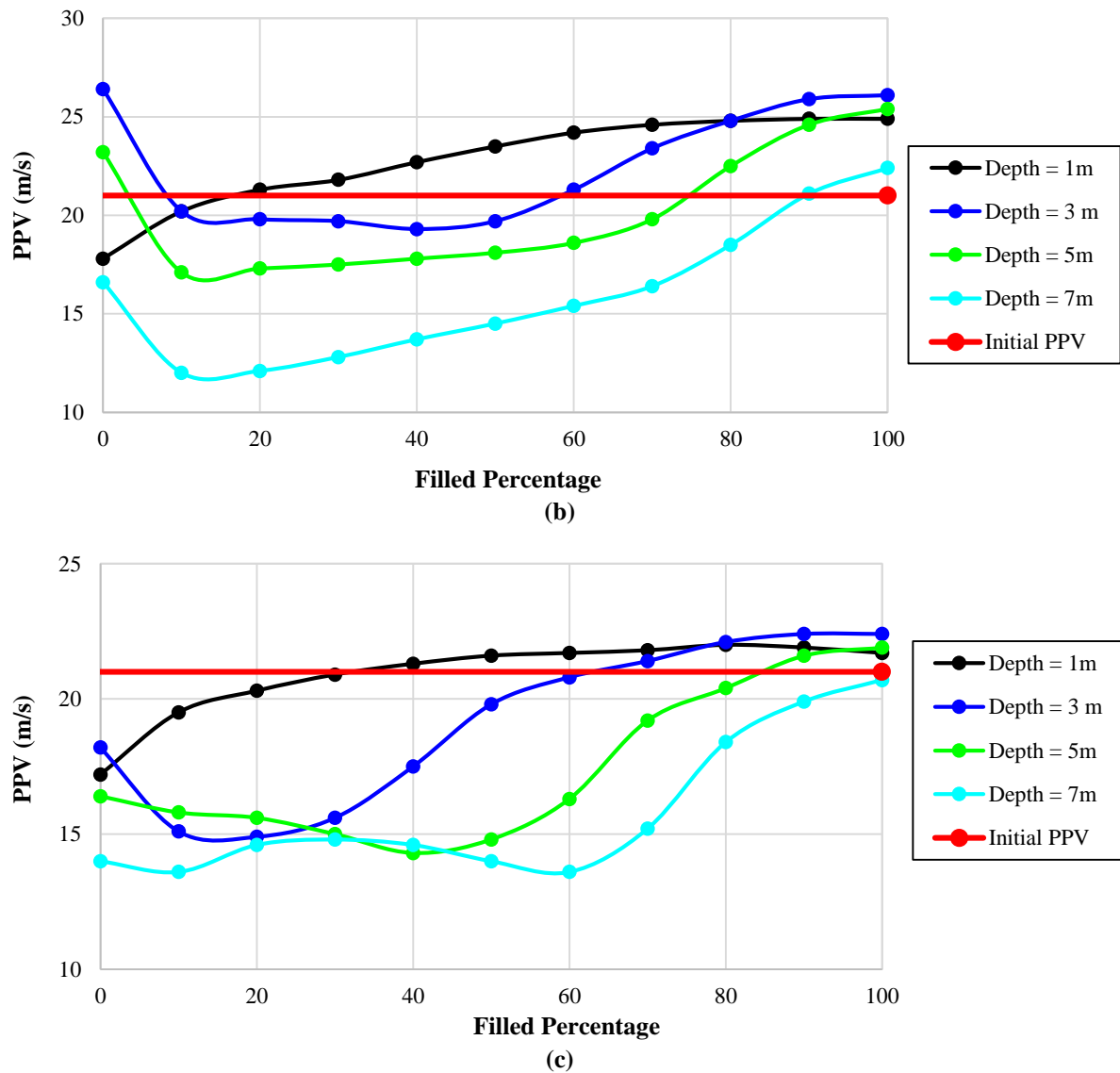


Fig. 12. Parametric study for partially concrete-filled single trenches located at: a) 4 m; b) 8 m; and c) 13 m

Figure 11 confirms the optimization procedure's accuracy. Figure 12 highlights the results in partially concrete-filled trenches. As observed, the minimum *PPV* is related to a trench that is 7 m deep and 10% filled, located at 8 m from the centerline. The optimization results report the same data, which indicates consistency and accuracy. Figure 13 justifies the optimization results for dual trenches, a 7 m deep and a 2.9 m deep trench located at 4 m and 12.2 m, respectively. Parametric studies were not conducted for the quadruple trench configuration due to the massive computational cost. Nevertheless, the accuracy of the optimization procedure in the single and dual trench systems provides a strong assurance of correctness for the

quadruple system.

9. Practical Implications of the Study

From a practical perspective, vibration control is a common concern in many civil engineering projects. With the findings of this research, vibrations can be reduced in cases where DC-induced vibrations are important. While the use of barriers, which require significant cost and time, may not be necessary for simple projects, they are essential near critical structures like power plants and oil pipelines. In such cases, the importance of reducing vibrations as much as possible is paramount, as demonstrated by Wang et al. (2023) that considered the effects of direct current on oil pipelines, and

utilized vibration isolation trenches to mitigate the resulting vibrations.

10. Conclusions

This research focuses on two main aspects: topology optimization of grout distribution within the design domain and the study of optimal rectangular trench configurations.

This paper provides a comprehensive study of various trench types, including open, infilled, single, dual, and quadruple, specifically in the context of DC-induced vibrations. In previous studies, many researchers have focused on investigating various factors affecting the performance of barriers. These problems need to be examined with a suitable tool due to the existing interdependencies between parameters, numerous affecting parameters, and the computational cost resulting from parametric studies. This research innovatively couples the finite element method and optimization to examine the

performance of wave barriers in the context of dynamic compaction. Furthermore, while genetic algorithms have been used in some studies, this research employs a new and suitable algorithm called Covariance Matrix Adaptation Evolution Strategy. Additionally, the dispersion of materials in the soil for this type of loading has not been studied. Another innovation of this research is introducing the partially-filled barriers.

The significant findings of the current paper are as follows:

- 1) It is observed that open trenches exhibit the highest MC value. Moreover, the best open trench is a deep active one, a 7 m trench located 4 m from the tamping point, which yields an MC of 46%.
- 2) Generally, the most critical design parameter of the trenches is the depth, affecting the results significantly; however, not directly. Generally, it is detected that installing partially-filled trenches can be an innovative and useful method that results in a marginally higher MC.

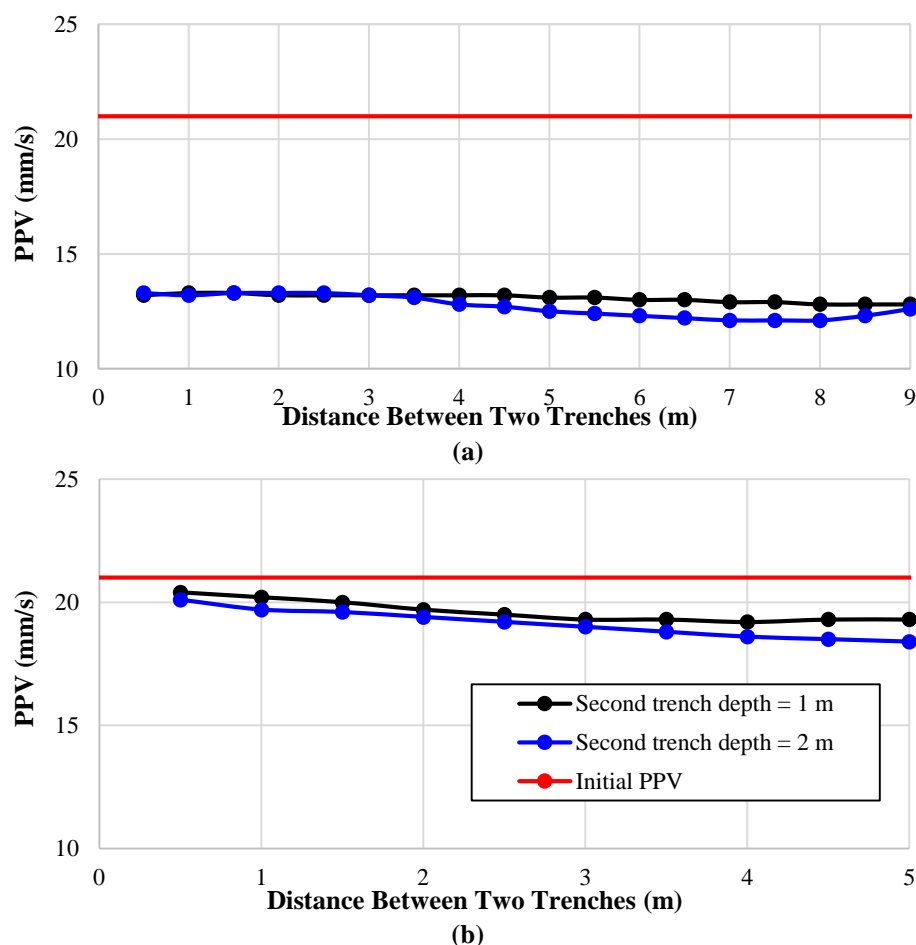


Fig. 13. Parametric study for dual-trenches. the first trench is located at: a) 4 m; and b) 8 m from the centerline

3) Using dual and quadruple trenches instead of single trenches cannot lead to larger MC values. The increase is minor, and not practically recommended due to the need for more excavation and difficulties in practice.

4) In the case of distributing the grout within the domain, the final optimized layout takes a W-shaped configuration. The grout is mainly concentrated near the excitation source and in the proximity of the receiving point. The overall shape of the grout traps the waves in between, diminishing the vibration level in the domain. The concentration of grout near the excitation source minimizes the initial influence on the surrounding structures, and putting the grout in the proximity of the receiving point ensures blocking the propagated waves before they reach the critical point.

5) The numerical results are verified against field measurements, and the comparison reveals a perfect match.

6) The optimization results are verified by conducting a comprehensive parametric study, and a good match between verifications and optimization results guarantees the reliability of the proposed CMA-ES/FE optimization method. The findings of this study can be utilized to optimize trench design and construction techniques, mitigating vibrations, and improving overall performance.

7) Addressing certain limitations in the current research methodology and scope is essential. There are always simplifications and assumptions in numerical modelling that can affect the results. The main limitation of numerical modelling lies in the limited representation of real-world complexity. First, simplifying the system as an axisymmetric model may cause differences with real behavior. Second, soil properties may vary in depth and length across the area of interest. Since the main consideration of this study is topology optimization, the model is simplified to a 2D model, and the variations of soil properties are not considered.

11. References

- Abaqus, F. (2014). *Dassault systemes simulia corporation*, Providence, Rhode Island, USA.
- Abedini, F., Rafiee-Dehkharghani, R. and Laknejadi, K. (2022). "Mitigation of vibrations caused by dynamic compaction considering soil nonlinearity", *International Journal of Civil Engineering*, 20(7), 809-826, [https://doi.org/10.1007/s40999-022-00700-9\(0123456789\(0..-volV\)\(0123456789,-\(0.volV\).](https://doi.org/10.1007/s40999-022-00700-9(0123456789(0..-volV)(0123456789,-(0.volV).)
- Ahmad, S. and Al-Hussaini, T. (1991). "Simplified design for vibration screening by open and in-filled trenches", *Journal of Geotechnical Engineering*, 117(1), 67-88, [https://doi.org/10.1061/\(ASCE\)0733-9410\(1991\)117:1\(67\).](https://doi.org/10.1061/(ASCE)0733-9410(1991)117:1(67).)
- Alzawi, A.M.A. (2011). "Vibration isolation using in-filled geofoam trench barriers", The University of Western Ontario, Canada, <https://ir.lib.uwo.ca/etd/265>.
- Bayat, M., Saadat, M. and Hojati, A. (2023). "Optimization of dynamic compaction procedure for sandy soils", *Civil Engineering Infrastructures Journal*, 57(1), 145-156, <https://doi.org/10.22059/CEIJ.2023.351287.1889>.
- Bian, X., Cheng, C., Jiang, J., Chen, R. and Chen, Y. (2016). "Numerical analysis of soil vibrations due to trains moving at critical speed", *Acta Geotechnica*, 11, 281-294, <https://doi.org/10.1007/s11440-014-0323-2>.
- Cho, I. (2021). "Wave energy dissipation by a floating horizontal porous plate in oblique incident waves", *Wave Motion*, 105, 102765, <https://doi.org/10.1016/j.wavemoti.2021.102765>.
- Chopra, A.K. (2007). *Dynamics of structures*, Pearson Education India,
- Croce, P., Flora, A. and Modoni, G. (2014). *Jet grouting: Technology, design and control*, CRC Press.
- Dolatshahi, K.M., Rezaie, A. and Rafiee-Dehkharghani, R. (2020). "Topology optimization of wave barriers for mitigation of vertical component of seismic ground motions", *Journal of Earthquake Engineering*, 24(1), 84-108, <https://doi.org/10.1080/13632469.2017.1398694>.
- Ekanayake, S.D., Liyanapathirana, D. and Leo, C.J. (2014). "Attenuation of ground vibrations using in-filled wave barriers", *Soil Dynamics and Earthquake Engineering*, 67, 290-300, <https://doi.org/10.1016/j.soildyn.2014.10.004>.
- Esmaili, M., Zakeri, J.A. and Mosayebi, S.A. (2014). "Investigating the optimized open v-shaped trench performance in reduction of train-induced ground vibrations", *International Journal of Geomechanics*, 14(3), 04014004,

- [https://doi.org/10.1061\(ASCE\)GM.1943-5622.0000331](https://doi.org/10.1061(ASCE)GM.1943-5622.0000331).
- Fathi Afshar, N., Hamidi, A. and Tavakoli Mehrjardi, G. (2024). "Impact of diffraction on screening of dynamic compaction waves with barriers", *Innovative Infrastructure Solutions*, 9(6), 184, <https://doi.org/doi.org/10.1007/s41062-024-01502-9>.
- Feng, S., Li, J., Zhang, X., Chen, Z., Zheng, Q. and Zhang, D. (2019). "Numerical analysis of buried trench in screening surface vibration", *Soil Dynamics and Earthquake Engineering*, 126, 105822, <https://doi.org/10.1016/j.soildyn.2019.105822>.
- Gao, M. and Shi, Z. (2019). "A wave guided barrier to isolate antiplane elastic waves", *Journal of Sound and Vibration*, 443, 155-166, <https://doi.org/10.1016/j.jsv.2018.11.042>.
- Groenwold, A.A. and Etman, L. (2010). "A quadratic approximation for structural topology optimization", *International Journal for Numerical Methods in Engineering*, 82(4), 505-524, <https://doi.org/10.1002/nme.2774>.
- Hansen, N. (2019). "A global surrogate assisted CMA-ES", *Proceedings of the Genetic and Evolutionary Computation Conference*, 664-672, <https://doi.org/10.1145/3321707.3321842>.
- Hansen, N. and Auger, A. (2014). "Evolution strategies and CMA-ES (covariance matrix adaptation)", *Proceedings of the Companion Publication of the 2014 Annual Conference on Genetic and Evolutionary Computation*, <https://dl.acm.org/doi/10.1145/2598394.2605347>.
- Hansen, N., Auger, A., Ros, R., Finck, S. and Pošík, P. (2010). "Comparing results of 31 algorithms from the black-box optimization benchmarking BBOB-2009", *Proceedings of the 12th Annual Conference Companion on Genetic and Evolutionary Computation*, <https://dl.acm.org/doi/10.1145/1830761.1830790>.
- Herbut, A. (2020). "Vibration mitigation efficiency of an inclined, curved, open trench", *PloS one*, 15(2), e0229010, <https://doi.org/10.1371/journal.pone.0229010>.
- Jayawardana, P., Achuhan, R., De Silva, G.S. and Thambiratnam, D. (2018). "Use of in-filled trenches to screen ground vibration due to impact pile driving: experimental and numerical study", *Heliyon*, 4(8), e00726, <https://doi.org/10.1016/j.heliyon.2018.e00726>.
- Jayawardana, P., Thambiratnam, D.P., Perera, N. and Chan, T. (2019a). "Dual in-filled trenches for vibration mitigation and their predictions using artificial neural network", *Soil Dynamics and Earthquake Engineering*, 122, 107-115, <https://doi.org/10.1016/j.soildyn.2019.04.006>.
- Jayawardana, P., Thambiratnam, D.P., Perera, N., Chan, T. and De Silva, G.S. (2019b). "Use of artificial neural network to evaluate the vibration mitigation performance of geof foam-filled trenches", *Soils and Foundations*, 59(4), 874-887, <https://doi.org/10.1016/j.sandf.2019.03.004>.
- Jelušič, P. and Žlender, B. (2018). "Optimal design of pad footing based on MINLP optimization", *Soils and Foundations*, 58(2), 277-289, <https://doi.org/10.1016/j.sandf.2018.02.002>.
- Juang, C.H. and Wang, L. (2013). "Reliability-based robust geotechnical design of spread foundations using multi-objective genetic algorithm", *Computers and Geotechnics*, 48, 96-106, <https://doi.org/10.1016/j.compgeo.2012.10.003>.
- Kermani, A., Hamidi, A. and Asemi, F. (2024). "Mitigation of transient vibrations induced by dynamic compaction: a numerical study on the efficacy of open trench and borehole barriers", *Proceedings of the Ninth International Conference on Seismology and Earthquake Engineering*, Tehran, Iran.
- Lukas, R. (1986). *Dynamic compaction for highway construction*, Design and Construction Guidelines, Vol. I, Federal Highway Administration Report FHWA-RD-86-133, https://rosap.nhtl.bts.gov/view/dot/68405/dot_68405_DS1.pdf.
- Mahdavisefat, E., Heshmati, A., Salehzadeh, H., Bahmani, H. and Sabermahani, M. (2017). "Vibration screening by trench barriers, A review", *Arabian Journal of Geosciences*, 10, 1-14, <https://doi.org/10.1007/s12517-017-3279-3>.
- Majumder, M. and Venkatraman, S. (2023). "A state-of-the-art review paper on the vibration screening techniques using open and in-filled trenches", *Asian Journal of Civil Engineering*, 24(7), 2693-2708, <https://doi.org/doi.org/10.1007/s42107-023-00613-5>.
- Mayne, P.W. and Jones Jr, J.S. (1983). "Impact stresses during dynamic compaction", *Journal of Geotechnical Engineering*, 109(10), 1342-1346, [https://doi.org/10.1061/\(ASCE\)0733-9410\(1983\)109:10\(1342\)](https://doi.org/10.1061/(ASCE)0733-9410(1983)109:10(1342)).
- Mehdipour, S. and Hamidi, A. (2017). "Impact of tamper shape on the efficiency and vibrations induced during dynamic compaction of dry sands by 3D Finite Element modeling", *Civil Engineering Infrastructures Journal*, 50(1), 151-163, <https://doi.org/10.7508/CEIJ.2017.01.009>.
- Moussa, A. and El Naggar, H. (2020). "Numerical evaluation of buried wave barriers performance", *International Journal of Geosynthetics and Ground Engineering*, 6, 1-13, <https://doi.org/10.1007/s40891-020-00240-z>.
- Norén-Cosgriff, K., Bjørnarå, T.I., Dahl, B.M. and

- Kaynia, A.M. (2019). "Advantages and limitation of using 2-DFE modelling for assessment of effect of mitigation measures for railway vibrations", *Applied Acoustics*, 155, 463-476, <https://doi.org/10.1016/j.apacoust.2019.06.013>.
- Pan, J. and Selby, A. (2002). "Simulation of dynamic compaction of loose granular soils", *Advances in Engineering Software*, 33(7-10), 631-640, [https://doi.org/10.1016/S0965-9978\(02\)00067-4](https://doi.org/10.1016/S0965-9978(02)00067-4).
- Persson, P. (2013). "Reduction in ground vibrations by the use of wave obstacles", Licentiate Thesis, Lund University, Faculty of Engineering (LTH), Division of Structural Mechanics, <https://lucris.lub.lu.se/ws/portalfiles/portal/3853659/4058477.pdf>.
- Rafiee-Dehkharghani, R., Bansal, D., Aref, A.J. and Dargush, G.F. (2018). "Analysis and optimal design of stress wave intensity attenuation in layered structures", *International Journal of Structural Stability and Dynamics*, 18(01), 1850015, <https://doi.org/10.1142/S0219455418500153>.
- Rezaie, A., Rafiee-Dehkharghani, R., Dolatshahi, K.M. and Mirghaderi, S.R. (2018). "Soil-buried wave barriers for vibration control of structures subjected to vertically incident shear waves", *Soil Dynamics and Earthquake Engineering*, 109, 312-323, <https://doi.org/10.1016/j.soildyn.2018.03.020>.
- Sadeghi, S., Abedini, F., Rafiee-Dehkharghani, R. and Laknejadi, K. (2021). "Covariance matrix adaptation evolution strategy for topology optimization of foundations under static and dynamic loadings", *Computers and Geotechnics*, 140, 104461, <https://doi.org/10.1016/j.compgeo.2021.104461>.
- Saikia, A. and Das, U.K. (2014). "Analysis and design of open trench barriers in screening steady-state surface vibrations", *Earthquake Engineering and Engineering Vibration*, 13, 545-554, <https://doi.org/10.1007/s11803-014-0261-x>.
- Scott, R. and Pearce, R. (1975). "Soil compaction by impact", *Geotechnique*, 25(1), 19-30, <https://doi.org/10.1680/geot.1975.25.1.19>.
- Seitz, K.F. and Grabe, J. (2016). "Three-dimensional topology optimization for geotechnical foundations in granular soil", *Computers and Geotechnics*, 80, 41-48, <https://doi.org/10.1016/j.compgeo.2016.06.012>.
- Sigmund, O., Schevenels, M., Lazarov, B.S. and Lombaert, G. (2016). "Topology optimization of two-dimensional elastic wave barriers", *Journal of Sound and Vibration*, 376, 95-111, <https://doi.org/10.1016/j.jsv.2016.04.039>.
- Svinkin, M.R. (2004). "Minimizing construction vibration effects", *Practice Periodical on Structural Design and Construction*, 9(2), 108-115, [https://doi.org/10.1061\(ASCE\)1084-0680\(2004\)9:2\(108\)](https://doi.org/10.1061(ASCE)1084-0680(2004)9:2(108)).
- Tandon, K., Kumar, D., Ayothiraman, R., Manna, B. and Ramana, G. (2023). "Numerical evaluation of tire chips-filled trench barriers for effective vibration isolation", *Journal of Low Frequency Noise, Vibration and Active Control*, 42(1), 325-344, <https://doi.org/10.1177/146134842211189>.
- Toraldo, C., Modoni, G., Ochmański, M. and Croce, P. (2018). "The characteristic strength of jet-grouted material", *Geotechnique*, 68(3), 262-279, <https://doi.org/10.1680/jgeot.16.P.320>.
- Wang, G., Yin, Y. and Wang, J. (2023). "Vibration safety evaluation and vibration isolation control measures for buried oil pipelines under dynamic compaction: A case study", *Soil Dynamics and Earthquake Engineering*, 167, 107783, <https://doi.org/10.1016/j.soildyn.2023.107783>.
- Yarmohammadi, F. and Rafiee-Dehkharghani, R. (2020). "An optimal design procedure of wave barriers for mitigation of underground and above-ground railway vibrations", *International Journal of Structural Stability and Dynamics*, 20(11), 2050121, <https://doi.org/10.1142/S0219455420501217>.
- Yarmohammadi, F., Rafiee-Dehkharghani, R., Behnia, C. and Aref, A. (2018). "Topology optimization of jet-grouted overlapping columns for mitigation of train-induced ground vibrations", *Construction and Building Materials*, 190, 838-850, <https://doi.org/10.1016/j.conbuildmat.2018.09.156>.
- Zakeri, J.A., Esmaeili, M. and Mosayebi, S.A. (2014). "Numerical investigation of the effectiveness of a step-shaped trench in reducing train-induced vibrations", *Proceedings of the Institution of Mechanical Engineers, Part F: Journal of Rail and Rapid Transit*, 228(3), 298-306, <https://doi.org/10.1177/0954409712473094>.



This article is an open-access article distributed under the terms and conditions of the Creative Commons Attribution (CC-BY) license.



Predicting the Efficiency of Using Empty Fruit Bunch of Oil-Palm Fibre in Reinforcing Structural Concrete: A Statistical Analysis

Kilani, A.J.^{1*}, Olubambi, A.², Ikotun, B. D.³, Onjefu, L.⁴ and Abdulwahab, R.⁵

¹ Ph.D. Candidate, Department of Civil and Environmental Engineering and Building Science, University of South Africa, Florida Science Campus, South Africa.

² Ph.D. Candidate, Department of Civil Engineering Science, University of Johannesburg, Auckland Park Kingsway Campus, South Africa; and Department of Construction Engineering, Triumphant College, Khomasdal Campus, Windhoek, Namibia.

³ Professor, Department of Civil and Environmental Engineering and Building Science, University of South Africa, Florida Science Campus, South Africa.

⁴ Senior Lecturer, Department of Civil Engineering, Namibia University of Science and Technology; and Department of Construction Engineering, Triumphant College, Khomasdal Campus, Windhoek, Namibia.

⁵ Senior Lecturer, Department of Civil and Environmental Engineering and Building Science, University of South Africa, Florida Science Campus, South Africa.

© University of Tehran 2024

Received: 21 Sep. 2023;

Revised: 16 Jul. 2024;

Accepted: 5 Aug. 2024

ABSTRACT: This study evaluates the performance, curing age importance and strength increment efficiency of using Empty Fruit Bunch of Oil Palm Fibre (EFBOPF) in structural concrete through a statistical model. The prediction was carried out using some concrete structural parameters (properties) through a one-way Analysis of Variance (ANOVA) model. These parameters include density, tensile and compressive strengths, and durability. The influences of EFBOPF on concrete density, compressive strength and durability were examined using $150 \times 150 \times 150$ mm (for density and compressive strength) and $100 \times 100 \times 100$ mm concrete cubes (for durability). Also, the strength performance of EFBOPF in concrete against tensile splitting and cracks was determined using 150×300 mm cylindrical concretes. The compressive strengths were evaluated at 28 days; tensile strengths at 28, 90 and 120 days; and durability performance was assessed at 28 and 90 days. All these parameters were tested using a Universal Testing Machine, weighing balance and durability testing apparatus. The results of the experiments were modelled with ANOVA. In the process of modelling, the correlations among the percentage of EFBOPF included, curing age, and the rate of concrete's strength increment were predicted. In accordance with ANOVA's prediction, the compressive strengths of concrete were greatly enhanced at 0.2 and 0.4% of EFBOPF. In addition, the split tensile strengths and durability capacity of EFBOPF- concrete were efficiently increased at 1.0% and 0.8-1.2% of EFBOPF inclusion, accordingly. The results of the modelling proved that EFBOPF increased the concrete strengths against compressive and tensile failures efficiently. Also, it was evident that EFBOPF enhanced the durability performance of concrete greatly. Although the application of EFBOPF in concrete as well as curing have great impacts on the hydration process of the concrete and its high strength yielding capacity. However, its capacity to increase the concrete's strengths does not depend on the rate of EFBOPF included or the long curing ages of concrete but depends on the reinforcement strength of EFBOPF used.

Keywords: Concrete Structural Properties, Empty Fruit Bunch, Oil Palm Fibre, Efficiency, Analysis of Variance (ANOVA), Modelling.

* Corresponding author E-mail: abiodun_kilani@yahoo.com; 20994680@mylife.uniza.ac.za

1. Introduction

Concrete is a composite material that consists of coarse and fine aggregates closely bound together with cement paste, which solidified over time. It is referred to as the second most used material in the world, especially in the construction of building structures (Hanson, 2020). The use of concrete for structural construction has been helping in providing a safe and healthy environment for the regulation of the high global population. It is the most essential material in the construction industry after water. Concrete possesses high durability capacity and good mechanical properties. Its proper production makes the concrete structures perform well under loading. From the engineering point of view, concrete is an excellent material (Carroll, 2023; Pillay et al., 2022).

Reinforced concrete is concrete made from a mixture of fine and coarse aggregates, cement, and water with steel bars embedded in it in such a way that the two are mingled together to resist the intended forces (Britannica, 2020). Concrete is said to be strong in compression but weak in tension. In several findings, most of the concrete tensile strengths were less than 10% of their compressive strengths as a result of their weak capacity against cracking and shrinkage (Mezher et al., 2020; Mack et al., 2024). Despite the application of steel bars in concrete to cater for its low tensile capacity, the issue of cracking persists.

Fibres were introduced into concrete to improve its structural properties and control flaws such as low tensile strength, cracks and shrinkage. It is defined as a reinforcing material with certain quality properties. A fibre is either flat or circular. Its aspect ratio was commonly calculated by dividing the length by its diameter. This ratio usually falls between 30 and 150 for some fibres.

Application of fibres in concrete controls some defects that are usually caused by concrete's weak properties, such as high rate of water permeability, cracking

and shrinkage (Gamage et al., 2024). Also, application of natural admixtures (such as natural fibres) as a partial substitute of concrete's aggregate has really helped in reducing the high rate of Carbon Dioxide (CO₂) and Green House Gases (GHGs) emission from concrete (Kilani and Fapohunda, 2022). According to the statistical data, almost half of the waste and raw materials generated by industries were consumed in the construction industries. As estimated, up to 70 - 80% and 40% of GHGs and global energy were respectively generated from concrete industries (Sizirici et al., 2021; Miller et al., 2021).

Agricultural waste products such as Palm Oil Fuel (POFPA), Silica fume, wood ash and fly ash were rich in Silica elements for accurate binding of aggregates and performing the function of cement in concrete (Rodier et al., 2019; Thomas, 2018). Fibres from agricultural wastes (natural fibres) are currently being appreciated in the construction industries. The major reinforcement and enhancement feedback received from their application in concrete has really proved their indelible strength toward the growth of the concrete and construction industries. Some of these developments are that natural fibres are used to increase the concrete's durability, tensile, and compressive strengths. One of the outstanding reports is that most of the agro-wastes were performing better in concrete than the synthetic and metallic fibres. For instance, as reported by Shadheer et al. (2021), coconut fibres performed better than synthetic fibres in reinforcing concrete.

Also, the result of applying treated oil palm fibre ash as a partial substitute for cement in concrete, as conducted by Omoniyi (2019), proved that concrete with fibre ash decreased in compressive strength compared to that of the control after being cured for 7 to 28 days. It was observed that the treatment of oil palm fibre with sodium hydroxide caused a decrease in strength. Thus, treating oil palm fibres before applying them to the concrete is not

necessary, as it does not cause a reduction in strength. On the contrary, the concrete reinforced with Empty Fruit Bunch of Oil Palm Fibre (EFBOPF) showed an increase in compressive strength up to 4.46% and 11.43% at 90 days of curing under natural weather conditions than that of the control (Lim et al., 2018). Also, as investigated by Sheng et al. (2019), the application of EFBOPF in concrete increased the concrete compressive strength by 2.07%. Therefore, the findings of Omoniyi (2019) and those of other scholars including Rao and Ramakrishna (2022) clearly showed that the application of EFBOPF in concrete could increase the concrete compressive strength up to 11.43%. Also, as experimented by Aguiar et al. (2003), up to 32% of specimens tested in the groups were unable to establish their characteristic compressive strengths.

Concrete in C20 and C25 groups had the characteristic strengths that were below the exigency, while that of C30 was above the exigency, as expected. Several existing building structures had low compressive strength, and the strength variation was very significant. The average compressive strength of buildings was in the normal distribution (Yuva, 2023). Therefore, fibres such as EFBOPF should be applied to such concrete to complement the strength capacity. In concreting, several methods of statistical analysis have been applied to evaluate the reinforcement performance of fibres in concrete. However, the analysis has not been extended to evaluate the efficiency of applying EFBOPF to the concrete and the dependency of concrete on the strength yielding capacity of EFBOPF on the hardening properties of concrete (BS EN 196-12, 2024).

This is the trust of this experimental analysis. In this experiment, one-way Analysis of Variance (ANOVA) model is used to evaluate the level of strength yielding capacity of EFBOPF in concrete, deviation, variance and variation ratio of the results obtained from the standard of concrete hardening properties (such as

tensile strength, compressive strength and durability). In the analysis and modelling, the efficiency of EFBOPFs in reinforcing the concrete structural properties was determined and the optimum predicted values were noticed. These were values were evaluated based on the experimental results. Thus, this analysis focuses on the application of the statistical method in predicting the level of strength enhancement generated by incorporating EFBOPF into the concrete (BS EN 197-2, 2020) and to show the level of efficiency brought by the application of EFBOPF in reinforcing structural concrete.

This study also aimed at predicting the level of dependence of concrete strengths on the quantities of EFBOPFs applied. This aim was achieved through the following objectives: i) To determine the rate of strength increment generated through the application of EFBOPF in concrete; ii) To determine the level of efficiency achieved in reinforcing the concrete's properties with application of EFBOPF; iii) To evaluate the level of concrete's strength deviation from the standard when EFBOPF is included; iv) To determine the level of variations in strengths of concrete with EFBOPF using ANOVA model; and v) To build a standard conclusion from the statistical data obtained from experimental results as modelled by ANOVA.

2. Materials and Methods

2.1. Treatment of Materials

The empty bunches of oil palm used were collected from a dumping site of a palm oil producing mill at Asin Ekiti, Ikole, Ikole Local Government Area (LGA), Ekiti State, Nigeria. The collected bunches were split into pieces with the aid of a sharp cutlass. Before the splitting operation, the bunches were soaked in warm water at an amber temperature to kill the germs and remove some harmful chemicals. After 5 hr, the soaked bunches were removed from the water and cut into filaments. The filaments were sun-dried for two weeks to dry off all

their moisture content. The dry materials were slashed into 20 mm lengths each for it to easily and perfectly mixing with other concrete aggregates. The coarse (granite) and fine (sand) aggregates used were supplied from a quarry site located at Oloko, Ikole LG. The aggregates were dried for 14 days and sieved with sieve no. 200 (75 μ m) to remove the impurities and clay. The Portland cement of grade 42.5N was used for this investigation. Its production was based on BS EN 196-12 (2024) and BS EN 197-2 (2020) of British standards. Portable water was used for the mixing of the aggregates with fibre. The oil palm bunches were treated and processed into

fibres by following the methods and processes as presented in Figures 1 and 2.

2.2. Chemical and Physical Properties of Oil Palm Fibre

The chemical and physical properties of fibre extracted from EFBOP were determined at the soil laboratory of the agronomy department, at the Ladok Akintola University of Technology (LAUTECH), Ogbomosho, Oyo state, Nigeria. In the Laboratory, the diameter and length of each EFBOPF were determined with micrometer screw-gauge and meetr rule, respectively.

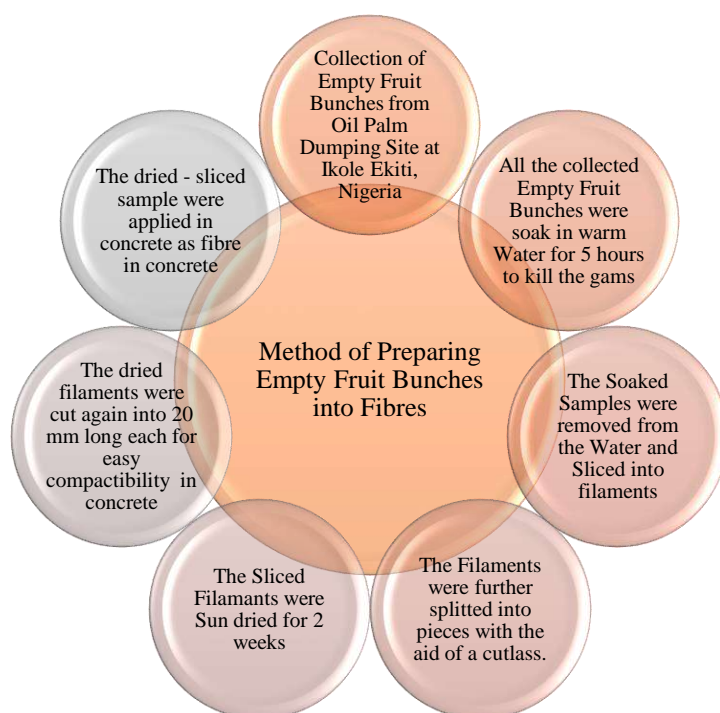


Fig. 1. Method of preparing empty fruit bunches of oil palm into fibre

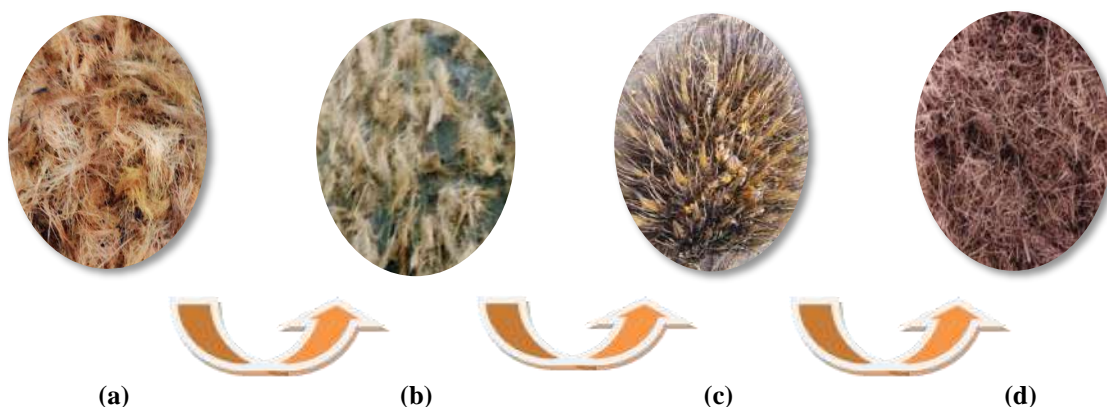


Fig. 2. a) An empty bunch of oil palm; b) Wet split bunches in filament form; c) Split bunches sun-dried; and d) Extracted fibres from empty bunches of oil palm, which were cut into 20 mm lengths each

Other properties of EFBOPF, like lignin, ash, hemicelluloses, cellulose and extraction, were also determined. These were done to capture the behavioural pattern of the fibre used, and its fitness for concrete operation. Cellulose possesses certain reinforcement properties required for concrete enhancement. The processes of determining the lignin, ash, hemicelluloses, cellulose and extraction content of EFBOPFs are in the order of Karunakaran et al. (2020). The ash content in EFBOPFs is determined by weighing a certain mass of dried EFBOPF on the scale as M_1 .

The measured sample is placed in a porcelain cup. The sample in the porcelain cup was heated and later burnt in the electric furnace for 5 hours at 550 °C until it became grey (ash). The cup was taken out of the furnace and allowed to cool. The weight of grey sample is determined as mass 2 (M_2).

The ash content of the fibre is calculated using Eq. (1).

$$\text{Ash Content (\%)} = \frac{M_1 - M_2}{M_1} \times 100 \% \quad (1)$$

where M_1 : is the weighed mass of dried EFBOPF, and M_2 : is the mass of grey sample. Also, the cellulose content of EFBOPF was determined by measured a certain quantity of Acid Detergent Fibre (ADF) on the balance noted as M_A . Then, the 72% of tetraoxosulphate (VI) acid solution was applied to the ADF sample and soaked in the solution for 3 hr. After 3 hr, the soaked sample was rinsed in a solution of acetone and hot water. The rinsed sample is then dried in the oven at 110 °C for 4 hours to remove all its moisture content. After 4 hours, the sample was taken from the oven, allowed to cool and weighed.

This weight was noted as M_B . The percentage of cellulose content in EFBOPF was calculated using Eq. (2).

$$\text{Cellulose Content} = \frac{M_A - M_B}{M_1} \times 100\% \quad (2)$$

where M_A : is the weighed mass of the ADF sample, and M_B : is the weighed mass of the

oven-dried sample. The percentage of hemicelluloses in EFBOPF was determined using the approach of determining the cellulose content of EFBOPF. In addition, percentage of lignin content of EFBOPF was determined by burning some weighed sample of the rinsed and oven-dried sample from cellulose test noted as M_B in a furnace at 600 °C. The burnt sample was weighed on the scale as Mass D (M_D). Then, the percentage of lignin content was calculated using Eq. (3).

$$\text{Lignin Content (\%)} = \frac{M_B - M_D}{M_1} \times 100\% \quad (3)$$

where M_D : is the mass of the sample after being burnt in the furnace at 600 °C. The extraction content of EFBOPF was obtained after all the other contents were determined.

2.3. Aggregates (Coarse and Fine) Properties

The coarse and fine aggregates used were characterised through sieve analysis. From the gradation curve, some properties of aggregates, like moisture content, coefficient of uniformity, bulk density, and coefficient of curvature, were determined to ascertain their suitability for concreting.

2.4. Concrete Mix Proportion and Operation

The weights of aggregates (coarse and fine), cement and water used for concrete production were determined from a 1:2:4 mix proportion, and a 0.5 water/cement ratio. The addition of EFBOPF to concrete aggregates was from 0 to 1.2% by weight of cement. The percentage of fibre in concrete was increasing by 0.2% until 7 samples were produced, including a control (with 0% of EFBOPF). The above proportion was adopted to formulate a concrete mix design for cylindrical and cube specimens as presented in Table 1. Using a mix proportion of 1:2:4, concrete specimens were produced at the concrete section of civil engineering's Laboratory of Federal University, Oye Ekiti (FUOYE), Nigeria. In the batching processes, 685.8 kg/m³ of

dried sand was measured on a weighing balance and spread on a clean tray in the laboratory. The 342.8 kg/m^3 of cement was also measured on a scale and spread on dried sand. The two aggregates were thoroughly mixed with spades and trowels.

Likewise, 1371.5 kg/m^3 of coarse aggregate (granites) were added to the mixture of sand and cement. The three aggregates were mixed thoroughly for the second time. After the mixing of granite, sand and cement, $0.81\text{--}4.89 \text{ kg/m}^3$ of EFBOPF was spread on the mixed aggregates of granite, sand and cement per batching, and the materials were mixed properly for the third time till all the aggregates were mingled. Finally, 171.5 kg/m^3 of water was evenly applied to the mixed aggregates. The four mixed aggregates with water were thoroughly mixed again for the fourth time until the paste was formed with other composite materials. These procedures were adopted for the production of $100 \times 100 \times 100 \text{ mm}$ concrete cubes, $150 \times 150 \times 150 \text{ mm}$ concrete cubes, and $150 \times 300 \text{ mm}$ cylindrical concretes with the application of $0\text{--}1.2\%$ of EFBOPF with an increase interval of 0.2% .

2.5. Determination of EFBOPF -Cement Pastes Consistency and Setting Times

The consistency of cement paste with EFBOPF was determined using BS EN 196-3 (2005) standard. At the initial stage of the experiment, the Vicat apparatus was placed in a stable place in the laboratory.

The dashpot's top of the apparatus was unscrewed to allow the plunger to be worked upon severally. 400 g of cement was weighed into an empty pan. Also, a certain volume of water was measured in a separate beaker. Moreover, through the

weight of the cement used, a certain mass of EFBOPF was weighed into another container. The three: cement, EFBOPF and water were mixed thoroughly until the paste was formed. The stopwatch was set, likewise, the Vicat apparatus. The mixed cement paste with EFBOPF was placed inside the Vicat mould, and its top was levelled with a scapula to have a smooth surface. At this stage, the plunger of the Vicat device was lowered to the top*surface of the paste inside the Vicat mould. At a set time, the plunger was released quickly to penetrate the paste inside the mould. This procedure was repeated until the plunger penetrated a distance value that fall within $5\text{--}7 \text{ mm}$ while the consistency of the paste mixed with EFBOPF was recorded. Also, the setting times of concrete's cement paste with EFBOPF were determined using BS EN 196-3 (2005) standard. In the laboratory, 400 g of 42.5N grade of cement was measured into a bowl and a certain mass of EFBOPF by the weight of cement was weighed into another bowl. A volume of water was measured using the value of fibre-cement paste consistency (0.85 P) determined earlier.

The stopwatch was set for reading. The cement, EFBOPF and water were mixed thoroughly until they form a paste. Immediately the water was added to the mixture of cement and EFBOPF, the stopwatch was started and recorded as time $1 (T_1)$.

The paste was placed inside the Vicat mould with the aid of trowels. The surface of the paste was levelled with a scapula to have a smooth surface. The needle was attached to the Vicat's plunger. The Vicat's plunger with needle was moved close to the top of the test block inside the Vicat mould.

Table 1. Concrete mix proportion for cylindrical and cube specimens

% of Fibre Content (%)	0.0	0.2	0.4	0.6	0.8	1.0	1.2
Granite (kg/m^3)	1371.5	1371.5	1371.5	1371.5	1371.5	1371.5	1371.5
Sand (kg/m^3)	685.8	685.8	685.8	685.8	685.8	685.8	685.8
Cement (kg/m^3)	342.8	342.8	342.8	342.8	342.8	342.8	342.8
Water (kg/m^3)	171.5	171.5	171.5	171.5	171.5	171.5	171.5
Fibre (kg/m^3)	0.00	0.81	1.63	2.44	3.26	4.07	4.89

The Vicat's plunger with needle was set and quickly released to penetrate into the testing block. The procedure was repeated after 2 min (which is a time interval) until the needle could not penetrate the test block up to 5 mm. At this stage, the paste setting time is recorded as time 2 (T_2). Instead of a needle, the plunger device was attached to the annular disc, and the procedure was repeated. The annular attachment was released to pierce the test block. The paste with EFBOPF was considered to be set finally when the application of the annular disc could not make an impact on the test block but that of the plunger needle was able to do so. The time recorded at this stage was referred to as time 3 (T_3). The initial and final setting times of concrete paste with EFBOPF were determined using Eqs. (4) and (5).

$$T_i = T_2 - T_1 \quad (4)$$

$$T_f = T_3 - T_1 \quad (5)$$

where T_1 : is the recorded time when the water was first applied to the cement to form paste, T_2 : is the time recorded when the penetration of the needle failed to reach between 5 and 7 mm, T_3 : is the time recorded when the impression was made on the test block annular disc but the needle failed to do so, T_i : is the initial setting time of cement paste mixed with EFBOPF, and T_f : is the final setting time of cement paste mixed with EFBOPF.

2.6. Concrete Workability and Its Density

The workability of concrete can be

greatly influenced by its water-cement ratio, consistency and the proportion of the aggregate used for its batching. In the investigation, the workability of concrete with EFBOPF paste was conducted using BS EN 12350-2 (2019) standard.

This was measured through the slump and compacting factor of the concrete produced. During the slump test conducted, the slump mould was held firmly after proper cleansing, and the prepared fresh concrete was placed inside the mould in four layers. Each layer was tamped with 35 strokes of blows from the tamping rod. The slump values received were recorded for analysis as shown in Figure 3.

$$\text{Volume of cylindrical concrete} = \pi r^2 h \quad (6)$$

Concrete density

$$= \frac{\text{Mass of cylindrical concrete (kg)}}{\text{Volume of cylindrical concrete (m}^3\text{)}} \quad (7)$$

where r : is the radius of the circular base of the cylindrical concrete, and h : is the height of each of the cylindrical concrete.

The density of the concrete with EFBOPF was measured using the BS EN 12350-6 (2000) standard. $100 \times 100 \times 100$ mm moulds were used to determine the density of small concrete cubes for the durability test, while the $150 \times 150 \times 150$ mm concrete cubes were used for the compressive tests.

The volumes of cylindrical concrete specimens were calculated from the diameter of the mould (150 mm) and the height of the mould using Eq. (6). The density of the cylindrical concrete was determined using Eq. (7).

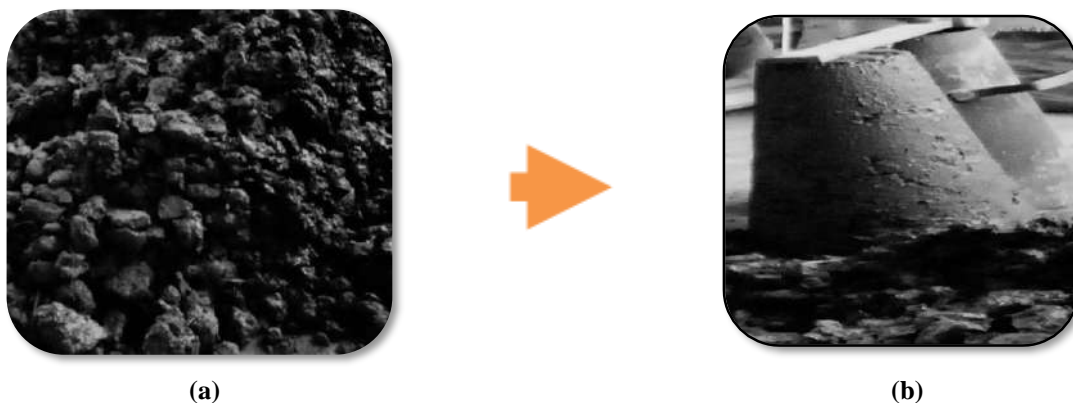


Fig. 3. a) Freshly mixed concrete with EFBOPF; and b) Compacted slump concrete with its cone

2.7. Concrete Compressive and Tensile Splitting Strength of Concrete Reinforced with EFBOPF

The strengths of concrete against compression stresses were determined using $150 \times 150 \times 150$ mm cube moulds and BS EN 12390-3 (2009) standard. During the experiment, the freshly mixed concrete with EFBOPF was placed inside the compressive moulds in four layers after a proper cleansing of the moulds. Each layer was compacted with 35 strokes of blows from the tamping rod. The top surface of the concrete in the moulds was levelled and smoothened with a trowel. The cast specimens were kept in a dry and cool place in the laboratory for 24 hr till the specimens gain enough strength. After 24 hr of casting, the specimens were removed from moulds and immersed in water for 7, 14, 28, 60, 90 and 120 days, until their crushing days. On a crushing day, the soaked specimens were removed from the water. The water on them was cleaned and allowed to air-dry for a little time, and they were positioned inside the UTM of a 1560 kW WAW-2000 B capacity model for accurate crushing. The concrete strength values gotten were recorded. The concrete cylindrical specimens were used to determine the tensile strength of concrete reinforced with EFBOPF. The specimens were formed from a 150×300 mm cylindrical mould.

This test was conducted in the laboratory using BS EN 12390-6 (2023) standards. After the proper preparation of the mould, the concrete with EFBOPF freshly prepared was placed inside the mould and compacted with 35 strokes of tamping from the rod, each in four layers. The top of the specimen was smoothened and levelled with a hand trowel. After a few hours, when the concrete started to be hardened, the specimens were labelled for identification.

After the labelling, the cast specimens were de-moulded and soaked in clean water for 7, 14, 28, 60, 90 and 120 days until their crushing day. The cured specimens were crushed using UTM of a 1560KN WAW-

2000 B capacity. The crushed values on the machine were recorded. The splitting strength of the crushed concrete was determined using Eq. (8).

$$\text{Concrete's tensile splitting strength} \left(\frac{\text{N}}{\text{mm}^2} \right) = \frac{2P}{\pi LD} \quad (8)$$

where T : is the tensile strength of cylindrical concrete, P : is the maximum indicated load when applied by machine (N), D : is the specimen's diameter (mm), L : is the specimen's length, and Π : Pi.

2.8. Durability of Concrete: Coefficient of Water Absorption

The concrete's coefficient of water absorption test was conducted to determine the rate of water permeability into the concrete with EFBOPF. This was ascertained by determining the speed at which water is being taken up into the dried concrete. The specimens were prepared using $100 \times 100 \times 100$ mm concrete cubes with the application of ASTM C1585-13 standard for the experiment. The concrete was prepared according to the prescription in the concrete mix design. After the concrete casting, the de-moulded concrete cubes were immersed in water for 28 and 90 days to complete the cement-water hydration process in concrete until their testing time. Before the testing, after the concrete was removed from the water, the concrete specimens were prepositioned inside the oven for 7 days to dry off all their moisture at a temperature of 60°C . On the 7th day, the dried specimens were weighed on a scale balance until a constant weight was observed. Then, the dried specimens were allowed to cool for 3 days in a sealed container. After all, each specimen's edge was coated with transparent epoxy to allow the flow of water in one direction.

Big and thick white bowls were filled with water up to 7 mm. The coated specimens were placed inside the bowls with their base at a 5 mm level of the water in the bowls, as presented in Figure 4. The

data gotten from the experiment were analysed using Eq. (9).

$$K_a = \left\{ \frac{Q}{A} \right\} \times \frac{1}{t} \quad (9)$$

where K_a : is the water absorption coefficient (m^2/s), Q : is the quantity of water absorbed, t : is the time taken to perform the experiment (3600 s), and A : is the penetration area of the concrete cube in water (m^2).

2.9. Predictions of the Rate of Strength Yielding Capacity

One-way AVONA is one of the statistical analysis methods that are good in predicting the efficiency of a material in application. The use of ANOVA in concrete will help in predicting the rate of strength development in concrete with the inclusion of EFBOPF.

The prediction was based on the analysis of experimental data obtained through the results of EFBOPF -concrete properties tested, such as compressive strength, density, tensile strength and durability.

Also, ANOVA in predicting the percentage of strength increment yielded by EFBOPF in concrete. For effective modelling of EFBOPF -concrete's experimental results with ANOVA, some essential parameters were firstly determined such as Sum of the Squares

(SS), Degree of Freedom (DF), Correlation factor (C), sum of square of treatment, a Ground Total (GT) of the data, number of replicates by treatment (n), number of treatment (k), the standard deviation (S), variance (S^2) and variance ratio. With these parameters, the rate of strength deviation and variation in EFBOPF -concrete were determined.

2.9.1. Determination of Standard Deviation and Variance of Concrete's Strengths from Experimental Data of Concrete Reinforced with EFBOP Fibre

All the values of the sample analysed in the experiment were grouped and represented by X_n vertically downward in the group, where n is the number of data presented in the group.

The addition of all the data in each group was done using $\sum X_n$. The means of the group data were determined using Eq. (10).

$$\text{Mean of the group data } (\bar{X}_n) = \frac{(\sum X_n)}{N} \quad (10)$$

where N : is the total number of data in the group, and n : is the number of data in the group. The group explains the number of observing data in each of concrete properties, such as compressive and tensile strengths data, durability data, and density data.



Fig. 4. 100 × 100 × 100 mm concrete cubes coated with transparent epoxy partially immersed to a depth of 5 mm at one end for varieties of time intervals: a) 7 concrete cubes immersed in water, first part; and b) 7 concrete cubes immersed in water, second part

The difference between each of the data in a group and the mean of each group is determined using $X_n - \bar{X}_n$. The values gotten from $X_n - \bar{X}_n$ were squared. Then, the rate of deviation in concrete strength when EFBOPF was applied to the concrete was calculated using Eq. (11). N and n have been defined earlier.

Standard deviation

$$\text{of concrete's strength (S)} = \sqrt{\left[\frac{\sum (X_n - \bar{X}_n)^2}{N - 1} \right]} \quad (11)$$

The variances in concrete strengths' deviations after being reinforced with EFBOPF were predicted using Eq. (12). N and n in the equation have been defined earlier with other parameters.

Variance in concrete strengths' deviation

$$= \left[\frac{\sum (X_n - \bar{X}_n)^2}{N - 1} \right] \quad (12)$$

2.9.2. Determination of Concrete Strength Variation Ratio from Experimental Data

To predict the rate of strengths yielded by EFBOPF in concrete and the rate of dependence of concrete on the strength increment yielded by EFBOPF in concrete, two hypotheses theories were formulated: 1) Null hypothesis (H_0); and 2) Alternate hypothesis (H_a) using $\alpha = 0.05$ as the level of significant for the hypothesis.

The Null hypothesis (H_0) states that the rate of strength increment in concrete reinforced with EFBOPF does not depend on the depth of increasing the percentage of EFBOPF included, while the Alternate Hypothesis (H_a) states that the rate of increase in concrete strengths depends on the increase in the percentage of EFBOPF included. After a careful consideration of the obtained experimental results, the null hypothesis theorem was adopted for this prediction. This is because the null hypothesis adopted was based on the 99.95% assurance of the experimental data with a 0.05 level of uncertainty (α). The

analyses of data for the right prediction of the certainties were conducted using the equations and formulas below. First of all, the degree of freedom of statistical group data was determined using Eq. (13).

Degree of concrete

$$\text{strengths' freedom (DF)} = (R - 1) \times (C - 1) \quad (13)$$

where R : is the number of rows, and C : is the number of columns. Secondly, the GT of the concrete strengths was determined from Eq. (14). The correlation within the concrete samples analyzed was determined using Eq. (15).

Concrete strengths' ground total (GT)

$$= \sum X_1 + \sum X_2 + \sum X_3 + \dots + \sum X_n \quad (14)$$

$$\text{Correlation factor (C)} = \frac{(GT)^2}{K \times n} \quad (15)$$

where K : is the number of columns, and n : is the number of rows. Then, the sum of squares of experimental strengths obtained (SS) and its Sum of Squares of Treatment (SST) were calculated using Eqs. (16) and (17).

$$\begin{aligned} \text{Total sum of square (SS)} &= [\sum X_n^2 - C] \\ &= [\sum X_1^2 + \sum X_2^2 + \sum X_3^2 + \dots + \sum X_n^2] - C \end{aligned} \quad (16)$$

where n : is the number of samples, C : is the concrete strengths' correlation factor, and X : is resulted from experimental data.

Sum of square of treatment (SST)

$$\begin{aligned} &= (\sum X_n)^2 / (N) - C \\ &= [(\sum X_1)^2 + (\sum X_2)^2 + (\sum X_3)^2 + \dots + (\sum X_n)^2] / N - C \end{aligned} \quad (17)$$

where N : is the number of data presented in a group column. Likewise, the standard rate of concrete strengths' deviation and its strengths variance were predicted using Eqs. (18) and (19).

Standard deviation of concrete'

$$\text{strengths } (S) = \sqrt{\left[\frac{\sum (X_n - \bar{X}_n)^2}{N - 1} \right]} \quad (18)$$

$$\begin{aligned} \text{Variance of concrete' strengths } (S^2) \\ = \left[\frac{\sum (X_n - \bar{X}_n)^2}{N - 1} \right] \end{aligned} \quad (19)$$

where N : is the number of rows, and n : is the number of samples. Having determined the values of the above parameters using Eqs. (13) to (19), the actual variation ratio of concrete strength calculated ($F_{cal.}$) was determined from the computed values as shown in Table 2. The statistical values gotten from Table 3 were used to determine the value of the Sum of Square Error (SSE) of concrete strengths using Eq. (20).

$$\begin{aligned} \text{Sum of square error } (SSE) \text{ of concrete's} \\ \text{strengths} = SS - SST \end{aligned} \quad (20)$$

where SS : is sum of square, and SST : is sum of square treatment.

3. Results and Discussions

The 20 mm length of each EFBOPF used, as shown in Table 3, was adopted for the smooth mingle of EFBOPFs with other aggregates during concrete mixing. As investigated, the adopted length (20 mm) of EFBOPF used was similar to that of Omoniyi (2019) and Ekelene et al. (2021) and falls within the range of 15-25 mm.

This proves that the 20 mm length of EFBOPF used is suitable for concrete enhancement. The Young Modulus (5.21 GPa), tensile strength (172.50 GPa), and Pentosan (21.50%) values of EFBOPF determined are all in line with the specified standard, which is good for the production of workable concrete according to ACI (1990). Also, with 35.78% water absorption of EFBOPF, up to 36% of the water required for concrete mixing might have been absorbed by the dried fibre, leading to the production of stiff concrete.

Therefore, it is advisable to soak the dried fibre (EFBOP) in water for some minutes to avoid unexpected water

absorption within the concrete aggregate's mixing, thus, reducing the cement-water hydration process in concrete. As shown in Table 3, the 1.07 g/cm³ density of EFBOPF and its aspect ratio of 53 shows that EFBOPF is suitable for the production of light-weight concrete. From another perspective, the results of the chemical composition of EFBOPF also contributed to the best performance of EFBOPF in concrete. As shown in Table 3, EFBOPF is made up of 38.50% cellulose, which is the firm component of plants required for high-strength yielding in concrete (Kilani et al., 2022a,b). From deep observation of the results presented in Table 3, the three main chemical properties of EFBOPF (Lignin-19%, Hemi-cellulose-12.6%, and cellulose-38.5%) needed for the enhancement of concrete properties were summed up to 70.1% which is a good result for the reinforcement of concrete structural properties. This percentage (70.1%) equates to the specified standard stated by ACI 232.1R (2012) for a good pozzolanic material to be used for concrete production (70%).

This also supports that the EFBOPF is fit for concrete reinforcement according to the physical characterisation tests' results obtained. Also, the moisture content of EFBOPF (0.014%) observed in Table 3 signified that EFBOPF will absorb a large quantity of water required for concrete cement-water hydration due to its high dried quantity. The 0.45% value of extraction of the fibre shows that the percentage of impurity in EFBOPF is minimal, less than 0.5%. It means, no dangerous material was found in the fibre, and it is chemical-free of toxic substances that are harmful to human health. The chemical and physical fitness of using EFBOPF in concrete is high compared to that of Ekelene et al. (2021) and Omoniyi (2019)'s findings. The properties of concrete's coarse and fine aggregates as analyzed through sieve analysis were presented as shown in Table 4. Considering the results in Table 4, it was observed that

both coarse and fine aggregates have good uniformity for concrete operation. Also, as presented in the gradation curve in Figure 5,

the values of the aggregates' coefficient of curvature were less than 1.00.

Table 2. Determination of the concrete strengths' variation ratio from calculated data ($F_{cal.}$)

Source of variation	Sum of squares	Degree of freedom	Mean squares	$F_{cal.}$
Treatment	SST	$k-1$	$MST = SST / (k-1)$	MST / MSE
Error	SSE	$k(n-1)$	$MSE = SSE / k(n-1)$	
Total	SS	$(kn-1)$		

Table 3. Physical and chemical properties of EFBOPF

Physical properties	Value	Chemical properties	Value
Young modulus (GPa)	5.21	Ashes (%)	5.25
Tensile strength (GPa)	172.50	Extraction (%)	0.45
Pentosan (%)	21.50	Lignin (%)	19.00
Water absorption (%)	35.78	Cellulose (%)	38.50
Density (g/cm ³)	1.07	Hemi-cellulose (%)	12.60
Aspect ratio	53	Moisture content (%)	0.014
Diameter (single fibre) (mm)	0.25-0.50		
Length (single fibre) (mm)	20		
Colour	Brown		

Table 4. Properties of coarse and fine aggregates

Properties	Value(s)	
	Coarse	Fine
Coefficient of uniformity (C_u)	2.43	3.00
Coefficient of curvature (C_c)	0.98	0.88
Moisture content (%)	0.00	0.00
Water absorption (%)	2.00	2.00
Bulk density (kg/m ³)	1641.67	1666.67
Specific gravity	2.67	2.63

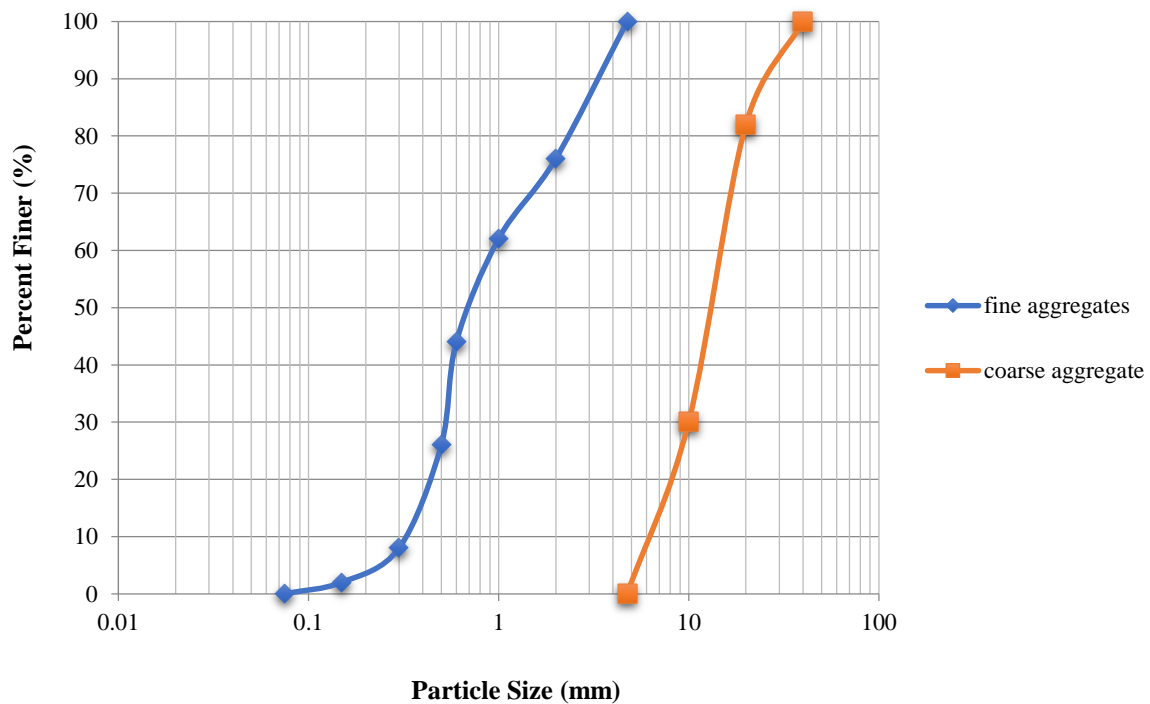


Fig. 5. Particle size distribution (gradation) curve

As estimated, the values of the coefficient observed were 67% better than expected. This proves their suitability for concrete production. As investigated, the percentage of moisture content and water absorption of coarse and fine aggregates were observed to be 0.00% and 2.00%, respectively. This indicated that both aggregates used are very dry; their application in concrete cannot increase the percentage of the water required for workable concrete production. The 2% of water absorption observed in both the coarse and fine aggregates was low compared to that of the specified limit allowable for concrete water absorption for good concreting (0-8%) as specified by ACI 318R (1999). Also, according to the ACI 318R (1999) standard, the aggregates' bulk density should be within the range of 1280-1920 kg/m³ before it can be adopted for concrete production. The bulk density of the aggregates (coarse and fine) observed in this experiment was recorded as 1641.67 and 1666.67 kg/m³, respectively (Table 4).

These values (1641.67 and 1666.67 kg/m³) are in agreement with the ACI 318R (1999) specified limit (1280-1920 kg/m³). The aggregates' coefficient of uniformity (C_u) observed from the analysis (2.43 and 3.0 for coarse and fine aggregates, respectively) is 4.0, which is also in line with the ACI 318R (1999) standard. Likewise, the specific gravity of both aggregates (2.67 for coarse and 2.63 for

fine) are within the limit (2.6-2.8) specified by ACI 318R (1999) as good material for concrete production. With these low specific gravities of both aggregates (2.67 and 2.63), it shows that both aggregates possess low surface areas for perfect compatibility and stability of concrete aggregates. In addition, the water-absorbing capacity of both aggregates is limited. This will assist in producing the workable concrete without segregation. With the critical observation of the presented results, both coarse and fine aggregates have good properties that fit into the ACI 318R (1999) specification; thus, the aggregates have good properties for concrete production, most importantly for research work.

3.1. Results of EFBOP Fibre-Cement Paste Consistency and Setting Times

As shown in Figure 6, the concrete consistency increased by 2.94% up to 0.8% inclusion of EFBOPF when compared with that of the control. The increase in consistency up to 1.2% EFBOPF inclusion with the increase percentage of 5.88%. The increase in concrete's paste consistency required more volume of water to attain the standard consistency of concrete's paste at the inclusion of EFBOPF in concrete production. Therefore, it is advisable to use a higher water-cement ratio for the production of concrete with EFBOPF to achieve the standard consistency of EFBOP fibre-cement paste concrete.

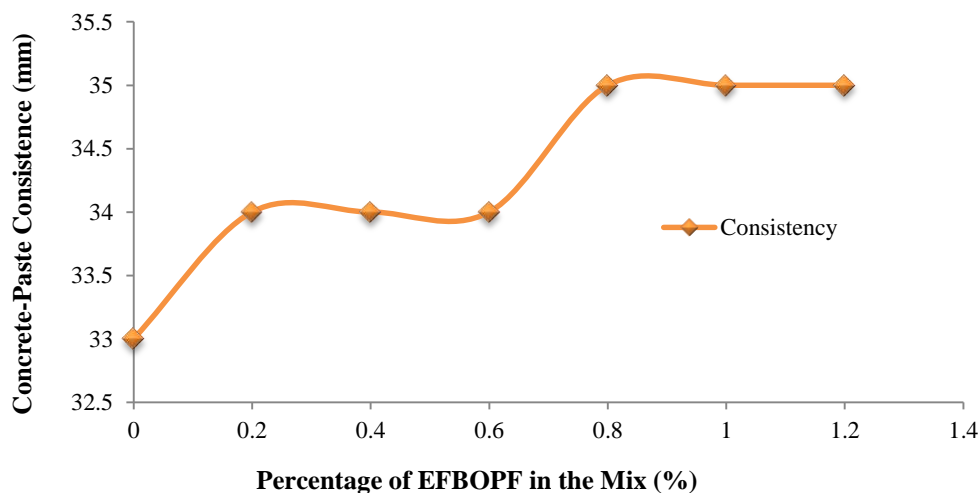


Fig. 6. Concrete's EFBOP fibre-cement paste consistency

3.3. Result of Concrete Density Reinforced with EFBOPF

The density values of concrete with 0% to 1.2% of EFBOPF with a fibre increment interval of 0.2% are presented as shown in Figure 8. The density values of EFBOPF fibre-concrete obtained after 7, 14, 28, 60, 90 and 120 days of curing range from 2330.9 kg/m³ to 2500.7 kg/m³. The values fall within the specified range (2200-2550 kg/m³) stated by ACI 318R (1999) for the

density of normal concrete. Thus, EFBOPF is good for the production of lightweight and normal-weight concrete.

3.4. Concrete Compressive Strengths with EFBOPF

As shown in Figure 9, the compressive strength of concrete with EFBOPF developed increases in strength up to 0.6% of EFBOPF inclusion at 28 and 60 days of curing.

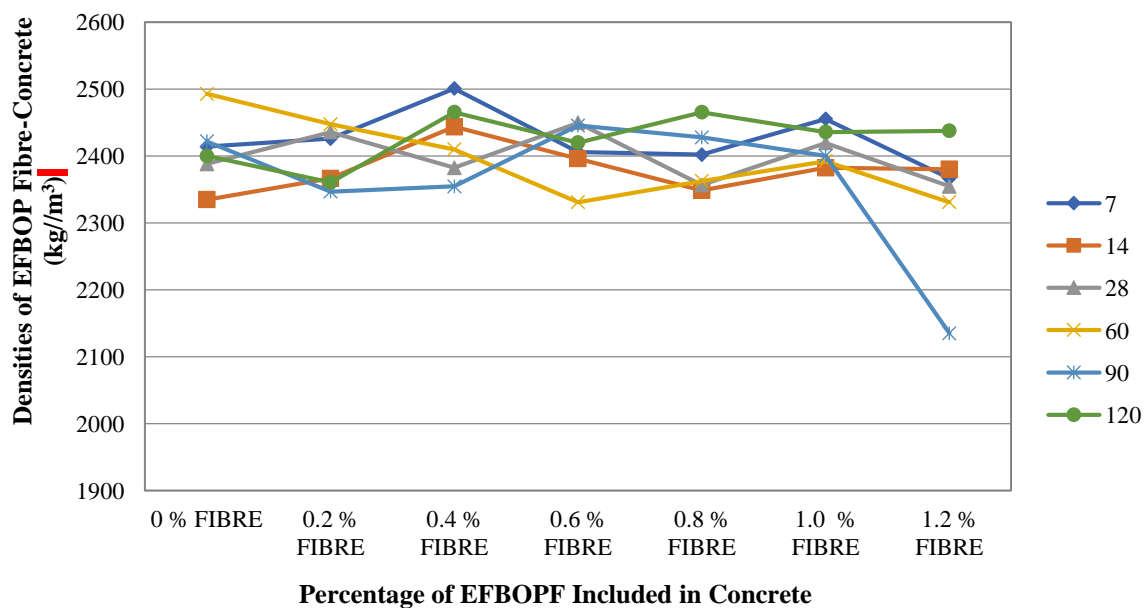


Fig. 8. Densities of EFBOP fibre-concrete with their curing ages

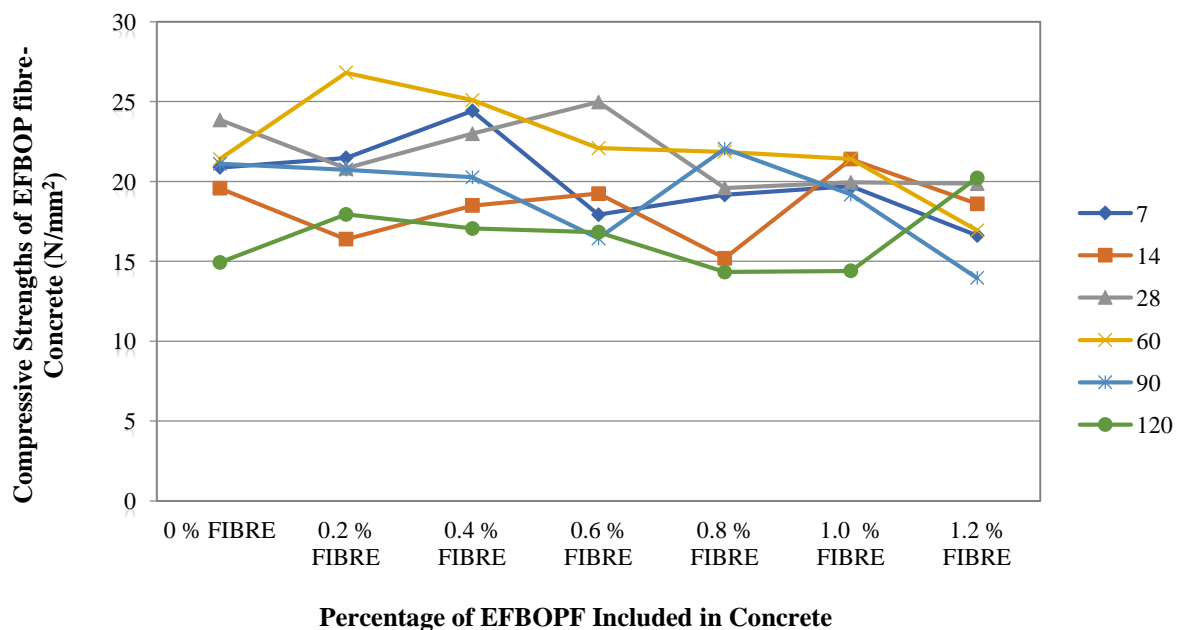


Fig. 9. Compressive strengths of EFBOP fibre-concrete with curing ages

At the 28th day of curing, the concrete compressive strength increased by 3.8% with 0.6% of EFBOPF as a percentage of optimum strength increment. Also, after 60 days of curing, the concrete compressive strength increased from 21.40 to 26.81 N/mm² (25.3% increment) with 0.2% of EFBOPF as a percentage for optimum strength increment. The output showed that up to 25.3% of strength increment was yielded by applying EFBOPF to concrete. This result is similar to the finding of Sheng et al. (2019), who reported that the application of EFBOPF in concrete increased the concrete's compressive strength by 33.8% (from 20.6 MPa to 31.13 MPa), after 28 days of curing. Contrary to the finding of Sheng et al. (2019), the report of Omoniyi (2019) shows that the application of EFBOPF in concrete reduced the concrete's compressive strength up to 62.5% with a substitution percentage of 0 to 30% replacement of cement. The results of this experiment prove that the application of EFBOPF in concrete increases its strength and toughness properties, which is in line with Rao and Ramakrishna (2022) report.

For maximum strength increment, the inclusion of EFBOPF in concrete should

not exceed 0.2% and the curing age should be limited to 60 days.

3.5. Result of Concrete Tensile Strength

The EFBOPF possesses great potential for concrete reinforcement against cracking and splitting stresses. As presented in Figure 10, the concrete tensile strength increased from 0.994 N/mm² to 1.099 N/mm² after 7 days of curing with 0.2% of EFBOPF as a percentage of optimum strength increment. With the trend of strength increment after 7 days of curing, the tensile strength of the concrete increased to 1.024 N/mm² from 0.854 N/mm² after 14 days of curing, with 0.6% as a percentage of the optimum strength increment yielded by EFBOPF in concrete. The observed optimum strength of concrete with EFBOPF was after 28 days of curing with 0.4% EFBOPF as a percentage of optimum strength increment (Figure 10). From 28 days' result, it was observed that about 33.6% of the strength increment was yielded with the application of 0.2% of EFBOPF in concrete. The result proves that 0.2% of EFBOPF is the best percentage for optimum strength increment in concrete.

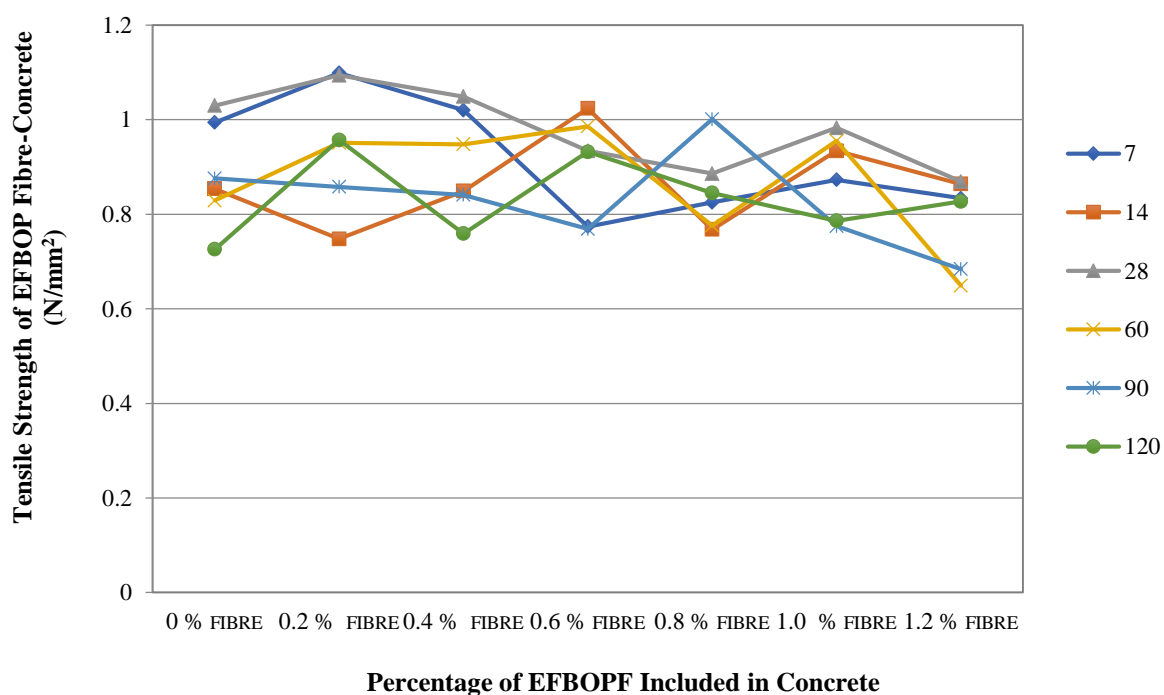


Fig. 10. Concrete tensile splitting strength reinforced with EFBOPF

In comparison, the percentage of strength generated by including EFBOPF in concrete was 13.3% more than that of compressive strength. The strength-yielding quality of the EFBOPF can be improved when it is treated with chemicals like sodium hydroxide (NaOH) to increase its bonding matrix to increase the toughness of concrete against cracking and splitting.

The finding of Futami et al. (2021) is in support of the result of the concrete tensile strength increment observed in this study with the inclusion of EFBOPF. According to the author, the enhancement of concrete properties with EFBOPF had increased the concrete tensile strength up to 70%.

With high strength yielding capacity of EFBOPF in concrete (most especially from 33.6 to 70%), it proves that application of EFBOPF in concrete will control the high effect of sudden splitting and cracks in concrete. In support of the above result, the experimental report of Mazlan and Abdul (2012) also proved that the application of EFBOPF in concrete has a high capacity of increasing the concrete's tensile strength. Considering the agreement between the findings of Futami et al. (2021) and Mazlan and Abdul (2012) and that of this experimental result, it could be deduced

that, achievement of high tensile strength in concrete with the application of EFBOPF should not exceed 3% to prevent strength yielding reduction. This suggestion is in correlation with the percentage of EFBOPF observed for optimum tensile strength increment (0.2%) in concrete, which is equivalent to 33.6%.

3.6. Result of Concrete Coefficient of Water Absorption

The inability of permitting the penetration of water into the dried concrete is one of the properties that prolongs the life span of a concrete structure. The penetration of water or liquid into the concrete has been causing a lot of damage to concrete toughness through weakening of the concrete's strength. As observed in this study, after 28 days of curing, the concrete coefficient of water absorption rate increased from 0.05 to 0.06 at the inclusion of 0.6% of EFBOPF (Figure 11). This result proved that concrete with dried EFBOPF (most especially, with 0.6% of EFBOPF) tends to absorb more water meant for the hydration process in concrete, and this can accelerate its initial setting time, thus, cause production of poor strength concrete.

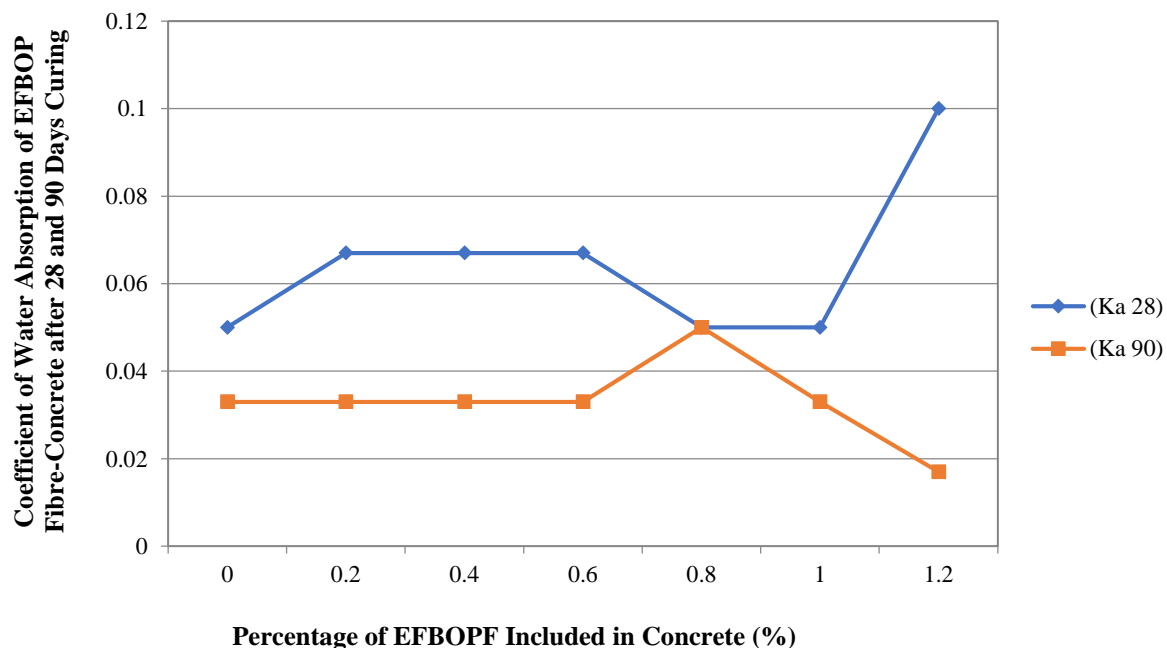


Fig. 11. Coefficient of water absorption of EFBOP fibre-concrete (K_a) after 28 and 90 days of curing

On the other hand, the application of 0.1% of EFBOPF in concrete has reduced its coefficient of water absorption by 48.5% after 90 days of curing (Figure 11). This might be a result of the long hydration process of EFBOP fibre-concrete. This might have developed the concrete properties against porosity, pores and holes formation within the concrete's aggregates.

As shown in Figure 10, application of 0.8% of EFBOPF in concrete will reduce the high rate of water penetration in concrete after 28 days of curing, while the application of 1.2% of EFBOPF in concrete will improve its durability strength against capillarity of water if its curing age is prolonged till 90 days. On the high rate of water absorption in concrete after 28 days of curing, the experimental report of Basiran and Ja'afar (2022), and Futami et al. (2021) support the fact that an increase in the percentage of EFBOPF included in concrete can influence its high rate of water absorption. Based on this observation, it could be deduced that EFBOPF has absorbed a large percentage of water meant for the hydration process in concrete. It was suggested that the percentage of EFBOPF in concrete should be limited to prevent the production of harsh concrete, which is bad for construction purposes.

3.7. Prediction of Concrete Strength Yielding Capacity of EFBOPF in the Concrete

3.7.1. Standard Deviation of Concrete's Compressive Strength Reinforced with EFBOPF

The results of deviation in EFBOP fibre-concrete strength from the specified standard were presented as shown in Figure 12. As predicted by ANOVA, the trend of EFBOP fibre-concrete strength yielding deviated from 0.120 to 3.227 on the 7th day of curing after being immersed in water at 0.4% of fibre inclusion in concrete. The optimum deviation in concrete's compressive strength was observed at 7 days of concrete's curing according to the

prediction from ANOVA. This deviation occurred at the inclusion of 0.4% of EFBOPF. The strength deviation observed was by 96.3% out of the specified standard. This gap is too wide. This deviation in strength might have occurred because concrete has not yet attained its full hydration process at the 7th day of curing. At the point that curing of concrete reached 14 days, its deviation in strength ranges from 0.224 to 1.728, which is about 87.04%. It could be deduced that the increase in concrete curing age influenced the deviation in its strength. This was observed by considering the 7-14 days curing deviation difference (96.3% to 87.04%, respectively). According to the strength development trend in concrete, it was expected that at the 28th day of curing, up to 99% of concrete strength would have been developed during the hydration process. At this point, there should be a reduction in the strength deviation of the concrete. As predicted by ANOVA, concrete compressive strength deviation at 28th day of curing ranges from 0.756 to 1.760, which is about 57.04%. The trend of deviation here doubled the initial one, and this was recorded at the inclusion of 0.6% of EFBOPF. Likewise, the inclusion of 0.6% of EFBOPF in concrete also contributed to this deviation in the strength trend. Considering the results of applying 0.2% and 0.4% of EFBOPF in concrete with 28 days curing, the strength deviation observed was almost zero (0.0182 and 0.0723), compared with that of concrete with 0% of EFBOPF (0.756) as predicted by ANOVA. Therefore, it is suggested that the application of EFBOPF in concrete should be limited to 0.2% and 0.4% to prevent unexpected deviation in concrete compressive strength according to ANOVA's prediction. Also, its curing age should be limited to 28 days. The strength deviation observed at 60 and 90 days of curing concrete with EFBOPF is from 0.115 (control) to 4.68; and from 0.667 (control) to 4.400, which have 85.7% and 84.8% strength deviation differences, respectively.

Also, the maximum percentage in EFBOP fibre concrete's compressive strength deviation after 120 days of concrete curing is 81.2%. Critically considering the results obtained from the application of 0.2-1.2% of EFBOPF to concrete with their curing ages, which ranged from 7 to 120 days (Figure 12), it was observed that the application of 0.6% of EFBOPF in concrete developed no strength deviation for all the concrete specimens cured and tested. Therefore, the application of EFBOPF in

concrete should be limited to 0.6% for maximum compressive strength enhancement.

3.7.2. Standard Deviation of Concrete's Tensile Strength Reinforced with EFBOPF

The standard deviation observed as predicted by ANOVA within the tensile strengths of concrete reinforced with EFBOPF are presented in Figure 13.

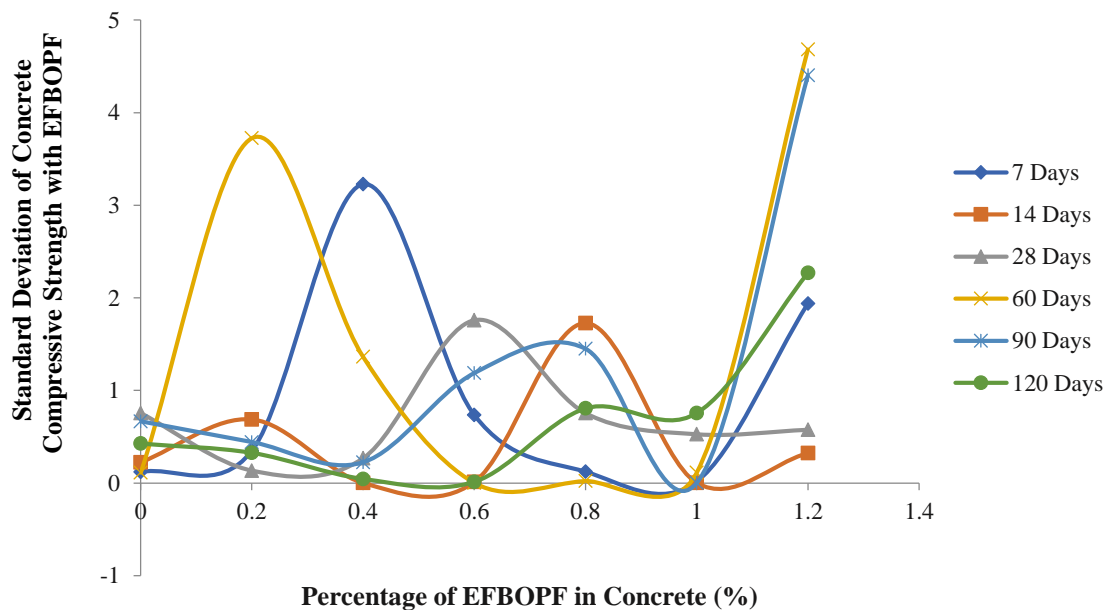


Fig. 12. Standard deviation of concrete compressive strength with EFBOPF

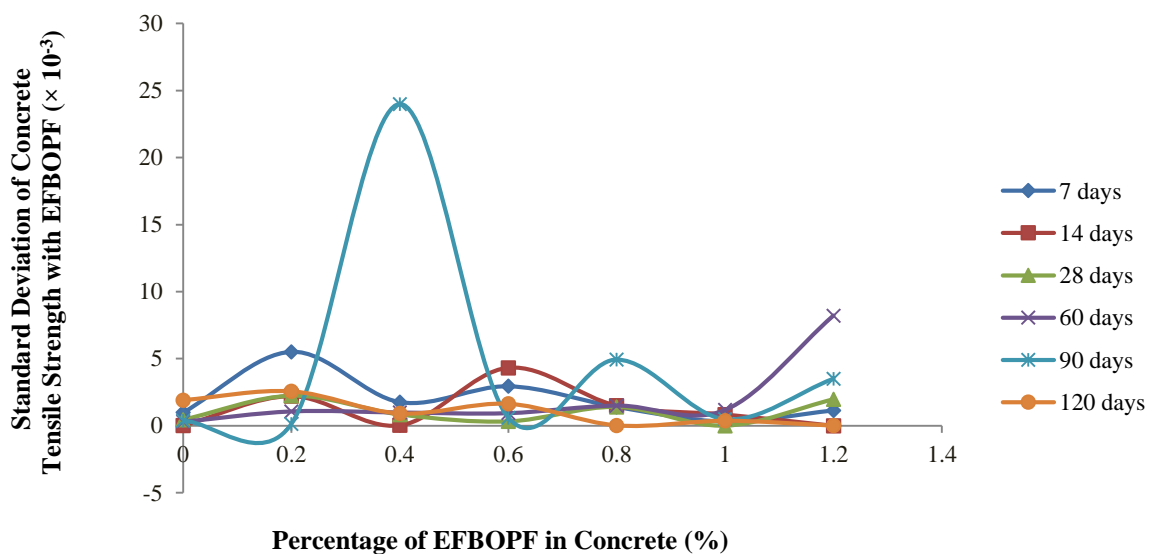


Fig. 13. Standard deviation of concrete tensile strength reinforced with EFBOPF

Generally, the deviation in concrete tensile strength was minimal compared to that of the compressive strength. Almost all the deviations observed from the prediction of ANOVA, as shown in Figure 13, are zero (0-0.025). It is therefore observed that concrete tensile strength increases with no deviation in strength at the application of 0.2-1.2% of EFBOPF despite its long curing ages of 7-120 days. As presented in Figure 13, the maximum strength deviation observed at the concrete tensile zones for 7 to 120 days of curing were 1.1482×10^{-3} for 7 days, 1.5042×10^{-3} for 14 days, 1.41067×10^{-3} for 28 days, 1.067×10^{-3} for 60 days, 0.024 for 90 days and 1.6335×10^{-3} for 120 days at 1.2, 0.8, 0.8, 0.2, 0.4, and 0.6% of EFBOPF inclusion, respectively. All are almost zero. For the control, only the concrete sample cured for 120 days was observed to have a maximum deviation in strength (1.9082×10^{-3}). Others were minimal and they are approximately zero.

As predicted by ANOVA, the application of EFBOPF has a great potential for increasing the concrete's toughness, delaying expansion in concrete that could lead to cracks, increasing the concrete's tensile strength, and blocking pores that can cause absorption of water into the concrete, which can reduce its durability, strength and also initiate cracks. Though the concrete

tensile strength increases with the inclusion of different percentages of EFBOPF, its enhancement capacity does not depend on the high percentages of EFBOPF included. According to Figure 13, the ANOVA prediction proved that application of EFBOPF in concrete will develop no deviation in strength, most especially, when concrete with 0.2% of EFBOPF is cured in water for 7 days, and that of 0.4%, 0.6%, 0.8%, 1.0% and 1.2% for 14, 28, 120, 28 and 120 days, respectively. Having observed the above results, 1.0% of EFBOPF is suggested as the best percentage for concrete tensile reinforcement and 120 days for curing duration.

3.7.3. Deviation in Concrete Durability's Strength with EFBOPF

The results of statistical analysis conducted on concrete durability data obtained from the laboratory experimental results were presented as shown in Figure 14. As predicted by ANOVA, the deviation in concrete's strength with the coefficient of water absorption at 28 and 90 days of curing were observed to be minimal. According to Figure 14, the maximum strength deviation values obtained were recorded as 3.267×10^{-5} and 3.267×10^{-9} for 28 and 90 days of curing, respectively.

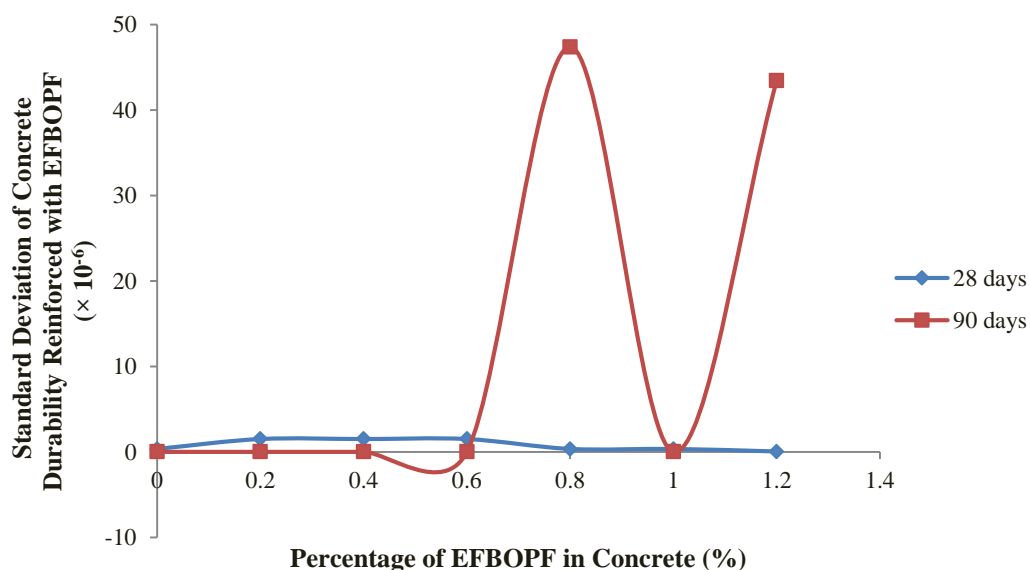


Fig. 14. Deviation of EFBOP fibre-concrete durability

These values are very minimal, approximately zero, even compared to that of controls (3.267×10^{-5} and 3.267×10^{-9} for 28 and 90 days curing, respectively). With these results, it could be observed that application of EFBOPF in concrete is effective in blocking holes and pores developed within the concrete composites, which might result into the permeability of water into concrete. Also, the inclusion of EFBOPF in concrete has improved its toughness property against deformation and developed its thickness against cracks. Thus, EFBOPF has great potential for the reinforcement of concrete durability properties for its more sustainability and durability. As predicted by ANOVA, it could be inferred that, application of EFBOPF in concrete should be limited to 0.8 and 1.2% for 28 days curing, and 0.2, 0.4, 0.6 and 1.0% for 90 days curing to attain maximum concrete's reinforcement.

3.7.4. Variances of Concrete Compressive Strength Reinforced with EFBOPF

The variations in concrete's compressive strength with the application of 0.2 to 1.2% of EFBOPF were observed in this section. As shown in Figure 15, the curing of 0.2 to 1.2% of EFBOP fibre-concrete was carried out as stipulated for 7 to 120 days. On the 7th day of curing, the concrete compressive strength has a variation in strength ranged from 0.0145

(control) to 10.4113, most especially, at the application of 0.4% of EFBOPF to concrete. The strength variation observed was about 99.9% which is very high. This might have occurred as a result of improper mixing of concrete aggregates with EFBOPF.

Also, it might be a result of the poor concrete's aggregate compaction rate. Or it might be a result of irregularity in concrete strength's development. At this stage of curing (7th day), less than 50% of the concrete strength might has not been formed. After 14th day of curing, the variation in concrete's compressive strength reduced from 10.4113 (that of 7th day) to 2.9862 (that of 14th day with 0.8% of EFBOPF). This is about 71.3% in strength variation. The in-uniformity among the compressive strengths of concrete is too wide (from 71.3% to 99.9%).

More efficient method is required for the application of EFBOPF in concrete. The concrete mixing method also needs improvement to give room for uniformity in concrete strengths produced after curing and crushing. As shown in Figure 15, the concrete compressive strength variation observed at 28th day was about 67.7%. The strength variation here is still high. Though, the increase in concrete's curing age leads to a decrease in concrete compressive strength variation, still, there was strength increment at the concrete compression zone.

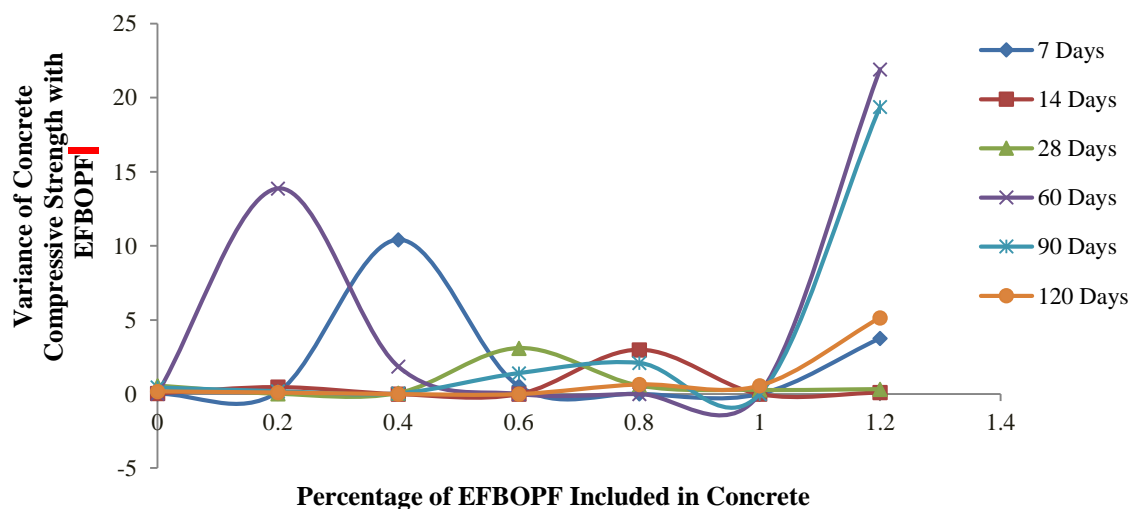


Fig. 15. Variance of concrete compressive strength with EFBOPF

At the 60, 90 and 120 days of concrete curing, the strength variations observed were 21.9180, 19.3888, and 5.1500, respectively. Compared to that of controls, the level of strengths' variation observed were 99.93%, 97.71% and 96.47% at 60, 90 and 120 days of curing, respectively. With all the above high strengths variation values observed at concrete's compression zones, it could be suggested that concrete with EFBOPF should be properly mixed and produced for uniformity in high quality. As predicted by ANOVA (Figure 15), to obtain uniformity in concrete compressive strength, application of EFBOPF in concrete should be from 0.2-0.6% for 120 days curing, while that of 0.8%, 1.0% and 1.2% of EFBOPF should be for 90-, 14- and 28 days curing, respectively. Any alteration of prediction can result in concrete strengths' variations, which can affect the effectiveness of concrete in service.

3.7.5. Variances of Concrete Tensile Strength Reinforced with EFBOPF

The tensile strengths' variation among the samples of concrete reinforced with EFBOPF as predicted by ANOVA are very minimal, approximately zero. As shown in Figure 16, the tensile splitting results of concrete with 0.2%-1.2% of EFBOPFs

produced the following variations, that is, 9.76×10^{-7} to 1.318×10^{-6} for 7 days curing; 1.823×10^{-10} to 2.779×10^{-14} for 14 days curing; 2.031×10^{-7} to 1.736×10^{-11} for 28 days curing; 8.643×10^{-8} to 8.789×10^{-7} for 60 days curing; 1.355×10^{-7} to 1.965×10^{-8} for 90 days curing, and 3.642×10^{-6} to 3.6×10^{-11} for 120 days curing. All the concrete tensile strength variations observed are zero, except that of the 7 days curing value with a small variation. With this outstanding performance of concrete tensile strength with EFBOPF, the application of EFBOPF in concrete will really have a better enhancement on concrete's tensile strength against splitting, cracks and deflections. For better strength increment, the application of 0.2%-1.2% of EFBOPF in concrete should undergo long curing ages, that is, from 7 to 120 days, so as to improve its toughness properties against splitting without strength variation.

3.7.6. Variances of Concrete Durability Strength After Being Reinforced with EFBOPF

The strength variations of concrete durability as predicted by ANOVA for 28 and 90 days curing were presented as shown in Figure 17.

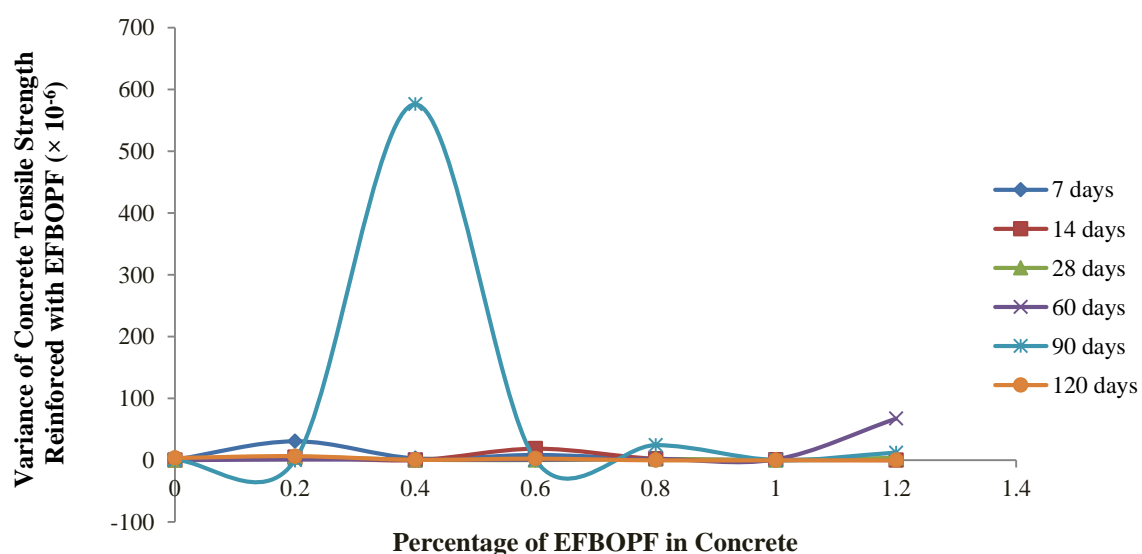


Fig. 16. Variance of concrete tensile strength with EFBOPF

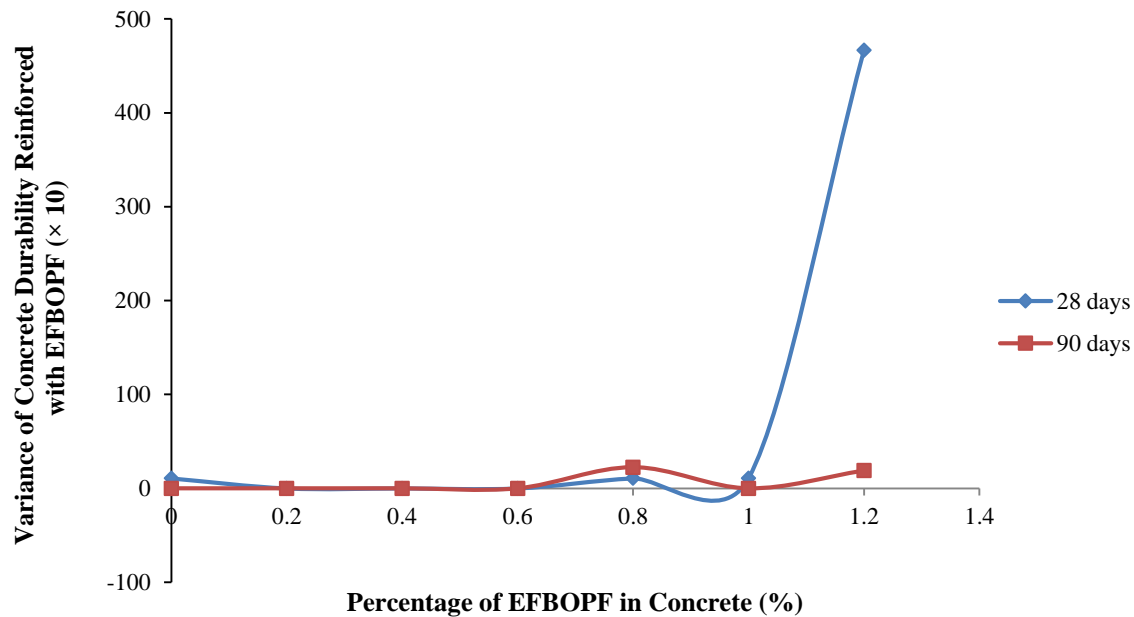


Fig. 17. Variance of concrete durability reinforced with EFBOPF

As observed, the variation in concrete's durability strengths with the inclusion of EFBOPF were from 1.067×10^{-9} to 2.25×10^{-12} for 28 days, and from 1.0673×10^{-17} to 1.0673×10^{-17} for 90 days of curing. The variation here is approximately zero. Thus, the inclusion of EFBOPF in concrete prevented the penetration of water into the concrete significantly and thus increased its durable properties. For excellent durability results, the addition of EFBOPF in concrete should be adopted but limited to 0.2%, 0.4%, 0.6% and 1.0% for 28 to 90 days of curing.

3.7.7. Variation Ratio (F) of Concrete Compressive Strength with EFBOPF

From the experimental and analysis results of concrete compressive strength, the maximum variation ratio (F_{max}) of

concrete strength observed was 5.5852. While the result of the concrete variation ratio (F) from the group data of its compressive strength, as presented in Table 6, with 99.95% ($\alpha = 0.05\%$) level of strength certainty was 5.3288. Also, from the experimental results, the maximum variation ratio (F_{max}) of concrete tensile strength was calculated to be 54.6393. The variation ratio (F) from the group data of concrete tensile strength is 2.132, as shown in Table 7. As shown in Tables 6 and 7, since $F = 5.3288 < F_{max} = 5.5852$ for concrete compressive strength, and $F = 2.132 < F_{max} = 54.6393$ for concrete's tensile strength, then, the null hypothesis (H_0) which stated that, the rate of increase in EFBOP fibre-concrete strengths does not depend on the increase in the percentage of EFBOPF included, is accepted.

Table 6. Variation ratio (F) of concrete EFBOP fibre - compressive strength

Source of variation	Sum of squares	Degree of freedom	Mean squares	F
Treatment	170.3149	5	34.0630	5.3288
Error	230.1202	36	6.3922	
Total	400.4351	41		

Table 7. Variation ratio (F) of EFBOP fibre - concrete tensile strength

Source of variation	Sum of squares	Degree of freedom	Mean squares	F
Treatment	0.113	5	0.0226	2.132
Error	0.382	36	0.0106	
Total	0.495	41		

The statistical result clearly shows that the concrete compressive strength increment does not depend on the large percentage EFBOPF included and also, it does not depend on the long curing age of concrete for strength increment but still contributed solely to stability, durability and sustainability of concrete. These results negate the finding of Musa et al. (2017), who said, an increase in concrete curing days brought about a steady increment in concrete compressive strength. Likewise, the results of Okonkwo and Nwokike (2015) also support this fact that concrete compressive strength varies with variation in curing methods.

4. Conclusions and Recommendations

Concrete is a good construction material that is commonly used for the construction of major infrastructures. It is globally acceptable because of its good structural properties, such as high compressive and flexural strengths, good durability, and high sustainability capacity. One of the major challenges in concreting is its weak ability to resist tensile stress, and this has been developed into a lot of deficiencies, such as cracks and shrinkage. Despite the application of steel bars to concrete to reinforce its weak tensile properties, its crack problem is still unsolved. From the research point of view, the application of natural fibre in concrete is one of the best solutions to these problems of cracks and deformation. Empty Fruit Bunch of Oil Palm Fibre (EFBOPF) is one of the natural fibres that possess good properties for structural concrete enhancement. In this study, EFBOPF is used as a concrete properties' enhancement material to improve its performance in service. As investigated in this experiment, the influence of EFBOPF on concrete's structural properties has been carefully evaluated using an ANOVA model. From ANOVA prediction, it was deduced that the application of EFBOPF in concrete influenced its structural properties

positively; however, its structural influence does not depend on a high percentage of EFBOPF included for sequential strength increment.

From the experimental point of view, EFBOPF is good for the production of lightweight and normal-weight concrete. This fact is in agreement with the value of EFBOP fibre-concrete densities observed from the experimental results. Likewise, the experimental result of EFBOP fibre-concrete's mechanical properties, such as compressive and tensile strengths, and durability increased in strengths with the inclusion of EFBOPF. The increase in the percentage of EFBOPF included in concrete is not the determinant factor for strength increment in concrete. Thus, the application of fibres such as EFBOPF in concrete could increase or decrease the strength of concrete. Also, the curing of EFBOP fibre-concrete beyond 30 days does not determine that its strength increment will be progressive with the increase in curing age.

From the experimental results, it was observed that the application of EFBOPF in concrete improved its toughness properties, and blocked pores and holes that normally cause cracking due to applied tensile force or thermal expansion. Also, it increases the concrete strength against deflection, compression and shrinkage, but the rate of strength increment yielding does not depend on a high percentage of EFBOPF included. Considering the results of analysis obtained from ANOVA, since the values of F are less than those of F_{max} from the variation ratio results, therefore, the null hypothesis (H_0), which states that the rate of strength increment in concrete reinforced with EFBOPF does not depend on the depth of increasing the percentage of EFBOPF included is accepted. It can be concluded that only a certain percentage of EFBOPF influence the concrete's strength increment, and the increase in EFBOP fibre-concrete's curing ages does not guarantee its progressive strength increment. According to ANOVA prediction, for maximum strength increment, the inclusion of

EFBOPF in concrete should not exceed 0.2% and the curing age should be limited to 60 days. For high concrete tensile strength, the percentage of EFBOPF in concrete should not exceed 3%. From the experimental result, it was observed that the EFBOPF absorbed a large percentage of water meant for the hydration process in concrete. Thus, the percentage of EFBOPF applied to concrete should be limited, to prevent the production of harsh concrete.

Likewise, the application of EFBOPF for concrete compressive strength increment after 28 days of curing should be limited to 0.2% and 0.4% which gave a zero deviation in strength as predicted by ANOVA. Also, 1.0% of EFBOPF was suggested as the best percentage for concrete's tensile increment and 120 days as its good curing age. As predicted by ANOVA, the application of EFBOPF in concrete should be limited to 0.8 and 1.2% for 28 days curing, and 0.2, 0.4, 0.6, and 1.0% for 90 days curing for optimum strength increment, and to prevent concrete's strength deviation. 1.0% of EFBOPF is suggested for the reinforcement of concrete compressive strength for optimum strength yielding at 7, 14, 28, 60, 90 and 120 days of curing with no strength variation. The inclusion of EFBOPF in concrete for its tensile strength reinforcement should be limited to 0.4% and 1.0%, and 7 to 120 days for curing ages, in order to have optimum tensile strength increment without any variation in strength. The application of EFBOPF in concrete improved its strength against water weakening, thus, making it more durable than the ordinary concrete. It was recommended that, application of EFBOPF in concrete should be limited to 0.2%, 0.4% and 0.6% and that of curing age should be limited to 28 and 90 days for concrete's better durability.

5. Acknowledgements

The authors appreciate the effort of laboratory technologists, Mr. Babatude and

Engr. Dr. Omofunmi of Federal University, Oye Ekiti, Nigeria for their immeasurable contribution towards the success of this research and its analysis.

6. References

- ACI 318R. (1999). *Building code requirements for structural concrete and commentary*, American Concrete Institute, <https://www.scribd.com/document/512845989/ACI-318R-99-Building-Code-Requirements-for-Structural-Concrete-and-Commentary>.
- ACI 232.1R. (2012). Report on the use of raw or processed natural Pozzolans in concrete, American Concrete Institute, <https://standards.globalspec.com/std/1540638/ac-232-1r>.
- ACI Manual of Concrete Practice. (1990). *Part 1, materials and general properties of concrete*, Guide for Structural Lightweight Aggregate Concrete, American Concrete Institute, <https://trid.trb.org/View/348409>.
- Aguiar, J., Verga, E. and Oliveira, P. (2003). "Statistical analysis of compressive strength of concrete specimens", *A New Era of Building: Proceedings of the International Conference on the Performance of Construction Materials in the New Millennium*, Cairo, Egypt, 18-20, <https://hdl.handle.net/1822/5387>.
- ASTM C1585-13. (2020). *Standard test method for measurement of rate of absorption of water by hydraulic cement concretes*, Advancing Standards Transforming Markets, <https://doi.org/10.1520/C1585-13>.
- Basiran, I. and Ja'afar, A. (2022). "To study the effect of oil palm empty fruit bunch (OPEFB) fibre ratio on the mechanical properties of EFB cement board for panelling", *Progress in Engineering Application and Technology*, 3(1), 297-305, <https://publisher.uthm.edu.my/periodicals/index.php/peat/article/view/6350>.
- BS EN 196-12. (2024). *Method of testing cement*, British Standards Institution, <https://doi.org/10.3403/BSEN196>.
- BS EN 12350-6. (2000). *Testing fresh concrete- Part 6: Density*, British Standards Institution, London, <https://www.scribd.com/document/653156944/BS-EN-12350-6-2000>.
- BS EN 196-3. (2005). *Methods of testing cement- Part 3: Determination of setting time and soundness*, British Standards Institution, <https://standards.iteh.ai/catalog/standards/cen/483fd029-2859-43a2-b3ec-eb3bf21ae307/en-196-3-2005>.
- BS EN 12390-3. (2009). *Testing hardened concrete- Part 3: Compressive strength of test specimens*,

- British Standards Institution, <https://www.scirp.org/reference/referencespapers?referenceid=3549078>.
- BS EN 12350-2. (2019). *Testing fresh concrete- Part 2: Slump test*, British Standards Institution, <https://knowledge.bsigroup.com/products/testing-fresh-concrete-slump-test-2?version=tracked>.
- BS EN 197-2. (2020). *Cement-assessment and verification of constancy of performance*, British Standards Institution, <https://knowledge.bsigroup.com/products/cement-assessment-and-verification-of-constancy-of-performance?version=tracked>.
- BS EN 12390-6. (2023). *Testing hardened concrete, tensile splitting strength of test specimens*, British Standards Institution, <https://doi.org/10.3403/30454320>.
- Carroll, S. (2023). "An introduction to concrete and its strengths and weaknesses", *Engineering Skills*, <https://www.engineeringskills.com/posts/introduction-to-concrete>.
- Ekelene, A.C., Ugwu, E.I., Njoku, C.E., Amanamba, E.C., Arinze, E.E., Ibearugbulani, O.H., Patrick, I.O. and Jagba, A.S. (2021). "Effect of palm bunch ash on the compressive strength of concrete", *International Conference on Engineering for Sustainable World (ICESW 2020)*, *IOP Conference Series: Materials Science and Engineering*, 1107, 012171, <https://doi.org/10.1088/1757-899X/1107/1/012171>.
- Futami, E., Shafigh, P., Katman, H.Y.B. and Ibrahim, Z. (2021). "Recent progress in the application of coconut and palm oil fibres in cement-based materials", *Sustainability*, 13(22), 12865, <https://doi.org/10.3390/su132212865>.
- Gamage, N., Patrisia, Y., Gunasekara, C., Law, D.W., Houshyar, S. and Setunge, S. (2024). "Shrinkage induced crack control of concrete integrating synthetic textile and natural cellulosic fibres: comparative review analysis", *Construction and Building Materials*, 427, 136275, <https://doi.org/10.1016/j.conbuildmat.2024.136275>.
- Hanson (2020). "The importance of concrete in construction", Heidelberg Cement Group, <https://www.hanson.my/en/importance-concrete-construction>.
- Karunakaran, V., Abd-Talib, N. and Yong, T.L.K. (2020). "Lignin from oil palm empty fruit bunches (EFB) under subcritical phenol conditions as a precursor for carbon fiber production", *Material Today: Proceedings*, 31, 100-105, <https://doi.org/10.1016/j.matpr.2020.01.252>.
- Kilani, A. and Fapohunda, C. (2022). "Economizing the road drainage construction's cost using standard design, offsetting and setting out method: a case study of Ogbomosho - Oke - Osogbo road, Nigeria", *Research on Engineering Structures and Materials*, 8(2), 403-420, <http://dx.doi.org/10.17515/resm2022.342st0930tn>.
- Kilani, A., Adeleke, O. and Fapohunda, C. (2022a). "Application of machine learning models to investigate the performance of concrete reinforced with oil palm empty fruit bunch (OPEFB) fibres", *Asian Journal of Civil Engineering*, 23, 299-320, <https://doi.org/10.1007/s42107-022-00424-0>.
- Kilani, A., Fapohunda, C., Adeleke, O. and Metiboba, C. (2022b). "Evaluating the effects of agricultural wastes on concrete and composite mechanical properties: A review", *Research on Engineering Structures and Materials*, 8(2), 307-336, <http://doi.org/10.17515/resm2021.339st0912>.
- Lim, S.K., Tiong, H.Y. and Woon, K.S. (2018). "Compressive strength and dimensional stability of palm oil empty fruit bunch fibre reinforced foamed concrete", *International Conference on Civil and Environmental Engineering (ICCEE 2018)*, *E3S Web of Conference*, 65, 02001, <https://doi.org/10.1051/e3sconf/20186502001>.
- Mack, V., Salehfard, R. and Habibnejad Korayem, A. (2024). "Comparative study of the effects of key factors on concrete-to-concrete bond strength", *Civil Engineering Infrastructures Journal*, 57(1), 205-223, <https://doi.org/10.22059/CEIJ.2023.353447.1903>.
- Mazlan, D. and Abdul, A. (2012). "Properties of cement based composites containing oil palm stem as fiber reinforcement", *Malaysian Journal of Civil Engineering*, 24(2), 107-117, <https://doi.org/10.11113/mjce.v24.15829>.
- Mezher, T.M., Hiswa, A.A.M.R. and Shubber, M.S. (2020). "Improvement of mechanical properties of concrete by using polypropylene fibers and admixture", *Defect and Diffusion Forum*, 398, 167-172, <https://doi.org/10.4028/www.scientific.net/DDF.398.167>.
- Miller, S.A., Habert, G., Myers, R.J. Harvey, J.T. (2021). "Achieving net zero greenhouse gas emissions in the cement industry via value chain mitigation strategies", *One Earth*, 4(10), 1398-1411, <https://doi.org/10.1016/j.oneear.2021.09.011>.
- Musa, A.G., Rajoria, N. and Mohammed, A.G. (2017). "Effect of palm oil fiber on laterized concrete", *International Journal of Engineering Technology, Management and Applied Sciences*, 5(5), 686-695, <https://www.academia.edu/81271528/effect-of->

- [palm-oil-fiber-on-laterized-concrete](#).
- Okonkwo, V.O. and Nwokike, V.M. (2015). "Effect of curing age on the compressive strength of concrete made from local granite chippings", *Journal of Multidisciplinary Engineering Science and Technology (JMEST)*, 2(10), 2671-2675, <https://www.jmest.org/wp-content/uploads/JMESTN42350600.pdf>.
- Omoniyi, T.E. (2019). "Potential of oil palm (*Elaeisguineensis*) empty fruit bunch fibres cement composites for building application", *AgriEngineering*, 1(2), 153-163, <https://doi.org/10.3390/agriengineering1020012>.
- Pillay, D.L., Olalusi, O.B., Kiliswa, M.W., Awoyera, P.O., Kolawole, J.T. and Babafemi, A.J. (2022). "Engineering performance of metakaolin based concrete", *Journal of Cleaner Engineering and Technology*, 6, 100383, <https://doi.org/10.1016/j.clet.2021.100383>.
- Shadheer Ahamed, M., Ravichandran, P. and Krishnaraja, A.R. (2021). "Natural fibers in concrete - a review", *IOP Conference Series Materials Science and Engineering*, 1055, 012038, <https://doi.org/10.1088/1757-899X/1055/1/012038>.
- Sizirici, B., Fseha, Y., Cho, C.S., Yildiz, I. and Byon, Y.J. (2021). "A review of carbon footprint reduction in construction industry, from design to operation", *Materials (Basel)*, 14(20), 6094, <https://doi.org/10.3390/ma14206094>.
- Rao, P.R. and Ramakrishna, G. (2022). "Oil palm empty fruit bunch fiber: surface morphology, treatment, and suitability as reinforcement in cement composites - A state of the art review", *Cleaner Materials*, 6, 100144, <https://doi.org/10.1016/j.clema.2022.100144>.
- Rodier, L., Villar-Cocina, E., Ballesteros, J.M. and Junior, H.S. (2019). "Potential use of sugarcane bagasse and bamboo leaf ashes for elaboration of green cementitious materials", *Journal of Cleaner Production*, 231, 54-63, <https://doi.org/10.1016/j.jclepro.2019.05.208>.
- Sheng, C.V., John, C., Zahid, M.H. Syakur, M.R. (2019). "Effect of empty fruit bunch (oil palm) in concrete", Final Year Project Report, Polytechnic Sultan Salahuddin Abdul Aziz Shah, Malaysia, <http://repository.psa.edu.my/bitstream/123456789/1926/1/Effect%20of%20Empty%20Fruit%20Bunch%20%28Oil%20Palm%29%20in%20Concrete.pdf>.
- Thomas, B.S. (2018). "Green concrete partially comprised of rice husk ash as a supplementary cementitious material - A compressive review", *Renewable and Sustainable Energy Reviews*, 82, 3913-3923, <https://doi.org/10.1016/j.rser.2017.10.081>.
- Yuva, Y. (2023). "Low-strength concrete properties

in existing structures using NDT and core test results", *Journal of Building Engineering*, 76, 107281, <https://doi.org/10.1016/j.jobe.2023.107281>.



This article is an open-access article distributed under the terms and conditions of the Creative Commons Attribution (CC-BY) license.



Permeable Triangular Vanes Effect on Turbulent Flow Field

Ahmadi Adli, S.¹, Abbaspour, A.^{2*}, Hosseinzadeh Dalir, A.³ and Parsa, J.²

¹ Ph.D., Department of Water Science and Engineering, Faculty of Agriculture, University of Tabriz, Tabriz, Iran.

² Associate Professor, Department of Water Science and Engineering, Faculty of Agriculture, University of Tabriz, Tabriz, Iran.

³ Professor, Department of Water Science and Engineering, Faculty of Agriculture, University of Tabriz, Tabriz, Iran.

© University of Tehran 2024

Received: 05 Sep. 2023;

Revised: 8 May 2024;

Accepted: 10 Jun. 2024

ABSTRACT: In this study, a Large Eddy Simulation (LES) model was used to simulate the turbulent flow field around the triangular vanes affected by different permeability rates and vanes angle. Depth-averaged velocity and bed shear stress distributions are affected due to the local effects of the triangular vanes structure; however, by increasing the permeability rate, these structures impacts on the flow field have been reduced. On average, maximum bed shear stress values around the simulated vanes were 3.47 times the τ_{Mean} . Tip velocity near the bed region for the 70% permeable vane with $\theta = 58^\circ$ and $\theta = 68^\circ$ was 1.13 times the V_{app} . The thalweg line alignment was affected by the flow field constriction and local flow structure. Due to the triangular vanes' cross-sectional opening and smoother flow deflection, which varied between 4° and 30° , the thalweg line generally showed a minor deflection from the channel centerline.

Keywords: Large Eddy Simulation, Permeability, Triangular Vanes, Turbulent Flow, Vanes Angle.

1. Introduction

In recent years, new river restoration techniques such as bank-attached triangular vanes have been proposed not only to protect river banks and stabilize the river bed but also to improve the river ecosystem regarding the growing awareness of the environmental issues (Pagliara and Kurdistan, 2017).

Bhuiyan et al. (2010) studied the effect of bank-attached triangular vanes on flow pattern and bed topography variations in the large-scale meandering channel. They concluded that the induction of a secondary flow near the outer bank counteracts the

main spiral flow in the bend, and horizontal vortices are not formed behind these structures. Kang et al. (2011) investigated the effect of the different geometry and permeability rates on turbulent flow characteristics around the rectangular and triangular-shaped groins. Generally, they concluded that weaker vortices occurred around triangular-shaped groins, and these structures are appropriate for multipurpose design. Teraguchi et al. (2011) studied the scour-deposition process and flow characteristics affected by permeable and impermeable groins. Results showed that velocity has been decreased around permeable groins, and the absence of strong

* Corresponding author E-mail: akabbaspour@yahoo.com

eddies around these structures prevents excessive siltation. Fang et al. (2014) employed a Large Eddy Simulation (LES) model to study the effect of groin head shape, aspect ratio, and length on flow characteristics around non-submerged groin in a shallow open channel flow.

Bahrami Yarahmadi and Shafai Bejestan (2015) studied scour-deposition and flow patterns affected by different triangular vane spacing in a 90° mild flume bend. Results showed that due to the vanes presence in the channel, counter-clockwise secondary flow near the outer bank forms, which counteracts the clockwise main secondary flow along the bend. Ferro et al. (2019) proposed a new technique, which is a combination of a permeable groin and a triangular vane, and they evaluated the effectiveness of this technique in river bends. Different combinations and flow rates were considered in this study. Results showed that the triangular vane enhances the performance of the permeable groin. Wang et al. (2020) investigated turbulent flow features in the wide and narrow channels using an Acoustic Doppler Velocimeter (ADV). In this study, turbulent kinetic energy, Reynolds shear stress, and turbulent intensities were investigated. Shampa et al. (2020) focused on the effects of the different installation angles and spur dikes position on three-dimensional flow characteristics. Three-dimensional velocity variations, flow depth fluctuations, and bed shear stress distribution were analysed to evaluate the efficiency of these structures.

Abdou et al. (2021) used LES to study flow characteristics in a 193° sharp laboratory flume bend. Water depth fluctuations, stream wise and transverse velocity distributions at different sections and over the whole channel were investigated. Iqbal et al. (2021) used Fluent model and Reynolds Stress Model (RSM) to study velocity profiles, turbulent intensities, and turbulent kinetic energy at different selected points in the horizontal plane around permeable rectangular spur dikes. Results showed that strong turbulent

flows do not occur around the tip region of the permeable spur dikes, and turbulent flow features have been decreased around these structures. Jafari and Sui (2021) studied turbulence structure and velocity variations around the non-submerged spur dikes having different orientation angles under the ice covered conditions using ADV. Results showed that tip region was critical and strong velocity fluctuations mainly occurred in this region, also ice cover on the water surface affects the bed shear stress and turbulence intensities. Haider et al. (2022) used Fluent to study the turbulent flow characteristics affected by the permeable spur dikes with different staggered pores having varying angles. Different permeability rates and staggered pores angles were considered. Velocity distributions, turbulent kinetic energy, turbulence intensity, and wall shear stress were compared around the considered permeable spur dikes. Mostafa et al. (2023) studied the flow structure and velocity around hybrid groins affected by different angles and geometry orientations using ADV.

To understand the effect of the channel constriction due to the groins presence on flow characteristics, longitudinal and transverse velocity variations at the groins tip were investigated. Most of the previous works related to triangular vanes mainly considered the impermeable form of these structures and focused on the local scour characteristics, morphological changes, and bed deformations affected by the vanes spacing in the straight and meandering channel conditions. Detailed results about turbulent flow features have not been presented for these structures. In this paper, LES model is employed to understand the effect of different permeability rates and vanes angles on turbulent flow characteristics around these structures. LES model is used due to its capability of modelling the wakes and vortices more accurately.

2. Materials and Methods

2.1. Governing Equations

LES is a turbulent model applied in a wide variety of engineering applications in which by filtering the partial differential equations, continuity and Navier-Stokes equations for incompressible flows are written as follows:

$$\frac{\partial \bar{u}_i}{\partial x_i} = 0 \quad (1)$$

$$\frac{\partial \bar{u}_i}{\partial t} + \frac{\partial (\bar{u}_i \bar{u}_j)}{\partial x_j} = -\frac{1}{\rho} \frac{\partial \bar{p}}{\partial x_i} + 2\nu \frac{\partial}{\partial x_j} \bar{S}_{ij} \quad (2)$$

where \bar{u}_i : is the filtered velocity component x_i and x_j : are the spatial coordinate, t : is time variable, ρ : is fluid density, ν : is kinematic viscosity, \bar{p} : is the filtered pressure field, \bar{S}_{ij} : is the rate-of-strain tensor, $\bar{u}_i \bar{u}_j$: is a nonlinear filtered term which needs to be modeled since the unfiltered velocity field is unknown. The term can be split up, and the filtered Navier-Stokes equations are written as below:

$$\bar{u}_i \bar{u}_j = \tau_{ij} + \bar{u}_i \bar{u}_j \quad (3)$$

$$\frac{\partial \bar{u}_i}{\partial t} + \frac{\partial (\bar{u}_i \bar{u}_j)}{\partial x_j} = -\frac{\partial \bar{p}}{\rho \partial x_i} + 2\nu \frac{\partial}{\partial x_j} \bar{S}_{ij} - \frac{\partial \tau_{ij}}{\partial x_j} \quad (4)$$

Smagorinsky-Lilly subgrid-scale model was used to model the unclosed residual stress tensor τ_{ij} . Eddy-viscosity is modelled in this subgrid-scale model and the governing equations of Smagorinsky-Lilly model can be written as follows (Smagorinsky, 1963):

$$\tau_{ij} - \frac{1}{3} \tau_{kk} \delta_{ij} = -2\mu_t \bar{S}_{ij} \quad (5)$$

$$\mu_t = \rho (C_s \Delta)^2 |\bar{S}| \quad (6)$$

$$\bar{S} = \sqrt{2S_{ij}S_{ij}} \quad (7)$$

where C_s , μ_t , ρ and Δ : are the model constant (0.1 - 0.2), eddy viscosity, density, and cube root of the local grid cell volume, respectively. τ_{kk} : is the isotropic part of the subgrid stresses, δ_{ij} : is kronecker delta and

$|\bar{S}|$: is magnitude of the resolved strain-rate tensor.

2.2. Numerical Model

2.2.1. Model Setup

The computational domain composed of a rectangular channel and non-submerged triangular vanes of varying permeability rates and angles which was created and meshed using Gambit. Channel length (L) and width (B) were considered as 2 m and 0.5 m and contraction ratio (L_v / B) was 0.25, where L_v : is the length of the vane.

Cylindrical tubes of 6 mm diameter with different intervals were considered to adjust the different permeability rates (P) (Figure 1). Boundary conditions at the channel inlet, outlet, and solid surfaces, such as vanes, channel bed, and side walls were defined as pressure inlet, pressure outlet, and wall, respectively. For the free surface, a pressure inlet boundary condition was used.

Fluent was used to simulate turbulent flow around triangular vanes. Inlet flow depth (H), approach flow velocity (V_{app}), flow Froude and Reynolds numbers were 0.15, 0.66, 0.54, and 61875, respectively.

Stream wise distance from the vanes, transverse distance from the channel sidewall, and vertical distance from the channel bed are defined by X , Y , and Z , respectively. Negative and positive values refer to sections located upstream and downstream of the vanes.

2.2.2. Data Validation

In this paper, the results of the tip velocity (V_{tip}/V_{app}), flow separation angle (β°) and downstream flow separation width (W_s/B) of impermeable triangular groins of the experimental study of Kang et al. (2011) were used to evaluate the applied numerical model accuracy and determine the appropriate number of nodes. Numerical simulations were performed under the same conditions, except for channel length, which was reduced to 3 m to avoid large mesh numbers.

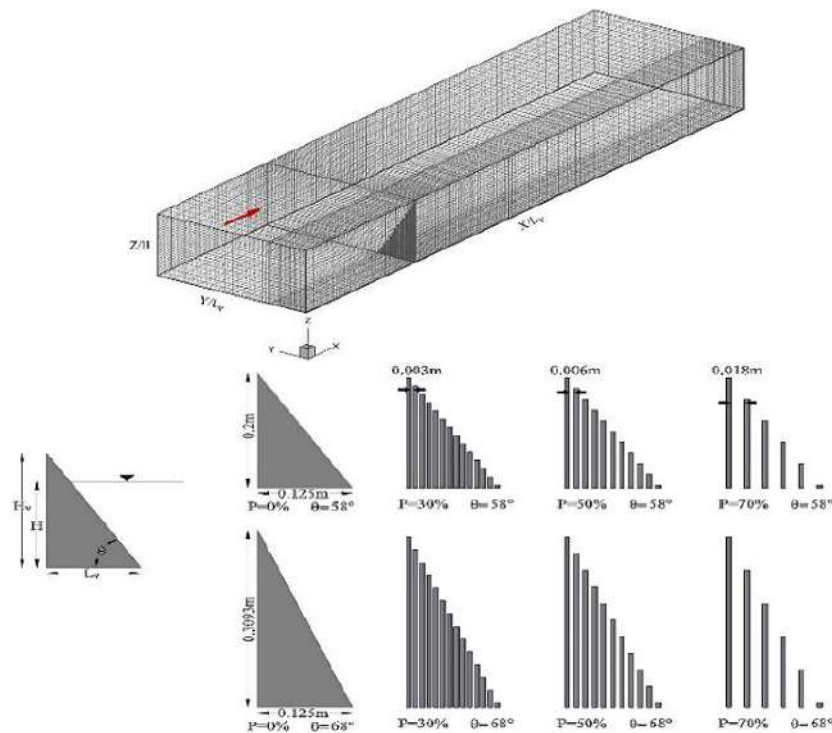


Fig. 1. Computational domain and dimensions of simulated vanes

Since the relative error values of the compared parameters are less than 10%, LES model can resolve the turbulent flow field accurately (Table 1). Furthermore, mesh independence test results for impermeable triangular groin ($\theta = 45^\circ$) showed a negligible difference (4.6%) between experimental and simulated values of the tip velocity by increasing the number of nodes; thus, a mesh composed of approximately 151400 to 170600 nodes was applied to all models (Figure 2).

3. Results and Discussions

3.1. Depth-Averaged Velocity

Velocity distribution in all simulated models clearly showed that due to the local effects of vanes' structure and channel constriction as a result of the vanes' protrusion, two zones are formed in the flow field, which are the main flow field, upstream, and downstream separation region (Figure 3).

These zones are separated by a fully turbulent and dynamic flow named detached shear layer. In the upstream of the impermeable vanes, $-1.6 \leq X/L_v \leq 0$, flow velocities near the channel side wall reduced due to the backwater effect. At the $X/L_v = 0$ section, local flow has been affected and velocity values have been increased due to the flow deflection. In the downstream region, presence of the recirculation zone, detached shear layer, different wakes and vortices significantly affected the flow field and maximum velocities occurred in this region. On average, maximum velocity values are $1.46V_{app}$.

Generally presence of the horseshoe vortices and high velocity zone near the bed and vanes tip region effects the local scour hole characteristics. Tip velocity in this critical region has a declining trend with increasing permeability rates and decreases up to 25% for the 70% permeable vane with $\theta = 58^\circ$ and 31.8% in the $\theta = 68^\circ$ case.

Table 1. Numerical simulation validation results

Crest angle (θ)	V_{tip} / V_{app}	β°	W_s / B
35	5.86%	6.25%	6.52%
45	4.6%	6.06%	6.66%

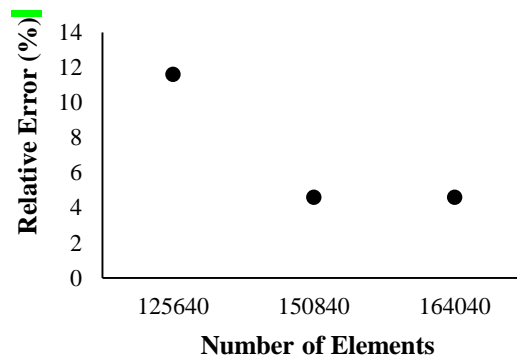


Fig. 2. Average relative error of experimental and simulated tip velocity of impermeable triangular groin ($\theta = 45^\circ$)

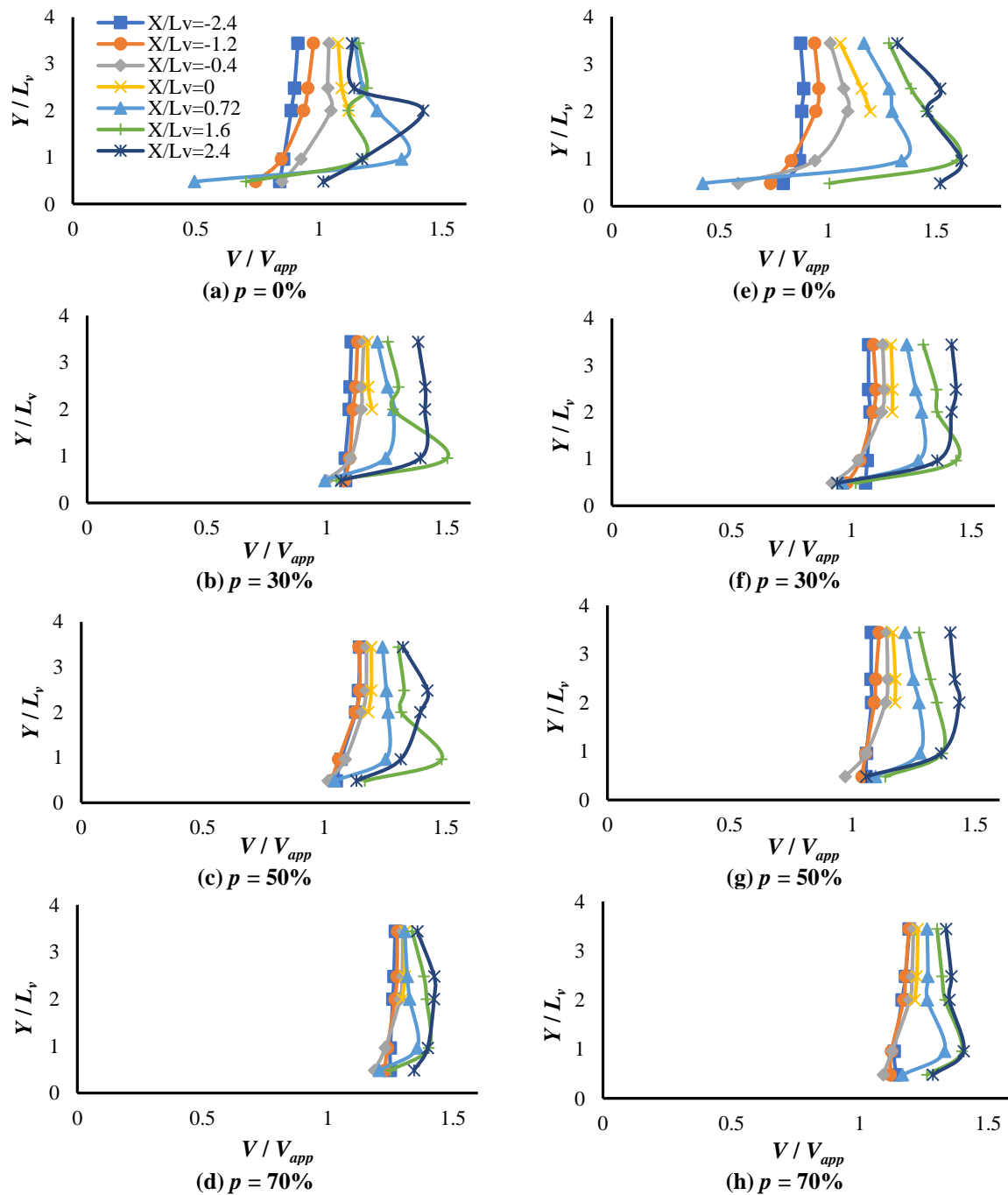


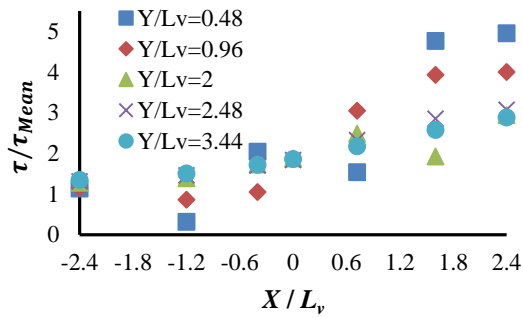
Fig. 3. Depth-averaged velocity distribution around triangular vanes; a, b, c, and d) $\theta = 58^\circ$; and e, f, g, and h) $\theta = 68^\circ$

3.2. Bed Shear Stress

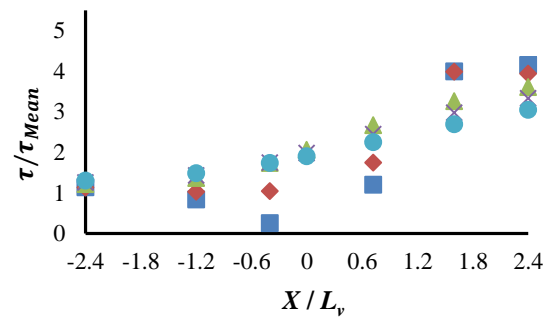
In this study, bed shear stress variation around the triangular vanes is plotted using the dimensionless parameter (τ / τ_{Mean}), where τ_{Mean} is the average bed shear stress of the impermeable rectangular vane at the channel entrance (Figure 4).

Generally, due to the complex condition

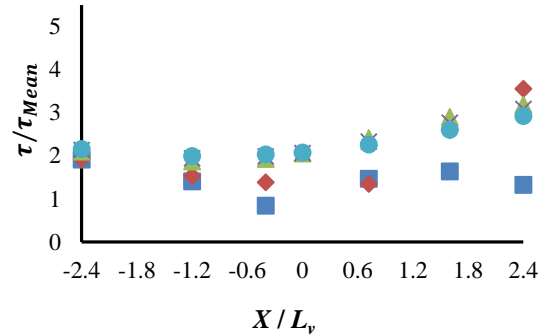
of the downstream region, such as flow deflection within the different layers of the flow field, formation of the strong eddies, secondary flows within the recirculation zone, and their subsequent interaction with different wakes or vortices, maximum bed shear stress values mainly occurred at $X / L_v = 2.4$ section.



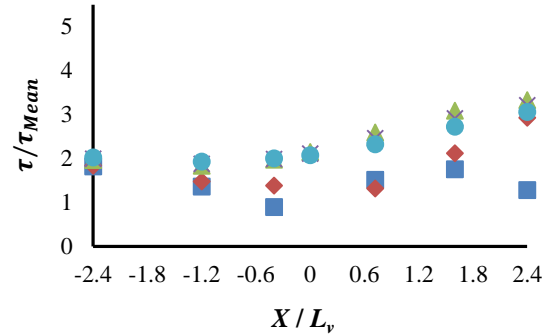
(a) $p = 0\%$



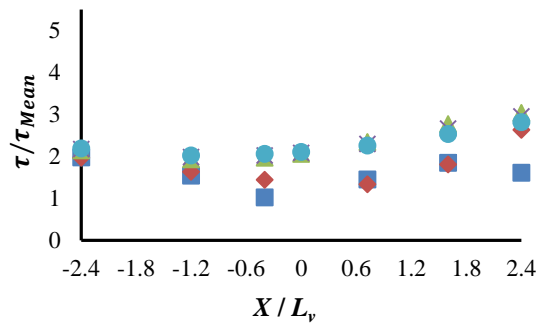
(e) $p = 0\%$



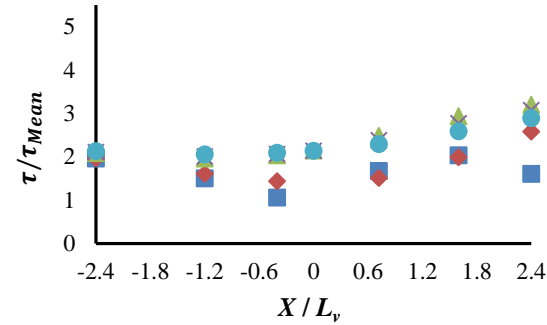
(b) $p = 30\%$



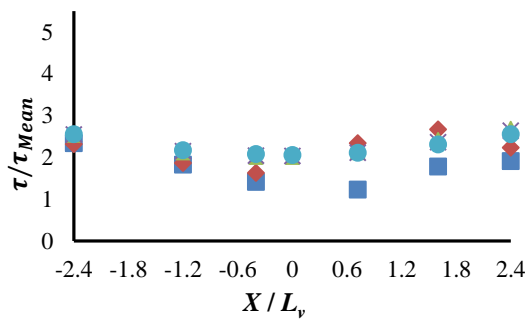
(f) $p = 30\%$



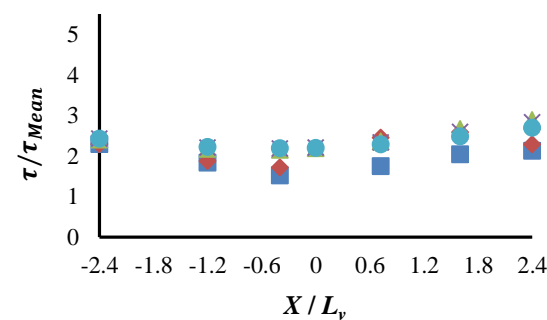
(c) $p = 50\%$



(g) $p = 50\%$



(d) $p = 70\%$



(h) $p = 70\%$

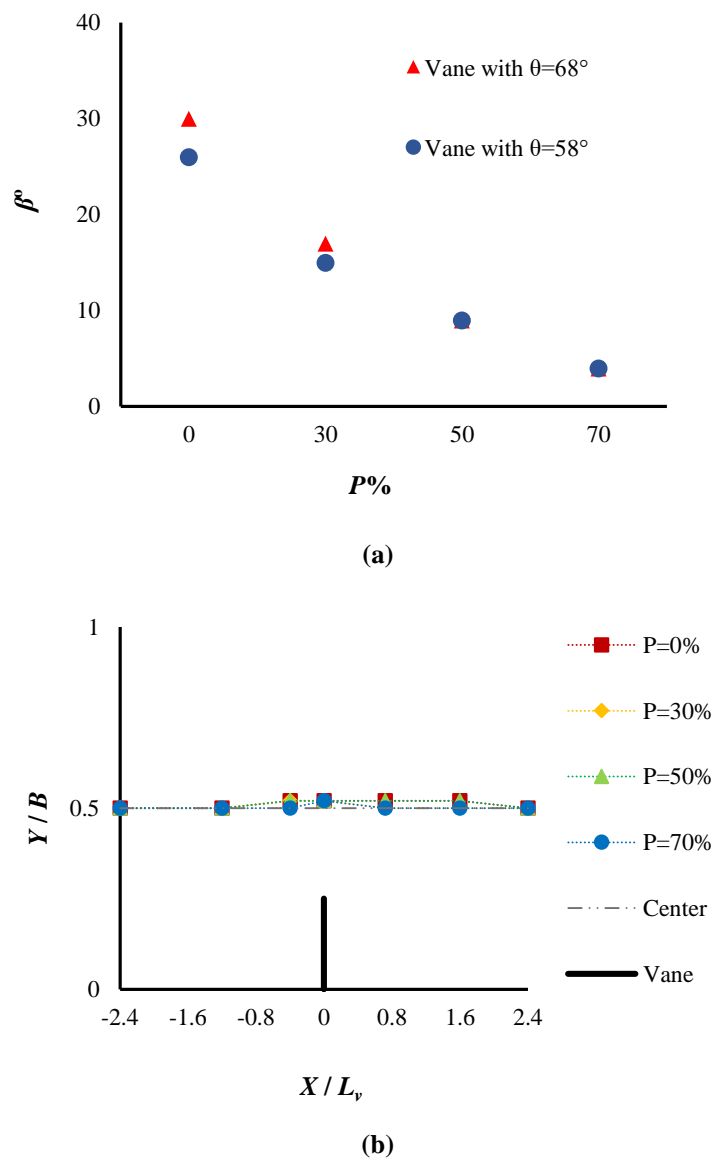
Fig. 4. Bed shear stress variations around simulated triangular vanes; a, b, c, and d) $\theta = 58^\circ$; and e, f, g, and h) $\theta = 68^\circ$

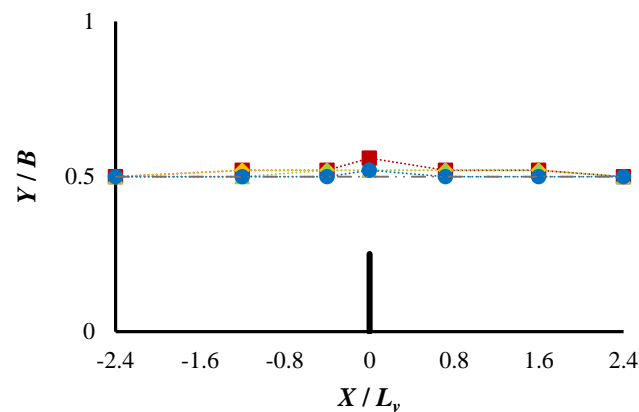
Maximum bed shear stress decreases up to 45.6% for the 70% permeable vane with $\theta = 58^\circ$ and 30.3% in the $\theta = 68^\circ$ case. Furthermore, maximum bed shear stress values shifted to the channel centreline by increasing the permeability rates of the triangular vane. Maximum values of the friction coefficient for all of the simulated triangular vanes vary between $0.006 \leq C_{fmax} \leq 0.018$ along the $-2.4 \leq X/L_v \leq 2.4$ region.

3.3. Thalweg Line Variation

The maximum stream wise velocity line, which is considered as the deepest flow line in alluvial rivers, is defined as the thalweg line. Upstream of the impermeable vanes, as flow reaches the vicinity of the

structure, it begins to bend, and velocity magnitude values increase. The highest velocity values occur at the $X/L_v = 0$ section. In the downstream, as the vanes' presence impact on the main flow field decreases, the thalweg line gradually returns to the channel centerline. The main flow field constriction and local flow structure affected by the vanes' protrusion mainly deflect the thalweg line from the channel centerline. Generally, by increasing the permeability rate of the vanes, the downstream recirculation zone does not form due to the smaller flow deflection angles (Figure 5a); thus, for 70% permeable triangular vanes, the thalweg line is almost coincident with the channel centerline (Figures 5b and 5c).





(c)

Fig. 5. Flow deflection angle and thalweg line variations; a) Flow deflection angle; b) $\theta = 58^\circ$; and c) $\theta = 68^\circ$

4. Conclusions

Numerical model accuracy assessed using experimental results of the tip velocity, flow separation angle, and downstream flow separation width of impermeable triangular groins of Kang et al. (2011) study.

The experimental and numerical results agreed well, since the average relative error values were less than 10%. Depth-averaged velocity distribution and bed shear stress variations showed that the presence of the impermeable triangular vanes significantly affected the downstream flow field due to the formation of the strong and stable vortices. Maximum velocities in all cases generally occurred in the $1.6 \leq X/L_v \leq 2.4$ region. Furthermore, at the near-bed region, tip velocity increased up to 10% for the impermeable triangular vane with $\theta = 68^\circ$.

Depth-averaged velocity variations clearly showed the presence of two different zones in the flow field, flow separation and turbulence due to the interaction of different wakes and vortices affected the flow velocities and sediment deposition process in these regions. Bed shear stress variation results showed that by increasing the vane angle from 58° to 68° in impermeable cases, maximum bed shear stress decreases up to 16.3%. Generally, for all simulated vanes, the maximum shear stress ratio (τ_{Max}/τ_{Mean}) varies between 2.6 and 4.9. Furthermore, maximum shear stress values shifted towards the channel centerline in

permeable cases; thus, this could be considered as one of the advantages of these structures in comparison to the impermeable ones for the river bank protection. However, it must be noted that vanes with higher permeability rates do not have a noticeable effect on controlling the local flow characteristics and velocity decreasing. Channel lateral constriction reduced due to the triangular vanes' cross-sectional opening; thus, weaker vortices occurred in the flow field, and in all of the simulated cases, the thalweg line shifts closer to the channel centerline.

5. References

- Abdou, S.S., ElMoustafa, A.M. and Samy, M. (2021). "Assessing flow bends in open channels", *International Research Journal of Advanced Engineering and Science*, 6(2), 49-54, <http://irjaes.com/wp-content/uploads/2021/04/IRJAES-V6N2P55Y21.pdf>.
- Bahrami Yarahmadi, M. and Shafai Bejestan, M. (2015). "Sediment management and flow patterns at river bend due to triangular vanes attached to the bank", *Journal of Hydro-environment Research*, 10, 64-75, <https://doi.org/10.1016/j.jher.2015.10.002>.
- Bhuiyan, F., Hey, R.D. and Wormleaton, P.R. (2010). "Bank-attached vanes for bank erosion control and restoration of river meanders", *Journal of Hydraulic Engineering*, 136(9), 583-596, [https://doi.org/10.1061/\(ASCE\)HY.1943-7900.0000217](https://doi.org/10.1061/(ASCE)HY.1943-7900.0000217).
- Fang, H., Bai, J., He, G. and Zhao, H. (2014). "Calculations of nonsubmerged groin flow in a shallow open channel by large-eddy

- simulation”, *Journal of Engineering Mechanics*, 140(5), 04014016, [https://doi.org/10.1061/\(ASCE\)EM.1943-7889.0000711](https://doi.org/10.1061/(ASCE)EM.1943-7889.0000711).
- Ferro, V., Shokrian Hajibehzad, M., Shafai Bejestan, M. and Kashefipour, S.M. (2019). “Scour around a permeable groin combined with a triangular vane in river bends”, *Journal of Irrigation and Drainage Engineering*, 145(3), 04019003, [https://doi.org/10.1061/\(ASCE\)IR.1943-4774.0001380](https://doi.org/10.1061/(ASCE)IR.1943-4774.0001380).
- Haider, R., Qiao, D., Yan, J., Ning, D., Ahmed Pasha, G. and Iqbal, S. (2022). “Flow characteristics around permeable spur dike with different staggered pores at varying angles”, *Arabian Journal of Science and Engineering*, 47, 5219-5236, <https://doi.org/10.1007/s13369-021-06435-4>.
- Iqbal, S., Pasha, G.A., Ghani, U., Ullah, M.K. and Ahmad, A. (2021). “Flow dynamics around permeable spur dike in a rectangular channel”, *Arabian Journal for Science and Engineering*, 46, 4999-5011, <https://doi.org/10.1007/s13369-020-05205-y>.
- Jafari, R. and Sui, J. (2021). “Velocity field and turbulence structure around spur dikes with different angles of orientation under ice covered flow conditions”, *Water*, 13(13), 1844, <https://doi.org/10.3390/w13131844>.
- Kang, J., Yeo, H., Kim, S. and Ji, U. (2011). “Permeability effects of single groin on flow characteristics”, *Journal of Hydraulic Research*, 49(6), 728-735, <https://doi.org/10.1080/00221686.2011.614520>.
- Mostafa, M.M., Ameen, M.A., Mohamed, H.I. and Ahmed, H.S. (2023). “Optimal flow pattern around hybrid groins with various orientations to improve fish habitat via experimental investigation using acoustic doppler velocimeter”, *SVU-International Journal of Engineering Sciences and Applications*, 4(2), 98-106, <https://doi.org/10.21608/svusrc.2023.189730.1096>.
- Pagliara, S. and Kurdistani, S.M. (2017). “Flume experiments on scour downstream of wood stream restoration structures”, *Geomorphology*, 279(2), 141-149, <https://doi.org/10.1016/j.geomorph.2016.10.013>.
- Shampa, S., Hasegawa, Y., Nakagawa, H., Takebayashi, H. and Kawaike, K. (2020). “Three-dimensional flow characteristics in slit-type permeable spur dike fields: Efficacy in riverbank protection”, *Water*, 12(4), <https://doi.org/10.3390/w12040964>.
- Smagorinsky, J. (1963). “General circulation experiments with the primitive equations I, the basic experiment”, *Monthly Weather Review*, 91(3), 99-164.
- Teraguchi, H., Nakagawa, H., Kawaike, K., Baba, Y. and Zhang, H. (2011). “Effects of hydraulic structures on river morphological process”, *International Journal of Sediment Research*, 26(3), 283-303, [https://doi.org/10.1016/S1001-6279\(11\)60094-2](https://doi.org/10.1016/S1001-6279(11)60094-2).
- Wang, W., Liao, W. and Qi, L. (2020). “Experiment of turbulent characteristics of flow in wide and narrow Channels”, *Advances in Water Science*, 31(3), 394-403, <https://doi.org/10.14042/j.cnki.32.1309.2020.03.009>.



This article is an open-access article distributed under the terms and conditions of the Creative Commons Attribution (CC-BY) license.



Optimizing the Performance of L-Shaped Concrete-Filled Steel Tube Columns Under Eccentric Loading

Labibzadeh, M.^{1*} , Kordi, M.², Hosseinlou, F.³ , Rezaeian, A.¹ and Khayat, M.³

¹ Associate Professor, Department of Civil Engineering, Faculty of Civil Engineering and Architecture, Shahid Chamran University of Ahvaz, Ahvaz, Iran.

² M.Sc. Student, Department of Civil Engineering, Faculty of Civil Engineering and Architecture, Shahid Chamran University of Ahvaz, Ahvaz, Iran.

³ Assistant Professor, Department of Civil Engineering, Faculty of Civil Engineering and Architecture, Shahid Chamran University of Ahvaz, Ahvaz, Iran.

© University of Tehran 2024

Received: 21 Feb. 2024;

Revised: 5 Apr. 2024;

Accepted: 21 Apr. 2024

ABSTRACT: Special-Shaped Concrete-Filled Steel Tube (SCFST) columns have a higher bearing capacity, ductility, and energy absorption compared to other columns. Due to their special shape, the columns can be utilized in different parts of the building without protrusion of member. In L-shaped CFST columns, this study investigated the effect of various parameters (such as yield stress of the steel wall, characteristic strength of the concrete, height of the column, thickness of the steel wall, and geometry of the stiffeners) on the eccentric load-bearing capacity. In other words, the bearing capacity has been measured based on the optimal performance of these columns under the effect of axial and eccentric loads. Also, the ratio of load-to-weight (p/w) has been considered. Load-displacement diagrams and the weight of steels used in different columns are compared. Based on the obtained results, the changing of the thickness and strength of the steel wall has a significant effect on increasing the bearing capacity. Whereas, the concrete strength has a lesser impact on the bearing capacity of the columns. The column with greater thickness performs better than the column with less thickness in terms of ductility and energy absorption capacity under eccentric loading.

Keywords: Special-Shaped Column, Concrete-Filled Steel Tube Column, Eccentric Bearing Capacity, Optimal Performance.

1. Introduction

Special-Shaped Concrete-Filled Steel Tube (SCFST) columns have a lower steel consumption ratio and more stiffness than normal steel columns, and this is due to the presence of concrete inside the steel pipe. Also, in a reinforced concrete column, only transverse reinforcements create confinement pressure for the concrete core, while in the steel column filled with

concrete, the entire steel wall plays the role of confinement for the concrete core. In buildings, columns with a special shape do not occupy much space, and as a result, they are generally useful in terms of architecture.

There is no cost of column formatting when using the concrete-filled steel tube columns (Hatzigeorgiou and Beskos, 2005; Dundar et al., 2008). Despite all the advantages of SCFST columns, the use of these columns has limitations. The

* Corresponding author E-mail: labibzadeh_m@scu.ac.ir

complexity of connecting beams to these columns and the lack of experience in construction are the most important limitations. Also, when the steel wall yields, the pressure on the concrete core increases greatly. Therefore, studying the behavior of SCFST columns under axial loading requires extensive studies (Ghandi et al., 2024; Zhou et al., 2024). Zhi-hua et al. (2009) used laboratory tests to investigate the mechanical properties and failure processes of SCFST columns under compressive loads. In order to compare the final load capacities and failure modes from their simulations with the experimental observations, they also carried out a finite element analysis. They also created methods to forecast these SCFST columns' compressive strength.

Zhang et al. (2018) investigated the behavior of seven SCFST columns featuring double plate connections subjected to axial compressive forces. Their study assessed how variations in the height and width of these connecting plates affected column performance and led to the formulation of equations for calculating the columns' load-bearing capacity. The tests demonstrated that the double LCFST columns exhibited strong axial compressive performance and that the single columns performed effectively within the double LCFST column's structural framework. They also utilized 3D nonlinear finite element models to analyze the mechanical properties and axial compressive behavior of the double LCFST columns, finding that the model results were consistent with the experimental data. Their parametric studies, based on these models, explored the impact of factors such as the thickness and width of vertical steel plates, the slenderness ratio, and the size and thickness of the steel pipe, and they proposed a new method for calculating the slenderness ratio.

Chen et al. (2021) conducted five sets of eccentric compression tests to look at the mechanical characteristics of SCFST columns under axial stresses and bending moments around the center of mass's main

axis. Their work, which followed international standards and integrated finite element calculations and experimental testing, produced a formula for evaluating the in-plane stability of SCFST columns that were bent and subjected to axial forces around the main axis.

Chen et al. (2021) investigated the effects of uniaxial eccentric compression on CFST composite columns with double sheet connections, taking into account varying eccentricities and loading directions. Axial load-displacement curves and fracture models from experimental testing, as well as finite element calculations, were compared. They proposed a new formula for the stability capacity of CFST composite columns with double plate connections. They introduced a theoretical formula for predicting the bearing capacity of specimens under uniaxial eccentric compression. They achieved this by applying the superposition principle and slenderness ratio calculation methods based on steel structure design standards.

The temperature distribution, axial deformation, fire resistance, and failure modes of LCFST columns were investigated by Yang et al. (2022). Their parametric research showed that fire resistance is highly dependent on factors such as component thickness, eccentricity ratio, slenderness ratio, and thickness of the fire protection layer. In comparison to the current CFST column fire design standards, they found that a thicker fire protection layer could result in higher fire resistance ratings for LCFST columns. They also proposed simplified formulas for determining fire resistance and the required thickness of the fire protection layer, which could result in a 50% reduction in thickness.

Liu et al. (2024a,b) investigated a novel L-shaped irregular concrete-filled steel tube column design, which offers enhanced convenience for installation and construction. Their study included tests on two full-scale specimens under axial compression and two under eccentric compression, and they developed finite

element models to simulate the loading process. The results from the FE models were in close agreement with the experimental findings. Ma et al. (2025) studied L-shaped columns constructed from recycled aggregate concrete-filled steel tubes using eccentric compression tests and numerical validation, developing an N-M relationship curve for improved safety predictions. Chen et al. (2024) designed and tested a steel cage featuring transverse steel bars for ultra-thin high-strength steel tube high-strength concrete medium-long column specimens. Their findings showed that the steel cage effectively mitigated bulging in the specimens and enhanced the steel pipe's restraint on the concrete.

A review of existing research highlights ongoing limitations in understanding the behavior of CFST columns with specific shapes under eccentric loading conditions. This manuscript addresses these gaps by employing finite element modeling to study SCFST columns and exploring methods to improve their performance under eccentric loading scenarios. For the first time, this study considers the load-to-weight ratio (p/w) as a key factor for optimizing SCFST column performance under eccentric loading, aiming to identify the most effective columns based on their p/w . This study evaluates a wide range of samples and distinguishes between the five best-performing and five weakest-performing

columns across two categories: short and long columns.

2. Numerical Simulation

In fact, the SCFST columns are a special form of CFST columns that are made up of several single columns connected by sheets and stiffeners. These columns are divided into different types based on the shape of the cross-section and the placement of single columns and their connections. Some examples of these columns are shown in Figure 1. In this study, the simulation of SCFST columns is conducted using the finite element software ABAQUS. The numerical simulation process involves several key steps: modeling the column geometry, simulating the material behavior, defining boundary conditions and interactions between model components, selecting appropriate element types, creating a mesh, applying the specified loading conditions to the model, and choosing the suitable analysis type.

2.1. The Geometry and Materials

The SCFST column consists of several components, including a square steel tube, connecting plates, concrete, transverse stiffeners, loading plates, and both upper and lower column stiffeners, as illustrated in Figure 2. In the ABAQUS software, these components are modeled separately.

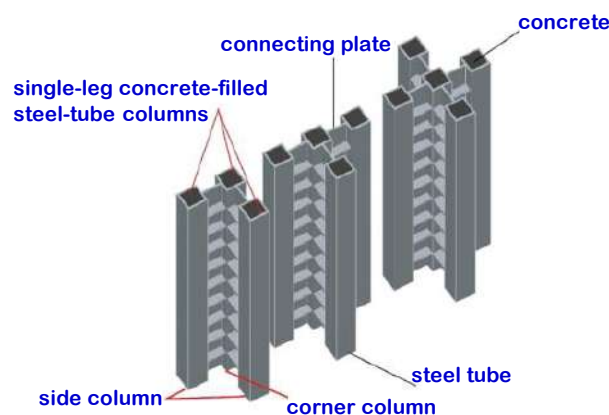


Fig. 1. Different configurations of SCFST columns (Chen et al., 2020)

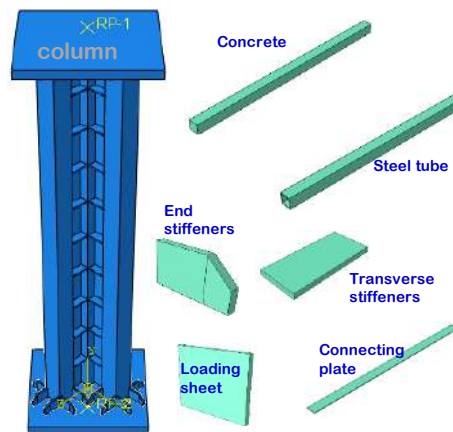


Fig. 2. The column and its components modeled in ABAQUS

The modeling process involves first constructing the steel column and stiffeners, then filling the space with concrete, and finally placing the loading plate on top of the column to apply the force (Chen et al., 2024; Wang, 2024). To simulate the SCFST columns, both concrete and steel materials are utilized. The Concrete Damage Plasticity (CDP) model from the ABAQUS material library is employed to define the concrete's behavior. This model is based on two primary mechanisms for concrete failure: tensile cracking and compressive crushing (Labibzadeh et al., 2017 and 2018). The CDP model is capable of capturing the complex behavior of concrete through isotropic elastic damage coupled with plasticity for both compressive and tensile forces. It is also designed to handle dynamic, one-way, and cyclic loading conditions (Labibzadeh and Hamidi, 2017). The majority of credible research studies use the CDP model for concrete. For defining the elastic properties of concrete, the modulus of elasticity and Poisson's ratio are required, which can be obtained from laboratory tests or estimated using ACI 318 (2011) standards.

3. Results

3.1. Eccentric Bearing Capacity of SCFST Columns

To investigate the effect of different parameters on the eccentric bearing capacity of SCFST columns, different models with varied specifications are built.

For this purpose, all the investigated parameters are considered fixed (L0, C20, F250, H2, A25) and only one of them is changed. Then, the column is subjected to eccentric loading.

3.1.1. Effect of Steel Tube Thickness

To compare the energy absorption and ductility of SCFST columns under eccentric load, three specimens with thicknesses of 4, 6, and 8 mm have been considered. In the specimens simulated in ABAQUS, the specifications of examined columns are considered constant (C20, F250, H2000, A25), and only the thickness of the steel tube has changed ($t = 4, 6, \text{ and } 8 \text{ mm}$). The dimensions of the steel tube are 100 mm.

Energy is equal to the area under the load-displacement diagram up to the peak point of the curve. In Figure 3, the bearing capacity of columns with different thicknesses and eccentric loading are compared. In Table 1, the amount of energy absorption of each column under eccentric loading is also listed. It can be seen that the amount of energy absorption of the column with a tube thickness of 8 mm under loading with eccentricity of -120 mm is about 3.7 times more than the column with a tube thickness of 4 mm and 1.7 times more than the column with a tube thickness of 6 mm. Also, the energy absorption of the column with a thickness of 8 mm under loading with eccentricity of 120 mm is 2.5 times more than the column with a thickness of 4 mm and 1.5 times more than the column with a thickness of 6 mm.

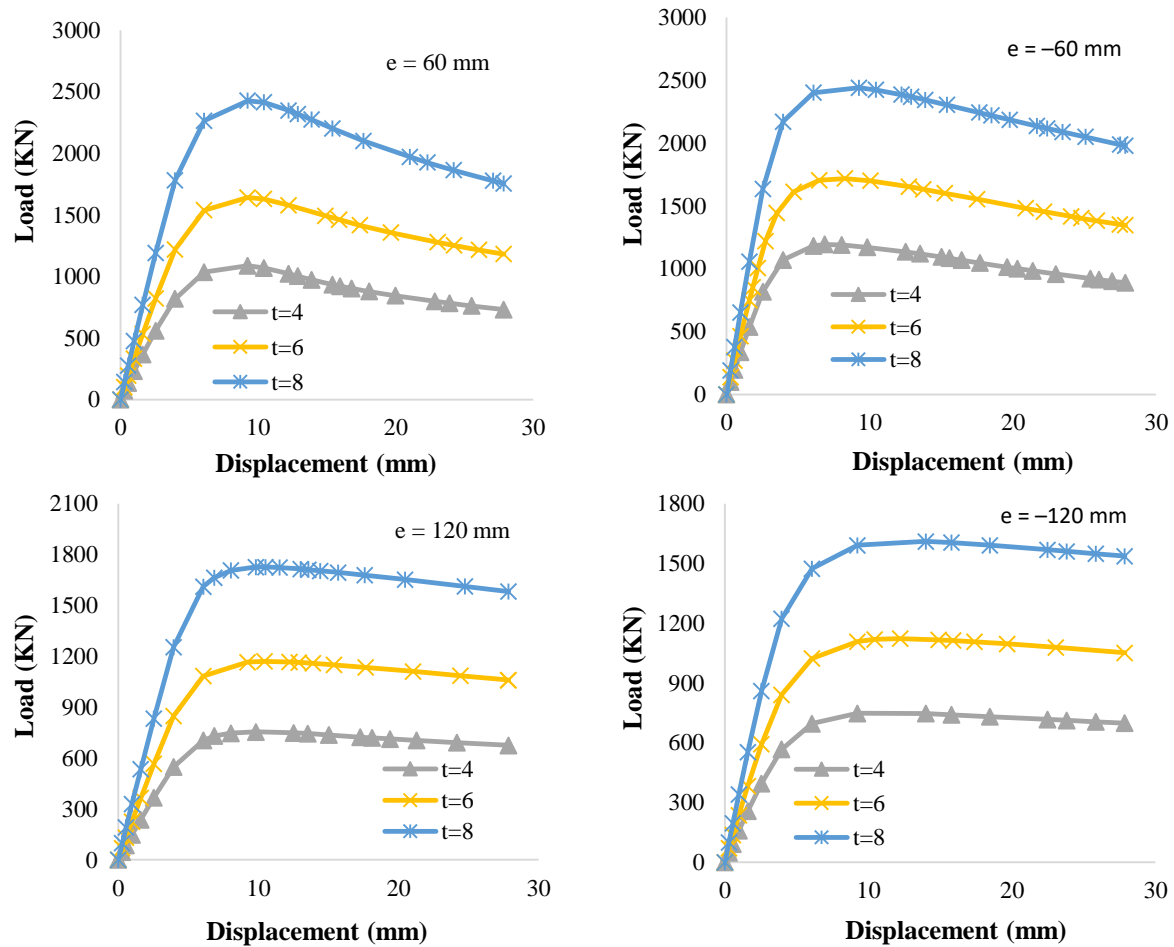


Fig. 3. Effect of steel tube thickness on load-carrying capacity under eccentric loading

Table 1. Comparison of energy absorption of SCFST columns

Feature	E (kN.mm)	E (kN.mm)	E (kN.mm)	E (kN.mm)
Eccentricity (mm)	$e = 60$	$e = -60$	$e = 120$	$e = -120$
$t = 4$ mm	4822.198	5234.006	5732.06	7035.35
$t = 6$ mm	10457.41	8734.964	10601.38	10468.35
$t = 8$ mm	17910.99	13100.36	17315.1	15359.85

The ductility of a member is the ability to deform plastic without a significant loss of strength before failure. Deformation capacity is generally utilized to acquire ductility. The ductility of the column is calculated considering the $P-\Delta$ diagram.

Eq. (1) is applied to calculate the ductility of columns (Tao et al., 2008; Dancygier and Berkover, 2016).

$$\mu_{0.85} = \frac{\Delta_{0.85}}{\Delta_y} \quad (1)$$

where $\Delta_{0.85}$: is the displacement corresponding to the point where capacity degrades to 85% of its peak.

According to Figure 3 and Table 1, it

can be stated that the eccentric bearing capacity of the column with a tube thickness of 8 mm under loading with $e = -120$ mm is about 1.4 times more than the bearing capacity of the column with a tube thickness of 6 mm and 2.15 times more than the column with a tube thickness of 4 mm. Meanwhile, the weight of steel used in the column with a tube thickness of 8 mm is 1.09 and 1.2 times more than the weight of steel used in the column with a tube thickness of 6 mm and 4 mm, respectively. Also, the ductility of examined columns with the tube thickness of 8 mm under loading with $e = -120$ mm is 1.02 and 1.05 times that of the column with tube thickness of 6 mm and 4 mm, respectively (Table 2).

Table 2. Comparison of energy absorption

Feature	P_u (kN)	P_u (kN)	P_u (kN)	P_u (kN)	$\mu_{0.85}$	$\mu_{0.85}$	$\mu_{0.85}$	$\mu_{0.85}$
Eccentricity (mm)	$e = 60$	$e = -60$	$e = 120$	$e = -120$	$e = 60$	$e = -60$	$e = 120$	$e = -120$
$t = 4$ mm	1088	1193	1635	748	3.18	5.3	6.04	8.4
$t = 6$ mm	1640	1718	2342	1123	3.42	5.59	6.48	8.6
$t = 8$ mm	2427	2420	2872	1610	3.65	6.48	6.95	8.8

3.1.2. Columns with Different Eccentricities

According to the outputs, it is clear that the best performance is for the specimen without eccentricity and the lowest height. Accordingly, in this sub-section, the effects of eccentricity are studied only on the short columns ($H = 2$ m). Figure 4 presents the load-displacement curves for a column with a height of 2 meters subjected to various levels of eccentricity.

The results demonstrate that eccentricity has a considerable effect on the column's load-bearing capacity. As eccentricity increases from 0 to 60 mm, the column's capacity drops by 95%, whereas increasing eccentricity from 0 to -60 mm leads to a 99% reduction in capacity. Furthermore, when eccentricity is increased to 120 mm and -120 mm, there is a 181% and 207% decrease in capacity, respectively. The column exhibits its poorest performance under the conditions of maximum height and the greatest negative eccentricity.

3.2. Performance of the Columns Based on the p/w Index

In this study, the numerical models

simulated in ABAQUS have five different eccentricities ($L = 0, 60, -60, 120, -120$ mm), three types of concrete resistance ($C = 15, 20, 40$ MPa), two types of steel tubes ($F = 250, 400$ MPa), three types of steel wall thickness ($t = 4, 6, 8$ mm), five types of height ($H = 2, 3, 4, 5, 6$ m). Moreover, there are three types of columns with the stiffeners at different intervals ($A = 20, 25, 35$ mm). Also, due to the fact that the distance between the stiffeners has no effect on the bearing capacity of the column, a distance of 25 mm has been applied in all the models.

According to the change of material and dimensions of each specimen, a total of 1100 models are evaluated. The load-to-weight ratio (p/w) is used to seek the best performance. In other words, the optimal column is the one that has the highest ratio of load-to-weight. To compare the overall performance of the columns, the specimens are divided into two types of short and long columns. Then, each of the short and long columns is examined separately, and the performance of each is studied according to the load-to-weight ratio.

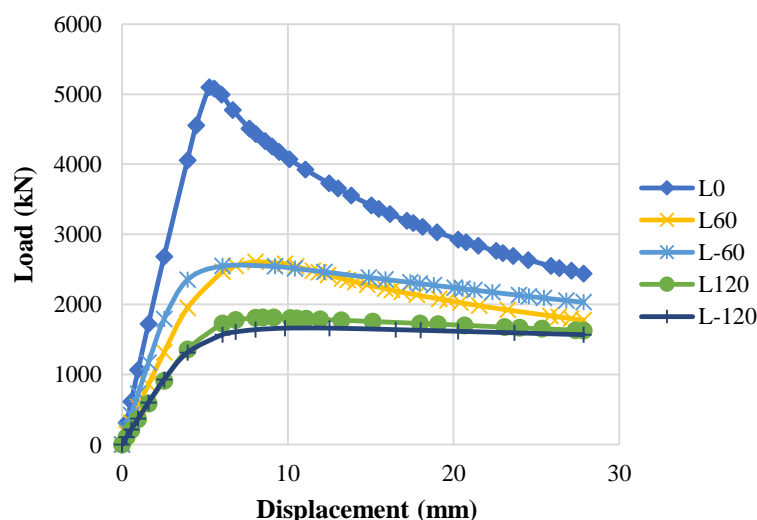


Fig. 4. Load-displacement curve of column ($H = 2$ m) with different eccentricities

In Table 3, the best and weakest performances of the considered columns are summarized. In the last column of Table 3, the failure behavior of each specimen is referred. In this regard, the behavior of the column in the state of failure is revealed in Figures 5 to 7. In each figure, three points “A”, “B”, and “C” are specified along with the von-Mises yield criterion. Point “A” is related to the yield stress of the column, point “B” is related to the maximum bearing capacity of the column, and point “C” represents the column's ductility. Also, P_u :

is the ultimate load, Δ_u : is the ultimate displacement, P_y : is the yield load, and Δ_y : is the yield displacement. It is worth noting that $\mu_{0.85}$: indicates the ductility of the column.

Based on the results, it is interesting that the specimen (column) with better performance based on the p/w index has less ductility than the specimen with lower performance. Also, the specimen with better performance based on the p/w index has the highest carrying capacity.

Table 3. Short columns with the best and weakest performance based on the p/w index

Performance	Height (m)	Wall thickness (mm)	Yield stress of steel (MPa)	Compressive strength of concrete (MPa)	Eccentricity (mm)	(p/w)	Behavior
best	2	8	400	40	0	1.34	Figure 11
weakest	4	4	250	15	-120	0.15	Figure 12

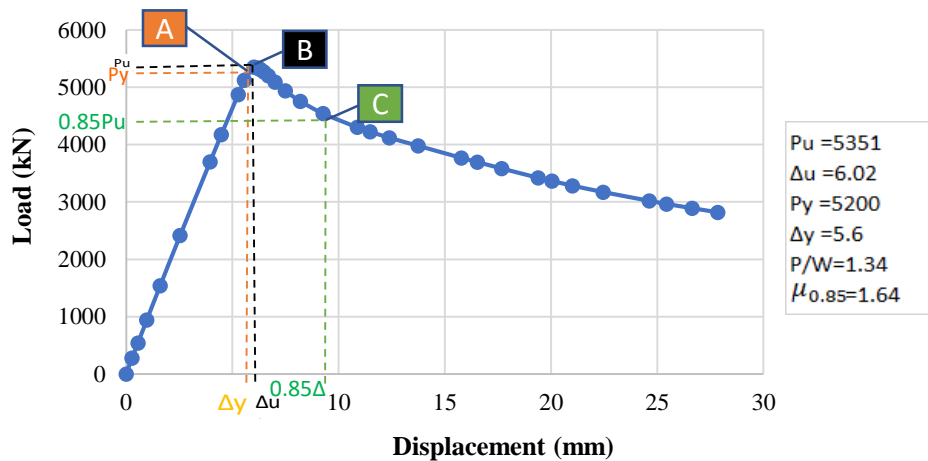


Fig. 5. Failure status of the best performance short column with $P/W = 1.34$

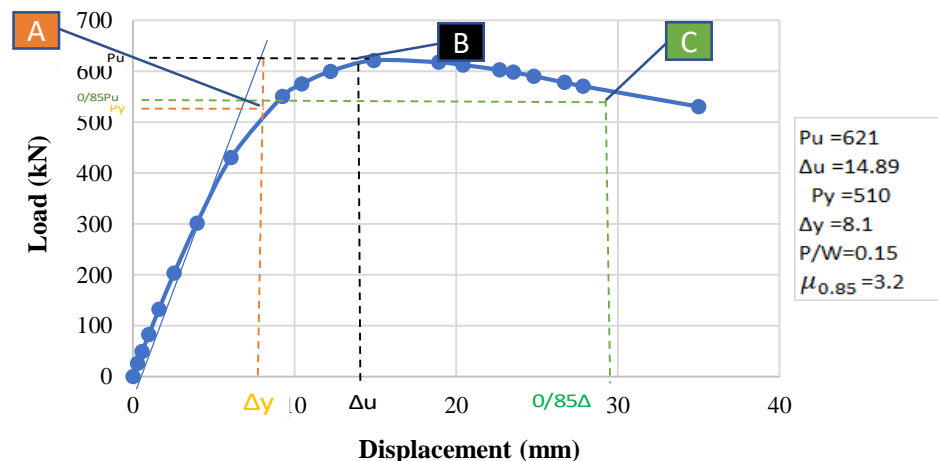


Fig. 6. Failure status of the weakest performance short column with $P/W = 0.15$

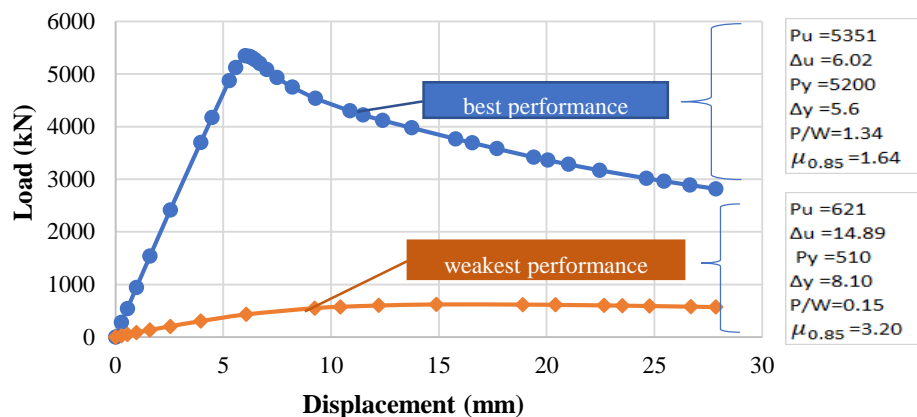


Fig. 7. Performance comparison between the strongest and weakest short columns

4. Conclusions

In this manuscript, the L-shaped CFST columns with different eccentricities were studied. Numerical modeling was done using ABAQUS software to evaluate these columns under the effect of axial and off-axis loading. The changes in the eccentric bearing capacity of the studied columns were analyzed and compared based on the strength of steel and concrete. Also, the optimal performance of the examined columns was assessed according to the p/w ratio (load-to-weight). The results of these analyzes were fully presented in the previous sections, and in this section, the most important results are briefly stated:

- Under the effect of eccentric loading, the columns with thicknesses of 4, 6, and 8 mm did not have a significant difference in term of ductility. The biggest difference (7%) was observed in the eccentricity of 120 mm.

- The energy absorption of the column with a tube thickness of 8 mm under loading with the eccentricity of -120 mm was 3.7 times more than the column with a tube thickness of 4 mm and 1.7 times more than the column with a tube thickness of 6 mm.

- In the comparison of the columns in terms of peak load under eccentric loading, the column with a tube thickness of 8 mm had 74% and 25% more capacity than the column with a tube thickness of 4 mm and the column with a tube thickness of 6 mm (on average), respectively.

- Among the different parameters, the

biggest impact on the eccentric bearing capacity of the columns was related to the thickness of the steel tube. Also, the least impact was related to the distance between connecting plate and the compressive strength of concrete.

- According to the acquired data, it is quite clear that the increase in height decreases the carrying capacity (i.e., reduction of p/w ratio). The important point is that by simultaneously increasing the height of the column and its weight, reducing the thickness of the steel tube can optimize the columns performance of the same rank (due to weight loss).

- For the column with a tube thickness of 8 mm, loading under $e = -120$ mm caused the greatest absorption of energy. For the column with a tube thickness of 6 mm, loading under $e = -60$ mm caused the greatest absorption of energy. For the column with a tube thickness of 4 mm, loading under $e = 60$ mm caused the greatest absorption of energy.

5. References

- ACI 318-11. (2011). *Building code requirements for structural concrete (ACI 318-11)*, American Concrete Institute, MI, USA.
- Chen, X., Zhou, T., Chen, Z., Liu, J. and Jiang, B. (2020). "Mechanical properties of special-shaped concrete-filled steel tube columns under eccentric compression", *Journal of Constructional Steel Research*, 167, 105779, <https://doi.org/10.1016/j.jcsr.2019.105779>.
- Chen, R.P., Ma, Q.L., Zhang, Y., Wu, H.N. (2021). "Experimental study on the mechanical behavior of eccentric compression short

- columns strengthened by ultra-high-performance fiber-reinforced concrete", *Structures*, 33, 508-522, <https://doi.org/10.1016/j.istruc.2021.04.078>.
- Chen, J., Li, J., Guo, M., Ding, F., Hu, H., Xiang, P. (2024). "Mechanical performances of thin-walled high-strength concrete-filled steel tube columns with high strength reinforced cages under biaxial eccentric compression", *Structures*, 61, 105976, <https://doi.org/10.1016/j.istruc.2024.105976>.
- Dancygier, A.N. and Berkover, E. (2016). "Cracking localization and reduced ductility in fiber-reinforced concrete beams with low reinforcement ratios", *Engineering Structures*, 111, 411-424, <https://doi.org/10.1016/j.engstruct.2015.11.046>.
- Dundar, C., Tokgoz, S., Tanrikulu, A.K. and Baran, T. (2008). "Behavior of reinforced and concrete-encased composite columns subjected to biaxial bending and axial load", *Building and Environment*, 43(6), 1109-1120, <https://doi.org/10.1016/j.buildenv.2007.02.010>.
- Ghandi, E., Mohammadi, R.N. and Esmaeili Niari, S. (2024). "Parametric analysis of axially loaded partially concrete-filled cold-formed elliptical columns subjected to lateral impact load", *Civil Engineering Infrastructures Journal*, 58(1), 49-70, <https://doi.org/10.22059/ceij.2024.364758.1955>.
- Hatzigeorgiou, G.D. and Beskos, D.E. (2005). "Minimum cost design of fibre-reinforced concrete-filled steel tubular columns", *Journal of Constructional Steel Research*, 61(2), 167-182, <https://doi.org/10.1016/j.jcsr.2004.06.003>.
- Labibzadeh, M., Hashemi Tabatabaei, S.M.J. and Ghafouri, H.R. (2018). "An efficient element free method for stress field assessment in 2D linear elastic cracked domains", *Computational and Applied Mathematics*, 37, 6719-6737, <https://doi.org/10.1007/s40314-018-0710-7>.
- Labibzadeh, M., Firouzi, A. and Ghafouri, H.R. (2017). "Structural performance evaluation of an aged structure using a modified plasticity model in inverse solution method", *Inverse Problems in Science and Engineering*, 26(9), 1326-1355, <https://doi.org/10.1080/17415977.2017.1400028>.
- Labibzadeh, M. and Hamidi, R. (2017). "Effect of stress path, size and shape on the optimum parameters of a brittle-ductile concrete model", *Engineering Structures and Technologies*, 9(4), 195-206, <https://doi.org/10.3846/2029882X.2017.1414636>.
- Liu, W.H., Bai, W.H., Guo, Y.L. and Wang, X. (2024a). "Design method of irregular-shaped concrete-filled steel tube column joints with inner semi-diaphragm", *Structures*, 60, 105883, <https://doi.org/10.1016/j.istruc.2024.105883>.
- Liu, W.H., Wang, X., Guo, Y.L., Tian, Z.H., Li, J.Y. Bai, W.H. (2024b). "Experimental and numerical study of L-shaped irregularly concrete-filled steel tube columns under axial compression and eccentric compression", *Journal of Building Engineering*, 84, 108572, <https://doi.org/10.1016/j.jobe.2024.108572>.
- Ma, W., Wang, P., Yan, Y., Liu, Z., Lu, Y. (2025). "Axially loaded square CFST columns strengthened with circular steel tubes and sandwiched concrete jackets", *Advances in Structural Engineering*, 28(16), 13694332251344661, <https://doi.org/10.1177/13694332251344661>.
- Tao, Z., Han, L.H. and Wang, D.Y. (2008). "Strength and ductility of stiffened thin-walled hollow steel structural stub columns filled with concrete", *Thin-Walled Structures*, 46(10), 1113-1128, <https://doi.org/10.1016/j.tws.2008.01.007>.
- Wang, L., Yang, X.J., Li, Z.Q., Yu, L.S., Zhou, X.F., Yin, P. (2024). "Investigation of interfacial bond strength of circular CFST columns based on ordinary and inorganic polymers through advanced machine learning method", *Structures*, 69, 107252, <https://doi.org/10.1016/j.istruc.2024.107252>.
- Yang, Y., Wang, G., Yang, W., Wei, X. and Frank-Chen, Y. (2022). "Experimental research on fire behavior of L-shaped CFST columns under axial compression", *Journal of Constructional Steel Research*, 198, 107505, <https://doi.org/10.1016/j.jcsr.2022.107505>.
- Zhang, W., Chen, Z. and Xiong, Q.Q. (2018). "Performance of l-shaped columns comprising concrete-filled steel tubes under axial compression", *Journal of Constructional Steel Research*, 145, 573-590, <https://doi.org/10.1016/j.jcsr.2018.03.007>.
- Zhi-hua, C., Bin, R. and Fafitis, A. (2009). "Axial compression stability of a crisscross section column composed of concrete-filled square steel tubes", *Journal of Mechanics of Materials and Structures*, 4(10), 1787-1799, <https://doi.org/10.2140/jomms.2009.4.1787>.
- Zhou, T., Yang, Z., Chen, Z. and Yu, Y. (2024). "Seismic behavior of connections between H-beams and L-shaped column composed of concrete-filled steel tube mono-columns connected by double vertical plates", *Journal of Constructional Steel Research*, 198, <https://doi.org/10.1016/j.jcsr.2022.107513>.



This article is an open-access article distributed under the terms and conditions of the Creative Commons Attribution (CC-BY) license.

Reviewers

The Editorial Board of the Civil Engineering Infrastructures Journal (CEIJ) would like to express sincere thanks to all reviewers of papers submitted to CEIJ during years 2024 and 2025 for their time and efforts in evaluating papers for this journal.

- Abdelkader, B.
University of Khemis Miliana
- Abdelraheem Farghaly, A.
Sohag University
- Abedinejad, S.
Alzahra University
- Adresi, M.
Shahid Rajaei Teacher Training University
- Aghabayk, K.
University of Tehran
- Aghayari, R.
Razi University
- Ahmadi, J.
Zanjan University
- Akbari, Z.
University of Tehran
- Alavi, S.M.Z.
University of Tehran
- Alielahi, H.
Islamic Azad University, Zanjan Branch
- Alshkane, Y. M.A.
University of Sulaimani
- Al-Zwainy, F.
Al-Nahrain University
- Amelsakhi, M.
Qom University of Technology
- Anand, N.
Karunya Institute of Technology and Sciences
- Apaza, F. R.
University Gustave Eiffel Nantes
- Arabani, M.
University of Guilan
- Arvin, M.R.
Fasa University
- Asadi, P.
Isfahan University of Technology
- Asakereh, A.
Semnan University
- Askari, F.
International Institute of Earthquake Engineering and Seismology
- Atmaca, N.
Gaziantep University
- Azhari, M.
Isfahan University of Technology (IUT)
- Badiei, P.
University of Tehran
- Barghi (Rezvani Sharif), M.
K.N. Toosi University of Technology
- Bazargan, J.
University of Zanjan
- Behnam, B.
Amirkabir University of Technology
- Behnam Far, F.
Isfahan University of Technology
- Bitaraf, M.
University of Tehran
- Brito, J.
ICIST Research Institute
- Cao, V.
Ho Chi Minh City University of Technology
- Cha, Y. J.
University of Manitoba
- Chen, Z.W.
Shenzhen University
- Chini, M.
Housing and Urban Development Research Centre
- Chowdhury, Sh. R.
Ahsanullah University of Science and Technology
- Dabiri, R.
Islamic Azad University, Tabriz Branch
- Deiranlou, M.
Bu-Ali Sina University
- Duarte, L.
University of Porto
- Ebead, U.
Qatar University
- Emami-Skardi, M. J.
University of Mazandaran
- Eskandari-Ghadi, M.
University of Tehran
- Eslamian, S.
Isfahan University of Technology
- Esmailpour, J.
University of Calgary
- Fadaee, M.J.
Shahid Bahonar University of Kerman
- Farahani, S.
Shahid Chamran University
- F. Irassar, E.
Universidad Nacional del Centro de la Provincia de Buenos Aires
- GhalandarZade, A.
University of Tehran
- Ghani, S.
Sharda University

Reviewers

- Gholampour, A. A.
Flinders University
- haghnazar, R.
Virginia Tech
- Hainin, M. R.
Universiti Teknologi Malaysia
- Haj Najafi, L.
Islamic Azad University
- Hesami, Z.
*Environment and Sustainable Development
Department of Tehran Municipality*
- Hong, Ch.
Zhejiang University
- Hoque, Md. I.
*Khulna University of Engineering and
Technology*
- Hoseini Vaez, S.R.
University of Qom
- Hosseini, S. M.
University of Tehran
- Hristova, T.
University of Mining and Geology
- Izadpanah, M.
Kermanshah University of Technology
- Jafari, M.
Babol Noshirvani University of Technology
- Jahed Armaghani, D.
University of Technology Sydney
- Jalali, M.
Shahrood University of Technology
- Janalizadeh Choobbasti, A.
Babol Noshirvani University of Technology
- Kalantary, F.
K. N. Toosi University of Technology
- Kamaruddin, H. K.
Universiti Teknologi MARA
- Kaminski, M.
Lodz University of Technology
- Kardan, N.
Shahid Madani University
- Kaushik, A.
University of Georgia
- Kavianpour, M. R.
K.N. Toosi University of Technology
- Kaźmierowski, M.
*Wrocław University of Environmental and Life
Sciences*
- Keshtegar, B.
University of Zabol
- Khabiri, M. M.
Yazd University
- Kijjanon, A.
Rambhai Barni Rajabhat University
- Kumar, Y.
National Institute of Technology Patna
- Kumar, P.
Mohan Babu University
- Lam, T. Q. K.
Mien Tay Construction University
- Li, L.
Victoria University
- Li, S.Q.
Heilongjiang University
- Madani, S.H.
Graduate University of Advanced Technology
- Mahdikhani, M.
Imam Khomeini International University
- Mahjuri, N.
K.N. Toosi University of Technology
- Maleki, M.
Bu-Ali Sina University
- Marchione, F.
Università Politecnica delle Marche
- Martínez-Barrera, G.
Autonomous University of the State of Mexico
- M. Dehcheshmeh, E.
Western University
- Memarzadeh, P.
Islamic Azad University,
- Moghadasi, M.
Bu-Ali Sina University
- Moghadas Nejad, F.
Amirkabir University of Technology
- Mohd Hashim, M. H.
Universiti Teknologi MARA
- Mohd Sani, M. S.
Universiti Teknologi Mara Pahang
- Mohd Yunus, N. Z.
Universiti Teknologi Malaysia
- Mokhtari, M.
Yazd University
- Momeni, E.
Lorestan University
- Navayi Neya, B.
Babol Noshirvani University of Technology
- Noormohammadi, N.
Isfahan University of Technology
- Nourani, M.
Islamic Azad University
- Odeyemi, S. O.
Kwara State University
- Ouhadi, V.R.
Bu-Ali Sina University
- Oulapour, M.
Shahid Chamran University
- Ozturk, B.
Hacettepe University
- Pacheco-Torgal, F.
University of Minho
- Paidoussis, M. P.
McGill University

- Pourakbar, Sh.
Universiti Putra Malaysia
- Pratap, B.
Graphic Era University
- Rabczuk, T.
Bauhaus University Weimar
- Rahami, H.
University of Tehran
- Rajabi Bhaabadi, M.
Yazd University
- Ramezaniapour, A.M.
University of Tehran
- Rashid Salimi, M.
University of Kurdistan
- Rasoolan, I.
Chamran University
- Saadeghvaziri, M.
New Jersey Institute of Technology
- Sadeghi, H.
Sharif University of Technology
- Sadrimoghaddam, Sh.
K.N. Toosi University of Technology
- Salahuddin, H.
*University of Engineering and Technology,
Taxila, Pakistan*
- Salehi Neyshabouri, S.A.A.
Tarbiat Modares University
- Salih Mohammed, A.
American University of Iraq
- Samerei, A. R.
University of Tehran
- Sartaj, M.
University of Ottawa
- Serjun, V.
*Slovenian National Building and Civil
Engineering Institute*
- Shao, R.
University of Technology Sydney
- Sharifi, R.
Shiraz University
- Sharma, V.
Government Engineering College, Rajkot
- Shishegaran, A.
IU International University of Applied Sciences
- Singh, S.
Srinath University
- Sobhani, J.
*Road, Housing & Urban Development Research
Center (BHRC)*
- Sohrabi, A.
University of Tehran
- Sreevalli, I. Y.
VIT University
- Taheriyoun, M.
Isfahan University of Technology
- Taherkhani, H.
University of Zanjan
- Tavakoli, H.R.
Babol Noshirvani University of Technology
- Thomas, S.
*International and Inter University Centre for
Nanoscience and Nanotechnology (IIUCNN)*
- Torabian, A.
University of Tehran
- Tornabene, F.
University of Salento
- Trépanier, M.
Polytechnique Montréal
- Uniyal, Kh.
Deemed to be University
- Wang, Sh.
Engineering Institute of Technology
- Yadav, J.
*National Institute of Technology Kurukshetra
India*
- Zakaria, Z.
University of Malta
- Zarrati, A.R.
Amirkabir University of Technology

AIMS AND SCOPE

Since the College of Engineering (Former Faculty of Engineering, FOE) of the University of Tehran has renewed its policy toward scientific publication, the Civil Engineering transaction of the well- built 45 years old Persian journal of "*Nashrieh Daneshkadeh Fanni*" is to be published in English and as separate independent journal with the name of ***Civil Engineering Infrastructures Journal***.

Civil Engineering Infrastructures Journal is an international journal which publishes high quality scientific papers in all areas of engineering and management of civil infrastructures. The civil infrastructures include, but are not limited to: buildings, bridges, dams, transportation systems, geotechnical structures, underground constructions, water distribution systems, offshore platforms, pipelines, ocean structures, airports and power plants.

The scope of this journal encompasses, but is not restricted to the following aspects of engineering and management of infrastructures:

- Mathematical modeling
- Computational and experimental methods
- Environmental Impact assessment
- Passive defense and security issues
- Monitoring and assessment
- Construction and design for durability
- Deterioration modeling and aging
- Failure analysis
- Field testing
- Financial planning
- Inspection and diagnostics
- Life-cycle analysis and prediction

- Maintenance, rehabilitation, repair and replacement strategies
- Non-destructive testing
- Optimization of maintenance and management
- Specifications and codes
- Reliability and risk management
- Supervisory Control and Data Assimilation (SCADA)
- Automation and Robotics in Construction
- Smart civil infrastructure Systems
- Sustainable civil infrastructure systems
- Case studies

Audiences of *Civil Engineering Infrastructures Journal* are researchers and practitioners as well as people working in infrastructure design, construction, maintenance and operation. Papers considered for publication must contain a clear and well-defined engineering component and make a significant contribution to the engineering and management of civil infrastructures. All articles submitted to this journal will undergo a rigorous peer review by anonymous independent experts.

Additional information can be obtained from:

Civil Engineering Infrastructures Journal

College of Engineering,

University of Tehran

P.O. Box: 11155- 4563

Tehran, Iran

Tel/ Fax: +98-21-88956097

Web Site: www.ceij.ir

Email: ceij@ut.ac.ir



University of Tehran
College of Engineering

Copyright Transfer Agreement

In order to protect the author(s), from the consequences of unauthorized use, the publisher requests that all author(s) sign the appropriate statement below:

The author(s) undersigned hereby approves submission of this work and all subsequent revisions for publication and transfers, assigns, or otherwise conveys copyright ownership to the Civil Engineering Infrastructures Journal (CEIJ). I (we) acknowledge that i) the submitted material represents original material, ii) does not infringe upon the copyright of any third party, and iii) that no part of the work has been published or under consideration for publication elsewhere unless and until it is rejected by Civil Engineering Infrastructures Journal (CEIJ). I (we) agree to indemnify the publisher against any loss or damages arising out of a breach of this agreement. In the event that my (our) submission is not published, copyright ownership shall revert to the author (s).

Manuscript Title:

Corresponding Author

Author:

Date:

Signature;

Author:

Date:

Signature:

Author:

Date:

Signature:

Author:

Date:

Signature:

Please submit the signed agreement with the final manuscript to:

Civil Engineering Infrastructures Journal (CEIJ)

School of Civil Engineering,

College of Engineering, University of Tehran

Enghelab Ave., P.O. Box: 11155-4563, Tehran, Iran.

Tel: 88956097

Fax: 66498981

E-mail: cej@ut.ac.ir

Website: www.cej.ir

CIVIL ENGINEERING INFRASTRUCTURES JOURNAL (CEIJ)

is indexed and abstracted in the bibliographical databases including:



Web of Science (ESCI)
<http://science.thomsonreuters.com>



Scopus
<https://www.scopus.com>



Islamic World Science Citation
Center;
<http://www.isc.gov.ir>



Directory of Open Access Journals
(DOAJ)
<https://doaj.org>



Google Scholar
<https://scholar.google.com>



General Impact Factor (GIF)
<http://generalimpactfactor.com>



Scientific Indexing Services (SIS)
<http://www.sindexs.org>



International Institute of
Organized Research (I2OR)
<http://www.i2or.com>



Information Matrix for the Analysis
of Journals (MAIR)
<http://miar.ub.edu>



ROAD: the Directory of Open
Access scholarly Resources
<http://road.issn.org>



Scientific World Index
<http://www.sciwindex.com>



International Innovative Journal
Impact Factor (IIJIF)
<http://www.ijif.com>



Science library index
<http://scinli.com>



Journal Factor
<http://www.journalfactor.org>



Open Academic Journals Index
(OAJI)
<http://oaji.net>



Electronic Journals Library (EZB)
<https://rzblx1.uni-regensburg.de>



Systematic Impact Factor
(SIF)
<http://www.sifactor.org>



COSMOS IMPACT FACTOR
<http://www.cosmosimpactfactor.com>

INDEX COPERNICUS
INTERNATIONAL
Polish Ministry of Science and
Higher Education (MSHE)
<https://journals.indexcopernicus.com>



Magiran
<http://www.magiran.com>



Scientific Information Database
(SID); Iran;
<http://www.Sid.ir>

Ministry of Science, Research and Technology of Iran has granted the Science and Research (Elmi-Pajouheshi) credit to CEIJ according to the letter No. 3/252445 at 25 Feb. 2012.

CONTENTS

Review Paper

The Utilization of Plastic Waste for Stabilizing Expansive Soil Subgrade: 203

A Critical Review

Kumar, M., Pratap, B., Azhar, M.D., Mondal, S. and Singh, R.P.

Research Papers

A Comparative Study on the Effect of Fineness of Low-Grade Calcined 231

Clays on Engineering Properties of Binary and Ternary Blended Concretes

Moodi, F., Fazelhashemi, A., GivKashi, M.R., Banar, R., Ramezaniapour, A.M. and Ramezaniapour, A.A.

Effects of Macro-Synthetic Fibres Incorporation on the Dimensional 253

Change Properties of Bacillus Subtilis Bacterial Concrete

Ghoniem, A.G., Aboul Nour, L. and Hassan, H.

The Free Vibration Characteristics of a Concrete Arch Gravity 265

Dam Using Finite Element Technique

Sougata, M. and Nallasivam, K.

Enhancing Cable-Stayed Bridge Structural Health Assessment 287

Using Phase Space Trajectory and Load Pattern Variability

Mohseni Moghaddam, M., Dehghani, E. and Bitaraf, M.

Impact of High-Strength Reinforcement on Ductility of 309

Normal-Strength Reinforced Concrete Column

Ulfa, A.A. and Piscesa, B.

Date Palm Fibers to Improve Tensile Strength in Self-Compacting 333

Concrete with Silica Fume

Mirzaie Aliabadi, M., Derakhshan Nezhad, A.H., Shahidzadeh, M.S. and Dadpour, A.

Lightweight Fiberglass Concrete Beams of Varying 351

Steel Reinforcement and Shear-Span Depth Ratios

Ghoniem, A., Gamal, M. and Aboul Nour, L.

Topology Optimization of Wave Barriers for Mitigating Dynamic 369

Compaction-Induced Vibrations Using a Coupled CMA-ES/Finite-Element Method

Abedini, F., Rafiee-Dehkharghani, R. and Laknejadi, K.

Predicting the Efficiency of Using Empty Fruit Bunch of Oil-Palm 391

Fibre in Reinforcing Structural Concrete: A Statistical Analysis

Kilani, A.J., Olubambi, A., Ikotun, B. D., Onjefu, L. and Abdulwahab, R.

Technical Notes

Permeable Triangular Vanes Effect on Turbulent Flow Field 419

Ahmadi Adli, S., Abbaspour, A., Hosseinzadeh Dalir, A. and Parsa, J.

Optimizing the Performance of L-Shaped Concrete-Filled Steel 429

Tube Columns Under Eccentric Loading

Labibzadeh, M., Kordi, M., Hosseini, F., Rezaeian, A. and Khayat, M.